

# Dissecting the Wholistic Impedance Profile of GPCR Signaling by Combining Functional Assays



## DISSERTATION

ZUR ERLANGUNG DES DOKTORGRADES DER  
NATURWISSENSCHAFTEN  
(DR. RER. NAT.) DER FAKULTÄT CHEMIE UND PHARMAZIE DER  
UNIVERSITÄT REGENSBURG

vorgelegt von **Saphia Sarah Azzam**

aus München

im Jahr **2024**



Diese Arbeit entstand im Zeitraum Januar 2020 bis März 2023 unter der Anleitung von Herrn Prof. Dr. Wegener am Institut für Analytische Chemie, Chemo- und Biosensorik der Fakultät für Chemie und Pharmazie der Universität Regensburg.

**Promotionsgesuch eingereicht am:** 21.08.2024

**Kolloquiumstermin:**

**Prüfungsausschuss:**

Vorsitzender: Apl. Prof. Dr. Thomas Hirsch

Erstgutachter: Prof. Dr. Joachim Wegener

Zweitgutachter: Prof. Dr. Max Keller

Drittgutachterin: Prof. Dr. Ursula Storch



This work was financially supported by the German Research Foundation (DFG) and the Research Training Group GRK1910 *Medicinal Chemistry of Selective GPCR Ligands*.





*Für meine Familie*



*“What we know is a drop, what we  
don’t know is an ocean.”*

Isaac Newton



# Danksagung

Zuallererst möchte ich mich bei **Prof. Dr. Joachim Wegener** für die Aufnahme in die Arbeitsgruppe, die nette Betreuung und das spannende und herausfordernde Promotionsthema innerhalb des Graduiertenkollegs GRK1910 bedanken. Danke für Deine guten Ratschläge und die Ungezwungenheit während unserer Gespräche, Joe.

Für die Übernahme des Zweitprüfers und der Drittprüferin möchte ich mich bei **Dr. Max Keller** und **Prof. Dr. Ursula Storch** bedanken. Danke, dass Sie sich die Zeit genommen haben meine Arbeit zu lesen und zu bewerten. Auch dem Prüfungsvorsitz **Dr. Thomas Hirsch** gebührt mein Dank.

A great thank you to associate professor **Dr. Nicholas Holliday** and his postdoc **Dr. Nicola Dijon** for supervising me during my stay abroad in Nottingham. I admire your GPCR knowledge and have learned a lot during my visit. You were always very patient and friendly and made my time in Notts very memorable.

Ein großes danke an **PD Dr. Max Keller** und **Dr. Carina Höring** für Eure Zelllinien, Substanzen und Gerätschaften, die ich mitbenutzen durfte. Danke für die gute Zusammenarbeit. Ohne Euch wäre diese Arbeit nicht möglich gewesen.

Danke an **Dr. Michael Skiba** für Deine großartige Vorarbeit, das Einlernen und die fachlichen Diskussionen.

Großer Dank gebührt **Dr. Daniel Lachmann**, **Dr. Timo Littmann**, **Dr. Lukas Grätz** und **Dr. Ulrike Wirth**. Danke für Eure Liganden, Lichtquellen, zellulären Systeme und die gute Zusammenarbeit.

Ein großes Danke an meine Masterandin **Julia Erl** und meine Bachelorandin **Annalena Bock** für Eure Unterstützung und Eure Beiträge zu meiner Arbeit.

Danke an alle Korrekturleser und Korrekturleserinnen. Thank you for revising my thesis. Special thanks to **Dr. Laura Humphrys**, **Dr. Nicola Dijon**, **Dr. Christian Kade** and **Julia Erl**.

Ein großes Danke an die gesamte **Arbeitsgruppe Wegener**: Julia, Steffi, Judith K., Judith St., Neha, Tobi, Anne, Max, Jannik, Sandra, Linda, Pierre, Lisa, Maria, Chrissi, Anja, Barbara, Nadja, Sarah, Nicole, Michi, Flo, Simone, Kuni, Susi, Rudi, Maren, Zlatko und Chris. Ihr habt die Zeit in der Gruppe für mich zu etwas Besonderem gemacht. Besonderer Dank gilt Julia – du bist mehr als eine Kollegin für mich <3 xoxo

Natürlich möchte ich mich auch bei meiner **Familie, meinen Freunden und meinem Freund Alex** bedanken. Ohne Euch gäbe es diese Arbeit nicht. Ihr seid immer für mich da und erinnert mich in schweren Zeiten daran, dass es sich lohnt nicht aufzugeben und dass ich gut bin wie ich bin. I love you <3







## Table of Contents

1	Introduction .....	1
1.1	G Protein-Coupled Receptors .....	1
1.1.1	Structure and Classification.....	1
1.1.2	Signal Transduction .....	4
1.1.3	Relevance of Minimal G Proteins .....	8
1.2	Assay Platforms to Study G Protein-Coupled Receptors .....	9
1.2.1	G Protein-Dependent Assays.....	11
1.2.2	G Protein-Independent Assays.....	12
1.2.3	Second Messenger Assays.....	13
1.2.4	Reporter Gene Assays.....	14
1.2.5	Dimerization Assays.....	14
1.2.6	Label-Free Assays .....	15
1.3	Assays Based on Nanoluciferase to Investigate G Protein-Coupled Receptors .....	16
1.3.1	Significance of Bioluminescence and Development of Nanoluciferase 16	
1.3.2	Nanoluciferase Binary Technology .....	18
1.4	G Protein-Coupled Receptors as Photopharmacological Targets.....	19
2	Objectives .....	22
3	Materials and Methods .....	24
3.1	Cell Culture Conditions.....	24
3.1.1	General.....	24
3.1.2	Cell Lines and Transfectants.....	24
3.1.3	Relevance of the G Protein-Coupled Receptors Under Study .....	28
3.1.4	Buffers and Solutions .....	31
3.1.5	Subcultivation.....	35
3.1.6	Cryopreservation and Recultivation.....	36
3.2	Molecular Biology.....	37

## Table of Contents

---

3.2.1	Generation of a SNAP-H2R-LgBiT Vector .....	37
3.2.2	Transformation of E. coli .....	40
3.2.3	Miniprep .....	41
3.2.4	Maxiprep .....	42
3.2.5	Transient Transfection .....	42
3.3	Preparation of Cell Culture Substrates .....	43
3.3.1	Substrate Types .....	43
3.3.2	Surface Coatings .....	45
3.4	Microscopy .....	46
3.4.1	Phase Contrast Microscopy .....	46
3.4.2	Stereomicroscopy .....	47
3.5	Impedance Spectroscopy .....	48
3.5.1	Theoretical Background .....	48
3.5.2	Electric Cell-Substrate Impedance Sensing .....	50
3.5.3	Workflow at the Impedance Measurement Devices .....	54
3.5.4	Impedance Data Analysis and Representation .....	60
3.6	Split Luciferase Complementation .....	64
3.6.1	Workflow at the Luminescence Measurement Devices .....	68
3.6.2	Luminescence Data Analysis and Representation .....	72
3.7	Calcium Second Messenger Assay .....	76
3.7.1	Workflow at the Flexstation 3 to Measure Agonist-Induced Calcium Mobilization by Fluorescence .....	77
3.7.2	Fluorescence Data Analysis and Representation .....	78
3.8	Setup for Simultaneous Measurements of Luminescence and Impedance	79
3.8.1	Workflow for Simultaneous Measurements of Luminescence and Impedance .....	82
3.8.2	Analysis and Representation of Simultaneously Recorded Luminescence and Impedance Data .....	83
4	Development and Optimization of a Setup for the Simultaneous Measurement of Luminescence and Impedance of One Cell Population .....	85

4.1	Characterization and Optimization of the Adherence of Human Embryonic Kidney and Chinese Hamster Ovary Cells with Impedance Spectroscopy .....	86
4.2	Characterization of Muscarinic and Histaminergic GPCR Responses with Impedance Spectroscopy .....	99
4.2.1	Impedance Profiles in the Absence of Coelenterazine h.....	100
4.2.2	Impedance Profiles in the Presence of Coelenterazine h .....	112
4.3	Characterization of Muscarinic and Histaminergic GPCR Responses with the MiniG Protein Recruitment Assay .....	116
4.4	Optimization of the Impedance Assay .....	127
4.4.1	Electrode Coatings.....	127
4.4.2	Coelenterazine h Aging.....	134
4.4.3	Cell Density.....	136
4.4.4	Measurement Buffer.....	143
4.5	Optimization of the MiniG Protein Recruitment Assay .....	149
4.5.1	Plate Coatings and Plate Color .....	149
4.5.2	Integration Time and Gain.....	158
4.5.3	Coelenterazine h Concentration.....	161
4.5.4	Different Cultivation Times .....	166
4.5.5	Additional Washing Step .....	171
4.5.6	Coelenterazine h Aging.....	175
4.5.7	Measurement Buffer.....	180
4.6	Combination of Impedance and MiniG Protein Recruitment Assay in One Experimental Setup .....	186
4.7	Summary and Outlook.....	216
5	Unraveling the Impedance Signal After GPCR Stimulation.....	225
5.1	Pathway-Specific Inhibitors and Activators .....	225
5.1.1	Imitation of the G <sub>s</sub> -Pathway and cAMP Signaling with Forskolin and 8-CPT-cAMP .....	226
5.1.2	Inhibition of the G <sub>s</sub> -Pathway with Cholera Toxin .....	229
5.1.3	Imitation of the G <sub>q</sub> -Pathway and Calcium Ion Signaling with Calcimycin	

## Table of Contents

---

5.2	Calcium Second Messenger Assay .....	236
5.3	$\beta$ -Arrestin2 Recruitment Assay .....	246
5.4	Summary and Outlook.....	260
6	Monitoring the Bioactivity of Photochromic Ligands Using Impedance Assays 265	
6.1	Characterization of Chinese Hamster Ovary Cells.....	266
6.2	Characterization of Photoswitchable Ligands with Impedance Spectroscopy 267	
6.3	Switching and Toggling of Photoswitchable Ligands .....	273
6.4	Insights Into the Switching Mechanism.....	281
6.5	Summary and Outlook.....	286
7	Summary.....	289
8	Zusammenfassung.....	291
9	References.....	294
	Appendix .....	323
9.1	Supplementary Figures .....	323
9.2	Abbreviations .....	353
9.3	Materials and Instrumentation .....	358
	Curriculum Vitae.....	361
	Eidesstattliche Erklärung.....	363





# 1 Introduction

## 1.1 G Protein-Coupled Receptors

Cellular receptors are capable of molecular recognition that initiates a biological response (Finlay et al., **2020**, Miller, Lappin, **2022**). Physiologically, the signal is generated by mechanosensory processes, photons or the binding of a ligand secreted by another cell, which, for instance, leads to an altered gene transcription and changes in the cell morphology. Depending on the location of the receptors they are classified as cell surface receptors (transmembrane receptors) or intracellular receptors. While transmembrane receptors include ligand-gated ion channels, enzyme-linked receptors and G protein-coupled receptors (GPCR), intracellular receptors, for instance, entail steroid hormone receptors.

Cell surface receptors are primarily activated by hydrophilic ligands or molecules that are too large to cross the plasma membrane. These receptors commonly consist of an extracellular binding domain, a membrane-spanning region and an intracellular domain essential for downstream signaling. GPCRs form the largest family of transmembrane receptors (Cong et al., **2017**, Fredriksson et al., **2003**). In the human genome, more than 800 GPCRs were identified, which corresponds to 4% of the human protein-coding genome (Fredriksson et al., **2003**, Takeda et al., **2002**). GPCRs transfer extracellular signals to heterotrimeric guanosine triphosphate binding proteins (G proteins) in the cell interior. The ligands for these receptors are diverse and, for instance, comprise odorants, peptides and hormones. Furthermore, GPCRs mediate a myriad of cellular responses and can either be activating or inhibiting. Since GPCRs are widely expressed in all tissues, they possess great physiological and pathophysiological relevance. Current medical and pharmacological research focuses on GPCRs as therapeutic drug targets because of their involvement in the regulation of sensory inputs like smell and taste but also in processes like neurotransmission, immune responses, cell metabolism, differentiation, proliferation and apoptosis (Cong et al., **2017**, Lefkowitz, **2013**, Wright, Bouvier, **2021**). More than a third of all authorized drugs target GPCRs, underlining their importance in drug discovery (Hauser et al., **2017**).

### 1.1.1 Structure and Classification

GPCRs consist of seven transmembrane (TM) domains, an extracellular N-terminus and an intracellular C-terminus. The ligand binding site (orthosteric binding site) is



Glutamate (G), Rhodopsin (R), Adhesion (A), Frizzled/Taste2 (F) and Secretin (S) family (short: GRAFS) (Schiöth, Fredriksson, **2005**). The main difference between both systems is that the former class B was subdivided into Secretin and Adhesion GPCRs. Furthermore, Taste2 receptors were added and the Rhodopsin family was divided into subgroups. Today, both systems are common practice. A short overview of the receptor classification is given in **Table 1**.

*Table 1. Overview of GPCR families, the corresponding number of human GPCRs, types of ligands and length of the N-termini (Congreve et al., **2020**, Isberg et al., **2014**, Lagerström, Schiöth, **2008**, Munk et al., **2016**).*

GPCR Family	Number (human)	Type of Ligand	Extended N-termini
Rhodopsin / class A	719	Amines, peptides, proteins, lipids, nucleotides, odorants, ...	No
Secretin / class B1	15	Peptides, proteins	No
Adhesion / class B2	33	Proteins, glycosaminoglycans	Yes
Glutamate / class C	22	Amino acids, cations, small organic compounds, carbohydrates	Yes
Frizzled / class F	11	Glycoproteins	Yes
Taste2 / class T	25	Small organic compounds	Yes
Other / class O	5	Unknown (orphan)	No

The Rhodopsin family is the largest class of GPCRs with 719 human receptors, corresponding to approximately 85% of all GPCRs. They are characterized by short N-termini in contrast to most other GPCR families and are activated by a myriad of different ligands. These include amines, peptides, proteins, lipids, nucleotides, odorants, chemokines, opioids and glycoproteins. Since the N-terminus is quite short, ligands bind to a cavity between TM3, TM5 and TM6. The only exception are glycoprotein receptors, which utilize the N-terminus as a ligand binding domain. In general, the orthosteric binding domain is highly conserved among class A GPCRs and constitutes a small, deep binding pocket. The Rhodopsin family is subdivided into four subgroups ( $\alpha$ ,  $\beta$ ,  $\gamma$  and  $\delta$ ) and 13 subbranches ascertained by phylogenetic investigations. Class A GPCRs are the most extensively studied receptor class since they are of great pharmacological importance; indeed, 94% of GPCR drugs target the Rhodopsin family (Cong et al., **2017**, **2017**, Lagerström, Schiöth, **2008**, Schiöth, Fredriksson, **2005**).

## 1.1.2 Signal Transduction

GPCRs transfer extracellular signals triggered by a ligand to an intracellular membrane-bound transducer protein. Depending on the ligand-receptor combination, certain transducer molecules are activated inside the cell. There are three main classes of proteins that transduce extracellular signals: G proteins, arrestins and GPCR kinases (GRK).

### 1.1.1.1 G Proteins

G proteins are heterotrimeric proteins consisting of three subunits ( $\alpha$ ,  $\beta$  and  $\gamma$ ). They transduce signals conveyed from a GPCR to effector proteins, triggering further downstream signaling. GPCRs are activated by binding of an extracellular ligand to the orthosteric binding site (**Figure 2**). In the case of class A GPCRs, it is usually found deep inside the transmembrane regions between helices 3, 5 and 6. The binding of the ligand leads to a conformational change within the GPCR: the cytoplasmic ends of TM5 and TM6 move outward and, therefore, create a G protein binding cavity (Gurevich, Gurevich, **2017**, **2019**). The membrane-bound heterotrimeric G protein binds to the GPCR, forming a ternary complex. Once bound, a conformational change takes place within the G protein by segregating the Ras-like domain and helical domain 5 of the  $\alpha$ -subunit, enabling an exchange of bound guanosine diphosphate (GDP) with guanosine triphosphate (GTP) (Gurevich, Gurevich, **2017**, Voss, Müller, **2022**). As a result, the heterotrimer dissociates into the  $\alpha$ -subunit and a  $\beta/\gamma$ -dimer. Both activate further downstream signaling. Since the  $\alpha$ -subunit possesses intrinsic GTPase activity, GTP is hydrolyzed to GDP followed by reconstitution of the  $\alpha$ - and  $\beta/\gamma$ -subunits.

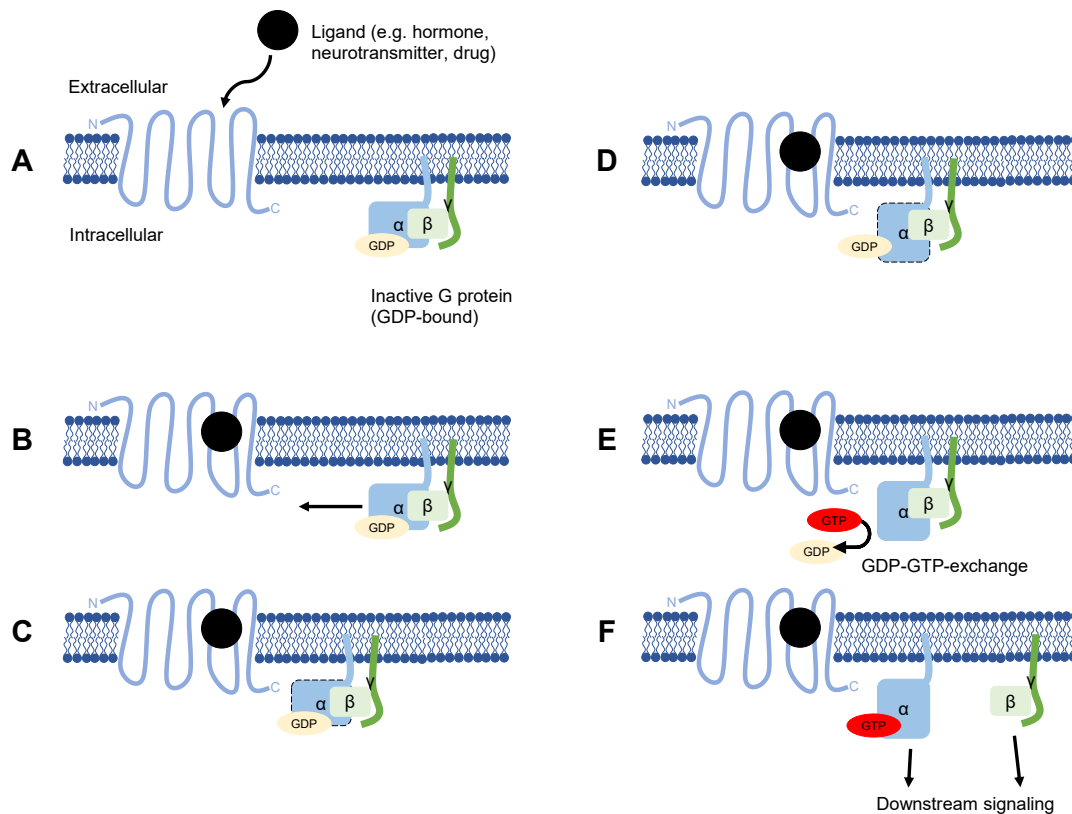


*Figure 2. GPCR signaling via guanine nucleotide-binding proteins (G proteins). Ligand approaching the GPCR (A). When the ligand binds to the receptor's orthosteric binding site (B), a conformational change takes place within the GPCR, enabling binding of the G protein (C). In turn, a conformational change takes place within the  $\alpha$ -subunit of the G protein (D) leading to a GDP-GTP exchange (E) and dissociation into the  $\alpha$ -subunit and the  $\beta/\gamma$ -dimer (F). Both G protein parts trigger further downstream signals.*

GPCRs mainly interact with the  $\alpha$ -subunit of the G protein. The  $\alpha$ -helical domain ( $\alpha$ H) is one of the key factors for GPCR-G protein interaction. Furthermore, the  $\alpha$ -subunit is anchored to the membrane by an N-terminal helix ( $\alpha$ N) and consists of three linker or switch regions that change their conformation dependent on the bound nucleotide (Voss, Müller, **2022**). The human genome encodes for 16 different  $G\alpha$ -subunits, which are clustered into four groups according to sequence similarity:  $G\alpha_{q/11}$ ,  $G\alpha_s$ ,  $G\alpha_{i/o}$  and  $G\alpha_{12/13}$  (short:  $G_q$ ,  $G_s$ ,  $G_i$ ,  $G_{12/13}$ ). Each group provokes individual signaling cascades (**Figure 3**).  $G_q$  proteins stimulate the membrane-bound protein phospholipase C- $\beta$  (PLC- $\beta$ ) that hydrolyzes phosphatidylinositol phosphate ( $PIP_2$ ) into diacylglycerol (DAG) and inositol triphosphate ( $IP_3$ ). Once  $IP_3$  binds to  $IP_3$ -sensitive calcium channels ( $IP_3R$ ) in the membrane of the endoplasmic reticulum (ER), calcium ions are released into the cytosol. Elsewhere, DAG activates  $Ca^{2+}$  dependent protein kinase C (PKC), which phosphorylates many substrates and thereby impacts the further downstream signaling and alters gene transcription. The  $G_s$ - and  $G_i$ -pathways both regulate the activity of adenylate cyclases (AC). While  $G_s$  proteins stimulate ACs and lead to increased cyclic adenosine monophosphate (cAMP) concentrations,  $G_i$

proteins inhibit ACs, lowering cAMP levels. This modifies the activity of cAMP-dependent protein kinase A (PKA) and activated extracellular signal-regulated kinases 1 and 2 (ERK1/2) both modifying gene transcription processes further downstream. cAMP signaling is terminated by phosphodiesterases (PDE), which degrade cAMP to adenosine monophosphate (AMP) (Newton et al., 2016).  $G_{12/13}$  proteins strongly interact with RhoGTPase enhancing factors (RhoGEFs) and RhoGTPase activating proteins, leading to the activation of the monomeric GTPase RhoA. This triggers the activation of Rho kinase (ROCK), which further affects cellular junctions, cell contractility and the cytoskeleton (Chaudhary, Kim, 2021, Dorsam, Gutkind, 2007, Siehler, 2007). As well as the effects of the  $\alpha$ -subunits, the  $\beta/\gamma$ -subunit induces separate signaling processes and interacts with several effector proteins like phosphoinositide 3-kinase (PI3K), PLC- $\beta$ , ion channels and ACs (Dorsam, Gutkind, 2007, Tuteja, 2009).

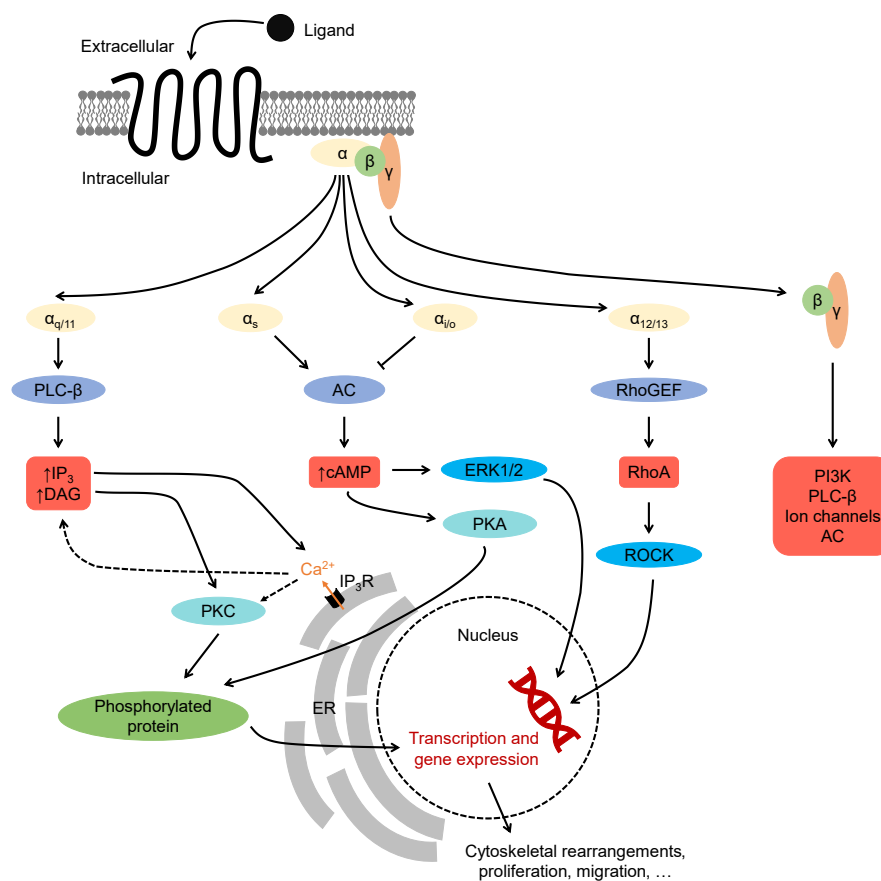


**Figure 3. GPCR signaling pathways.** After stimulation of the transmembrane receptor by a ligand approaching from the extracellular side, an intracellular mechanism is activated. The heterotrimeric G protein dissociates into the  $\alpha$ - and  $\beta/\gamma$ -subunit. Depending on the  $\alpha$ -subtype ( $G_{q/11}$ ,  $G_s$ ,  $G_{i/o}$ ,  $G_{12/13}$ ), different downstream processes are triggered. The  $\beta/\gamma$ -unit provokes independent signaling. PLC- $\beta$ : phospholipase C- $\beta$ , AC: adenylate cyclase, RhoGEF: RhoGTPase enhancing factor,  $IP_3$ : inositol triphosphate, DAG: diacylglycerol, cAMP: cyclic adenosine monophosphate, ERK1/2: extracellular signal-regulated kinases 1/2, PKA: protein kinase A, ROCK: Rho kinase, PI3K: phosphoinositide 3-kinase, PKC: protein kinase C,  $Ca^{2+}$ : calcium,  $IP_3R$ : inositol triphosphate receptor, ER: endoplasmic reticulum.

### 1.1.1.2 G Protein-Coupled Receptor Kinases and Arrestins

GRKs belong to the superfamily of AGC-kinases (named after protein kinases A, G and C). They are involved in numerous diseases and are one of three transducer molecules for GPCR signaling. In vertebrates, seven different GRKs are known. GRK1 and GRK7 are only expressed in cones and rods. The remaining GRKs (GRK2-GRK6) are ubiquitously expressed, apart from GRK4, which is only expressed in the testes, kidneys, brain and uterus. Generally, GRKs phosphorylate serine and threonine residues of GPCRs in the third intracellular loop (ICL3) and the C-terminus, which facilitates GPCR desensitization, i.e. uncoupling GPCRs from G protein signaling (cf. **chapter 1.1.1.1**). GRKs are not activated by phosphorylation but upon conformational changes. They consist of multiple domains with a central catalytic region, a C-terminal domain important for membrane targeting and an N-terminal domain homologous to regulators of GPCR signaling, which is essential for GPCR phosphorylation and stabilizing its active conformation (Gurevich, Gurevich, **2017, 2019**, Nogués et al., **2018**). In addition, GRKs phosphorylate various other proteins such as tyrosine kinases, transcription factors and cytoskeletal proteins. Therefore, they play a significant role in cell growth, death, motility, attachment, proliferation, immunity and pathophysiology. Furthermore, GRKs partly engage in  $G_q$ - and  $G_{\beta/\gamma}$ -signaling by protein-protein interactions (Gurevich, Gurevich, **2019**).

After GPCR phosphorylation, arrestins are recruited to the receptor. There are four types of arrestins present in the human body: two visual arrestins (arrestins 1 and 4) and two ubiquitously expressed arrestins (arrestins 2 and 3 or  $\beta$ -arrestin 1 and 2, respectively). Structurally, they comprise an N-terminal and an elongated C-terminal domain, connected by loops to form a sandwich-like architecture with seven antiparallel  $\beta$ -strands. Arrestins bind to phosphorylated GPCRs. Subsequently, a release of the C-terminal domain of the arrestins into the G protein binding cavity is observed. In contrast to G proteins, arrestins do not dissociate from the GPCR and, hence, block the binding cavity for G protein interactions. Therefore, arrestins are inevitable for desensitization mechanisms of GPCRs and facilitate internalization of the receptors, for instance, by the formation of clathrin-coated pits (Gurevich, Gurevich, **2017, 2019**).

Besides preventing G protein coupling to the receptors by blocking the interhelical binding cavity, arrestins and GRKs promote distinctive GPCR-dependent or GPCR-independent signaling. For instance, arrestins are involved in the activation of mitogen-activated protein kinases (MAPK, e.g. JNK3) and ERK1/2.

### 1.1.3 Relevance of Minimal G Proteins

To develop optimal drugs for GPCRs, it is essential to understand the structural changes upon ligand binding and GPCR activation. Active-state GPCRs were first crystallized with the help of G protein-derived peptides or nanobodies (antibody fragments derived from the variable domain of heavy chain-only camelid antibodies) (Carpenter, **2018**). However, both G protein mimetics had their issues: while the peptides only offer limited use because only certain receptor types are stabilized, nanobodies are difficult to prepare and do not imitate the GPCR-G protein interface well. Additionally, nanobodies must be generated individually for every GPCR, including an immunization and selection procedure that are both time-consuming and cost-intensive. Minimal G proteins (miniG, mG) overcome these problems and provide a retained coupling specificity and similar conformational changes compared to heterotrimeric G proteins (Carpenter, **2018**).

The first miniG protein  $mG_s$  was used for the structural resolution of the  $\beta 2AR$  in its active conformation (Carpenter, Tate, **2016**). In short, it is an engineered G protein mimetic only consisting of the GTPase domain of the  $\alpha$ -subunit since the GTPase domain is the main interaction partner between the G protein and GPCR (> 97% interaction) (Carpenter, Tate, **2016**). Apart from removing the  $\alpha H$  domain and replacing it with a short glycine linker, the  $\alpha N$  domain is deleted, removing the membrane anchorage. Furthermore, the link to the  $\beta/\gamma$ -dimer is cut, leading to a reduced mass of 30 kDa compared to the 90 kDa heterotrimer. Additionally, several point mutations were introduced to thermally stabilize the miniG protein, improve its expression level and prevent the GPCR-miniG-nucleotide complex from dissociation (Carpenter, **2018**, Wan et al., **2018**). Since  $mG_s$  proteins are limited to a certain number of GPCRs, the scope of miniG proteins was expanded. Inasmuch as the GPCR-G protein interface determines the coupling specificity, modifications and mutations within this region were implemented. Chimeric miniG proteins were developed by replacing the  $\alpha H$  domain to match the residues of other  $G_\alpha$  proteins (Nehmé et al., **2017**).

To date, miniG proteins are not only used to stabilize GPCRs in their active conformation to structurally elucidate binding modes with X-ray crystallography or cryo-EM, but they are also versatile and robust tools to study GPCR signaling behavior. For instance, Wan *et al.* demonstrated that the cytoplasmic miniG proteins are translocated to the plasma membrane after ligand binding by a bioluminescence resonance energy transfer (BRET) approach (Wan et al., **2018**). Additionally, they bind to active GPCRs in intracellular compartments like the Golgi apparatus, making

miniG proteins useful tools for detecting intracellular signaling events. Furthermore, they might pave the way for studying the determinants of GPCR coupling specificity and avail biased ligands to prevent adverse side effects of pharmaceuticals and drugs (Kroning, Wang, **2022**, Wan et al., **2018**).

## 1.2 Assay Platforms to Study G Protein-Coupled Receptors

Developing assays and biosensor platforms to characterize GPCRs and their signaling behavior is often challenging. Many signaling pathways undergo crosstalk downstream of the signaling cascade. Furthermore, the discovery of biased agonism (or functional selectivity) of certain ligands offers great opportunities in drug discovery to circumvent adverse side effects but is often overlooked since researchers mainly focus on a single signal transducer and might miss the response of another (Wright, Bouvier, **2021**). To date, GPCR assays are divided into binding studies and functional assays. While binding studies focus on characterizing ligands and their binding affinity, functional assays address the signal outcome and functional responses.

For a long time, binding assays were exclusively based on radiolabeled ligands (e.g.  $^3\text{H}$  or  $^{125}\text{I}$ ). However, they suffer from a lack of ligand availability and heterogenous, non-physiological readouts since membrane preparations and several filtration and washing steps are often necessary. Furthermore, the disposal of radioactive waste poses a challenge and involves high costs and safety risks. Besides these problems, it is not possible to classify whether the ligand is a full, partial, neutral or inverse agonist or antagonist because only the affinity of the ligand towards the GPCR is determined. Advanced methods of binding studies avoid radioactivity by utilizing fluorescence- or bioluminescence-based techniques. Instead of using radiolabels, the ligands and GPCRs are tagged with fluorophores or bioluminescent probes to enable resonance energy transfer (RET). This facilitates higher throughputs and minimizes the risk associated with the synthesis of radiolabeled probes and waste disposal. Moreover, measured association and dissociation kinetics as well as binding affinities are comparable to radio-based assays. The binding of labeled ligands can either be detected and visualized directly by fluorescence microscopy or identified with plate readers, allowing for time-resolved luminescence readouts with increased signal-to-noise ratios. Nonetheless, attaching fluorophores or bioluminescent molecules to ligands and receptors might lead to changes in the binding capacity because of steric hindrance and an increased total mass or volume, which should be kept in mind when designing such an assay platform. Still, fluorescence- and luminescence-based

techniques have outgrown radioactivity-based approaches (Sykes et al., **2019**, Zhang, Xie, **2012**).

Functional assays are subdivided into proximal and distal assays depending on the readout parameter. Proximal events take place at the beginning of the signaling cascade and are less prone to false-positive results. Distal processes are found downstream of the signaling cascade and often display larger signal-to-noise ratios because of signal enhancement. Ideally, a functional assay is simple to perform, robust, homogeneous, does not implement radioactive substances, is amendable to higher throughputs, can be automated and is conducted under physiological conditions in live cells without the need for any labels. Classical functional assays harness second messengers, gene reporters or promiscuous G proteins or  $G_{\alpha}$ -subunits with variable GPCR interactions and a distinct second messenger readout. However, neither of those assays is capable of distinguishing the intrinsically activated G proteins with certainty. Therefore, a shift towards the detection of specific protein-protein interactions by RET approaches or by protein fragment complementation assays (PCA) is necessary (Guo et al., **2022**). In the former case, a light-sensitive donor molecule (e.g. luciferase, fluorophore) transfers its energy to a light-sensitive acceptor molecule (e.g. fluorophore) with overlapping spectral properties if both are less than 10 nm apart. The energy transfer takes place by non-radiative dipole-dipole interactions making RET extremely sensitive to changes in the distance between donor and acceptor. Similar to RET, PCAs detect protein-protein interactions by labeling the two proteins of interest with a third protein (often enzyme or fluorescent protein, **Figure 4**). The latter is split into two fragments that ideally do not display any activity on their own and only possess low affinity towards one another. Once the split protein recombines, it either exhibits an enzymatic activity or fluorescence, indicating the interplay of the two proteins of interest.

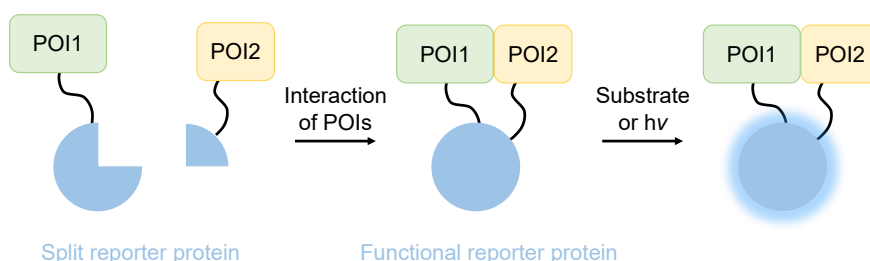


*Figure 4. Principle of a protein fragment complementation assay (PCA). Two proteins of interest (POI) are labeled with complementary fragments of an enzyme or a fluorescent protein (reporter). If the two POI interact, the reporter fragments combine and retrieve their functionality. In the case of an enzymatic reporter, a biochemical reaction is observed in the presence of its substrate. In the case of a fluorescent protein, fluorescence is observed if the protein is illuminated with the appropriate excitation wavelength.*

### 1.2.1 G Protein-Dependent Assays

G protein recruitment illustrates the most proximal functional response after GPCR activation. Formerly, it was detected by the accumulation of non-hydrolyzable  $^{35}\text{S}$ -GTP $\gamma$ S at the plasma membrane.  $^{35}\text{S}$ -GTP $\gamma$ S is a radiolabeled analog of GTP, which replaces GDP at the  $G_{\alpha}$ -subunit after G protein activation (Thomsen et al., **2005**, Zhang, Xie, **2012**). Since the assay has several drawbacks such as low signal-to-background ratios, a radiometric readout and restricted applicability (primarily  $G_{i/o}$ ), advancements toward fluorescence- and luminescence-based approaches and chimeric proteins have been required (Olsen, English, **2023**, Wright, Bouvier, **2021**, Zhou et al., **2021**).

Fusion or chimeric proteins are generated by joining two or more genes (coding for proteins with distinct functionality) in one expression vector. When the fusion gene is transcribed and translated, proteins with properties of both original genes are expressed. Chimeric G proteins with altered  $G_{\alpha}$ -coupling profiles are created by the replacement of the C-terminus of the original  $G_{\alpha}$  with a C-terminus of a different  $G_{\alpha}$  protein. One example is the  $G_{i/q}$  chimera: instead of measuring the inhibition of AC, the activation of PLC is measured by calcium mobilization. This method is highly adaptable and useful for elucidating the  $G_{\alpha}$ -coupling profiles of orphan GPCRs but does not directly measure the GPCR- $G_{\alpha}$  engagement (Olsen, English, **2023**, Wang et al., **2009**).

A more direct approach is recruitment-based biosensors to detect protein-protein interactions. Hereby, usually, the receptor and the G protein (also feasible for miniG proteins,  $\beta$ -arrestins or GRKs) are labeled with a RET system consisting of fluorophores and/or luciferases with overlapping spectral bands. If the GPCR and the G protein are adjacent to each other (< 10 nm apart), Förster or bioluminescence RET (FRET/BRET) is measurable indicating protein-protein interaction. Recent advances involve the sensor platforms: systematic protein affinity strength modulation (SPASM), G protein effector membrane translocation assays (GEMTA) and BRET biosensors with ER/K linker and yellow fluorescent protein (BERKY). SPASM utilizes a FRET acceptor-labeled GPCR with the fluorophore linked to the C-terminus of a FRET donor-labeled  $G_{\alpha}$ . After the association of the cognate  $G_{\alpha}$  to the receptor, FRET increases. GEMTA or enhanced bystander BRETs rely on markers in the plasma membrane and a second tag at the transducer or effector protein. If the latter is approaching the receptor and, thus, the plasma membrane, RET is observed. BERKY detects the formation of the GTP-bound form of  $G_{\alpha}$  or free  $G_{\beta\gamma}$ . Similar to GEMTA, BERKY sensors carry a membrane motif based on NanoLuciferase (NanoLuc, NLuc)

connected to yellow fluorescent protein (YFP) via a long linker. If  $G_{\alpha}$ -GTP is available close to the plasma membrane after GPCR activation, the linker bends and BRET is observed between NanoLuc and YFP. With these assays, it is not only possible to detect protein-protein interactions but also receptor trafficking to different cellular compartments like the Golgi apparatus. Assays like BERKY are also suitable for measurements of endogenous GPCRs (Olsen, English, **2023**, Wright, Bouvier, **2021**, Zhou et al., **2021**).

Lastly, there are also assays measuring the activation of the more physiologically relevant heterotrimeric G proteins. An example is the  $G_{\alpha\beta\gamma}$  (Gaby) sensor or more specifically the transducer pathway (TRUPATH) assay addressing the proximity change between  $G_{\alpha}$  and  $G_{\beta/\gamma}$  (Olsen et al., **2020**). Hereby, the  $G_{\alpha}$ -subunit is labeled with a luciferase and the  $\beta/\gamma$ -unit is tagged with a fluorophore, measuring changes in BRET once the G protein dissociates. The TRUPATH assay covers a spectrum of 14 different G protein pathways by 16  $G_{\alpha}$ -, 4  $G_{\beta}$ - and 12  $G_{\gamma}$ -subunits and uses optimized donor insertion sites at the  $G_{\alpha}$  protein. The principle is adaptable to FRET and enzyme complementation and can address the reassociation of a split G protein as well (Guo et al., **2022**, Olsen, English, **2023**, Wright, Bouvier, **2021**, Zhou et al., **2021**).

### 1.2.2 G Protein-Independent Assays

As discussed in **chapter 1.1.2**, following G protein recruitment, GPCRs are phosphorylated and bind arrestins. Then, GPCRs are internalized and either recycled back to the plasma membrane or degraded in the lysosome. Different assays are required to monitor receptor desensitization. Since  $\beta$ -arrestins are cytoplasmic proteins, translocation and receptor trafficking assays are often easier to perform than for G proteins, which suffer from high background signals because of their membrane anchorage (Guo et al., **2022**).

Early  $\beta$ -arrestin recruitment assays were designed by labeling  $\beta$ -arrestin with green fluorescent protein (GFP) and tagging the receptor with *Renilla* luciferase (RLuc), forming a BRET system. By now, many more donor-acceptor combinations are available. The enhanced bystander BRET for  $\beta$ -arrestins allows real-time measurements and detection of trafficking between the plasma membrane and endosomes. Besides BRET and FRET systems, the Tango assay is a common example of a protease-activated reporter gene assay detecting  $\beta$ -arrestin recruitment. Hereby,  $\beta$ -arrestin is tagged with a protease. The investigated GPCR carries a cleavage site for this protease connected to a transcription factor. When  $\beta$ -arrestin is recruited to the receptor and the transcription factor is cleaved off, gene transcription

is altered and can be monitored by reporter gene expression (Guo et al., **2022**, Zhou et al., **2021**).

Another example of the detection of  $\beta$ -arrestin engagement is PCAs. For instance, in the PathHunter assay, fragments of  $\beta$ -galactosidase are linked to  $\beta$ -arrestin and the GPCR. Promega's Nanoluciferase Binary Technology (NanoBIT) relies on the same principle but utilizes NanoLuc as an enzyme (cf. **chapter 1.3.2**). If both enzyme fragments complement and the respective substrate is present, a colorimetric, fluorometric or bioluminescent signal can be read (Guo et al., **2022**).

### 1.2.3 Second Messenger Assays

GPCR signals originate from ligands (first messengers) that bind to an extracellular receptor site. These signals are relayed via effector proteins to generate second messengers, which are normally the small molecules and ions calcium, cAMP, inositol phosphate (IP) and DAG. Second messengers translate extracellular signals into an intracellular response and usually interact with proteins and enzymes to alter their activity (Newton et al., **2016**).

Calcium and IPs are commonly investigated second messengers after PLC activation. Calcium assays usually utilize fluorescent dyes (e.g. fluo-3 or fluo-4) that bind calcium ions with high affinity. They are composed of a calcium-chelating backbone (e.g. BAPTA, EDTA, EGTA) and acetoxymethyl ester (AM) moieties, rendering the dyes membrane-permeable (Cobbold, Rink, **1987**, Gee et al., **2000**, Oheim et al., **2014**). Once the dye enters the cells, the AM groups are cleaved off by unspecific PDEs, trapping the dye in the cell interior. This allows for both the real-time detection of calcium mobilization in an automated high-throughput manner (plate reader) and visualization by fluorescence microscopy. Another method to detect calcium is photoproteins specifically binding to calcium ions. For instance, in the AequoScreen assay, a bioluminescent signal is created by the photoprotein aequorin in the presence of coelenterazine and calcium.

In IP assays,  $IP_1$  or inositol is detected since  $IP_3$  is very unstable and gets hydrolyzed easily by cellular phosphatases ( $IP_3 \rightarrow IP_2 \rightarrow IP_1 \rightarrow$  inositol). Detection of  $IP_1$  is possible if its degradation towards inositol is inhibited by the addition of lithium ions.  $IP_1$  accumulates and can be detected by time-resolved FRET between labeled anti- $IP_1$  antibody and  $IP_1$  with the IP-One technology. Other approaches quantify inositol phosphates by IP accumulation using tritium-labeled IP ( $^3H$ -IP) or fluorescently labeled IP (Siehler, **2008**, Zhang, Xie, **2012**).

cAMP accumulation in  $G_s$ -coupled systems is regularly measured after the addition of PDE inhibitors (e.g. 3-isobutyl-1-methylxanthine, IBMX) to prevent cAMP hydrolysis. cAMP levels are often quantified by immunodetection and the displacement of labeled cAMP by non-labeled cAMP. In the AlphaScreen and HitHunter assay, both the antibody and cAMP are labeled, e.g. by enzyme fragment complementation or a FRET/BRET pair. In the case of  $G_i$ -coupled systems, titration and prestimulation steps with the GPCR-independent AC activator forskolin are necessary to recognize an inhibitory effect on ACs (Siehl, **2008**, Zhang, Xie, **2012**).

#### 1.2.4 Reporter Gene Assays

Reporter genes are genes inserted and attached to a gene of interest by molecular biology techniques. The reporter gene DNA is composed of a promoter (gene of interest), where transcription factors bind to and regulate gene transcription, the reporter gene itself and a transcriptional stop signal. Reporter genes translate into measurable proteins like enzymes (e.g. luciferases) or fluorescent proteins (e.g. GFP) to indicate the regulation of the gene of interest. In GPCR research, promoters are often related to second messengers. For instance, the cAMP response elements (CRE), the nuclear factor of activated T-cells (NFAT) and the activator protein 1 (AP-1) are often utilized promoters to investigate  $G_s$ - and  $G_q$ -coupled receptors, respectively. Reporter gene assays are very distal to GPCR activation and, thus, can yield false-positive results from confounding factors upstream in cells. Nonetheless, they offer great sensitivity and signal-to-noise ratios, especially with luciferases (Hill et al., **2001**, Zhang, Xie, **2012**).

#### 1.2.5 Dimerization Assays

Many GPCRs form dimers or higher-order oligomers, which can alter GPCR signaling (Caniceiro et al., **2022**, Wouters et al., **2019**). In particular, class C GPCRs are known to generate heterodimers that are essential for their functionality. But also class A GPCRs are capable of homo- or heterodimerization. Receptor dimers are thought to be involved in many diseases, for example, schizophrenia, depression and neurodegenerative diseases (Caniceiro et al., **2022**, Wouters et al., **2019**). Therefore, several dimerization assays were developed to study the emergence, distribution and function of receptor dimers. Most assays are based on PCA where the GPCRs of interest are fused to complementary protein fragments of a fluorescent or bioluminescent protein. As soon as the GPCRs dimerize or oligomerize, the protein

label becomes fully active and can be detected by FRET, BRET and NanoBiT assays (cf. **chapter 1.3.2**) (Guo et al., **2022**, Wouters et al., **2019**, Zhang, Xie, **2012**, Zhou et al., **2021**). However, large receptor expression often leads to false-positive results as observed in a BRET study of the  $\beta$ 2AR homodimerization (Lan et al., **2015**).

### 1.2.6 Label-Free Assays

Traditional GPCR assays are mostly radio- or fluorescence-based and often interfere with the cellular system under investigation. Therefore, over the years the need for label-free techniques to measure physiologically relevant systems has increased, for example, to measure endogenous receptors or primary cells. Label-free assays usually capture an overall morphological cell response with intermediate- to high-throughput and do not engage with the system under investigation. They provide unbiased yet pathway-specific kinetic responses of live cells (Grundmann, **2017**, Lundstrom, **2017**). Two main assay formats for label-free investigations of GPCR signaling in living cells are available: (i) optical dynamic mass redistribution (DMR) biosensors and (ii) electrochemical impedance biosensors. DMR sensors include resonance waveguide grating (RWG) and surface plasmon resonance (SPR) (**Figure 5**).

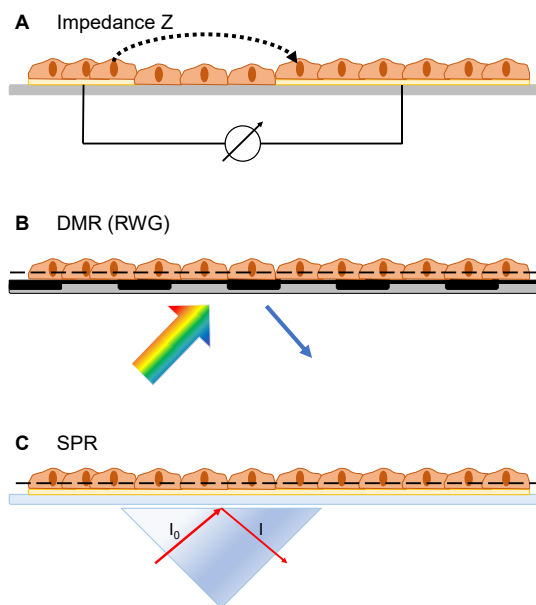


*Figure 5. Label-free assay techniques for the investigation of GPCRs. A: Electric cell-substrate impedance sensing (ECIS). Morphological changes are detected by applying an electrical field. B: Dynamic mass redistribution (DMR) on a resonance waveguide grating (RWG). After illumination of the waveguide structure with polychromatic light, an evanescent field (dashed line) is generated reaching 100-200 nm into the cells. Depending on refractive index changes at their basal side, the reflected wavelength changes. C: Surface plasmon resonance (SPR). Cells are grown on a gold-coated glass substrate, which is illuminated by a laser or LED. An evanescent field (dashed line) is created at the gold surface, reaching into the bottom of the cells and leading to the formation of surface plasmons. Refractive index changes are detected by alterations in the reflected light intensity or angle.*

In contrast to DMR, electrochemical impedance spectroscopy is not restricted to the basal side of the cells but is a holistic technique sensitive for cellular adherence, cell viability and morphological changes. Two gold film electrodes of different size (small working electrode, large counter electrode) are deposited on a culture substrate or microtiter plate. If cells are confluent grown on these electrodes and a small alternating current (AC) is applied, the current is forced to flow below, between or through the cells that behave as insulating particles. Consequently, impedance relies on an intact cell layer and strongly depends on the cells' morphology. Therefore, the electrode coverage, cell shape changes or modified barrier functions can be detected depending on the applied AC frequency. As impedance integrates over the entire cell layer, all cumulative responses are measured rather than one signaling event as in most label-based functional assays. This allows studying endogenous receptors because of the great sensitivity and distal character of impedance-based readouts. Nonetheless, this also implies that impedance spectroscopy is prone to false-positive or false-negative results and can not fully resolve underlying cellular mechanisms. For instance, mechanisms like  $G_s$ - and  $G_i$ -coupling that display converse outcomes might be overlooked when co-occurring, leading to false-negative results (Grundmann, 2017, Lieb et al., 2016b, Skiba et al., 2022, Zhang, Xie, 2012). To deconvolve the assay outcome, pathway inhibitors to selectively switch off a certain signaling cascade as well as additional functional assays are often used. Furthermore, bioengineering by mutational or genetic ablation of signaling proteins is a frequently used method but requires expertise in molecular biology and alters the cells' physiology (Grundmann, 2017).

## 1.3 Assays Based on Nanoluciferase to Investigate G Protein-Coupled Receptors

### 1.3.1 Significance of Bioluminescence and Development of Nanoluciferase

Light behaves as an electromagnetic wave and is divided into incandescence and luminescence. While incandescence describes *hot light*, which arises after heating material until it glows, luminescence is *cold light* emerging at lower temperatures (Murthy, Virk, 2013). The most utilized types of luminescence are photoluminescence, chemiluminescence and bioluminescence. In photoluminescence, molecules are excited by photons to either create fluorescence or phosphorescence. Thereby, electrons are elevated to an excited electronic singlet or triplet state by the energy of

photons and eventually drop down to the electronic ground state while emitting light of a certain wavelength. Chemiluminescence and bioluminescence are the result of chemical or biochemical reactions, respectively (Murthy, Virk, **2013**). Bioluminescence is an often-observed phenomenon in nature. For instance, bioluminescence is necessary for some marine organisms to communicate, defend themselves and reproduce. There are also terrestrial organisms such as glow-worms, bacteria, beetles, fungi and fireflies that harness bioluminescence (Haddock et al., **2010**, Murthy, Virk, **2013**). The common principle of bioluminescence is the oxidation of a luciferin with oxygen catalyzed by a luciferase or photoprotein, which leads to a release of energy as visible light. Many luciferases and photoproteins depend on the presence of bivalent cations (e.g. calcium or magnesium) and adenosine triphosphate (ATP, **Table 2**). The presence of oxygen is required for luciferases but not for photoproteins (Haddock et al., **2010**, Krasitskaya et al., **2020**).

Table 2. Overview of luciferases with their abbreviations, organisms they originate from, substrates, cofactors and molecular weight.

Luciferase	Organism	Substrate	Cofactors	Molecular Weight / kDa
<b>FLuc</b>	<i>Photinus pyralis</i> Firefly	D-luciferin	ATP, Mg <sup>2+</sup>	61
<b>CBLuc</b>	<i>Pyrophorus plagiophthalmus</i> Click Beetle	D-luciferin	ATP, Mg <sup>2+</sup>	64
<b>RLuc</b>	<i>Renilla reinformis</i> Sea Pansy	Coelenterazine	-	36
<b>GLuc</b>	<i>Gaussia princeps</i> Copepod	Coelenterazine	-	20
<b>OLuc</b>	<i>Oplophorus gracilirostris</i> Deep-sea shrimp	Coelenterazine	-	19 (Full size: 106)
<b>NanoLuc / NLuc</b>	<i>Oplophorus gracilirostris</i> Deep-sea shrimp (engineered)	Coelenterazine Furimazine	-	19

Luciferases are widely used in genetic engineering for reporter gene studies and protein-protein interaction assays. In particular, firefly and *Renilla* luciferase (FLuc and RLuc) are often used in bioanalytical applications. Over the years, more luciferases, predominantly from marine organisms, were discovered, for example, luciferases from the copepod *Gaussia princeps* (GLuc) or the deep-sea shrimp *Oplophorus gracilirostris* (OLuc). They are usually smaller and much brighter than other luciferases and, hence, increase the assay sensitivity and reduce undesired interactions. Nonetheless, luminescence signals decay rapidly, some luciferins are

chemically unstable and high autoluminescence backgrounds can cause unwanted noise. To overcome these problems, the enzymatic 19 kDa subunit of OLuc (KAZ) was modified and mutated based on the investigations of Inouye *et al.* to generate a novel luciferase named Nanoluciferase (NanoLuc, NLuc) (Inouye *et al.*, **2000**). It exhibits exceptional brightness, improved physical and chemical properties and great compatibility with mammalian cells. Furthermore, the original luciferin coelenterazine was engineered to create a more stable and brighter luciferin called furimazine, which displays less background signal. By now, many differently substituted coelenterazine analogs outperform furimazine with respect to its bioluminescence intensity and stability (Coutant *et al.*, **2020**). NanoLuc in tandem with furimazine exhibits a glow-type luminescence with a half-life of  $> 2$  h and a 150-fold increased brightness compared to RLuc and FLuc (England *et al.*, **2016**, Hall *et al.*, **2012**). It is highly stable at elevated temperatures, over a wide pH range and in urea-containing and NaCl-rich media. NanoLuc is uniformly expressed in mammalian cells and remains stable over several hours since there are no posttranslational modifications. It has been used as a fusion reporter for monitoring cellular metabolism and protein trafficking in real-time and is a versatile tool to study protein-protein interactions, genetic regulation and cell signaling with the help of NanoBRET and NanoBiT assays (cf. **chapter 1.3.2**).

### 1.3.2 Nanoluciferase Binary Technology

NanoLuc is used as a split protein in the so-called NanoLuc Binary Technology (NanoBiT) (Dixon *et al.*, **2016**, Hall *et al.*, **2012**). It is a very sensitive and optimized assay to quantify protein-protein interactions and was refined in terms of fragment affinity, fragment size, expression levels and temperature stability of NanoLuc. The final NanoBiT assay consists of an 11 amino acid (1.3 kDa) fragment called Small BiT (SmBiT) and a larger 18 kDa fragment called Large BiT (LgBiT) that weakly associate ( $K_D = 190 \mu\text{M}$ ) even at high expression levels (Dixon *et al.*, **2016**). There are also medium- and high-affinity variants discerned by variations of the small NanoLuc fragment. When the native peptide, which is the 13 amino acid precursor of SmBiT, is used,  $K_D$  lies at  $1 \mu\text{M}$ . The high-affinity 11 amino acid fragment of NanoLuc is called High BiT (HiBiT) and displays a  $K_D$  of  $1 \text{ nM}$ . In GPCR research, SmBiT is usually linked to the C-terminus of the GPCR and LgBiT is bound to the G protein or  $\beta$ -arrestin transducer protein to study GPCR activation or desensitization without biased interferences (Guo *et al.*, **2022**). However, it is also feasible to tag the receptor's C-terminus with LgBiT and the transducer protein with SmBiT (Martins, Prazeres, **2021**). Besides GPCR activation, the NanoBiT assay can also be used to study protein

dimerization, protein trafficking, posttranslational modifications and protein expression (Krasitskaya et al., **2020**).

## 1.4 G Protein-Coupled Receptors as Photopharmacological Targets

*Optogenetics* is a technique to express light-sensitive proteins (e.g. receptors) in neurons and other cell types to optically control their activity (Duebel et al., **2015**). Similarly, *photopharmacology* regulates the activity of certain proteins such as enzymes, ion channels and GPCRs by utilizing photosensitive molecules. Unlike optogenetics, photopharmacology does not rely on the genetic engineering of light-sensitive receptors but rather on soluble light-addressable molecules added to the system under investigation. This allows for better spatial and temporal control of drug therapy and minimizes side effects (Duebel et al., **2015**, Ricart-Ortega et al., **2019**, Wijtmans et al., **2022**). Photopharmacology is divided into two subgroups: *photocaging* and *photoswitching*. Photocaging incorporates the illumination of a caged, inactive ligand that is uncaged and activated by light. Usually, this reaction is irreversible since the ligand is cleaved off. Photoswitching also makes use of the change in the shape of the ligand upon illumination. However, it is based on the isomerization of the photoswitchable or photochromic ligand, allowing reversible reactions with better temporal control. The most utilized photoswitchable moiety is the azobenzene group. Azobenzenes have the advantage that they are very stable, easy to synthesize and allow reversible *cis/trans*-transitions. By attaching a pharmacophore to the photoswitch moiety, a photopharmacologically active, light-sensitive substance is generated. Besides azobenzenes, there are also other photoswitchable moieties such as heteroaryl azo groups, fulgimides and dithienylethenes (**Figure 6**). The latter two depend on a cyclization reaction between the *open* and *closed* isoform of the photoswitchable moiety. Most photoswitchable ligands are diffusible (non-tethered) but there are also some covalently bound (tethered) to the target of interest (Wijtmans et al., **2022**).

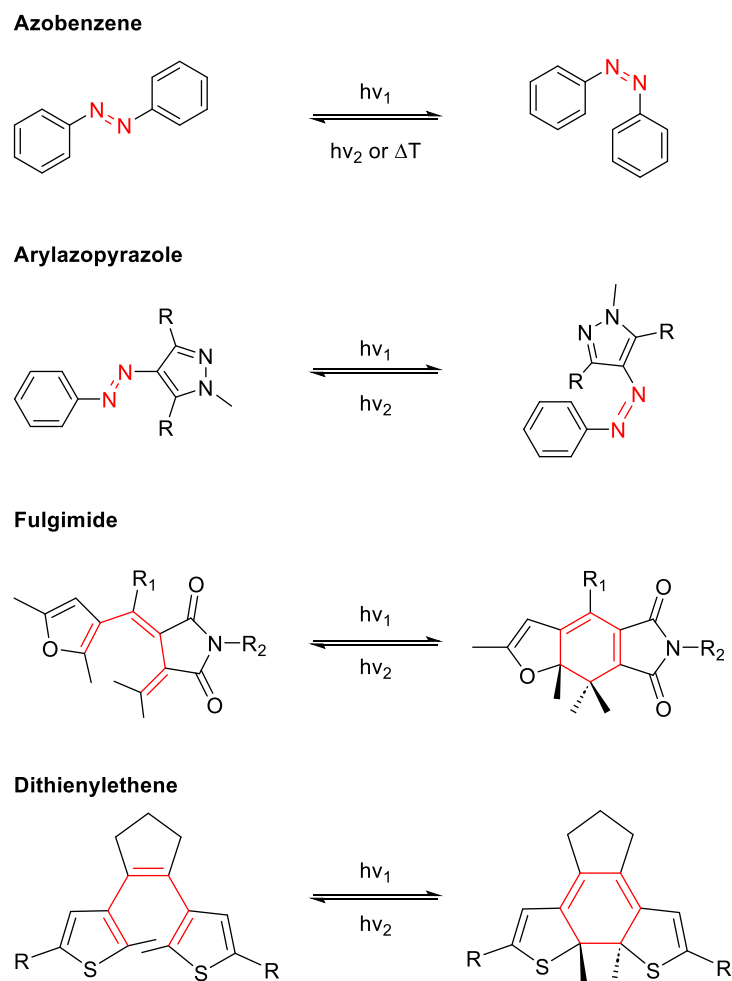


Figure 6. Common photoswitchable ligand moieties including azobenzenes, arylazopyrazoles, fulgimides and dithienylethenes. The first two are switched between *cis*- and *trans*-isoforms, while fulgimides and dithienylethenes are isomerized between open and closed isoforms.

Decorating GPCR ligands with photoswitchable moieties finetunes their bioactivity and regulates their signaling behavior in a spatiotemporal fashion. Class A GPCRs are the most addressed targets in photopharmacology research (Ricart-Ortega et al., **2019**). The photoswitchable ligands are optimized in terms of their absorption and switching wavelengths, their photostationary states (PSS), the switching efficiency and their thermal half-lives by customized substitution of the aryl rings. The PSS describes the ratio of both ligand isoforms in equilibrium after irradiation with one switching wavelength (Wijtmans et al., **2022**). Generally, it is desirable to reach high PSS for both ligand isoforms. Ideally, this gives rise to “switch on/switch off” systems allowing full control of the bioactivity.

To characterize photoswitchable ligands for GPCRs, binding and functional assays are performed to identify ligand affinity, conformational changes, second messenger release, gene regulation and protein-protein interactions (Wijtmans et al., **2022**). Many of those assays are based on non-dynamic endpoint measurements because

switching during the assay is often challenging. Particularly, optical readouts might interfere with the optical switching of the photoswitchable ligands and lead to unintended isomerization and inaccurate results. Since most photoswitchable ligands are switched in a broad range of wavelengths (e.g. azobenzenes: *cis* 350-400 nm, *trans* 400-550 nm), it is fundamental to work in the dark or under dark red light conditions during synthesis and assay performance to prevent undesired switching. Non-optical, label-free techniques like impedance spectroscopy offer an innovative strategy to hurdle these problems (Wirth et al., **2023**). Additionally, they allow real-time measurements and, thus, provide a more dynamic insight into cellular processes and switching.

## 2 Objectives

A major number of assays to investigate the physiologically highly relevant receptor class of G protein-coupled receptors (GPCR) relies on label-based endpoint measurements and focuses on one single readout parameter. But since GPCR signaling is extremely complex and most often includes cross talk downstream of the activated cascade, single time point and single parameter readouts are not representative and do not always mirror the system under investigation well. Many signaling processes might be missed or misinterpreted, especially if the readout time point is not optimized or if converse effects are induced. To approach these problems, in this work, integrative and label-free impedance measurements are used to temporally resolve GPCR stimulation and the subsequent activation of further downstream processes.

Since impedance detects all processes that induce morphological changes of the cells, it includes more information compared with a single molecular readout parameter such as the intracellular calcium concentration. Nonetheless, it is often problematic to explain where the impedance signal emanates from and what exactly evokes a decrease or increase in impedance. To gain a better understanding of the impedance response after GPCR stimulation, in the first project (i) electric cell-substrate impedance sensing (ECIS) shall be combined with the Nanoluciferase Binary Technology (NanoBiT), monitoring minimal G protein (miniG, mG) activation (**chapter 4**). While ECIS is a distal and holistic technique, the NanoBiT assay detects proximal miniG protein recruitment by a luminescence readout. A novel and elaborative setup for the simultaneous detection of impedance and luminescence of one individual cell population needs to be developed. This setup must be optimized in terms of the adhesiveness of the cells, the cell density, the proper handling of the luciferin and both signal intensities. Simultaneously recorded impedance and luminescence data shall be correlated to unravel molecular mechanisms that give rise to the recorded impedance response, in particular by comparing different readout time points. Additionally, the pharmacological characterization of the cell lines and ligands under study is compared between dual and individual measurement setups. To cover the signaling profiles of different G protein pathways, two  $G_q$ -coupled and one  $G_s$ -coupled human embryonic kidney (HEK) cell lines shall be investigated.

Another approach to elucidate the impedance response after GPCR stimulation is targeted in the second project (ii) (**chapter 5**): independent functional assays and pathway-specific inhibitors and activators shall be used to clarify the impedance signal of HEK cells expressing the muscarinic acetylcholine 1 receptor (M1R) and histamine

2 receptor (H2R) after stimulation with carbachol (M1R) and histamine (H2R). To deconvolve the underlying molecular mechanisms, calcium and  $\beta$ -arrestin2 assays shall be performed. Furthermore, pathway-specific activators and inhibitors will be applied.

Improved spatiotemporal control of GPCR activation can be achieved by the application of so-called photoswitchable ligands, consisting of a pharmacophore (pharmacologically active molecule) and a light-sensitive moiety that changes its conformation upon illumination. In project part (iii), two photoswitchable ligands for the neuropeptide Y4 receptor (Y4R) and the dopamine 2 receptor (D2R) expressed in Chinese hamster ovary (CHO) cells shall be assayed with impedance spectroscopy (**chapter 6**). Impedance is chosen as a measurement technique since it is a non-optical, label-free technique, not interfering with the switching of the ligands. First, both ligands shall be pharmacologically characterized to find optimal conditions for switching their bioactivity. Then, switching and toggling experiments shall be performed and the switching location shall be elucidated.

## 3 Materials and Methods

### 3.1 Cell Culture Conditions

#### 3.1.1 General

In order to maintain sterile conditions and prevent contamination of *in vitro* cell cultures with bacteria or fungi, the following precautions were taken. All cell culture operations were conducted under laminar flow in a biological safety cabinet. Unsterile solutions were either autoclaved or sterile-filtered (pore size: 0.2  $\mu\text{m}$ ). Before usage, all solutions were warmed up to 37°C in a water bath to sustain physiological conditions. The cells were cultivated in polystyrene flasks with a growth area of 25 cm<sup>2</sup> or 75 cm<sup>2</sup> and stored inside a humidified incubator with 5% (v/v) CO<sub>2</sub>. Subcultivation of the cells took place at 80-90% confluence (see **chapter 3.1.5**).

#### 3.1.2 Cell Lines and Transfectants

In this work, different transfectants of human embryonic kidney 293 (HEK) cells and Chinese hamster ovary (CHO) cells were used (**Table 3**). They either overexpress the native form or a mutant of a G protein-coupled receptor (GPCR). Their behavior was compared with wild type (wt) cells or a cell line exclusively expressing the GPCR without any tag (e.g. Nanoluciferase).

### 3 Materials and Methods

*Table 3. Overview of cell lines used in this work with their cellular origin, the vectors used for genetic engineering and their overexpressed receptor system. CHO = Chinese hamster ovary, HEK = human embryonic kidney. pcDNA = plasmid cloning DNA. ECL = extracellular loop. NLuc = Nanoluciferase. NanoBiT = Nanoluciferase Binary Technology. SmBiT and LgBiT = Small and large fragment of Nanoluciferase. miniGx = minimal G protein. \* = calcium phosphate precipitation was originally used for transfection (Hayes et al., 1992).*

Cell Line	Origin	Vectors	Overexpressed receptor system
CHO D2L	CHO K1	pAXhD2A*	Dopamine receptor 2, long splicing variant
CHO K1	Wild Type	-	-
CHO M1R	CHO K1	pcDNA3.1/M1R	Muscarinic acetylcholine receptor 1
CHO M5R	CHO K1	pcDNA3.1/M5R	Muscarinic acetylcholine receptor 5
CHO NPY	CHO K1	pcDNA3/Y4R pcDNA3.1/hygro-G <sub>q5</sub> pcDNA3.1/zeo-mtAEQ	Neuropeptide Y receptor 4
CHO NTS1R	CHO K1	pcDNA3.1/NTS1R	Neurotensin receptor 1
HEK293T	Wild Type	-	-
HEK293 H2R	HEK293	pIRESneo3/H2R	Histamine receptor 2
HEK293T LgBiT-miniG <sub>q</sub> /SmBiT-M1R	HEK293T	pIRESpuro3/LgBiT-mG <sub>q</sub> pcDNA3.1/SmBiT-M1R	Muscarinic acetylcholine receptor 1, NanoBiT
HEK293T LgBiT-miniG <sub>q</sub> /SmBiT-M5R	HEK293T	pIRESpuro3/LgBiT-mG <sub>q</sub> pcDNA3.1/SmBiT-M5R	Muscarinic acetylcholine receptor 5, NanoBiT
HEK293T LgBiT-miniG <sub>s</sub> /SmBiT-H2R	HEK293T	pIRESpuro3/LgBiT-mG <sub>s</sub> pcDNA3.1/SmBiT-H2R	Histamine receptor 2, NanoBiT
HEK293T NTS1R intraNLucT227	HEK293T	pcDNA3.1/NTS1R (intraNLucT227)	Neurotensin receptor 1, NLuc fused to ECL2 (Threonine 227)
HEK293T SmBiT β-Arrestin2	HEK293T	pcDNA3.1/SmBiT-β-arrestin2	SmBiT-labeled β-arrestin2

#### Chinese Hamster Ovary Cells

In 1957, Puck *et al.* first isolated euploid ovary cells from an adult Chinese hamster (CHO cells) with the aim of cultivating them on a long-term basis (Puck et al., 1958). The mammalian cell line was found to be very robust and showed a constant growth behavior over 10 months. The cells grow adherently in fibroblastic monolayers (Figure 7) and have a doubling time of approximately 24 h (Ham, 1965). In 1968, the CHO K1 subclone was derived from the original cell line by reducing the chromosomal number from 21 to 20 (Kao, Puck, 1968). In general, CHO cells are easily transfectable and, thus, an often-used model for molecular biology studies.

In this work, several transfectants of the wild type CHO K1 cells have been used (Table 3). CHO K1 cells were kindly provided by the group of Prof. Dr. Koch (University of Regensburg). CHO D2L cells expressing the long splicing variant of the dopamine 2 receptor (D2L) were kindly provided by Prof. Dr. John Shine (Garvan

Institute of Medical Research, Australia). In contrast to CHO D2S cells, the CHO D2L cell line expresses the dopamine 2 receptor with an insert of 29 amino acids in the intracellular loop 3 (ICL3), leading to an altered coupling profile generating second messengers like calcium and cyclic adenosine monophosphate (cAMP) (Hayes et al., 1992). CHO M1R and CHO M5R cells were kindly provided by the group of Prof. Dr. Koch (University of Regensburg). In this instance, pcDNA3.1/M1R (**Appendix 1**) or pcDNA3.1/M5R (**Appendix 2**) encoding for the human muscarinic acetylcholine receptors 1 or 5 (M1R or M5R) was stably transfected into CHO K1 cells (cDNA Resource Center, Bloomsberg, USA). The CHO NPY cells, expressing the human neuropeptide Y (NPY) receptor of type 4 (Y4R), were kindly provided by Prof. Dr. Buschauer and Dr. Ralf Ziemek (University of Regensburg). To obtain this cell line, CHO K1 cells were successively transfected with the vectors pcDNA3-hY<sub>4</sub> (**Appendix 3**), pcDNA3.1/hygro-G<sub>q15</sub> (**Appendix 4**) and pcDNA3.1/zeo-mtAEQ (**Appendix 5**) using the FuGENE6 reagent. This leads to an expression of the Y4R, the chimeric G protein G<sub>q15</sub> and mitochondrially targeted apoaequorin (Ziemek et al., 2007). CHO NTS1R cells expressing the Neurotensin 1 receptor (NTS1R) were kindly provided by Dr. Lukas Grätz (University of Regensburg). They were generated by stably transfecting CHO K1 cells with pcDNA3.1/NTS1R (**Appendix 6**) encoding for the NTS1R.

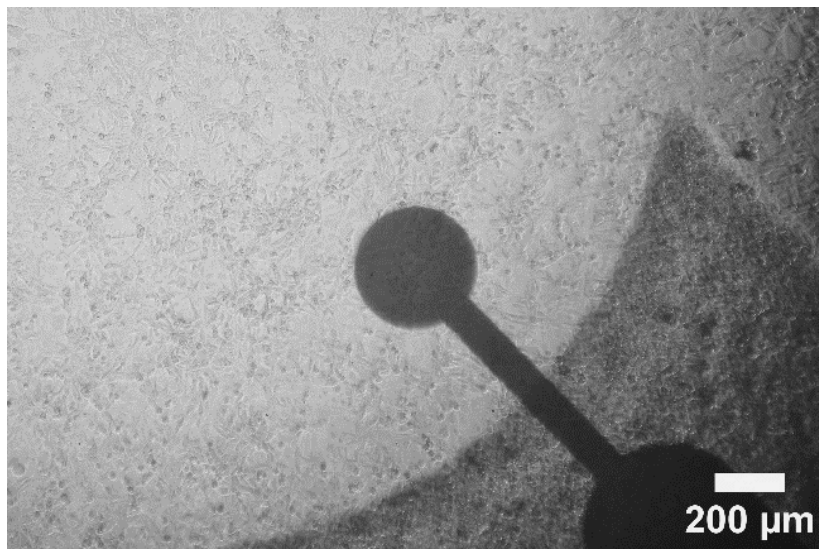


*Figure 7. Phase contrast micrograph of CHO K1 cells on a 96W1E+ electrode array. The image was taken with a 4x objective at the Nikon Diaphot microscope.*

### **Human Embryonic Kidney Cells**

In 1977, the first adenoviral transformation of a human cell line was accomplished. Primary human embryonic kidney (HEK) cells were transfected with adenovirus type 5 DNA. The obtained HEK293 cell line showed an epithelioid morphology (Graham et

al., 1977). Later on, HEK293T cells, a variant of HEK293 cells, carrying a plasmid containing a mutant of SV40 large T antigen, were derived from the original cell line (DuBridge et al., 1987, Lebkowski et al., 1985, Rio et al., 1985). HEK293T cells are highly transfectable and grow adherently with a fibroblastic to oval morphology (**Figure 8**). The doubling time amounts to 24-30 h (dsmz.de; **August 10, 2024**).

In this work, several transfectants of HEK cells have been used (**Table 3**). The wild type HEK293T cells were kindly provided by Prof. Gmeiner (University of Erlangen). HEK293T NTS1R intraNLucT227 cells carrying a Nanoluciferase (NanoLuc, NLuc, Promega Corporation) fused to the extracellular loop 2 (ECL2) at position threonine 227 (T227) of the NTS1R were kindly provided by Dr. Lukas Grätz (University of Regensburg). The cells were established by transfecting HEK293T cells with pcDNA3.1/NTS1R (intraNLucT227) (**Appendix 7**) encoding for the GPCR-luciferase system. HEK293 H2R cells expressing the human histamine 2 receptor (H2R) were kindly provided by Dr. Ulla Seibel-Ehlert (University of Regensburg). To obtain these, HEK293 cells were stably transfected with a pIRESneo3/H2R vector (**Appendix 8**) encoding for a Flag-tagged H2R. Nanoluciferase Binary Technology (NanoBiT, Promega Corporation) expressing HEK293T cells, carrying complementary NanoLuc fragments at the receptor and the corresponding “canonical” minimal G protein (miniG, mG), were kindly provided by Dr. Carina Höring (University of Regensburg). For the generation of those cell lines, HEK293T cells were stably transfected with pcDNA3.1/SmBiT-M1R (**Appendix 9**), pcDNA3.1/SmBiT-M5R (**Appendix 10**) or pcDNA3.1/SmBiT-H2R (**Appendix 11**) encoding for the GPCR of interest, which is C-terminally labeled with an 11 amino acid long fragment (1.3 kDa, small BiT, SmBiT) of NanoLuc. Additionally, the cells were transfected with a pRESpuro3/LgBiT-mG<sub>q</sub> (**Appendix 12**) or pRESpuro3/LgBiT-mG<sub>s</sub> (**Appendix 13**) vector leading to the expression of the respective miniG protein labeled with the complementary 18 kDa fragment of NanoLuc (large BiT, LgBiT). HEK293T SmBiT- $\beta$ -Arrestin2 cells, which stably express SmBiT fused to  $\beta$ -arrestin2 (**Appendix 14**), were kindly provided by Dr. Nicola Dijon (University of Nottingham, UK). In later experiments, these cells were transiently transfected with pcDNA3.1/SNAP-GPCR-LgBiT (cf. **Figure 13**) encoding for a C-terminally LgBiT-tagged receptor (see **chapter 3.2.5**,  $\beta$ 2AR, H2R, M1R).

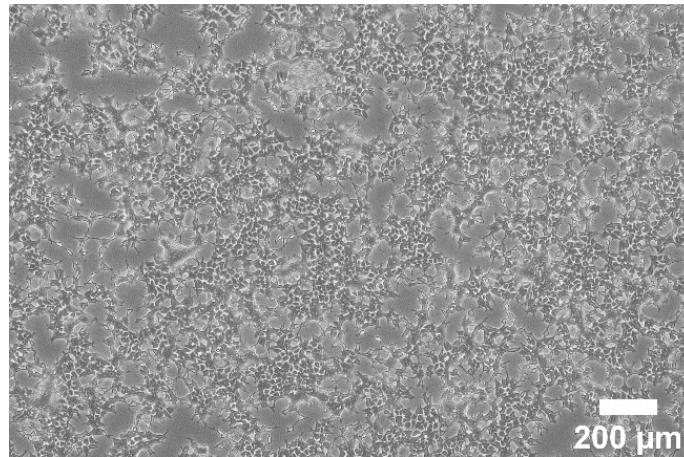


Figure 8. Phase contrast micrograph of HEK293T wild type cells on a cell culture flask. The image was taken with a 4x objective at the Nikon Diaphot microscope.

In the further course of this work, the names of the cell lines used will be abbreviated as listed in **Table 4**.

Table 4. Full name of HEK cell lines with their corresponding abbreviations used throughout this work. For a detailed explanation of the cell lines see **Table 3** and above.

Full name	Abbreviation
HEK293T (wild type)	HEK wt
HEK293 H2R	HEK H2R
HEK293T LgBiT-miniG <sub>q</sub> /SmBiT-M1R	HEK M1R/mG <sub>q</sub>
HEK293T LgBiT-miniG <sub>q</sub> /SmBiT-M5R	HEK M5R/mG <sub>q</sub>
HEK293T LgBiT-miniG <sub>s</sub> /SmBiT-H2R	HEK H2R/mG <sub>s</sub>
HEK293T NTS1R intraNLucT227	HEK NTS1R iL
HEK293T SmBiT $\beta$ -Arrestin2	HEK SmBiT $\beta$ -Arr.2
HEK293T SmBiT $\beta$ -Arrestin2 <i>transiently transfected with LgBiT-<math>\beta</math>2AR DNA</i>	HEK $\beta$ 2AR/ $\beta$ -Arr.2
HEK293T SmBiT $\beta$ -Arrestin2 <i>transiently transfected with LgBiT-H2R DNA</i>	HEK H2R/ $\beta$ -Arr.2
HEK293T SmBiT $\beta$ -Arrestin2 <i>transiently transfected with LgBiT-M1R DNA</i>	HEK M1R/ $\beta$ -Arr.2

### 3.1.3 Relevance of the G Protein-Coupled Receptors Under Study

In this work, the signaling of five different class A GPCRs was investigated (see **chapters 4, 5 and 6**). Their physiological relevance, their canonical coupling pathways as well as their individual ligands are summarized in the following. An overview is found in **Table 5**.

### **Dopamine 2 Receptor (D2R)**

Dopamine receptors are mainly expressed in the brain and are important drug targets for the treatment of neuropsychiatric disorders such as schizophrenia, Parkinson's disease, bipolar disorders and depression (Beaulieu et al., **2015**). They are also involved in the regulation of movements, sleep, olfaction, vision and cognitive functions. Dopamine, a neurotransmitter produced in the neuronal terminals, acts as endogenous ligand at all five dopamine receptor subtypes (D1R-D5R) (Martel, Gatti McArthur, **2020**). They are subdivided into two groups: the D1-like receptors, which contain the D1R and D5R, and the D2-like receptors, including the D2R, D3R and D4R (Seeman, van Tol, **1994**). While D1-like receptors mainly couple to G<sub>s</sub> proteins, the D2-like receptors canonically couple to G<sub>i</sub> proteins (Beaulieu et al., **2015**, Polit et al., **2020**). There are two splicing variants of the D2R: a short splicing variant D2S, which misses 29 amino acids in the ICL3, and a long splicing variant D2L. In this work, the D2L signaling was investigated by utilization of the photoswitchable ligand **1**, acting as a D2L receptor agonist (see **chapter 6**). Quinpirole, a D2R receptor agonist, was used as a positive control (Kostrzewa et al., **2018**).

### **Histamine 2 Receptor (H2R)**

The histamine 2 receptor (H2R) belongs to the group of histaminergic receptors (H1R-H4R) and was first discovered by Sir James Black in 1972 (Black et al., **1972**). It is highly expressed in gastric mucosa cells and different regions of the brain but also in many other cell types like smooth muscle cells, T and B lymphocytes as well as cardiac cells (O'Mahony et al., **2011**). In contrast to the other histaminergic receptor subtypes, the H2R is known to canonically couple G<sub>s</sub> proteins, leading to intracellular cAMP level increases and protein kinase A activation (Bongers et al., **2010**). In some cells, the H2R is also known for its G<sub>q</sub>-coupling, the involvement in ERK1/2 activation and pathways associated with tyrosine kinase receptors (Monczor, Fernandez, **2016**). Physiologically, the H2R is essential for gastric acid secretion, which is triggered by the endogenous ligand histamine (Fernández et al., **2017**). Therefore, many drugs acting at the H2R are designed for the treatment of gastric acid-related diseases, e.g. dyspepsia and gastric ulcers. The most famous drugs are cimetidine, famotidine and ranitidine, which behave as H2R antagonists and thereby reduce the activity of histamine. In this work, the agonist histamine and the antagonist cimetidine were investigated at the H2R (see **chapters 4 and 5**).

### **Muscarinic Acetylcholine Receptors 1 and 5 (M1R and M5R)**

The family of muscarinic acetylcholine receptors consists of five subtypes M1R-M5R. Their endogenous ligand is acetylcholine, a neurotransmitter released from presynaptic nerve terminals (Felder, **1995**, Haga, **2013**). The receptors are mainly expressed in the central nervous system (CNS) but also in peripheral tissue (Dwomoh et al., **2022**). In this work, the focus was set on the M1R and M5R. At the M1R, the agonists iperoxo, carbachol and acetylcholine and the subtype-selective antagonist pirenzepine were investigated (see **chapters 4 and 5**) (Calcutt et al., **2017**). At the M5R, the two agonistic ligands iperoxo and carbachol were assayed (see **chapter 4**). The M1R is primarily found in the forebrain where it is inevitable for glutamatergic neurotransmission, functions of the memory and learning behavior (Dwomoh et al., **2022**). It is also expressed in the vasculature, cardiomyocytes and the gastrointestinal tract. Here, it plays a role in the regulation of the blood pressure, K<sup>+</sup> channels and smooth muscle contraction. During receptor malfunction, neurodegenerative diseases or disorders such as schizophrenia, Alzheimer's or Parkinson's disease might develop, which makes the M1R a compelling drug target (Dwomoh et al., **2022**, Wong et al., **2023**). The M5R is only expressed in the CNS, predominantly in dopamine-containing neurons of the midbrain (Garrison et al., **2022**). It is the least studied muscarinic acetylcholine receptor subtype but is assumed to be involved in opioid use disorder (Dwomoh et al., **2022**, Garrison et al., **2022**). Therefore, future M5R drugs might help to manage and minimize drug addiction and misuse. Both the M1R and M5R are G<sub>q</sub>-coupled GPCRs, which stimulate phospholipase C and subsequent inositol triphosphate and Ca<sup>2+</sup> level increases (Felder, **1995**, Ishii, Kurachi, **2006**).

### **Neuropeptide Y4 Receptor (Y4R)**

Neuropeptide Y (NPY), peptide YY and pancreatic polypeptide (PP) are endogenous ligands for the family of neuropeptide Y receptors (Reichmann, Holzer, **2016**). Five of seven neuropeptide Y receptors are expressed in humans with the Y1R, Y2R, Y4R and Y5R being the best studied ones. While NPY exhibits a large affinity for Y1R, Y2R and Y5R, PP predominantly binds to the Y4R (Sánchez et al., **2023**). The four receptors as well as NPY itself are largely expressed in the CNS, including the brain and spinal cord, but also in the sympathetic nervous system (Brothers, Wahlestedt, **2010**). In this work, the signaling behavior of the Y4R was studied by utilizing the peptide-derived photoswitchable ligand **2** (see **chapter 6**). Human pancreatic polypeptide (hPP) served as a reference agonist. The Y4R is particularly expressed in the brain but is also localized in the gastrointestinal tract, pancreas and prostate (Li

et al., **2015**). It is assumed to be involved in the food intake behavior and energy metabolism (Zhu et al., **2023**). As with all other NPY receptors, the Y4R primarily couples to  $G_i$  proteins, leading to decreased intracellular cAMP concentrations (Brothers, Wahlestedt, **2010**, Czarnecka et al., **2019**).

*Table 5. Overview of GPCRs studied in this work including their expression, (physiological) relevance, canonical coupling pathway and the ligands used in this work. \* = antagonist. GIT = gastrointestinal tract. CNS = central nervous system.*

Receptor	Expression	Relevance	Canonical Pathway	Investigated Ligands
<b>D2R</b>	CNS	Movement, sleep, memory, cognition	$G_i$	Photoswitchable ligand <b>1</b> , quinpirole
<b>H2R</b>	Gastric mucosa, brain, smooth muscles, lymphocytes, heart	Gastric acid regulation	$G_s$	Histamine, cimetidine*
<b>M1R</b>	CNS, heart, vasculature, GIT	Regulation of $K^+$ channels, learning, memory	$G_q$	Iperoxo, carbachol, acetylcholine, pirenzepine*
<b>M5R</b>	CNS	Management of drug addiction and misuse (e.g. opioids)	$G_q$	Iperoxo, carbachol
<b>Y4R</b>	Brain, GIT, pancreas, prostate	Appetite, energy metabolism	$G_i$	Photoswitchable ligand <b>2</b> , human pancreatic polypeptide (hPP)

### 3.1.4 Buffers and Solutions

In this work, several buffers and media, either for subcultivation or experimental procedures, were used. In the case of long-term cultivation and measurements without optical readout, culture medium containing phenol red was used. For shorter experimental sequences, phenol red-free media like Leibovitz' 15 (L15), phosphate-buffered saline (PBS), Hank's balanced salt solution (HBSS) or HEPES-buffered saline (HBS) were used. In the following section, the medium and buffer compositions are summarized.

#### **Leibovitz' 15 (L15)**

L15 medium was developed in 1963 by Albert Leibovitz (Leibovitz, **1963**). His idea was to utilize free amino acids as buffer components instead of using a classical phosphate buffer. Besides amino acids, L15 contains inorganic salts, vitamins and

galactose. Since it does not contain any carbonate, it is commonly used at 0% (v/v) CO<sub>2</sub>. The pH value is reported to be in a range of 7.4-7.8 (sigmaaldrich.com #1; **August 10, 2024**). The buffer composition is given in **Table 6**.

#### **Dulbecco's Phosphate-Buffered Saline (DPBS, PBS)**

Dulbecco's PBS belongs to the balanced salt solutions, which were first developed in 1885 by Sydney Ringer. It is commonly used as a measurement buffer or for washing and diluting mammalian cells since its pH value is in the physiological range (pH 6.9-7.1) and it provides osmotic balance (sigmaaldrich.com #2; **August 10, 2024**). PBS is available with (PBS<sup>++</sup>) or without (PBS<sup>-</sup>) the bivalent cations calcium and magnesium. In general, PBS<sup>++</sup> is used if adherence to the substrate is crucial since calcium and magnesium ions act as so-called adhesion cofactors and by that are inevitable for cell-cell and cell-substrate contacts. In contrast, PBS<sup>-</sup> loosens cellular contacts and is often used as a washing buffer for subcultivation (see **chapter 3.1.5**). Since PBS does not contain any carbonate buffer system, it was routinely used at 0% (v/v) CO<sub>2</sub>. The buffer composition is given in **Table 6**.

#### **Hank's Balanced Salt Solution (HBSS)**

Like PBS, HBSS belongs to the balanced salt solutions developed after Sydney Ringer and Maurice Vejux Tyrode (sigmaaldrich.com #3; **August 10, 2024**). HBSS is a phosphate-buffered system, which contains inorganic salts and glucose. It provides a pH of 7.0-7.4 (sigmaaldrich.com #4; **August 10, 2024**) as well as an osmotic balance. It is commonly used at 0% (v/v) CO<sub>2</sub>. The buffer composition is given in **Table 6**.

#### **HEPES-Buffered Saline (HBS)**

4-(2-hydroxyethyl)-1-piperazineethanesulfonic acid (HEPES) was first synthesized and described in 1966 by Norman E. Good (Good et al., **1966**). It belongs to the so-called Good's buffers that overcome many problems of other buffer systems like poor buffer capacity, undesired reactivity or toxicity. By now, HBS is an often-used buffer system in biological research. It buffers pH values in a wide range between 6.8-8.2 (sigmaaldrich.com #5; **August 10, 2024**). Unlike the buffers outlined above, HBS was not purchased but prepared in the laboratory. It contains HEPES, a zwitterionic amino sulfonic acid (**Figure 9**), as well as inorganic salts, pyruvate and glucose. The buffer composition is given in **Table 6**.

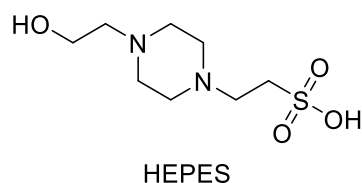


Figure 9. Structure of 4-(2-hydroxyethyl)-1-piperazineethanesulfonic acid also called HEPES. By deprotonation of the sulfonic acid and protonation of one amino group, it becomes zwitterionic.

In the following **Table 6**, the buffer compositions of L15, PBS<sup>++</sup>, HBSS and HBS are described in more detail.

Table 6. Composition of measurement buffers including amino acids, inorganic salts, HEPES, sodium pyruvate, sugars and vitamins. In L15 the following amino acids are contained: glycine, L-alanine, L-arginine, L-asparagine, L-cysteine, L-glutamine, L-histidine, L-isoleucine, L-leucine, L-lysine, L-methionine, L-phenylalanine, L-serine, L-threonine, L-tryptophan, L-tyrosine, L-valine. Furthermore, it contains the following vitamins: choline chloride, D-calcium pantothenate, folic acid, niacinamide, pyridoxine hydrochloride, sodium riboflavin 5'-phosphate, thiamine monophosphate, i-inositol.

Component	Concentration / mg·L <sup>-1</sup>			
	L15	PBS <sup>++</sup>	HBSS	HBS
<b>Amino acids</b>	Yes, see table heading	No	No	No
<b>CaCl<sub>2</sub></b>	140	133	185.4	144.3
<b>HEPES</b>	-	-	-	2384
<b>KCl</b>	400	200	400	373
<b>KH<sub>2</sub>PO<sub>4</sub></b>	60	200	60	-
<b>MgCl<sub>2</sub></b>	93.7	100	-	-
<b>MgSO<sub>4</sub></b>	97.67	-	200	246
<b>Na<sub>2</sub>HPO<sub>4</sub></b>	190	1150	90	-
<b>NaCl</b>	8000	8000	8000	8470
<b>NaHCO<sub>3</sub></b>	-	-	350	126
<b>Sodium Pyruvate</b>	550	-	-	220
<b>Sugar</b>	D-Galactose 900	No	D-Glucose 1000	D-Glucose 1800
<b>Vitamins</b>	Yes, see table heading	No	No	No

### Dulbecco's Modified Eagle Medium (DMEM)

Dulbecco's modified Eagle medium (DMEM) is a culture medium used for many adherent mammalian cell lines. It contains up to four times the amount of amino acids and vitamins compared to the original Eagle medium (sigmaaldrich.com #6; **August 10, 2024**). In this work, different DMEM formulations were used supplemented with

fetal bovine serum (FBS), L-glutamine (L-glu) as a carbon and nitrogen source and antibiotics (penicillin, streptomycin) as indicated in **Table 7**. High glucose concentrations are necessary because glucose serves as a carbon source and is essential for cellular growth. Since DMEM contains a carbonate buffer system, it was used at 5% (v/v) CO<sub>2</sub> for maintaining a physiological pH value.

### Ham's F12 Medium

Ham's nutrient mixture F12 was originally designed for the growth of CHO cells (Ham, McKeehan, **1979**). Historically it was used without protein supplementation but nowadays it is supplemented with serum depending on the cell line in use. In this work, Ham's F12 was used for most CHO cell lines as indicated in **Table 7**. FBS, L-glu and antibiotics (penicillin, streptomycin) were added to the basal medium to improve cellular growth and prevent microbial contaminations. The medium was used at 5% (v/v) CO<sub>2</sub> to maintain a constant physiological pH value.

For the cultivation of CHO D2L cells, a commercially available 1:1 mixture of DMEM and Ham's F12 was used as basal medium as shown in **Table 7**.

*Table 7. Composition of culture media of different HEK and CHO cell lines. The basal medium was supplemented with fetal bovine serum (FBS), L-glutamine (L-glu) and two antibiotics as indicated below. NaHCO<sub>3</sub> was added to the CHO D2L medium to maintain physiological pH values. All media and supplements were purchased from Sigma (order number for basal media given in brackets).*

Cell Line	Basal Medium	D-glucose / g·L <sup>-1</sup>	FBS / % (v/v)	L-glu / mM	Penicillin Streptomycin / µg·mL <sup>-1</sup>
CHO D2L	DMEM/F12 (D8062) + NaHCO <sub>3</sub> (0.5 mg/mL)	3.15	10	-	100
Other CHO cell lines	Ham's F12 (N4888)	1.802	10	2	100
HEK SmBiT β-Arr.2	DMEM (D6429)	4.5	10	-	-
Other HEK cell lines	DMEM (D5671)	4.5	10	2	100

### 3.1.5 Subcultivation

#### HEK Cells

HEK cells were subcultivated when reaching 80-90% confluency. For subcultivation, the cells were washed with 5 mL PBS<sup>-</sup> and were incubated with 1 mL 0.05% (w/v) trypsin-ethylenediaminetetraacetic acid (EDTA, 1 mM) in PBS<sup>-</sup> for 3-5 min. PBS<sup>-</sup> removes dead cells and serum residues. Trypsin belongs to the group of endopeptidases and hydrolyzes peptide bonds of basic amino acids. After detaching the cells, trypsinization was stopped by the addition of 5-6 mL culture medium per flask. The cell suspension was centrifuged at 100 g and room temperature (r.t.) for 10 min. Subsequently, the supernatant was aspirated and the cell pellet was resuspended in 3 mL culture medium per flask. The cells were seeded in a density of 1/10 or 1/20 relative to the original growth area onto new flasks. Selection antibiotics were added where necessary (**Table 8**). To determine the cell concentration, 10  $\mu$ L of the cell suspension were diluted in 80  $\mu$ L culture medium and the cells were manually counted with a hemocytometer. Then the cell suspension was diluted to reach the desired cell concentration and, subsequently, was seeded onto the respective substrates.

#### CHO Cells

CHO cells were subcultivated when a confluency of 80-90% was reached. For subcultivation, the cells were washed with 5 mL PBS<sup>-</sup> and were incubated with 1 mL 0.05% (w/v) trypsin-EDTA (1 mM) in PBS<sup>-</sup> for 5 min. After detachment of the cells, 5-6 mL culture medium per mL trypsin were added to stop trypsinization. The cells were centrifuged at 100 g and r.t. for 10 min before resuspension in 3 mL culture medium per flask. New flasks were seeded with a dilution of 1/10 relative to the original growth area in culture medium, containing selection antibiotics where necessary (**Table 8**). To determine the cell concentration, 30  $\mu$ L of the cell suspension were diluted in 60  $\mu$ L of medium and the cells were counted with a hemocytometer. Then, the cell concentration was adjusted to the desired value and the cells were seeded onto the different substrates.

Table 8. Selection antibiotics and respective concentrations added to HEK and CHO cells during routine cell culture.

Cell Line	Selection Antibiotics / $\mu\text{g}\cdot\text{mL}^{-1}$			
	Geneticin	Puromycin	Zeocin	Hygromycin B
CHO D2L				
CHO M1R				
CHO M5R	600	-	-	-
CHO NTS1R				
HEK H2R				
HEK NTS1R iL				
CHO NPY	400	-	250	400
HEK GPCR/mG <sub>x</sub>	600	1	-	-
HEK SmBIT $\beta$ -Arr.2	-	-	2.5	-

### 3.1.6 Cryopreservation and Recultivation

For cryopreservation, T75 flasks with a confluency of 80-90% were washed with PBS and trypsinized following the procedure described above (see **chapter 3.1.5**). After washing the cells in a centrifugation step, the cells were resuspended in FBS with 10% (v/v) dimethyl sulfoxide (DMSO). DMSO serves as a cryoprotectant as it prevents the formation of ice crystals and cell damage. Per cryo vial, 1.8 mL cell suspension, which corresponds to cells on one T25 flask, were frozen. The aliquots were slowly cooled down to  $-80^{\circ}\text{C}$  overnight with the help of a freezing container. Finally, the cryo vials were transferred to liquid nitrogen ( $-196^{\circ}\text{C}$ ) for long-term storage.

To recultivate cells, the desired cryo vial was carefully taken out of the liquid nitrogen tank and was slowly warmed up to  $-20^{\circ}\text{C}$  over a period of 1-2 h. Following this, the vial was slowly defrosted in a water bath at a temperature of  $37^{\circ}\text{C}$ . The complete cell suspension was transferred to a 50 mL tube and was slowly heated up to  $37^{\circ}\text{C}$  by dropwise addition of 5-10 mL preheated culture medium. Excess DMSO was diluted and osmolarity was slowly adjusted in this step. After centrifugation at 100 g and r.t. for 10 min, the supernatant was removed and the cells were carefully resuspended in 4 mL culture medium. Usually, cells were seeded in different densities in four T25 flasks (1x1/2, 1x1/4, 2x1/8). For very sensitive, weakly adhering cells, the complete cell suspension was used to seed one T25 or T75 flask. Cell culture medium was exchanged in regular intervals of 2-3 days. When 80-90% confluency was reached, the next subcultivation was conducted. From then on, selection antibiotics were added to the flasks (**Table 8**). Before performing first experiments, at least two subcultivation cycles using selection antibiotics were completed after revitalization.

## 3.2 Molecular Biology

### 3.2.1 Generation of a SNAP-H2R-LgBiT Vector

A HEK H2R/ $\beta$ -Arr.2 cell line was engineered by transient transfection of HEK SmBiT  $\beta$ -Arr.2 cells with DNA encoding the H2R labeled with the LgBiT fragment of NanoBiT. First, DNA encoding for the H2R, intracellularly labeled with LgBiT, was generated by modification of the pIRESneo3 H2R vector used for creating stably transfected HEK H2R cells (kindly provided by Dr. Seibel-Ehlert, University of Regensburg) (this chapter). Then, the obtained SNAP-H2R-LgBiT vector was transiently transfected into HEK SmBiT  $\beta$ -Arr.2 cells (kindly provided by Dr. Nicola Dijon, University of Nottingham, UK) to generate a split luciferase complementation system (**chapter 3.2.5**). This allows for the detection of  $\beta$ -arrestin2 recruitment at the H2R (Dixon et al., **2016**).

#### 3.2.1.1 Polymerase Chain Reaction and Creation of Linearized H2R DNA Insert

To generate an H2R insert with flanking BamHI and XhoI restriction enzyme sites, 1 ng of HEK H2R template DNA (**Appendix 8**), forward (GGATCCGGGATGGCACCCAATGGCACAGCCTCTTCCTTTT) and reverse (CTCGAGCCTGTCTGTGGCTCCCTGGGGGGCCGTGACTTCT) primers at 10  $\mu$ M each, 10  $\mu$ L of Q5 reaction buffer and 200  $\mu$ M deoxynucleotide triphosphates (dNTPs) were mixed. A Hot Start protocol (New England Biolabs) used an initial 2 min DNA denaturing step (94°C) and holding at 55°C, at which point Q5 High-Fidelity DNA polymerase was added. A negative control reaction was prepared without Q5 High-Fidelity DNA polymerase. The polymerase chain reaction (PCR) was continued with 25 cycles of denaturation (94°C, 2 min), annealing of the primers (55°C, 1 min) and the extension of DNA by the polymerase (72°C, 2 min) with a final elongation step of 7 min at 72°C. Following DpnI restriction enzyme treatment, loading dye (5-fold concentration) was added to each PCR mixture. Subsequently, the DNA was analyzed using gel electrophoresis (cf. **chapter 3.2.1.3**) and isolated and purified using a GenElute gel extraction kit (Sigma).

### 3.2.1.2 Ligation of Linearized H2R DNA Insert with pJET1.2/blunt Vector

The linearized H2R DNA (cf. **chapter 3.2.1.1**) was ligated with a commonly available pJET1.2/blunt vector (**Figure 10A and Appendix 15**). For this, 10  $\mu\text{L}$  of ligation buffer (2-fold concentration), 50 ng of the linearized H2R DNA, 1  $\mu\text{L}$  of the pJET1.2/blunt vector (50 ng/ $\mu\text{L}$ ), 1  $\mu\text{L}$  of T4 ligase and water (added to reach a total volume of 20  $\mu\text{L}$ ) were mixed and left at 16°C overnight. The ligation product was transformed into *E. coli* (**chapter 3.2.2**). A colony was picked and the DNA was purified by a GenElute Miniprep kit (Sigma, **chapter 3.2.3**). A pJET1.2/H2R vector with approximately 4000 base pairs (bps) was generated (**Figure 10B**).

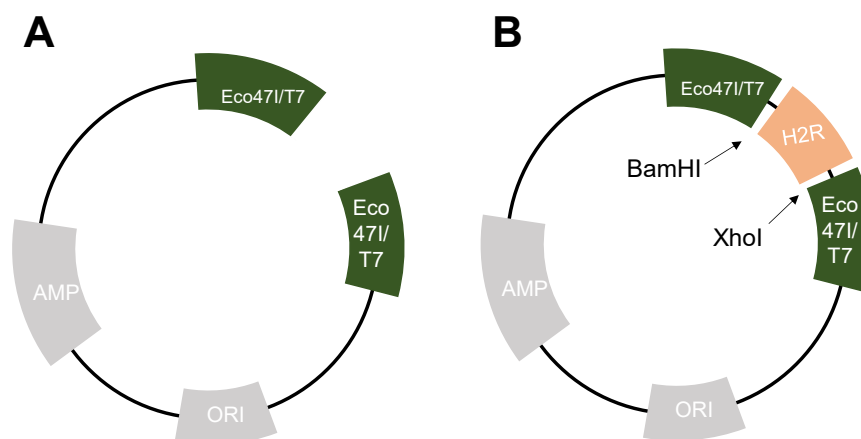


Figure 10. Schematic vector map of the pJET1.2/blunt vector (A) and pJET1.2/H2R vector (B). For more details see **Appendix 15**.

### 3.2.1.3 Digestion of pJET1.2/H2R Vector and Gel Electrophoresis

To create an H2R insert with sticky ends out of the pJET1.2/H2R vector (**chapter 3.2.1.2**), a restriction enzyme digestion was performed. 2  $\mu\text{L}$  FD green buffer (10-fold concentration), 1  $\mu\text{L}$  BamHI, 1  $\mu\text{L}$  XhoI and 16  $\mu\text{L}$  of the pJET1.2/H2R DNA were incubated for 1 h at 37°C. To stop the digestion, the enzymes were denatured by increasing the temperature to 65°C for 20 min. After that, the DNA was kept at 4°C until it was analyzed by gel electrophoresis. For gel electrophoresis, a 1% (w/v) agarose gel in Tris-borate-EDTA (TBE) buffer containing 0.001% (v/v) ethidium bromide was prepared. After loading the gel with the DNA samples and a Quick-Load Purple 1kb DNA Ladder, a voltage of 80 V (corresponds to 90 mA) was applied for at least 40 min to separate the DNA fragments by their length. Subsequent to sufficient separation, the gel was imaged under UV light to ensure the correct insert size.

### 3.2.1.4 Digestion of SNAP- $\beta$ 2AR-LgBiT Vector and Shrimp Alkaline Phosphatase Treatment

The SNAP- $\beta$ 2AR-LgBiT vector (**Figure 11A and Appendix 16**) was kindly provided by Dr. Nicola Dijon (University of Nottingham, UK). It encodes for a  $\beta$ 2-adrenoceptor ( $\beta$ 2AR) labeled with a SNAP-tag and the LgBiT subunit of NanoLuc. The  $\beta$ 2AR gene was removed by restriction enzyme digestion with BamHI and XhoI as described in **chapter 3.2.1.3**. The remaining vector was alkaline phosphatase treated according to a commonly available protocol (Thermo Fisher) to prevent vector re-ligation. Thereafter, the DNA was purified by a GenElute PCR clean-up kit (Sigma). In the following, the obtained vector is referred to as SNAP---LgBiT (**Figure 11B**).

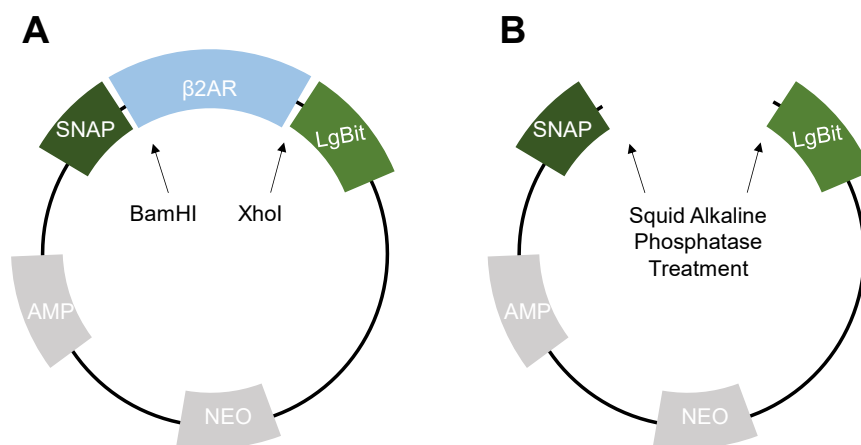


*Figure 11. SNAP- $\beta$ 2AR-LgBiT vector with BamHI and XhoI restriction enzyme sites (A) and respective vector after restriction enzyme digestion and shrimp alkaline phosphatase treatment (B). The vector in B is referred to as SNAP---LgBiT vector.*

### 3.2.1.5 Ligation of Digested H2R Insert with SNAP---LgBiT Vector

The H2R insert with sticky ends (**chapter 3.2.1.3**) was ligated with the SNAP---LgBiT vector (**chapter 3.2.1.4**). 1  $\mu$ L of ligation buffer (10-fold concentration), 1  $\mu$ L 50 ng/ $\mu$ L of the SNAP---LgBiT vector, 25 ng of the H2R DNA (3:1 insert-to-vector molar ratio), 1  $\mu$ L of T4 ligase and water (added to reach a total volume of 10  $\mu$ L) were mixed and left at 16°C overnight. The ligation product was transformed into *E. coli*. Colonies were picked and the DNA was purified using a GenElute Plasmid Miniprep kit (Sigma, **chapter 3.2.3**). The purified DNA was digested with BamHI and XhoI to confirm the ligation of the H2R insert with the SNAP---LgBiT vector. A gel electrophoresis according to **chapter 3.2.1.3** was performed with the different DNA preparations to ensure a correct alignment and size of the product DNA (**Figure 12A-B**). For later

transformations, DNA sample 1-1 (**Figure 12A**) was further multiplied in a maxiprep (**chapter 3.2.4**).

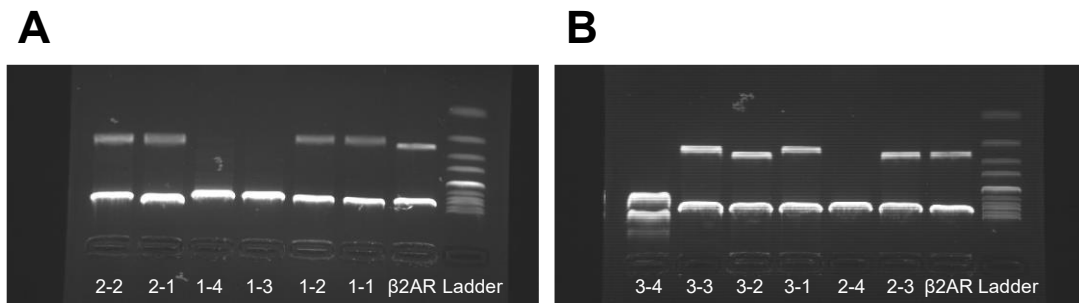


**Figure 12.** Agarose gel imaged under UV light. Several DNA samples (1-1 to 3-4), a digested reference vector ( $\beta$ 2AR) and a Quick-Load Purple 1kb Ladder (Ladder) were loaded in an agarose gel. The samples were separated at 80 V for 40 min and imaged under UV light by an ethidium bromide staining. Samples 1-1, 1-2, 2-1, 2-2, 3-1 and 3-3 were identified as hits as they show two bands with the hits having a smaller base pair fragment (1077 bp) than the reference vector ( $\beta$ 2AR, 1233 bp). This indicates that the H2R insert indeed has ligated with the SNAP---LgBiT vector and no original  $\beta$ 2AR DNA is remaining.

The final vector used in transfection experiments is depicted in **Figure 13**.

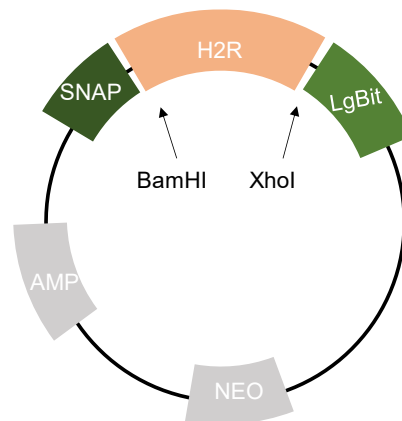


**Figure 13.** Final SNAP-H2R-LgBiT vector. The correct alignment of the vector was confirmed by an agarose gel electrophoresis (see **Figure 12**).

### 3.2.2 Transformation of *E. coli*

For the preparation of agar plates for bacterial culture of *E. coli* transformations, 20 mL freshly autoclaved LB broth with agar in the recommended concentration (35 g per 1 L water) containing 100  $\mu$ g/mL ampicillin were poured into petri dishes with a diameter of 10 cm under semi-sterile conditions (Bunsen burner). Once set at r.t., the dishes were put inside an incubator at 37°C until further use or were sealed with parafilm and stored at 4°C until needed.

TOP10F chemically competent *E. coli* were stored at  $-80^{\circ}\text{C}$  until use. For transformation,  $16\ \mu\text{L}$  of bacteria suspension were mixed with  $1.6\ \mu\text{L}$  of the desired DNA. After 20 min on ice, the bacteria were heat-shocked at  $42^{\circ}\text{C}$  for 30 s to ensure the DNA enters the cells before returning to ice for 2 min. Subsequently,  $100\ \mu\text{L}$  LB broth were added to the bacteria. They were shaken at  $37^{\circ}\text{C}$  for at least 1 h. Thereafter,  $50\text{-}100\ \mu\text{L}$  of bacteria suspension were spread on agar plates under semi-sterile conditions (Bunsen burner). After 5 min, the plates were inverted and put inside an incubator at  $37^{\circ}\text{C}$  to enhance bacterial growth overnight.

Per seeded agar plate two 30 mL tubes were filled with 5 mL LB broth under semi-sterile conditions (Bunsen Burner).  $10\ \mu\text{L}$  of 50 mg/mL ampicillin solution were added to each tube. After that, single circular bacterial colonies were picked with a  $100\ \mu\text{L}$  Eppendorf pipette. The pipette tip was expelled into the respective tube. Each picked colony was defined as a clone, e.g. 1-1, 1-2. Subsequently, the tubes were shaken at  $37^{\circ}\text{C}$  and 225 rpm overnight to ensure bacterial growth without oxygen depression.

#### 3.2.3 Miniprep

DNA was harvested and purified from overnight bacterial culture using a Miniprep kit (GenElute Plasmid Miniprep kit, Sigma). First, 1.5 mL of the bacteria suspension were centrifuged in a 1.5 mL Eppendorf tube for 5 min at 4000 rpm. After the removal of the supernatant, this step was repeated. Then, the bacteria were resuspended in  $200\ \mu\text{L}$  RNase buffer to remove RNA followed by the addition of  $200\ \mu\text{L}$  lysis buffer and inverting the Eppendorf tube six times to ensure good mixing. After 2-3 min at r.t.,  $350\ \mu\text{L}$  neutralizing buffer were added to stop the lysis. The mixture was centrifuged for 10 min at 14000 rpm. The supernatant was carefully removed with a pipette and added to a prepared column. After centrifuging the DNA mixture for 1 min at 14000 rpm, the DNA, now immobilized on the column material, was washed with  $500\ \mu\text{L}$  washing buffer and was centrifuged for 1 min at 14000 rpm. After removing the liquid, the column was dry-spun for 2 min at 14000 rpm to remove remaining ethanol-containing wash buffer. Subsequently, the DNA was eluted with  $100\ \mu\text{L}$  of water. The DNA concentration and purity were determined by measuring the absorption ratio at 260 nm and 280 nm with the Nanodrop spectrophotometer ( $260\ \text{nm}/280\ \text{nm} = 1.7\text{-}1.9$ , Thermo Fisher).

### 3.2.4 Maxiprep

For further amplification of the final SNAP-H2R-LgBiT DNA, a maxiprep was conducted. In the first step, a starter culture was set up by mixing 5 mL of LB broth, 10  $\mu$ L of 50 mg/mL ampicillin and 100  $\mu$ L of bacteria suspension (sample 1-1, **chapter 3.2.1.5**). After shaking the bacteria suspension at 37°C and 225 rpm for 4-6 h, the entire suspension was added to 120 mL of fresh LB broth, supplemented with 180  $\mu$ L of 50 mg/mL ampicillin. The bacterial culture was shaken at 37°C overnight. The maxiprep itself was performed using a QIAfilter Plasmid Maxi Kit (Qiagen). In short, the bacteria were centrifuged (2000 g, 15 min), resuspended in RNase-containing buffer and lysed to release the desired DNA. After neutralization of the reaction mixture, the DNA was loaded into a column and washed twice using gravity flow. After elution with 15 mL of elution buffer, the DNA was washed with 10.5 mL isopropyl alcohol, centrifuged (6000 g, 60 min) and dried. The DNA was resuspended in 300  $\mu$ L Tris-EDTA (TE) buffer. 30  $\mu$ L of 3 M sodium acetate solution and 660  $\mu$ L of 100% cold ethanol (EtOH) were added. The mixture was centrifuged again, washed with 200  $\mu$ L cold 70% (v/v) EtOH and was dried. Finally, the DNA was resuspended in TE buffer to receive a final concentration of 1  $\mu$ g/ $\mu$ L.

### 3.2.5 Transient Transfection

In order to transfect HEK293T SmBiT  $\beta$ -Arr2. cells with SNAP-H2R-LgBiT DNA (**chapter 3.2.1.5**), a four-day protocol was applied. Initially, the cells were subcultivated according to **chapter 3.1.5** and were seeded with a density of  $6.3 \cdot 10^4$  c/cm<sup>2</sup> on poly-D-lysine coated (cf. **chapter 3.3**) transparent 6-well plates. After 24 h the cells were transfected with the Lipofectamine 3000 reagent (Invitrogen) according to the following protocol. Per well 2.5  $\mu$ g SNAP-H2R-LgBiT DNA, 125  $\mu$ L Opti-MEM (OM) and 5  $\mu$ L of P-3000 reagent were mixed in one tube. In a second tube, 3.75  $\mu$ L of Lipofectamine (LF) and 125  $\mu$ L OM were mixed. By pipetting 125  $\mu$ L of the LF/OM reaction mix into the first tube, a reaction was started and left for 5 min (longer runtimes reduce the transfection efficiency). Meanwhile, the 6-well plate was washed and loaded with 1 mL OM per well. After 5 min DNA/LF incubation, 250  $\mu$ L of the transfection mixture was added to each well in a dropwise fashion. As a control, empty vector DNA or DNA with a well-behaved control insert (SNAP- $\beta$ 2AR-LgBiT, cf. **chapter 3.2.1.4**) was used. The cells were kept inside a humidified incubator with 37°C and 5% (v/v) CO<sub>2</sub>. After 24 h, the cells were washed and trypsinized according to **chapter 3.1.5** and were seeded on a poly-D-lysine coated white 96-well plate with

transparent bottom. The cell density in complete medium was set to  $1.18 \cdot 10^5$  c/cm<sup>2</sup>. Plated cells were then placed inside a humidified incubator with 37°C and 5% (v/v) CO<sub>2</sub> for 24 h before the NanoBiT assay was performed. The experimental protocol is explained in **chapter 3.6**.

### 3.3 Preparation of Cell Culture Substrates

In this work, several different cell culture substrates for impedance readouts, luminescence measurements, second messenger assays and microscopic analyses were used (**chapter 3.3.1**). They were either preincubated with serum-containing culture medium or coated with gelatin, crosslinked gelatin or poly-D-lysine (**chapter 3.3.2**). In the following, each substrate is described briefly and the different coating protocols are explained.

#### 3.3.1 Substrate Types

In the case of impedance measurements, different electrode arrays manufactured by Applied BioPhysics or Nanion Technologies were utilized. For 96-well measurements with the ECIS Z or ECIS Z $\theta$  device (Applied BioPhysics), commercial transparent 96W1E+ arrays and custom-made black 96W1E+ arrays with transparent bottom were used. Both array types contain two planar, circular gold-film electrodes with a diameter of 350  $\mu$ m that are deposited on the well bottom opposite to each other (**Figure 14A**). The total electrode area per well amounts to 0.256 mm<sup>2</sup> including the feed lines (biophysics.com #2; **August 10, 2024**). For 8-well measurements, 8W1E arrays with one circular working electrode per well were used (**Figure 15**). The electrode has an area of 0.049 mm<sup>2</sup>, the electrode diameter amounts to 250  $\mu$ m (biophysics.com #1; **August 10, 2024**). In case of an impedance measurement with the CardioExcyte 96 (CE96, Nanion Technologies), transparent or custom-made black 96-well plates with a circular working electrode of 0.6 mm in diameter in the center of the well and a horseshoe-shaped counter electrode at the rim of the well (CardioExcyte 96 NSP-96 Sensor Plates; nanion.de; **August 10, 2024**) were used (**Figure 14B**).

All electrode arrays were used for three to five experiments. Upon completion of one experiment, the cells were trypsinized off the substrates by incubation with 0.05% (w/v) trypsin-EDTA in PBS at 37°C for at least 0.5 h. Then, the wells were washed five times with sterile water and dried inside the safety cabinet overnight.

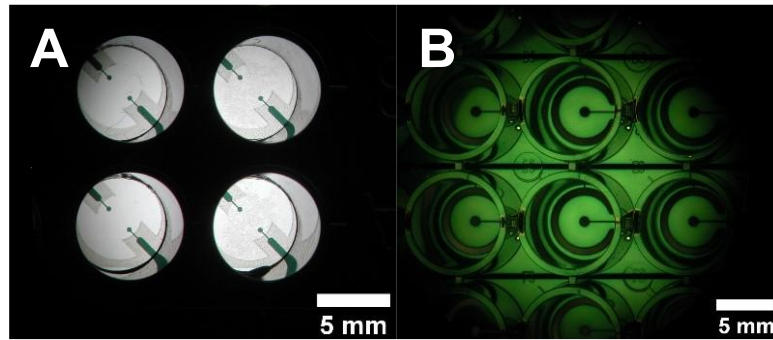


Figure 14. Stereomicroscopic pictures of electrode arrays used for impedance measurements. A: 96W1E+ Array (Applied BioPhysics). Two opposite circular gold-film electrodes with a diameter of  $350\ \mu\text{m}$  are deposited on the bottom of one well. B: Nanion Technologies NSP-96 sensor plate (Nanion Technologies). One circular working electrode with a diameter of  $0.6\ \text{mm}$  is deposited in the center of the well. The horseshoe-shaped counter electrode is found at the rim of the well.

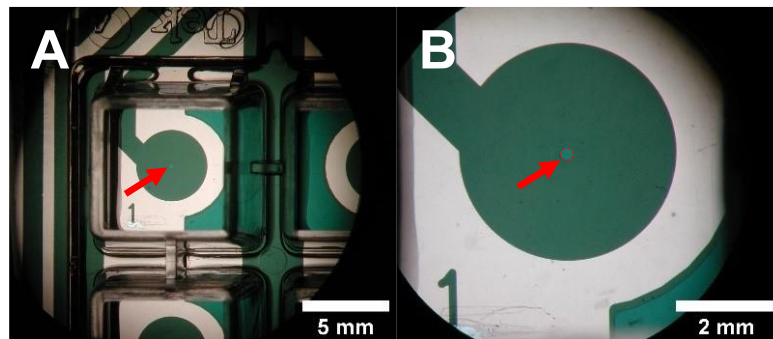


Figure 15. Stereomicroscopic images of 8W1E electrode arrays (Applied BioPhysics) used for impedance measurements. In the center of each well one working electrode with a diameter of  $250\ \mu\text{m}$  is located (red arrow). Around the working electrode, the gold-film is coated with photopolymer to precisely define the electrode size. B is a magnification of A.

For luminescence-based miniG protein recruitment assays (see **chapter 3.6.1.1**), 96-well plates of different colors were tested. White (Brand), black (Greiner) as well as transparent (Greiner) plates with flat bottoms that were of the same material and color as the 96-well body of the plates were used. Furthermore, transparent and custom-made black 96W1E+ arrays with transparent bottom (Applied BioPhysics) were utilized (**Figure 14A**).

For microscopic studies, cells were seeded onto transparent 24-well plates (Thermo Fisher). Calcium assays (see **chapter 3.7.1**) were performed with black 96-well plates with transparent bottom (Corning, VWR). In  $\beta$ -arrestin2 assays (see **chapter 3.6.1.2**), white 96-well plates with transparent bottoms were used (Greiner). For transient transfection (see **chapter 3.2.5**), transparent 6-well plates were necessary (Corning).

### 3.3.2 Surface Coatings

Before cells were seeded, the cell culture substrates were sterilized with Argon plasma for 30 s to 1 min. By that, biological remnants and chemical contaminations are removed from metallic surfaces like the gold-film electrodes and the substrate becomes more hydrophilic, which leads to better spreading of waterborne media and buffers. To further increase the adhesion of cells to the described substrates (**chapter 3.3.1**), different surface coatings were tested. Preincubation with serum-containing medium was compared to a coating with gelatin, crosslinked gelatin and poly-D-lysine.

For medium preincubation, serum-containing culture medium (10% (v/v) FBS, cf. **chapter 3.1.4**) was added to the substrates after plasma treatment and was left on for at least 0.5 h. After that, the medium was removed and the cells were seeded on the substrates. For the gelatin coating, the plasma-treated substrates were incubated with 50  $\mu\text{L}$  (96-well plates), 200  $\mu\text{L}$  (8-well plates) or 500  $\mu\text{L}$  (24-well plates) 0.5% (w/v) gelatin (from bovine skin) solution in water for at least 0.5 h. After that, the substrates were washed twice with culture medium before seeding the cells. In the case of a crosslinked gelatin coating, the sterilized substrates were incubated with 0.5% (w/v) gelatin solution as described above. After an incubation period of 1.5-2 h, the gelatin was removed and crosslinked with the same volume of 2.5% (v/v) glutardialdehyde in water for 10 min. Thereby,  $\epsilon$ -amino residues of lysine within the proteins are crosslinked by Schiff's base formation (**Figure 16**). Thereafter, the substrates were washed 8-12 times with water. For later use, the substrates were stored loaded with water at 4°C. Immediately before seeding, the substrates were washed twice with culture medium.

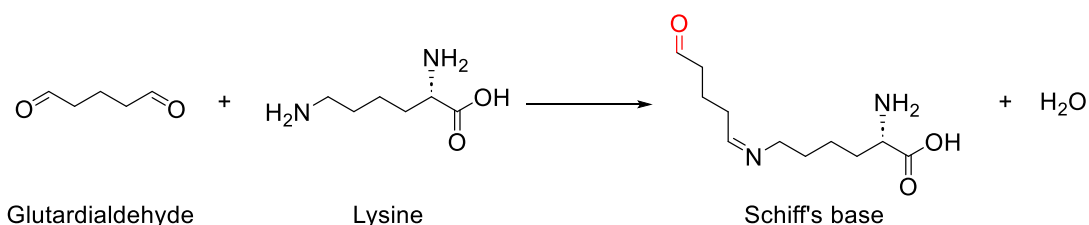


*Figure 16. Reaction scheme of glutardialdehyde with an  $\epsilon$ -amino residue of lysine to create a Schiff's base. The red glutardialdehyde residue can undergo another reaction of the same type to crosslink two proteins. This reaction takes place during crosslinking of gelatin (Farris et al., 2010).*

For coating with poly-D-lysine, the substrates were incubated with 50  $\mu\text{L}$  (96-well plates) 10  $\mu\text{g}/\text{mL}$  poly-D-lysine solution in PBS for at least 0.5 h. After that, the plates were washed with culture medium twice followed by cell seeding.

## 3.4 Microscopy

### 3.4.1 Phase Contrast Microscopy

Phase contrast microscopy is one of the most important techniques used in any biological or microbiological laboratory. It allows optical studies of nearly transparent samples like cells, tissues and microorganisms. Typically, these samples do not absorb a lot of light and only induce small phase shifts because of their thinness and their relatively constant refractive index throughout the specimen. Those small phase shifts can not be recognized by eye but can be converted into amplitude differences by phase contrast microscopy to enhance image contrast.

The development of the first phase contrast microscope goes back to Fritz Zernike, who published his initial findings in 1942 (Zernike, **1942**). Assuming that the incident light is a plane wave, he suggested that light passing a thin transparent object can be divided into *direct* and *diffracted light*. While *direct light* remains unchanged and is not diffracted when passing the sample, *diffracted light* represents all perturbed light waves (Zernike, **1955**).

By introducing a phase annulus close to the aperture of the condenser in front of the focal plane, the illumination light is focused on the specimen. In the focal plane of the specimen, the phase of the *diffracted light* is shifted about  $-90^\circ$  compared to the *direct light* due to the thickness and refractive index of the sample. To specifically modify the phase shift of the *direct light* and enhance image contrast, a phase plate optically conjugated to the phase annulus is integrated in the objective. The phase plate, which is a glass plate with a slightly elevated or lowered circular area (phase ring), shifts the incident wavelength of the *direct light* either by  $-90^\circ$  or  $+90^\circ$ , leading to a net phase shift between *direct* and *diffracted light* of  $0^\circ$  or  $180^\circ$ . Furthermore it reduces the amplitude of the *direct light* by absorbing part of it. The overall phase shifts either induce constructive ( $0^\circ$  phase difference, negative phase contrast) or destructive ( $180^\circ$  phase difference, positive phase contrast) interference of *direct* and *diffracted light* giving rise to amplitude changes and, hence, enhanced image contrast. A schematic illustration of an upright phase contrast microscope is depicted in **Figure 17**.

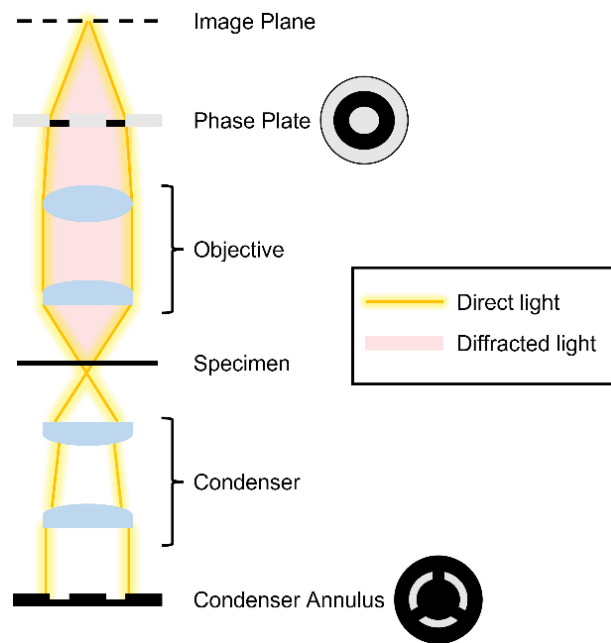


Figure 17. Setup of a commercial phase contrast microscope. In contrast to brightfield microscopes, a phase plate and a condenser annulus are introduced to the light path to allow discrimination between direct and diffracted light and to enhance image contrast of nearly transparent specimens.

In this work, phase contrast microscopy was applied for the documentation of the viability, morphology and confluency of mammalian cells. Accordingly, a Nikon Diaphot microscope including a 4x objective (Plan, 4x, NA = 0.13) and a 10x objective (Plan, 10x, NA = 0.25) was used. For image acquisition, a Nikon D 5000 camera was utilized. Scale bars were inserted with the image analysis software ImageJ (Wayne Rasband, NIH). To convert pixels (px) into micrometers ( $\mu\text{m}$ ), micrographs of a standard hemocytometer with known distances were used as a reference.

### 3.4.2 Stereomicroscopy

In 1671, the first stereomicroscope was invented by Cherubin d'Orleans but unfortunately, this microscope suffered from image dissection. It was only possible to obtain an image by utilizing supplemental lenses. More than 200 years later, in the 1890s, Horatio Saltonstall Greenough developed the preliminary version of the modern stereomicroscope together with the Zeiss Group (Carl Zeiss AG, Oberkochen, Germany). It was the first microscope utilizing erecting prisms for image acquisition (microscopyu.com; **August 10, 2024**). Greenough-type microscopes use two light paths, each of them consisting of an eyepiece and an objective. This enables great numerical apertures (NA), thus, leading to better resolution in comparison to common main objective (CMO) microscopes where one large objective is shared between the two light paths. Furthermore, samples can be visualized in a 3D manner

(Wilson et al., **2020**). Stereomicroscopes are mainly used for biological preparations and to investigate and document non-transparent, big samples. Therefore, they are important for material research, quality assurance and biological dissections.

In this work, a Nikon SMZ 1500 CMO stereomicroscope was used for the documentation and quality control of several cell culture substrates. The magnification was varied between 0.75x and 11.25x depending on the selected objectives. Scale bars were inserted with the image analysis software ImageJ (Wayne Rasband, NIH). Pixels (px) were converted into millimeters (mm) by taking micrographs of a ruler with known distances.

### 3.5 Impedance Spectroscopy

Electrochemical impedance spectroscopy (EIS) is a powerful tool to determine electrochemical and physical properties of materials and their interfaces (Macdonald, Johnson, **2018**). EIS measures the complex resistance, namely the impedance  $Z$ , for an applied sinusoidal alternating current (AC) over a wide frequency range (Abasi et al., **2022**, Irvine et al., **1990**). Since it allows non-destructive, label-free measurements, it circumvents the drawbacks of standard microscopic techniques (e.g. fluorescence microscopy) and allows the investigation of cells, 3D tissues and other biological systems (Krukiewicz, **2020**).

#### 3.5.1 Theoretical Background

Impedance measures the complex resistance of a system when a sinusoidal AC or voltage is applied. According to Ohm's law, the impedance  $Z$  is defined as

$$Z(t) = \frac{U(t)}{I(t)} \quad (1)$$

$$\text{with } U(t) = U_0 \cdot (\sin \omega t) = U_0 \cdot e^{i\omega t} \quad (2)$$

$$\text{and } I(t) = I_0 \cdot \sin(\omega t - \varphi) = I_0 \cdot e^{i(\omega t - \varphi)} \quad (3)$$

Here,  $U_0$  and  $I_0$  are the amplitudes of voltage  $U$  and current  $I$ ,  $\omega$  is the angular frequency in rad/s,  $t$  describes the time and  $\varphi$  the phase shift in  $^\circ$  between voltage and current.  $i$  is defined as  $\sqrt{-1}$ . The angular frequency  $\omega$  can also be expressed as

$$\omega = 2\pi f \quad (4)$$

with  $f$  being the frequency given in Hertz (Hz). Consequently, impedance must be represented as  $Z(t,f)$  or  $Z(t,\omega)$  since it is not only time-dependent but also frequency-dependent. In contrast, the resistance  $R$  of an ideal resistor is defined as

$$R = \frac{U}{I} \quad (5)$$

with  $U$  describing the voltage and  $I$  being the current. The resistance  $R$  is independent of time and frequency. Additionally, alternating currents and voltages through an ideal resistor are in phase with each other.

With **equations 1,2 and 3** the impedance  $Z$  can also be expressed as

$$Z(t, \omega) = \frac{U_0}{I_0} \cdot e^{i\varphi} = |Z| \cdot e^{i\varphi} \quad (6)$$

Here,  $|Z|$  is a measure of the impedance magnitude. By converting the polar coordinates  $|Z|$  and  $\varphi$  into Cartesian coordinates, two new quantities can be defined: the resistance  $R$  and the reactance  $X$ . While the resistance  $R$  describes the real part ( $Re$ ) of the impedance, the reactance  $X$  stands for the imaginary part ( $Im$ ).

$$Z = Re + i \cdot Im = R + iX \quad (7)$$

$$Re = R = |Z| \cdot \cos \varphi \quad (8)$$

$$Im = X = |Z| \cdot \sin \varphi \quad (9)$$

With Cartesian and polar coordinates in hand, impedance can be depicted as a vector in a complex plane, also called Argand or Nyquist diagram (**Figure 18**). The negative imaginary part  $-Im$ , describing the reactance  $X$ , is plotted against the real part  $Re$  representing the resistance  $R$ . Moreover, the length of the vector is given by the impedance magnitude  $|Z|$ . The angle between the x-axis and the vector is described by the phase shift  $\varphi$ .

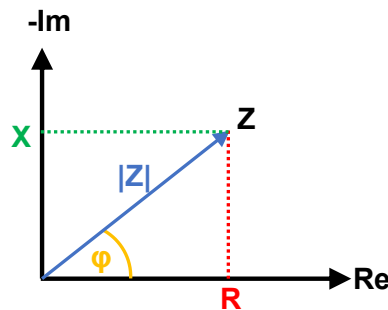


*Figure 18. Impedance  $Z$  plotted as a vector (blue) in a Nyquist diagram. On the x-axis, the real part  $Re$  is plotted. On the y-axis, the negative imaginary part  $-Im$  is depicted. Since impedance is a complex measure, it can either be described by the Cartesian coordinates  $R$  (resistance, real part) and  $X$  (reactance, imaginary part) or with the polar coordinates  $|Z|$ , describing the length of the vector, and  $\varphi$ , which is the angle between x-axis and vector.*

Real impedance components are of resistive behavior and show current in phase with the applied voltage ( $\varphi = 0^\circ$ , x-axis contribution). By contrast, imaginary impedance elements originate from current  $90^\circ$  out of phase with the voltage (y-axis contribution). Besides the Nyquist representation, impedance can also be depicted in a so-called Bode plot. Whereas the Nyquist diagram gives information about the single impedance components ( $R$ ,  $X$ ), the Bode plot contains frequency information. In a

Bode plot, the impedance  $Z$  and phase  $\varphi$  are plotted against the applied frequency for one certain time point in a double- or semi-logarithmic way.

To unravel the impedance signal and characterize the system at hand, fitting an equivalent circuit model to the impedance data is necessary. For that purpose, common components known from electronic circuitry such as resistors, capacitors and inductors are used. Furthermore, a constant phase element (CPE) is introduced to mimic the double layer behavior at the electrode surface. Their impedance contributions and phase shifts are given in **Table 9**.

*Table 9. Components for equivalent circuit modeling of impedance  $Z$ . Resistances, capacitors, inductors and constant phase elements (CPE) are used to describe the impedance  $Z$  of any system. Their single impedance values can be calculated from the formulas in column two. Thereby,  $R$  is the resistance,  $C$  the capacitance,  $i$  stands for  $\sqrt{-1}$ ,  $\omega$  is the angular frequency,  $L$  describes the inductance,  $A$  is a CPE parameter in  $F \cdot s^{n-1}$  and  $n$  describes the respective order, which varies between 0 and 1. The phase shift  $\varphi$  for the equivalent circuit components is given in column three.*

Equivalent circuit component	Impedance $Z$	Phase $\varphi$
Resistance	$R$	$0^\circ$
Capacitor	$\frac{1}{C \cdot i \cdot \omega}$	$-90^\circ$
Inductor	$L \cdot i \cdot \omega$	$90^\circ$
Constant Phase Element CPE	$\frac{1}{A_n \cdot i^n \cdot \omega^n}$ with $0 < n < 1$	$-n \cdot 90^\circ$

As mentioned above, resistances are non-complex and are independent of the frequency, i.e. current and voltage are in phase ( $\varphi = 0^\circ$ ) across a resistor. However, capacitors, inductors and CPEs possess imaginary components and are frequency-dependent. In fact, inductors and capacitors merely consist of an imaginary component and, hence, exhibit a phase shift of  $\varphi = 90^\circ$  or  $\varphi = -90^\circ$ , respectively. The CPE describes the double layer capacitance of an electrode-electrolyte interface. Its phase is frequency-independent and interpolates between capacitors and resistors described by the order  $n$  ( $0 < n < 1$ ).

### 3.5.2 Electric Cell-Substrate Impedance Sensing

In 1984, the first paper explaining electric cell-substrate impedance sensing (ECIS) was published by I. Giaever and C. R. Keese (Giaever, Keese, **1984**). ECIS is a special form of EIS where adherent cells are seeded onto thin gold film electrodes. It reads morphological changes of cells and allows the study of several different cellular processes like cell attachment, cell adhesion, cell growth, cell migration and wound healing. Moreover, cell viability and motility can be monitored, which enables cytotoxicity screenings of a variety of compounds in a high-throughput manner. In

addition, electroporation, cell fusion and signal transduction (e.g. after GPCR stimulation) can be followed. By using serial dosing protocols in single wells, the throughput can be increased even more, e.g. to record full concentration-response curves of GPCR agonists (Stolwijk et al., 2019).

In general, ECIS is measured with a two-electrode system consisting of a small working electrode (WE) and an about 500-1000 times larger counter electrode (CE), both deposited on common cell culture substrates (**Figure 19**) (Stolwijk et al., 2015). When cells are seeded on the electrodes and a small non-lethal AC current of a few  $\mu\text{A}$  is applied, the in- and out-of-phase voltage (few mV) can be measured yielding the impedance (Stolwijk, Wegener, 2019). Due to the big difference in electrode size, the major voltage drop occurs at the WE (bottleneck effect), meaning the total impedance signal is dominated by the cells growing on the WE. In contrast, contributions of the bulk medium and the CE become negligible.

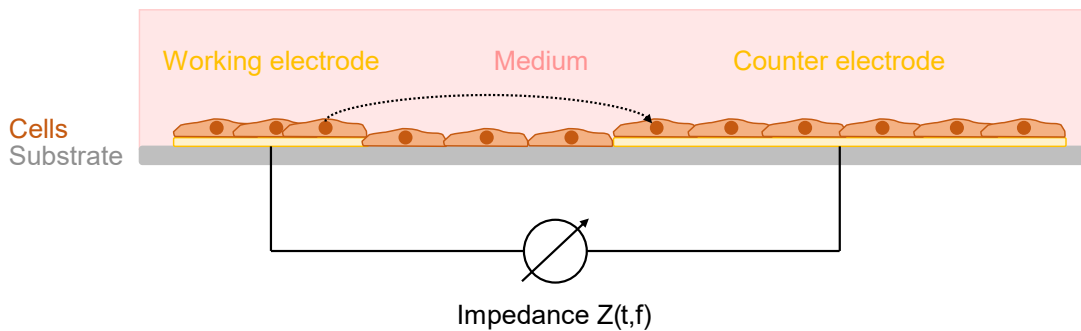


*Figure 19. Setup for electric cell-substrate impedance sensing (ECIS). The setup consists of a small working electrode (WE,  $0.05 \text{ mm}^2$ ) and an about 500-1000 times larger counter electrode (CE,  $25\text{-}50 \text{ mm}^2$ ). When cells are adhered to the surface and a small AC current is applied between the electrodes, the impedance is dominated by the cell-covered WE.*

Since cells behave as insulating particles, impedance rises when they are seeded on the electrodes. However, depending on the applied AC frequency, different phenomena are observed. For frequencies  $f < 10 \text{ kHz}$ , the current prefers the paracellular pathway to cross the cell layer. In this case, the barrier function dominates the impedance signal. For frequencies  $f > 10 \text{ kHz}$ , the current couples through the cells, meaning transcellular pathways are favored. Here, the membrane capacitance strongly influences impedance (**Figure 20**).

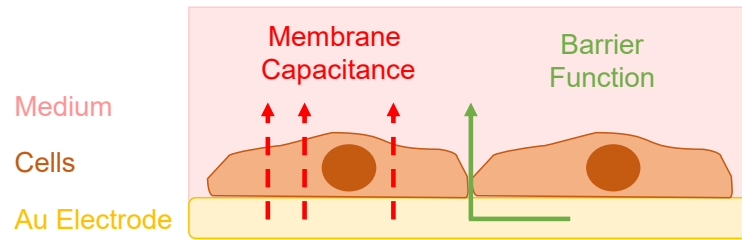


Figure 20. Current pathways in electric cell-substrate impedance sensing (ECIS). Depending on the applied AC frequency the current is either choosing the paracellular pathway (green,  $f < 10$  kHz) dominated by cellular junctions or the transcellular pathway (red,  $f > 10$  kHz) determined by the membrane capacitance of the cells.

In general, ECIS is either conducted in *multi-frequency vs. time* (MFT) mode or in *single-frequency vs. time* (SFT) mode. Whereas the MFT-mode is conducted with several different frequencies between 1-10<sup>5</sup> Hz, the SFT-mode only uses one frequency (usually the most sensitive frequency). In both cases, impedance is recorded at the respective frequencies over time. Accordingly, the MFT-mode is often used to record impedance spectra, to determine the most sensitive frequency (biggest impedance difference between cell-free and cell-covered electrode) and to obtain information about paracellular (< 10 kHz) and transcellular (> 10 kHz) components of impedance. The SFT-mode is preferred if the most sensitive frequency is known and better time resolution is required, e.g. to detect receptor activation or other processes with fast kinetics.

The impedance of every biological system can be approximated with an equivalent circuit. In the case of a cell-covered ECIS electrode, the bulk resistance of the medium is modeled by a resistor  $R_{\text{bulk}}$ . For the impedance of the cell layer ( $Z_{\text{cl}}$ ), capacitive (e.g. cell membrane,  $C_{\text{cl}}$ ) and resistive (e.g. cell junctions,  $R_{\text{cl}}$ ) components must be considered. The electrode-electrolyte interface behaves as a non-ideal capacitor with double layer formation. Since no electrotechnical component is available to perfectly describe its behavior, a CPE is introduced to describe the behavior at the interface of the polarizable gold electrode. The resulting equivalent circuit is depicted in **Figure 21**. However, it must be noted that the depicted model is only an approximation of the real conditions.

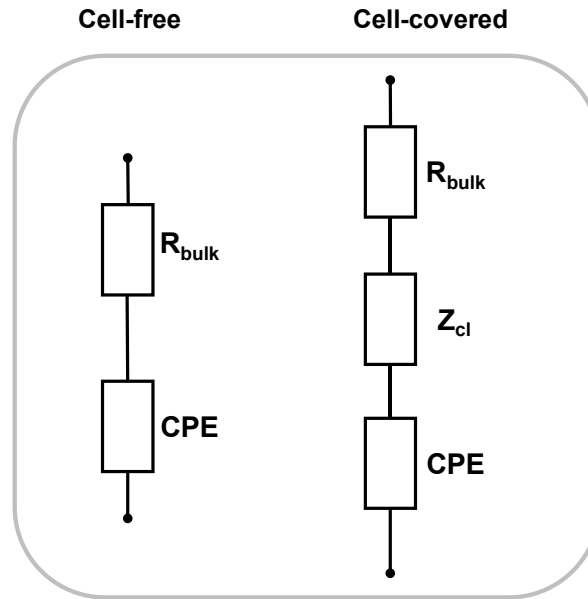


Figure 21. Simplified equivalent circuit for cell-free (left) and cell-covered (right) electrodes of ECIS. While the circuit model for the cell-free electrode only consists of a  $R_{bulk}$  resistor and a CPE element, the equivalent circuit of the cell-covered electrode additionally considers the impedance  $Z_{cl}$  originating from the cell layer.  $Z_{cl}$  is composed of resistive ( $R_{cl}$ ) and capacitive ( $C_{cl}$ ) components.

As seen in **Figure 21**, the three impedance contributions of the cell-covered electrode ( $R_{bulk}$ ,  $Z_{cl}$  and CPE) are connected in series. For cell-free electrodes, only the medium resistivity  $R_{bulk}$  and the CPE element are of importance. With these equivalent circuits in hand, impedance data can be fitted by which the single impedance contributions are elucidated. However, equivalent circuits do not always describe the biological system at hand perfectly, which is why the two ECIS founders Giaever and Keese came up with another idea. In 1991, they developed a first mathematical model to deconvolve the measured impedance signal (Giaever, Keese, **1991**). They approximated cells as circular disks with a radius  $r_c$ . Furthermore, they defined the frequency-dependent impedance of the cell-free electrode as  $Z_n$  and the impedance emerging by the capacitive nature of the cell membranes as  $Z_m$ . Eventually, they ended up with a differential equation that could be solved by modified Bessel functions of orders 0 and 1, giving rise to two new parameters  $\alpha$  and  $R_b$ .  $\alpha$  is the impedance contribution arising from the current flow between the cell layer and substrate. It is defined as

$$\alpha = r_c \sqrt{\frac{\rho}{h}} \quad (10)$$

given in  $\sqrt{\Omega cm}$  with  $\rho$  being the specific resistivity of the electrolyte and  $h$  being the height difference between cells and substrate, which usually ranges between 25-150 nm (Reiss, Wegener, **2015**).  $R_b$  is defined as the barrier resistance between two adjacent cells and is usually given in  $\Omega cm^2$ . The higher  $R_b$ , the tighter the cell barriers.

$\alpha$  and  $R_b$  are of special interest if the applied AC current finds its way underneath the cells and through the paracellular cleft. However, if it passes through the cells by capacitively coupling through their upper and lower membrane, the membrane impedance  $Z_m$  has to be considered. It is defined as

$$Z_m = \frac{2}{i\omega C_m} \quad (11)$$

with  $i = \sqrt{-1}$ ,  $\omega$  being the angular frequency and  $C_m$  describing the membrane capacitance. In **Figure 22**, all important model parameters are illustrated.

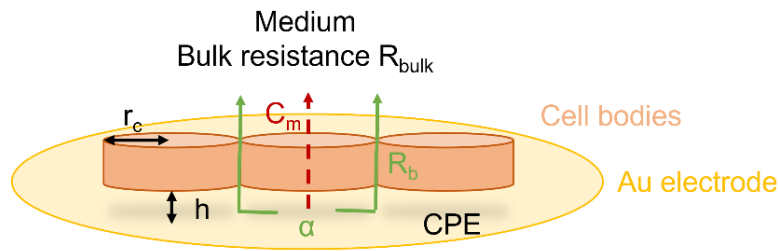


*Figure 22. Schematic of ECIS model and respective parameters. The cells are approximated as small cylinders with radius  $r_c$ . Their distance from the electrode is described by  $h$ . The total impedance of this system is given by the impedance of the electrode  $Z_{el}$ , the impedance of the cell layer  $Z_{cl}$  and the bulk resistance  $R_{bulk}$ . The electrode impedance  $Z_{el}$  is influenced by the constant phase element (CPE) of the electrode-electrolyte interface. The impedance of the cell layer  $Z_{cl}$  is determined by the impedance from cell adhesion sites  $\alpha$ , cellular barriers  $R_b$  and the membrane capacitance  $C_m$ . The Figure was adapted from Wegener et al. (Wegener et al., 2000a).*

Ultimately, the total impedance is given by the impedance of the electrode  $Z_{el}$ , the impedance of the cell layer  $Z_{cl}$  and the resistance of the medium above the cells  $R_{bulk}$ .  $Z_{el}$  is approximated with a CPE, which models the double layer behavior of the gold electrode, a non-ideal capacitor. The impedance of the cell layer is determined by  $\alpha$ ,  $R_b$  and  $C_m$ . In summary, the ECIS model uses five parameters to characterize the impedance of a cellular system, specifically  $\alpha$ ,  $R_b$ ,  $C_m$ ,  $R_{bulk}$  and the CPE.

### 3.5.3 Workflow at the Impedance Measurement Devices

In this work, different ECIS devices were used. On one hand, the ECIS Z and the ECIS Z $\theta$  device, both manufactured by Applied BioPhysics, were utilized for 8-well and 96-well measurements. In special cases, self-assembled setups for 8-well measurements as depicted in **Figure 23** were used. This setup will be referred to as *ECIS self-assembled* (ECIS SA) in the further course of this work. It uses a Solartron Si-1260 (Schlumberger Instruments, Farnborough, UK) as an impedance analyzer, a self-built relay to switch between the single electrodes and a LabView-based software (kindly provided by Prof. Wegener, University of Regensburg) to operate the system.

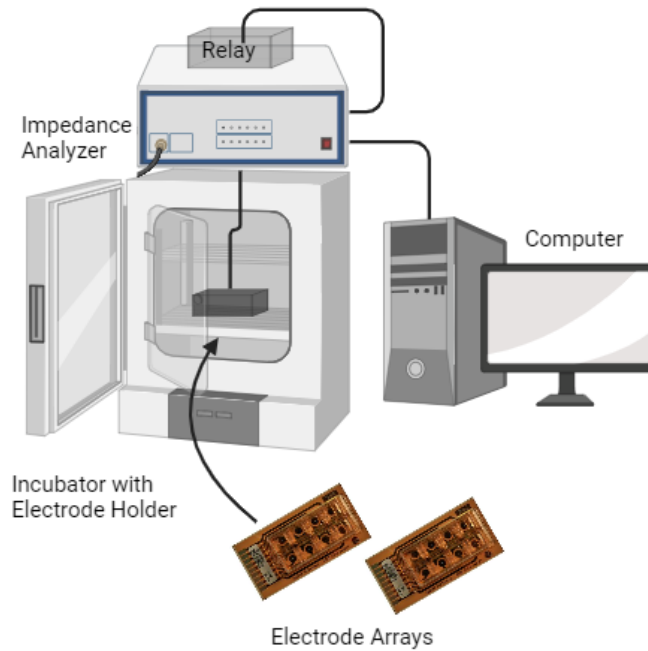


*Figure 23. Manual setup for 8-well electrode impedance measurements at the ECIS SA. The electrode arrays are mounted to an 8-well holder placed inside an incubator at 37°C. The holder is connected to a relay that selects and switches between the single electrodes. The relay is linked to an impedance analyzer, which reads the impedance and passes it on to the computer. This figure was created with biorender.com. Images of 8W1E arrays from biophysics.com.*

On the other hand, the CardioExcyte 96 device (CE96, Nanion Technologies) was used. It was originally developed for impedance measurements to monitor the beating of cardiomyocytes and has the advantage that its time resolution is extremely advanced (1 ms). Furthermore, no big incubator is necessary because the measurement chamber is implemented inside a small incubation system with external environmental control and a gas mixer (**Figure 24**). During the measurement, the lid of the 96-well chamber can be removed for substance addition and further cell manipulation.



*Figure 24. CardioExcyte 96 (CE96, Nanion Technologies) tabletop device with external humidity and gas control. In comparison to most impedance devices, no incubator is necessary (image from nanion.de).*

### 3.5.3.1 Workflow at the ECIS Z, ECIS Z $\theta$ and ECIS SA to Measure Agonist-Induced GPCR Activation

For all measurements at the ECIS Z, ECIS Z $\theta$  and ECIS SA, Applied BioPhysics electrode arrays were used (**chapter 3.3.1**). Before cell seeding, the arrays were sterilized in Argon plasma for 30 s and were coated as described in **chapter 3.3.2**. Thereafter, the cells were seeded on the electrodes. For HEK cells, a density of  $3 \cdot 10^5$  c/cm<sup>2</sup> was used. CHO cells were seeded in a density of  $10^5$  c/cm<sup>2</sup>.

When recording frequency spectra in MFT-mode to document cellular attachment and adhesion and to find the most sensitive frequency, the arrays were mounted to the holders before or directly after cell seeding to ensure the first measured spectrum is for cell-free electrodes (0 h spectra). Usually, the *impedance magnitude*  $|Z|$  (to simplify, the term will be abbreviated with *impedance* in the further course of this work) was measured at the frequencies 4/12/16/32/64/96 kHz if not indicated differently. The time resolution was approximately 10 min. The incubator was set to a physiological temperature of 37°C and 5% (v/v) CO<sub>2</sub>. After about 24 h, the measurement was paused and the cell culture medium was exchanged. After another 24 h, the adhesion measurement was stopped and the confluency of the cell layer was validated by phase contrast microscopy. In consecutive 96-well experiments (detailed below), the culture medium was exchanged with 75  $\mu$ L (w/ preincubation step) or 100  $\mu$ L (w/o preincubation step) measurement buffer (see **chapter 3.1.4**). In 8-well experiments, 100  $\mu$ L (w/ preincubation step) or 200  $\mu$ L (w/o preincubation step) of measurement buffer were used. After exchanging the medium, the cells were equilibrated for 2-2.5 h (HEK cells) or 4 h (CHO cells) at 37°C and 0% (v/v) CO<sub>2</sub>. An impedance measurement in SFT-mode was started at the sensitive frequency of  $f = 12$  kHz and an impedance baseline was recorded for at least 0.5 h. After that, the cells were exposed to different substances, usually executed by 1:1 additions of double concentrated solutions to guarantee thorough mixing (e.g. addition of 100  $\mu$ L double concentrated solution of substance x to 100  $\mu$ L of buffer). After the last addition, impedance was recorded for at least one more hour. The time resolution throughout SFT-experiments amounts to approximately 50 s.

#### **Optimization of the Impedance Readout at the ECIS Z, ECIS Z $\theta$ and ECIS SA**

Different influences on the impedance signal during cell adhesion and after GPCR stimulation were tested in **chapter 4**. The impact of different plate coatings, coelenterazine h itself, aging of coelenterazine h, the cell density and the measurement buffer was investigated by impedance measurements.

### Plate Coatings

The plate coatings described in **chapter 3.3.2**, specifically a preincubation with serum-containing culture medium and coatings with gelatin and crosslinked gelatin, were compared in cellular adhesion and GPCR stimulation measurements (cf. **chapters 4.1 and 4.4.1**).

### Influence of Coelenterazine h

The influence of the luciferin coelenterazine h on impedance was tested by preincubating the cells with a final concentration of 1  $\mu\text{M}$  in L15 buffer for 0.15-0.25 h before stimulation of the cells with ligand solution. The results were compared to a stimulation in the absence of coelenterazine h (cf. **chapter 4.2**).

### Coelenterazine h Aging

In addition to the study described above, differently treated coelenterazine h solutions were tested to check its light sensitivity, temperature stability and vulnerability towards oxygen and humidity (cf. **chapter 4.4.2**). Four coelenterazine h solutions were prepared and compared with ECIS.

- (1) **Control**: the solution was freshly prepared on the day of the experiment and was stored at 4°C in the dark until use
- (2) **Three warm-cold-cycles**: the solution was prepared on the day of the experiment but underwent heating-up to 37°C and cooling down to 4°C in 5 min intervals three times, respectively
- (3) **4°C dark**: the solution was prepared one day before the experiment and was kept at 4°C protected from light until use
- (4) **r.t. illuminated**: the solution was prepared one day before the experiment and was kept at r.t. not protected from light until use

### Seeding Density and Cell Growth

In these experiments, either the seeding density was altered (cf. **chapters 4.1 and 4.4.3.1**) or the same seeding density was used but the cultivation time was varied (cf. **chapter 4.4.3.2**). Both experiments study the influence of the cell number on the impedance signal. In the case of varying the seeding density, HEK cells were seeded either with  $3 \cdot 10^5$  c/cm<sup>2</sup> (standard condition),  $2 \cdot 10^5$  c/cm<sup>2</sup>,  $10^5$  c/cm<sup>2</sup> or  $5 \cdot 10^4$  c/cm<sup>2</sup>. The adhesion behavior and the differences after ligand stimulation were monitored with ECIS. In case of shortening or extending the culturing time in comparison to the standardized protocol (two-day cultivation), the cells were able to grow one, two or

three days, respectively. Eventually, their agonist-induced impedance response was compared.

### Measurement Buffers

Three typical measurement buffers, in particular L15, HBSS and PBS, were compared in GPCR stimulation experiments using impedance measurements (cf. **chapter 4.4.4**). The ligands under study were dissolved in the respective buffer before addition to the cells.

### 3.5.3.2 Workflow at the CE96 to Measure Light-Controllable GPCR Activation

With the tabletop CE96 device, so-called photoswitchable ligands and their impact on impedance were investigated. They are constituted of a photoswitchable moiety and a pharmacophore that is able to activate certain GPCRs. Its receptor-activating properties rely on the configuration of the photoswitchable moiety (*cis/trans* or *open/closed*). An illumination with different wavelengths allows switching between the two isomers. In this work, one ligand for the D2L, namely ligand **1**, and one ligand for the Y4R, namely ligand **2**, was investigated by impedance measurements. Their structures are given in **Figure 25** and **Figure 26**. For ligand **1**, a working concentration of 200 nM was chosen. Ligand **2** was routinely used in a working concentration of 50 nM.

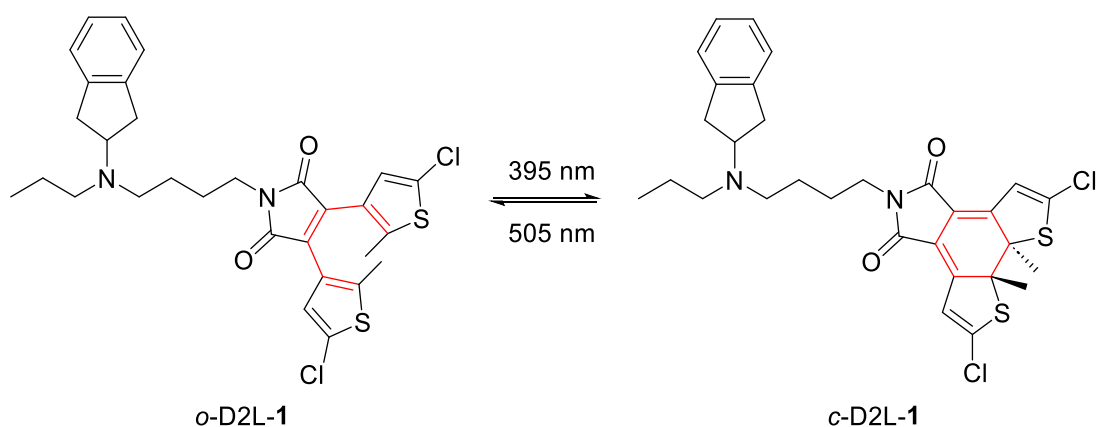


**Figure 25.** Structure and switching behavior of ligand **1**. The D2L ligand is dithienylmaleimide-based and is switched with a wavelength of  $\lambda = 395$  nm to the closed isomer (c) and with  $\lambda = 505$  nm to the open isoform (o). The switching moiety is shown in red.

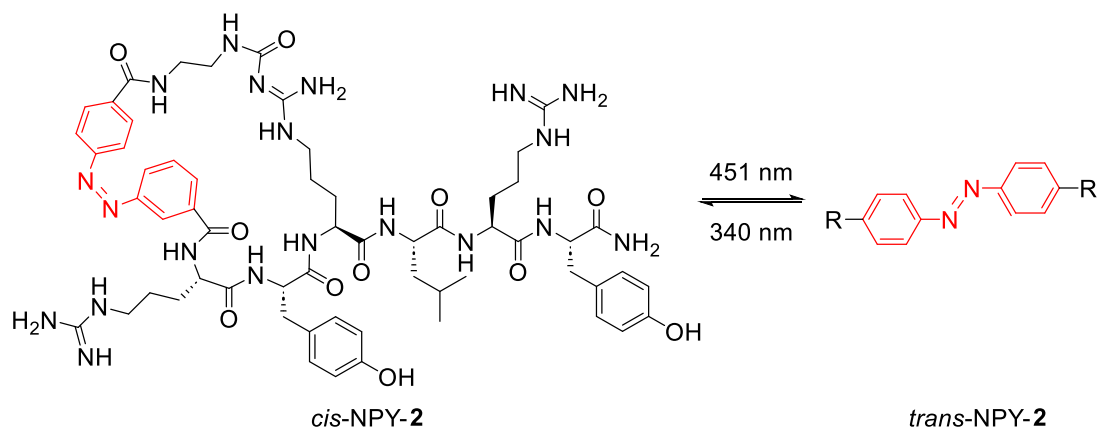


Figure 26. Structure and switching behavior of the Y4R ligand 2. The photoswitchable ligand consists of a cyclo-peptidic pharmacophore and an azobenzene moiety as photoswitchable part. Switching is performed at wavelengths of  $\lambda = 340$  nm to obtain the *cis*-isoform and at  $\lambda = 451$  nm to generate the *trans*-isoform. The azobenzene switching moiety is shown in red. The cyclopeptide is abbreviated with R in the right structure.

Before cell seeding on the CE96 electrode arrays (cf. **chapter 3.3.1**), the electrodes were sterilized with Argon plasma for 30 s. After medium preincubation for at least 0.5 h, the cells were seeded on the substrates. A cell density of  $10^5$  c/cm<sup>2</sup> was used for both CHO cell lines under test (CHO D2L, CHO NPY, cf. **chapter 3.1.2**).

Similar to the ECIS devices (see **chapter 3.5.3.1**), the CE96 can also be used in MFT- and SFT-mode. The former was used to determine the most sensitive frequency of the cell lines and to document attachment and adhesion on the electrodes. 21 logarithmically distributed frequencies between 1-100 kHz were chosen. The SFT-mode was preferred for cellular stimulation and illumination experiments. The time resolution amounts to 60 s in MFT-mode and 22 s for one frequency ( $f = 12$  kHz) in SFT-mode. Experiments were conducted similar to ECIS experiments (see **chapter 3.5.3.1**) but since photosensitive substances were investigated, all experiments and preliminary steps were performed in the dark. The only light source available was a red light-emitting diode (LED) with a wavelength of  $\lambda = 645$  nm (700 mA). This wavelength has proven to not interfere with any switching wavelength of the ligands under study. For intended illumination, single LEDs (340 nm, 451 nm, 505 nm) or 96-well LED plates (395 nm, 505 nm) were used (kindly provided by Prof. König, University Regensburg). To obtain the respective isoform of a certain photochromic ligand, the ligand stock solutions were irradiated with the respective wavelengths for 3 min before serial dilutions and the experiments were conducted. During switching experiments, non-irradiated wells (dark controls) were covered with aluminum foil to avoid unintentional switching. To prevent stray light formation, black 96-well plates were preferred (see **chapter 3.3.1**).

While equilibrating the CHO cells for 4 h in 50  $\mu$ L L15 measurement buffer, the impedance  $|Z|$  was recorded with the SpectraControl Software (Nanon Technologies)

at the CE96 until a stable baseline level was observed. Subsequently, the cells were preincubated with 50  $\mu\text{L}$  0.8  $\mu\text{M}$  forskolin (FSK) in L15 for 0.25-0.33 h (final concentration of 0.4  $\mu\text{M}$ ). After that incubation time, 100  $\mu\text{L}$  double-concentrated ligand solution dissolved in 0.4  $\mu\text{M}$  FSK in L15 was added. At least 0.33 h after stimulation with the photoswitchable ligand, switching experiments were performed with an illumination time of 3 min and varying illumination wavelengths. In the case of concentration-response studies, photoswitching was not applied.

### 3.5.4 Impedance Data Analysis and Representation

For the ECIS Z, ECIS Z $\theta$  and ECIS SA data extraction, the commercially available software *ECIS* (Applied BioPhysics) or a self-written LabView-based software (kindly provided by Prof. Wegener, University of Regensburg) was used. The CE96 data was extracted with the SpectraControl Software (Nanon Technologies). The ECIS and CE96 data were evaluated and plotted with the OriginLab software (OriginLab Corporation). In the following, the data analysis procedures will be explained in detail.

#### **Sensitive Frequency**

The sensitive frequency is defined as the frequency where the cells contribute most to the impedance signal relative to the impedance of the cell-free electrode. To determine the most sensitive frequency, impedance spectra at different time points after cell seeding were recorded in MFT-mode. The measured data for cell-free electrodes ( $t = 0$  h) and cell-covered electrodes ( $t \geq 30$  h) was plotted against the applied AC frequency in a double-logarithmic manner. From the ratio between the two curves ("cell-covered divided by cell-free"), usually a Gaussian-shaped curve is obtained. The frequency at the maximum of the curve mirrors the most sensitive frequency. In this work, a frequency of 12 kHz proved to be satisfactory for all cell lines investigated (see **chapters 4.1 and 6.1**). Accordingly, all measurements in SFT-mode were performed at 12 kHz.

#### **Baseline Values**

Since HEK cells are weakly adhering and quickly detach from the substrate surface (Faussner et al., **2022**, Jayakumar, J. A. K. J. et al., **2020**), the impedance baseline values were expected to vary from experiment to experiment. Baseline impedance values, also referred to as *basal impedance*, were calculated from the impedance raw data at the sensitive frequency 12 kHz to compare the electrode coverage between experiments. For each experiment and each condition, a mean baseline value was

determined by averaging 11 raw data points before the first compound addition. The averaged baseline values are given in the captions of the figures and the main body of the text. The impact of different assay parameters on the basal impedance is investigated in **chapter 4.1 and 4.4**.

### Adhesion Data

For the analysis of the adhesion data (**chapter 4.1**), the averaged, non-normalized raw data of impedance was plotted and analyzed. By averaging the raw data, the baseline impedance values determined in other experiments can be correlated with the electrode coverage apparent from the adhesion data.

### Normalization of Impedance Values

In pharmacological stimulation experiments, the impedance response was normalized to the time point of stimulus addition (if not stated otherwise) by pursuing the following steps for each well:

- 1) The time value of stimulus addition was subtracted from all given time values to set the start of compound exposure to time zero.
- 2) The impedance value at the time point of stimulus addition was subtracted from all measured impedance values (for each well) to express all changes from the baseline impedance.

The obtained impedance values represent the absolute change of the impedance magnitude over time and will be called  $\Delta|Z|$  accordingly. The  $\Delta|Z|$  values of equally treated wells were averaged by calculating the mean and standard error in accordance with the following equations:

$$\Delta|Z|_{mean} = \frac{1}{n} \sum_{i=1}^n \Delta|Z_i| \quad (12)$$

$$SD = \sum_{i=1}^n \sqrt{\frac{(\Delta|Z_i| - \Delta|Z|_{mean})^2}{n-1}} \quad (13)$$

$$SE = \frac{SD}{\sqrt{n}} = \sum_{i=1}^n \sqrt{\frac{(\Delta|Z_i| - \Delta|Z|_{mean})^2}{n(n-1)}} \quad (14)$$

$\Delta|Z|_{mean}$  is the averaged impedance change,  $n$  is the number of replicates per experiment,  $SD$  describes the standard deviation and  $SE$  is the standard error of the mean (often abbreviated with  $SEM$ ). If not indicated differently,  $\Delta|Z|_{mean} + SE$  was plotted over time for reasons of clarity and comprehensibility. In the case of averaging multiple experiments, Gaussian error propagation was applied. The corresponding number of replicates ( $N$ ) is given in the figure captions.

### Concentration-Response Curves

To generate concentration-response curves after stimulus addition, different techniques for analyzing the data have been compared. Besides plotting (i) the

impedance change  $\Delta|Z|$  after a certain time point against the logarithm of the ligand concentration, it is also possible to plot (ii) the area under the curve (AUC) for a particular time interval or (iii) the maximum impedance against the logarithmic ligand concentration. In this work, the method of choice was the analysis of  $\Delta|Z|$  after a certain time point as it turned out to be the simplest analysis technique but at the same time yielded consistent results similar to both other analysis methods as confirmed in **Figure 27**.

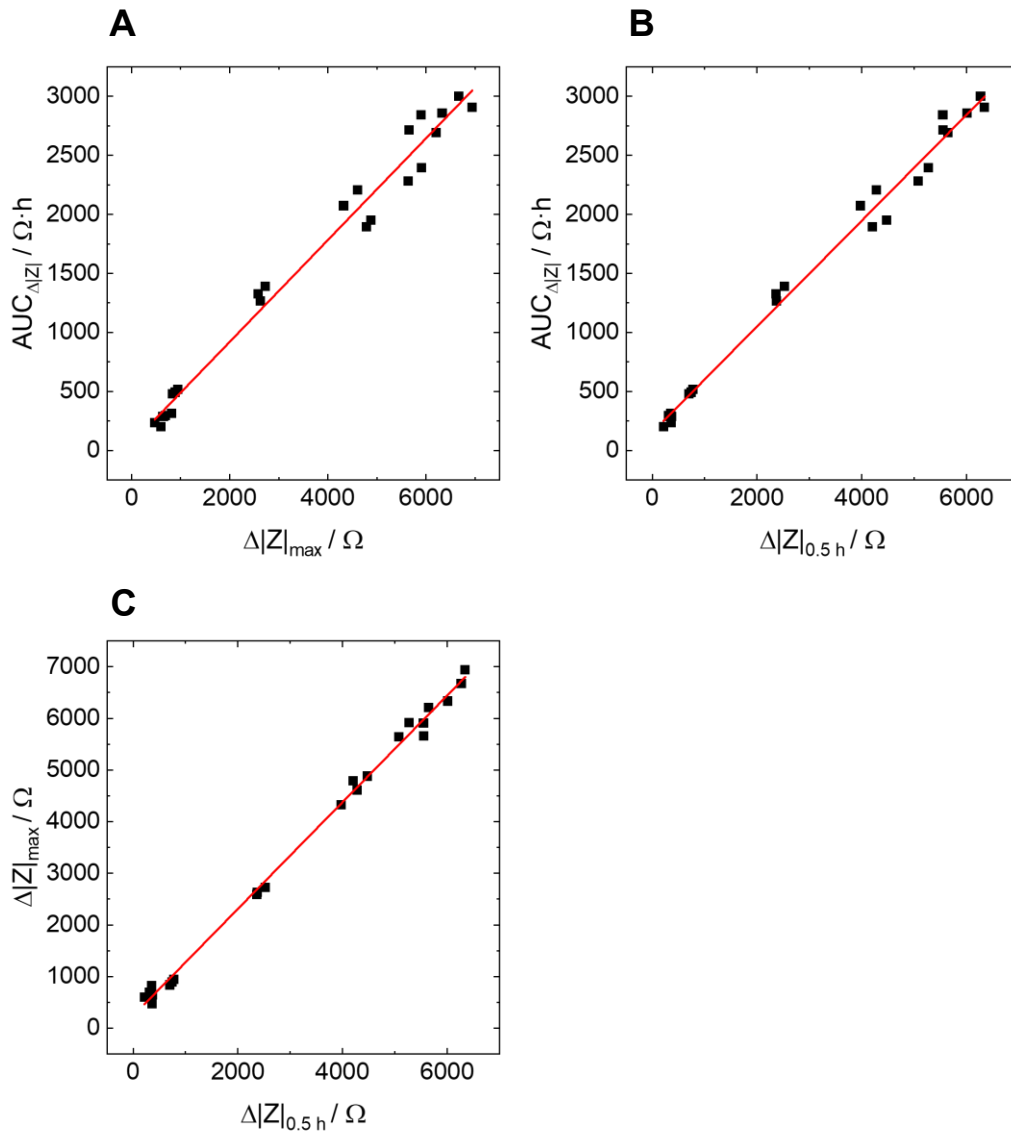


**Figure 27.** Comparison of three impedance data analysis techniques, in particular the analysis of (i)  $\Delta|Z|_{0.5h}$  after a certain time point (0.5 h after stimulus addition), (ii) the analysis of the area under the curve (AUC) of  $\Delta|Z|$  for a certain time interval and (iii) the analysis of the impedance maximum  $\Delta|Z|_{max}$ . Shown here is the impedance data for HEK M1R/mGq cells after stimulation with increasing concentrations of the ligand carbachol (concentrations increase from the bottom left to the top right). The results of the three methods are plotted against each other, respectively. A:  $AUC_{\Delta|Z|}$  versus impedance maximum  $\Delta|Z|_{max}$ , B:  $AUC_{\Delta|Z|}$  versus impedance  $\Delta|Z|_{0.5h}$  after 0.5 h, C: impedance maximum  $\Delta|Z|_{max}$  versus impedance  $\Delta|Z|_{0.5h}$  after 0.5 h. A linear dependency is found in every case, which means independent of the analysis method, equivalent results are obtained. A:  $R^2 = 0.98$ , B:  $R^2 = 0.99$ , C:  $R^2 = 1$ .

The evaluated time point at which impedance was determined was set to  $t = 0.5$  h because stable and maximal impedance signals are usually obtained after this time. The respective  $\Delta|Z|_{\text{mean}} + \text{SE}$  values are plotted against the logarithm of the applied ligand concentration to generate concentration-response curves. They are fitted with a four-parametric dose-response fit. A Levenberg-Marquardt-algorithm was applied, fitting non-linear data sets by the least-square method. The data was weighted instrumentally using the weighing factor  $\omega_i = \frac{1}{\sigma_i^2}$  if not stated otherwise.  $\sigma_i$  represents the SE of one data point. The fitting equation is given by

$$y = A_1 + \frac{A_2 - A_1}{1 + 10^{(\log x_0 - x) \cdot p}} \quad (15)$$

$A_1$  and  $A_2$  describe the lower and upper asymptote, respectively. The  $A_2$  value is also often denoted as efficacy or  $E_{\text{max}}$ , which mirrors the maximal response after stimulation.  $x_0$  represents the EC50 value, which is the ligand concentration that results in the half-maximal response, with

$$\log x_0 = -pEC50 \quad (16)$$

The potency or pEC50 value is more illustrative and intuitive than the EC50 value because it takes smaller, more handy values. Therefore, pEC50 values were calculated and compared throughout this work. Hereby, the vehicle control (CTRL) was always represented by  $\log(c/M) = -20$  in concentration-response curves. The Hill slope  $p$  defines the steepness of the curve and takes a value of 1 in the ideal case. The fit parameters are also depicted in **Figure 28**.

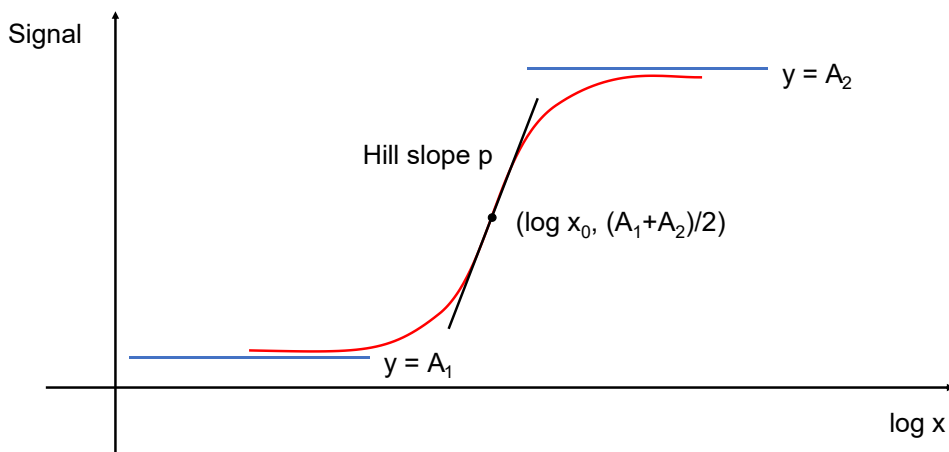


Figure 28. Schematic concentration-response curve according to **equation 15**.  $A_1$  and  $A_2$  define the lower and upper asymptotes,  $\log x_0$  represents the concentration with half-maximal effect (negative pEC50). The steepness of the linear part of the curve is given by the Hill slope  $p$ .

For concentration-response analysis of the photoswitchable ligands **1** and **2** (cf. **chapter 6.2**), the impedance at time point  $t = 0.33$  h or the AUC of impedance between a time interval of  $t = 0.33$ - $0.67$  h was evaluated. The fit data was weighted

instrumentally for ligand **1** or not weighted for ligand **2**. These procedures yielded better fits of the experimental data.

### 3.6 Split Luciferase Complementation

In 1989, Stanley Fields and Ok-kyu Song developed the first version of a protein fragment complementation assay (PCA) called the yeast two-hybrid system (Y2H) (Fields, Song, **1989**). With this assay, protein-protein interactions can be investigated. Fields and Song analyzed the GAL4 protein in *Saccharomyces cerevisiae*. GAL4 is a transcriptional factor in gene regulation and consists of a DNA-binding domain (BD) and a C-terminal domain activating gene transcription (activating domain, AD). Two-hybrid systems, composed of genes encoding for the GAL4 DNA-binding domain linked to yeast protein SNF1 (GAL4(1-147)-SNF1) and encoding for part of the GAL4 C-terminal domain linked to protein SNF4 (SNF4-GAL4(768-881)), were created. If the proteins SNF1 and SNF4, generally also called *bait* and *prey* proteins, interact with each other, both GAL4 fragments reconstitute and become functional, leading to transcription of the bound Gal1-lacZ reporter gene (**Figure 29**).

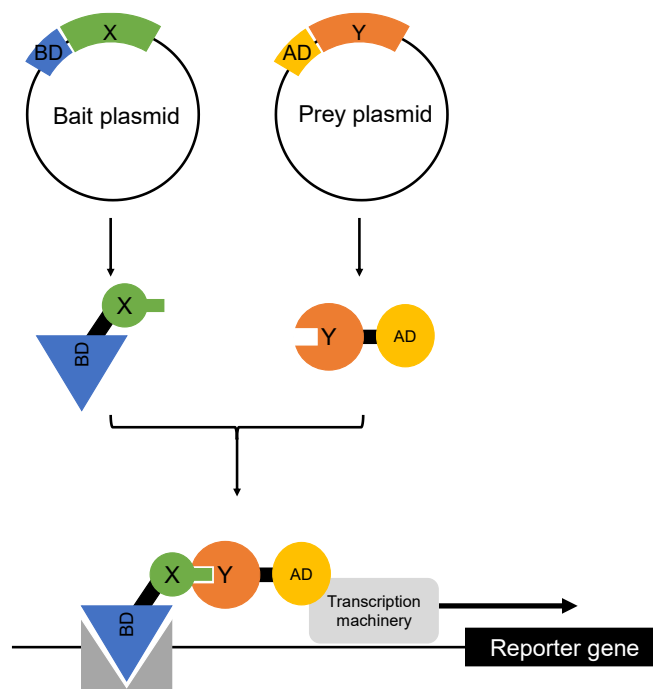


*Figure 29. Schematic of the yeast two-hybrid system (Y2H). The bait plasmid, encoding for a DNA binding domain (BD) and one protein of interest X, and the prey plasmid, encoding for the transcription activating domain (AD) and a second protein of interest Y, were introduced into yeast cells. After protein expression, transcription of a reporter gene is observed if the two proteins X and Y interact.*

More recently, PCAs rely on enzymes and fluorescent proteins, e.g. luciferases or green fluorescent protein (GFP). When they are split into two complementary fragments and are bound to two proteins of interest, the single fragments remain inactive provided that no protein interaction takes place. As soon as the two proteins of interest re-bind, the split enzyme or fluorescent protein re-complements and becomes functional again. In contrast to the Y2H system, the re-complementation can be read directly by fluorescence microscopy or in a microtiter plate format without any further protein biosynthesis.

In this work, a split luciferase complementation assay for the detection of miniG protein recruitment (cf. **chapters 4.3 and 4.5**) or  $\beta$ -arrestin2 recruitment (cf. **chapter 5.3**) was used. It is based on the NanoBiT technology (Dixon et al., **2016**) and utilizes a split NanoLuc, which is an engineered and very small luciferase with exceptional brightness and stability (Hall et al., **2012**). NanoLuc is split into a small 1.3 kDa fragment consisting of 11 amino acids (SmBiT) and a large 18 kDa fragment (LgBiT), which are fused to two proteins of interest. A schematic depiction of the miniG protein recruitment assay is shown in **Figure 30A-G**.

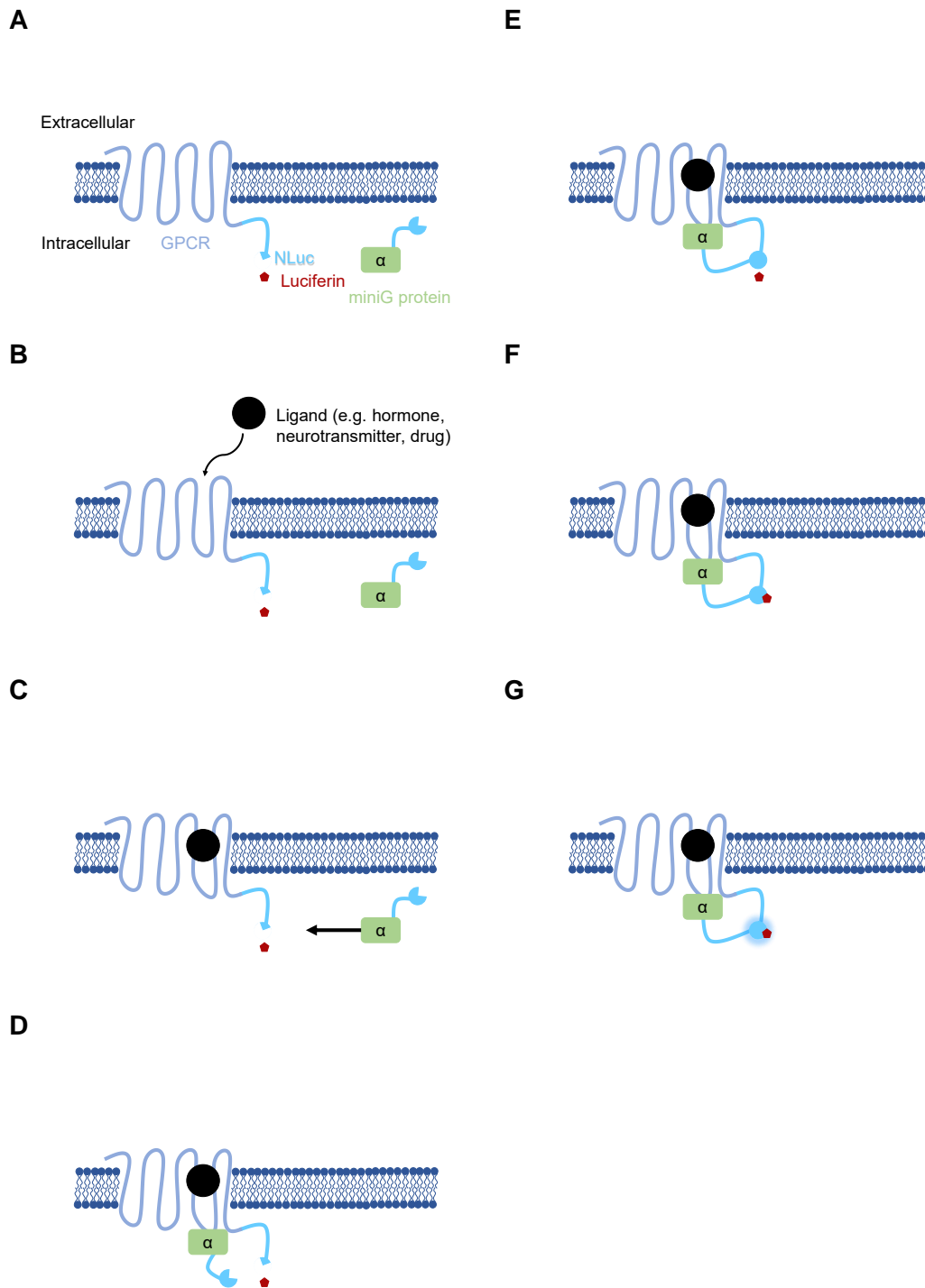


*Figure 30. Schematic of the NanoBiT-based miniG protein recruitment assay. A small NanoLuc fragment (SmBiT) is fused to the C-terminus of the GPCR. The fusion protein is expressed by stable transfection. The complementary NanoLuc fragment (LgBiT) is bound to the respective miniG protein and the fusion protein is also expressed by stable transfection (A). If an agonist ligand binds extracellularly to the GPCR (B), a conformational change takes place at transmembrane helices 5 and 6 (TM5, TM6) of the GPCR and an intracellular signaling cascade is triggered (C). The miniG protein is recruited to the receptor (D) by which the two NanoLuc fragments re-complement (E). NanoLuc becomes fully active again, catalyzing the oxidation of its luciferin (here: coelenterazine h)(F) to create a bioluminescence (G) that is dependent on the ligand concentration.*

With the miniG protein recruitment assay, interactions between the GPCR and the miniG protein are investigated by reading the bioluminescence. SmBiT is fused to the C-terminus of the GPCR, LgBiT is fused to the respective miniG protein and both are expressed by stable transfection (**Figure 30A**). A signaling cascade is started by the binding of a ligand to the extracellular binding site of the GPCR (**Figure 30B**). After conformational changes within transmembrane domains 5 and 6 (TM5, TM6) of the GPCR (**Figure 30C**), the miniG protein is recruited to the receptor intracellularly (**Figure 30D**) (Gurevich, Gurevich, **2017, 2019**). By that, the two NanoLuc fragments re-bind (**Figure 30E**). NanoLuc becomes active again, leading to a reaction with its luciferin (**Figure 30F**). The resulting luminescence (**Figure 30G**) is dependent on the luciferin concentration. Coelenterazine h was used as luciferin. Its oxidation reaction is depicted in **Figure 31**.

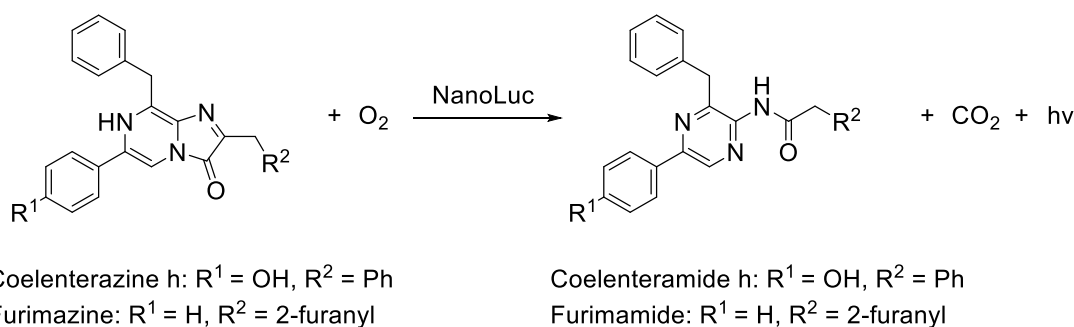


*Figure 31. Reaction of the luciferins coelenterazine h or furimazine with oxygen by catalysis of NanoLuc to coelenteramide h or furimamide, carbon dioxide and light. Coelenterazine h was used in all miniG protein recruitment assays throughout this work and is derived from the luciferin coelenterazine (**Appendix 17**). Furimazine was used in all  $\beta$ -arrestin2 recruitment assays throughout this work and is an engineered substrate for NanoLuc that shows very bright luminescence.*

In the  $\beta$ -arrestin2 recruitment assay, SmBiT is genetically fused to the N-terminus of  $\beta$ -arrestin2 and stably expressed in HEK SmBiT  $\beta$ -Arr.2 cells, whereas LgBiT is bound to the C-terminus of the GPCR, expressed by transient transfection of the respective plasmid DNA (see **chapters 3.2.1 and 3.2.5**). The working principle is similar to the miniG protein recruitment assay (cf. **Figure 30A-G**). After agonist stimulation of the GPCR at the extracellular binding site, an intracellular signaling cascade is triggered, leading to SmBiT-tagged  $\beta$ -arrestin2 recruitment to the GPCR. The re-complemented NanoLuc becomes fully active again and reacts with its substrate (here: furimazine) to create a ligand-dependent bioluminescence. The reaction of furimazine used in the  $\beta$ -arrestin2 recruitment assay is depicted in **Figure 31** as well.

Both luciferins (coelenterazine h and furimazine) get oxidized in the NanoLuc reaction to create the respective amide, carbon dioxide and light with a wavelength of approximately  $\lambda = 450$  nm (**Figure 32**). In contrast to D-luciferin, which is the native

substrate for firefly luciferase, coelenterazine h and furimazine are oxidized in the absence of adenosine triphosphate (ATP) and magnesium ions (cf. **chapter 1.3**).

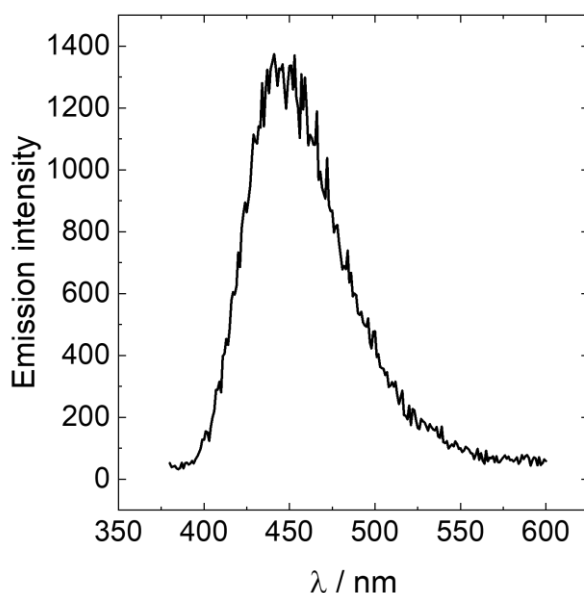


Figure 32. NanoLuc emission spectrum recorded for HEK M1R/ $\beta$ -Arr.2. cells. Furimazine was used as luciferin in a final dilution of 1/600 relative to the stock solution (no molar concentration given by the manufacturer). The cells were stimulated with 100  $\mu$ M carbachol. 1 h after stimulation this spectrum was recorded at the CLARIOstar plate reader (BMG Labtech). The emission maximum is found at a wavelength of  $\lambda = 450$  nm.

### 3.6.1 Workflow at the Luminescence Measurement Devices

For the miniG protein recruitment assay and  $\beta$ -arrestin2 recruitment assay, different workflows were pursued. MiniG protein recruitment was recorded at the Tecan Genios plate reader (Tecan Group AG, **chapter 3.6.1.1**), while  $\beta$ -arrestin2 recruitment was measured with the PHERAstar FS plate reader (BMG Labtech, kindly provided by Prof. Holliday (University of Nottingham, UK), **chapter 3.6.1.2**).

#### 3.6.1.1 Workflow at the Tecan Genios to Measure Agonist-Induced G Protein Activation

In the following, the experimental protocol for the miniG protein recruitment assay at the Tecan Genios plate reader is described. This protocol was modified parameter-wise in later experiments to optimize the luminescence readout.

##### Main Protocol

The cells were subcultivated according to **chapter 3.1.5** and were seeded on a white uncoated 96-well plate with a density of  $3 \cdot 10^5$  c/cm<sup>2</sup>. After 24 h, the medium was

renewed to sustain cell growth and viability. On the day of the experiment, the culture medium was exchanged with 75  $\mu$ L phenol red-free L15 buffer. The cells were equilibrated for 2-2.5 h at 0% (v/v) CO<sub>2</sub> and 37°C. Next, 75  $\mu$ L of 4  $\mu$ M coelenterazine h in L15 were added to the cells (final concentration of 1  $\mu$ M) and a luminescence baseline was recorded for a time interval of 0.15-0.25 h with the software XFLUOR4 version V4.40 at the Tecan Genios device. Subsequently, the measurement was discontinued for ligand addition. 150  $\mu$ L double-concentrated ligand solutions in L15 were added in a 1:1 manner. Another luminescence measurement was started and monitored for 1 h. The duration of the measurements was influenced by the number of wells and was adjusted by altering the number of measurement cycles. The minimal time resolution for one cycle and 96 wells amounts to 56 s. Throughout one measurement, the instrument settings were kept constant. An overview of the instrument settings is given in **Table 10**.

*Table 10. Measurement parameters set at the Tecan Genios plate reader (Tecan Group AG) for the main protocol of the miniG protein recruitment assay.*

Parameter	Main protocol
<b>Measurement mode</b>	Luminescence (no emission filter slide) Top read
<b>Integration time</b>	100 ms
<b>Gain</b>	150
<b>Plate definition</b>	96-well, white, F-bottom
<b>Temperature</b>	37°C
<b>Number of wells</b>	According to experiment
<b>Number of cycles</b>	According to experiment Usually resulting in 0.15-0.25 h for baseline Usually resulting in 1 h for ligand addition

### Optimization of the Luminescence Readout

Different influences on the luminescence signal were investigated in additional experiments. The impact of plate coatings and plate color (**chapter 4.5.1**), the integration time and gain (**chapter 4.5.2**), the coelenterazine h concentration (**chapter 4.5.3**), the cell density (**chapter 4.5.4**), an additional washing step (**chapter 4.5.5**), coelenterazine h aging (**chapter 4.5.6**) and the measurement buffer (**chapter 4.5.7**) was tested.

#### Plate Coatings and Plate Color

As described in **chapter 3.3.2**, different coatings were studied on 96-well plates with different colors. In particular, plates incubated with serum-containing medium were

compared to gelatin and crosslinked gelatin-coated plates. Either transparent, white or black 96-well plates were used (cf. **chapter 3.3.1**).

#### Integration Time

The integration time defines the time span during which a signal (here luminescence) is measured and integrated. It was varied between 100 ms, 250 ms, 500 ms and 1000 ms. Signal-to-noise (S/N) ratios were determined to find the optimal integration time. This study was combined with the optimization of the gain (see below).

#### Gain

The gain is an amplification factor describing the extent to which a signal (here luminescence) is enhanced. The gain was varied between 100, 150, 200 and 250. S/N ratios were determined to find the optimal gain. This study was combined with the optimization of the integration time (see above).

#### Coelenterazine h Concentration

Since luminescence signals and kinetics might be influenced by the coelenterazine h concentration, final concentrations of 0.5  $\mu\text{M}$ , 1  $\mu\text{M}$ , 1.5  $\mu\text{M}$  and 2  $\mu\text{M}$  coelenterazine h were tested. S/N ratios were determined to find the optimal coelenterazine h concentration.

#### Cell Density

The impact of different cell numbers on the luminescence signal was compared by seeding the cells with a density of  $3 \cdot 10^5$  c/cm<sup>2</sup> on three white 96-well plates and letting them grow for one, two (control conditions) or three days. A medium exchange took place every day.

#### Additional Washing Step

Whereas the cells are routinely cultured in phenol red-containing medium, the luminescence measurements took place in phenol red-free L15 buffer. The influence of phenol red remnants was investigated by introducing an additional washing step before cell equilibration.

#### Coelenterazine h Aging

It is known that luciferins are readily oxidized in the absence of their luciferases (Jiang et al., **2016**, Kaskova et al., **2016**, Nakajima et al., **2021**). Furthermore, luciferins are light- and temperature-sensitive reagents. Therefore, a coelenterazine h aging study

was performed. Four differently treated coelenterazine h solutions were prepared and compared in the miniG protein recruitment assay.

- (1) **Control**: the solution was freshly prepared on the day of the experiment and was stored at 4°C in the dark until use
- (2) **Three warm-cold-cycles**: the solution was prepared on the day of the experiment but underwent heating-up to 37°C and cooling down to 4°C in 5 min intervals three times, respectively
- (3) **4°C dark**: the solution was prepared one day before the experiment and was kept at 4°C protected from light until use
- (4) **r.t. illuminated**: the solution was prepared one day before the experiment and was kept at r.t. not protected from light until use

By repeated heating and cooling, the temperature stability of coelenterazine h was tested. By preparation of the solutions one day before the experiment, the influence of a prolonged oxidation and hydrolysis time was investigated and by storing the coelenterazine h solution at r.t. without any protection from light, the temperature and light sensitivity were tested. The results were compared to a freshly prepared solution that was stored at 4°C in the dark until use.

#### Buffer

The impact of three different measurement buffers on bioluminescence was investigated. L15 buffer was compared with PBS and HBSS. None of the buffers contains phenol red but their formulations vary (see **chapter 3.1.4**). Coelenterazine h and all ligands were diluted in the respective buffers.

#### [3.6.1.2 Workflow at the PHERAstar FS to measure Agonist-Induced \$\beta\$ -Arrestin2 Recruitment](#)

In the following, the experimental protocol for the  $\beta$ -arrestin2 recruitment assay at the PHERAstar FS plate reader is described. After transiently transfecting HEK SmBiT  $\beta$ -Arr.2 cells according to **chapter 3.2.5**, they were seeded on a white poly-D-lysine coated 96-well plate with a density of  $1.18 \cdot 10^5$  c/cm<sup>2</sup>. Cell cultures were incubated in a humidified incubator (37°C, 5% (v/v) CO<sub>2</sub>) for 24 h. The NanoBiT assay was performed at the PHERAstar FS device (BMG Labtech). First, the plate was washed once with 50  $\mu$ L HBS containing 0.1% (w/v) bovine serum albumin (BSA), which were replaced with 40  $\mu$ L HBS with 0.1% (w/v) BSA. After 0.17 h equilibration time at 37°C

inside the device, 10  $\mu$ L furimazine (1/100 in HBS with 0.1% (w/v) BSA; no molar concentration of the stock solution is given by the manufacturer) were added to each well. After 0.08 h, a baseline measurement was started. Three cycles with a time resolution of 2 min (96-well plate) were measured. Subsequently, 10  $\mu$ L of 6-fold concentrated ligand solutions were added with a multichannel pipette, resulting in a final furimazine dilution of 1/600. Another 19 or 32 cycles were recorded, resulting in a total measurement time of 0.5 h or 1 h. An overview of the instrument settings is given in **Table 11**.

*Table 11. Measurement parameters set at the PHERAstar plate reader (BMG Labtech) for the  $\beta$ -arrestin2 recruitment assay.*

Parameter	Main protocol
Measurement mode	Luminescence Top read
Integration time	1 s
Gain	3600
Plate definition	96-well, white, F-bottom
Temperature	37°C
Number of wells	96
Number of cycles	19 or 32 (first 3 cycles: baseline measurement)
Time resolution	2 min per cycle

In the case of investigating antagonists, the cells were equilibrated in 40  $\mu$ L HBS with 0.1% (w/v) BSA containing antagonist (1.5-fold concentration) for 0.25-0.33 h. Thereafter, 10  $\mu$ L of furimazine (1/100 in HBS with 0.1% (w/v) BSA) were added and the cells were incubated for 5 min. A luminescence baseline was recorded as described above. Finally, 10  $\mu$ L of 6-fold concentrated ligand solution were added and luminescence was monitored for 19 or 32 cycles.

### 3.6.2 Luminescence Data Analysis and Representation

#### 3.6.2.1 Tecan Genios Data

All measurements performed at the Tecan Genios are discontinuous measurements, i.e. between the baseline measurement and the measurement of receptor stimulation the reading is paused for ligand addition outside the plate reader. In later figures, the curves for the baseline and stimulation measurement are connected by a line plot. The delay in time between subsequent measurements was always factored in.

### Baseline Values

Since HEK cells are poorly adhering and quickly detach from the substrate surface during medium exchange (Faussner et al., **2022**, Jayakumar, J. A. K. J. et al., **2020**), the luminescence baseline values were expected to vary between experiments. Furthermore, an altered intrinsic activity or protein expression of NanoLuc, the receptor or the miniG protein may lead to changes in the basal luminescence. For better comparison between experiments, baseline luminescence values were calculated from the non-normalized luminescence raw data. For each experiment and each condition, a mean baseline value was determined by averaging 11 raw data points before compound addition. The averaged baseline values are given in the captions of the figures and the continuous text. The impact of different assay parameters on the basal luminescence is investigated in **chapter 4.5**.

### Smoothing and Normalization of Luminescence Values

Since the raw data obtained from measurements at the Tecan Genios was quite noisy, it was first smoothed by an *unweighted moving average* with a window size of three. Considering the first three measured luminescence values (first window), the respective averaged value was calculated, resulting in the first smoothed value. By shifting the window forward value by value and repeating the calculation of the average luminescence, a smoothed curve was received.

After smoothing the data, it was normalized to the time point of ligand addition as described for impedance (cf. **chapter 3.5.4**). In short, the time point of substance addition was subtracted from all other time points. Furthermore, the luminescence value at the time point of substance addition was subtracted from all measured luminescence values. This was repeated for every well and yields  $\Delta BL$  values given in bioluminescence units (BLU). Hereafter, the average change of bioluminescence  $\Delta BL_{mean}$  was calculated for equally treated wells. The following equations were used:

$$\Delta BL_{mean} = \frac{1}{n} \sum_{i=1}^n \Delta BL_i \quad (17)$$

$$SD = \sum_{i=1}^n \sqrt{\frac{(\Delta BL_i - \Delta BL_{mean})^2}{n-1}} \quad (18)$$

$$SE = \frac{SD}{\sqrt{n}} = \sum_{i=1}^n \sqrt{\frac{(\Delta BL_i - \Delta BL_{mean})^2}{n(n-1)}} \quad (19)$$

$n$  represents the number of replicates per experiment, SD is the standard deviation and SE (also SEM) describes the standard error of the mean. Usually,  $\Delta BL_{mean} + SE$  was plotted against the time to obtain the luminescence time courses. In the case of averaging multiple experiments, Gaussian error propagation was applied. By analogy with the impedance data (cf. **chapter 3.5.4**),  $N$  represents the total number of replicates and is given in the figure captions.

### Concentration-Response Curves

Instead of evaluating the AUC or maximum of luminescence, a time point of  $t = 0.5$  h was chosen for concentration-response analysis. Indeed, all three data evaluation techniques deliver similar results as shown in **Appendix 18**. However, the analysis of the time point  $t = 0.5$  h is very simple and enables a comparison of impedance and luminescence data for cells in a similar state. This is particularly important for the combination of both measurement techniques in a dual setup where both impedance and luminescence are measured simultaneously for one cell population (cf. **chapter 4.6**).

To generate concentration-response curves, the  $\Delta BL_{\text{mean}}$  values 0.5 h after stimulation were extracted and plotted against the logarithmic ligand concentration. By fitting the curve with a four-parametric dose-response fit (see **equation 15**), potencies (pEC50 values) and efficacies ( $E_{\text{max}}$  values, i.e. upper asymptote) were obtained. The data was weighted instrumentally using the weighing factor  $\omega_i = \frac{1}{\sigma_i^2}$ . Thereby,  $\sigma_i$  represents the SE of one data point. The vehicle control (CTRL) was always set to a defined value of  $\log(c/M) = -20$ .

### Signal-to-Noise Ratios and Statistical Significance

A useful quantity to characterize the quality of the luminescence readout is the signal-to-noise (S/N) ratio. It was used to find the optimal measurement parameters and compare the different assay conditions. To calculate S/N ratios, non-normalized data was used. For each well, the averaged baseline value  $\pm SD_{\text{Baseline}}$  and the maximum luminescence value  $\text{max}_{\text{Stim}}$  of the stimulation measurement were determined. By division, the S/N is calculated:

$$\frac{S}{N} = \frac{\text{max}_{\text{Stim}}}{SD_{\text{Baseline}}} \quad (20)$$

The S/N ratios for wells that were treated equally were averaged and plotted with their standard errors SE (see above) to generate bar charts. Statistical significance (\*) was assessed with Tukey's range test. Thereby, the p-value is a measure of the probability that the null hypothesis ( $H_0$ ) is rejected (\*  $p \leq 0.05$ , \*\*  $p \leq 0.01$ , \*\*\*  $p \leq 0.001$ ). The  $H_0$  states that the compared means are the same.

#### 3.6.2.2 PHERAstar FS Data

##### Baseline Values

In analogy to the Tecan Genios data analysis protocol described in **chapter 3.6.2.1**, the baseline luminescence of the PHERAstar FS data was calculated. The raw data

points of the first three cycles (baseline measurement) were averaged to compare fluctuations in the protein expression and intrinsic activity between experiments.

### Normalization of Luminescence Values

To obtain luminescence time courses, the raw data of bioluminescence was not smoothed but normalized as described for the Tecan Genios data in **chapter 3.6.2.1**. Smoothing was not necessary because the data was less noisy compared to the Tecan Genios data. The normalized data was averaged according to **equations 17-19**.

### Concentration-Response Curves

To generate concentration-response curves, the luminescence values 0.5 h after stimulation (cycle 19) relative to the response of a reference ligand were plotted against the logarithmic ligand concentration. The luminescence value of the vehicle control (CTRL; HBS with 0.1% (w/v) BSA) was set to 0%, while the value of the reference ligand was set to 100%. The obtained  $R_{\max}$  (relative  $E_{\max}$ ) values allow a relative comparison between the effects of different ligands. A four-parametric dose-response fit was applied (**equation 15**) with the vehicle control taking a value of  $\log(c/M) = -20$ . The data was weighted instrumentally using the weighing factor  $\omega_i = \frac{1}{\sigma_i^2}$ . Thereby,  $\sigma_i$  represents the SD of one data point. In the case of averaging concentration-response curves, Gaussian error propagation was applied. Mean  $pEC_{50}$  and  $R_{\max}$  values were extracted. N represents the number of replicates given in the figure captions.

### Schild Analysis

If antagonist assays were evaluated, the antagonists were generally treated as competitive and surmountable antagonists. Accordingly,  $R_{\max}$  was fixed and set to 100%. From the obtained  $pEC_{50}$  values in presence of different antagonist concentrations, Schild plots were generated. First, the identified  $pEC_{50}$  values were transferred into the respective  $EC_{50}$  values. By dividing the  $EC_{50}$  values in the presence of  $x \frac{mol}{L}$  antagonist by the  $EC_{50}$  value in the absence of the antagonist, dose ratios  $DR_x$  were calculated.

$$DR_x = \frac{EC_{50}(\text{in presence of } x \frac{mol}{L} \text{ antagonist})}{EC_{50}(\text{in absence of antagonist})} \quad (21)$$

The dose ratios were converted into logarithmic values to obtain a linear relationship between the  $\log(DR_x - 1)$  and the logarithm of the molar antagonist concentration  $\log x$ .

By linear regression of the Schild plot, the antagonist affinity ( $pK_B$  or  $K_B$ ) was determined from the x-intercept as depicted in **Figure 33**.

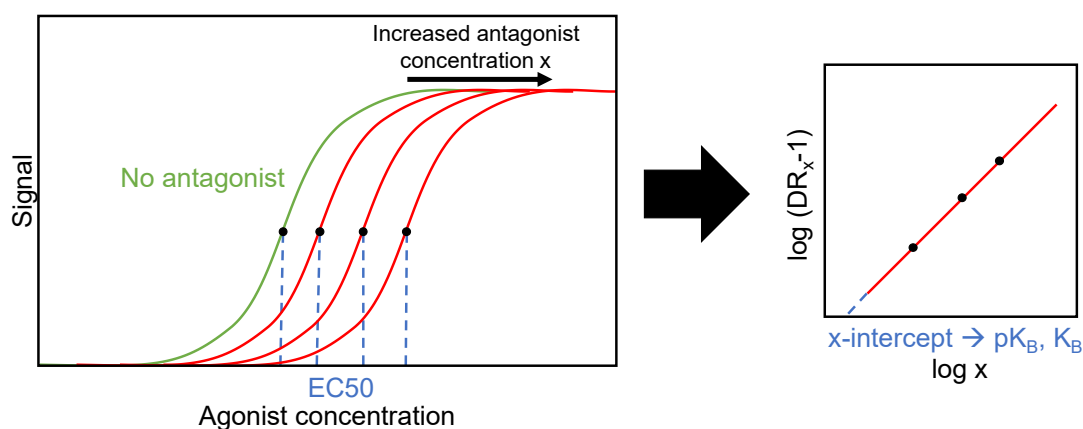
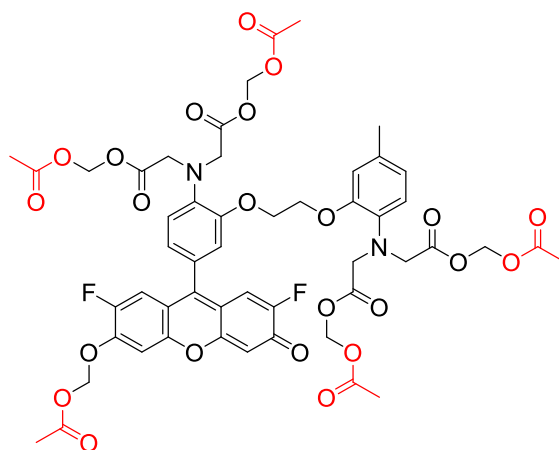


*Figure 33. Depiction of Schild analysis. The concentration-response curves (left) in the presence of different antagonist concentrations  $x$  are evaluated. From the  $EC_{50}$  values, dose ratios  $DR_x = \frac{EC_{50}(\text{in presence of } x \frac{\text{mol}}{\text{L}} \text{ antagonist})}{EC_{50}(\text{in absence of antagonist})}$  are calculated. If the  $\log(DR_x - 1)$  is plotted against the logarithmic antagonist concentration  $\log x$ , Schild plots (right) are generated. From the x-intercept, the antagonist affinity  $pK_B$  or  $K_B$  is determined.*

### 3.7 Calcium Second Messenger Assay

Intracellular calcium  $Ca^{2+}$  is a second messenger for GPCR signaling. It is well known that calcium is correlated to  $G_q$ -coupling, where it is released from the endoplasmic reticulum by  $IP_3$ . The intracellular calcium ion concentration can rise to  $100 \mu\text{M}$  (Liu et al., **2010**). However, an increase in calcium levels can also be initiated by other pathways or downstream processes (Ma et al., **2017**).

There are different possibilities to investigate the calcium ion mobilization after GPCR stimulation in whole cells. The most prominent ones rely on calcium-sensitive fluorescent dyes such as Fura-2, Fluo-3, Fluo-4 and FLIPR assays (cf. **chapter 1.2.3**) (Guo et al., **2022**). But there are also bioluminescence-based assays like the AequoScreen assay (Thomsen et al., **2005**). With all those assays, the rather transient calcium ion signal can be monitored kinetically with a plate reader or can be resolved spatially and temporally by fluorescence microscopy. In most fluorescence-based calcium assays, the dyes are first present in their acetoxymethyl ester (AM) form. They are readily membrane-permeable and, thus, can easily enter intact cells. After cleavage of the ester bond by cytosolic esterases, the dye becomes membrane impermeable and is trapped inside the cells (**Figure 34**). If intracellular calcium levels are elevated, the dye either changes its spectral properties (excitation and emission wavelengths, fluorescence intensity) or it starts to fluoresce since calcium binds to it (Ma et al., **2017**).



Fluo-4 AM

Figure 34. Structure of fluo-4 AM. This fluorescent dye is commonly used for calcium ion assays. It is depicted in its acetoxymethyl ester (AM) form and can easily enter cells via the plasma membrane. As soon as endogenous esterases cleave the ester bonds (here indicated in red), the dye becomes membrane impermeable. It specifically binds calcium ions and, hence, increases its fluorescence at 516 nm.

In this work, a fluo-4 assay was utilized to test the calcium ion mobilization of different GPCRs in whole cells. An Invitrogen assay kit was used. The execution and analysis of the fluo-4 assay will be described in the following chapters.

### 3.7.1 Workflow at the Flexstation 3 to Measure Agonist-Induced Calcium Mobilization by Fluorescence

The cells of interest were seeded on black poly-D-lysine coated 96-well plates with a density of  $1.18 \cdot 10^5$  c/cm<sup>2</sup> and were grown to 80-90% confluency overnight in a humidified incubator (37°C, 5% (v/v) CO<sub>2</sub>). The next day, the calcium assay was performed. The seeding medium was aspirated and replaced with 100 µL of 1.5 µM fluo-4 AM dye for (45 ± 5) min. The plate was washed once with 100 µL HBS containing 0.1% (w/v) BSA and 2.5 mM probenecid. Probenecid is an organic anion-transport inhibitor and prevents the leakage of the de-esterification product of fluo-4 AM. Subsequently, the wells were loaded with 100 µL HBS with 0.1% (w/v) BSA and probenecid. After an equilibration time of 10-20 min inside the preheated device (Flexstation 3, Invitrogen) and a 15 s baseline recording, 20 µL of 6-fold concentrated ligand solution in assay buffer were added automatically by the device to allow for fast data acquisition of the transient calcium signal. The cells were stimulated column by column resulting in a total measurement time of 105 s per column and a time resolution of 1.6 s. The measurement parameters are given in **Table 12**. The data was recorded and extracted with the SoftMax Pro 7.1 software (Invitrogen).

Table 12. Measurement parameters set at the Flexstation 3 plate reader (Invitrogen) for the fluo-4 assay detecting calcium mobilization.

Parameter	Fluo-4 Assay Settings
Measurement mode	Fluorescence, Flex
Excitation wavelength $\lambda_{exc}$	485 nm (6 flashes)
Emission wavelength $\lambda_{em}$	525 nm
Gain	High
Flashes per read	6
Plate definition	96-well, black, F-bottom clear
Temperature	37°C
Number of cycles	66
Time resolution	1.6 s
Measurement Time per Column	105 s (including 15 s baseline)

The composition of the loading and washing/assay buffer is given in **Table 13**. If not already available, a 50  $\mu\text{g}$  aliquot of fluo-4 AM was dissolved in 25  $\mu\text{L}$  DMSO and 50  $\mu\text{L}$  of 20% (w/v) pluronic F-127. Pluronic F-127 is a non-ionic surfactant and serves as a dispersing reagent for the nonpolar fluo-4 AM dye in aqueous solution.

Table 13. Composition of loading medium and washing/assay buffer for the fluo-4 calcium ion assay.

Loading Medium	Washing / Assay Buffer
DMEM + 10% (v/v) FBS	HBS
+ 1.5 $\mu\text{M}$ Fluo-4 AM	+ 0.1% (w/v) BSA
+ 2.5 mM Probenecid	+ 2.5 mM Probenecid

### 3.7.2 Fluorescence Data Analysis and Representation

#### Normalization of Fluorescence Values

The fluorescence raw data at  $\lambda_{em} = 525$  nm was normalized to the first measured time point, i.e. the fluorescence data at the time point before ligand addition was subtracted from all other fluorescence data points (for each well). This yields the change of fluorescence  $\Delta F$  in fluorescence units (FLU). After averaging  $\Delta F$  for equally treated wells according to **equations 17-19**,  $\Delta F_{mean} + SE$  was plotted against the time. In the case of averaging multiple experiments, Gaussian error propagation was applied.  $N$  represents the number of replicates.

#### Concentration-Response Curves

To generate concentration-response curves, the maximum  $\Delta F_{mean}$  value relative to the maximum  $\Delta F_{mean}$  value of a reference agonist is plotted against the logarithm of the ligand concentration. Thereby, the vehicle control (CTRL) was set to a defined

fluorescence value of 0% and  $\log(c/M) = -20$ , while the fluorescence value of the reference agonist was set to 100%. After fitting with a four-parametric dose-response fit (see **equation 15**), pEC50 and  $R_{\max}$  (relative  $E_{\max}$ ) values were determined. The data was weighted instrumentally using the weighing factor  $\omega_i = \frac{1}{\sigma_i^2}$ . Thereby,  $\sigma_i$  represents the SD of one data point.

### 3.8 Setup for Simultaneous Measurements of Luminescence and Impedance

In this work, the ECIS method (see **chapter 3.5.2**) was combined with the miniG protein recruitment assay based on a luminescence readout (see **chapter 3.6**). A novel setup for monitoring the impedance and luminescence of one single cell population in parallel was developed. First, it was necessary to connect a common 96W1E+ array (Applied BioPhysics) to the impedance analyzer to enable a simultaneous impedance and luminescence measurement inside the Tecan Genios plate reader (Tecan Group AG). Two measurement methods were developed referred to as *manual* and *circuit board contacting*.

#### Manual Contacting

The contact pads on the bottom of a sterilized and tightly closed 96W1E+ array were manually contacted with copper wires and silver conductive paint to two RS232 connectors (**Figure 35**). The length of the wires varied between 60-80 cm depending on the wells contacted. If wells in the upper rows were contacted, longer wires were chosen to facilitate free movement of the plate inside the plate reader without the risk of the cables getting caught inside the device. To ensure high conductivity, silver conductive paint was applied on the contacts. The wires were secured properly using adhesive tape. In total, a maximum of 16 wells (8 per RS232 connector) was contacted, not including the two counter electrodes. The electrical connections were tested with a multimeter.

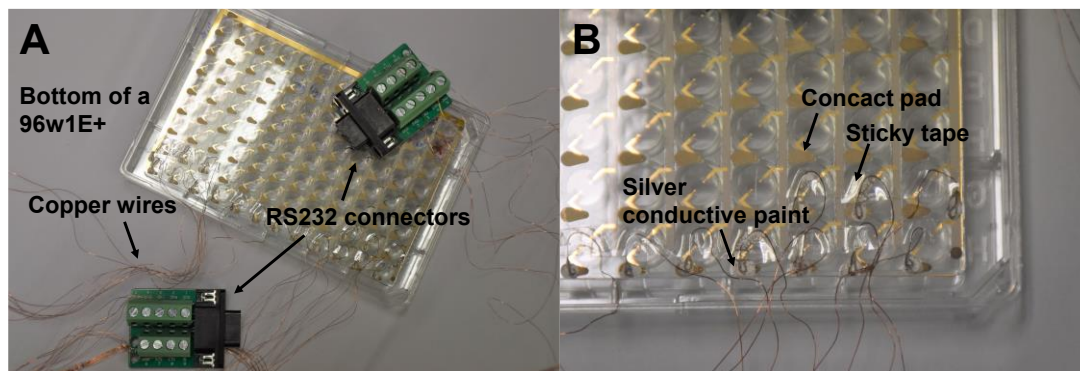


Figure 35. 96W1E+ array manually connected to two electric RS232 connectors using copper wires, silver conductive paint and sticky tape. In total, 16 wells can be contacted, not including the two counter electrodes. The silver conductive paint increases electric conductivity. The sticky tape ensures a constant position of the wires. B is a magnification of A.

To start a measurement, the array was placed inside the holder of the luminescence plate reader with the cables pointing out of the device. The plugs were connected to an impedance analyzer. Then, simultaneous luminescence and impedance measurements could be started.

### Circuit Board Contacting

For circuit board contacting of 96W1E+ arrays, four different circuit boards were designed and manufactured in cooperation with the electronics workshop (University of Regensburg). With each of the circuit boards, 16 different wells could be contacted, simply by placing the 96-well plate on top of the circuit board. The plate was fixed by mounting clamps on each side of the plate. The setup is shown in **Figure 36**.

Each circuit board possesses 24 spring contacts in two rows that align with the contact pads of a standardized 96W1E+ array. 16 of those spring contacts were connected at once to two RS232 connectors with copper wires (**Figure 36A**). The wires were soldered on the spring contacts (**Figure 36B**). For contacting the two counter electrodes, two additional spring contacts were added at the edges of the circuit boards (in alignment with the respective contact pads). With each of the circuit boards, 16 wells could be measured:

- Circuit board A/C: wells A1-8 and C1-8
- Circuit board B/D: wells B1-8 and D1-8
- Circuit board E/G: wells E1-8 and G2-9
- Circuit board F/H: wells F1-12 and H1-4

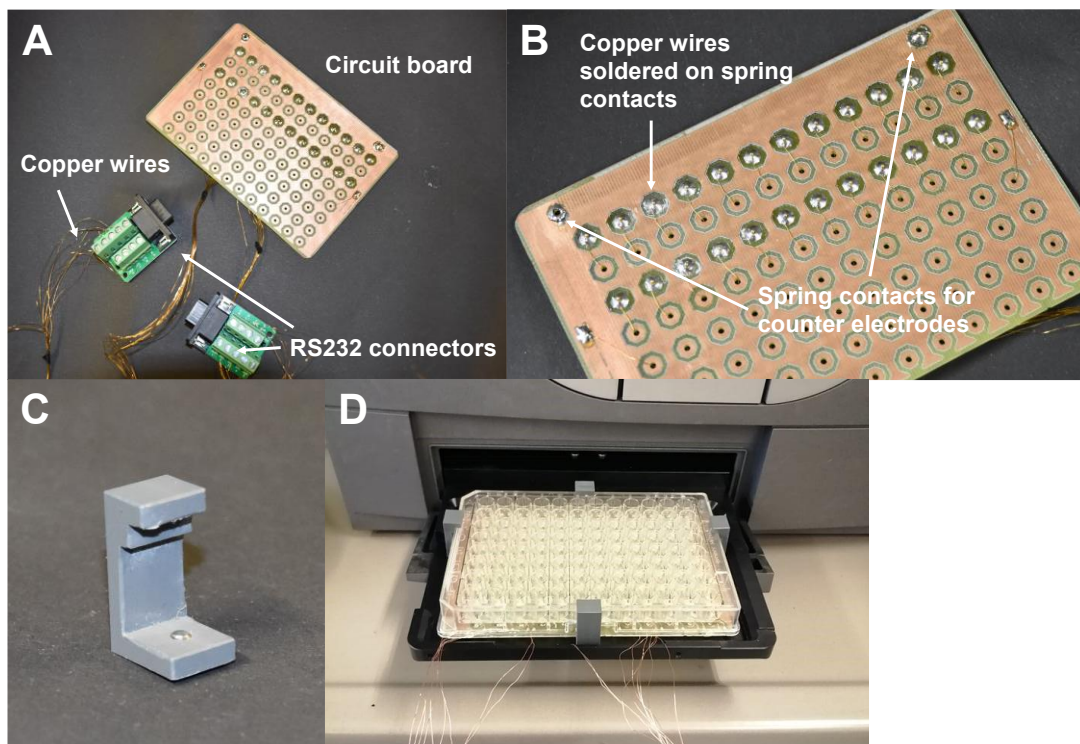


*Figure 36. One of the four circuit boards for contacting a 96W1E+ array to an impedance analyzer (A,B). Clamp for mounting a 96W1E+ array to the circuit boards (C). A 96W1E+ array contacted to an impedance analyzer using one circuit board (D). The contacted array is placed inside the Tecan Genios plate holder with the cables pointing out of the device.*

To start a measurement, the 96W1E+ array was placed on top of the circuit board, the lid was taken off and the plate was mounted to the circuit board by using four clamps designed and manufactured together with the mechanics workshop (University of Regensburg) (**Figure 36C**). The clamps were secured by tightening up a small screw at their bottom side. The plate was placed inside the luminescence plate holder with the wires pointing out of the device and the RS232 plugs were connected to the impedance analyzer (**Figure 36D**).

In the case of one spring contact becoming fully inoperable, a different spring contact of the two indicated rows was used instead. In total, the four circuit boards allowed the measurement of 64 wells of one 96W1E+ plate in four consecutive experiments.

For reading the cells' luminescence, a Tecan Genios plate reader (Tecan Group AG) was used that is placed close to the impedance setup to prevent contact loss due to the limited length of the copper wires. The complete dual luminescence-impedance setup is depicted in **Figure 37**.

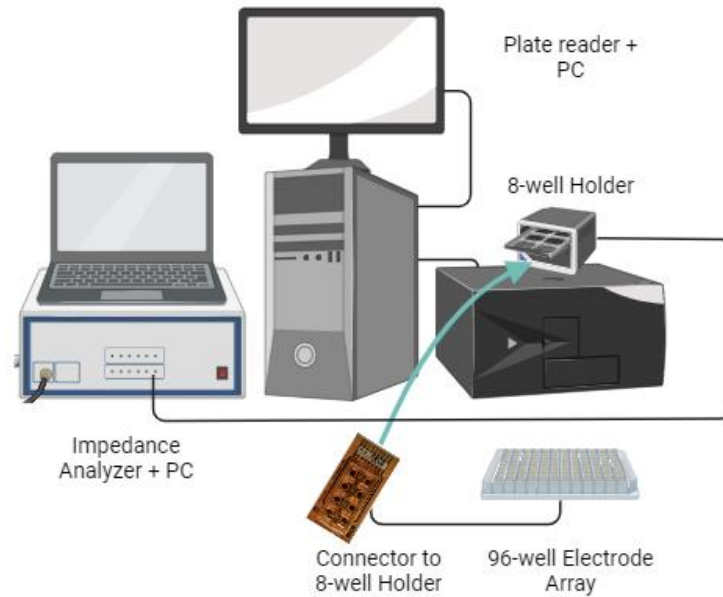


*Figure 37. Setup for dual luminescence-impedance measurements. For monitoring the impedance, the electrode array is connected to an impedance analyzer (ECIS Z, Applied BioPhysics) via an 8-well holder (Applied BioPhysics) either by manual or circuit board contacting. The impedance is measured with the help of the ECIS software (Applied BioPhysics) and monitored on a laptop. To simultaneously measure luminescence, a plate reader (Tecan Genios, Tecan Group AG) is necessary. It is connected to another computer that records the luminescence with the XFLUOR4 software (version V4.40). The figure was created with biorender.com.*

### 3.8.1 Workflow for Simultaneous Measurements of Luminescence and Impedance

HEK cells expressing the NanoBiT technology for the detection of miniG protein recruitment were seeded in a density of  $3 \cdot 10^5$  c/cm<sup>2</sup> on sterile gelatin or crosslinked gelatin-coated transparent 96W1E+ arrays. In the case of manual contacting, 16 wells per 96W1E+ array were seeded. If circuit board contacting was the method of choice, only the wells that were contacted with the respective circuit board(s) were filled with cell suspension. One day after seeding, the medium was exchanged to ensure cellular viability and growth. On the next day, the dual luminescence-impedance experiment was performed. First, the growth medium was exchanged with 75  $\mu$ L L15 buffer and the spaces between the wells were filled with sterile water to prevent the wells from drying out inside the plate reader. The cells were equilibrated at 0% (v/v) CO<sub>2</sub> and 37°C inside a humidified incubator for 2 h. Afterward, the 96W1E+ array was connected to the impedance analyzer either by manual or circuit board contacting and an impedance baseline was recorded for 0.5 h inside the preheated plate reader (37°C, Tecan Genios). In the case of circuit board contacting, the array was covered with aluminum foil to prevent evaporation of liquid inside the preheated device since the lid was removed. After recording an impedance baseline, the 96-well plate was

moved out of the device (without stopping the baseline measurement of impedance) and 75  $\mu\text{L}$  4  $\mu\text{M}$  coelenterazine h in L15 were added in a 1:1 ratio. A baseline measurement of luminescence was started in parallel to the on-going impedance measurement for 0.15-0.25 h. Thereafter, the plate was moved out again (without stopping the impedance measurement) and 150  $\mu\text{L}$  double-concentrated ligand solution in L15 was added in a 1:1 manner, yielding a final coelenterazine h concentration of 1  $\mu\text{M}$ . A second luminescence recording was started while impedance was recorded continuously. After 1 h, both measurements were stopped. In general, impedance was measured in SFT-mode ( $f = 12$  kHz) at the ECIS Z device. Here, the time resolution for 16 wells amounts to approximately 16 s. For luminescence, the parameters are similar as described in **chapter 3.6.1.1** but the plate setting was adjusted to transparent 96-well plates. The cycle and well number, both influencing time resolution, were adapted individually to reach the indicated measurement times (0.15-0.25 h baseline, 1 h stimulation). Since it is not possible to choose separate wells with the XFLUOR4 software, usually more than the desired wells were measured. The time resolution for the measurement of 8 neighboring wells in the luminescence setup amounts to approximately 15 s. The minimal time resolution for the measurement of 16 wells (usually this includes the measurement of several undesired wells) ranges between 20-30 s.

### 3.8.2 Analysis and Representation of Simultaneously Recorded Luminescence and Impedance Data

The impedance and luminescence data were analyzed as described in the **chapters 3.5.4 and 3.6.2.1**, respectively. In brief, the luminescence raw data was smoothed and the changes in impedance and luminescence were calculated ( $\Delta|Z|$ ,  $\Delta\text{BL}$ ), averaged and plotted against the time. Concentration-response curves were generated by extraction of the values at  $t = 0.5$  h and plotting them against the logarithm of the ligand concentration (vehicle control (CTRL):  $\log(c/M) = -20$ ). The data was fitted with a four-parametric dose-response fit (see **equation 15**) to calculate  $\text{pEC}_{50}$  and  $E_{\text{max}}$  values (i.e. upper asymptote values). In addition, for the simultaneous luminescence-impedance measurements, the two impedance and luminescence data sets were correlated in different plots shortly explained in the following.

To gain a deeper understanding of the kinetic correlations, the non-averaged time courses for the change of impedance and luminescence for every ligand concentration were plotted in one graph with two y-axes ( $\Delta|Z|$  and  $\Delta\text{BL}$ ). The x-axis,

corresponding to the time scale, is the same for both parameters. Furthermore, the non-averaged  $\Delta Z$  and  $\Delta BL$  curves were analyzed in three ways. Firstly, the values at time point  $t = 0.5$  h were determined and averaged for each concentration. Secondly, the AUC for a time interval between  $t = 0-0.75$  h was calculated for every single curve and the values were averaged for each concentration. Thirdly, the signal maxima were determined and averaged for each concentration. These calculations were done with the impedance and luminescence data independently. Finally, the impedance values were plotted against the corresponding luminescence values (e.g. AUC of impedance vs. AUC of luminescence) to determine if both parameters are dependent on each other and to find a potential correlation between impedance and luminescence. To quantify how well the data correlates, Spearman correlation coefficients  $r_s$  were calculated. They indicate to what extent two data sets correlate monotonically in a non-linear way. The Spearman  $r_s$  takes values of  $-1 < r_s < 1$  and is calculated with the help of the following formula:

$$r_s = 1 - 6 \sum \frac{d^2}{N(N^2-1)} \quad (22)$$

with  $d$  being the difference of the ranks of the two compared parameters (here impedance and luminescence).  $N$  is equal to the number of data points. If  $r_s > 0$ , both parameters correlate in a positive fashion. This implicates an increase in  $y$  for an increase in  $x$ . If  $r_s < 0$ , the opposite is true and one parameter increases while the other one decreases. If  $r_s$  is close to zero ( $r_s \sim 0$ ) no correlation is observed. The closer  $r_s$  is to  $\pm 1$ , the stronger and more reliable is the monotone, non-linear correlation.

## 4 Development and Optimization of a Setup for the Simultaneous Measurement of Luminescence and Impedance of One Cell Population

G protein-coupled receptors (GPCR) are of crucial importance in biological and medical research (cf. **chapter 1.1**). They play a major role in several pathophysiological processes and diseases like metabolic and immunological disorders (Sloop et al., **2018**), neurodegenerative diseases (Huang et al., **2017**), cardiovascular diseases or cancer (Nieto Gutierrez, McDonald, **2018**), which is the reason why they are relevant targets for more than a third of all FDA-approved drugs. However, these drugs only target about 100 of the 800 human GPCRs (Peterson et al., **2023**). The yet untargeted GPCRs are important therapeutic targets in the future to further expand the repertoire of medical interventions. To identify new drug targets, ligand libraries are screened with cell-based assays, molecular docking studies and biomolecular assays (Kumari et al., **2015**). Cell-based functional assays are often performed as endpoint assays, i.e. the signaling dynamics and kinetics are not taken into account, which might lead to a misunderstanding and misinterpretation of molecular processes. Accordingly, more attention should be given to time-resolved assays, where the cellular behavior can be followed continuously over time.

The aim of this chapter was to combine two rather different functional assays in a novel setup to investigate the signaling patterns of different GPCRs with both readouts simultaneously. Impedance and luminescence-based minimal G protein (miniG, mG) recruitment were measured simultaneously for one cell population. Both techniques deliver different pieces of information and in combination help to better understand the activation profile of GPCRs. The focus was on the muscarinic acetylcholine receptors 1 and 5 (M1R, M5R), which canonically couple to G<sub>q</sub>-proteins, and the histamine 2 receptor (H2R) favoring the G<sub>s</sub>-pathway (see **chapter 3.1.3**). All GPCRs under test were solely expressed in human embryonic kidney (HEK) cells (HEK M1R/mG<sub>q</sub>, HEK M5R/mG<sub>q</sub>, HEK H2R/mG<sub>s</sub>, **chapter 3.1.2**). Iperoxo, carbachol (M1R, M5R) and histamine (H2R) were utilized as agonistic ligands (see **chapter 3.1.3**).

First, the cells were characterized in adhesion measurements to identify their optimal seeding density, improve their adherence and find the sensitive frequency for impedance measurements (see **chapter 4.1**). Second, single impedance and luminescence readouts were conducted for the three GPCR/miniG protein cell lines to monitor the cellular behavior after ligand addition independently (see **chapters 4.2 and 4.3**). The results were compared to cell lines expressing the same receptor but

no luciferase or miniG protein (control cell lines: CHO M1R, CHO M5R, HEK H2R, **chapter 3.1.2**). Furthermore, HEK wt cells were used as a reference not expressing the GPCRs under study. Next, the impedance as well as the luminescence assay was optimized with respect to the experimental parameters with the help of the model cell line HEK M1R/mG<sub>q</sub> (see **chapters 4.4 and 4.5**). Lastly, impedance and miniG protein recruitment, detected by a luminescence readout, were combined in a simultaneous measurement to correlate signaling dynamics (see **chapter 4.6**).

## 4.1 Characterization and Optimization of the Adherence of Human Embryonic Kidney and Chinese Hamster Ovary Cells with Impedance Spectroscopy

To characterize the cell lines used in this work, adhesion studies were performed using impedance spectroscopy (see **chapter 3.5.3.1**). Four cell concentrations of HEK cells were examined to find the optimal seeding density. The adhesion behavior of HEK cells was also tested by means of 8W1E gold-film electrodes preincubated with serum-containing medium, coated with gelatin or crosslinked gelatin (cf. **chapter 3.3.2**). Furthermore, the adhesion profiles of Chinese hamster ovary (CHO) cells on the three coatings were compared using 8W1E electrode arrays.

To find the optimal seeding concentration for all HEK cell lines, four densities of the model cell line HEK M1R/mG<sub>q</sub> were tested:  $5 \cdot 10^4$  c/cm<sup>2</sup>,  $10^5$  c/cm<sup>2</sup>,  $2 \cdot 10^5$  c/cm<sup>2</sup> and  $3 \cdot 10^5$  c/cm<sup>2</sup>. HEK M1R/mG<sub>q</sub> cells were seeded on crosslinked gelatin-coated 8W1E arrays. Subsequently, impedance was measured at the ECIS SA device in *multi-frequency vs. time* (MFT) mode for 41 frequencies between 0.1-100 kHz evenly distributed on a logarithmic scale. The spectra at time points  $t = 0$  h (i.e. immediately after seeding) and  $t = 40$  h were extracted for the different cell densities. They are plotted in **Figure 38A-D**.

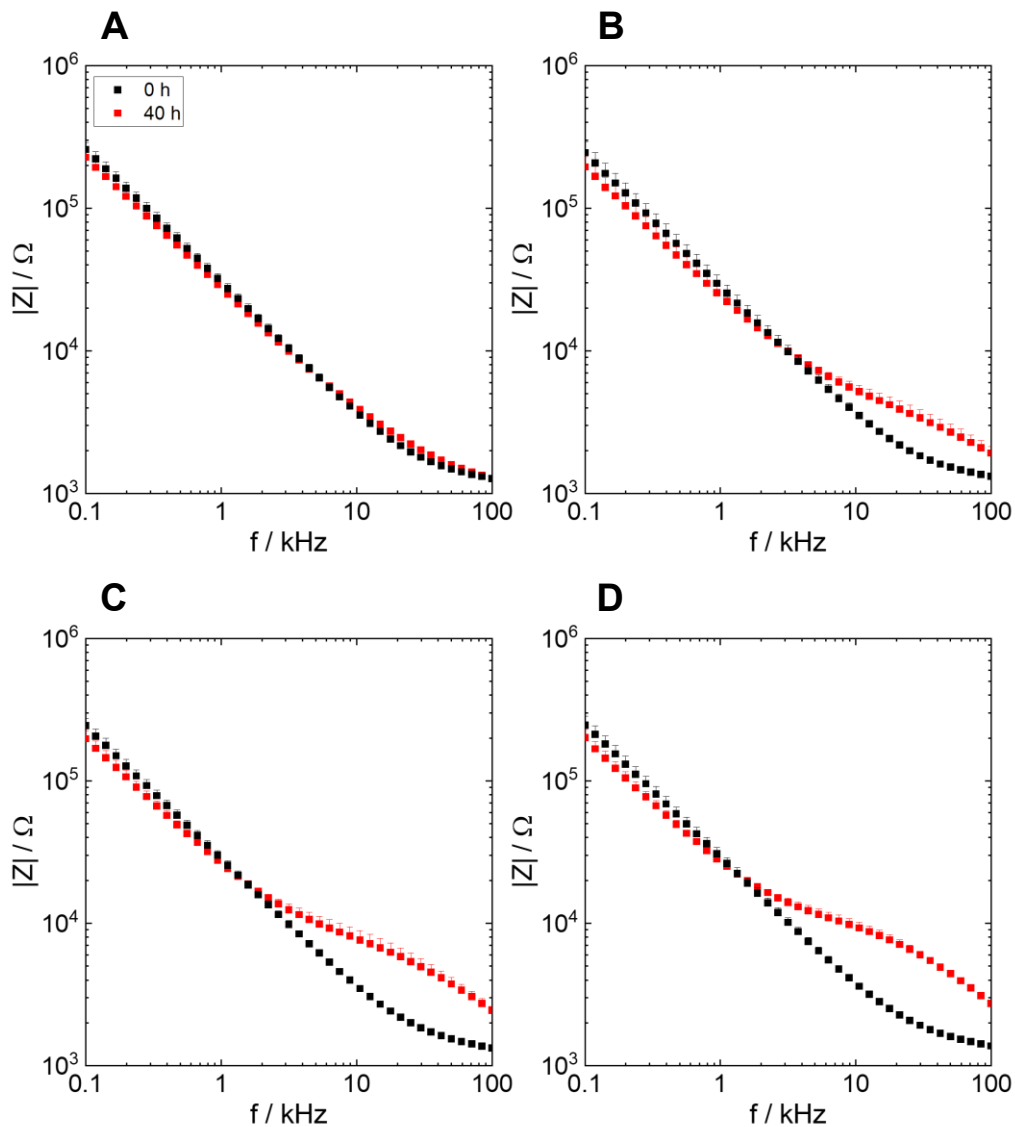


Figure 38. Impedance spectra immediately after (0 h, black) and 40 h after seeding (red) of **HEK M1R/mG<sub>q</sub>** cells. The impedance was measured at 41 frequencies between 0.1-100 kHz evenly distributed on a logarithmic scale in MFT-mode with 8W1E electrode arrays that were coated with crosslinked gelatin. At time point  $t = 0$  h, **different cell densities** were seeded (A:  $5 \cdot 10^4$  c/cm<sup>2</sup>, B:  $10^5$  c/cm<sup>2</sup>, C:  $2 \cdot 10^5$  c/cm<sup>2</sup> and D:  $3 \cdot 10^5$  c/cm<sup>2</sup>). Mean + SE,  $N = 6$ , two independent experiments. Temperature: 37°C.

At  $t = 0$  h, all spectra look very similar (**Figure 38A-D, black**). They show a linear decrease of impedance between 0.1-10 kHz with increasing frequency. For  $f > 10$  kHz, impedance slowly declines and converges to an impedance value of approximately 1000 Ω. 40 h after cell seeding (**Figure 38A-D, red**), differences between the spectra for the different cell densities are observed. For a density of  $5 \cdot 10^4$  c/cm<sup>2</sup>, the spectra after 0 h and 40 h can not be discriminated (**Figure 38A**). For higher cell densities (**Figure 38B-D**), the spectra after 0 h show slightly larger impedance values than the spectra after 40 h between 0.1-4 kHz. At frequencies

> 4 kHz, the 40 h spectra show larger impedance values in comparison to the 0 h spectra with a slow decrease of impedance up to 20 kHz followed by a more drastic impedance decrease for  $f > 20$  kHz. At the high-frequency end, the 0 h and 40 h spectra are converging, respectively. The differences between both spectra are most pronounced for frequencies between 9-15 kHz. Furthermore, with larger seeding density, the 40 h curve exhibits larger impedance values at intermediate frequencies (4-20 kHz).

In the case of the 0 h spectra (**Figure 38A-D, black**), the electrodes are still cell-free since the cells did not have enough time to attach, spread and adhere to the electrodes. This is why only contributions of the medium ( $R_{\text{bulk}}$ ) at the high-frequency end and the gold-film electrodes at the low-frequency end (constant phase element CPE) are observed (cf. **chapter 3.5.2**) (Arndt et al., **2004**, Stolwijk et al., **2015**). Since the bulk resistance behaves as an Ohmic resistor, impedance converges to a value of approximately  $1000 \Omega$  for frequencies  $f > 10$  kHz (resistive behavior; horizontal line), which is a typical value for 8W1E electrodes. In contrast, the CPE behaves more as a capacitor and, hence, shows a frequency-dependent behavior below 10 kHz.

The differences between the 0 h and 40 h spectra are attributed to the cell bodies themselves. After 40 h (**Figure 38A-D, red**), the cells have already attached and adhered to the electrodes, which was confirmed by phase contrast micrographs (**Appendix 19**). However, the confluency of the cells differed depending on the seeding density. With increasing seeding density, the confluency of the cell layer is increased, which is confirmed by the larger impedance values after 40 h. Only for  $f = 0.1-4$  kHz the 0 h curves show smaller impedance values than the 40 h curves. This is attributed to cysteine depositing on the gold electrodes, which removes electrode contaminations and, thus, increases the electrode capacitance and decreases impedance (Janshoff et al., **1996**). The relatively constant impedance between 4-20 kHz (**Figure 38B-D, red**) is explained by the barrier function of the cells, which behaves like an Ohmic resistor ( $R_b$ , cf. **chapter 3.5.2**) (Arndt et al., **2004**, Stolwijk et al., **2015**). At  $f > 20$  kHz, the current mainly couples through the cells, since the cell membrane behaves as a capacitor, resulting in a frequency-dependent impedance contribution ( $C_m$ , cf. **chapter 3.5.2**). This leads to decreasing impedance values at the high-frequency end of the spectrum. The largest difference in the impedance spectra of cell-free and cell-covered electrodes is observed for intermediate frequencies (9-15 kHz). Accordingly, in all following *single-frequency vs. time* (SFT) measurements with HEK cells, a frequency of 12 kHz was chosen as sensitive measurement frequency.

In addition to the impedance spectra, the time courses of impedance at the sensitive frequency  $f = 12$  kHz were plotted for the different seeding densities. They are shown in **Figure 39**.

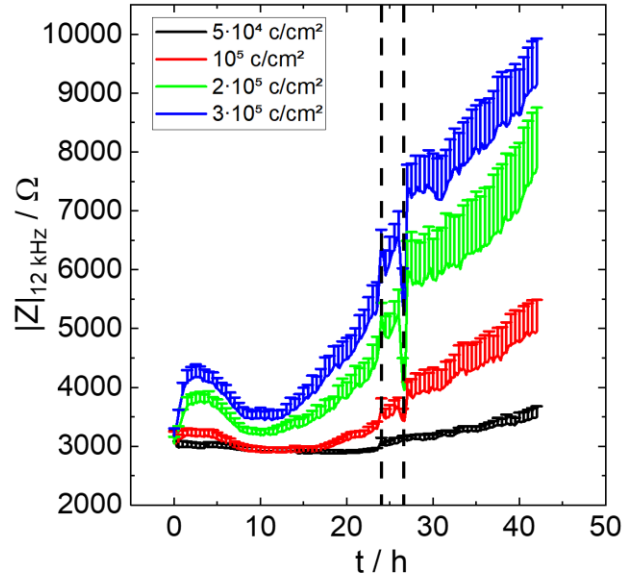


*Figure 39. Impedance time courses of HEK M1R/mG<sub>q</sub> cells at a frequency of 12 kHz. At  $t = 0$  h, the cells were seeded on 8W1E electrode arrays with **different cell densities** (black:  $5 \cdot 10^4$  c/cm<sup>2</sup>, red:  $10^5$  c/cm<sup>2</sup>, green:  $2 \cdot 10^5$  c/cm<sup>2</sup> and blue:  $3 \cdot 10^5$  c/cm<sup>2</sup>). The arrays were coated with crosslinked gelatin. The vertical lines indicate the time points of medium exchange. Mean + SE,  $N = 6$ , two independent experiments. Temperature: 37°C.*

In all cases, impedance at 12 kHz gradually increases from a starting value of about 3000  $\Omega$  to final values of  $(3500 \pm 200)$   $\Omega$  for  $5 \cdot 10^4$  c/cm<sup>2</sup> (**Figure 39, black**),  $(5000 \pm 500)$   $\Omega$  for  $10^5$  c/cm<sup>2</sup> (**Figure 39, red**),  $(8000 \pm 1000)$   $\Omega$  for  $2 \cdot 10^5$  c/cm<sup>2</sup> (**Figure 39, green**) and  $(9100 \pm 800)$   $\Omega$  for  $3 \cdot 10^5$  c/cm<sup>2</sup> (**Figure 39, blue**). Only for the two highest seeding densities of  $2 \cdot 10^5$  c/cm<sup>2</sup> and  $3 \cdot 10^5$  c/cm<sup>2</sup>, a local impedance maximum of about 700  $\Omega$  ( $2 \cdot 10^5$  c/cm<sup>2</sup>) and 1000  $\Omega$  ( $3 \cdot 10^5$  c/cm<sup>2</sup>) between  $t = 0$  h and  $t = 5$  h and a subsequent decrease of impedance until  $t = 10$  h is observed followed by a continuous increase in impedance until the measurement was stopped. The highest impedance values are observed for a cell density of  $3 \cdot 10^5$  c/cm<sup>2</sup> followed by lower seeding densities in descending order.

The varying confluency can not only be recognized with the help of the impedance spectra (**Figure 38A-D**) but also with the impedance time courses at 12 kHz. At  $t = 0$  h, the electrodes are still cell-free, resulting in a minimal impedance value of 3000  $\Omega$  (**Figure 39**). Over time, more and more cells attach and adhere to the surface, leading to an increase in impedance over time due to the insulating behavior of the

cells (Stolwijk et al., **2015**, Voiculescu et al., **2021**, Wegener et al., **2000b**). The highest impedance value among the investigated cell densities is reached after  $t > 40$  h for a seeding density of  $3 \cdot 10^5$  c/cm<sup>2</sup> (**Figure 39, blue**). After that time, the cells have reached confluency, which was confirmed by phase contrast microscopy (**Appendix 19**). For smaller cell densities (**Figure 39, black, red, green**), the cells are not as densely packed or have not reached full confluency yet. Therefore, the current flow between the electrodes is less hindered and lower impedance values are observed. For later experiments, a seeding density of  $3 \cdot 10^5$  c/cm<sup>2</sup> was chosen because for this density the impedance values of cell-free and cell-covered electrodes can be discriminated best. Between  $t = 0-10$  h the impedance does not increase continuously for cell densities of  $2 \cdot 10^5$  c/cm<sup>2</sup> and  $3 \cdot 10^5$  c/cm<sup>2</sup> (**Figure 39, green, blue**) but a local maximum of impedance is observed. This is ascribed to the crosslinked gelatin coating and HEK cells adhering to this coating, which was further investigated below.

In a second experiment, different electrode coatings were compared for HEK NTS1R iL cells, which were used as a HEK model cell line. The cells were seeded with a density of  $3 \cdot 10^5$  c/cm<sup>2</sup> on gelatin or crosslinked gelatin-coated 8W1E electrodes or 8W1E electrodes that were preincubated with medium containing serum proteins (see **chapter 3.3.2**). Impedance was monitored in MFT-mode for 6 frequencies at the ECIS SA over 45 h starting right after cell seeding. The impedance spectra are given in **Figure 40A-C**.

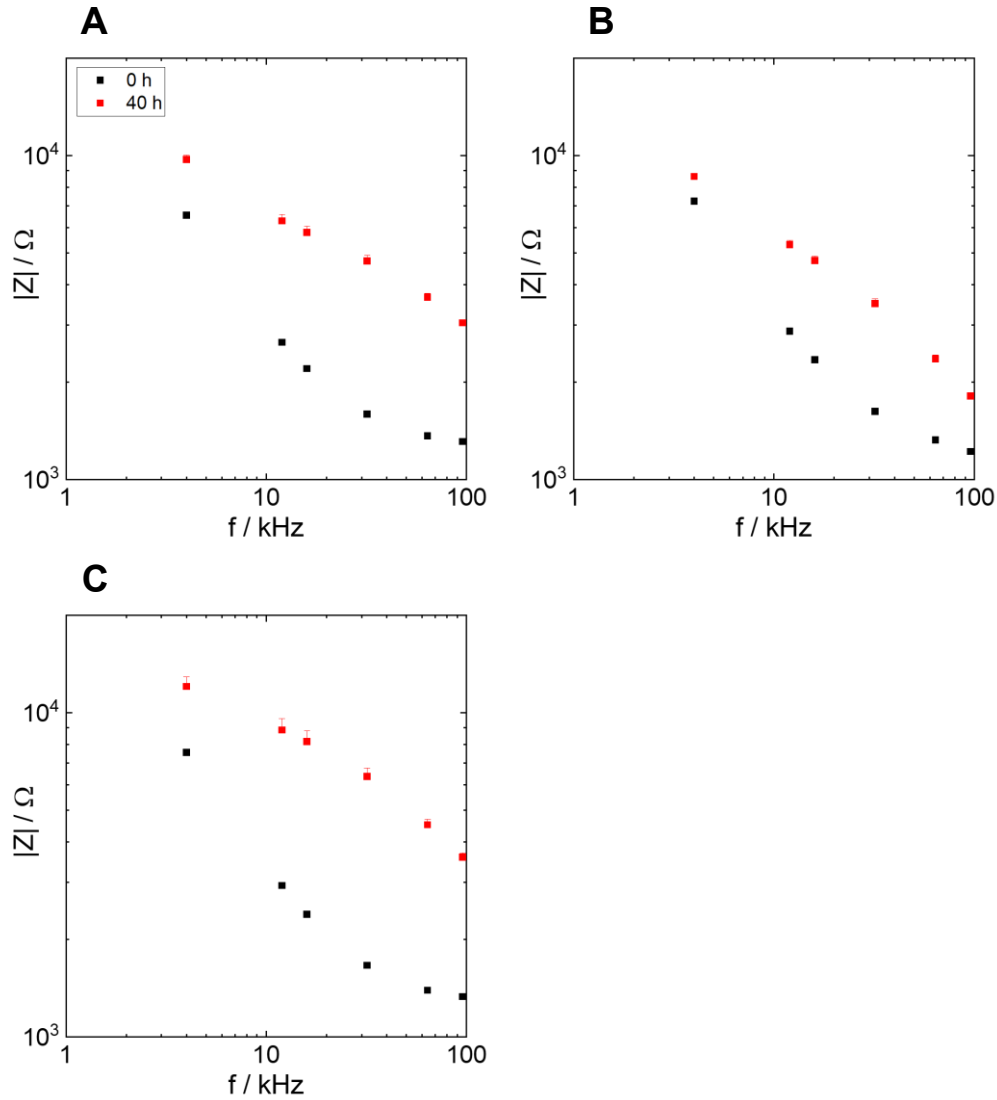


Figure 40. Impedance spectra immediately after (0 h, black) and 40 h after seeding (red) of **HEK NTS1R iL** cells with a density of  $3 \cdot 10^5$   $c/cm^2$ . The impedance was measured at the frequencies 4/12/16/32/64/96 kHz in MFT-mode with an 8W1E electrode array that was **preincubated with medium (A), coated with gelatin (B) or crosslinked gelatin (C)**. Mean + SE,  $N = 3-4$ , single experiment. Temperature: 37°C.

If the 0 h curves are compared between the different coatings, the differences in impedance for medium (**Figure 40A, black**), gelatin (**Figure 40B, black**) and crosslinked gelatin (**Figure 40C, black**) are not very pronounced. After  $t = 40$  h, the differences between the coatings are more pronounced. The largest impedance values are observed for the crosslinked gelatin coating (**Figure 40C, red**), followed by medium preincubated electrodes (**Figure 40A, red**) and gelatin coated electrodes (**Figure 40B, red**). If the values at a frequency of 12 kHz and  $t = 40$  h are compared between the coatings, crosslinked gelatin shows the largest value with  $(8800 \pm 800)$   $\Omega$  followed by medium with  $(6300 \pm 300)$   $\Omega$  and gelatin with  $(5300 \pm 200)$   $\Omega$ .

Compared with **Figure 38A-D** the same trends in the impedance spectra are visible in **Figure 40A-C**. At the beginning of the measurement ( $t = 0$  h, **Figure 40A-C, black**), the bare electrode impedance is measured. The current is allowed to flow between the electrodes without any cellular resistance, resulting in lower impedance values than after  $t = 40$  h (**Figure 40A-C, red**). After 40 h, the cells are adhered to the electrode surface and, hence, lead to increased impedance values because the current flow is hampered by the dielectric bodies. The increase in cellular attachment and confluency on the different coatings was also confirmed by phase contrast microscopy (**Appendix 20**). Since the impedance values at  $t = 40$  h are larger on crosslinked gelatin-coated and medium preincubated plates compared to gelatin-coated ones (**Figure 40A-C, red**), the former two coatings presumably enhance the cellular attachment and adhesion strength of HEK cells by reduction of the distance  $h$  between cells and electrodes, leading to an increased impedance contribution  $\alpha$  (**equation 10**) and, hence, an increased total impedance  $Z$ . Another explanation could be larger cellular radii on crosslinked gelatin coated and medium preincubated electrodes, affecting  $\alpha$  in a proportional manner (**equation 10**). Besides cell-matrix contacts, a larger number of cell-cell contacts (increased  $R_b$ ) on crosslinked gelatin and medium preincubated electrodes would also lead to a greater impedance value compared to a gelatin coating. To confirm the coatings' impact on the cell-matrix contacts, capacitance measurements at high frequencies could be performed (cf. **chapter 3.5.2**). In analogy, the impact of cell-cell contacts could be confirmed by measurements of the resistance at low frequencies (cf. **chapter 3.5.2**).

In **Figure 41** the corresponding impedance time courses of HEK NTS1R iL cells on different coatings and at a measurement frequency of 12 kHz are plotted.

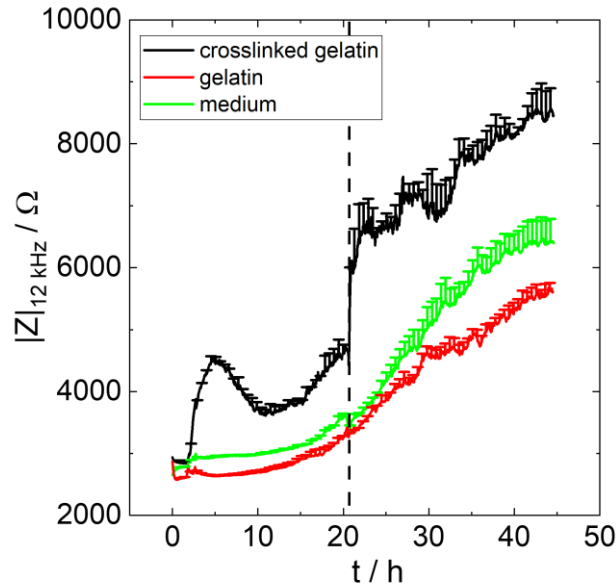


Figure 41. Impedance time courses of **HEK NTS1R iL** cells at a frequency of 12 kHz. At  $t = 0$  h, the cells were seeded with a density of  $3 \cdot 10^5$  c/cm<sup>2</sup> on 8W1E electrode arrays that were coated with **crosslinked gelatin (black)**, **gelatin (red)** or that were **preincubated with medium (green)**. The vertical line indicates the time point of medium exchange. Mean + SE,  $N = 2-4$ , single experiment. Temperature: 37°C.

All three curves start at similar values of 2600-2900  $\Omega$  for crosslinked gelatin (**Figure 41, black**), gelatin (**Figure 41, red**) and medium preincubation (**Figure 41, green**). They all show an overall increase of impedance at 12 kHz between  $t = 0-45$  h. Only for a coating with crosslinked gelatin, an impedance rise in the first five hours followed by a decrease in the next five hours is observed. In addition, the curves for varying coatings reach different final values after 45 h. For crosslinked gelatin, a value of  $(8500 \pm 400)$   $\Omega$  is achieved at the end of the measurement, for medium, a value of  $(6400 \pm 300)$   $\Omega$  is reached and for gelatin, the final value lies at  $(5600 \pm 100)$   $\Omega$ . The curve for crosslinked gelatin is comparable to the one recorded in **Figure 39, blue**.

The impedance values of the cell-free electrodes ( $t = 0$  h) are similar for crosslinked gelatin-coated (**Figure 41, black**), gelatin-coated (**Figure 41, red**) and medium preincubated (**Figure 41, green**) electrodes. Consequently, the coating itself does not impact the impedance of the cell-free electrodes significantly. However, over time, more drastic differences in the cellular impedance on different coatings are observed because the cells start to attach and adhere to the electrode surface (Wegener et al., **2000b**). The cells adhere faster on crosslinked gelatin (**Figure 41, black**) because for the same amount of time, larger impedance values are reached compared to gelatin or medium. The accelerated adhesion on crosslinked gelatin was also observed for HEK M1R/mG<sub>q</sub> cells in a microscopic study (**Appendix 21**) and HEK293T cells in the literature (He et al., **2023**). Furthermore, the cells adhere stronger to the electrode

surface on crosslinked gelatin (**Figure 41, black**) since the maximum impedance on crosslinked gelatin is about 2900  $\Omega$  larger than on gelatin (**Figure 41, red**) and about 2000  $\Omega$  larger than on medium preincubated electrodes (**Figure 41, green**). When crosslinked gelatin is used as a coating, gelatin forms a polymer-like network with glutardialdehyde, which is more densely packed than gelatin or serum proteins themselves (Oryan et al., **2018**). This might bring the cells closer to the electrode surface by which the impedance contribution  $\alpha$  and, hence, the total impedance is increased compared to a gelatin coating or preincubation with medium (cf. **chapter 3.5.2**) (Janshoff et al., **2010**). Since crosslinked gelatin leads to higher impedance values and ensures better adherence to the gold film electrodes, which is essential for impedance spectroscopy, it was favored in subsequent impedance studies of HEK cells. The local impedance maximum for crosslinked gelatin in the first 10 h must be attributed to HEK cells in combination with the crosslinked gelatin coating itself since no local maximum was observed in combination with gelatin or medium preincubated electrodes. Moreover, this behavior was observed for several different HEK cell lines throughout this work and was not present for CHO cells in an analogous experiment described below. It could be explained by attachment and spreading of the HEK cells on the coating. Compared to gelatin and medium, 5 h after seeding, the cells on crosslinked gelatin must either be closer to the electrode by formation of cell-matrix contacts or have increased their radius after spreading, leading to an impedance increase. The formation of cell-cell contacts is not considered accountable for the local impedance maximum since cell-cell contacts, e.g. tight junctions, are usually formed after  $\geq 10$  h depending on the cell line under study (Heitmann et al., **2007**). The following impedance decrease could be explained by shrinkage of the cells due to proliferation and space restrictions or a modification of the cell-substrate contacts over time. However, it must be noted that proliferation usually leads to an overall increase of impedance or decrease of capacitance since the electrode coverage increases (Stolwijk, Wegener, **2019**). Consequently, it is rather attributed to modified cell-substrate contacts.

In this work, CHO cells were used in several control experiments. Consequently, CHO cells were characterized by impedance spectroscopy as well to find a sensitive measurement frequency and optimize their adherence. CHO NTS1R cells, which served as a CHO model cell line, were seeded with a density of  $10^5$  c/cm<sup>2</sup> on 8W1E arrays preincubated with medium, coated with gelatin or coated with crosslinked gelatin. Impedance was recorded at the ECIS SA in MFT-mode to monitor cell

adhesion. The impedance spectra immediately after seeding ( $t = 0$  h) and 40 h after inoculation are depicted in **Figure 42A-C**.

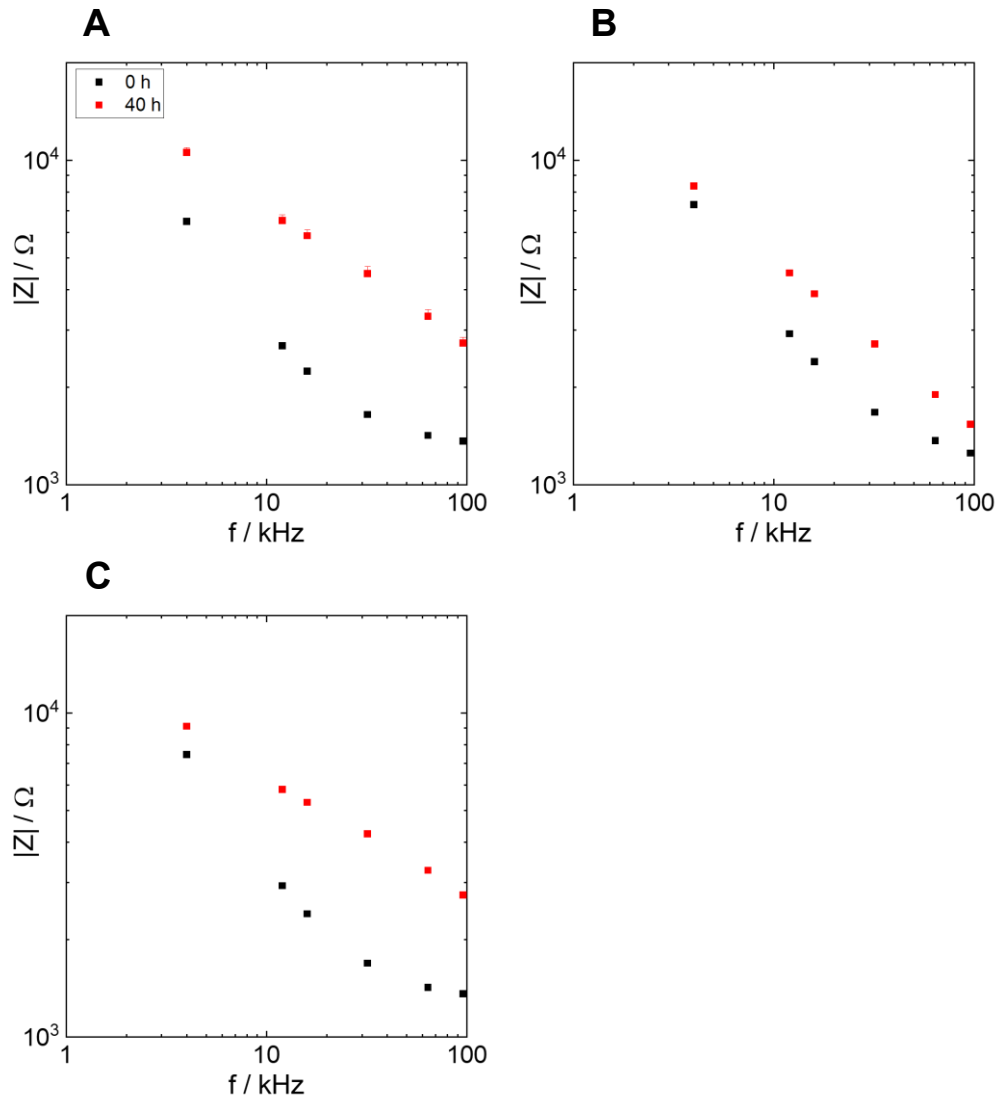


**Figure 42.** Impedance spectra of **CHO NTS1R** cells immediately after seeding (0 h, black) and 40 h after seeding (red). The impedance was measured at the frequencies 4/12/16/32/64/96 kHz in MFT-mode with an 8W1E electrode array that was preincubated with **medium (A)**, **coated with gelatin (B)** or **crosslinked gelatin (C)**. Mean + SE,  $N = 4$ , single experiment. Temperature: 37°C.

At  $t = 0$  h, the spectra for all coatings (**Figure 42A-C**, black) only show minor differences. The impedance values at  $t = 40$  h (**Figure 42A-C**, red) are increased up to three times in comparison to the 0 h curves with a maximal difference at intermediate frequencies (12-32 kHz). If the curves after 40 h are compared between the three coatings, the impedance on medium preincubated (**Figure 42A**, red) and crosslinked gelatin-coated (**Figure 42C**, red) electrodes is enhanced compared to gelatin-coated electrodes (**Figure 42B**, red). More specifically, at  $t = 40$  h and at a sensitive frequency of 12 kHz, the impedance of medium preincubated electrodes lies

at  $(6500 \pm 500) \Omega$ , the impedance value of crosslinked gelatin-coated electrodes is  $(5800 \pm 200) \Omega$  and the impedance of gelatin-coated electrodes takes a value of  $(4500 \pm 100) \Omega$ .

Many extracellular matrix (ECM) proteins such as vitronectin and fibronectin are known to facilitate cellular adhesion (Cai et al., **2020**). They contain a short peptide sequence Arg-Gly-Asp (RGD), which promotes the binding of certain integrins and, thus, the formation of cell-matrix contacts (Bachmann et al., **2019**). An impact of varying ECM proteins and substrate coatings on the adhesion of CHO cells was detected here as well. From the spectral data in **Figure 42A-C, black** it can be concluded that at  $t = 0$  h impedance only comprises the bulk resistance ( $R_{\text{bulk}}$ ) and the electrode interface impedance (CPE). This is because the electrode surface is still cell-free and the current flow is unhampered independent of the coating. After 40 h (**Figure 42A-C, red**), the cells are attached and adhered to the gold film electrodes, which was confirmed by phase contrast microscopy (**Appendix 20**). Accordingly, the increased impedance after 40 h is explained by the impedance contribution of the cells. The largest impact of the cells on impedance is observed for intermediate frequencies between 12-32 kHz. Consequently, a frequency of 12 kHz was chosen as sensitive measurement frequency in successive experiments. In addition, a dependency of the adhesion strength on the surface coating is observed after 40 h. Cells seeded on medium preincubated and crosslinked gelatin-coated electrodes attach stronger than on gelatin-coated electrodes indicated by enhanced impedance values (for explanation see analogous experiment with HEK cells above).

In addition to the impedance spectra, the time courses at  $f = 12$  kHz were evaluated for CHO NTS1R cells on different coatings. They are depicted in **Figure 43**.

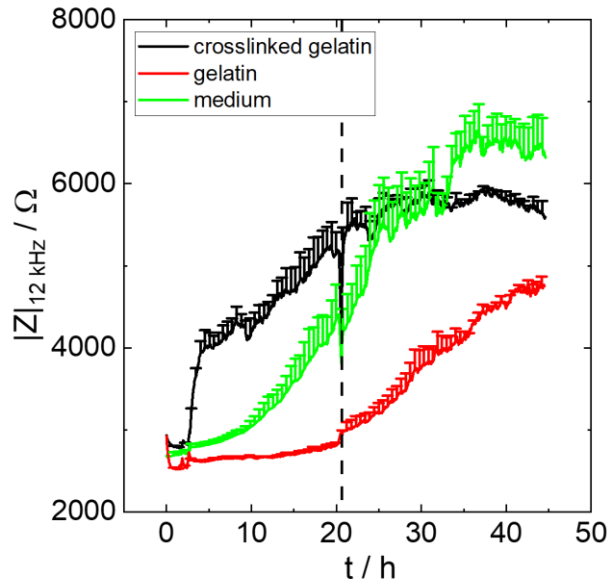


Figure 43. Impedance time course of **CHO NTS1R** cells at a frequency of 12 kHz. At  $t = 0$  h, the cells were seeded on an 8W1E electrode array that was **coated with crosslinked gelatin (black), gelatin (red) or that was preincubated with medium (green)**. The vertical line indicates the time point of medium exchange. Mean + SE,  $N = 4$ , single experiment. Temperature: 37°C.

For all three coatings (**Figure 43, black, red, green**), the impedance at 12 kHz generally increases over the recorded period. The starting values ( $t = 0$  h) for all coatings are similar with impedance values between 2600-2900  $\Omega$ . On crosslinked gelatin, impedance increases after 2.5 h and reaches a first plateau of  $(4000 \pm 200)$   $\Omega$  after 4.5 h (**Figure 43, black**). Subsequently, impedance starts to increase again after 9.5 h until a stable value of 5500-6000  $\Omega$  is reached after 22 h. On electrodes preincubated with medium, impedance rises slower but more continuously (**Figure 43, green**). A constant maximum value of  $(6300 \pm 200)$   $\Omega$  for medium preincubation is obtained after 35 h and is about 13% larger than for crosslinked gelatin. The impedance values for the gelatin coating only slightly increase in the first 20 h. After a medium exchange, impedance rises continuously to a final value of  $(5600 \pm 100)$   $\Omega$ .

**Figure 43** reveals different kinetics of attachment and spreading and different adhesion strength of CHO cells on varying surface coatings (Janshoff et al., **2010**, Stolwijk, Wegener, **2019**, Wegener et al., **2000b**). The adhesion process is accelerated on crosslinked gelatin (**Figure 43, black**) since impedance rises faster in comparison to the other coatings and reaches a stable level after 22 h already. In contrast, the adhesion is slower on medium preincubated electrodes (**Figure 43, green**). Here, the maximal impedance is reached after 35 h, i.e. the adhesion process takes 13 h longer than on crosslinked gelatin. However, the developed cell-matrix

and/or cell-cell contacts are stronger in comparison with crosslinked gelatin because 13% larger maximal impedance values are achieved on medium preincubated electrodes. This might be attributed to variations in the cell radii or distance between cells and electrodes, both impacting  $\alpha$ , or differences in  $R_b$ . To deconvolve the cell-cell and cell-matrix contributions of impedance, high-frequency capacitance measurements and low-frequency resistance measurements could be performed (cf. **chapter 3.5.2**). In the case of a simple gelatin coating (**Figure 43, red**), an attenuated increase in impedance is observed. In addition, the final impedance value is smaller compared to the other coatings and no stable impedance level is identified. Presumably, the cells need more time to reach a fully equilibrated state with an impedance level comparable to that of crosslinked gelatin or medium. Consequently, in most following experiments with CHO cells, the arrays were incubated with medium before seeding. By this, the time-consuming coating protocol for crosslinking the gelatin and toxic components such as glutardialdehyde, risking cell viability, were circumvented (Adamiak, Sionkowska, **2020**).

Overall, adhesion monitored by impedance spectroscopy depends on the cell density and coating of the electrode surface. The latter was already observed in 1986 by the electric cell-substrate impedance sensing (ECIS) pioneers Giaever and Keese. They found different impedance responses after seeding mammalian cells on substrates coated with gelatin, fibronectin, bovine serum albumin (BSA) and fetuin with fibronectin enhancing adhesive forces (Giaever, Keese, **1986**). Later, Wegener *et al.* investigated the attachment and adhesion of Madin-Darby Canine Kidney (MDCK) cells by impedance measurements and detected a dependency of the adhesion kinetics on the surface coating (Wegener *et al.*, **2000b**). In this work, crosslinked gelatin greatly enhanced the adhesion of poorly adhering HEK cells (Faussner *et al.*, **2022**, Jayakumar, J. A. K. J. *et al.*, **2020**). A cell density of  $3 \cdot 10^5$  c/cm<sup>2</sup> in combination with crosslinked gelatin allows the best discrimination between cell-free and cell-covered electrodes at a sensitive frequency of 12 kHz. However, crosslinking with glutardialdehyde is very time-consuming (intense washing) and must be conducted properly since toxic glutardialdehyde residues might remain inside the wells, kill the cells and, hence, reduce the throughput if the wells are not washed enough. This problem is solved by lowering the glutardialdehyde content. Concentrations down to 1% (v/v) have been tested throughout this work (data not shown) and proved as sufficient as the standard concentration of 2.5% (v/v). The local maximum of impedance between  $t = 0-10$  h turned out to be specific for HEK cells adhering to crosslinked gelatin (**Figure 41, black**) since CHO cells did not display this behavior

(**Figure 43, black**). In addition, HEK cells grown on gelatin-coated and medium preincubated plates did not show a local maximum either (**Figure 41, red, green**). This behavior only observed for HEK cells must be attributed to attachment and spreading mechanisms and an alternation of cellular radii.

As with HEK cells, CHO cells adhere most rapidly to crosslinked gelatin. However, the greatest adhesion strength of CHO cells is found for medium preincubated plates. Since CHO cells generally adhere stronger to surfaces than HEK cells and to circumvent the time-consuming crosslinking protocol, coating the substrates with serum-containing medium was preferred for CHO cells in later experiments.

Comparing the results for HEK and CHO cells, CHO cells adhere faster on crosslinked gelatin compared to HEK cells. While adhesion of CHO cells on crosslinked gelatin is completed after 22 h, HEK cells need 40 h at minimum to reach a stable impedance level. This might be attributed to differences in the extracellular matrix (ECM) composition and the varying medium proteins necessary for cellular adhesion (Croset et al., **2012**, Jaluria et al., **2008**, Schlie-Wolter et al., **2013**). In general, the discrepancies in the adhesion forces and strength of the cell-cell contacts, indicated by differing maximal impedance values, can also be explained by variations in the ECM composition (Schlie-Wolter et al., **2013**, Stolwijk, Wegener, **2019**). The ECM is largely influenced by the coating and cell line under study. Consequently, it affects the expression of cellular junction proteins and, hence, the impedance outcome.

## 4.2 Characterization of Muscarinic and Histaminergic GPCR Responses with Impedance Spectroscopy

Depending on the GPCR system, ligands known to interact with the receptor of interest and triggering a signaling cascade well described in the literature were selected (cf. **chapter 3.1.3**). For both muscarinic acetylcholine receptors (M1R and M5R), the agonists iperoxo and carbachol were chosen (Ishii, Kurachi, **2006**). For the H2R, the agonist histamine was investigated (Walter, Stark, **2012**). Each receptor was expressed recombinantly in HEK cells that co-express either miniG<sub>q</sub> proteins (M1R, M5R) or miniG<sub>s</sub> proteins (H2R). While the GPCR was intracellularly labeled with SmBiT, the respective miniG protein was labeled with LgBiT using the Nanoluciferase (NanoLuc, NLuc) Binary Technology (NanoBiT) (cf. **chapter 3.1.2**).

To develop a dual setup for the simultaneous detection of impedance and luminescence of one cell population (see **chapter 4.6**), these cell lines were initially characterized by impedance measurements only. First, the impedance profiles after agonist addition were examined (see **chapter 4.2.1**). In addition, the influence of the

luciferin coelenterazine h, which is needed for the luminescence-based miniG protein recruitment assay, was studied for intrinsic impact on the impedance signal (see **chapter 4.2.2**).

#### 4.2.1 Impedance Profiles in the Absence of Coelenterazine h

HEK M1R/mG<sub>q</sub>, HEK M5R/mG<sub>q</sub> and HEK H2R/mG<sub>s</sub> cells were seeded with a density of  $3 \cdot 10^5$  c/cm<sup>2</sup> on gelatin or crosslinked gelatin-coated 96W1E+ electrodes according to the standardized protocol (see **chapter 3.5.3.1**). Two days after cell seeding, the cells were equilibrated in Leibovitz' 15 (L15) buffer and a baseline of impedance was recorded at a frequency of 12 kHz in SFT-mode at the ECIS Z $\theta$ . Then, different concentrations of agonists in L15 were added and impedance was monitored for 1 h. At the M1R, seven iperexo concentrations between 0.1 nM and 10  $\mu$ M (**Figure 44A,C**) and seven carbachol concentrations between 100 nM to 1 mM (**Figure 44B,D**) were used in addition to a vehicle control (CTRL). At the M5R, seven iperexo concentrations between 0.1 nM and 1  $\mu$ M (**Figure 46A,C**) and seven carbachol concentrations between 10 nM and 100  $\mu$ M (**Figure 46B,D**) were investigated in addition to a CTRL. Six histamine concentrations between 1 nM and 100  $\mu$ M and a CTRL were tested at the H2R (**Figure 48**). The respective concentration-response curves are given in **Figure 45A-B** (M1R), **Figure 47A-B** (M5R) and **Figure 49** (H2R).

After recording a stable baseline of HEK M1R/mG<sub>q</sub> cells in L15 ( $(5540 \pm 40) \Omega$  and  $(5530 \pm 40) \Omega$ ), a CTRL and different iperexo (**Figure 44A,C**) and carbachol (**Figure 44B,D**) concentrations were added. The change of impedance was recorded for 1 h and is depicted in **Figure 44A-D**.

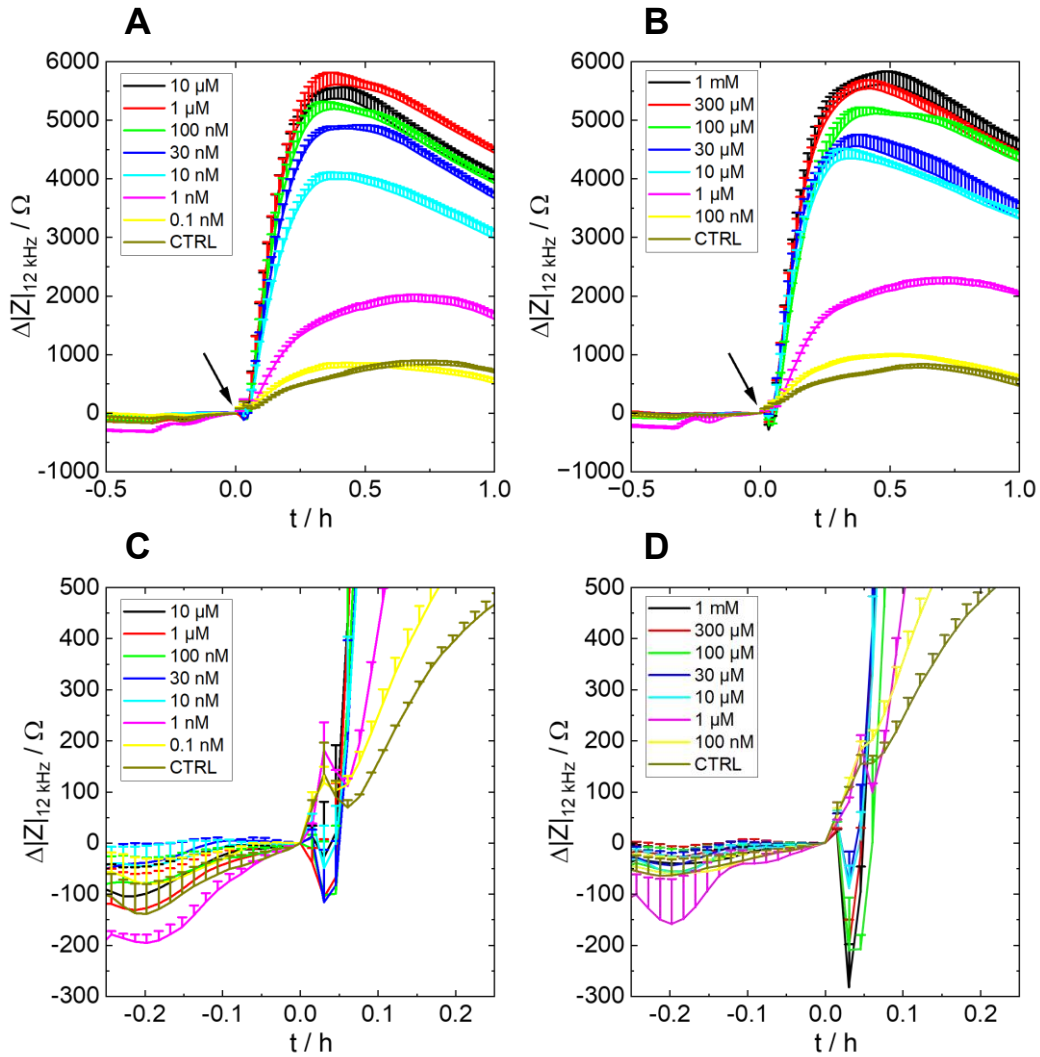
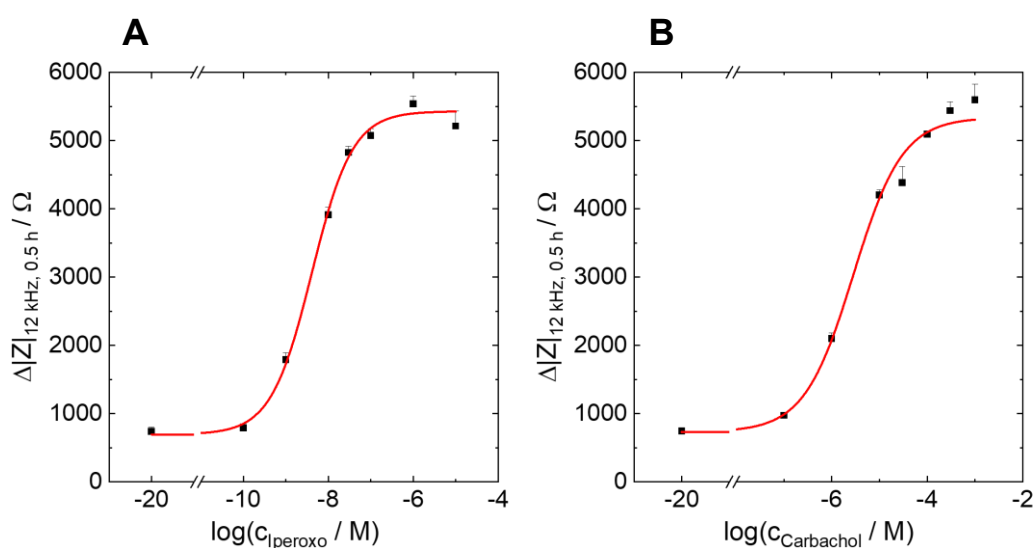


Figure 44. Impedance change over time of **HEK M1R/mG<sub>q</sub>** cells at a frequency of 12 kHz. The cells were cultivated on a 96W1E+ electrode array that was coated with crosslinked gelatin. After a baseline recording, the cells were stimulated with different concentrations of **iperoxo (A,C)** or **carbachol (B,D)** at  $t = 0$  h. In (C) and (D) zoom-ins of (A) and (B) are shown, respectively. A,C: black 10  $\mu\text{M}$ , red 1  $\mu\text{M}$ , green 100 nM, blue 30 nM, cyan 10 nM, pink 1 nM, yellow 0.1 nM, brown CTRL. B,D: black 1 mM, red 300  $\mu\text{M}$ , green 100  $\mu\text{M}$ , blue 30  $\mu\text{M}$ , cyan 10  $\mu\text{M}$ , pink 1  $\mu\text{M}$ , yellow 100 nM, brown CTRL. Baseline A:  $(5540 \pm 40) \Omega$ , mean + SE,  $N = 3-7$ , two independent experiments. Baseline B:  $(5530 \pm 40) \Omega$ , mean + SE,  $N = 3-13$ , three independent experiments. CTRL = vehicle control. Temperature: 37°C.

Immediately after stimulation, a transient, concentration-dependent 100-300  $\Omega$  decrease in impedance is observed (**Figure 44C,D**). Subsequently, impedance increases, reaches a maximum after  $t = 0.4-0.5$  h and slowly decreases again. The maxima for concentrations below 1 nM iperoxo and 1  $\mu\text{M}$  carbachol (**Figure 44A-B, pink, yellow, brown**) are more delayed in time and emerge between  $t = 0.5-0.75$  h. The CTRL (**Figure 44A-B, brown**) shows an 800  $\Omega$  increase over a period of 0.6-0.75 h and slowly decreases afterward. With higher ligand concentrations, the overall impedance signal and maximum impedance increase. The only exception is the curve

for 1  $\mu\text{M}$  of iperexo (**Figure 44A, red**), which runs slightly higher in comparison to the maximum concentration of 10  $\mu\text{M}$  iperexo (**Figure 44A, black**). A maximal impedance of  $(5600 \pm 200) \Omega$  is reached by a concentration of 1  $\mu\text{M}$  iperexo after  $t = 0.4$  h. For carbachol, a maximum signal of  $(5600 \pm 200) \Omega$  is achieved by a concentration of 1 mM (**Figure 44B, black**) at  $t = 0.48$  h. Nonetheless, the curves for the three highest concentrations of iperexo (**Figure 44A, black, red, green**) and the two highest concentrations of carbachol (**Figure 44B, black, red**) do not vary significantly. No further increase of impedance is observed for concentrations above 100 nM of iperexo and 300  $\mu\text{M}$  of carbachol. For the smallest concentrations of 0.1 nM iperexo and 100 nM carbachol (**Figure 44A-B, yellow**), no significant difference to the CTRL is measured.

From **Figure 44A-B**, concentration-response curves were extracted as described in **chapter 3.5.4**. In short, the impedance changes at  $t = 0.5$  h and  $f = 12$  kHz were plotted against the logarithm of the ligand concentrations and the graphs were fitted with a four-parametric dose-response fit (**equation 15**). The results are depicted in **Figure 45A** for iperexo and **Figure 45B** for carbachol.



**Figure 45.** Concentration-response curves of **HEK M1R/mG<sub>q</sub>** cells after stimulation with different concentrations of **iperexo (A)** or **carbachol (B)**. The impedance data at a frequency of 12 kHz and 0.5 h after stimulation (black squares) is plotted as a function of the ligand concentration and was extracted from **Figure 44A-B**. The concentration-response fits (red solid line, **equation 15**) reveal a  $pEC_{50}$  of  $8.39 \pm 0.06$  for iperexo and a  $pEC_{50}$  of  $5.55 \pm 0.06$  for carbachol. The  $E_{max}$  is  $(5400 \pm 100) \Omega$  for iperexo and  $(5340 \pm 90) \Omega$  for carbachol. A: Mean + SE,  $N = 3-7$ , two independent experiments. B: Mean + SE,  $N = 3-13$ , three independent experiments. Temperature: 37°C.

For both ligands, a sigmoidal curve is obtained (**Figure 45A-B**). The CTRL and smallest agonist concentrations of 0.1 nM iperexo and 100 nM carbachol display similar impedance values of 700-900  $\Omega$ . By increasing the concentration,  $\Delta|Z|$  is

increased and reaches a saturation above 100 nM of iperoxo and 100  $\mu$ M of carbachol (5000-6000  $\Omega$ , respectively). For iperoxo, a pEC50 of  $8.39 \pm 0.06$  and an  $E_{\max}$  value of  $(5400 \pm 100) \Omega$  is found (**Figure 45A**). In contrast, the pEC50 of carbachol (**Figure 45B**) is smaller and equals  $5.55 \pm 0.06$ . The  $E_{\max}$  value for carbachol is  $(5340 \pm 90) \Omega$ .

In **Figure 46A-D**, HEK M5R/mG<sub>q</sub> cells were treated with a CTRL or stimulated with different concentrations of the ligands iperoxo (**Figure 46A,C**) and carbachol (**Figure 46B,D**) after recording a baseline on gelatin-coated 96W1E+ arrays for 0.5 h ( $(5350 \pm 10) \Omega$  and  $(5180 \pm 10) \Omega$ ). At  $t = 0$  h the cells were stimulated and the change of impedance was recorded for 1 h.

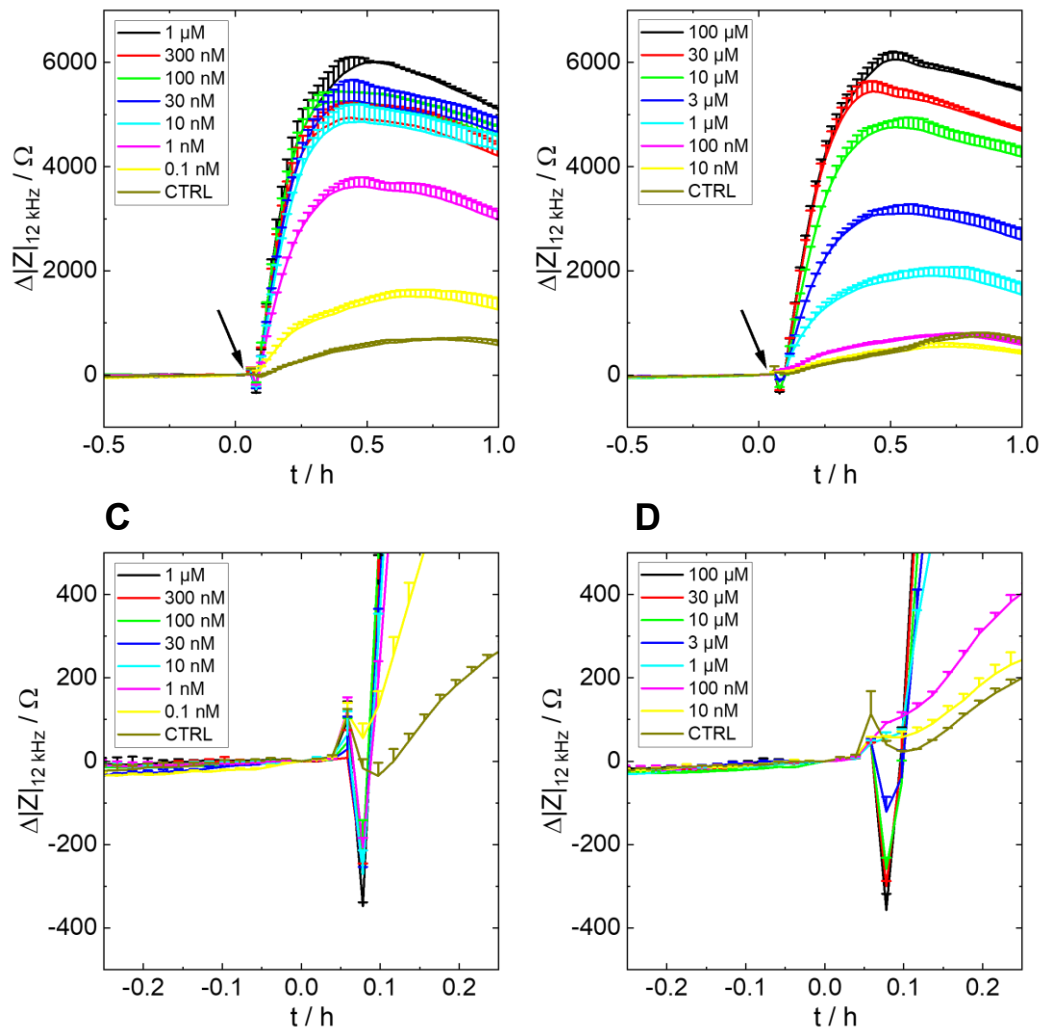


Figure 46. Impedance change over time of **HEK M5R/mG<sub>q</sub>** cells at a frequency of 12 kHz. The cells were cultivated on a 96W1E+ electrode array that was coated with gelatin. After a baseline recording, the cells were stimulated with different concentrations of **iperoxo (A,C) or carbachol (B,D)** at  $t = 0$  h. In (C) and (D) zoom-ins of (A) and (B) are shown, respectively. A,C: black 1  $\mu\text{M}$ , red 300 nM, green 100 nM, blue 30 nM, cyan 10 nM, pink 1 nM, yellow 0.1 nM, brown CTRL. B,D: black 100  $\mu\text{M}$ , red 30  $\mu\text{M}$ , green 10  $\mu\text{M}$ , blue 3  $\mu\text{M}$ , cyan 1  $\mu\text{M}$ , pink 100 nM, yellow 10 nM, brown CTRL. Baseline A and B:  $(5350 \pm 10) \Omega$ ,  $(5180 \pm 10) \Omega$ . Mean + SE,  $N = 3-4$ , single experiment. CTRL = vehicle control. Temperature: 37°C.

When the ligands are added ( $t = 0$  h), a 250-300  $\Omega$  transient decrease of impedance for iperoxo concentrations above 0.1 nM (**Figure 46C, black, red, green, blue, cyan, pink**) and a 100-350  $\Omega$  concentration-dependent, transient decrease of impedance for carbachol concentrations above 1  $\mu\text{M}$  (**Figure 46D, black, red, green, blue**) is observed. The higher the ligand concentration, the more distinct the decrease. Thereafter, impedance rises, reaches a maximum and slowly falls off again. With increasing ligand concentration, the impedance generally rises. The curves for the CTRL (**Figure 46A-B, brown**) show a minor impedance increase of about 700  $\Omega$  over

0.8 h but overall remain at a relatively constant level over the measurement period. For iperoxo, impedance increases for concentrations between 0.1-10 nM (**Figure 46A, cyan, pink, yellow**). Between 10-300 nM of iperoxo (**Figure 46A, red, green, blue, cyan**), a saturation behavior is observed: no further increase in impedance is achieved by increasing the concentration. Only the largest iperoxo concentration of 1  $\mu\text{M}$  (**Figure 46A, black**) shows a further increase in impedance compared to 10-300 nM iperoxo. The maximal change of impedance of  $(6400 \pm 400) \Omega$  is reached by 1  $\mu\text{M}$  iperoxo after 0.5 h.

In the case of carbachol, the curves for the two smallest concentrations (**Figure 46B, pink, yellow**) run with the CTRL curve. By continuously increasing the carbachol concentration, the impedance change is increased. In contrast to iperoxo, no saturation behavior is observed for carbachol for the concentrations under study. The greatest impedance value is found for 100  $\mu\text{M}$  carbachol (**Figure 46B, black**) after 0.5 h and amounts to  $(6100 \pm 200) \Omega$ .

Concentration-response curves were generated with the data at  $t = 0.5$  h (**Figure 46A-B**). The data points were plotted against the logarithmic ligand concentrations and were fitted by a four-parametric dose-response fit (**equation 15**). The concentration-response curves for iperoxo and carbachol are depicted in **Figure 47A-B**.

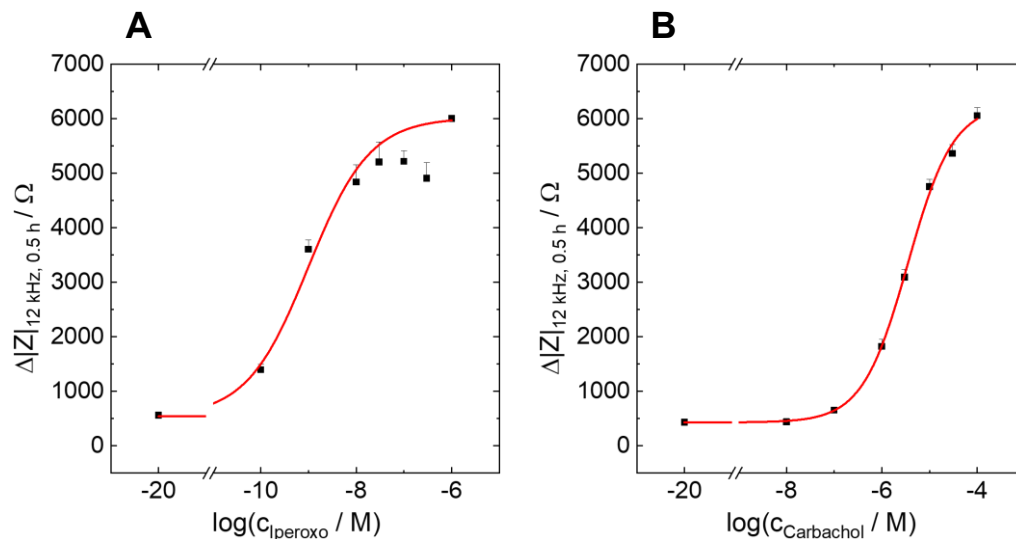


**Figure 47.** Concentration-response curves of **HEK M5R/mG<sub>q</sub>** cells after stimulation with different concentrations of **iperoxo (A)** or **carbachol (B)**. The impedance data at a frequency of 12 kHz and 0.5 h after stimulation (black squares) is plotted as a function of ligand concentration and was extracted from **Figure 46A-B**. The concentration-response fits (red solid line, **equation 15**) reveal a  $pEC_{50}$  of  $9.0 \pm 0.2$  for iperoxo and a  $pEC_{50}$  of  $5.46 \pm 0.04$  for carbachol. The  $E_{max}$  values are  $(6000 \pm 100) \Omega$  for iperoxo and  $(6300 \pm 100) \Omega$  for carbachol. Mean + SE,  $N = 3-4$ , single experiment. Temperature: 37°C.

With increasing ligand concentration, impedance generally increases. For iperoxo (**Figure 47A**), a continuous increase of the impedance change is observed up to a concentration of 30 nM iperoxo. Between 30-300 nM iperoxo, a saturation behavior is observed exceeded by a concentration of 1  $\mu\text{M}$ . The dose-response fit does not describe the experimental data of iperoxo well, especially for the concentrations 100-300 nM. Instead, the fit in **Figure 47B** represents the carbachol data almost perfectly. For concentrations up to 100 nM, the change of impedance remains at the level of the CTRL. By further increasing the carbachol concentration, impedance rises steadily. No saturation behavior is observed for large carbachol concentrations. However, the steepness of the curve is decreased for 30-100  $\mu\text{M}$  of carbachol. A  $\text{pEC}_{50}$  value of  $9.0 \pm 0.2$  and an  $E_{\text{max}}$  value of  $(6000 \pm 100) \Omega$  were determined for iperoxo, while the  $\text{pEC}_{50}$  for carbachol is  $5.46 \pm 0.04$  and its  $E_{\text{max}}$  is  $(6300 \pm 100) \Omega$ .

In a further experiment, HEK H2R/ $\text{mG}_s$  cells were investigated. A baseline of  $(5810 \pm 30) \Omega$  was measured in L15 buffer for 0.5 h before the addition of a CTRL or stimulation with varying concentrations of histamine (**Figure 48**).

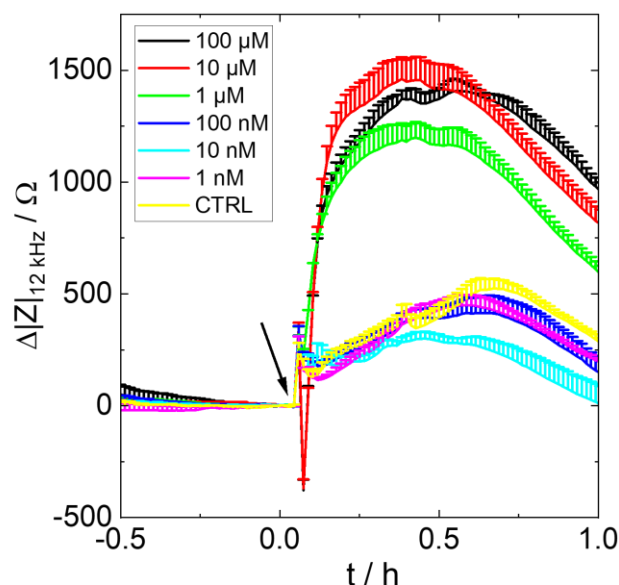


*Figure 48. Impedance change over time of HEK H2R/ $\text{mG}_s$  cells at a frequency of 12 kHz. The cells were cultivated on a 96W1E+ electrode array that was coated with crosslinked gelatin. At  $t = 0$  h, the cells were stimulated with different concentrations of histamine (black 100  $\mu\text{M}$ , red 10  $\mu\text{M}$ , green 1  $\mu\text{M}$ , blue 100 nM, cyan 10 nM, pink 1 nM, yellow CTRL). Baseline:  $(5810 \pm 30) \Omega$ . Mean + SE,  $N = 3$ , single experiment. CTRL = vehicle control. Temperature:  $37^\circ\text{C}$ .*

As observed for the HEK M1R/ $\text{mG}_q$  and HEK M5R/ $\text{mG}_q$  cells, an immediate impedance decrease is observed after ligand addition at  $t = 0$  h for histamine concentrations of 10-100  $\mu\text{M}$  (**Figure 48, black, red**). Then, impedance increases,

reaches a maximum after  $t = 0.4-0.6$  h and gradually falls off again. The CTRL shows an impedance increase of about  $500 \Omega$  until  $0.67$  h and subsequently decreases again (**Figure 48, yellow**). Similar behavior is observed for histamine concentrations between  $1-100$  nM (**Figure 48, blue, cyan, pink**). Up to  $t = 0.5$  h, the curve for  $100 \mu\text{M}$  histamine (**Figure 48, black**) displays lower impedance values than the curve for  $10 \mu\text{M}$  histamine (**Figure 48, red**). The curve for  $1 \mu\text{M}$  histamine (**Figure 48, green**) runs below the curve for  $100 \mu\text{M}$  histamine. No stringent concentration dependency is observed for the impedance signals. A maximal impedance change of  $(1500 \pm 100) \Omega$  is achieved by a histamine concentration of  $10 \mu\text{M}$   $0.4$  h after stimulation.

The experimental data at  $t = 0.5$  h was extracted and plotted against the logarithm of the histamine concentration. The data points were fitted with a four-parametric dose-response fit (**equation 15**). The corresponding concentration-response curve is shown in **Figure 49**.

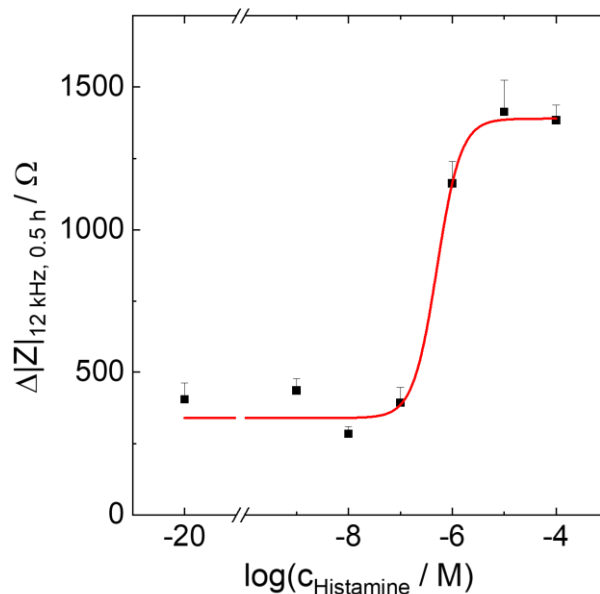


**Figure 49.** Concentration-response curve of **HEK H2R/mGs** cells after stimulation with **histamine**. The cells were grown on a crosslinked gelatin-coated 96W1E+ array. The impedance data at a frequency of  $12$  kHz and  $0.5$  h after stimulation (black squares) is plotted as a function of histamine concentration and was extracted from **Figure 48**. The concentration-response fit (red solid line, **equation 15**) reveals a  $pEC_{50}$  of  $6.3 \pm 0.2$  and an  $E_{\text{max}}$  of  $(1400 \pm 100) \Omega$ . Mean + SE,  $N = 3$ , single experiment. Temperature:  $37^\circ\text{C}$ .

For histamine concentrations up to  $100$  nM, the impedance does not change significantly and remains at the level of the CTRL (**Figure 49**). By further increasing the histamine concentration to  $1 \mu\text{M}$ , impedance increases significantly about  $1000 \Omega$ . Above  $1 \mu\text{M}$  of histamine, a saturation of impedance is observed. The steepest part of the curve (between  $100$  nM and  $1 \mu\text{M}$  histamine) is not determined well by the

experimental data points. The dose-response fit for histamine reveals a pEC<sub>50</sub> of  $6.3 \pm 0.2$  and an E<sub>max</sub> value of  $(1400 \pm 100) \Omega$ .

For HEK M1R/mG<sub>q</sub>, HEK M5R/mG<sub>q</sub> and HEK H2R/mG<sub>s</sub> cells, the basal impedance in L15 lies in a similar range between 5180-5800  $\Omega$  (**Figure 44A-D, Figure 46A-D and Figure 48**). These values are smaller than the impedance values detected for HEK cells in culture medium after a cultivation time of two days (cf. **chapter 4.1: Figure 39, blue and Figure 41, black**). During the medium exchange, several cells might have been washed off since HEK cells are only weakly adhering (Faussner et al., **2022**, Jayakumar, J. A. K. J. et al., **2020**), leading to decreased impedance values in this chapter. However, the confluency of the cells after medium exchange was routinely confirmed with phase contrast microscopy. The change of the basal impedance could also be ascribed to the different cell media and their varying conductivity. Furthermore, the osmolality inside the cells might depend on the medium in use. In L15, a osmolality of 300-336 mOs/kg is present, while the osmolality in DMEM amounts to 317-351 mOs/kg not including effects of fetal bovine serum (FBS) or other supplements (sigmaaldrich.com #7; **August 10, 2024**, sigmaaldrich.com #10; **August 10, 2024**, thermofisher.com; **August 10, 2024**).

For the three cell lines under study, a decrease in impedance is observed immediately after the addition of large agonist concentrations (**Figure 44A-D, Figure 46A-D and Figure 48**). This indicates an initial cellular reaction to ligand addition and is often observed for G<sub>q</sub>-coupled systems such as the M1R or M5R (Scott, Peters, **2010**, Verdonk et al., **2006**) and, for instance, was also observed in various cell lines expressing the G<sub>q</sub>-coupled histamine 1 receptor (H1R) (Lieb et al., **2016a**, Skiba, **2022**, Stolwijk et al., **2019**). However, the HEK H2R/mG<sub>s</sub> cells investigated in this work also show this behavior. This suggests that HEK H2R/mG<sub>s</sub> cells are not merely G<sub>s</sub>-coupled but may also couple via G<sub>q</sub>-proteins. The G<sub>q</sub>-coupling behavior of the H2R was also detected in literature before (Höring, **2022**, Kühn et al., **1996**, Wellner-Kienitz et al., **2003**) and will be further investigated in **chapter 5**.

Overall, the impedance time courses of HEK M1R/mG<sub>q</sub>, HEK M5R/mG<sub>q</sub> and HEK H2R/mG<sub>s</sub> cells are similar. After an initial transient decrease in impedance, it generally increases to reach a maximum and then slowly declines (**Figure 44A-D, Figure 46A-D and Figure 48**). In this, impedance behaves concentration-dependent. For increased ligand concentrations, larger impedance signals are observed. This means by ligand addition and subsequent GPCR activation, the resistive behavior of the cells changes and impedance increases, e.g. by alterations in the cell-matrix adhesion, the

cell shape or the barrier function and by cytoskeletal rearrangements (Doijen et al., **2019**, Stolwijk, Wegener, **2019**, Szénási et al., **2023**).

To exclude that the impedance changes occur because of GPCR-independent interactions between the ligands and the cells, control experiments with HEK wt cells were performed in a similar manner (**Appendix 22**). No concentration dependency of the impedance signal was observed after the addition of varying concentrations of iperoxo, carbachol or histamine to HEK wt cells. However, the cells showed a response of several 100  $\Omega$  after approximately 0.75 h for every ligand concentration, which might be explained by the activation of endogenous GPCRs like the muscarinic acetylcholine receptor 3 (M3R) or the H1R (Atwood et al., **2011**, Meisenberg et al., **2015**) or by GPCR-independent effects like mechanosensitive responses and liquid handling (Belly et al., **2022**, Saffioti et al., **2020**, Wilde et al., **2022**). The latter might also be an explanation for the impedance increase between 0.6-0.8 h observed for the CTRLs of HEK M1R/mG<sub>q</sub>, HEK M5R/mG<sub>q</sub> and HEK H2R/mG<sub>s</sub> cells (**Figure 44A-D**, **Figure 46A-D** and **Figure 48**).

In addition, the impedance signals of the three investigated NanoBiT systems were compared to CHO M1R (**Appendix 23**), CHO M5R (**Appendix 24**) and HEK H2R cells (**Appendix 25**), only expressing the native GPCRs but neither miniG proteins nor NanoLuc. Both CHO cell lines did not exhibit an immediate impedance decrease after stimulation, whereas HEK M1R/mG<sub>q</sub> and HEK M5R/mG<sub>q</sub> cells did display an initial decrease in impedance. Furthermore, CHO M1R cells displayed a biphasic behavior for iperoxo concentrations above 1 nM (**Appendix 23A**, **black**, **red**, **green**, **blue**, **cyan**) and carbachol concentration above 3  $\mu$ M (**Appendix 23B**, **black**, **red**, **green**, **blue**), which was not observed for HEK M1R/mG<sub>q</sub> cells. In addition, the highest iperoxo concentration of 10  $\mu$ M (**Appendix 23A**, **black**) led to decreased impedance values of CHO M1R cells compared to smaller iperoxo concentrations, indicating a toxic or hook effect (Ross et al., **2020**). This means above a certain ligand concentration the system saturates by which unspecific binding becomes more probable and might lead to a change of the functional readout. With few exceptions, the impedance signals of CHO M1R and CHO M5R cells did not decrease after  $t = 0.4-0.6$  h, as observed for HEK M1R/mG<sub>q</sub> and HEK M5R/mG<sub>q</sub> cells, but increased gradually over the measurement period. Moreover, the impedance signal of HEK H2R cells (**Appendix 25**) is more stable compared with HEK H2R/mG<sub>s</sub> cells (**Figure 48**). The differences between the impedance time courses of HEK M1R/mG<sub>q</sub> and CHO M1R cells, HEK M5R/mG<sub>q</sub> and CHO M5R cells and HEK H2R/mG<sub>s</sub> and HEK H2R cells can be explained by the expression of NanoLuc and miniG proteins that potentially influence the native GPCR signaling behavior. Furthermore, the variations

might be attributed to the different cell lines (HEK versus CHO). Depending on the tissue or species the cell line originates from, GPCR signaling might be altered (Hao, Tatonetti, **2016**, Michelotti et al., **2000**). Nonetheless, all control cell lines showed a concentration-dependent increase in impedance when agonists were added. From this, it can be deduced that the activation of the M1R, M5R and H2R indeed can be detected by impedance spectroscopy. **Table 14** gives an overview of the pEC50 and  $E_{max}$  values determined for the HEK cells expressing the NanoBiT technology (HEK M1R/mG<sub>q</sub>, HEK M5R/mG<sub>q</sub>, HEK H2R/mG<sub>s</sub>) compared to cells expressing the native GPCRs (CHO M1R, CHO M5R, HEK H2R). The values were determined according to **chapter 3.5.4**.

*Table 14. Comparison of pEC50 and  $E_{max}$  values of HEK M1R/mG<sub>q</sub> cells with CHO M1R cells, HEK M5R/mG<sub>q</sub> cells with CHO M5R cells and HEK H2R/mG<sub>s</sub> cells with HEK H2R cells. NanoBiT-labeled cells are compared with cells only expressing the respective native GPCR (no luciferase, no miniG protein). The muscarinic systems (M1R and M5R) were stimulated with iperoxo and carbachol. The H2R was activated by the addition of histamine. All values were determined by analysis of  $t = 0.5$  h of the impedance change after compound addition and concentration-response analysis according to **chapter 3.5.4**. For details see **Figure 44A-D** to **Figure 49** (NanoBiT systems) and **Appendix 23** to **Appendix 25** (native GPCRs). \* = CHO cells were used as control cell line.*

		NanoBiT system		Native GPCR	
		pEC50	$E_{max} / \Omega$	pEC50	$E_{max} / \Omega$
<b>M1R</b>	Iperoxo	8.39 ± 0.06	5400 ± 100	8.2 ± 0.2*	720 ± 70*
	Carbachol	5.55 ± 0.06	5340 ± 90	5.8 ± 0.2*	700 ± 50*
<b>M5R</b>	Iperoxo	9.0 ± 0.2	6000 ± 100	9.60 ± 0.06*	1640 ± 60*
	Carbachol	5.46 ± 0.04	6300 ± 100	6.18 ± 0.07*	1530 ± 60*
<b>H2R</b>	Histamine	6.3 ± 0.2	1400 ± 100	6.70 ± 0.04	830 ± 30

The pEC50 values are similar between the NanoBiT and native cell lines (cf. **Table 14**). The small differences in the pEC50 might indicate tissue- or species-dependent receptor behavior. Dependent on the species or tissue the cell line originates from, other signaling pathways might possibly be activated (Gao et al., **2022**), leading to distinct impedance responses for HEK and CHO cells. Furthermore, it must be considered that HEK and CHO cells were seeded in different cell densities and display varying impedance values after a cultivation time of two days (cf. **chapter 4.1**), which might lead to varying impedance responses.

By extracting the time course data of HEK M1R/mG<sub>q</sub>, HEK M5R/mG<sub>q</sub> and HEK H2R/mG<sub>s</sub> cells at  $t = 0.5$  h (**Figure 44A-D**, **Figure 46A-D**, **Figure 48**), concentration-response curves were obtained (**Figure 45A-B**, **Figure 47A-B**, **Figure 49**). They are well-fitted for HEK M1R/mG<sub>q</sub> cells. However, the curves for HEK M5R/mG<sub>q</sub> and HEK H2R/mG<sub>s</sub> cells are not well-described by the four-parametric dose-response fit, which

is also indicated by the larger errors of the pEC50 values compared to HEK M1R/mG<sub>q</sub> cells. At the M5R, larger carbachol concentrations (> 100 μM) should be investigated for a better determination of the upper asymptote and the E<sub>max</sub> value (**Figure 47B**). In addition, more histamine concentrations between 100 nM and 1 μM should be tested on HEK H2R/mG<sub>s</sub> cells for a more reliable determination of the pEC50 value (**Figure 49**). For the muscarinic systems, the pEC50 values of iperoxo are at least two orders of magnitude (logarithmic scale) larger than those for carbachol, rendering iperoxo more potent (**Table 14**). At the M1R, the pEC50 values of  $8.39 \pm 0.06$  for iperoxo and  $5.55 \pm 0.06$  for carbachol are in good agreement with the literature. For iperoxo, values of  $7.80 \pm 0.04$  and  $9.42 \pm 0.05$  and for carbachol, pEC50 values of  $4.69 \pm 0.05$ ,  $6.12 \pm 0.08$  and  $6.6 \pm 0.1$  have been described in the literature with the latter obtained by an impedance measurement with CHO cells expressing the M1R (Höring, **2022**, Littmann et al., **2018**, Scott, Peters, **2010**). At the M5R, values of  $9.0 \pm 0.2$  for iperoxo and  $5.46 \pm 0.04$  for carbachol were determined (**Table 14**). These values are also in accordance with the literature. For iperoxo, values between  $7.95 \pm 0.06$  and  $9.80 \pm 0.07$  have been found in luminescence-based G protein recruitment and inositol phosphate assays (Höring, **2022**, Littmann et al., **2018**, Randáková et al., **2021**). The pEC50 for carbachol at the M5R ranges between  $5.30 \pm 0.06$  and  $6.78 \pm 0.06$  in the literature (Höring, **2022**, Littmann et al., **2018**, Randáková et al., **2021**). In general, the efficacies for both iperoxo and carbachol are very similar in the impedance assay, even though iperoxo is often described as a superagonist with higher E<sub>max</sub> values than carbachol (Kloeckner et al., **2010**, Schrage et al., **2013**, Volpato et al., **2020**). This suggests that the efficacy depends on the readout parameter and whether it is more proximal or distal. In proximal miniG protein recruitment and inositol 1,4,5-trisphosphate (IP<sub>3</sub>) accumulation assays, the efficacies of both ligands differ significantly (Höring, **2022**, Randáková et al., **2021**), while for a more distal assay like the impedance assay they assimilate and both ligands act as full agonists. Since iperoxo and carbachol both activate the M1R and M5R, they prove to be non-selective agonists (Randáková et al., **2020**, Volpato, Holzgrabe, **2018**). Histamine exhibits a pEC50 of  $6.3 \pm 0.2$  at the H2R (**Table 14**). This value is similar to literature values of  $6.93 \pm 0.05$  found in a miniG protein recruitment assay (Höring, **2022**) and 6.16 received in a guinea pig right atrium assay (Pockes et al., **2018**). Overall, HEK M1R/mG<sub>q</sub>, HEK M5R/mG<sub>q</sub> and HEK H2R/mG<sub>s</sub> cells display similar behavior in the impedance assay. The time courses are similar and show an initial transient decrease in impedance, a subsequent impedance rise to a maximum and a slow decline of impedance. Nonetheless, the maximal impedance values differ between the cell lines. HEK H2R/mG<sub>s</sub> cells show maximal values of about 1500 Ω

(**Figure 48**), while HEK M1R/mG<sub>q</sub> (**Figure 44A-B**) and HEK M5R/mG<sub>q</sub> (**Figure 46A-B**) cells display maxima around 5000-6500  $\Omega$ , which is also mirrored by the different  $E_{\max}$  values determined by concentration-response analysis (**Table 14**). These variations in the maximal impedance might be attributed to the different signaling pathways (G<sub>q</sub> versus G<sub>s</sub>) and potentially also to varying expression levels of the receptors and the respective miniG proteins. However, for HEK H2R/mG<sub>s</sub> cells, about 10-fold the amount of receptors per cell was determined in radioligand saturation binding experiments in contrast to HEK M1R/mG<sub>q</sub> and HEK M5R/mG<sub>q</sub> cells (Höring, **2022**), which weakens this argument. Another explanation could be that a secondary coupling pathway, e.g. coupling to G<sub>q</sub> proteins, is (primarily) observed for HEK H2R/mG<sub>s</sub> cells by impedance spectroscopy while miniG<sub>s</sub>-coupling is insufficiently detectable or not detectable at all. As discussed above, the initial decrease of impedance after ligand addition is often observed for G<sub>q</sub>-coupled cells. Since HEK H2R/mG<sub>s</sub> cells also show a transient impedance decrease, G<sub>q</sub>-coupling might be a possible explanation for the impedance results. Furthermore, G<sub>q</sub>-coupling was also observed for HEK H2R/mG<sub>s,q</sub> cells in literature before (Höring, **2022**). Since the miniG<sub>s</sub> proteins are overexpressed in HEK H2R/mG<sub>s</sub> cells in contrast to the native G<sub>q</sub> proteins, the percentage of G<sub>q</sub>-coupling might be reduced, leading to smaller impedance maxima in comparison with the muscarinic receptor systems. To find out if impedance spectroscopy is potentially “blind” for certain signaling pathways, the G<sub>s</sub>-coupling behavior of HEK H2R cells was further investigated in **chapter 5.1**.

#### 4.2.2 Impedance Profiles in the Presence of Coelenterazine h

The influence of the cell-permeable luciferin coelenterazine h was investigated in impedance experiments analogous to **chapter 4.2.1** to ascertain possible interferences in the dual luminescence-impedance setup (see **chapter 4.6**). HEK M1R/mG<sub>q</sub> cells were used as a model cell line. They were seeded on crosslinked gelatin-coated 96W1E+ arrays as described in **chapter 3.5.3.1**. After a two-day cultivation and an equilibration in L15 buffer, a baseline measurement of impedance at 12 kHz was started using the ECIS Z $\theta$  device. Subsequently, 1  $\mu$ M coelenterazine h dissolved in L15 was added and impedance was recorded for 0.25 h. Finally, a vehicle control (CTRL) and seven concentrations of iperoxo (between 0.1 nM and 10  $\mu$ M) or seven concentrations of carbachol (between 100 nM and 1 mM) were added. The change of impedance was recorded for 1 h and is depicted in **Figure 50A-B**.

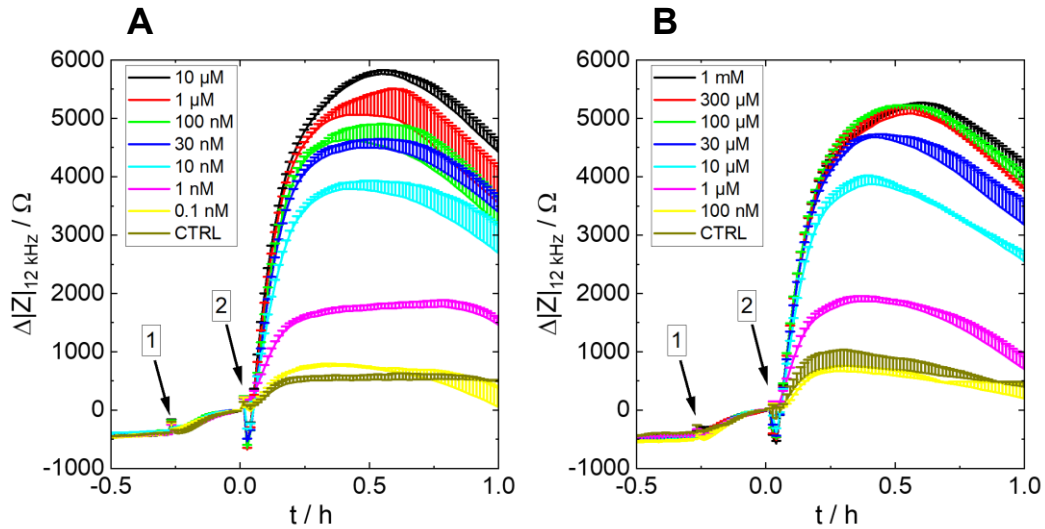


Figure 50. Impedance change over time of **HEK M1R/mG<sub>q</sub>** cells at a frequency of 12 kHz. The cells were cultivated on a 96W1E+ electrode array that was coated with crosslinked gelatin. At  $t = -0.25$  h,  $1 \mu\text{M}$  **coelenterazine h** (arrow 1) was added. At  $t = 0$  h, the cells were stimulated with different concentrations of **iperoxo (A)** or **carbachol (B)** (arrow 2). A: black  $10 \mu\text{M}$ , red  $1 \mu\text{M}$ , green  $100 \text{ nM}$ , blue  $30 \text{ nM}$ , cyan  $10 \text{ nM}$ , pink  $1 \text{ nM}$ , yellow  $0.1 \text{ nM}$ , brown CTRL. B: black  $1 \text{ mM}$ , red  $300 \mu\text{M}$ , green  $100 \mu\text{M}$ , blue  $30 \mu\text{M}$ , cyan  $10 \mu\text{M}$ , pink  $1 \mu\text{M}$ , yellow  $100 \text{ nM}$ , brown CTRL. Baseline A and B:  $(5650 \pm 10) \Omega$  and  $(5590 \pm 10) \Omega$ . Mean + SE,  $N = 3$ , single experiment. CTRL = vehicle control. Temperature:  $37^\circ\text{C}$ .

After the baseline has stabilized (**Figure 50A**:  $(5650 \pm 10) \Omega$  and **Figure 50B**:  $(5590 \pm 10) \Omega$ ),  $1 \mu\text{M}$  coelenterazine h was added, which is accompanied by a slight impedance increase of  $400\text{-}500 \Omega$  over  $0.25$  h for every curve. When the ligands are added, impedance decreases concentration-dependently for the five highest ligand concentrations of iperoxo and carbachol, respectively (**Figure 50A-B**, **black, red, green, blue, cyan**). Then impedance increases, reaches a maximum between  $t = 0.4\text{-}0.5$  h and slowly declines. For the CTRLs and the lowest concentrations of  $0.1 \text{ nM}$  iperoxo and  $100 \text{ nM}$  carbachol (**Figure 50A-B**, **yellow, brown**), impedance rises about  $500\text{-}800 \Omega$  within  $0.25$  h and remains relatively constant over the measurement period. For larger ligand concentrations, the impedance change is more pronounced. Impedance rises concentration-wise as observed in **chapter 4.2.1**. For iperoxo, only the curves for  $100 \text{ nM}$  and  $30 \text{ nM}$  overlay (**Figure 50A**, **green, blue**). For carbachol concentrations between  $100 \mu\text{M}$  and  $1 \text{ mM}$  (**Figure 50B**, **black, red, green**), the curves superimpose indicating saturation.

From **Figure 50A-B**, concentration-response plots were generated by extracting the values at  $t = 0.5$  h and plotting them against the logarithm of the ligand concentration. The experimental data was fitted with a four-parametric dose-response fit according to **equation 15**. The concentration-response relationships for iperoxo and carbachol are given in **Figure 51A-B** below.

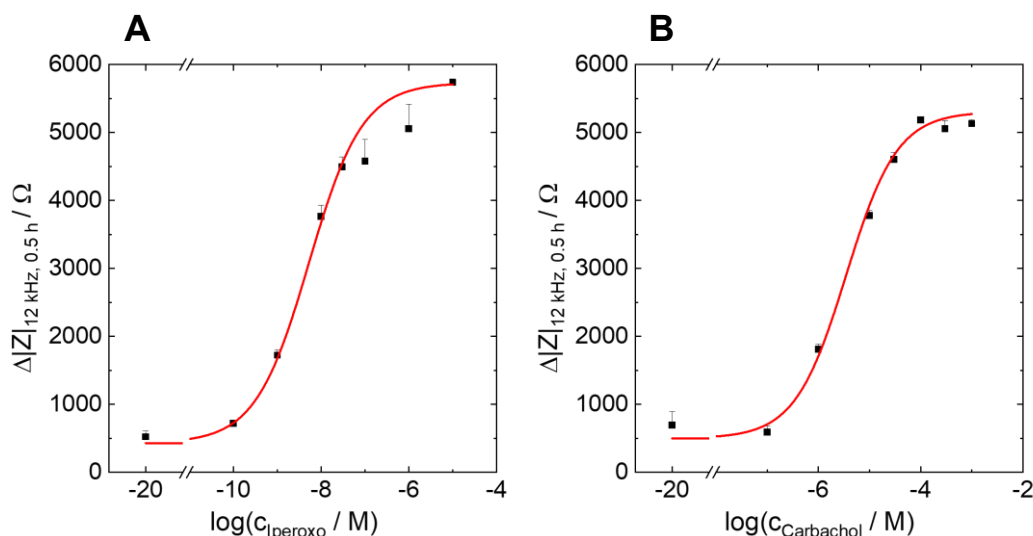


Figure 51. Concentration-response curves of **HEK M1R/mG<sub>q</sub>** cells after incubation with **1 μM coelenterazine h** and stimulation with **iperoxo (A)** or **carbachol (B)**. The impedance data at a frequency of 12 kHz and 0.5 h after stimulation (black squares) is plotted as a function of the agonist concentration and was extracted from **Figure 50A-B**. The concentration-response fits (red solid line, **equation 15**) reveal a **pEC<sub>50</sub>** of  $8.28 \pm 0.07$  for iperoxo and a **pEC<sub>50</sub>** value of  $5.5 \pm 0.1$  for carbachol. The **E<sub>max</sub>** values amount to  $(5730 \pm 80) \Omega$  for iperoxo and  $(5300 \pm 100) \Omega$  for carbachol. Mean + SE,  $N = 3$ , single experiment. Temperature: 37°C.

For iperoxo (**Figure 51A**) and carbachol (**Figure 51B**), the impedance change increases with increasing concentration. A sigmoidal curve shape is obtained with a saturation behavior above 100 nM iperoxo and 100 μM carbachol. The values of 0.1 nM iperoxo and 100 nM carbachol remain at the level of the CTRL. The concentration-response fits reveal a **pEC<sub>50</sub>** of  $8.28 \pm 0.07$  and an **E<sub>max</sub>** of  $(5730 \pm 80) \Omega$  for iperoxo and a **pEC<sub>50</sub>** of  $5.5 \pm 0.1$  and an **E<sub>max</sub>** of  $(5300 \pm 100) \Omega$  for carbachol. An overview of the determined **pEC<sub>50</sub>** and **E<sub>max</sub>** values for HEK M1R/mG<sub>q</sub> cells compared to the values from **chapter 4.2.1** (in the absence of coelenterazine h) is given in **Table 15**.

Table 15. Overview of **pEC<sub>50</sub>** and **E<sub>max</sub>** values determined for HEK M1R/mG<sub>q</sub> cells with the impedance assay. The  $\Delta|Z|_{12 \text{ kHz}, 0.5 \text{ h}}$  values in the presence (**Figure 51A-B**) and absence (**Figure 45A-B**) of **1 μM coelenterazine h** and after stimulation with iperoxo and carbachol are compared and were determined by a four-parametric dose-response fit as described in **chapter 3.5.4**.

		<b>pEC<sub>50</sub></b>	<b>E<sub>max</sub> / Ω</b>
<b>M1R</b>	Iperoxo (w/o coelenterazine h)	$8.39 \pm 0.06$	$5400 \pm 100$
	Carbachol (w/o coelenterazine h)	$5.55 \pm 0.06$	$5340 \pm 90$
	Iperoxo (w/ coelenterazine h)	$8.28 \pm 0.07$	$5730 \pm 80$
	Carbachol (w/ coelenterazine h)	$5.5 \pm 0.1$	$5300 \pm 100$

The pEC50 and  $E_{\max}$  values in the presence (this chapter) and absence (**chapter 4.2.1, Figure 45A-B**) of coelenterazine h determined by impedance analysis are similar. For iperoxo, pEC50 values of  $8.39 \pm 0.06$  in the absence and  $8.28 \pm 0.07$  in the presence of coelenterazine h were determined. Carbachol features pEC50 values of  $5.55 \pm 0.06$  in the absence and  $5.5 \pm 0.1$  in the presence of coelenterazine h. The efficacies in the form of  $E_{\max}$  values are found to be  $(5400 \pm 100) \Omega$  in the absence and at  $(5730 \pm 80) \Omega$  in the presence of coelenterazine h for the ligand iperoxo. For carbachol, values of  $(5340 \pm 90) \Omega$  in the absence and  $(5300 \pm 100) \Omega$  in the presence of coelenterazine h were determined. The largest difference is found between the  $E_{\max}$  values determined after stimulation with iperoxo: in the presence of coelenterazine h,  $E_{\max}$  is about  $300 \Omega$  larger than in the absence of coelenterazine h.

The time courses with (this chapter) and without (**chapter 4.2.1, Figure 44A-B**) preincubation with coelenterazine h only show minor differences. If coelenterazine h is added, a  $400\text{-}500 \Omega$  increase in impedance becomes visible (**Figure 50A-B**). This is explained by the high membrane permeability of coelenterazine h (Krasitskaya et al., **2020**, Shimomura, **1997**). It enters the cells easily, by which the osmolarity of the cells might change and, hence, the total impedance might be altered. Possibly, the  $400\text{-}500 \Omega$  increase also indicates intrinsic activity of the  $G_{\alpha}$ -GTPase or split NanoLuc after coelenterazine h addition (Maziarz et al., **2020**, Spalding, Burstein, **2006**). Another explanation could be liquid handling since all curves show the same impedance increase. Nonetheless, the  $400\text{-}500 \Omega$  increase in impedance after the addition of coelenterazine h is negligible compared to the subsequent impedance rise after ligand addition ( $5000\text{-}6000 \Omega$ , **Figure 50A-B**).

Independent of the presence of coelenterazine h, impedance rapidly decreases followed by an impedance rise to a maximum and a subsequent decrease of impedance after ligand addition. Only a few discrepancies between the curves in the absence and presence of coelenterazine h are identified. In the presence of coelenterazine h, the highest concentration of  $10 \mu\text{M}$  iperoxo (**Figure 50A, black**) displays a larger impedance than  $1 \mu\text{M}$  iperoxo (**Figure 50A, red**). By contrast, in the absence of coelenterazine h, the curve for  $10 \mu\text{M}$  iperoxo (**Figure 44A, black**) shows impedance values between the values of  $1 \mu\text{M}$  and  $100 \text{ nM}$  of iperoxo (**Figure 44A, red, green**). For  $10 \mu\text{M}$  carbachol, the impedance values in the absence of coelenterazine h are similar to those of  $30 \mu\text{M}$  carbachol (**Figure 44B, blue, cyan**), whereas in the presence of coelenterazine h, they are lowered compared to  $30 \mu\text{M}$  carbachol (**Figure 50B, blue, cyan**). These small variations of impedance in the

presence and absence of coelenterazine h are reduced to variations in the cellular behavior between experiments and not to an altered response to coelenterazine h itself. If the latter were true, for every ligand concentration, differences in the absence and presence of coelenterazine h would be expected.

The  $pEC_{50}$  and  $E_{max}$  values of iperoxo and carbachol in the presence of coelenterazine h (**Figure 51A-B**) hardly change in comparison to **Figure 45A-B**, where the cells were not preincubated with coelenterazine h (see **Table 15**). The only exceptions are the efficacies determined for iperoxo. In the presence of coelenterazine h, the  $E_{max}$  value of iperoxo is about 300  $\Omega$  larger. This is attributed to the dose-response fit in the presence of coelenterazine h, which does not represent the data for high iperoxo concentrations as well as in the absence of coelenterazine h (**Figure 51A**). The actual  $E_{max}$  in the presence of coelenterazine h is potentially smaller.

In summary, coelenterazine h does not have a significant impact on the impedance time courses, impedance maxima, potencies and efficacies after agonist addition. It is considered to be a suitable luciferin for dual luminescence-impedance measurements (**chapter 4.6**). In later experiments, the impedance assay conditions were further optimized regarding the electrode coatings, coelenterazine h aging, cell density and measurement buffers (see **chapter 4.4**).

### 4.3 Characterization of Muscarinic and Histaminergic GPCR Responses with the MiniG Protein Recruitment Assay

In contrast to most endpoint assays, the impedance assay described in **chapter 4.2** has great sensitivity and is a label-free holistic method to monitor GPCR activation in real-time. However, its integrative character has the drawback that elucidating the underlying mechanisms and signaling pathways is complicated. Deconvolution of the on-going processes can either be achieved by applying pathway-specific inhibitors or activators (cf. **chapter 5**) or by knocking down or knocking out certain pathways (Doijen et al., **2019**). Another possibility is to perform additional GPCR assays, e.g. second messenger assays, to compare impedance with a more proximal signal readout (cf. **chapter 5**).

In this work, a so-called NanoBiT assay is used to monitor miniG protein recruitment after GPCR activation in real-time. Stably transfected HEK M1R/mG<sub>q</sub>, HEK M5R/mG<sub>q</sub> and HEK H2R/mG<sub>s</sub> cells (cf. **chapter 3.1.2**) were used, labeled with a large NanoLuc fragment (Large BiT, LgBiT) at the miniG protein and a small NanoLuc fragment (Small BiT, SmBiT) at the receptor C-terminus. If the GPCR signaling cascade is

activated by the addition of an agonistic ligand, the miniG protein is recruited to the receptor and both NanoLuc fragments recombine, catalyzing a chemical reaction producing a bioluminescence in the presence of its luciferin (cf. **chapter 3.6**). In the following, the luminescence time courses of HEK M1R/mG<sub>q</sub>, HEK M5R/mG<sub>q</sub> and HEK H2R/mG<sub>s</sub> cells were investigated in the presence of iperoxo, carbachol (M1R and M5R) or histamine (H2R). Coelenterazine h was utilized as luciferase substrate. Very briefly, the cells were seeded with a density of  $3 \cdot 10^5$  c/cm<sup>2</sup> on sterilized, non-coated white 96-well plates. Two days after cell inoculation, the culture medium was exchanged with L15 buffer and the cells were equilibrated for 2-2.5 h at 0% CO<sub>2</sub> and 37°C. Subsequently, 1 μM coelenterazine h was added to the wells and a 0.15-0.25 h baseline measurement of luminescence was started at the Tecan Genios plate reader. Baseline measurements without coelenterazine h did not generate any luminescence signal (data not shown), which is why they were omitted in all later experiments. Finally, the ligands were added in different concentrations and luminescence was monitored for 1 h. For a more detailed description see **chapter 3.6.1.1**.

The time courses for HEK M1R/mG<sub>q</sub> cells stimulated with iperoxo and carbachol are depicted in **Figure 52A-B**. A baseline of about 22-23 BLU was recorded for 0.15 h before adding increasing iperoxo (between 0.1 nM and 10 μM) and carbachol (between 100 nM and 1 mM) concentrations and a vehicle control (CTRL).

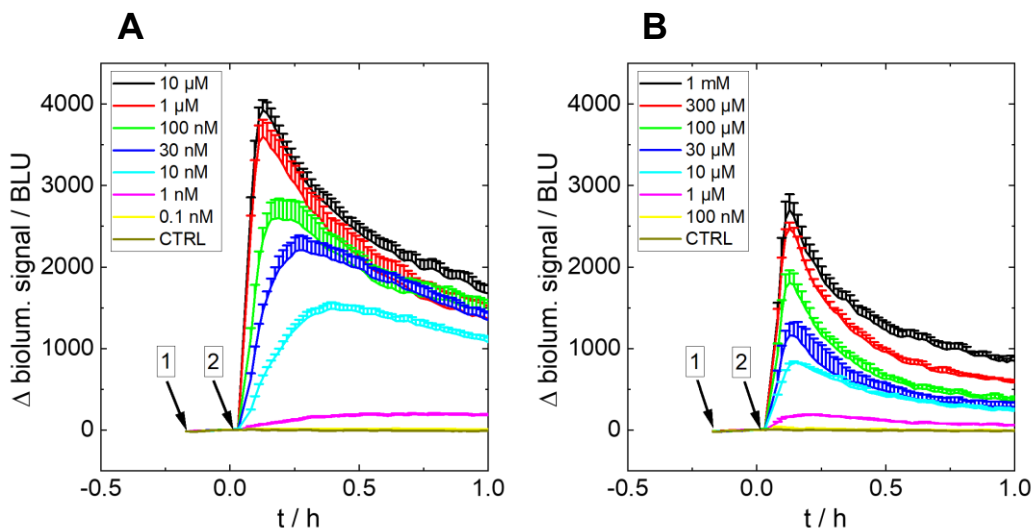


**Figure 52.** Luminescence change over time of **HEK M1R/mG<sub>q</sub>** cells. The cells were cultivated on a white 96-well plate. At  $t = -0.15$  h, 1 μM **coelenterazine h** was added (arrow 1). At  $t = 0$  h, the cells were stimulated with different concentrations of **iperoxo (A)** or **carbachol (B)** (arrow 2). A: black 10 μM, red 1 μM, green 100 nM, blue 30 nM, cyan 10 nM, pink 1 nM, yellow 0.1 nM, brown CTRL. B: black 1 mM, red 300 μM, green 100 μM, blue 30 μM, cyan 10 μM, pink 1 μM, yellow 100 nM, brown CTRL. Baseline A and B:  $(22.6 \pm 0.5)$  BLU and  $(22.6 \pm 0.6)$  BLU. Mean + SE, N = 6 (A) or 3 (B), single experiment. BLU = bioluminescence units. CTRL = vehicle control. Temperature: 37°C.

After the addition of iperoxo (**Figure 52A**) and carbachol (**Figure 52B**), the bioluminescence signal increases, reaches a maximum and rapidly decreases again over a measurement period of 1 h. Only the curves for the CTRL and 0.1 nM iperoxo and 100 nM carbachol (**Figure 52A-B, yellow, brown**) remain at the baseline level. With increasing ligand concentration, the signal maximum is enhanced. For iperoxo, a strong initial rise of luminescence is observed with steeper slopes for larger concentrations. A maximum signal of  $(3900 \pm 100)$  BLU is attained after 0.13 h for 10  $\mu\text{M}$  iperoxo (**Figure 52A, black**). The half-life of this bioluminescence level is  $t_{1/2} = 0.8$  h. With decreasing iperoxo concentration, the maximum is less pronounced in intensity and more delayed in time by which  $t_{1/2}$  is extended. The curves for the two highest iperoxo concentrations of 10  $\mu\text{M}$  and 1  $\mu\text{M}$  (**Figure 52A, black, red**) are not significantly different. In the case of carbachol, the slopes after ligand addition are steeper the higher the ligand concentration is. The maximum rises concentration-dependently and is observed after approximately  $t = 0.13$  h for every carbachol concentration. The biggest luminescence intensity is observed for the highest carbachol concentration of 1 mM with a value of  $(2700 \pm 200)$  BLU (**Figure 52B, black**). The half-life of this bioluminescence level is  $t_{1/2} = 0.44$  h.

From both luminescence data sets (**Figure 52A-B**), concentration-response curves were extracted. The luminescence data at  $t = 0.5$  h was plotted against the logarithmic ligand concentration and was fitted by a four-parametric dose-response relationship (**equation 15**). The concentration-response relations for iperoxo and carbachol are plotted in **Figure 53A-B**.

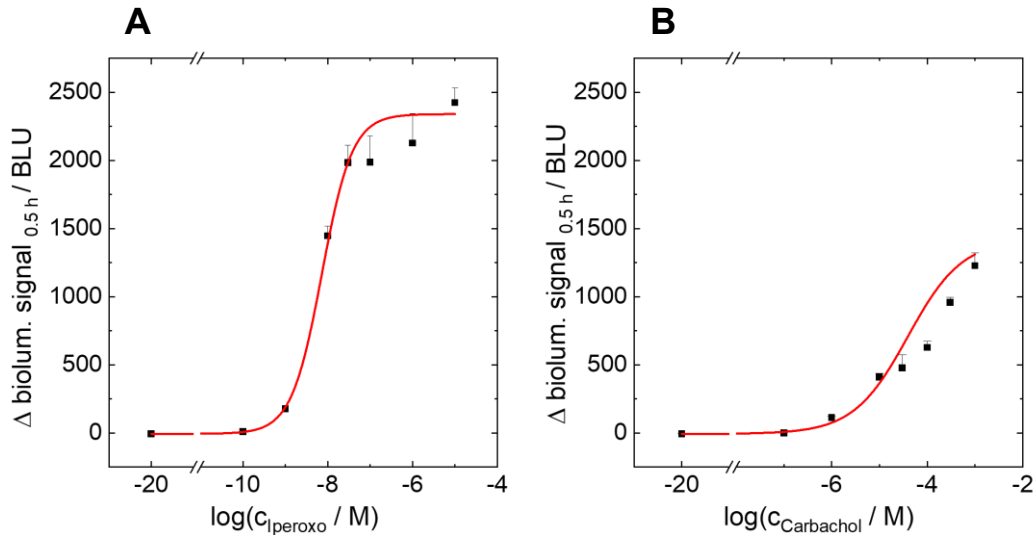


Figure 53. Concentration-response curves of **HEK M1R/mG<sub>q</sub>** cells on a white 96-well plate. After incubation with 1  $\mu\text{M}$  **coelenterazine h**, the cells were stimulated with different concentrations of **iperoxo (A)** or **carbachol (B)**. The luminescence data 0.5 h after stimulation (black squares) is plotted as a function of the ligand concentration and was extracted from **Figure 52A-B**. The concentration-response fits (red solid line, **equation 15**) reveal a  $pEC_{50}$  of  $8.14 \pm 0.06$  for iperoxo and a  $pEC_{50}$  of  $4.4 \pm 0.3$  for carbachol. The  $E_{max}$  values are  $(2300 \pm 100)$  BLU for iperoxo and  $(1400 \pm 300)$  BLU for carbachol. Mean + SE,  $N = 6$  (A) or 3 (B), single experiment. BLU = bioluminescence units. Temperature: 37°C.

Iperoxo in a concentration of 0.1 nM displays a similar luminescence value as the CTRL (**Figure 53A**). By further increasing the ligand concentration, the change of luminescence is increased. For 30 nM, 100 nM and 1  $\mu\text{M}$  of iperoxo, a relatively stable luminescence around 2100 BLU is observed. The highest iperoxo concentration of 10  $\mu\text{M}$  shows an even larger luminescence value. A sigmoidal curve shape is observed, which is best fitted for concentrations below 100 nM. For iperoxo, a  $pEC_{50}$  of  $8.14 \pm 0.06$  and an  $E_{max}$  of  $(2300 \pm 100)$  BLU is obtained. The readings for 100 nM carbachol (**Figure 53B**) feature a similar bioluminescence as the CTRL. By increasing the carbachol concentration, the luminescence change continuously increases. No saturation behavior is observed at the high-concentration end as for iperoxo. The curve is best fitted for concentrations below 30  $\mu\text{M}$  carbachol. A  $pEC_{50}$  of  $4.4 \pm 0.3$  and an  $E_{max}$  of  $(1400 \pm 300)$  BLU was determined for carbachol.

In another experiment, HEK M5R/mG<sub>q</sub> cells were investigated. After the addition of coelenterazine h at  $t = -0.26$  h, a baseline of luminescence was measured. Subsequently, different iperoxo (between 0.1 nM and 1  $\mu\text{M}$ ) and carbachol (between 10 nM and 100  $\mu\text{M}$ ) concentrations and a CTRL were added and luminescence was studied for 1 h. The luminescence time courses are displayed in **Figure 54A-B**.

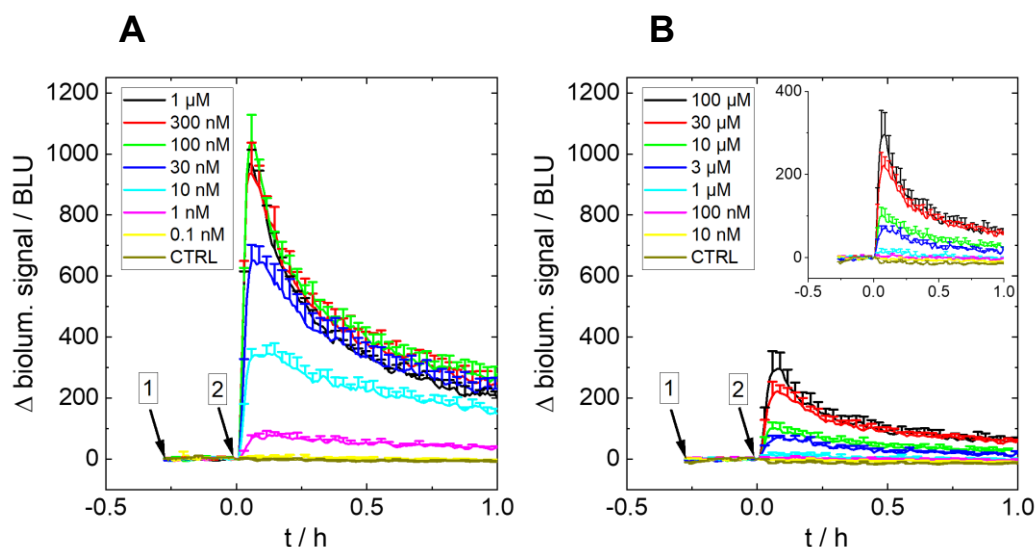


Figure 54. Luminescence change over time of **HEK M5R/mG<sub>q</sub>** cells. The cells were cultivated on a white 96-well plate. At  $t = -0.26$  h,  $1 \mu\text{M}$  **coelenterazine h** was added (arrow 1). At  $t = 0$  h, the cells were stimulated with different concentrations of **iperoxo (A)** or **carbachol (B)** (arrow 2). A: black  $1 \mu\text{M}$ , red  $300$  nM, green  $100$  nM, blue  $30$  nM, cyan  $10$  nM, pink  $1$  nM, yellow  $0.1$  nM, brown CTRL. B: black  $100 \mu\text{M}$ , red  $30 \mu\text{M}$ , green  $10 \mu\text{M}$ , blue  $3 \mu\text{M}$ , cyan  $1 \mu\text{M}$ , pink  $100$  nM, yellow  $10$  nM, brown CTRL. Baseline A and B:  $(17.9 \pm 0.4)$  BLU,  $(17.6 \pm 0.4)$  BLU. Mean + SE,  $N = 3$ , single experiment. BLU = bioluminescence units. CTRL = vehicle control. Temperature:  $37^\circ\text{C}$ .

After a constant baseline read at  $(17.9 \pm 0.4)$  BLU (**Figure 54A**) and  $(17.6 \pm 0.4)$  BLU (**Figure 54B**), luminescence increases concentration-dependently, peaks and steadily declines after reaching the maximum. In the case of iperoxo, the maxima are observed at  $t = 0.05$  h with an absolute maximum of  $(1050 \pm 80)$  BLU for  $100$  nM iperoxo (**Figure 54A, green**). The time  $t_{1/2}$  after which half of the maximum signal is observed is  $t_{1/2} = 0.28$  h for the three highest iperoxo concentrations (**Figure 54A, black, red, green**) and  $t_{1/2} = 0.5$  h for  $30$  nM iperoxo (**Figure 54A, blue**). The curves for  $\geq 100$  nM iperoxo saturate (**Figure 54A, black, red, green**). With decreasing concentrations, the signals get suppressed and the luminescence maxima are lowered. The curves for the CTRL and  $0.1$  nM iperoxo remain at the baseline level (**Figure 54A, yellow, brown**).

Carbachol displays way smaller luminescence values compared to iperoxo (**Figure 54B**). Nevertheless, the same concentration dependency is obtained. With larger carbachol concentrations, the luminescence signals increase. Only the curves for  $100 \mu\text{M}$  and  $30 \mu\text{M}$  carbachol (**Figure 54B, black, red**) slightly overlap. The absolute maximum of  $(300 \pm 50)$  BLU is observed for the  $100 \mu\text{M}$  carbachol after  $0.08$  h (**Figure 54B, black**). The kinetic behavior is similar to iperoxo as well. The luminescence maxima for carbachol concentrations between  $3$ - $100 \mu\text{M}$  (**Figure 54B, black, red, green, blue**) are reached between  $t = 0.05$ - $0.08$  h. The time after which half of the maximal response is observed increases with decreasing carbachol

concentration. For 100  $\mu\text{M}$  carbachol (**Figure 54B, black**),  $t_{1/2}$  amounts to 0.25 h, whereas it is 0.32 h for 30  $\mu\text{M}$  (**Figure 54B, red**) and 0.42 h for 10  $\mu\text{M}$  carbachol (**Figure 54B, green**).

Concentration-response curves of iperexo and carbachol were generated by analysis of the time point  $t = 0.5$  h. The experimental data was plotted against the logarithmic ligand concentration and fitted with a four-parametric dose-response relationship (**equation 15**) as shown in **Figure 55A-B**.

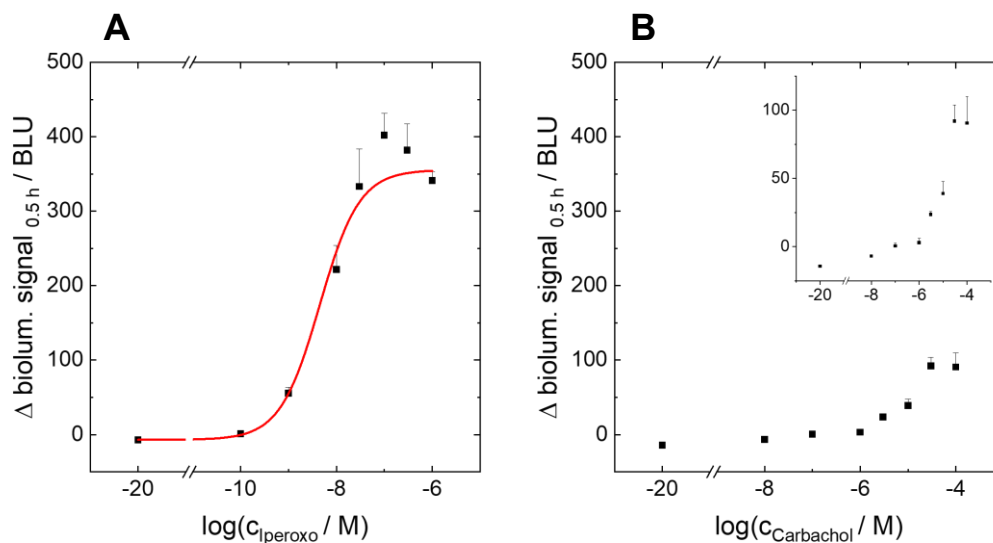


**Figure 55.** Concentration-response curves of **HEK M5R/mG<sub>q</sub>** cells on a white 96-well plate. After incubation with 1  $\mu\text{M}$  **coelenterazine h**, the cells were stimulated with different concentrations of **iperexo (A)** or **carbachol (B)**. The luminescence data 0.5 h after stimulation (black squares) is plotted as a function of the ligand concentration and was extracted from **Figure 54A-B**. The concentration-response fit (red solid line, **equation 15**) reveals a  $pEC_{50}$  of  $8.3 \pm 0.1$  and an  $E_{max}$  of  $(360 \pm 20)$  BLU for iperexo. For carbachol, a dose-response fit was only possible if the upper asymptote was set to  $(90 \pm 10)$  BLU (value for 30  $\mu\text{M}$  carbachol). Then, a  $pEC_{50}$  of  $4.8 \pm 0.3$  was determined. Mean + SE,  $N = 3$ , single experiment. BLU = bioluminescence units. Temperature: 37°C.

For iperexo (**Figure 55A**) and carbachol (**Figure 55B**), the luminescence increases with increasing ligand concentration. Sigmoidal curve shapes are observed. Only for the largest iperexo concentration of 1  $\mu\text{M}$ , the luminescence value after 0.5 h is lowered compared to 300 nM and 100 nM iperexo. In addition, the values for 0.1 nM iperexo and 10 nM, 100 nM and 1  $\mu\text{M}$  carbachol remain at the luminescence level of the CTRL. A  $pEC_{50}$  of  $8.3 \pm 0.1$  and an  $E_{max}$  of  $(360 \pm 20)$  BLU are determined for iperexo. The concentration-response curve for carbachol is markedly suppressed in comparison to iperexo and no sigmoidal fit is possible. Only if the upper asymptote ( $E_{max}$ ) is set to the maximal luminescence value of  $(90 \pm 10)$  BLU (30  $\mu\text{M}$  carbachol), a  $pEC_{50}$  of  $4.8 \pm 0.3$  is returned.

Furthermore, HEK H2R/mG<sub>s</sub> cells were investigated with the luminescence-based miniG recruitment assay. After a two-day cultivation and equilibration in L15 buffer according to **chapter 3.6.1.1**, a luminescence baseline of  $(2340 \pm 10)$  BLU was recorded after the addition of  $1 \mu\text{M}$  coelenterazine at  $t = -0.14$  h. Subsequently, different histamine solutions (between  $0.1 \text{ nM}$  and  $10 \mu\text{M}$ ) and a CTRL were added at  $t = 0$  h. The kinetic luminescence results are displayed in **Figure 56**.

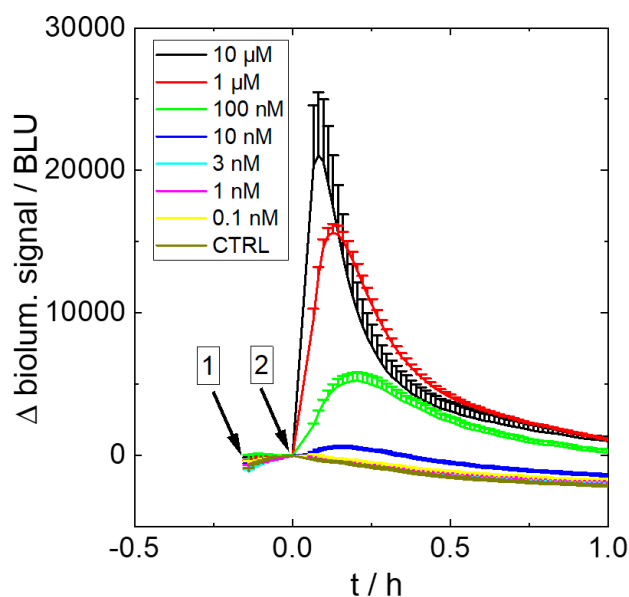


*Figure 56. Luminescence change over time of HEK H2R/mG<sub>s</sub> cells. The cells were cultivated on a white 96-well plate. At  $t = -0.14$  h,  $1 \mu\text{M}$  coelenterazine **h** was added and a luminescence measurement was started (arrow 1). At  $t = 0$  h, the cells were stimulated with different concentrations of histamine (arrow 2). Black  $10 \mu\text{M}$ , red  $1 \mu\text{M}$ , green  $100 \text{ nM}$ , blue  $10 \text{ nM}$ , cyan  $3 \text{ nM}$ , pink  $1 \text{ nM}$ , yellow  $0.1 \text{ nM}$ , brown CTRL. Baseline:  $(2340 \pm 10)$  BLU. Mean + SE,  $N = 6$ , single experiment. BLU = bioluminescence units. CTRL = vehicle control. Temperature:  $37^\circ\text{C}$ .*

Right after ligand addition, luminescence increases drastically for  $10 \mu\text{M}$  and  $1 \mu\text{M}$  histamine (**Figure 56, black, red**), reaches a maximum and decreases again. Similar behavior is observed for concentrations of  $100 \text{ nM}$  and  $10 \text{ nM}$  histamine (**Figure 56, green, blue**) but the initial slope is lowered for smaller histamine concentrations. Furthermore, the maxima are delayed in time and smaller in intensity with decreasing ligand concentration. For the highest concentration of  $10 \mu\text{M}$  histamine (**Figure 56, black**), a maximum of  $(21000 \pm 4000)$  BLU is found after  $t = 0.08$  h. The respective half-life is  $t_{1/2} = 0.2$  h. For  $1 \mu\text{M}$  histamine (**Figure 56, red**), the maximum lies at  $(15600 \pm 600)$  BLU after  $t = 0.13$  h and the curve for  $100 \text{ nM}$  histamine (**Figure 56, green**) shows a maximum of  $(5300 \pm 600)$  BLU after  $t = 0.2$  h. For  $10 \text{ nM}$  histamine (**Figure 56, blue**), the luminescence maximum lies at  $(500 \pm 100)$  BLU and is reached after  $t = 0.2$  h. The curves for the concentrations  $3 \text{ nM}$ ,  $1 \text{ nM}$ ,  $0.1 \text{ nM}$  and the CTRL

(Figure 56, cyan, pink, yellow, brown) are superimposing and remain at the baseline level.

By extracting the luminescence data at time point  $t = 0.5$  h, plotting it against the logarithmic histamine concentration and applying a four-parametric dose-response fit (equation 15), a concentration-response curve is generated, which is shown in Figure 57.

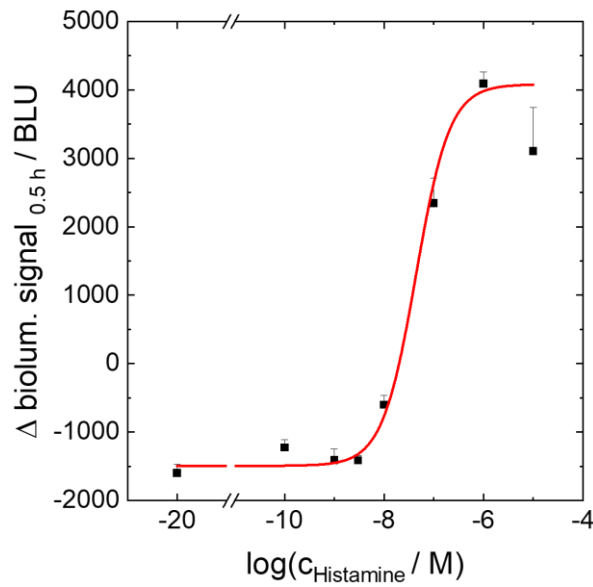


Figure 57. Concentration-response curve of **HEK H2R/mG<sub>s</sub>** cells after incubation with  $1 \mu\text{M}$  **coelenterazine h** and stimulation with **histamine**. The luminescence data  $0.5$  h after stimulation (black squares) is plotted as a function of histamine concentration and was extracted from **Figure 56**. The concentration-response fit (red solid line, **equation 15**) reveals a  $pEC_{50}$  of  $7.4 \pm 0.2$  and an  $E_{max}$  of  $(4100 \pm 400)$  BLU. Mean + SE,  $N = 6$ , single experiment. BLU = bioluminescence units. Temperature:  $37^\circ\text{C}$ .

With increasing histamine concentration, the luminescence change after  $0.5$  h rises (**Figure 57**). Only the values for  $0.1$  nM,  $1$  nM and  $3$  nM of histamine are similar to the value of the CTRL. Additionally, for the highest histamine concentration of  $10 \mu\text{M}$ , no further increase in the bioluminescence is observed but the luminescence value is reduced in comparison to the value for  $1 \mu\text{M}$  histamine. The sigmoid fit reveals a  $pEC_{50}$  of  $7.4 \pm 0.2$  and an  $E_{max}$  of  $(4100 \pm 400)$  BLU for histamine.

An overview of the  $pEC_{50}$  and  $E_{max}$  values of the three investigated cell lines (HEK M1R/mG<sub>q</sub>, HEK M5R/mG<sub>q</sub> and HEK H2R/mG<sub>s</sub>) and the respective agonistic ligands (iperoxo, carbachol and histamine) is presented in **Table 16**.

#### 4 Simultaneous Measurement of Luminescence and Impedance

Table 16. Overview of pEC50 and E<sub>max</sub> values determined for HEK M1R/mG<sub>q</sub>, HEK M5R/mG<sub>q</sub> and HEK H2R/mG<sub>s</sub> cells with the luminescence-based miniG protein recruitment assay. By a four-parametric dose-response fit of the luminescence data extracted at t = 0.5 h as described in **chapter 3.5.4**, values for iperoxo, carbachol (M1R, M5R) and histamine (H2R) were determined. BLU = bioluminescence units. \* = E<sub>max</sub> was fixed to the value for 30 μM carbachol.

		pEC50	E <sub>max</sub> / BLU
<b>M1R</b>	Iperoxo	8.14 ± 0.06	2300 ± 100
	Carbachol	4.4 ± 0.3	1400 ± 300
<b>M5R</b>	Iperoxo	8.3 ± 0.1	360 ± 20
	Carbachol	4.8 ± 0.3*	90 ± 10*
<b>H2R</b>	Histamine	7.4 ± 0.2	4100 ± 400

The E<sub>max</sub> for histamine at the H2R takes the highest value, followed by the E<sub>max</sub> values at the M1R and the M5R. For the latter two, the E<sub>max</sub> of iperoxo always display larger values than for carbachol. Additionally, the pEC50 of carbachol is always smaller compared to the pEC50 of iperoxo.

To prove that luminescence is ascribed to an interaction of the miniG protein with the receptor, similar experiments were conducted with HEK wt cells and CHO M1R, CHO M5R and HEK H2R cells that only express the native form of the GPCRs and (data only given for HEK wt, **Appendix 26**). The cells were first preincubated with 1 μM coelenterazine h and, subsequently, stimulated with different concentrations of iperoxo, carbachol or histamine. No change in luminescence is detectable but luminescence remains at the baseline level. Consequently, the luminescence signals of HEK M1R/mG<sub>q</sub>, HEK M5R/mG<sub>q</sub> and HEK H2R/mG<sub>s</sub> cells certainly indicate a receptor-miniG protein interaction and are not ascribed to unidentified or unspecific effects.

If the baseline values of luminescence are compared between the three cell lines, it is apparent that the baseline for HEK H2R/mG<sub>s</sub> cells (**Figure 56**) is > 100 times larger than for the muscarinic cell lines (**Figure 52A-B**, **Figure 54A-B**). Furthermore, the maximal luminescence values and E<sub>max</sub> values (**Table 16**) after stimulation of the H2R are larger compared to the M1R and M5R. This can be explained by different receptor and miniG protein expression. In previous radioligand saturation binding assays, varying amounts of binding sites per cell were determined (Höring, **2022**). For the HEK M1R/mG<sub>q</sub> system, (120000 ± 20000) sites/cell were determined (Höring, **2022**). In the HEK M5R/mG<sub>q</sub> cell line, (90000 ± 10000) sites/cell were found and for the HEK H2R/mG<sub>s</sub> cells, the receptor density amounts to (1000000 ± 200000) sites/cell (Höring, **2022**). The stoichiometry of the receptors to the miniG proteins was not measured. Nonetheless, the higher luminescence signals in the order of HEK H2R/mG<sub>s</sub> > HEK M1R/mG<sub>q</sub> > HEK M5R/mG<sub>q</sub> cells might be explained by an increased

receptor expression. Moreover, it is hypothesized that more constitutively active receptors are available in HEK H2R/mG<sub>s</sub> related to the higher receptor expression, leading to larger values for the baseline (Seifert, Wenzel-Seifert, **2002**, Threlfell et al., **2008**).

Additionally, the kinetics between the three cell lines were compared. Overall, a fast increase to a maximal luminescence value after  $t = 0.05\text{-}0.13$  h with a subsequent decline of luminescence is observed (**Figure 52A-B**, **Figure 54A-B**, **Figure 56**). The luminescence increase suggests that the labeled miniG protein is recruited to the receptor after ligand addition, the luciferase re-complements and catalyzes the oxidation of coelenterazine h (proximity assay). This happens on a second-to-minute time scale and proves the proximal nature of this assay. The luminescence decrease can either be explained by substrate depletion after oxidation, by receptor desensitization and internalization or by modifications in the miniG protein concentration because of potential changes in the cells' metabolism and a subsequent degradation of proteins (Hoare et al., **2020**, Hoare et al., **2021**, Reyes-Alcaraz et al., **2022**). In contrast to the luminescence kinetics, the maximal impedance response in similar experiments (see **chapter 4.2**) is established after  $t = 0.4\text{-}0.6$  h and remains relatively stable over a measurement time of 1 h. It is not as transient as the luminescence signal, confirming its integrative and distal character (Doijen et al., **2019**, Skiba et al., **2022**). Contrary to HEK M5R/mG<sub>q</sub> and HEK H2R/mG<sub>s</sub> cells, HEK M1R/mG<sub>q</sub> cells display more decelerated signaling dynamics. The luminescence maxima are hit after  $t = 0.13$  h at the earliest, whereas the maxima for HEK M5R/mG<sub>q</sub> and HEK H2R/mG<sub>s</sub> cells are attained between 0.05-0.08 h. Moreover, the luminescence signal at the M1R is more long-lived, since the half-live  $t_{1/2}$  of luminescence is elongated. The maximal concentrations of iperoxo and carbachol induce values of  $t_{1/2} = 0.8$  h at the M1R, respectively, while  $t_{1/2}$  ranges between 0.2-0.28 h for the other GPCR systems. For HEK M1R/mG<sub>q</sub> stimulated with iperoxo and HEK H2R/mG<sub>s</sub> stimulated with histamine, the luminescence maxima are delayed in time with decreasing ligand concentration. Concomitant,  $t_{1/2}$  is extended with decreasing concentrations. Additionally, steeper initial slopes are observed for enhanced ligand concentrations. This suggests that the kinetics are dependent on the investigated system and ligand and its concentration (Hoare et al., **2020**, Vilardaga, **2010**).

For all three investigated cell lines, the luminescence signal increases in a concentration-wise manner. More ligand evokes a faster and stronger miniG recruitment and subsequent luciferin oxidation. Moreover, above a certain ligand concentration, the signals often saturate in the concentration-response curves. This

is either explained by receptor reserve (Fernandez et al., 2020, Zhao, Furness, 2019) or a full occupation of the available receptors. In the former case, the maximal efficacy  $E_{\max}$  is reached if only a fraction of all available GPCRs is activated by a ligand. If the ligand concentration is increased further, no enhancement of  $E_{\max}$  is observed.

The pEC50 values determined in this chapter (**Table 16**) are similar to the literature. At the M1R, a pEC50 of  $8.14 \pm 0.06$  for iperoxo and a pEC50 of  $4.4 \pm 0.3$  for carbachol were determined (**Figure 53A-B**). In a complementary NanoBiT assay using the same cell line, pEC50 values of  $7.80 \pm 0.04$  for iperoxo and  $4.69 \pm 0.05$  for carbachol were found at the M1R (Höring, 2022). At the M5R, pEC50 values of  $8.3 \pm 0.1$  for iperoxo and  $4.8 \pm 0.3$  for carbachol were determined (**Figure 55A-B**). They match well with the values of  $7.95 \pm 0.06$  for iperoxo and  $5.30 \pm 0.06$  for carbachol found in the literature using the same cell line (Höring, 2022). The pEC50 of histamine at the H2R is found at  $7.4 \pm 0.2$  (**Figure 57**). In a similar assay using the same cell line, a value of  $6.93 \pm 0.05$  was determined for histamine (Höring, 2022), which is close to the value identified here. The small differences in the pEC50 values determined in this work and found literature might be attributed to the unique assay conditions, the use of different luciferins and measurement devices and the distinct data analysis protocols (Höring, 2022).

The concentration-response curves of carbachol (**Figure 53B, Figure 55B**) often lack a well-defined upper asymptote for the determination of reliable efficacy values. For a better determination of the  $E_{\max}$  value of carbachol, larger ligand concentrations should be tested. However, these concentrations (above 1 mM) are considered not physiological and, hence, were omitted. The carbachol concentration-response curve for HEK M5R/mG<sub>q</sub> cells (**Figure 55B**) can only be fitted if the upper asymptote is set to a fixed value of  $(90 \pm 10)$  BLU for 30  $\mu$ M carbachol. Still, it is recognized that the luminescence signals of carbachol are considerably suppressed in comparison to iperoxo (**Figure 55A**). Generally, higher maxima (**Figure 52A-B, Figure 54A-B**), pEC50 and  $E_{\max}$  values (**Figure 53A-B, Figure 55A-B, Table 16**) are found for iperoxo in contrast to carbachol. This indicates that iperoxo is more potent at both muscarinic receptors (M1R, M5R) and additionally can be classified as a superagonist (Schrage et al., 2016). In **chapter 4.2**, the impedance responses of iperoxo and carbachol were investigated at HEK M1R/mG<sub>q</sub> and HEK M5R/mG<sub>q</sub> cells in similar impedance experiments. There, iperoxo also displayed a larger potency in comparison with carbachol. However, iperoxo was classified as a full agonist and not as a superagonist and displayed a similar efficacy as carbachol in the impedance assay. These differences in the classification of iperoxo as a full agonist or superagonist are related to the assay readout parameter (Addis et al., 2023, Strange,

**2008**). Impedance is a very distal readout parameter, i.e. it integrates over several processes along the signaling cascade. This leads to an enhancement of the measured signal and, thus, to a lower discriminability between ligands that were classified as full agonists or superagonists in a more proximal assay like miniG protein recruitment (Skiba et al., **2022**, Stolwijk et al., **2019**).

In the concentration-response fits for HEK M5R/mG<sub>q</sub> and HEK H2R/mG<sub>s</sub> cells, the highest iperoxo and histamine concentration shows a reduced value in comparison with the second-highest ligand concentration (**Figure 55A and Figure 57**). This phenomenon is called hook effect and often appears in ternary complex bioassays, especially in indirect immunoassays. If an excess of target analyte is used, the capture and detector antibodies will be saturated with it, thus, reducing the immunocomplex formation and decreasing the signal (Ross et al., **2020**). Transferred to a two-sided ligand-receptor system, this could mean above a certain concentration, the ligand is saturating the system by which unspecific effects become more probable, potentially leading to an opposite effect on the functional readout.

In the course of this work, the NanoBiT assay was further optimized regarding the plate coatings and colors (**chapter 4.5.1**), integration time and gain (**chapter 4.5.2**), coelenterazine h concentration (**chapter 4.5.3**), cell number (**chapter 4.5.4**), an additional washing step (**chapter 4.5.5**), coelenterazine h aging (**chapter 4.5.6**) and the measurement buffer (**chapter 4.5.7**).

### 4.4 Optimization of the Impedance Assay

In order to find the optimal measurement parameters for a dual luminescence-impedance assay (**chapter 4.6**), several measurement settings and experimental conditions were tested in the impedance assay. It was optimized with regard to the electrode coating (**chapter 4.4.1**), the handling of the luciferin coelenterazine h (**chapter 4.4.2**), the seeded cell density (**chapter 4.4.3**) and measurement buffer (**chapter 4.4.3**). HEK M1R/mG<sub>q</sub> cells were used as a model cell line. Carbachol was utilized as ligand.

#### 4.4.1 Electrode Coatings

Strong adherence is crucial for ECIS. Only if cells are strongly attached to the gold film electrodes, current flow is impeded and a cellular signal becomes measurable (Lieb et al., **2016b**). Since HEK cells are poorly adhering cells (Faussner et al., **2022**, Jayakumar, J. A. K. J. et al., **2020**), three electrode coatings were tested to improve

cellular adherence. Coating with crosslinked gelatin was compared to coating with gelatin and preincubation with serum-containing medium (cf. **chapter 3.3.2**) In **chapter 4.1**, crosslinked gelatin already proved to be best suited for cellular attachment and adhesion. However, the impact of the different coatings on GPCR signaling has not been demonstrated yet. This will be addressed in the following.

HEK M1R/mG<sub>q</sub> cells were seeded according to the standardized protocol on 96W1E+ arrays coated with crosslinked gelatin, gelatin or medium (see **chapters 3.3.2 and 3.5.3.1**). On the day of the experiment, the culture medium was exchanged by L15 buffer, the cells were equilibrated and an impedance baseline was recorded at the ECIS Z $\theta$  at a frequency of 12 kHz for 0.5 h. Then, a vehicle control (CTRL) and seven different carbachol concentrations (between 100 nM and 1 mM) were added on-line and impedance was recorded for 1 h. The time courses are given in **Figure 58A-C**.

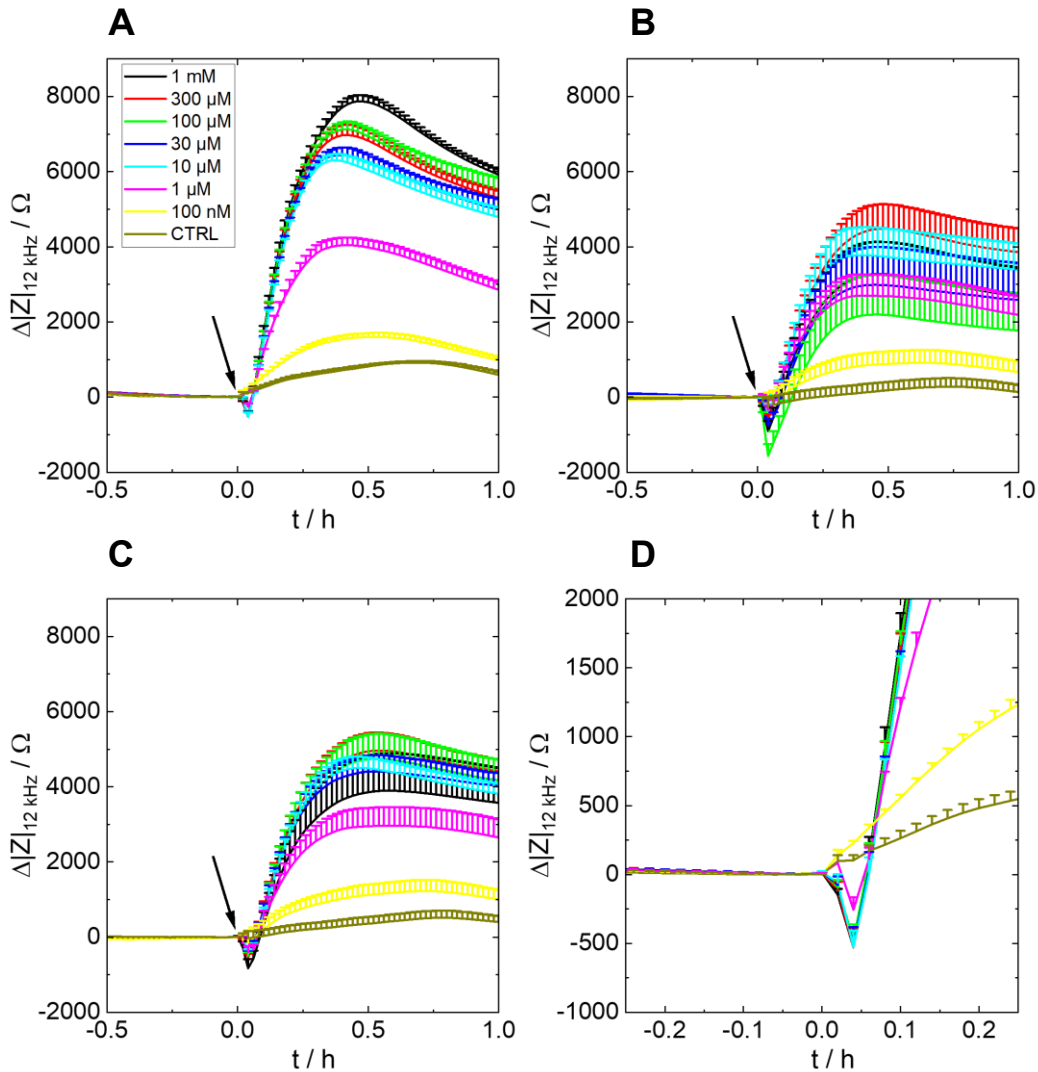


Figure 58. Impedance change over time of **HEK M1R/mG<sub>q</sub>** cells at a frequency of 12 kHz. The cells were cultivated on a 96W1E+ electrode array that was coated with **crosslinked gelatin (A,D)**, **gelatin (B)** or that was **preincubated with medium (C)**. After a baseline recording, the cells were stimulated with different concentrations of carbachol at  $t = 0$  h. D is a magnification of A and gives an example of the transient impedance decrease after stimulation. Black 1 mM, red 300  $\mu$ M, green 100  $\mu$ M, blue 30  $\mu$ M, cyan 10  $\mu$ M, pink 1  $\mu$ M, yellow 100 nM, brown CTRL. Baseline values from A to C:  $(5500 \pm 400)$   $\Omega$ ,  $(5400 \pm 800)$   $\Omega$ ,  $(5200 \pm 300)$   $\Omega$ . Mean + SE,  $N = 7-8$ , two independent experiments. CTRL = vehicle control. Temperature: 37°C.

After recording a stable baseline of 5200-5500  $\Omega$ , a transient decrease in impedance is identified after  $t = 0.04$  h. It is most pronounced for gelatin (**Figure 58B**) with a maximal change of about 1500  $\Omega$ , followed by medium (**Figure 58C**) with about 800  $\Omega$  and crosslinked gelatin (**Figure 58A,D**) with approximately 500  $\Omega$ . With few exceptions, the intensity of the transient impedance decrease is dependent on the carbachol concentration and is more pronounced for larger carbachol concentrations. Subsequently, impedance increases to reach a maximum and then slowly levels off. Only the impedance of the CTRL is relatively constant over time and remains at the baseline level (**Figure 58A-C, brown**).

For crosslinked gelatin, a distinct concentration dependency is observed: with larger ligand concentration, the impedance outcome increases. Only the curves for 300  $\mu\text{M}$  and 100  $\mu\text{M}$  carbachol (**Figure 58A, red, green**) as well as the curves for 30  $\mu\text{M}$  and 10  $\mu\text{M}$  (**Figure 58A, blue, cyan**) overlap. The maximal concentration of 1 mM carbachol shows the largest impedance signal (**Figure 58A, black**). In contrast to crosslinked gelatin, on gelatin-coated and medium preincubated electrodes, a concentration dependency is only observed up to a concentration of 10  $\mu\text{M}$  (gelatin, **Figure 58B, cyan**) and 300  $\mu\text{M}$  (medium, **Figure 58C, red**). Between 10-300  $\mu\text{M}$  of carbachol, the curves for medium preincubation saturate (**Figure 58C, red, green, blue, cyan**). The highest concentration of 1 mM carbachol displays lower impedance values than 10-300  $\mu\text{M}$  carbachol on medium preincubated electrodes (**Figure 58C, black**). On gelatin, the concentration dependency is completely lost above concentrations of 10  $\mu\text{M}$  carbachol. For instance, the impedance curves for concentrations of 30  $\mu\text{M}$  and 1 mM (**Figure 58B, black, blue**) overlap and display smaller impedance values than a concentration of 10  $\mu\text{M}$  carbachol (**Figure 58B, cyan**). Furthermore, the curve for 100  $\mu\text{M}$  carbachol (**Figure 58B, green**) exhibits lower values than 1  $\mu\text{M}$  carbachol (**Figure 58B, pink**). Generally, the error bars on gelatin are in a range of several hundred Ohms and underpin the lack of concentration dependency. Considering the error bars on medium preincubated electrodes, the curves for concentrations above 10  $\mu\text{M}$  can not be differentiated.

If the curves for individual carbachol concentrations are compared between the coatings, the impedance time courses of the two smallest carbachol concentrations of 100 nM and 1  $\mu\text{M}$  only feature insignificant variances: for all three coatings the curves rise to 1000-2000  $\Omega$  (100 nM, **Figure 58A-C yellow**) and 3000-4000  $\Omega$  (1  $\mu\text{M}$ , **Figure 58A-C, pink**), respectively, and slowly descend again. However, for concentrations  $\geq 10 \mu\text{M}$  (**Figure 58A-C, black, red, green, blue, cyan**), distinct differences are apparent between the coatings. On crosslinked gelatin, much higher impedance values (5000-8000  $\Omega$ ) are obtained. For instance, a value of  $(7900 \pm 200) \Omega$  is achieved by 1 mM carbachol on crosslinked gelatin, whereas  $(3300 \pm 900) \Omega$  and  $(4000 \pm 1000) \Omega$  are the maximum values for the same ligand concentration on gelatin and medium (all after approximately 0.5 h; **Figure 58A-C, black**). Furthermore, five to six times larger errors and, therefore, larger variances in impedance are measured on gelatin-coated and medium preincubated plates in comparison to crosslinked gelatin. A rough estimation of signal-to-noise (S/N) ratios by dividing the maximum values for 1 mM carbachol by the error of the impedance baseline results in values of 20, 4 and 13 for crosslinked gelatin, gelatin and medium preincubation, respectively.

The impedance data at  $t = 0.5$  h (**Figure 58A-C**) was extracted and plotted against the logarithm of the carbachol concentration for each coating. A four-parametric dose-response fit (**equation 15**) was used to analyze the curves. The concentration-response relationships are given in **Figure 59**.

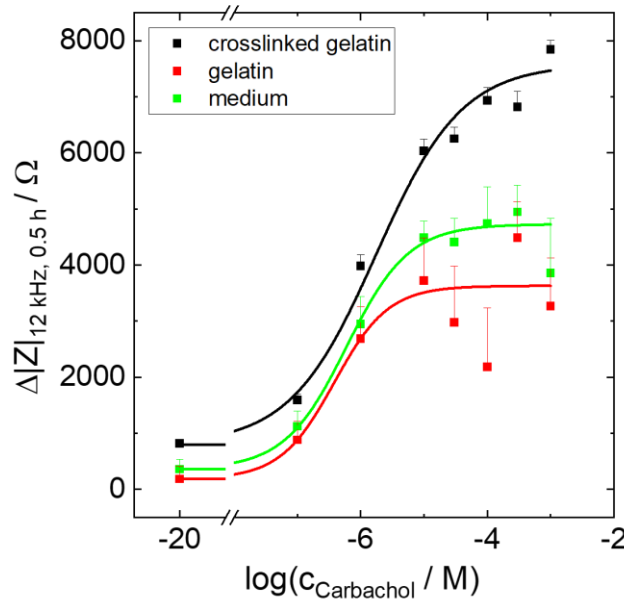


**Figure 59.** Concentration-response curves of HEK M1R/mG<sub>q</sub> cells on different coatings (**black: crosslinked gelatin, red: gelatin, green: medium**) after stimulation with different concentrations of carbachol. The change of impedance at a frequency of 12 kHz and 0.5 h after stimulation (squares) is plotted as a function of the carbachol concentration. The data was extracted from **Figure 58A-C**. The concentration-response fits (solid lines) reveal pEC<sub>50</sub> values of  $5.8 \pm 0.2$  on crosslinked gelatin,  $6.4 \pm 0.3$  on gelatin and  $6.2 \pm 0.1$  on medium. The  $E_{max}$  amount to  $(7600 \pm 400) \Omega$ ,  $(3600 \pm 400) \Omega$  and  $(4700 \pm 200) \Omega$  in the same order. Mean + SE,  $N = 7-8$ , two independent experiments. Temperature: 37°C.

The concentration-response curve of crosslinked gelatin (**Figure 59, black**) generally displays larger impedance values than the curves for gelatin (**Figure 59, red**) and medium (**Figure 59, green**). Moreover, the impedance values for medium are generally higher than for gelatin. Starting at a value of about 800 Ω (CTRL), the impedance magnitude on crosslinked gelatin continuously increases with increasing concentration. Only for 300 μM carbachol slightly lowered impedance values compared to 100 μM carbachol are observed. The impedance on gelatin-coated and medium preincubated electrodes also increases with larger carbachol concentrations. Both curves superimpose up to a concentration of 1 μM of carbachol with the CTRL exhibiting values between 200-400 Ω (**Figure 59, red, green**). Above a concentration of 1 μM carbachol, the impedance values are enhanced for medium in comparison to gelatin. On medium, a saturation behavior for concentrations between 10-300 μM is observed. The value for the highest concentration of 1 mM is lowered in comparison to 300 μM carbachol on medium preincubated electrodes (**Figure 59, green**). On

gelatin, a constant increase of impedance is observed until a concentration of 10  $\mu\text{M}$  is reached. Between 10-100  $\mu\text{M}$  of carbachol, the impedance constantly drops (local minimum for 100  $\mu\text{M}$  carbachol) (**Figure 59, red**). For 300  $\mu\text{M}$  carbachol, the maximal signal on gelatin is obtained and for 1 mM carbachol, impedance is lowered to the values of 10-30  $\mu\text{M}$  carbachol again. No real saturation behavior is observed in the high-concentration range but rather big fluctuations are obtained (**Figure 59, red**). When applying a dose-response fit, the data for gelatin is not fitted well as given by the  $R^2$  value of 0.94 in comparison with a  $R^2$  of 0.99 for crosslinked gelatin and medium. Furthermore, the highest carbachol concentration of 1 mM is not fitted well for medium preincubation (**Figure 59, green**). Concentration-response analysis yields  $pEC_{50}$  values of  $5.8 \pm 0.2$  on crosslinked gelatin,  $6.4 \pm 0.3$  on gelatin and  $6.2 \pm 0.1$  on medium. The identified  $E_{\text{max}}$  values are  $(7600 \pm 400) \Omega$  on crosslinked gelatin,  $(3600 \pm 400) \Omega$  on gelatin and  $(4700 \pm 200) \Omega$  on medium preincubated plates.

The transient impedance decrease after ligand addition is reduced on crosslinked gelatin (**Figure 58D**) in comparison with gelatin and medium. This might be attributed to less mechanical stimulation of the cells on crosslinked gelatin (Belly et al., **2022**, Saffioti et al., **2020**, Wilde et al., **2022**) but potentially also indicates less influence of  $G_q$ -coupling on the cells' morphology (Grogan et al., **2023**, Verdonk et al., **2006**). Additionally, its magnitude generally increases with the ligand concentration. Therefore, the initial impedance decrease arises from both the ligand-receptor interaction as well as the addition process itself interfering with cellular adhesion and mechano-stimulation.

Overall, the kinetics on all three coatings are similar to the kinetics observed in **chapter 4.2.1**. On crosslinked gelatin the only difference to **chapter 4.2.1** is that in this chapter the curves for 100  $\mu\text{M}$  and 300  $\mu\text{M}$  carbachol superimpose (**Figure 58A, red, green**), while in **chapter 4.2.1** the two highest concentrations of 300  $\mu\text{M}$  and 1 mM carbachol overlaid (**Figure 44B, black, red**). Furthermore, 1000-2000  $\Omega$  larger impedance values were detected in this chapter (**Figure 58A**). These differences can be explained by experimental variations such as varying protein expression levels and a modified cellular behavior depending on the passage number since the cell density is similar between experiments (see baseline values).

For small ligand concentrations, only small differences in the time courses are observed between the three coatings. However, for larger carbachol concentrations, the differences between the coatings are more distinct and the impedance values descend in this order: crosslinked gelatin > medium > gelatin. Consequently, the

signal change is most pronounced on crosslinked gelatin confirmed by the S/N estimation. This is attributed to stronger adhesion of the cells on crosslinked gelatin again, which reduces the distance between cells and electrodes and, thus, yields a more sensitive impedance readout, indicated by larger impedance changes (Janshoff et al., 2010, Stolwijk, Wegener, 2019).

Besides that, the measurement on crosslinked gelatin is less prone to scattering recognizable by the five to six times smaller error bars compared to the measurements on gelatin and medium preincubated electrodes. This implies that on gelatin-coated and medium preincubated plates the cells are not as strongly attached to the substrate surface as for crosslinked gelatin or that the cells partly detach after ligand addition because they are adhered weaker. This might give rise to larger impedance variations and losing the concentration dependency of the signals on gelatin and medium (e.g. 100  $\mu$ M curve on gelatin in **Figure 58B, green**; also noticeable in the concentration-response curve in **Figure 59, red**).

One similarity between the coatings is the emergence of the impedance maximum after approximately 0.5 h. By evaluating this time point, pEC50 and  $E_{\max}$  values were determined. The pEC50 of  $5.8 \pm 0.2$  on crosslinked gelatin is in good agreement with the pEC50 of  $5.55 \pm 0.06$  determined in **chapter 4.2.1**. However, the  $E_{\max}$  value is 42% larger in comparison to **chapter 4.2.1**. As explained above, this phenomenon might be attributed to variances in the protein expression that fluctuated contingent on the passage number and thawing cycle and can not be ascribed to an altered seeding density. The latter was similar for both experiments, since the baseline impedance took values of about 5500  $\Omega$ , respectively (**Figure 44 and Figure 58A**). Consequently, changes in the GPCR and miniG protein expression potentially led to changes in the absolute impedance magnitudes after stimulation. For gelatin and medium, the pEC50 values are 7-10% larger while the  $E_{\max}$  values are 38-52% smaller compared to crosslinked gelatin (**Figure 59**). The latter confirm the enhanced signal change on crosslinked gelatin compared to the other coatings. However, the concentration-response curves for gelatin and medium preincubation must be interpreted with care because the corresponding impedance time courses show larger error bars compared with crosslinked gelatin.

Summed up, crosslinked gelatin is considered the coating with the best performance. In **chapter 4.1**, crosslinked gelatin proved to enhance the adherence of HEK cells in comparison with gelatin and medium preincubation. In this chapter, crosslinked gelatin again revealed the best impedance results after GPCR stimulation concerning the reproducibility of the time courses, the signal intensity and a concentration dependency. Consequently, crosslinked gelatin is a strong candidate for subsequent

experiments where impedance and luminescence are combined in one setup (cf. **chapter 4.6**) but will be investigated in the luminescence assay first to test for potential interferences (see **chapter 4.5.1**).

#### 4.4.2 Coelenterazine h Aging

In this chapter, the impact of differently treated coelenterazine h solutions on the impedance outcome after GPCR stimulation of HEK M1R/mG<sub>q</sub> cells with carbachol is investigated. In **chapter 4.2.2**, no significant influence of coelenterazine h on impedance was found. Consequently, no effect on the impedance signals is expected here. Nonetheless, breakdown products after heating or light exposure and the oxidized or hydrolyzed form of coelenterazine h might be formed during assay preparation and could affect the impedance results. This will be tested in the following. HEK M1R/mG<sub>q</sub> cells were seeded according to the standardized protocol on a 96W1E+ array (**chapter 3.5.3.1**). Before the experiment, the culture medium was exchanged with L15 buffer and an impedance baseline was recorded at the ECIS Z<sub>0</sub>. At  $t = -0.14$  h, four differently prepared and handled coelenterazine h solutions (1  $\mu\text{M}$  respectively) were added (cf. **chapter 3.5.3.1**). The *control* solution was diluted freshly on the day of the experiment and was kept at 4°C in the dark until use. Another solution was prepared on the day of the experiment but was alternately preheated (37°C) and cooled (4°C) three times in 5 min intervals. It is referred to as “*three warm-cold-cycles*”. Two other solutions were prepared the day before the experiment. One of them, referred to as “*4°C dark*”, was stored at 4°C in the dark until the experiment but had a chance to undergo oxidation and hydrolysis at ambient air. The second one, referred to as “*r.t. illuminated*”, was kept at room temperature (r.t.) overnight. It was not protected from light. Furthermore, oxidation and hydrolysis could take place.

After the addition of 1  $\mu\text{M}$  of the differently treated coelenterazine h solutions to HEK M1R/mG<sub>q</sub> cells, the impact on the stimulation response was tested by the addition of 100  $\mu\text{M}$  carbachol or a vehicle control (CTRL) at  $t = 0$  h. Compared to **chapter 4.2.2**, 100  $\mu\text{M}$  carbachol should induce a maximal impedance response of approximately 5000  $\Omega$  after 0.5 h. Impedance was recorded for 1 h and is depicted in **Figure 60A-D**

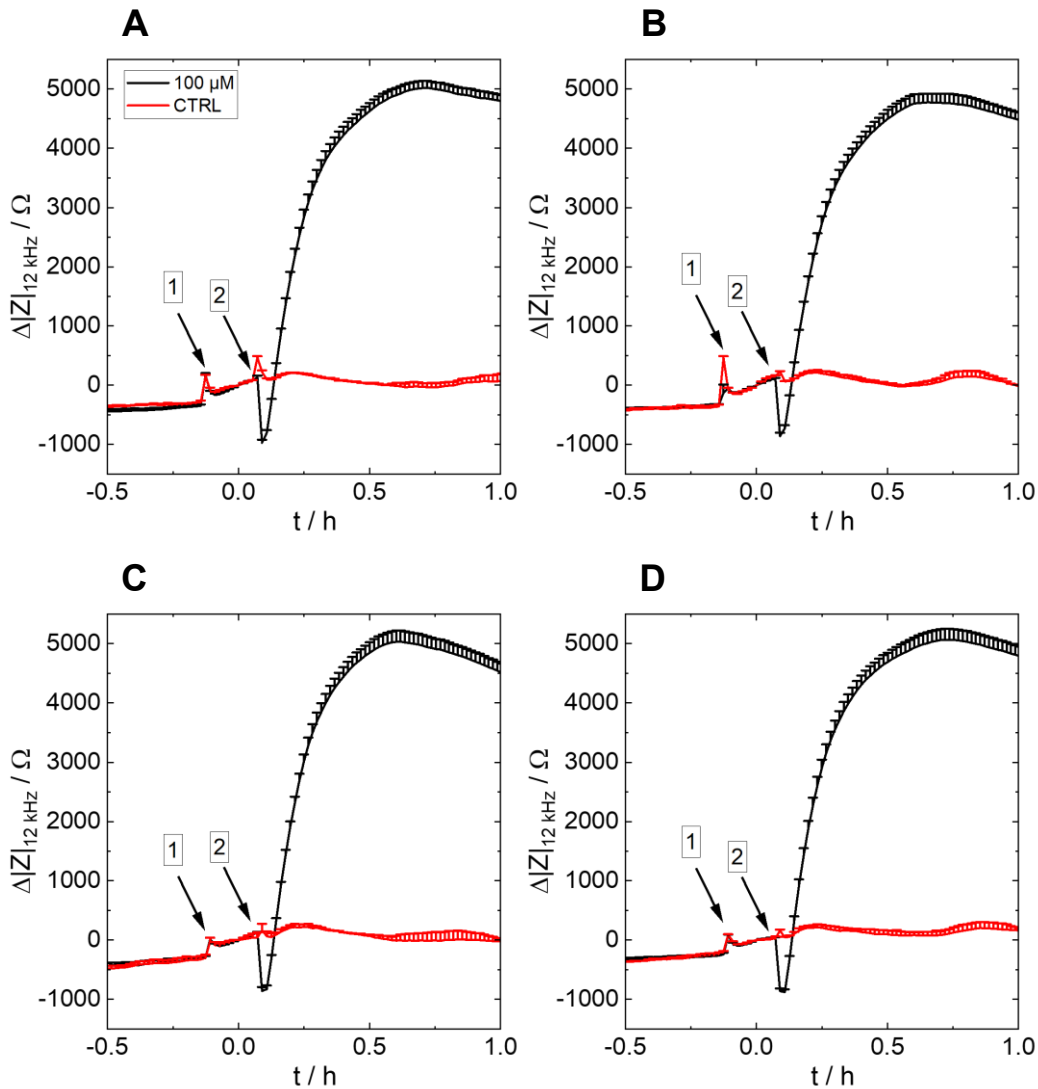


Figure 60. Impedance change over time of **HEK M1R/mG<sub>q</sub>** cells at a frequency of 12 kHz. The cells were cultivated on a 96W1E+ electrode array that was coated with gelatin. At  $t = -0.14$  h, differently treated coelenterazine h solutions ( $1 \mu\text{M}$  respectively) were added (**A: control; B: three warm-cold-cycles; C: 4°C dark; D: r.t. illuminated**, arrow 1). At  $t = 0$  h (arrow 2), the cells were treated with a CTRL (red) or stimulated with  $100 \mu\text{M}$  of carbachol (black). Baseline values from A to D:  $(5800 \pm 200) \Omega$ ,  $(6560 \pm 50) \Omega$ ,  $(6910 \pm 50) \Omega$ ,  $(6840 \pm 40) \Omega$ . Mean + SE,  $N = 2$  (CTRL) or 6 ( $100 \mu\text{M}$ ), single experiment. CTRL = vehicle control. Temperature:  $37^\circ\text{C}$ .

After a baseline recording ( $5800$ - $6910 \Omega$ ) and the addition of different luciferin solutions ( $1 \mu\text{M}$  respectively) (**Figure 60A-D**), impedance transiently increases about  $300$ - $800 \Omega$ . Then, impedance slightly rises about  $140$ - $300 \Omega$  over a time span of  $0.17$  h. Subsequently, carbachol or a CTRL was added. For the CTRL, again a small addition peak is observed but impedance remains relatively constant over the measurement period. For carbachol, impedance decreases by about  $1000 \Omega$  as observed in **chapter 4.2** and, subsequently, increases to reach a maximal value after approximately  $0.5$  h that is maintained over the measurement period. The maxima are  $(5000 \pm 100) \Omega$  for the *control* (**Figure 60A**),  $(4800 \pm 100) \Omega$  for *three warm-cold-*

*cycles (Figure 60B)*,  $(5000 \pm 200) \Omega$  for *4°C dark (Figure 60C)* and  $(5100 \pm 200) \Omega$  for *r.t. illuminated (Figure 60D)*.

The findings from this study imply that differently treated coelenterazine h solutions do not have a significant impact or toxic effect on the cells detected by impedance (Ngoc Le et al., 2019). Neither the time course after coelenterazine h addition nor the impedance profile after GPCR stimulation with carbachol is changed in comparison to *control* conditions. Furthermore, the time courses and kinetics are all similar to the results from **chapter 4.2.2**: the CTRLs take impedance values between  $-500 \Omega$  and  $1000 \Omega$  and remain relatively constant over time, while the curve for  $100 \mu\text{M}$  carbachol exhibits an impedance increase to a value of about  $5000 \Omega$  as previously observed in **Figure 50B, green**. This indicates that the products after potential coelenterazine h oxidation, hydrolysis, heating and illumination do not influence the impedance reading (Kaskova et al., 2016, Shimomura et al., 2001, White et al., 1961). But since luminescence strongly depends on the presence of a luciferin (Didiot et al., 2011, Kanie et al., 2020), the impact of the same coelenterazine h solutions on bioluminescence was analyzed in **chapter 4.5.6**.

### 4.4.3 Cell Density

In **chapter 4.1**, the impact of the cell density on the adhesion profile detected by impedance spectroscopy was investigated. There, the aim was to find an optimal seeding density for the best discrimination between cell-free and cell-covered electrodes. In this chapter, the impact of the cell density on GPCR stimulation detected by impedance measurements is examined. To identify a dependence of the impedance signal after receptor stimulation on the cell number, two kinds of experiments were conducted. On the one hand, different cell densities were seeded (**chapter 4.4.3.1**). After a medium exchange on day two, the measurement was performed on day three to ensure the cells had enough time to attach, adhere and grow and to guarantee a sufficient receptor and miniG protein expression. On the other hand, cells were seeded with the standard density of  $3 \cdot 10^5 \text{ c/cm}^2$  but were measured one, two and three days after subcultivation to allow for different growth and expression times (**chapter 4.4.3.2**).

## 4.4.3.1 Different Seeding Densities

HEK M1R/mG<sub>q</sub> cells were seeded with densities of  $5 \cdot 10^4$  c/cm<sup>2</sup>,  $10^5$  c/cm<sup>2</sup>,  $2 \cdot 10^5$  c/cm<sup>2</sup> and  $3 \cdot 10^5$  c/cm<sup>2</sup> on an 8W1E array coated with crosslinked gelatin. After a two-day cultivation, the culture medium was exchanged with L15 buffer and an impedance baseline was recorded at the ECIS SA. Finally, 300  $\mu$ M carbachol or a vehicle control (CTRL) were added and impedance was recorded for 1 h (**Figure 61**).

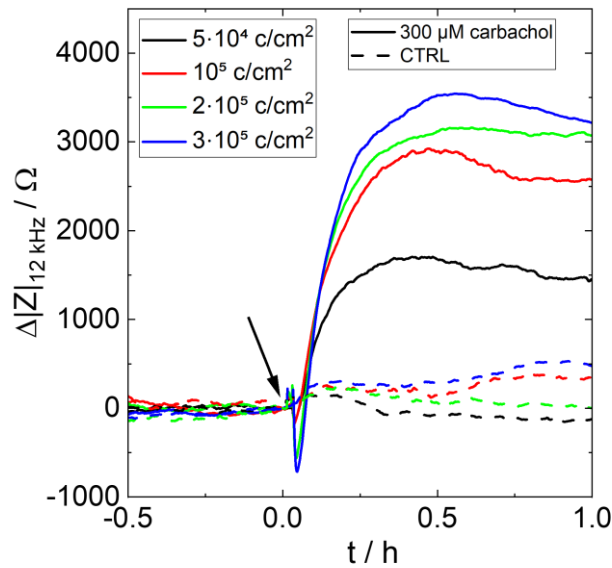


**Figure 61.** Impedance change over time of **HEK M1R/mG<sub>q</sub>** cells at a frequency of 12 kHz. The cells were seeded with different cell densities (**black:  $5 \cdot 10^4$  c/cm<sup>2</sup>**, **red:  $10^5$  c/cm<sup>2</sup>**, **green:  $2 \cdot 10^5$  c/cm<sup>2</sup>**, **blue:  $3 \cdot 10^5$  c/cm<sup>2</sup>**) on an 8W1E electrode array that was coated with crosslinked gelatin. After a baseline recording, the cells were either stimulated with 300  $\mu$ M of carbachol (solid lines) or treated with a CTRL (dashed lines) at  $t = 0$  h. Baseline from  $5 \cdot 10^4$  c/cm<sup>2</sup> to  $3 \cdot 10^5$  c/cm<sup>2</sup>:  $(3970 \pm 20)$   $\Omega$ ,  $(4950 \pm 80)$   $\Omega$ ,  $(6380 \pm 20)$   $\Omega$ ,  $(7200 \pm 20)$   $\Omega$ .  $N = 1$ , single experiment. CTRL = vehicle control. Temperature: 37°C.

The baseline impedance values for the increasing seeding densities differ significantly. With increasing cell number, the basal impedance rises from  $(3970 \pm 20)$   $\Omega$  for  $5 \cdot 10^4$  c/cm<sup>2</sup> to  $(4950 \pm 80)$   $\Omega$  for  $10^5$  c/cm<sup>2</sup>,  $(6380 \pm 20)$   $\Omega$  for  $2 \cdot 10^5$  c/cm<sup>2</sup> and  $(7200 \pm 20)$   $\Omega$  for  $3 \cdot 10^5$  c/cm<sup>2</sup> (**Figure 61**). The impedance response after the addition of the CTRL displays rather similar behavior for all seeding densities (**Figure 61, dashed lines**). No significant impedance difference is detected for varying seeding densities. After stimulation with 300  $\mu$ M carbachol (**Figure 61, solid lines**), impedance first decreases and then rises to different extents within 0.5 h. Then, for all four cell densities, impedance remains at a constant level over the measurement period. The largest impedance magnitudes are observed for  $3 \cdot 10^5$  c/cm<sup>2</sup> (**Figure 61, blue**) with an intensity of about 700  $\Omega$  for the initial impedance decrease and 3500  $\Omega$  for the maximum. With decreasing cell density, the initial

decrease takes continuously smaller values between 140-560  $\Omega$  (**Figure 61, black, red, green**). The maximum values are found at about 3200  $\Omega$  for  $2 \cdot 10^5$  c/cm<sup>2</sup>, 2900  $\Omega$  for  $10^5$  c/cm<sup>2</sup> and 1700  $\Omega$  for  $5 \cdot 10^4$  c/cm<sup>2</sup> after  $t = 0.5$  h.

From these findings, it is concluded that the basal impedance, the initial impedance decrease and the maximal signal depend on the seeding density. For a density of  $5 \cdot 10^4$  c/cm<sup>2</sup>,  $10^5$  c/cm<sup>2</sup> and  $2 \cdot 10^5$  c/cm<sup>2</sup> (**Figure 61, black, red, green**), the basal impedance was 45%, 31% and 11% lower compared to  $3 \cdot 10^5$  c/cm<sup>2</sup> (**Figure 61, blue**). Similar observations have been found in literature as well. Ebrahim *et al.* found different basal impedance values after seeding different cell densities of a human epithelial cell line on ECIS electrodes (Ebrahim *et al.*, **2022**). For instance, 4 h after seeding, a density of  $3 \cdot 10^4$  c/well displayed smaller impedance values and larger capacitance values compared to a density of  $6 \cdot 10^4$  c/well. The depression of the impedance maxima with decreasing cell number (**Figure 61**) amounts to 52%, 18% and 11% smaller values for  $5 \cdot 10^4$  c/cm<sup>2</sup>,  $10^5$  c/cm<sup>2</sup> and  $2 \cdot 10^5$  c/cm<sup>2</sup> in contrast to  $3 \cdot 10^5$  c/cm<sup>2</sup>. Similar observations were made by McGuinness *et al.* They measured the impedance response of eight cell densities of CHO M1R cells after stimulation with 10  $\mu$ M of the agonist oxotremorine and detected a reduction of the impedance signal with decreasing cell numbers (McGuinness *et al.*, **2009**). Likewise, the initial impedance decrease takes 80%, 76% and 22% smaller values for  $5 \cdot 10^4$  c/cm<sup>2</sup>,  $10^5$  c/cm<sup>2</sup> and  $2 \cdot 10^5$  c/cm<sup>2</sup> in comparison to  $3 \cdot 10^5$  c/cm<sup>2</sup>. Since impedance is an integrative technique (Doijen *et al.*, **2017**, Stolwijk *et al.*, **2019**) and the cell population on the electrode is greater for  $3 \cdot 10^5$  c/cm<sup>2</sup> than for  $5 \cdot 10^4$  c/cm<sup>2</sup>, which was confirmed by phase contrast microscopy images (**Appendix 19**), more intense changes of impedance are detected for larger cell densities. The larger basal impedance values for higher cell densities can be explained by the formation of more and stronger cellular contacts leading to increased  $R_b$  and  $\alpha$  values and a decreased capacitance that is proportional to the surface coverage of the electrodes (cf. **chapter 3.5.2**). As a result, small changes in the cell radii  $r_c$  or distance between cells and electrodes  $h$ , which might arise after agonist addition, are easier to identify for larger cell densities. Consequently, larger cell numbers amplify the initial impedance decrease and impedance maximum and react stronger to stimulation with a ligand.

As shown in **chapter 4.1**, a cell density of  $3 \cdot 10^5$  c/cm<sup>2</sup> is optimal to best discriminate between cell-free and cell-covered electrodes with impedance spectroscopy. In this chapter, this cell density also proved to be well-suited for the detection of GPCR stimulation by impedance readings. Therefore, in later experiments following a two-day cultivation protocol of HEK cells, a seeding density of  $3 \cdot 10^5$  c/cm<sup>2</sup> was used. In

future experiments, even larger seeding densities ( $> 3 \cdot 10^5$  c/cm<sup>2</sup>) should be tested to potentially further improve the sensitivity of impedance readings after GPCR activation.

### 4.4.3.2 Different Cultivation Times

In addition to reviewing different seeding densities (**chapter 4.4.3.1**), the cultivation time was considered as another parameter impacting the impedance readout after GPCR stimulation. It was tested by seeding HEK M1R/mG<sub>q</sub> cells with a density of  $3 \cdot 10^5$  c/cm<sup>2</sup> on crosslinked gelatin-coated 8W1E arrays. After one, two or three days of cultivation, equal experiments were performed. First, the culture medium was exchanged with L15 buffer. Then, the cells were equilibrated to the new conditions and an impedance baseline was measured for at least 0.5 h at the ECIS SA. Finally, a vehicle control (CTRL) and three concentrations of carbachol (1 mM, 300  $\mu$ M, 10  $\mu$ M) were added to find out if GPCR signaling behaves differently after varying cultivation periods (**Figure 62A-C**).

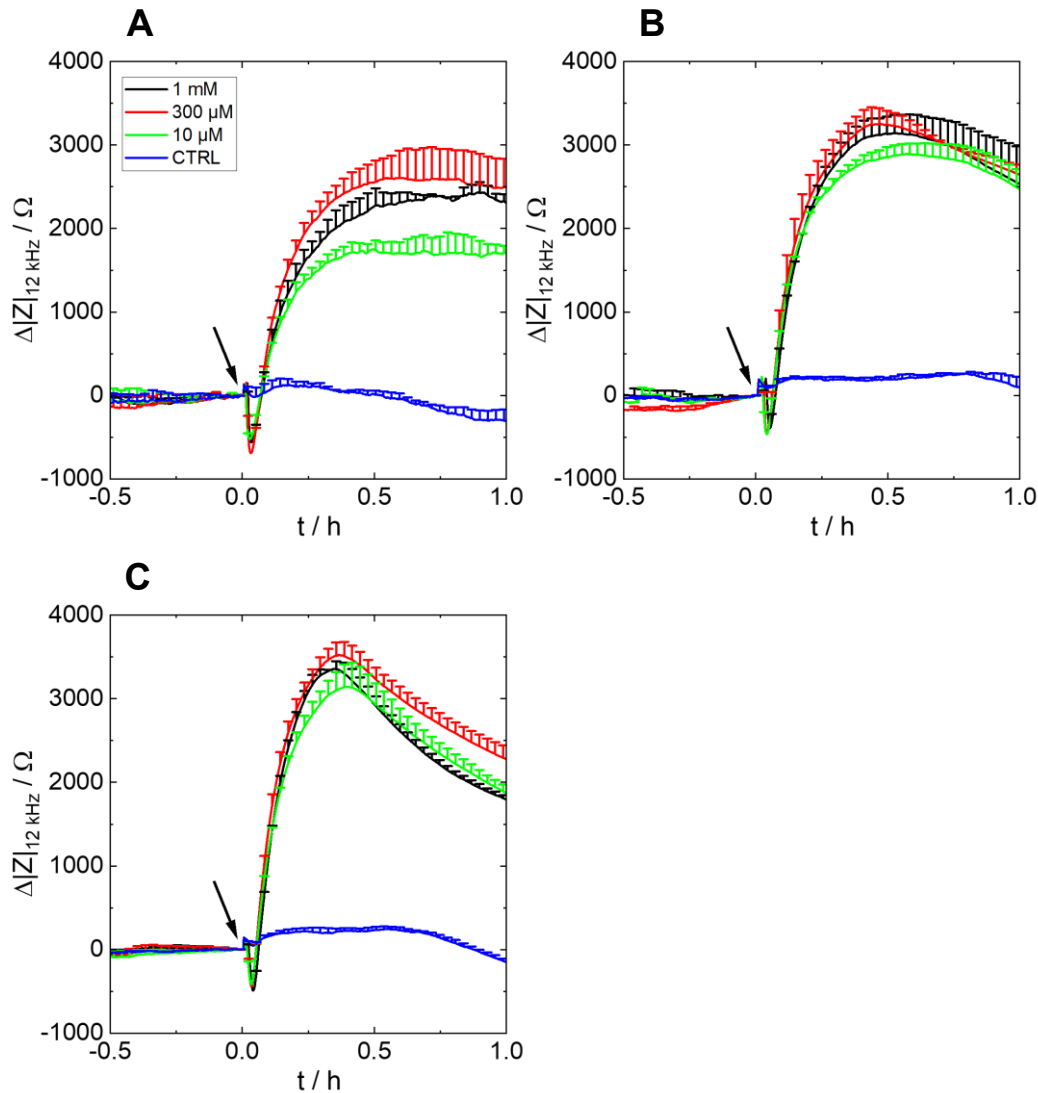


Figure 62. Impedance change over time of **HEK M1R/mG<sub>q</sub>** cells at a frequency of 12 kHz. The cells were seeded with a density of  $3 \cdot 10^5$  c/cm<sup>2</sup> on 8W1E electrode arrays that were coated with crosslinked gelatin. The cells had different times to grow (**A: one day, B: two days (standard) and C: three days of cultivation**). After a baseline recording, the cells were either stimulated with different concentrations of carchamol (black 1 mM, red 300  $\mu$ M, green 10  $\mu$ M) or were treated with a CTRL (blue) at  $t = 0$  h. Baseline from A to C:  $(5380 \pm 50) \Omega$ ,  $(6790 \pm 30) \Omega$ ,  $(7010 \pm 40) \Omega$ . Mean + SE,  $N = 2$ , single experiment. CTRL = vehicle control. Temperature: 37°C.

One (**Figure 62A**), two (**Figure 62B**) and three days (**Figure 62C**) after seeding, the measured baseline values show clear differences. With longer culturing time impedance increases from  $(5380 \pm 50) \Omega$  (one day of cultivation) to  $(6790 \pm 30) \Omega$  (two days of cultivation) and  $(7010 \pm 40) \Omega$  (three days of cultivation). All CTRL curves remain at a constant level throughout the measurements. As soon as carchamol is added, a transient impedance decrease is noticed. Then impedance constantly rises until  $t = 0.4$ - $0.5$  h and either remains at the same impedance level (one day of cultivation, **Figure 62A**) or decreases after reaching a maximum (two and three days of cultivation, **Figure 62B** and **Figure 62C**). For a cultivation time of one day, the

initial transient decrease of impedance amounts to about 550  $\Omega$  and impedance subsequently rises with 300  $\mu\text{M}$  (**Figure 62A, red**) exhibiting larger impedance values than 1 mM of carbachol (**Figure 62A, black**). Nonetheless, if the error bars are taken into consideration, both curves are not significantly different. Maxima are found at  $(2400 \pm 100) \Omega$  for 1 mM and  $(2600 \pm 300) \Omega$  for 300  $\mu\text{M}$  of carbachol, correspondingly. In comparison, the 10  $\mu\text{M}$  curve (**Figure 62A, green**) is somewhat depressed with a maximum at  $(1800 \pm 100) \Omega$ . After routine cultivation of two days (**Figure 62B**), an impedance decrease of about 400  $\Omega$  is observed after carbachol addition. A maximum of about 3000  $\Omega$  is found for the curves of 1 mM, 300  $\mu\text{M}$  and 10  $\mu\text{M}$  carbachol (**Figure 62B, black, red, green**), which all superimpose. In **chapter 4.2.1**, only the curves for 1 mM and 300  $\mu\text{M}$  carbachol overlaid and took maximal impedance values of about 6000  $\Omega$  (**Figure 44B, black, red**). In comparison, the curve for 10  $\mu\text{M}$  carbachol (**Figure 44B, cyan**) was suppressed and only reached a maximal impedance value of 4500  $\Omega$ . In this chapter, much lower impedance values are observed (**Figure 62B, black, red, green**). For a cultivation time of three days (**Figure 62C**), a transient impedance decrease of about 500  $\Omega$  is identified after the addition of carbachol. The time courses for 1 mM, 300  $\mu\text{M}$  and 10  $\mu\text{M}$  carbachol (**Figure 62C, black, red, green**) are overlaying and a maximum impedance of about 3500  $\Omega$  is measured. At  $t = 1$  h, the maximal signal for 1 mM carbachol has decreased by about 48% to a value of  $(1800 \pm 30) \Omega$  (**Figure 62C, black**). Similar observations are made for 300  $\mu\text{M}$  and 10  $\mu\text{M}$  of carbachol (**Figure 62C, red, green**) three days after cultivation, which indicates that the impedance signal on day three is not stable over time.

These findings suggest that the impedance response after GPCR stimulation somewhat depends on the time cells are able to grow and proliferate on the electrodes. Alongside a dependency of the baseline impedance on the cultivation time, a likewise enhancement of the signal with increasing cultivation time was observed for the maximum impedance (**Figure 62A-C**). Relative to the maximum signal of 1 mM carbachol on day three (**Figure 62C, black**), the signals on days one and two (**Figure 62A-B, black**) are 28% and 6% smaller, respectively. The change of the basal and maximum impedance could be attributed to different cell numbers and electrode populations (see phase contrast micrographs in **Appendix 27** and **chapter 4.4.3.1**). An increase in cell density and corresponding impedance with increasing cultivation time was already found elsewhere (McGuinness et al., 2009). However, the cells are usually seeded confluent to prevent an impact of proliferation and cell division in assays addressing signal transduction cascades. Consequently,

the variations in the baseline and maximal impedance with cultivation time are rather attributed to changes of the impedance contributions  $\alpha$ ,  $R_b$  and  $C_m$  by changes in the distance between cells, between cells and electrodes and an altered cellular behavior (Szulcek et al., 2014, Wegener et al., 2000b): with increasing cultivation time,  $\alpha$  and  $R_b$  might increase due to changes in the cell radius  $r_c$ , alteration of the cell-electrode distance  $h$  and formation of stronger cell-cell contacts (see **chapter 3.5.2**).  $C_m$  is potentially decreased over time by changes in the membrane topography or composition (Adam et al., 2009).

The more intense GPCR signal after ligand addition with increasing cultivation time might also be explained by enhanced expression of the receptor and miniG protein over time. However, this contradicts the phenomenon of receptor reserves (Stephenson, 1956). Even if the GPCR expression on day three is amplified, the same amount of ligand should lead to similar outcomes on days one and two, assuming that the signal on day one already includes spare receptors.

Moreover, the signal stability suffers with increasing cultivation time, especially after a three-day cultivation period (**Figure 62C**). A possible explanation is the activation of other signaling pathways, for instance  $\beta$ -arrestin recruitment, due to a change in cell metabolism over the time of cultivation. Another explanation could be a change of the ECM composition over time, rendering the cells more sensitive towards compound additions and potentially losing the strength of their cellular contacts.

Compared to **chapter 4.2.1 (Figure 44B)**, similar kinetics but much lower impedance magnitudes have been observed in this chapter for the standardized two-day cultivation protocol. This can not be reduced to a change of the electrode layout, because 8W1E electrodes (this chapter) and 96W1E+ electrodes (**chapter 4.2.1**) possess similar sensitivities. Both layouts behave like a single working electrode with a size of approximately  $5 \cdot 10^{-4} \text{ cm}^2$  in combination with a significantly bigger counter electrode. Consequently, the differences in the impedance values must be explained by a modified behavior of the cells, which might vary from passage number to passage number, or variances in the proliferation rate as is recognized when comparing the baseline impedance values (this chapter:  $6790 \Omega$ , **chapter 4.2.1**:  $5530 \Omega$ ). An enhanced cell number might imply an increased number of receptors per well and, hence, a larger change of the GPCR response monitored by impedance measurements.

In future experiments, the two-day protocol was followed to obtain larger signal intensities (compared to a one-day cultivation) and to prevent signal loss over time (compared to three days of cultivation).

In summary, a seeding density of  $3 \cdot 10^5$  c/cm<sup>2</sup> (**chapter 4.4.3.1**) and a cultivation time of two days (**chapter 4.4.3.2**) yield the best impedance results after GPCR stimulation. Consequently, these culturing conditions were used in all other experiments described in the following.

### 4.4.4 Measurement Buffer

It was reported that the impedance signal features drastic discrepancies with respect to GPCR stimulation in different buffer systems (Skiba, **2022**). This phenomenon is addressed in this chapter. The influence of the measurement buffer on the signaling behavior of HEK M1R/mG<sub>q</sub> cells was studied with ECIS. Routinely, L15 buffer was used as medium. Other buffers, in particular Hank's balanced salt solution (HBSS) and Dulbecco's phosphate-buffered saline (PBS), were tested and compared to L15 in the following experiment.

HEK M1R/mG<sub>q</sub> cells were seeded and cultivated according to the standardized protocol (**chapter 3.5.3.1**). On the day of the experiment, the cells were first equilibrated with L15, PBS or HBSS buffer before recording an impedance baseline at 12 kHz with the ECIS Z $\theta$ . After 0.5 h, a buffer control (CTRL) and seven carbachol concentrations (between 100 nM and 1 mM) in the respective buffer were added and impedance was monitored for 1 h. The results are given in **Figure 63A-C**.

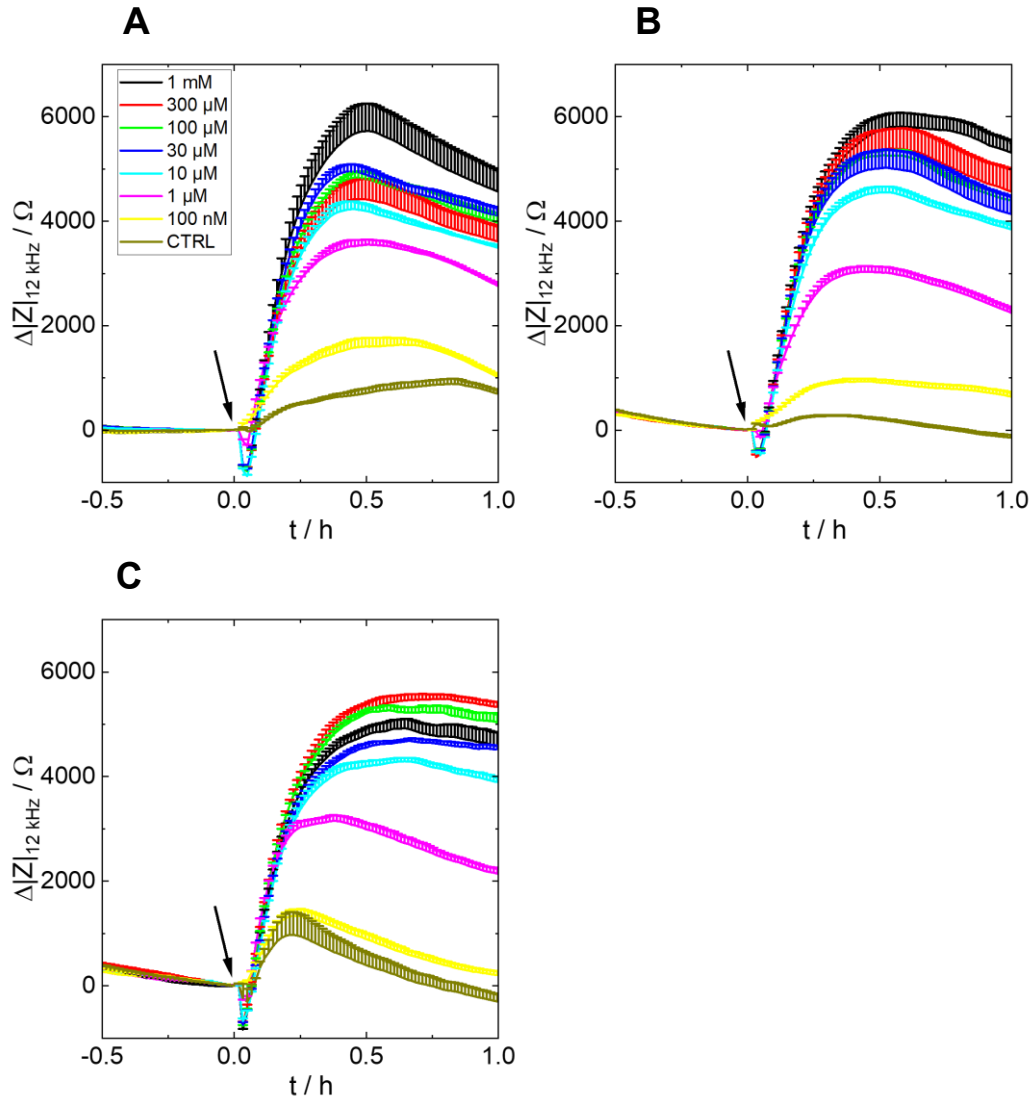


Figure 63. Impedance change over time of **HEK M1R/mG<sub>q</sub>** cells. The cells were cultivated on a 96W1E+ array that was coated with crosslinked gelatin. At  $t = 0$  h, the cells were stimulated with different concentrations of carbachol. Black 1 mM, red 300  $\mu$ M, green 100  $\mu$ M, blue 30  $\mu$ M, cyan 10  $\mu$ M, pink 1  $\mu$ M, yellow 100 nM, brown CTRL. Three different buffers were used as measurement medium (**A: L15**, **B: PBS**, **C: HBSS**). Baseline from A to C:  $(6140 \pm 10) \Omega$ ,  $(4810 \pm 10) \Omega$ ,  $(5490 \pm 20) \Omega$ . Mean + SE,  $N = 4$ , single experiment. CTRL = vehicle control. Temperature: 37°C.

Considering the baseline, average values of  $(6140 \pm 10) \Omega$  for L15 (**Figure 63A**),  $(4810 \pm 10) \Omega$  for PBS (**Figure 63B**) and  $(5490 \pm 20) \Omega$  for HBSS (**Figure 63C**) were found. Moreover, between  $t = -0.5$  h and  $t = 0$  h, a slight drop of the baseline impedance is noticed for PBS and HBSS in contrast to L15. After the addition of carbachol, a quick transient decrease in impedance is identified, which is followed by an impedance increase, an impedance maximum and a slow decline in impedance until  $t = 1$  h. In PBS, the smallest transient impedance decrease is observed after ligand addition. The individual decreases for 1 mM carbachol (**Figure 63A-C**, black) take values of about 800  $\Omega$  in L15 and HBSS and 400  $\Omega$  in PBS. Generally, they are

concentration-dependent since their magnitude increases with larger ligand concentration just as for the maximal impedance.

Up to a concentration of 10  $\mu\text{M}$  carbachol, the impedance curves are distinguishable for every buffer system (**Figure 63A-C, cyan, pink, yellow, brown**). In L15 and PBS, the curves for carbachol concentrations between 30-300  $\mu\text{M}$  (**Figure 63A-B, red, green, blue**) display larger values than the curve for 10  $\mu\text{M}$  (**Figure 63A-B, cyan**), but all superimpose. The highest carbachol concentration of 1 mM (**Figure 63A-B, black**) again shows an elevated impedance compared to all other concentrations. In HBSS, impedance increases concentration-wise up to a concentration of 300  $\mu\text{M}$  (**Figure 63C, red**). Thereby, the curves for 100  $\mu\text{M}$  and 300  $\mu\text{M}$  carbachol (**Figure 63C, red, green**) overlap. In contrast, the curve for 1 mM carbachol (**Figure 63C, black**) is lowered and takes values between 30  $\mu\text{M}$  and 100  $\mu\text{M}$  of carbachol (**Figure 63C, green, blue**). The error bars for L15 and PBS in a concentration range of 30  $\mu\text{M}$  to 1 mM (**Figure 63A-B, black, red, green, blue**) are approximately 2-12 times larger than for smaller concentrations in the respective buffer (**Figure 63A-B, cyan, pink, yellow, brown**).

The impedance maxima emerge after approximately 0.5 h for L15, but in PBS and in particular HBSS the time after which they arise seems dependent on the concentration. The maximum shifts to greater time values with increasing concentration. For instance, the impedance maxima for 1 mM and 1  $\mu\text{M}$  carbachol both emerge after 0.51 h in L15 (**Figure 63A, black, pink**). They amount to impedance magnitudes of  $(5700 \pm 500) \Omega$  for 1 mM and  $(3550 \pm 90) \Omega$  for 1  $\mu\text{M}$  carbachol. In PBS, the maxima for the same concentrations are found at 0.58 h for 1 mM ( $(5800 \pm 300) \Omega$ ) and 0.44 h ( $(3000 \pm 100) \Omega$ ) for 1  $\mu\text{M}$  carbachol (**Figure 63B, black, pink**), whereas they emerge after 0.64 h for 1 mM ( $(4900 \pm 200) \Omega$ ) and 0.38 h for 1  $\mu\text{M}$  carbachol ( $(3200 \pm 100) \Omega$ ) in HBSS (**Figure 63C, black, pink**). Strikingly, the HBSS CTRL curve also exhibits a maximum of  $(1000 \pm 400) \Omega$  after 0.22 h (**Figure 63C, brown**), while the L15 and PBS control curves do not exhibit a remarkable maximum.

For each buffer system, the impedance after 0.5 h was extracted and plotted against the logarithm of the carbachol concentration. A four-parametric dose-response fit (**equation 15**) was used to fit the experimental data. Three concentration-response curves are obtained and given in **Figure 64**.

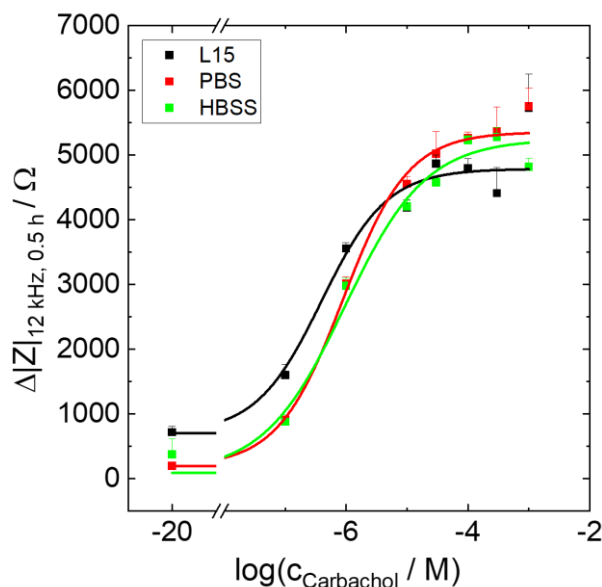


Figure 64. Concentration-response curves of **HEK M1R/mG<sub>q</sub>** cells after stimulation with different concentrations of carbachol in three different buffers (**black: L15**, **red: PBS**, **green: HBSS**). The change of impedance at a frequency of 12 kHz and 0.5 h after stimulation (squares) is plotted as a function of the carbachol concentration. The data was extracted from **Figure 63A-C**. The concentration-response fits (solid lines) reveal  $pEC_{50}$  values of  $6.4 \pm 0.1$  in L15,  $6.05 \pm 0.06$  in PBS and  $6.0 \pm 0.2$  in HBSS. The  $E_{max}$  values amount to  $(4800 \pm 200) \Omega$ ,  $(5400 \pm 100) \Omega$  and  $(5200 \pm 300) \Omega$  in the same order. Mean + SE,  $N = 4$ , single experiment. Temperature: 37°C.

The concentration-response curves for PBS (**Figure 64**, red) and HBSS (**Figure 64**, green) overlay, especially up to a carbachol concentration of 1  $\mu$ M. They reveal  $pEC_{50}$  values of  $6.05 \pm 0.06$  in PBS and  $6.0 \pm 0.2$  in HBSS. The  $E_{max}$  values amount to  $(5400 \pm 100) \Omega$  in PBS and  $(5200 \pm 300) \Omega$  in HBSS, which translates to a relative difference of 4%. In contrast, L15 shows a larger  $pEC_{50}$  of  $6.4 \pm 0.1$  but a smaller signal range (**Figure 64**, black). Not only the  $E_{max}$  value ( $(4800 \pm 200) \Omega$ ) is reduced in comparison to PBS and HBSS, but also the lower asymptote is lifted.

The baseline values in HBSS (**Figure 63C**) and PBS (**Figure 63B**) are 11% and 22% smaller compared to L15 (**Figure 63A**). This might be attributed to the buffer resistivity itself, which influences  $R_{bulk}$  and, therefore, the total impedance of the system. L15 is the only buffer that contains amino acids and vitamins (**Table 6**) and, thus, might display a larger basal impedance. Another explanation could be varying osmolalities or osmolarities (i.e. osmotically active particles per mass or volume of the solvent). Bellotti *et al.* have shown that increasing the osmolarity of the measurement buffer, leads to decreased impedance values since the barrier integrity is affected (Bellotti *et al.*, **2011**). For L15, osmolalities of 300-336 mOs/kg are given by the manufacturers (sigmaaldrich.com #7; **August 10, 2024**, thermofisher.com; **August 10, 2024**). For PBS, an osmolality of 275-304 mOs/kg is found (sigmaaldrich.com #8; **August 10,**

**2024**) and for HBSS a value of 260-300 mOs/kg is quoted (sigmaaldrich.com #9; **August 10, 2024**). Since L15 shows a larger osmolality than PBS and HBSS, which should lead to decreased impedance values according to Bellotti *et al.* (Bellotti *et al.*, **2011**), the osmolality can not be an explanation for the larger basal impedance in L15. Another explanation could be different contents of the divalent ions  $Mg^{2+}$  and  $Ca^{2+}$  in the different buffers. Both ions are responsible for the correct folding of integrins and the formation of cell-matrix ( $\alpha$ ) as well as intercellular ( $R_b$ ) contacts (Leitinger *et al.*, **2000**, Wegener *et al.*, **2000b**). However, since the  $Ca^{2+}$  concentration is larger in HBSS than in L15 and PBS and since the  $Mg^{2+}$  concentration descends in the following order L15 > PBS > HBSS (see **Table 18**), single  $Ca^{2+}$  or  $Mg^{2+}$  concentrations are not accountable for the varying baseline impedances but rather a combination of both. Furthermore, PBS has a larger ionic strength than L15 and HBSS (cf. **Table 18**), which might reduce the basal impedance. The utilized buffer might also have an impact on protein stability, leading to varying membrane protein expressions and, hence, to changed  $R_b$  and  $C_m$  values, influencing the total impedance (Giaever, Keese, **2012**, Senisterra, Finerty, **2009**).

In PBS and HBSS (**Figure 63B-C**), the impedance baseline appeared non-stable in contrast to L15 (**Figure 63A**) although the cells had the same time to equilibrate to the new conditions. One explanation could be that L15 buffer supplies the cells with ions and sugar but, in contrast with PBS and HBSS, also with several amino acids and vitamins (**Table 6**), which helps the cells to adjust to new conditions faster. Another explanation might be that L15 contains D-galactose, while PBS and HBSS contain D-glucose as a carbon source (**Table 6**). Galactose is involved in numerous metabolic processes, e.g. galactosylation, known to modulate cellular contacts as well as cell communication and signaling (Conte *et al.*, **2021**).

In PBS, the initial decrease of impedance after ligand addition is not as pronounced as for L15 and HBSS. This is very hard to interpret and needs to be further investigated. But since the coating and cell line were not altered, it must be attributed to the buffer itself. In general, the magnitude of the impedance decrease is concentration-dependent as observed in previous chapters (**chapters 4.2 and 4.4**). This is explained by larger cellular and morphological responses to increasing ligand concentrations. Another explanation is given by Parviz *et al.*, who investigated  $G_q$ -coupled H1R in HeLa cells with impedance measurements and a fluorescence-based  $Ca^{2+}$  mobilization assay (Parviz *et al.*, **2017**). They found a dependency of the initial impedance decrease after agonist addition and the mobilization of  $Ca^{2+}$  ions. The more pronounced the impedance decrease was, the larger the intracellular  $Ca^{2+}$

concentration has become. A more pronounced  $\text{Ca}^{2+}$  mobilization in HBSS and L15 might be the reason for a stronger impedance decrease compared to PBS.

In all buffers, the impedance signal intensities for one carbachol concentration are similar. Furthermore, the impedance signal is always dependent on the carbachol concentration. Consequently, ECIS can be used for the investigation of GPCR signaling in different buffers. The  $\text{pEC}_{50}$  and  $E_{\text{max}}$  values determined by concentration-response analysis (**Figure 64**) are similar for the three investigated buffer systems. Only minor differences are observed. From the concentration-response curves, it can be concluded that the signal range in L15 is slightly reduced in contrast to PBS and HBSS. This is attributed to the concentration-response analysis itself not considering any kinetic processes but focusing on a certain time point. If the entire kinetic traces are considered, the maximal impedance values do not vary significantly. Information like the cellular reaction to the addition of the HBSS CTRL and the rather constant signal of the L15 CTRL get lost. Instead of analyzing only one time point, in this particular case a comprehensive analysis of different time points or the area under the curve (AUC), integrating the signal over a certain time interval, is recommended. For L15, a potency of  $6.4 \pm 0.1$  was determined (**Figure 64**). Compared to the results in **chapters 4.2.1 and 4.4.1**, the time courses and  $\text{pEC}_{50}$  values in L15 are very similar. Nonetheless, the impedance maxima and concentration dependency vary between experiments. For instance, the highest concentration of 1 mM carbachol shows a maximum impedance of around 6000  $\Omega$  in this chapter (**Figure 63A, black**) and **chapter 4.2.1 (Figure 44B, black)** but displays a value of about 8000  $\Omega$  in **chapter 4.4.1 (Figure 58A, black)**. Furthermore, the perfect concentration dependency observed in **chapter 4.2.1** is lost here, especially for concentrations between 10-300  $\mu\text{M}$  (**Figure 63A, red, green, blue, cyan**). This is underpinned by the large error bars obtained for concentrations  $\geq 30 \mu\text{M}$  in **Figure 63A** as well. These observations are assigned to experimental variations, variations in the expression level of the proteins and an altered cell behavior with the passage number.

Yet the question arises as to why the HBSS CTRL (**Figure 63C, brown**) reacts in such a definite way. Since the coating and cell line were not altered, it must be ascribed to the buffer itself. One explanation could be that the cells react more sensitive to additions in HBSS (Belly et al., **2022**, Saffioti et al., **2020**, Wilde et al., **2022**). This might also affirm the observation that the maxima in HBSS are time-shifted with increasing concentrations. Supposing that cells in HBSS generally react to additions after 0.22 h (cf. maximum of CTRL) and assuming a similar reaction time to the GPCR ligand carbachol as for the measurement in L15, i.e.  $t = 0.5$  h, in theory,

two peaks should become visible for HBSS. However, impedance is an integrative technique and the two peaks are potentially converted into one big signal. With increasing carbachol concentrations, the peak after 0.5 h gains in height and influence, while the contribution of the addition peak after 0.22 h remains constant. As a consequence, the observed maxima are shifted to later time points with increasing ligand concentrations.

Overall, the buffer composition does not have a significant impact on impedance signaling. For all buffer systems, similar signal maxima, pEC50 values and  $E_{\max}$  values were determined. However, different kinetic behavior was observed for L15, PBS and HBSS. In HBSS, consideration must be given to sensitivity towards mechanical stimulation of the GPCRs during liquid handling. Therefore, L15 was chosen as a measurement buffer in subsequent experiments.

### 4.5 Optimization of the MiniG Protein Recruitment Assay

Bioluminescence is greatly influenced by the luciferase and luciferin concentration and luciferase stability at different pH values and temperatures (England et al., 2016). In this chapter, the impact of several other aspects on the luminescence signal of the miniG protein recruitment assay was addressed. Different plate coatings and plate colors were tested (**chapter 4.5.1**). Integration times and the signal amplifying gain of the luminescence readout were varied (**chapter 4.5.2**). Several coelenterazine h concentrations (**chapter 4.5.3**), the influence of the cell density (**chapter 4.5.4**) and an additional washing step (**chapter 4.5.5**) were examined. In addition, the aging of coelenterazine h (**chapter 4.5.6**) was investigated to check for temperature, oxygen and light sensitivity and, lastly, three measurement buffers (**chapter 4.5.7**) were compared. Similar aspects were also investigated in the impedance assay before (cf. **chapter 4.4**)

#### 4.5.1 Plate Coatings and Plate Color

For luminescence assays, white plates are widely recommended by most culture ware manufacturers (bmglabtech.com; **August 10, 2024**, corning.com; **August 10, 2024**, promega.de #1; **August 10, 2024**) because of their reflective properties and higher S/N ratios in comparison to black and transparent plates. This chapter aimed to find out if white plates indeed are the best choice and exhibit better S/N ratios than transparent plates and black plates commonly used for fluorescence readouts. Transparent and black plates are of special interest because they must be used in the

dual luminescence-impedance assay (**chapter 4.6**) since no white 96W1E+ arrays are commonly available to date (biophysics.com #2; **August 10, 2024**). In this chapter, white 96-well plates, custom-made black 96W1E+ arrays with transparent bottoms or commercially available transparent 96W1E+ arrays were used (cf. **chapter 3.3.1**). In addition, different coatings were tested on the different plates to investigate if the standardized crosslinked gelatin coating, used for impedance measurements, negatively impacts the luminescence signal.

HEK M1R/mG<sub>q</sub> cells were seeded on transparent and black 96W1E+ arrays and on completely white 96-well plates preincubated with serum-containing medium or coated with gelatin or crosslinked gelatin according to the previously described protocols (**chapters 3.3.2 and 3.6.1.1**). After a two-day cultivation, the medium was substituted with L15 buffer and the cells were equilibrated for 2-2.5 h. Then, 1  $\mu$ M coelenterazine h was added and a luminescence baseline was recorded with the common settings at the Tecan Genios device. Finally, a vehicle control (CTRL) and different carbachol concentrations in L15 (between 100 nM and 1 mM) were added and luminescence was monitored for 1 h. The results for the different plates and coatings are given in **Figure 65A-C** (white), **Figure 66A-C** (transparent) and **Figure 67A-C** (black).

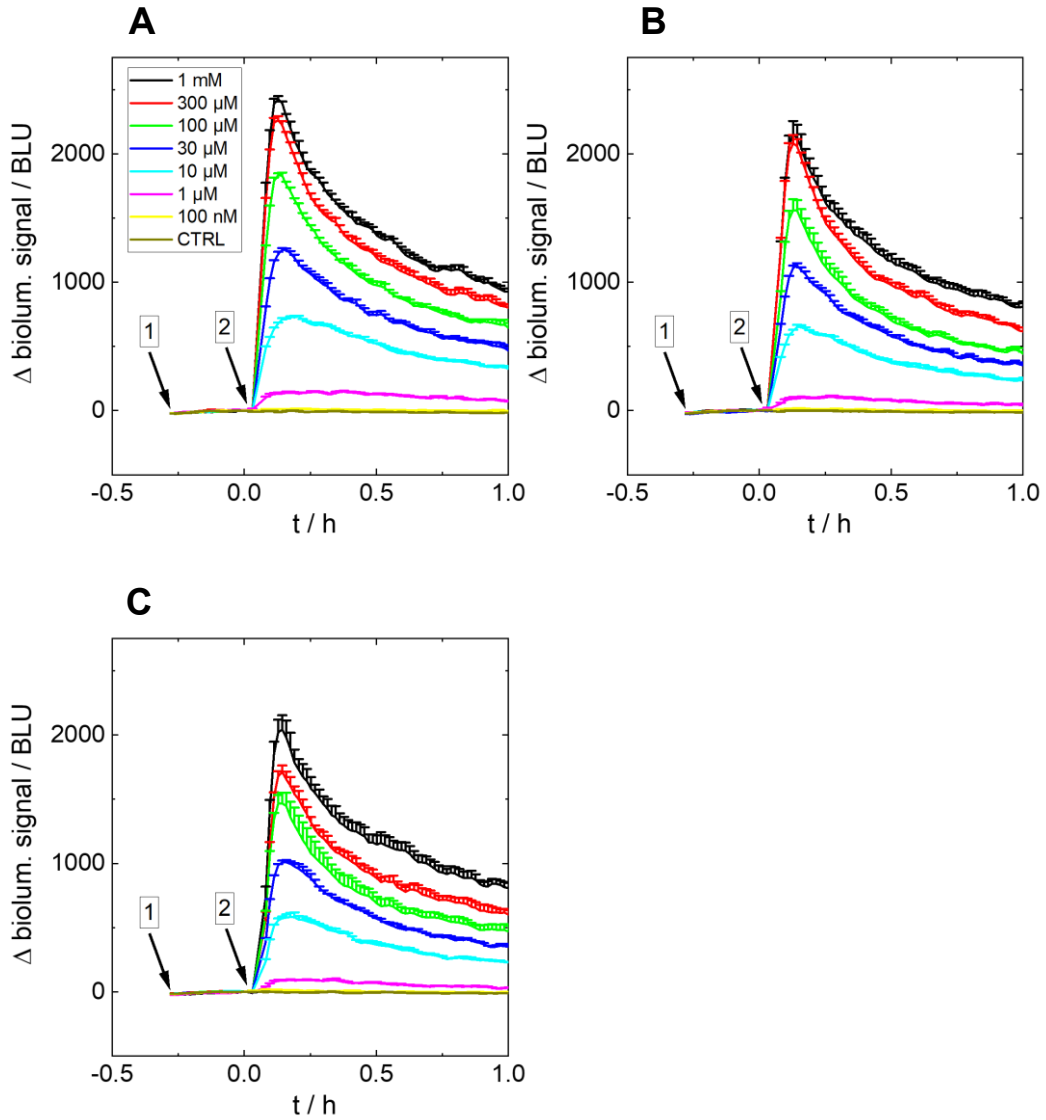


Figure 65. Luminescence change over time of **HEK M1R/mG<sub>q</sub>** cells. The cells were cultivated on a **white 96-well plate** that was coated with **crosslinked gelatin (A), gelatin (B) or medium (C)**. At  $t = -0.26$  h, 1  $\mu$ M coelenterazine h (arrow 1) was added. At  $t = 0$  h, the cells were stimulated with different concentrations of carbachol (arrow 2). Black 1 mM, red 300  $\mu$ M, green 100  $\mu$ M, blue 30  $\mu$ M, cyan 10  $\mu$ M, pink 1  $\mu$ M, yellow 100 nM, brown CTRL. Baseline from A to C:  $(29.9 \pm 0.5)$  BLU,  $(26.1 \pm 0.4)$  BLU,  $(23.3 \pm 0.4)$  BLU. Mean + SE,  $N = 4$ , single experiment. CTRL = vehicle control. BLU = bioluminescence units. Temperature: 37°C.

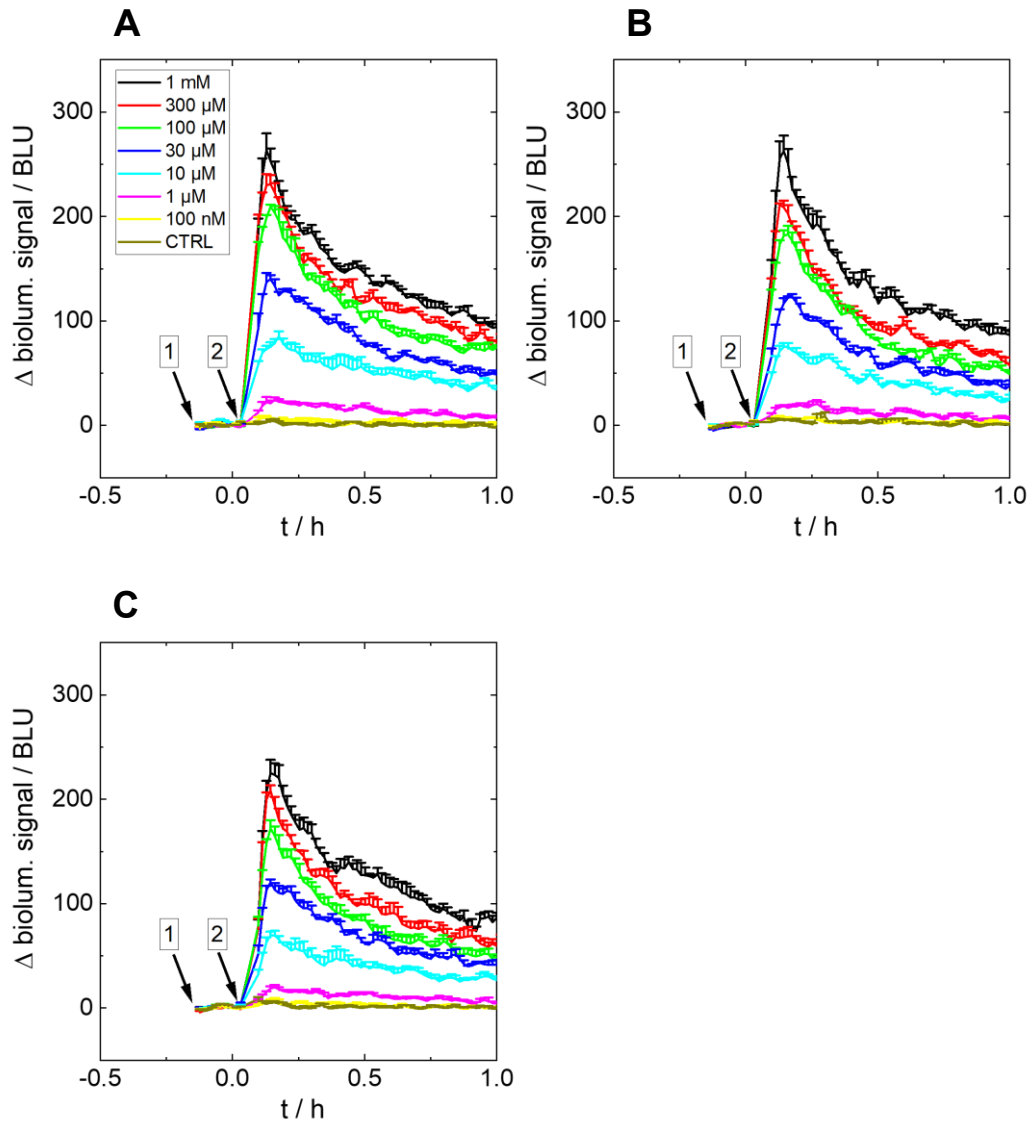


Figure 66. Luminescence change over time of **HEK M1R/mG<sub>q</sub>** cells. The cells were cultivated on a **transparent 96W1E+** array that was coated with **crosslinked gelatin (A)**, **gelatin (B)** or **medium (C)**. At  $t = -0.12$  h, 1  $\mu$ M coelenterazine h (arrow 1) was added. At  $t = 0$  h, the cells were stimulated with different concentrations of carbachol (arrow 2). Black 1 mM, red 300  $\mu$ M, green 100  $\mu$ M, blue 30  $\mu$ M, cyan 10  $\mu$ M, pink 1  $\mu$ M, yellow 100 nM, brown CTRL. Baseline from A to C:  $(5.6 \pm 0.2)$  BLU,  $(5.4 \pm 0.2)$  BLU,  $(5.5 \pm 0.2)$  BLU. Mean + SE,  $N = 4$ , single experiment. CTRL = vehicle control. BLU = bioluminescence units. Temperature: 37°C.

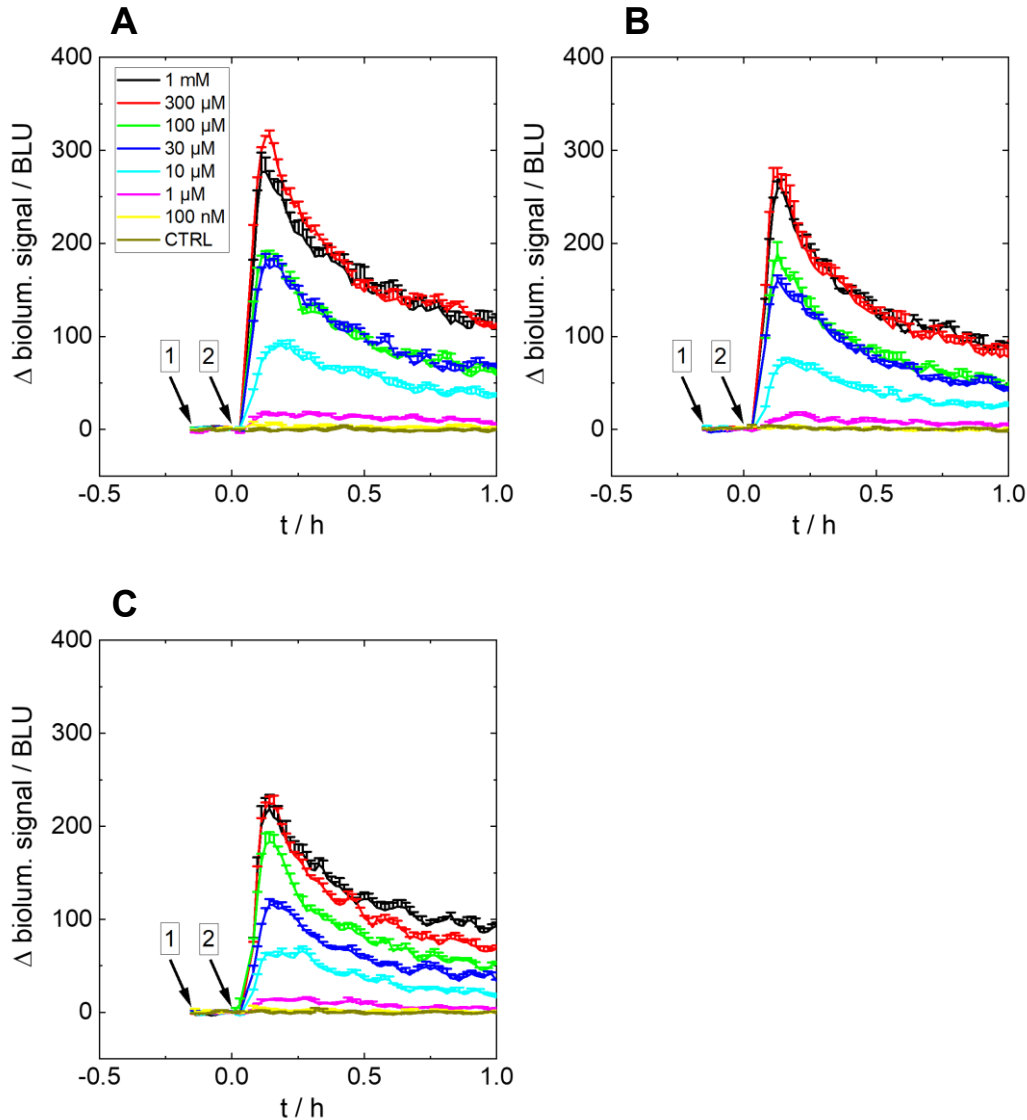


Figure 67. Luminescence change over time of **HEK M1R/mG<sub>q</sub>** cells. The cells were cultivated on a **black 96W1E+ array** that was coated with **crosslinked gelatin (A)**, **gelatin (B)** or **medium (C)**. At  $t = -0.14$  h, 1  $\mu$ M coelenterazine h (arrow 1) was added. At  $t = 0$  h, the cells were stimulated with different concentrations of carbachol (arrow 2). Black 1 mM, red 300  $\mu$ M, green 100  $\mu$ M, blue 30  $\mu$ M, cyan 10  $\mu$ M, pink 1  $\mu$ M, yellow 100 nM, brown CTRL. Baseline from A to C:  $(5.7 \pm 0.2)$  BLU,  $(5.6 \pm 0.2)$  BLU,  $(5.1 \pm 0.2)$  BLU. Mean + SE,  $N = 4$ , single experiment. CTRL = vehicle control. BLU = bioluminescence units. Temperature: 37°C.

The non-normalized baseline values on the white plate vary between 23-29 BLU (**Figure 65A-C**). In contrast, the baseline takes values between 5-6 BLU for the transparent (**Figure 66A-C**) and black (**Figure 67A-C**) 96W1E+ array. Consequently, the baseline values of the white plate are approximately 5 times larger than for the transparent and black electrode arrays.

In general, the time courses and kinetics for the three plates and the three coatings are alike. Luminescence immediately increases concentration-wise after compound addition and reaches a maximum after 0.13-0.14 h, respectively. Subsequently,

luminescence gradually decreases over the measurement period. For the white plate, the maxima for 1 mM carbachol amount to  $(2430 \pm 30)$  BLU on crosslinked gelatin,  $(2200 \pm 100)$  BLU on gelatin and  $(2000 \pm 100)$  BLU on medium (**Figure 65A-C, black**). The luminescence on the transparent and black plates only takes about 10% of the value of the white plate. On the transparent plate luminescence values of  $(260 \pm 20)$  BLU on crosslinked gelatin,  $(260 \pm 20)$  BLU on gelatin and  $(230 \pm 10)$  BLU on medium are observed for 1 mM carbachol, respectively (**Figure 66A-C, black**). On the black plate, values of  $(280 \pm 20)$  BLU for crosslinked gelatin,  $(260 \pm 8)$  BLU for gelatin and  $(220 \pm 20)$  BLU for medium preincubation are observed for 1 mM carbachol, respectively (**Figure 67A-C, black**). Overall, the signals for one ligand concentration decrease depending on the plate coating in the following order: crosslinked gelatin > gelatin > medium. Nonetheless, the differences between the coatings on one plate type are not significant. For each coating and plate color, the luminescence signals increase with increasing ligand concentration. With a few exceptions, a strict concentration dependency of bioluminescence is observed. On the black 96W1E+ array coated with crosslinked gelatin and gelatin, the curves for 1 mM and 300  $\mu$ M carbachol (**Figure 67A-B, black, red**) and the curves for 100  $\mu$ M and 30  $\mu$ M carbachol (**Figure 67A-B, green, blue**) superimpose. Irrespective of the plate coating and plate material, the CTRL (**Figure 65A-C, Figure 66A-C, Figure 67A-C, brown**) does not show any change in the luminescence signal over the measurement time. In every case, the 100 nM curve (**Figure 65A-C, Figure 66A-C, Figure 67A-C, yellow**) runs with the CTRL curve.

If the results for the medium preincubated white plate (**Figure 65C**) are compared with the outcome of **chapter 4.3**, a similar concentration dependency and similar kinetics are observed after stimulation with carbachol. The only difference is the signal intensity. For instance, in **chapter 4.3**, a concentration of 1 mM carbachol (**Figure 52B, black**) led to a maximal signal of about 3000 BLU, whereas in this chapter only a maximum signal of 2000 BLU is achieved (**Figure 65C, black**).

It is apparent that the luminescence on the transparent and black electrode array exhibits more fluctuations independent of the coating. To quantify this behavior, S/N ratios were calculated according to **chapter 3.6.2**. They are visualized in **Figure 68** for white, transparent and black plates and the three substrate coatings.

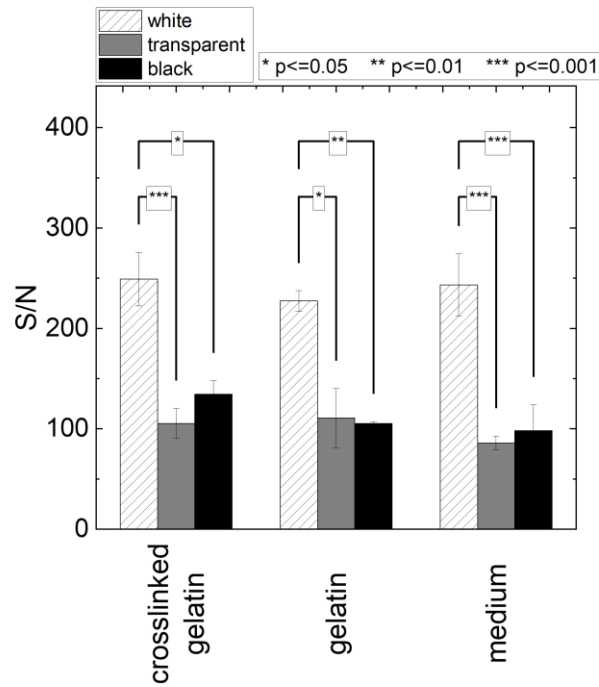
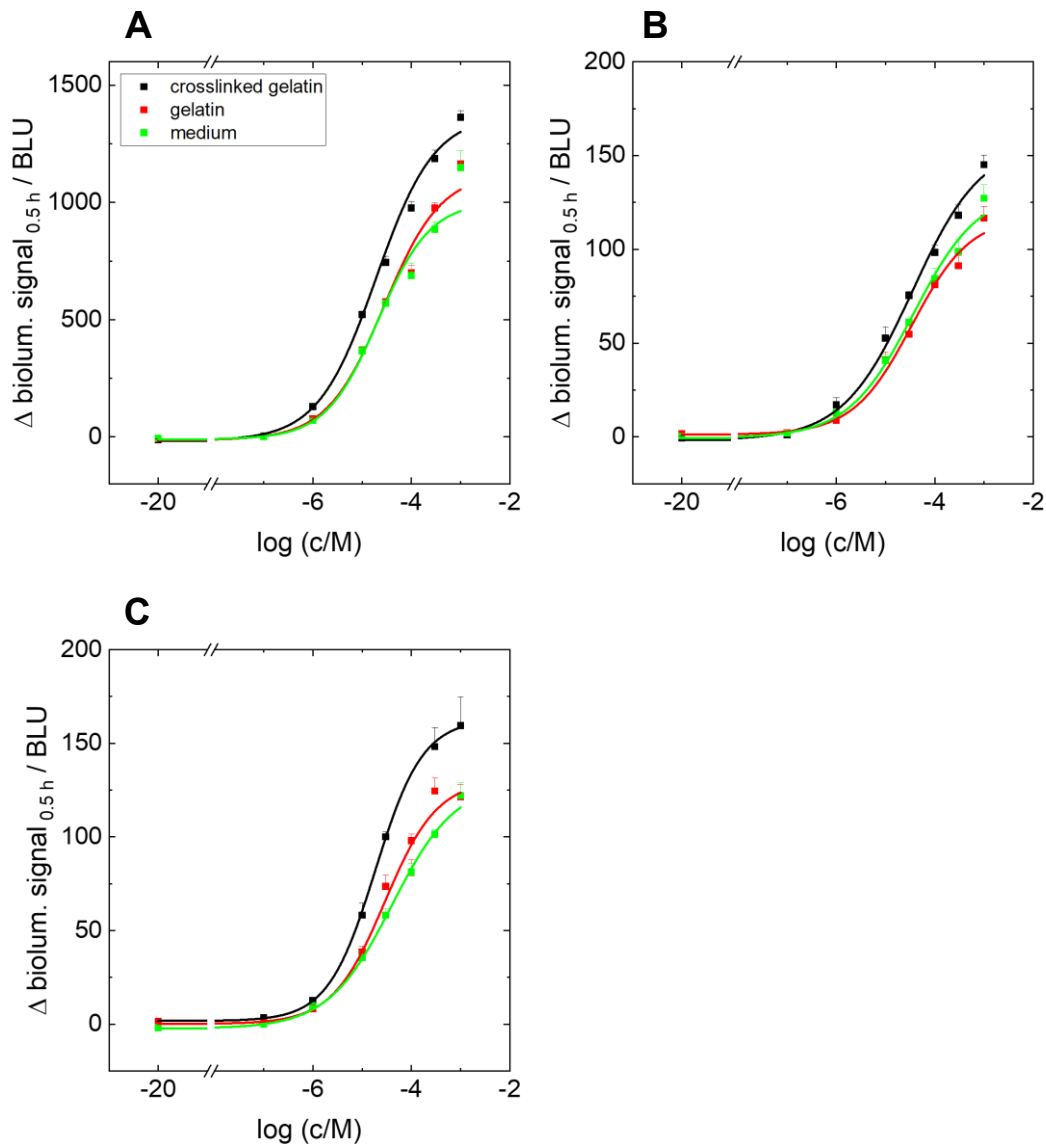


Figure 68. S/N ratios of the luminescence data of HEK M1R/mG<sub>q</sub> cells that were cultivated on a white 96-well plate (white bars), a transparent 96W1E+ array (grey bars) or a black 96W1E+ array (black bars) that were coated with crosslinked gelatin, gelatin or medium, respectively. After incubation with 1  $\mu$ M coelenterazine h, 1 mM of carbachol was added. The data processing protocol is described in chapter 3.6.2.1. Statistical significance (\*) was assessed with Tukey's range test. Mean  $\pm$  SE, N = 4, single experiment. Temperature: 37°C.

Overall, the S/N ratios are the largest on white plates. Thereby, the average values for crosslinked gelatin, gelatin and medium are  $250 \pm 30$ ,  $230 \pm 10$  and  $240 \pm 30$  not differing significantly (Figure 68, white). However, significant differences between the white and the other two plate materials are visible. For transparent plates (Figure 68, grey), values of  $100 \pm 20$  on crosslinked gelatin,  $110 \pm 30$  on gelatin and  $86 \pm 7$  on medium were determined. For black 96W1E+ arrays (Figure 68, black), the S/N values amount to  $130 \pm 10$  on crosslinked gelatin,  $105 \pm 2$  on gelatin and  $100 \pm 30$  on medium. Overall, the S/N values of transparent and black plates take about 30-50% of the S/N values of white plates. Furthermore, the S/N ratios on black and transparent plates are very similar and no significant differences are observed. In addition, the S/N values do not differ significantly when comparing the different coatings for one plate color.

For an even better comparison of the luminescence data on different plates with different coatings, pEC<sub>50</sub> and E<sub>max</sub> values were extracted from the time course data after t = 0.5 h. The data points were plotted against the logarithmic carbachol concentration. A four-parametric dose-response fit was used to fit the data (equation 15). The concentration-response curves are shown in Figure 69A (white),

**Figure 69B** (transparent) and **Figure 69C** (black). An overview of all  $pEC_{50}$  and  $E_{max}$  values is found in **Table 17**.



**Figure 69.** Concentration-response curves of **HEK M1R/mG<sub>q</sub>** cells on a **white 96-well plate (A)**, **transparent 96W1E+ array (B)** or **black 96W1E+ array (C)** with different coatings (**black: crosslinked gelatin, red: gelatin, green: medium preincubation**). The luminescence data 0.5 h after stimulation (squares) is plotted as a function of the carbachol concentration and was extracted from **Figure 65A-C**, **Figure 66A-C** and **Figure 67A-C** (1  $\mu$ M coelenterazine h). By applying a four-parametric dose-response fit (solid lines, **equation 15**),  $pEC_{50}$  and  $E_{max}$  values were determined. They are summarized in **Table 17**. Please note the different scales on the y-axes. Mean + SE,  $N = 4$ , single experiment. BLU = bioluminescence units. Temperature: 37°C.

#### 4 Simultaneous Measurement of Luminescence and Impedance

Table 17. Overview of  $pEC_{50}$  and  $E_{max}$  values of HEK M1R/mG<sub>q</sub> cells on a white 96-well plate, transparent 96W1E+ array or black 96W1E+ array. Crosslinked gelatin, gelatin and medium were tested as substrate coatings. The values were extracted from the concentration-response curves in **Figure 69A-C**. Mean  $\pm$  SE, N = 4, single experiment. BLU = bioluminescence units. \* = for a reliable fit, the concentration 100  $\mu$ M was excluded.

	Coating	$pEC_{50}$	$E_{max}$ / BLU
<b>White 96-well</b>	Crosslinked gelatin	4.72 $\pm$ 0.08	1370 $\pm$ 80
	Gelatin	4.5 $\pm$ 0.1	1130 $\pm$ 90
	Medium	4.68 $\pm$ 0.10	1000 $\pm$ 80
<b>Transparent 96W1E+</b>	Crosslinked gelatin	4.5 $\pm$ 0.1	160 $\pm$ 10
	Gelatin	4.5 $\pm$ 0.2	120 $\pm$ 10
	Medium	4.4 $\pm$ 0.1	130 $\pm$ 10
<b>Black 96W1E+</b>	Crosslinked gelatin	4.73 $\pm$ 0.06*	163 $\pm$ 9*
	Gelatin	4.5 $\pm$ 0.2	130 $\pm$ 10
	Medium	4.40 $\pm$ 0.08	129 $\pm$ 6

All curves display increasing luminescence values with larger carbachol concentrations (**Figure 69A-C**). Only the values for 100 nM and 1  $\mu$ M carbachol remain at the level of the CTRL. Furthermore, above concentrations of 300  $\mu$ M carbachol, the steepness of the concentration-response curves decreases, indicating a saturation-like effect. The concentration-response curves for crosslinked gelatin (**Figure 69A-C, black**) exhibit larger values of the bioluminescence than for gelatin and medium on all three plate types (**Figure 69A-C, red, green**). The  $E_{max}$  values on crosslinked gelatin are 20-30% larger compared to gelatin and medium on white, transparent and black plates, respectively (**Table 17**). The  $E_{max}$  values of gelatin and medium only differ by about 1-10%. Considering the different plate colors, the  $E_{max}$  values on transparent and black plates only take about 10% of the values on white plates. The  $pEC_{50}$  values on white plates are slightly elevated compared to transparent and black plates. Nonetheless, the differences in the  $pEC_{50}$  values between the different plate types are insignificant. All  $pEC_{50}$  values range between 4.4 and 4.73 (**Table 17**).

White plates (**Figure 65A-C**) display 5-6 times larger baseline values in contrast to transparent (**Figure 66A-C**) and black electrode arrays (**Figure 67A-C**) and are considered the method of choice regarding luminescence measurements (Garvin et al., 2021). Additionally, the maximum signal of luminescence is enhanced drastically (about 10-fold) for white plates, which is confirmed by the larger  $E_{max}$  values (**Table 17**). Moreover, the S/N ratios of white plates are approximately twice as big as for transparent and black plates (**Figure 68**) and fewer fluctuations in the luminescence are visible on white plates. This is explained by a higher reflectivity of

white plates in contrast to transparent plates and black plates that potentially absorb or scatter a part of the luminescence. An influence of the electrodes themselves was excluded by control experiments with purely white, black and transparent plates (data not shown).

Similar time courses, kinetics and concentration dependencies are observed in any case (**Figure 65A-C**, **Figure 66A-C** and **Figure 67A-C**) and similar pEC50 values can be extracted (**Table 17**), rendering all measurement conditions suitable for a pharmacological characterization and potency determination. The different coatings do not influence the concentration-response curves remarkably. Only in the high concentration range they have a small impact recognizable by the varying  $E_{\max}$  values (**Table 17**). The larger  $E_{\max}$  for crosslinked gelatin might be attributed to a larger adhered cell number, leading to increased luminescence in comparison to gelatin and medium preincubation, where cells might have washed off during medium exchange. The time courses on white medium preincubated plates (**Figure 65C**) are similar to **chapter 4.3 (Figure 52B)**. The only difference is the intensity of luminescence, which is about 1000 BLU higher in **chapter 4.3**. This is also demonstrated by the change in  $E_{\max}$ . In this chapter, a value of  $(1000 \pm 80)$  BLU was found for white medium preincubated plates (**Table 17**), whereas in **chapter 4.3** a value of  $(1400 \pm 300)$  BLU was determined. Nonetheless, similar pEC50 values of  $4.4 \pm 0.3$  (**chapter 4.3**) and  $4.68 \pm 0.10$  (this chapter) were identified. The differences in the luminescence values could be explained by varying receptor or miniG protein expression or passage-dependent alterations in the cellular behavior.

Although white plates performed the best in terms of signal intensities and S/N ratios, they could not be used in the dual luminescence-impedance setup (**chapter 4.6**), since no white 96W1E+ arrays were commercially available. Instead, transparent 96W1E+ plates were used. They illustrate a good alternative to white plates since the pEC50 values, kinetics and concentration dependencies were similar on both plate types. Crosslinked gelatin served as the coating of choice because a slightly amplifying effect on luminescence was observable. Furthermore, it enhances cellular adherence (cf. **chapter 4.1 and 4.4.1**), which is crucial for impedance readings.

#### 4.5.2 Integration Time and Gain

The integration time is the duration a detector collects and counts emitted photons (here luminescence). The longer the integration time, the more photons are detected, leading to larger signals for each data point. However, if the integration time is too large, short-lived luminescence processes will not be resolved since time resolution

is too bad. If the integration time takes too small values, low signals can not be distinguished from noise (Dijon et al., **2021**). The gain has a similar influence on the signal as the integration time but is a computational signal amplifying factor. If it is set too high, signals usually become noisy. If it is too small, signals and noise can not be discriminated any longer (Dijon et al., **2021**). In this work, the integration time was commonly set to 100 ms at the Tecan Genios plate reader. The gain was usually set to 150. The aim of this chapter was to find the optimal integration time and gain at the Tecan Genios plate reader in luminescence mode to optimize the S/N of the miniG protein recruitment assay independent of other assay conditions.

HEK M1R/mG<sub>q</sub> cells were seeded on white 96-well plates according to the standardized protocol (**chapter 3.6.1.1**). On the day of the experiment, the medium was exchanged with L15 buffer and short luminescence measurements were conducted as follows. After equilibration, 1  $\mu$ M coelenterazine h was added and a 5 min baseline was recorded at the Tecan Genios plate reader. Then seven carbachol concentrations (between 100 nM and 1 mM) and a vehicle control (CTRL) were added and luminescence was measured for another 15 min to ensure that the maximum luminescence (usually occurring after 8 min) was detected. In total, 16 combinations of integration times and gains were tested: the integration times were 100 ms (standard), 250 ms, 500 ms and 1000 ms and the gains were set to 100, 150 (standard), 200 and 250. The corresponding luminescence time courses are found in **Appendix 28**. From the maximal signals and standard deviations of the baseline readings, S/N ratios were calculated for each instrument setting using a carbachol concentration of 1 mM (cf. **chapter 3.6.2.1**). They are displayed in **Figure 70**.

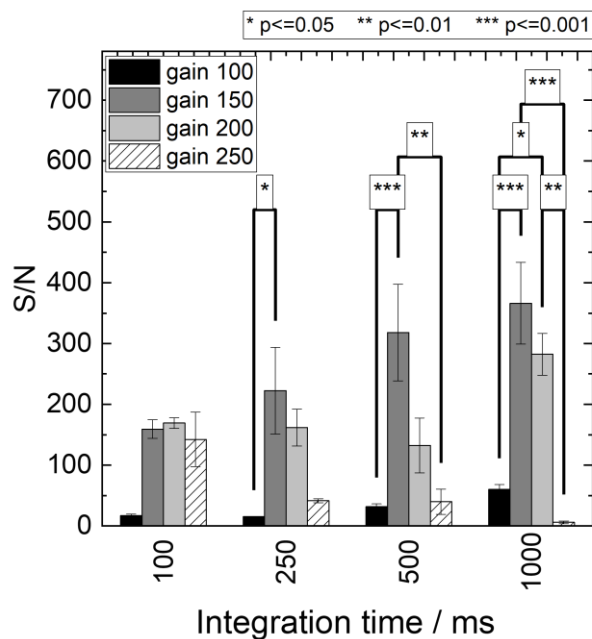


Figure 70. S/N ratios of the luminescence data of **HEK M1R/mG<sub>q</sub>** cells that were cultivated on a white 96-well plate. After incubation with 1  $\mu$ M coelenterazine h, 1 mM of carbachol was added. Different **integration times (100 ms, 250 ms, 500 ms, 1000 ms) and gains (100, 150, 200, 250)** were set at the Tecan Genios plate reader. The data processing protocol is described in **chapter 3.6.2.1**. Statistical significance (\*) was assessed with Tukey's range test. Mean  $\pm$  SE, N = 3, single experiment. Temperature: 37°C.

The luminescence signals increase with both longer integration times and larger gains (**Appendix 28**). However, the fluctuations considerably increase with the gain as well. Furthermore, at a gain of 250 and integration times between 250 ms and 1000 ms the signal threshold is exceeded for high carbachol concentrations. Nonetheless, S/N ratios were calculated for 1 mM carbachol (**Figure 70**). Given that the gains are 100 and 150, the S/N ratios increase with longer integration times. At a gain of 200, the S/N is stable for integration times between 100-500 ms and increases for an integration time of 1000 ms. For a gain of 250, an inverse relationship is observed: the S/N decreases with increasing integration times. Considering a single integration time, the S/N increases from a gain of 100 to 150 and decreases for larger gains. Only for an integration time of 100 ms, the S/N ratio rises up to a gain of 200 and then decreases again. The largest S/N is found for 1000 ms and a gain of 150 with a value of  $370 \pm 70$ . The smallest S/N with a value of  $6 \pm 2$  is found for 1000 ms and a gain of 250.

Except for a gain of 250, it is obvious that longer integration times are advantageous regarding the S/N (**Figure 70**) (Salama et al., **2004**). However, it must be considered that the time resolution suffers from longer integration times and kinetic information is lost. Consequently, it is always a question of the system under investigation, whether

to improve the S/N or time resolution. For HEK M1R/mG<sub>q</sub> cells, no significant data loss is visible when choosing larger integration times (**Appendix 28**), thus, 1000 ms is recommended as the best practice parameter.

By increasing the gain for one fixed integration time, an amplification of the S/N followed by a decrease in S/N is observed (**Figure 70**). This is due to increased standard deviations in the baseline. With larger gains not only the signal amplitude increases but also the noise, giving rise to lower S/N ratios. Therefore, an intermediate gain such as 150 should be chosen. Setting the gain to the highest possible value as suggested by Garvin *et al.* is not recommended by the demonstrated data (Garvin *et al.*, **2021**).

Overall, it is always important to evaluate the system under study with respect to both parameters. The integration time and gain should be adjusted to the cell line in use and its luminescence behavior and, additionally, must be customized according to the measurement device or plate reader. For instance, HEK H2R/mG<sub>s</sub> cells already exhibit large luminescence values for an integration time of 100 ms and a gain of 150 (cf. **chapter 4.3, Figure 56**) in contrast to HEK M1R/mG<sub>q</sub> cells. Therefore, a further increase of the integration time or gain will lead to a cut-off signal, especially for high ligand concentrations, because of the detector's threshold (**Appendix 29**).

### 4.5.3 Coelenterazine h Concentration

Luminescence is known to be dependent on the luciferin concentration (Didiot *et al.*, **2011**, Dijon *et al.*, **2021**). Yet, one possibility to enhance the luminescence signal in the miniG protein recruitment assay is to increase the coelenterazine h concentration. However, coelenterazine h is a significant expense factor (0.484 € per 1 µg coelenterazine h; promega.de #3; **August 10, 2024**). A balance between signal enhancement and cost must be established. Routinely, a final concentration of 1 µM coelenterazine h was used. In this chapter, two smaller concentrations (0.25 µM and 0.5 µM) and one larger concentration (2 µM) of coelenterazine h were tested in the miniG protein recruitment assay.

HEK M1R/mG<sub>q</sub> cells were seeded as described in **chapter 3.6.1.1** on white 96-well plates. After a two-day cultivation, the culture medium was exchanged with L15 buffer and the cells were equilibrated for 2-2.5 h. Then, four different coelenterazine h solutions (0.25 µM, 0.5 µM, 1 µM, 2 µM) were added and a baseline was recorded for 0.17 h at the Tecan Genios. Finally, a vehicle control (CTRL) and seven different carbachol concentrations (between 100 nM and 1 mM) were added and

luminescence was measured for one more hour. The time traces are depicted in **Figure 71A-D**.

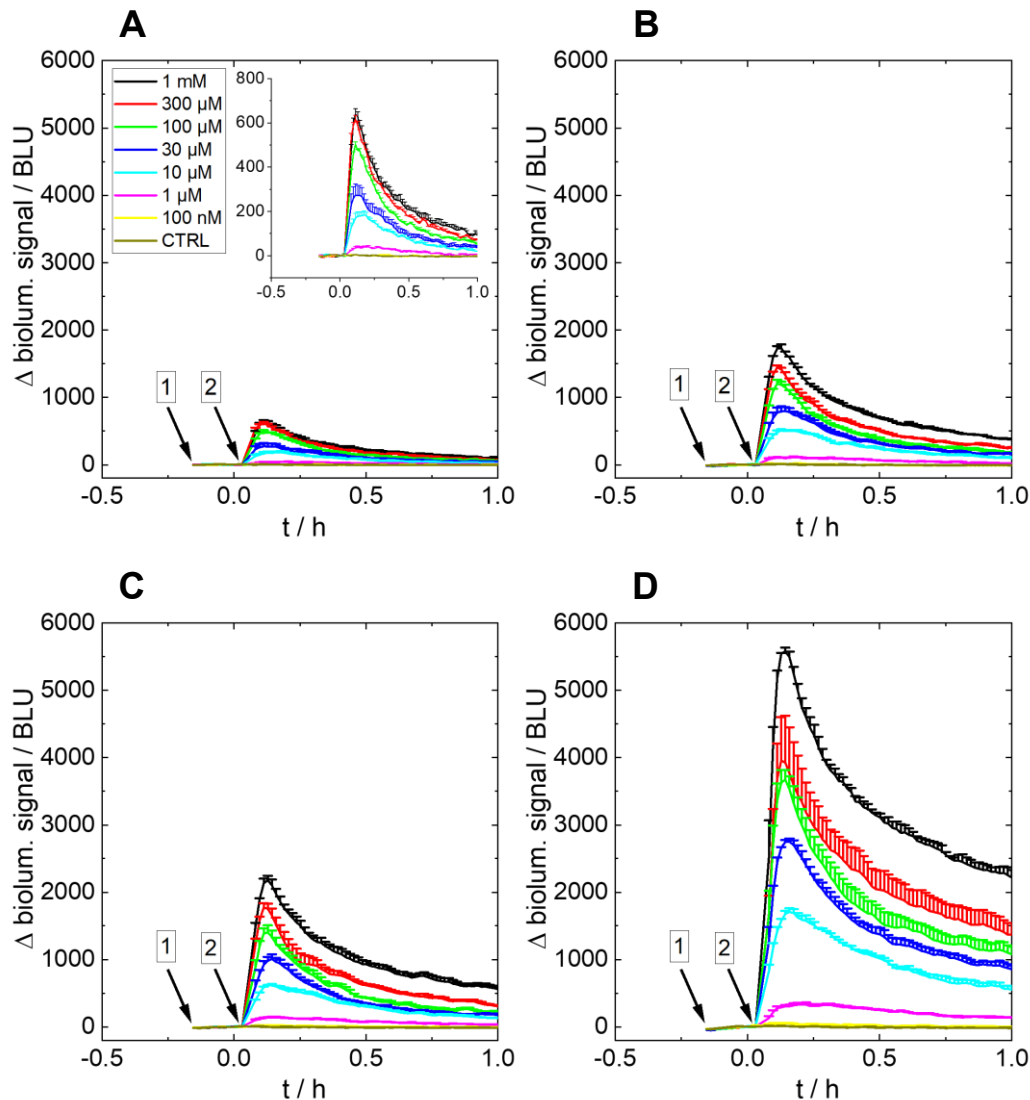


**Figure 71.** Luminescence change over time of **HEK M1R/mG<sub>q</sub>** cells. The cells were cultivated on a white 96-well plate. At  $t = -0.14$  h, four different **concentrations of coelenterazine h** (**A: 0.25  $\mu$ M**, **B: 0.5  $\mu$ M**, **C: 1  $\mu$ M**, **D: 2  $\mu$ M**) were added (arrow 1). At  $t = 0$  h, the cells were stimulated with different concentrations of carbachol (arrow 2). Black 1 mM, red 300  $\mu$ M, green 100  $\mu$ M, blue 30  $\mu$ M, cyan 10  $\mu$ M, pink 1  $\mu$ M, yellow 100 nM, brown CTRL. Baseline from A to D:  $(8.9 \pm 0.3)$  BLU,  $(16.9 \pm 0.6)$  BLU,  $(17.9 \pm 0.5)$  BLU and  $(37 \pm 1)$  BLU. Mean + SE,  $N = 3$ , single experiment. CTRL = vehicle control. BLU = bioluminescence units. Temperature: 37°C.

For the baseline luminescence, discrepancies between the different coelenterazine h concentrations are detected. The baseline values increase from  $(8.9 \pm 0.3)$  BLU for 0.25  $\mu$ M coelenterazine h (**Figure 71A**) to  $(16.9 \pm 0.6)$  BLU for 0.5  $\mu$ M coelenterazine h (**Figure 71B**),  $(17.9 \pm 0.5)$  BLU for 1  $\mu$ M coelenterazine h (**Figure 71C**) and  $(37 \pm 1)$  BLU for 2  $\mu$ M coelenterazine h (**Figure 71D**). After

stimulation at  $t = 0$  h, the luminescence increases rapidly in all four cases to reach a maximum after  $t = 0.11$ - $0.14$  h. In all cases, the luminescence signals increase with increasing carbachol concentration. The only exceptions are the curves of  $300 \mu\text{M}$  and  $1 \text{ mM}$  carbachol if the cells are preincubated with  $0.25 \mu\text{M}$  coelenterazine h (**Figure 71A, black, red**). Here, the two curves overlay. Furthermore, the luminescence signal is enhanced with increasing coelenterazine h concentration. For  $0.25 \mu\text{M}$  coelenterazine h and  $1 \text{ mM}$  carbachol, a maximum signal of  $(640 \pm 30)$  BLU is observed (**Figure 71A, black**). For increasing coelenterazine h concentrations, the luminescence signal increase is more pronounced with maximal values of  $(1730 \pm 50)$  BLU for  $0.5 \mu\text{M}$  coelenterazine h (**Figure 71B, black**),  $(2180 \pm 70)$  BLU for  $1 \mu\text{M}$  coelenterazine h (**Figure 71C, black**) and  $(5580 \pm 50)$  BLU for  $2 \mu\text{M}$  coelenterazine h (**Figure 71D, black**) and  $1 \text{ mM}$  carbachol, respectively.

To compare potencies and efficacies, concentration-response curves were generated by extracting the data at  $t = 0.5$  h and plotting it against the logarithmic ligand concentration. The data was fitted with a four-parametric dose-response fit (**equation 15**), which is depicted in **Figure 72** for the different coelenterazine h concentrations.

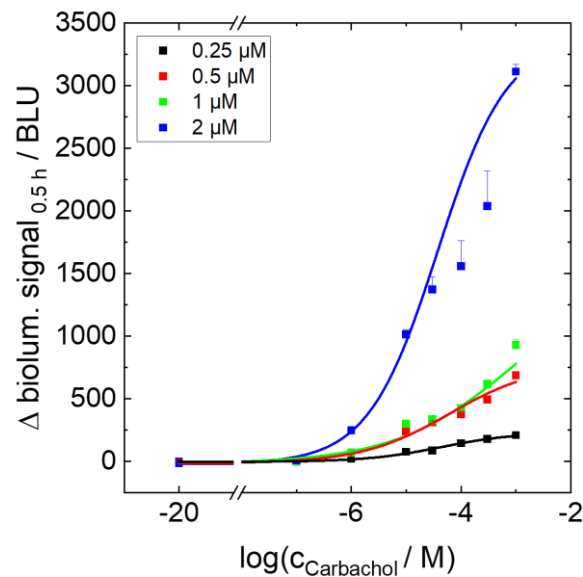


**Figure 72.** Concentration-response curves of **HEK M1R/mG<sub>q</sub>** cells grown on a white 96-well plate. After incubation with **0.25  $\mu\text{M}$  (black), 0.5  $\mu\text{M}$  (red), 1  $\mu\text{M}$  (green) or 2  $\mu\text{M}$  (blue) coelenterazine h**, the cells were stimulated with different concentrations of carbachol. The luminescence data 0.5 h after stimulation (squares) is plotted as a function of agonist concentration and was extracted from **Figure 71A-D**. The concentration-response fits (solid lines) reveal  $pEC_{50}$  values of  $4.4 \pm 0.1$  for  $0.25 \mu\text{M}$  coelenterazine h,  $4.2 \pm 0.4$  for  $0.5 \mu\text{M}$  coelenterazine h,  $3 \pm 2$  for  $1 \mu\text{M}$  coelenterazine h and  $4.4 \pm 0.2$  for  $2 \mu\text{M}$  coelenterazine h. The  $E_{max}$  values are  $(230 \pm 20)$  BLU,  $(800 \pm 200)$  BLU,  $(2000 \pm 2000)$  BLU and  $(3400 \pm 300)$  BLU in the same order. Mean + SE,  $N = 3$ , single experiment. BLU = bioluminescence units. Temperature:  $37^\circ\text{C}$ .

For each coelenterazine h concentration, the luminescence values of the CTRL and 100 nM carbachol remain close to zero (**Figure 72**). By further increasing the carbachol concentration, luminescence constantly increases. Thereby, the highest coelenterazine h concentration of 2  $\mu\text{M}$  (**Figure 72, blue**) displays the largest luminescence signals followed by 1  $\mu\text{M}$ , 0.5  $\mu\text{M}$  and 0.25  $\mu\text{M}$  of coelenterazine h. The curves for 1  $\mu\text{M}$  and 0.5  $\mu\text{M}$  coelenterazine h (**Figure 72, red, green**) superimpose up to a concentration of 100  $\mu\text{M}$  carbachol. Above that concentration, the curve for 1  $\mu\text{M}$  coelenterazine h shows larger values than 0.5  $\mu\text{M}$  coelenterazine h.

The pEC50 values are  $4.4 \pm 0.1$  for 0.25  $\mu\text{M}$  coelenterazine h (**Figure 72, black**),  $4.2 \pm 0.4$  for 0.5  $\mu\text{M}$  coelenterazine h (**Figure 72, red**),  $3 \pm 2$  for 1  $\mu\text{M}$  coelenterazine h (**Figure 72, green**), and  $4.4 \pm 0.2$  for 2  $\mu\text{M}$  coelenterazine h (**Figure 72, blue**). For all coelenterazine h concentrations, the pEC50 values are in a similar range. Only the value for 1  $\mu\text{M}$  coelenterazine h features a large error. The  $E_{\text{max}}$  values, in contrast, rise with increasing substrate concentration. They take values of  $(230 \pm 20)$  BLU for 0.25  $\mu\text{M}$  coelenterazine h,  $(800 \pm 200)$  BLU for 0.5  $\mu\text{M}$  coelenterazine h,  $(2000 \pm 2000)$  BLU for 1  $\mu\text{M}$  coelenterazine h and  $(3400 \pm 300)$  BLU for 2  $\mu\text{M}$  coelenterazine h. Again, the value for 1  $\mu\text{M}$  coelenterazine h exhibits a large error. For better comparison of the signal enhancement, S/N ratios were calculated according to **chapter 3.6.2.1**. They are given in **Figure 73** for the different coelenterazine h concentrations and a carbachol concentration of 1 mM.

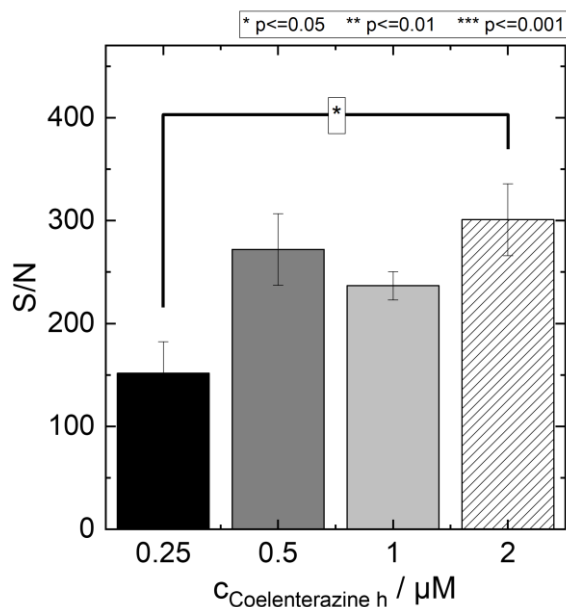


Figure 73. S/N ratios of the luminescence data of **HEK M1R/mG<sub>q</sub>** cells that were cultivated on a white 96-well plate. After incubation with **0.25  $\mu\text{M}$  (black)**, **0.5  $\mu\text{M}$  (dark grey)**, **1  $\mu\text{M}$  (light grey)** or **2  $\mu\text{M}$  (white) coelenterazine h**, 1 mM of carbachol was added. The data processing protocol is described in **chapter 3.6.2.1**. Statistical significance (\*) was assessed with Tukey's range test. Mean  $\pm$  SE, N = 3, single experiment. Temperature: 37°C.

**Figure 73** reveals S/N ratios of  $150 \pm 30$  for 0.25  $\mu\text{M}$  coelenterazine h,  $270 \pm 40$  for 0.5  $\mu\text{M}$  coelenterazine h,  $240 \pm 10$  for 1  $\mu\text{M}$  coelenterazine h and  $300 \pm 40$  for 2  $\mu\text{M}$  coelenterazine h. Only the values for 0.25  $\mu\text{M}$  and 2  $\mu\text{M}$  coelenterazine h are significantly different (\*,  $p \leq 0.05$ ).

From the baseline values of luminescence, it is implied that the background luminescence rises with increased coelenterazine h concentration (**Figure 71A-D**). This is attributed to the fact that more constitutively active receptors or intrinsically active NanoLuc molecules are detected when more coelenterazine h is present (Kenakin, **2006**, Milligan, **2003**). Another explanation is that coelenterazine h is oxidized spontaneously independent of the available ligand, GPCR or reassembled NanoLuc. The spontaneous oxidation of luciferins was evidenced by screening several NanoLuc substrates including furimazine *in vivo* without any luciferase present in nude mice (Gaspar et al., **2021**).

Generally, the signaling kinetics and potencies for all coelenterazine h concentrations (**Figure 71A-D** and **Figure 72**) are the same as described in **chapter 4.3**. The time courses first show a concentration-dependent signal increase with maxima found between 0.11-0.14 h. Then, luminescence gradually drops down. However, the signal intensity is changed with varying coelenterazine h concentrations. The luminescence maxima, S/N ratios and  $E_{\text{max}}$  values are enhanced for larger coelenterazine h

concentrations (**Figure 72 and Figure 73**). Besides that, close inspection reveals that the initial slopes become steeper with increasing coelenterazine h concentration. This is due to the fact that the rate of luminescence generation depends on the luciferin concentration as Michaelis and Menten proposed in 1913 (Michaelis et al., **2011**, Michaelis, Menten, **1913**, Seibert, Tracy, **2014**).

Overall, the pEC50 values for all coelenterazine h concentrations are in the same range (**Figure 72**) and similar to the one determined in **chapter 4.3** ( $4.4 \pm 0.3$ ). The large error of the pEC50 and  $E_{\max}$  value for a preincubation with 1  $\mu\text{M}$  coelenterazine h (**Figure 72, green**) is attributed to the concentration-response fit. No saturation is achieved for large carbachol concentrations. Concentrations above 1 mM carbachol must be evaluated with the miniG protein recruitment assay for a better definition of the upper asymptote. However, concentrations above 1 mM are not considered physiologically relevant. Therefore, the investigation of higher carbachol concentrations was omitted.

While 0.25  $\mu\text{M}$  coelenterazine h exhibits significantly smaller luminescence signals (**Figure 71A and Figure 72, black**), concentrations of 0.5  $\mu\text{M}$  (**Figure 71B and Figure 72, red**) and 1  $\mu\text{M}$  coelenterazine h (**Figure 71C and Figure 72, green**) generally feature similar  $E_{\max}$  and S/N values and only show a slight difference in the time courses. For 2  $\mu\text{M}$  coelenterazine h (**Figure 71D and Figure 72, blue**), the largest signal intensities and, hence, enhanced S/N ratios (**Figure 73**) are observed. Consequently, a concentration of 2  $\mu\text{M}$  of coelenterazine h should be favored with respect to the luminescence intensities. However, since 0.5  $\mu\text{M}$  and 1  $\mu\text{M}$  coelenterazine h deliver equivalent results, a concentration of 0.5  $\mu\text{M}$  is recommended as the best practice parameter for investigating HEK M1R/mG<sub>q</sub> cells to reduce the costs compared to 2  $\mu\text{M}$  coelenterazine h but at the same time obtain adequate luminescence signals. If the luciferase expression is very weak, it is worthwhile to elevate the coelenterazine h concentration instead of taking a loss of signal. As Feeney *et al.* claim, the luciferin concentration should be chosen dependent on the luciferase system (Feeney et al., **2016**).

#### 4.5.4 Different Cultivation Times

In this chapter, the impact of the cell number after different cultivation times on luminescence was investigated. HEK M1R/mG<sub>q</sub> cells were seeded with a density of  $3 \cdot 10^5$  c/cm<sup>2</sup> on white 96-well plates. After a one-, two- or three-day cultivation, the miniG recruitment assay was performed as described in **chapter 3.6.1.1**. Shortly, the culture medium was removed and exchanged with L15 buffer and the cells were

equilibrated to the new conditions for 2-2.5 h. Then, 1  $\mu\text{M}$  coelenterazine h was added and a luminescence baseline was recorded for 0.15 h with the Tecan Genios plate reader. Finally, a vehicle control (CTRL) and carbachol solutions of varying concentrations (between 100 nM and 1 mM) were added and luminescence was monitored for 1 h. The time courses one, two and three days after seeding are depicted in **Figure 74A-C**.

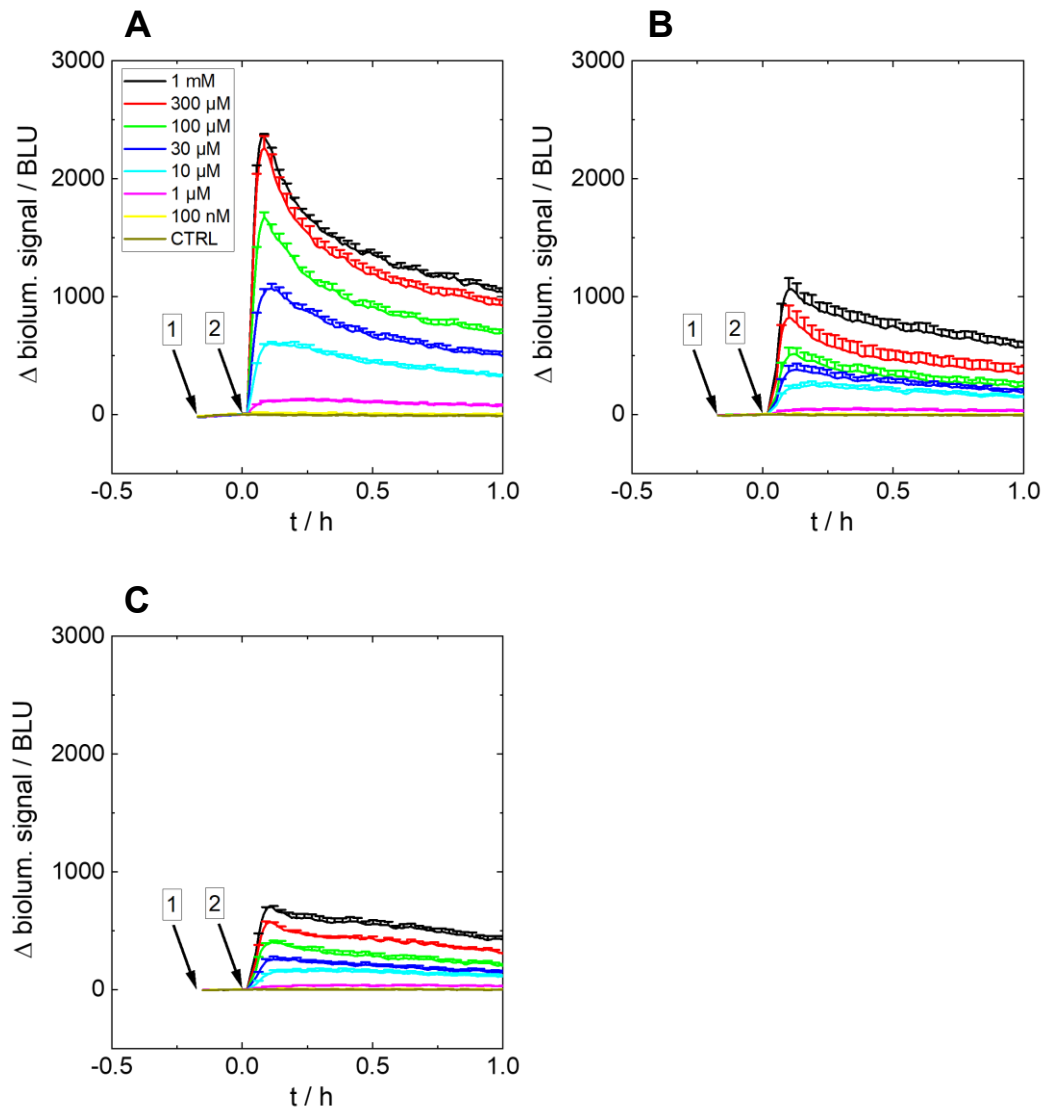
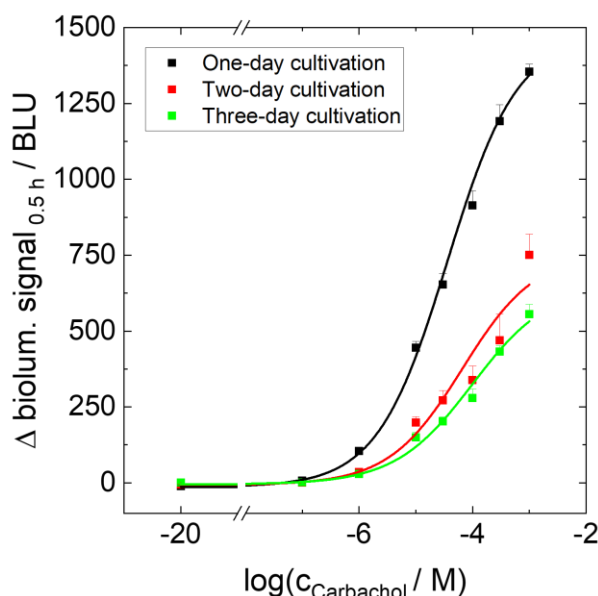


Figure 74. Luminescence change over time of **HEK M1R/mG<sub>q</sub>** cells. The cells were seeded with a density of  $3 \cdot 10^5$   $c/cm^2$  and cultivated on a white 96-well plate for **one (A), two (B) or three days (C)**. At  $t = -0.15$  h, 1  $\mu\text{M}$  coelenterazine h was added (arrow 1). At  $t = 0$  h, the cells were stimulated with different concentrations of carbachol (arrow 2). Black 1 mM, red 300  $\mu\text{M}$ , green 100  $\mu\text{M}$ , blue 30  $\mu\text{M}$ , cyan 10  $\mu\text{M}$ , pink 1  $\mu\text{M}$ , yellow 100 nM, brown CTRL. Baseline from A to C:  $(26.9 \pm 0.4)$  BLU,  $(13.3 \pm 0.3)$  BLU and  $(9.3 \pm 0.2)$  BLU. Mean + SE,  $N = 6$ , single experiment. CTRL = vehicle control. BLU = bioluminescence units. Temperature:  $37^\circ\text{C}$ .

The baseline values after a one-day cultivation are  $(26.9 \pm 0.4)$  BLU (**Figure 74A**), whereas on days two (**Figure 74B**) and three (**Figure 74C**) they are lower with values

of  $(13.3 \pm 0.3)$  BLU and  $(9.3 \pm 0.2)$  BLU, respectively. After ligand addition, luminescence quickly increases concentration-wise, then reaches a maximum and gradually decreases again over the measurement period. The kinetics are the same as described before (**chapter 4.3**). However, the signal intensities differ with the cultivation time. Comparing the different cultivation periods, a concentration of 1 mM carbachol leads to luminescence maxima of  $(2360 \pm 30)$  BLU (**Figure 74A**),  $(1100 \pm 100)$  BLU (**Figure 74B**) and  $(710 \pm 20)$  BLU (**Figure 74C**) with increasing cultivation time. Similar observations are made for smaller carbachol concentrations. For each cultivation time, the luminescence signals increase with increasing carbachol concentration. Only the curves for 300  $\mu$ M and 1 mM of carbachol partly superimpose for a cultivation time of one day (**Figure 74A, black, red**).

Potencies and efficacies were extracted from concentration-response curves derived from the data at time point  $t = 0.5$  h. The data for one, two and three days of cultivation was fitted with a four-parametric dose-response fit (**equation 15**), respectively, and is given in **Figure 75**.



*Figure 75. Concentration-response curves of HEK M1R/mG<sub>q</sub> cells on a white 96-well plate. The cells were cultivated for **one (black), two (red) or three (green) days**. After incubation with 1  $\mu$ M coelenterazine h, the cells were stimulated with different concentrations of carbachol. The luminescence data 0.5 h after stimulation (squares) is plotted as a function of carbachol concentration and was extracted from **Figure 74A-C**. The concentration-response fits (solid lines) reveal a pEC<sub>50</sub> of  $4.44 \pm 0.08$  and an  $E_{max}$  of  $(1470 \pm 50)$  BLU for a one-day cultivation, a pEC<sub>50</sub> of  $4.2 \pm 0.4$  and an  $E_{max}$  of  $(800 \pm 200)$  BLU for a two-day cultivation and a pEC<sub>50</sub> of  $4.0 \pm 0.3$  and an  $E_{max}$  of  $(700 \pm 100)$  BLU for a three-day cultivation. Mean + SE, N = 6, single experiment. BLU = bioluminescence units. Temperature: 37°C.*

For the CTRL and 100 nM carbachol, no differences in luminescence are visible and the curves for the different cultivation times overlay (**Figure 75**). With increasing

carbachol concentrations, the luminescence change increases. Above 1  $\mu\text{M}$  carbachol, larger discrepancies can be discerned for the different cultivation times. For a one-day cultivation (**Figure 75, black**), a steeper slope is observed compared to a two-day (**Figure 75, red**) or three-day (**Figure 75, green**) cultivation. Additionally, higher luminescence values are achieved after a one-day cultivation. A  $\text{pEC}_{50}$  of  $4.44 \pm 0.08$  and an  $E_{\text{max}}$  of  $(1470 \pm 50)$  BLU is calculated for the shortest cultivation period. The curve for a two-day cultivation lies above the curve for a three-day cultivation and reveals a  $\text{pEC}_{50}$  of  $4.2 \pm 0.4$  and an  $E_{\text{max}}$  of  $(800 \pm 200)$  BLU. For the curve of the three-day cultivation, values of  $4.0 \pm 0.3$  for the  $\text{pEC}_{50}$  and an  $E_{\text{max}}$  of  $(700 \pm 100)$  BLU are extracted. Taken together, the  $\text{pEC}_{50}$  values are in a similar range but the  $E_{\text{max}}$  values decrease for longer cultivation times. For a more extensive data analysis, S/N ratios were calculated for 1 mM carbachol. They are presented in **Figure 76**.

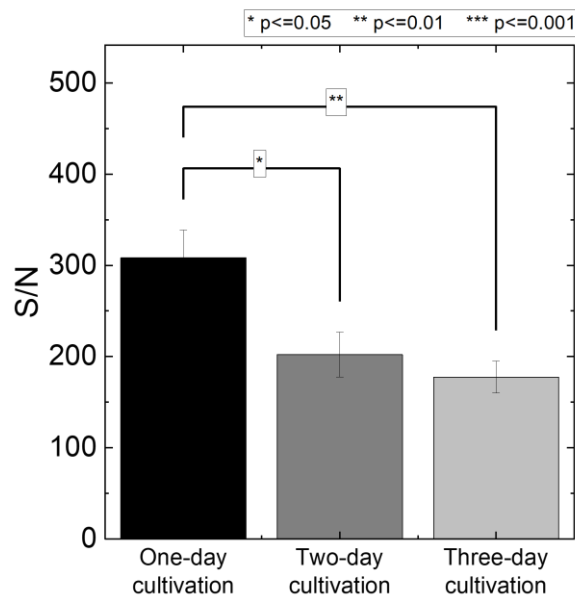


*Figure 76. S/N ratios of the luminescence data of HEK M1R/mG<sub>q</sub> cells that were cultivated on a white 96-well plate for one (black), two (dark grey) or three (light grey) days. After incubation with 1  $\mu\text{M}$  coelenterazine h, 1 mM of carbachol was added. The data processing protocol is described in **chapter 3.6.2.1**. Statistical significance (\*) was assessed with Tukey's range test. Mean  $\pm$  SE, N = 6, single experiment. Temperature: 37°C.*

For 1 mM carbachol, S/N values of  $310 \pm 30$ ,  $200 \pm 30$  and  $180 \pm 20$  were calculated for cultivation times of one, two and three days, respectively (**Figure 76**). This means the S/N decreases with longer cultivation. The value for a cultivation time of one day is considered significantly different from the value of a two-day (\*,  $p \leq 0.05$ ) or three-day (\*\*,  $p \leq 0.01$ ) cultivation.

In summary, luminescence is more pronounced after a cultivation time of one day compared to a two- or three-day cultivation. Both, baseline and stimulation values, are larger after one day than for longer cultivation times (**Figure 74A-C**). The baseline values on days two (**Figure 74B**) and three (**Figure 74C**) are reduced by about 51% and 65% in comparison with a one-day cultivation. Also, the maximal luminescence after stimulation on days two and three is reduced to 45% and 30% of the value of a one-day cultivation. Similar behavior is observed for the  $E_{\max}$  values (**Figure 75**). The S/N values confirm these observations (**Figure 76**). All these findings might be attributed to changes in the GPCR and miniG protein and, hence, luciferase expression over time (Lämmermann, Kastenmüller, **2019**). If the overall luciferase expression over time is decreased irrespective of an increased cell number, less signal is expected. However, in an analogous experiment, impedance signals increased with prolonged cultivation time (**chapter 4.4.3.2**), which suggests the exact opposite. The slight increase in impedance could be explained by an increased receptor-miniG protein expression, leading to more downstream signaling and, thus, larger impedance responses. At first, this is contradictory to the luminescence findings. However, considering both outcomes, the luminescence signal certainly indicates that less luciferase is present over longer cultivation times, either due to a degradation of the miniG proteins, the luciferase, the receptor or a combination of these. If this holds true, the amplified impedance signal with longer cultivation time is either emerging from interactions of the modified receptor and endogenous G proteins, possibly being more expressed over time in contrast to miniG proteins, or from an entirely different signaling pathway (e.g.  $\beta$ -arrestin, second messengers). Likewise, it is conceivable that solely a very downstream process, for instance  $Ca^{2+}$  release, and succeeding morphological changes are resolved with impedance spectroscopy. This hypothesis is supported by the fact that impedance is a holistic integrational technique (Doijen et al., **2019**, Stolwijk, Wegener, **2019**). Even if protein expression is attenuated and only a small number of receptors is activated after ligand addition, the triggered processes add up along the signaling cascade, leading to an extensive signal enhancement and a rapid saturation of impedance in contrast to a more proximal assay. This is also why the differences in impedance with longer cultivation time (**chapter 4.4.3.2**) are not as pronounced as the variations of luminescence (**Figure 74A-C**).

The determined pEC50 values of luminescence for a one-, two- or three-day cultivation (**Figure 75**) were all in the same range and are in accordance with the literature ( $4.69 \pm 0.05$ , (Höring, **2022**)). Furthermore, the pEC50 value for a two-day cultivation ( $4.2 \pm 0.4$ ) is similar to the one determined in **chapter 4.3** ( $4.4 \pm 0.3$ ).

Consequently, the cell number or cultivation time does not influence the potency of the ligand. A reproducible determination of the potency after a cultivation time of two days is feasible.

Concludingly, for luminescence, a measurement after a cultivation time of one day is recommended. Generally, higher signals and S/N are attained and a more sensitive characterization of the system under study is possible. In addition, it is more economical because time and costs, e.g. for culture medium, are saved and more experiments can be performed in the same amount of time. However, taking impedance measurements into account, a two-day cultivation is inevitable. Cell attachment, spreading and the formation of cellular contacts are only just completed after two days, which is required to ensure a reliable impedance readout (Janshoff et al., **2010**). Consequently, a two-day cultivation is necessary when combining both assays (cf. **chapter 4.6**) and strikes a good balance between the luminescence signal outcome and adherence.

### 4.5.5 Additional Washing Step

All cell lines were routinely cultured in medium containing the pH indicator phenol red. Phenol red is known to increase the background fluorescence and, hence, might also lead to inaccurate results when present in a bioluminescent framework with spectral properties overlaying with the excitation wavelength of the pH indicator (Stadtfield et al., **2005**). Its absorption maximum takes a value of around 440 nm, coinciding with the emission wavelength of NanoLuc (cf. **chapter 3.6, Figure 32**) (Ettinger, Wittmann, **2014**, Rovati et al., **2012**). To prevent the excitation of phenol red and, accordingly, a potential impact on luminescence after receptor stimulation, a washing step was introduced to remove phenol red remnants. The results of the standard protocol (no washing step) were compared to the results including a washing step.

In short, HEK M1R/mG<sub>q</sub> cells were seeded as usual on white 96-well plates (see **chapter 3.6.1.1**). On the day of the experiment, the wells were either washed once with L15 buffer before adding measurement buffer again (“washed”) or the culture medium was exchanged directly with L15 buffer (“non-washed”). After equilibration, a luminescence baseline was measured with 1  $\mu$ M coelenterazine h at the Tecan Genios device and, subsequently, miniG recruitment was initiated by stimulation with different carbachol solutions (between 100 nM and 1 mM). L15 buffer was used as a vehicle control (CTRL). Luminescence was monitored for 1 h and is depicted in **Figure 77A-B** for the washed and non-washed samples.

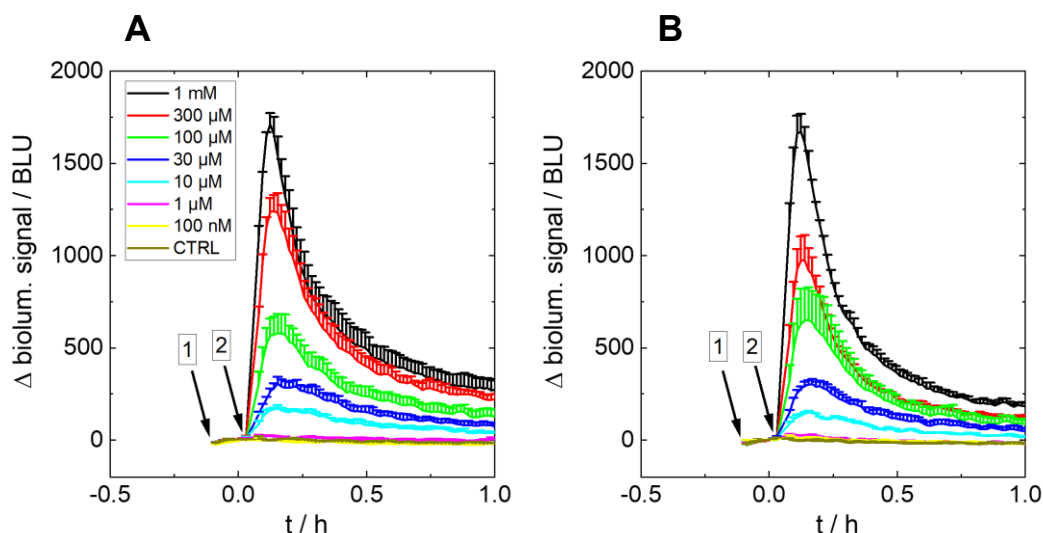
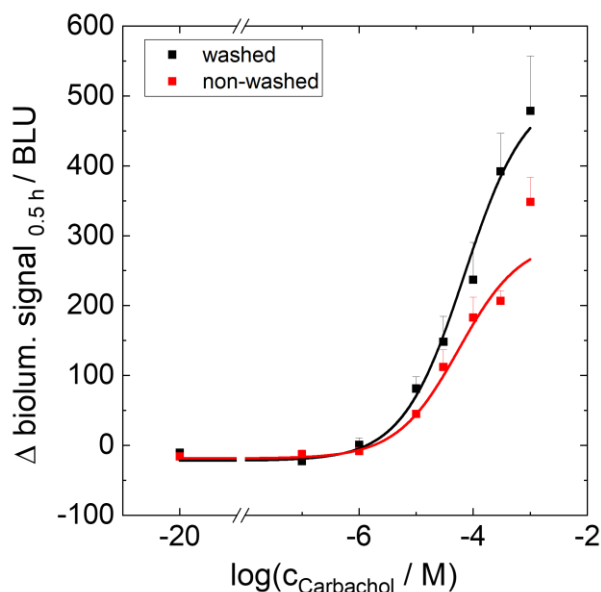


Figure 77. Luminescence change over time of *HEK M1R/mG<sub>q</sub>* cells. The cells were cultivated on a white 96-well plate. The wells were either **washed once with measurement buffer (A)** or **were not washed (B)** before exchanging the medium with L15. At  $t = -0.15$  h,  $1 \mu\text{M}$  coelenterazine h was added (arrow 1). At  $t = 0$  h, the cells were stimulated with different concentrations of carbachol (arrow 2). Black  $1 \text{ mM}$ , red  $300 \mu\text{M}$ , green  $100 \mu\text{M}$ , blue  $30 \mu\text{M}$ , cyan  $10 \mu\text{M}$ , pink  $1 \mu\text{M}$ , yellow  $100 \text{ nM}$ , brown CTRL. Baseline A and B:  $(30.4 \pm 0.9)$  BLU,  $(34.1 \pm 0.8)$  BLU. Mean + SE,  $N = 2-3$ , single experiment. CTRL = vehicle control. BLU = bioluminescence units. Temperature:  $37^\circ\text{C}$ .

Both baselines take similar values of  $(30.4 \pm 0.9)$  BLU for the washed (**Figure 77A**) and  $(34.1 \pm 0.8)$  BLU for the non-washed (**Figure 77B**) cells. After carbachol addition, the kinetics are the same as described in **chapter 4.3**: luminescence quickly rises, reaches a maximum and declines over the measurement period. The luminescence signals increase with increasing carbachol concentration. In general, similar luminescence intensities are observed for every carbachol concentration if washed and non-washed cells are compared. Solely, the maxima for  $300 \mu\text{M}$  (**Figure 77A-B, red**) differ. For the washed cells, it lies at  $(1240 \pm 90)$  BLU whereas it takes a value of  $(1000 \pm 100)$  BLU for the not washed cells. Nonetheless, all other maxima coincide. For instance,  $1 \text{ mM}$  carbachol leads to maximal values of  $(1710 \pm 60)$  BLU and  $(1700 \pm 100)$  BLU for washed and non-washed cells, respectively. Another difference between washed and non-washed cells is that the curves for  $300 \mu\text{M}$  and  $100 \mu\text{M}$  carbachol overlay for  $t \geq 0.25$  h in the case of the non-washed cells but not for the washed cells (**Figure 77A-B, red, green**). Additionally, the curves for  $1 \text{ mM}$  and  $300 \mu\text{M}$  carbachol superimpose for  $t \geq 0.25$  h in the case of the washed cells, which is not the case for the non-washed cells (**Figure 77A-B, black, red**).

By extracting the luminescence values after  $t = 0.5$  h and plotting them against the logarithmic carbachol concentration, concentration-response curves are generated. After fitting the data with a four-parametric dose-response fit (**equation 15**),  $\text{pEC}_{50}$

and  $E_{\max}$  values are determined. The experimental data and respective fits are depicted in **Figure 78**.



*Figure 78. Concentration-response curves of HEK M1R/mG<sub>q</sub> cells on a white 96-well plate that was either **washed with measurement buffer once (black)** or **that was not washed (red)** before starting the measurement. After incubation with 1  $\mu\text{M}$  coelenterazine h, the cells were stimulated with different concentrations of carbachol. The luminescence data 0.5 h after stimulation (squares) is plotted as a function of carbachol concentration and was extracted from **Figure 77A-B**. The concentration-response fits (solid lines) reveal  $pEC_{50}$  values of  $4.2 \pm 0.4$  for the washed cells and  $4.3 \pm 0.3$  for the non-washed cells. The  $E_{\max}$  values are  $(500 \pm 200)$  BLU for the washed cells and  $(290 \pm 70)$  BLU for the non-washed cells. Mean + SE,  $N = 3$ , single experiment. BLU = bioluminescence units. Temperature: 37°C.*

Up to a concentration of 1  $\mu\text{M}$ , both concentration-response curves overlay and take values close to 0 BLU (**Figure 78**). With increasing carbachol concentrations, the curves for the washed and non-washed cells increase continuously. However, the values of the non-washed cells are smaller compared to the values of the washed cells. The difference between both curves increases for larger ligand concentrations. Nevertheless, up to a concentration of 100  $\mu\text{M}$  carbachol, the data points are not significantly different.  $pEC_{50}$  values of  $4.2 \pm 0.4$  for the washed cells (**Figure 78, black**) and  $4.3 \pm 0.3$  for non-washed cells (**Figure 78, red**) were determined. The  $E_{\max}$  values lie at  $(500 \pm 200)$  BLU for the washed cells and  $(290 \pm 70)$  BLU for the non-washed cells. It must be noted that the 1 mM value is not fitted well for the non-washed cells.

For an even more comprehensive comparison, S/N ratios were calculated to obtain information about the data quality. The S/N values for 1 mM carbachol are shown in **Figure 79**.

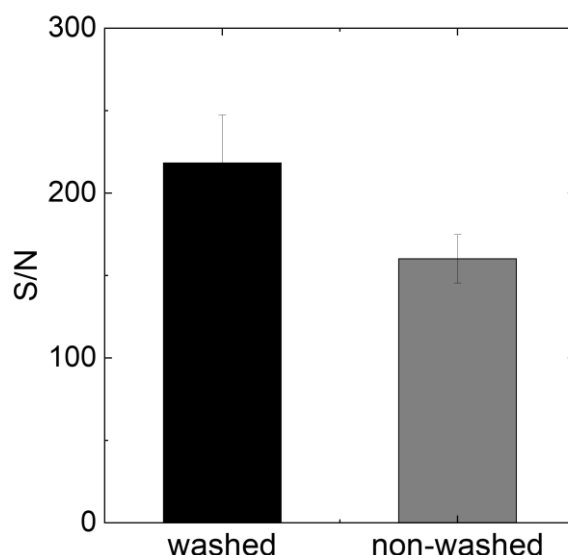


Figure 79. S/N ratio of the luminescence data of **HEK M1R/mG<sub>q</sub>** cells that were cultivated on a white 96-well plate. The wells were either **washed with measurement buffer once (black)** or **were not washed (grey)** before starting the experiment. After incubation with 1  $\mu$ M coelenterazine h, a concentration of 1 mM carbachol was added. The data processing protocol is described in **chapter 3.6.2.1**. Statistical significance (\*) was assessed with Tukey's range test. Mean  $\pm$  SE, N = 3, single experiment. Temperature: 37°C.

For the washed cells, a larger S/N value is observed than for the non-washed cells (**Figure 79**). However, no significant difference was detected between the two S/N values of  $220 \pm 30$  for washed and  $160 \pm 30$  for non-washed cells.

The results point to the fact that a washing step to remove phenol red remnants is dispensable. Neither the luminescence baseline nor the kinetics (**Figure 77A-B**) or potencies (**Figure 78**) are influenced significantly by introducing a washing step. Considering the concentration-response curves (**Figure 78**), the discrepancies between washed and non-washed cells at the high-concentration end led to a 72% larger  $E_{\max}$  value of  $(500 \pm 200)$  BLU for the washed cells in comparison with  $(290 \pm 70)$  BLU for the non-washed cells. Indeed, also higher S/N values were found for the washed cells. However, the concentration-response curve for the non-washed cells (**Figure 78, red**) is not well-fitted for a data point of 1 mM carbachol, which greatly impacts the efficacy outcome. Additionally, no significant difference was found between the S/N values of 1 mM carbachol (**Figure 79**). Since, it is more economical and time-saving to omit the washing step, in the following experiments, the washing step was excluded.

#### 4.5.6 Coelenterazine h Aging

Similar to **chapter 4.4.2**, the aging of coelenterazine h and its sensitivity towards heat, oxygen, hydrolysis and light exposure was evaluated in this chapter. Four differently treated coelenterazine h solutions (always 1  $\mu\text{M}$ ) were prepared and investigated with the help of the miniG protein recruitment assay (see **chapter 3.6.1.1**). First, a *control* solution was prepared that was freshly diluted on the day of the experiment and was stored at 4°C in the dark until use. Second, a solution that underwent *three warm-cold-cycles* (alternating temperatures of 37°C and 4°C in 5 min intervals) was prepared on the day of the experiment. Two more solutions were diluted, both one day before the experiment. One was kept at 4°C in the dark (referred to as *4°C dark*) but had the chance to oxidize and hydrolyze overnight. The other one was stored at r.t. with light exposure (referred to as *r.t. illuminated*) and had the possibility to oxidize and hydrolyze overnight.

The experiment was performed according to **chapter 3.6.1.1**. After seeding the cells and a medium exchange after 24 h, the culture medium was removed and L15 buffer was added. The cells were equilibrated at 0% (v/v) CO<sub>2</sub> for 2-2.5 h. Then, the four different coelenterazine h solutions (always 1  $\mu\text{M}$ ) were added and a luminescence baseline was recorded with the Tecan Genios luminescence reader. After 0.17 h, a vehicle control (CTRL) and carbachol in different concentrations (between 100 nM and 1 mM) were added and luminescence was measured for one more hour. The results are given in **Figure 80A-D** for the different coelenterazine h solutions.

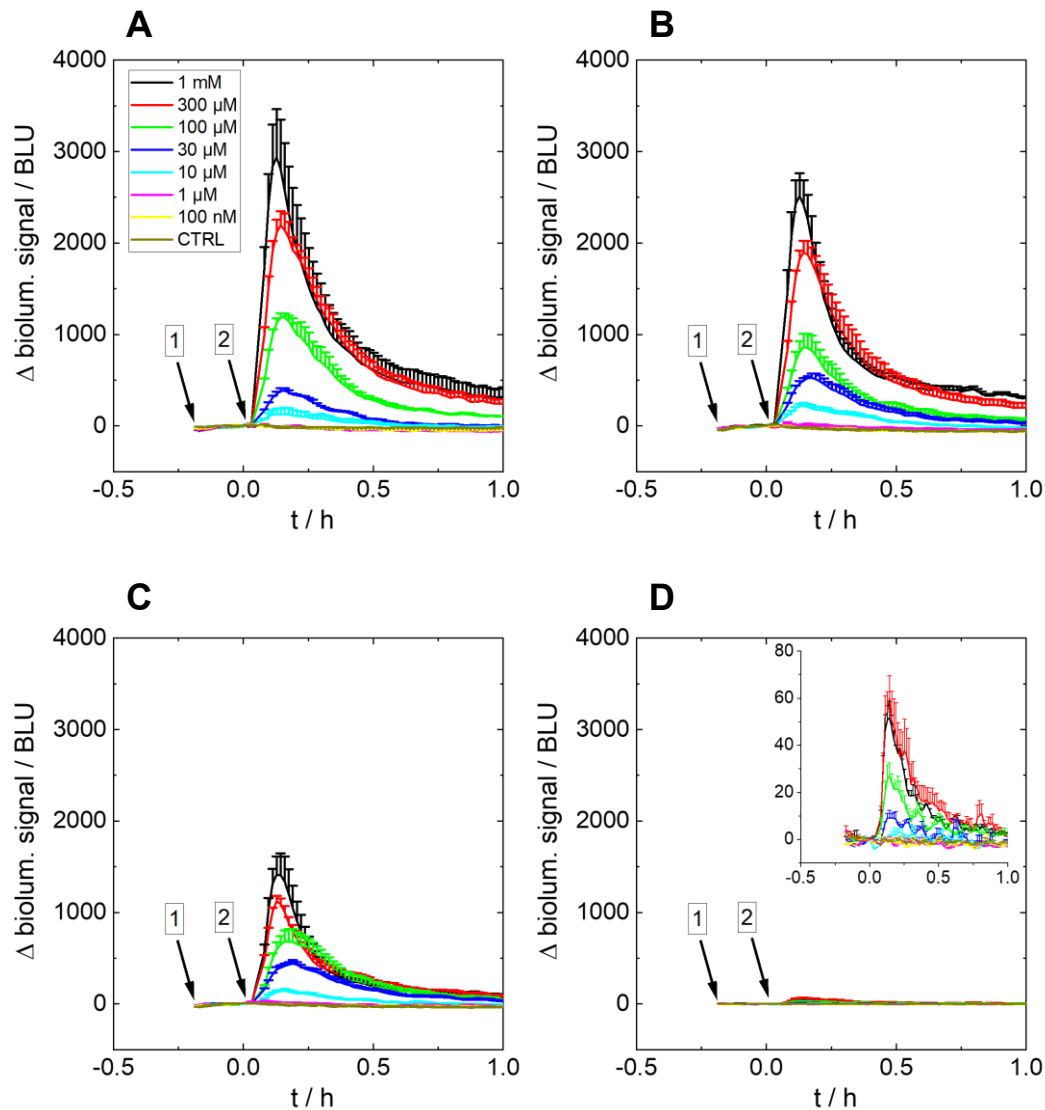
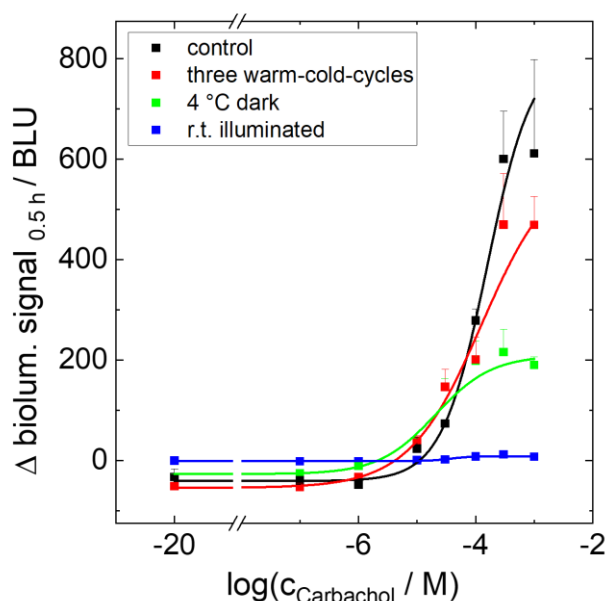


Figure 80. Luminescence change over time of **HEK M1R/mG<sub>q</sub>** cells. The cells were cultivated on a white 96-well plate. At  $t = -0.17$  h, differently treated coelenterazine  $h$  solutions ( $1 \mu\text{M}$ ) were added (arrow 1). **A: control, B: three warm-cold-cycles, C: 4°C dark, D: r.t. illuminated.** At  $t = 0$  h, the cells were stimulated with different concentrations of carbachol (arrow 2). Black  $1 \text{ mM}$ , red  $300 \mu\text{M}$ , green  $100 \mu\text{M}$ , blue  $30 \mu\text{M}$ , cyan  $10 \mu\text{M}$ , pink  $1 \mu\text{M}$ , yellow  $100 \text{ nM}$ , brown CTRL. Baseline from A to D:  $(63 \pm 1)$  BLU,  $(59 \pm 1)$  BLU,  $(41 \pm 1)$  BLU and  $(4.5 \pm 0.1)$  BLU. Mean + SE,  $N = 2-3$ , single experiment. CTRL = vehicle control. BLU = bioluminescence units. Temperature:  $37^\circ\text{C}$ .

The baseline values decrease from *control* conditions ( $(63 \pm 1)$  BLU, **Figure 80A**) to *three warm-cold-cycles* ( $(59 \pm 1)$  BLU, **Figure 80B**) to *4°C dark* ( $(41 \pm 1)$  BLU, **Figure 80C**) to *r.t. illuminated* ( $(4.5 \pm 0.1)$  BLU, **Figure 80D**). When carbachol is added, luminescence increases, reaches a maximum and gradually decreases again. With increasing ligand concentration, the luminescence signals are elevated. The CTRLs remain at the baseline level throughout the experiment. Akin to the baseline values, the luminescence intensities are higher for the *control* conditions, followed by the conditions *three warm-cold-cycles*, *4°C dark* and *r.t. illuminated*. Comparing the

maxima for 1 mM carbachol, values of  $(2900 \pm 500)$  BLU for *control* conditions,  $(2500 \pm 300)$  BLU for *three warm-cold cycles*,  $(1400 \pm 200)$  BLU for the  $4^\circ\text{C}$  *dark* sample and  $(52 \pm 7)$  BLU for the sample *r.t. illuminated* are found at  $t = 0.13\text{-}0.14$  h, respectively (**Figure 80A-D, black**). In the case of the *r.t. illuminated* treatment, the signal nearly vanishes in comparison with the other treatments.

The data at  $t = 0.5$  h was extracted and plotted against the logarithm of the carbachol concentration. By fitting with a four-parametric dose-response fit (**equation 15**),  $p\text{EC}_{50}$  and  $E_{\text{max}}$  values were determined for each coelenterazine h treatment. The plots are shown in **Figure 81**.



**Figure 81.** Concentration-response curves of *HEK M1R/mG<sub>q</sub>* cells on a white 96-well plate. After incubation with  $1 \mu\text{M}$  coelenterazine h that was pretreated differently (**black: control, red: three warm-cold-cycles, green:  $4^\circ\text{C}$  dark, blue: r.t. illuminated**), the cells were stimulated with different concentrations of carbachol. The luminescence data 0.5 h after stimulation (squares) is plotted as a function of agonist concentration and was extracted from **Figure 80A-D**. The concentration-response fits (solid lines) reveal  $p\text{EC}_{50}$  values of  $3.8 \pm 0.2$  (control),  $3.9 \pm 0.3$  (three warm-cold-cycles),  $4.7 \pm 0.2$  ( $4^\circ\text{C}$  dark) and  $4.4 \pm 0.2$  (r.t. illuminated). The  $E_{\text{max}}$  values are  $(800 \pm 200)$  BLU,  $(600 \pm 100)$  BLU,  $(210 \pm 30)$  BLU and  $(8 \pm 1)$  BLU in the same order. Mean + SE,  $N = 2\text{-}3$ , single experiment. BLU = bioluminescence units. Temperature:  $37^\circ\text{C}$ .

For concentrations up to  $10 \mu\text{M}$ , the data points mostly overlay for every coelenterazine h treatment (**Figure 81**). For concentrations above  $10 \mu\text{M}$ , the gaps between the curves increase, which also becomes evident in the efficacies.  $E_{\text{max}}$  values of  $(800 \pm 200)$  BLU (*control*, **Figure 81, black**),  $(600 \pm 100)$  BLU (*three warm-cold-cycles*, **Figure 81, red**),  $(210 \pm 30)$  BLU ( $4^\circ\text{C}$  *dark*, **Figure 81, green**) and  $(8 \pm 1)$  BLU (*r.t. illuminated*, **Figure 81, blue**) are observed. The  $p\text{EC}_{50}$  values lie at  $3.8 \pm 0.2$ ,  $3.9 \pm 0.3$ ,  $4.7 \pm 0.2$  and  $4.4 \pm 0.2$  in the same order and all take similar values, rendering an average  $p\text{EC}_{50}$  of  $4.2 \pm 0.2$ .

Furthermore, S/N ratios were calculated for an overall comparison of the data quality. They are given in **Figure 82** for a carbachol concentration of 1 mM.

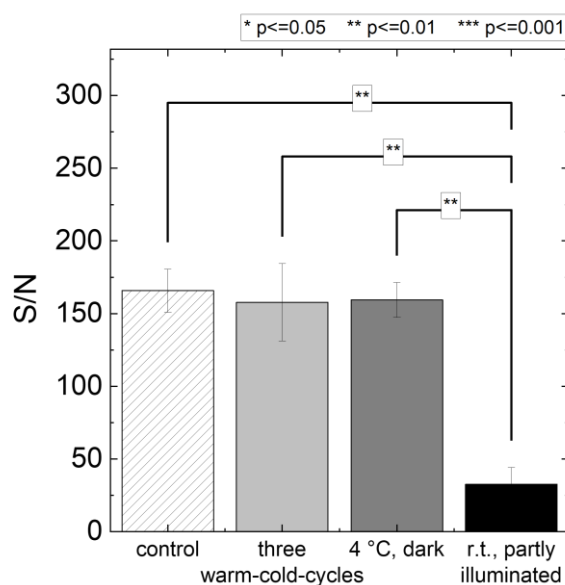


**Figure 82.** S/N ratio of the luminescence data of **HEK M1R/mG<sub>q</sub>** cells that were cultivated on a white 96-well plate. After incubation with 1  $\mu$ M coelenterazine h that was pretreated differently (**white: control, light grey: three warm-cold-cycles, dark grey: 4°C dark, black: r.t. partly illuminated**), 1 mM of carbachol was added. The data processing protocol is described in **chapter 3.6.2.1**. Statistical significance (\*) was assessed with Tukey's range test. Mean  $\pm$  SE, N = 3, single experiment. Temperature: 37°C.

The S/N values for the *control* condition (**Figure 82, white**), *three warm-cold-cycles* (**Figure 82, light grey**) and *4°C dark* (**Figure 82, dark grey**) amount to  $170 \pm 20$ ,  $160 \pm 30$  and  $160 \pm 10$ , respectively. On the contrary, the value for *r.t. illuminated* is  $30 \pm 10$  (**Figure 82, black**). The S/N for the *control* condition is not significantly different from the S/N of the conditions *three warm-cold-cycles* and *4°C dark*. For the condition *r.t. illuminated*, an 80% smaller S/N is observed compared with the other conditions, indicated by a statistical difference (\*\*,  $p \leq 0.01$ ).

As a matter of fact, differently treated coelenterazine h solutions yield different results in luminescence. It is known that luciferins, e.g. D-luciferin or coelenterazines, are prone to oxidation and are often hydrolyzed in solution (Cordeau, Kriz, **2012**, Kaskova et al., **2016**). Furthermore, they are light-sensitive and degrade at elevated temperatures (Cordeau, Kriz, **2012**, Giuliani et al., **2021**). Light exposure in combination with elevated temperature (in comparison to the recommended storage temperature of -20°C; promega.de #2; **August 10, 2024**) and a sufficient oxidation or hydrolysis time have the greatest impact on coelenterazine h, indicated by lowered luminescence values for the sample *r.t. illuminated* (**Figure 80D**). According to the

results, the 4°C *dark* sample shows the second highest influence on luminescence (temperature and oxidation or hydrolysis, **Figure 80C**). The least pronounced effect compared to *control* conditions (**Figure 80A**) is observed for the *three warm-cold-cycles* sample, where only temperature variations were tested (**Figure 80B**). These findings are not obvious when only the S/N ratios are considered (**Figure 82**). From those, one could speculate that only light exposure affects the coelenterazine h stability and accordingly luminescence outcomes. However, the kinetic results (**Figure 80A-D**) imply that light exposure, temperature and oxidation or hydrolysis need to be taken into account and affect luminescence. The large discrepancies in the  $E_{\max}$  values (**Figure 81**) are also explained by the luciferin's sensitivity towards light, temperature and oxidation or hydrolysis as observed for the luminescence intensities in general. Nonetheless, the pEC50 values for the four different conditions are very similar and range between 3.9-4.4.

In comparison with **chapter 4.4.2**, where no impact on the impedance response was observed after preincubation with differently treated coelenterazine h solutions and subsequent stimulation with carbachol (**Figure 60**), in this chapter, distinctively reduced luminescence signals are observed if coelenterazine h undergoes any kind of aging (**Figure 80A-D**). It is reasonable that the luminescence intensity decreases if coelenterazine h is degraded and becomes non-functional. The unaffected impedance signals can be explained by preserved (mini)G protein activation and further downstream effects, leading to rearrangements of the cytoskeleton. Impedance does not rely on functional coelenterazine h.

The results for the *control* condition in this chapter are compared with the results from the previous **chapter 4.3**. The kinetics, e.g. the maxima of luminescence after 0.13-0.14 h, are similar between both chapters and a concentration dependency is observed in both chapters as well. Furthermore, the luminescence signals are similar for carbachol concentrations of 300 µM and 1 mM (cf. **Figure 52B** and **Figure 80A, black, red**). However, in this chapter, the curves for intermediate concentrations between 1 µM and 100 µM carbachol (**Figure 80A, green, blue, cyan pink**) are lowered in comparison to **chapter 4.3**. Furthermore, the pEC50 and  $E_{\max}$  values (**Figure 81**) are smaller than the ones determined in **chapter 4.3** (**Figure 53B**). These differences are reduced to experimental variations, e.g. varying passage numbers or protein expressions of the GPCR, NanoLuc or miniG protein and, hence, varying cellular behavior.

Concludingly, it was verified that coelenterazine h is susceptible to oxidation, hydrolysis and elevated temperatures and undergoes photochemical reactions when exposed to light. These chemical and photochemical reactions might induce

degradation of coelenterazine h, which, consequently, can not be recognized and converted by NanoLuc anymore. This has a great impact on the luminescence outcome. For future work, it is recommended to always dilute coelenterazine h freshly on the day of the experiment and store it at  $\leq 4^{\circ}\text{C}$  not longer than a few hours.

### 4.5.7 Measurement Buffer

In analogy to **chapter 4.4.3**, three measurement buffers, L15, PBS and HBSS, were tested in the miniG protein recruitment assay to investigate the influence of the assay medium on luminescence. As described in **chapter 3.6.1.1**, HEK M1R/mG<sub>q</sub> cells were seeded with a density of  $3 \cdot 10^5$  c/cm<sup>2</sup> on a white 96-well plate. After a two-day cultivation, the medium was replaced with L15, PBS or HBSS and the cells were equilibrated at 0% (v/v) CO<sub>2</sub> and 37°C for 2-2.5 h. Then, the NanoLuc substrate coelenterazine h (1  $\mu\text{M}$ ), dissolved in the respective buffer, was added and a 0.17 h baseline of luminescence was recorded at the Tecan Genios. Finally, different carbachol concentrations (between 100 nM and 1 mM) in L15, PBS or HBSS were added and luminescence was followed for 1 h. The pure buffer solutions were utilized as controls (CTRL). The luminescence time courses are depicted in **Figure 83A-C**.

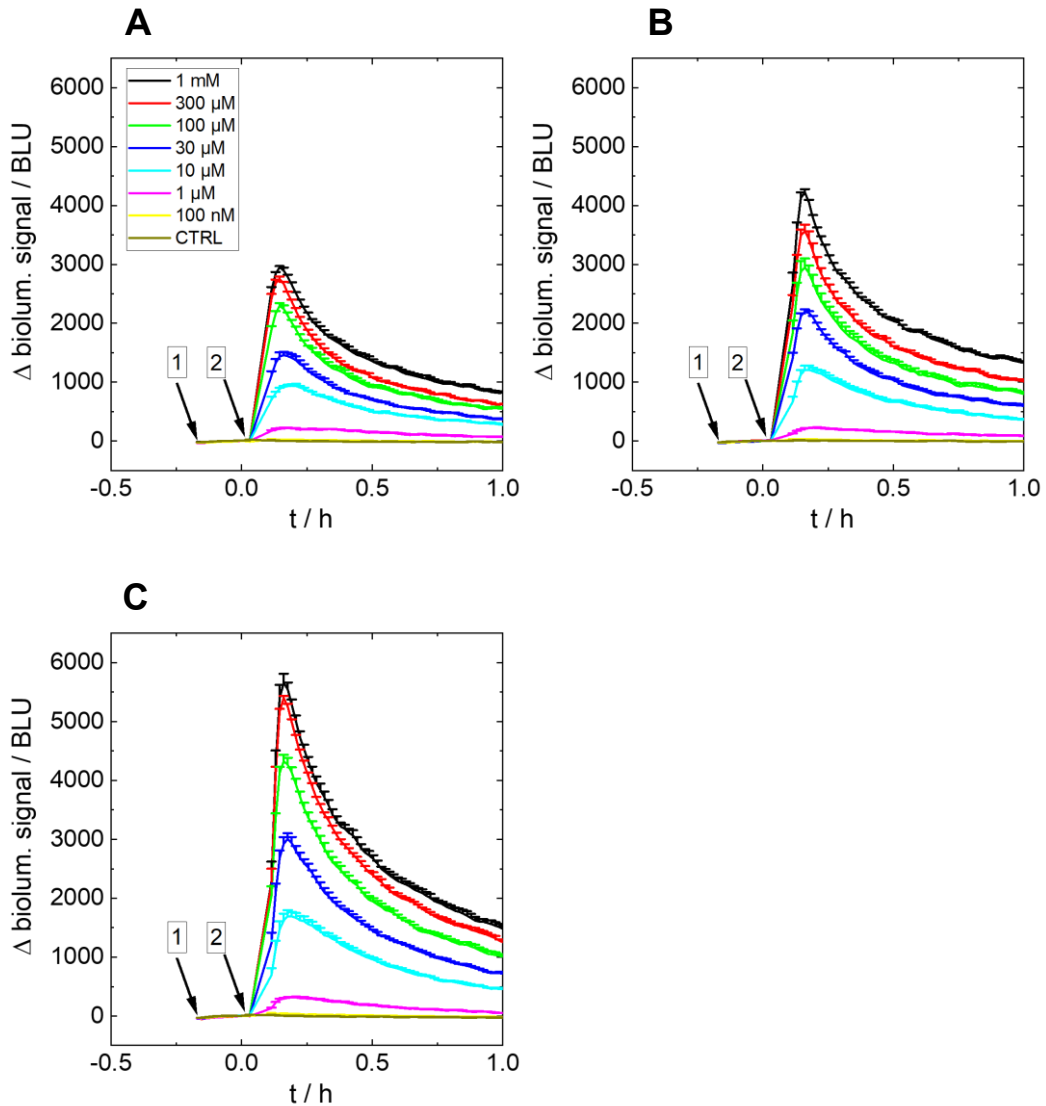
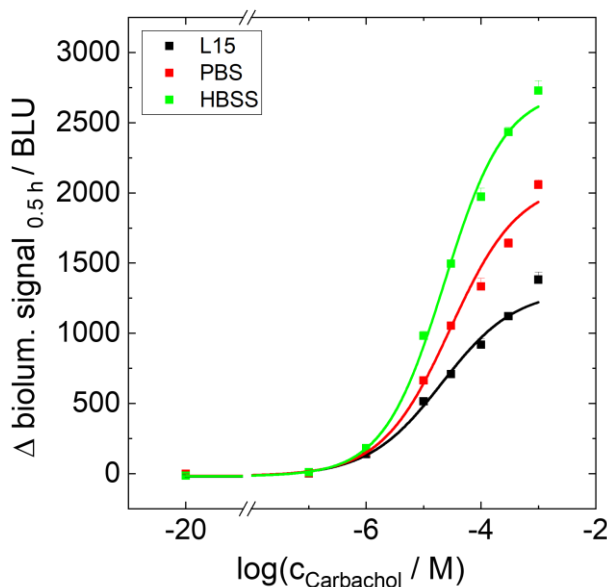


Figure 83. Luminescence change over time of **HEK M1R/mG<sub>q</sub>** cells. The cells were cultivated on a white 96-well plate. At  $t = -0.17$  h,  $1 \mu\text{M}$  coelenterazine h was added (arrow 1). At  $t = 0$  h, the cells were stimulated with different concentrations of carbachol (arrow 2). Black  $1 \text{ mM}$ , red  $300 \mu\text{M}$ , green  $100 \mu\text{M}$ , blue  $30 \mu\text{M}$ , cyan  $10 \mu\text{M}$ , pink  $1 \mu\text{M}$ , yellow  $100 \text{ nM}$ , brown CTRL. Three different buffers were used as assay medium (**A**: L15, **B**: PBS, **C**: HBSS). Baseline from A to C:  $(34.8 \pm 0.6)$  BLU,  $(35.0 \pm 0.6)$  BLU,  $(55.2 \pm 0.9)$  BLU. Mean + SE,  $N = 4$ , single experiment. CTRL = vehicle control. BLU = bioluminescence units. Temperature:  $37^\circ\text{C}$ .

While the baseline values are similar for L15 ( $(34.8 \pm 0.6)$  BLU, **Figure 83A**) and PBS ( $(35.0 \pm 0.6)$  BLU, **Figure 83B**), they are 60% larger in HBSS ( $(55.2 \pm 0.9)$  BLU, **Figure 83C**). After stimulation, in all cases, the same kinetics and a concentration dependency of the luminescence signal are observed as described in **chapter 4.3**. Luminescence increases to a maximum after carbachol is added and, subsequently, declines over the measurement period. With larger carbachol concentrations, a rise in the luminescence intensity is observed for all measurement buffers under study. However, the signal maxima differentiate and increase from L15 to PBS to HBSS. For instance, a ligand concentration of  $1 \text{ mM}$  carbachol induces maximal values of

( $2950 \pm 20$ ) BLU in L15, ( $4220 \pm 60$ ) BLU in PBS and ( $5700 \pm 200$ ) BLU in HBSS (**Figure 83A-C, black**).

By extracting the data at  $t = 0.5$  h and plotting it against the carbachol concentration, potencies and efficacies for each measurement buffer were determined. The data was fitted with a four-parametric dose-response fit (**equation 15**) and is given in **Figure 84**.



**Figure 84.** Concentration-response curves of **HEK M1R/mG<sub>q</sub>** cells on a white 96-well plate in different buffers (**black: L15, red: PBS, green: HBSS**). After incubation with  $1 \mu\text{M}$  coelenterazine h, the cells were stimulated with different concentrations of carbachol. The luminescence data 0.5 h after stimulation (squares) is plotted as a function of carbachol concentration and was extracted from **Figure 83A-C**. The concentration-response fits (solid lines) reveal  $pEC_{50}$  values of  $4.7 \pm 0.1$  in L15,  $4.5 \pm 0.2$  in PBS and  $4.64 \pm 0.05$  in HBSS. The  $E_{\text{max}}$  values are ( $1300 \pm 100$ ) BLU in L15, ( $2100 \pm 200$ ) BLU in PBS and ( $2740 \pm 90$ ) BLU in HBSS. Mean + SE,  $N = 4$ , single experiment. BLU = bioluminescence units. Temperature:  $37^\circ\text{C}$ .

The concentration-response curves are well-fitted to the data (**Figure 84**). For concentrations  $\leq 1 \mu\text{M}$ , all curves superimpose. The luminescence values for  $100 \text{ nM}$  are similar to the values of the CTRLs. By increasing the carbachol concentration, the luminescence signal increases but slowly starts to saturate for large ligand concentrations. Above  $1 \mu\text{M}$  carbachol, significant discrepancies become visible for the three assay buffers analogous to the time traces (**Figure 83A-C**). In HBSS (**Figure 84, green**), the largest luminescence change is observed resulting in an efficacy of ( $2740 \pm 90$ ) BLU, followed by PBS (**Figure 84, red**) with an  $E_{\text{max}}$  of ( $2100 \pm 200$ ) BLU and L15 (**Figure 84, black**) with an  $E_{\text{max}}$  of ( $1300 \pm 100$ ) BLU. The  $pEC_{50}$  values are  $4.64 \pm 0.05$  in HBSS,  $4.5 \pm 0.2$  in PBS and  $4.7 \pm 0.1$  in L15 and are similar in all buffers.

Besides efficacy and potency calculations, S/N ratios were determined for 1 mM carbachol, which are contrasted in **Figure 85**.

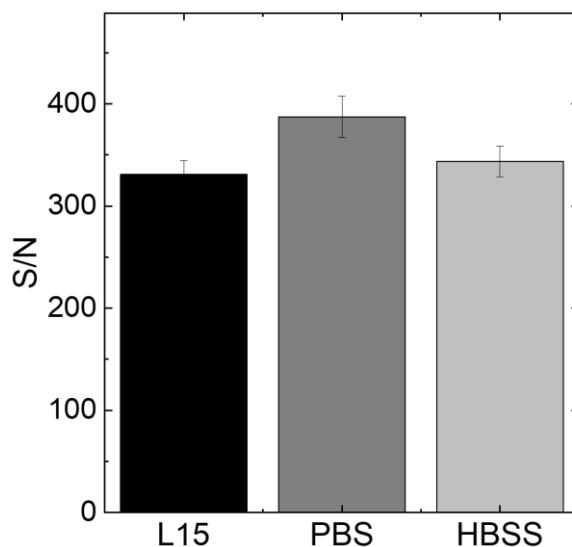


*Figure 85. S/N ratios of the luminescence data of HEK M1R/mG<sub>q</sub> cells in different buffers (black: L15, dark grey: PBS, light grey: HBSS). The cells were cultivated on a white 96-well plate. After incubation with 1 μM coelenterazine h, 1 mM of carbachol was added. The data processing protocol is described in chapter 3.6.2.1. Statistical significance (\*) was assessed with Tukey's range test. Mean ± SE, N = 4, single experiment. Temperature: 37°C.*

The S/N ratios in L15, PBS and HBSS and for a carbachol concentration of 1 mM are 330 ± 10 (**Figure 85, black**), 390 ± 20 (**Figure 85, dark grey**) and 340 ± 20 (**Figure 85, light grey**), respectively. No significant difference was detected between the S/N ratios of 1 mM carbachol in the different buffer systems.

Comparing the luminescence data in L15 (**Figure 83A, Figure 84, black**) with the data in **chapter 4.3**, the signaling kinetics as well as the concentration dependency are very similar for the addition of carbachol. The luminescence maxima, the  $E_{max}$  values and the pEC50 values are also in good agreement with the values found in this chapter.

In **chapter 4.4.4**, the GPCR activation of HEK M1R/mG<sub>q</sub> cells was investigated by impedance spectroscopy using L15, PBS and HBSS as measurement buffers. The results did not indicate a big influence of the buffer system on the impedance response. Contrary to the impedance data, the luminescence signal intensity is greatly influenced by the buffer system (**Figure 83A-C, Figure 84**). This has also been described in the literature for other luciferase systems (Goerke et al., **2008**, Kricka, Thorpe, **1983**, Nguyen et al., **1988**, Webster et al., **1980**). The reason why impedance is not influenced by the buffer system but luminescence is influenced must

be attributed to the fact that the buffers and their ingredients interact with the luciferase system itself but do not have a significant impact on distal signaling processes.

Characteristic features of luciferases are their pH-dependent activity and temperature sensitivity (England et al., **2016**, Markova et al., **2019**, Shimomura et al., **2001**). NanoLuc in particular exceeds other luciferases by an increased stability and luminescence at pH values  $\geq 6.5$  and temperatures up to  $60^{\circ}\text{C}$  (England et al., **2016**). However, in this experiment, those variables were kept constant. The pH value of all three buffers is set to physiological conditions (cf. **chapter 3.1.4**) and the temperature was kept at  $37^{\circ}\text{C}$ . Consequently, neither the pH value nor the temperature are the reason for changes in the luminescence in the three buffer systems.

Another explanation for the differing luminescence intensities is the varying salt composition of the different buffers. They are given in **Table 18** and were calculated from the manufacturer's data sheets (Sigma). On one hand, the folding of the ligand binding pocket of the GPCR might be impacted by varying salt concentrations. On the other hand the influence of divalent ions and sodium chloride (NaCl) on the correct folding of the luciferase and the luciferase activity is frequently researched. The optimal sodium chloride concentration, indicated by a high luciferase activity and large luminescence intensities, lies between 0.2-1 M (Markova et al., **2019**, Shimomura et al., **2001**). For higher and lower sodium chloride concentrations, a decrease in luminescence intensity is observed (Markova et al., **2019**, Shimomura et al., **2001**). The sodium chloride concentration in the buffers L15, PBS and HBSS used in this work amounts to 140 mM (**Table 18**, sigmaaldrich.com, October 2023). Since the concentration is the same in all three buffers, NaCl can not be the reason for the varying luminescence readouts in different buffers.

Sodium ions themselves are widely described as negative allosteric modulators for several class A GPCRs (Gutiérrez-de-Terán et al., **2013**, Katritch et al., **2014**, Schiffmann, Gimpl, **2018**) and also have an impact on GPCR signaling. However, the total sodium ion concentration in L15, PBS and HBSS takes values of 145 mM, 153 mM and 142 mM (**Table 18**), respectively, which are all in the same physiological range and supposedly are not responsible for the changes in luminescence intensity in different buffer systems.

Furthermore, inhibitory effects of other ions such as chloride ( $\text{Cl}^-$ ), calcium ( $\text{Ca}^{2+}$ ) and magnesium ( $\text{Mg}^{2+}$ ) on luciferases are known (Rodionova, Petushkov, **2006**). The latter is often a crucial cofactor for luciferases but this is not the case for NanoLuc (see **chapter 1.3.1**). In contrast to firefly luciferase, NanoLuc is independent of the presence of magnesium ions and adenosine triphosphate (ATP) (England et al.,

2016). In addition, the total  $\text{Cl}^-$  and  $\text{Ca}^{2+}$  concentrations are relatively constant among all three investigated buffers. An overview of the molar ion concentrations is given in **Table 18**.

Table 18. Total ion composition of L15, PBS and HBSS. All ion concentrations were calculated with the information provided by the manufacturer's data sheets (Sigma). In the last row the total ion strength  $I$  is given. It was calculated manually by consideration of the cation and anion concentrations:  $I = \frac{1}{2} \sum_{i=1}^n c_i z_i^2$  with  $c_i$  describing the ion concentration and  $z_i$  being the respective charge.

c / mM	L15	PBS	HBSS
$\text{Ca}^{2+}$	1.26	1.20	1.67
$\text{Cl}^-$	147	144	146
$\text{H}_2\text{PO}_4^-$	0.44	1.47	0.44
$\text{HCO}_3^-$	-	-	0.00417
$\text{HPO}_4^{2-}$	1.34	8.10	0.63
$\text{K}^+$	5.81	3.57	4.64
$\text{Mg}^{2+}$	1.12	1.05	0.27
$\text{Na}^+$	145	153	142
Pyruvate	5	-	-
$\text{SO}_4^{2-}$	0.13	-	0.27
<b>Ionic strength I</b>	<b>156</b>	<b>169</b>	<b>149</b>

Besides single ion concentrations, Altamash *et al.* claim that the ionic strength, representing all ions in a system, influences the luminescence of NanoLuc (Altamash *et al.*, 2021). With increased ionic strengths less intense signals are observed, which is attributed to altered interactions between substrate and luciferase. The ionic strength of L15 is 156 mM and takes a larger value than for HBSS (149 mM). However, PBS outreaches both values with an ionic strength of 169 mM. Consequently, the absolute ion concentration does not serve as an explanation for the trend in luminescence intensities.

The only explanation left in terms of the buffer composition are amino acids, sugars and vitamins. L15 is the only buffer that contains amino acids and vitamins (cf. **Table 6**). The aromatic amino acids phenylalanine, tryptophan and tyrosine absorb light at 280 nm and, hence, do not interfere with the emission at 400-500 nm of NanoLuc. But L15 also contains vitamins like riboflavin 5'-phosphate (R5P) that absorbs light with wavelengths of 380 nm and 450 nm, which overlaps with the luciferase emission (Redmond, Kochevar, 2019). Therefore, R5P could be an explanation for why luminescence intensities are decreased in comparison with PBS and HBSS: part of the emission light is reabsorbed by R5P and is emitted non-radiatively. Nonetheless, this still does not explain why the luminescence in PBS is lowered in contrast to HBSS. It is conceivable that the expression of GPCRs in high-

glucose media is more pronounced than in low-glucose media as observed for the cannabinoid 1 receptor (Mohammadi-Farani et al., **2014**). Since only HBSS contains glucose (HBSS 5.6 mM glucose  $\leftrightarrow$  L15: 5.0 mM galactose, PBS: no sugar), GPCR expression and, accordingly, luciferase intensities might be enhanced in HBSS.

Overall, significantly larger luminescence increases are observed in the order of HBSS > PBS > L15. With respect to signal intensity, HBSS is preferred. Still, similar potencies and S/N ratios are obtained in all three buffer systems. Consequently, the buffer should be chosen situation-dependently. For long-time measurements, L15 is recommended since it not only contains a carbon source (galactose) but also several nitrogen sources (amino acids) both essential for cellular growth.

### 4.6 Combination of Impedance and MiniG Protein Recruitment Assay in One Experimental Setup

According to current knowledge, the first and only setup that combines impedance spectroscopy of whole adherent cells with a luminescent technique to detect GPCR signaling was described in 2017 by Parviz *et al.* (Parviz et al., **2017**). There, the authors investigated HeLa cells, expressing the H1R, with impedance spectroscopy and fluorescence microscopy in parallel for one cell population. By addition of the endogenous ligand histamine to the cells, adherently grown on transparent indium-tin-oxide (ITO) electrodes, they were able to detect morphological changes such as actin cytoskeleton rearrangements as well as a calcium ion release from the endoplasmic reticulum (ER). This novel strategy enables a more comprehensive analysis of GPCR signaling events and their kinetics.

The aim of this thesis was to join a bioluminescence-based miniG protein recruitment assay with impedance spectroscopy in a dual setup akin to the system described by Parviz *et al.* (Parviz et al., **2017**). The idea was to measure proximal and distal events simultaneously for one cell population. Whilst miniG recruitment studies the first functional response along the GPCR signaling cascade, impedance monitors and integrates over downstream events. Taken together, this novel method might help to unravel signaling cascades more profoundly and, most recently, allows measuring two distinct kinetic GPCR responses for one single cell population. Impedance and luminescence data can be compared and correlated for each well since there are no variations in the seeding of the cells, the passage number or the phenotype of the cells, usually varying in separate experiments.

As described in **chapter 3.8.1**, a novel system, combining a 96-well plate reader for luminescence measurements with the common ECIS Z setup by Applied BioPhysics,

was developed. Therefore, 96-well electrode arrays, necessary for impedance measurements, were contacted to an impedance analyzer either manually or by a circuit board (cf. **chapter 3.8.1**). At the same time, they were measured in the Tecan Genios plate reader to detect luminescence. The setup is given in **Figure 37**. Different miniG protein systems that displayed distinct luminescence and impedance responses (cf. **chapters 4.2 and 4.3**) were investigated with the dual setup. Two  $G_q$ -coupled systems and one  $G_s$ -coupled system, namely HEK M1R/ $mG_q$ , HEK M5R/ $mG_q$  and HEK H2R/ $mG_s$  cells, were assayed.

Very briefly, the cells were seeded on 96W1E+ arrays coated with crosslinked gelatin or gelatin with a density of  $3 \cdot 10^5$  c/cm<sup>2</sup>. After a cultivation time of two days, the cells were equilibrated in L15 buffer for 2 h. Water was filled in the intermediate spaces between the wells to prevent the wells from drying out inside the preheated plate reader (37°C). After equilibration, an impedance baseline was recorded for 0.5 h inside the plate reader. The impedance measurement was not disrupted until the end of the luminescence measurement. Next, 1  $\mu$ M coelenterazine h was added and a luminescence baseline was recorded in parallel to impedance. Finally, the luminescence measurement was paused and different agonist concentrations (iperoxo, carbachol, histamine) were added to the respective cellular system. Immediately after addition, the luminescence measurement was continued. For more details see **chapter 3.8.1**.

The kinetic data and concentration-response results for HEK M1R/ $mG_q$  cells with iperoxo as ligand are found in **Figure 86A-H**, **Figure 87A-C** and **Appendix 30**. The simultaneously detected time courses of impedance and luminescence for single iperoxo concentrations are plotted in **Figure 86A-H**. Iperoxo concentrations of 0.1 nM to 10  $\mu$ M were used. L15 served as a vehicle control (CTRL). On the left y-axis (black) the change of impedance is plotted, while on the right y-axis (red) the change of luminescence is depicted, both for the same time scale (x-axis). In general, the impedance measurements already start at  $t = -1$  h (not fully shown) with a baseline recording ( $(6640 \pm 30) \Omega$ ). At  $t = -0.44$  h, 1  $\mu$ M coelenterazine h is added and a simultaneous luminescence measurement is started (manually contacted). The luminescence baseline amounts to  $(7.5 \pm 0.3)$  BLU.

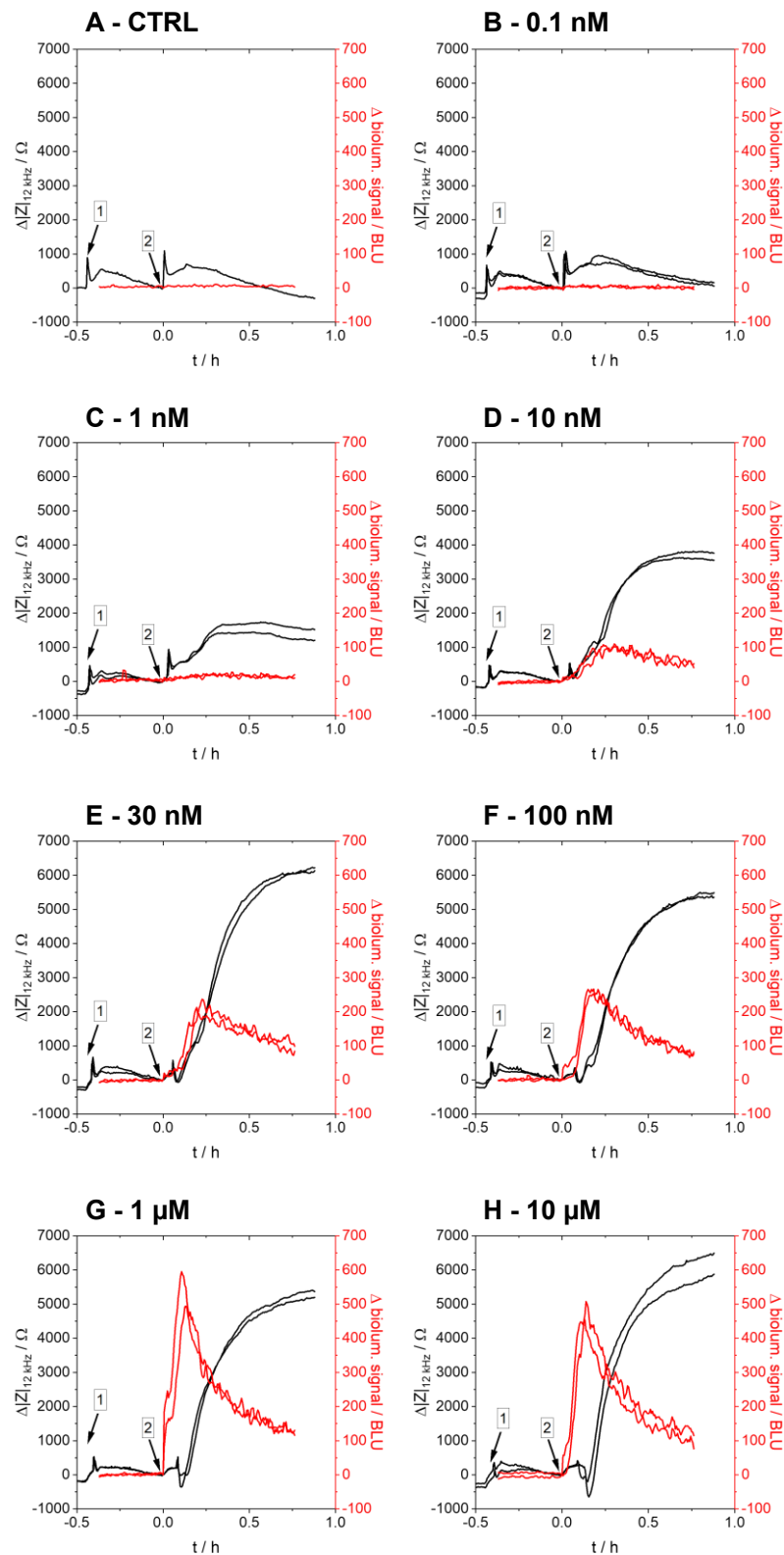


Figure 86. Correlated kinetic data for impedance (black) and luminescence (red) of **HEK M1R/mG<sub>q</sub>** cells that were seeded on transparent 96W1E+ arrays (manually contacted). The cells were preincubated with 1  $\mu\text{M}$  coelenterazine h (arrow 1) and stimulated with **iperoxo** (arrow 2). The ligand concentration increases from the CTRL (A) to 0.1 nM (B), 1 nM (C), 10 nM (D), 30 nM (E), 100 nM (F), 1  $\mu\text{M}$  (G) and 10  $\mu\text{M}$  (H).  $N = 1-2$ , single experiment. **Manually contacted**. CTRL = vehicle control. BLU = bioluminescence units. Temperature: 37°C.

After the addition of coelenterazine h, a small positive peak is discerned for impedance (400-500  $\Omega$ , **Figure 86A-H, black**). When iperoxo is added in different concentrations, impedance again exhibits a small positive peak and a transient decrease for concentrations  $\geq 30$  nM (**Figure 86E-H, black**). The decrease is most pronounced for 10  $\mu$ M iperoxo (**Figure 86H, black**) with a negative impedance change of about 700  $\Omega$ . Then, impedance slowly increases, reaches a maximum after  $t = 0.25$ - $0.5$  h and remains at a constant level over time. Only the curves for the CTRL and 0.1 nM iperoxo (**Figure 86A-B, black**) remain relatively constant. In all other cases, the impedance magnitude increases concentration-dependently. However, for concentrations above 30 nM iperoxo, no further increase of impedance is observed by increasing the ligand concentration. For the four highest iperoxo concentrations of 30 nM to 10  $\mu$ M (**Figure 86E-H, black**), maximal values around 5000-6000  $\Omega$  are noticed.

In contrast to impedance, luminescence immediately increases to reach a maximum that emerges between  $t = 0.14$ - $0.25$  h and, subsequently, decreases again for concentrations  $\geq 10$  nM (**Figure 86D-H, red**). All lower concentrations remain at the zero line (**Figure 86A-C, red**). The initial slope of luminescence rises with increasing concentrations. Moreover, the maxima for 1  $\mu$ M, 100 nM and 30 nM iperoxo (**Figure 86E-G, red**) emerge at the time points  $t = 0.14$  h,  $t = 0.20$  h and  $t = 0.25$  h, respectively. The maxima are delayed in time with decreasing ligand concentration. The absolute maximum is achieved by a concentration of 1  $\mu$ M with a value of  $(520 \pm 30)$  BLU. Overall, the luminescence signals increase with increasing iperoxo concentration. Only the curves for the 1  $\mu$ M and 10  $\mu$ M iperoxo overlay (**Figure 86G-H, red**).

While impedance already shows increased signals for smaller ligand concentrations, luminescence still rises when impedance is saturated ( $\geq 30$  nM, **Figure 86E-H, black**). Furthermore, for 1  $\mu$ M and 10  $\mu$ M iperoxo the maximum of luminescence seems to overlay with the initial decrease in impedance ( $t = 0.14$ - $0.16$  h, **Figure 86G-H**).

By evaluating the data at  $t = 0.5$  h and fitting it with a four-parametric dose-response fit (**equation 15, Appendix 30**), pEC50 and  $E_{\max}$  values were determined for luminescence and impedance. This time point was chosen for both measurement techniques to compare luminescence and impedance signals from cells in the same state. A pEC50 value of  $8.5 \pm 0.1$  for impedance and a pEC50 value of  $8.0 \pm 0.1$  for luminescence was determined for iperoxo.  $E_{\max}$  lies at  $(4900 \pm 200)$   $\Omega$  and  $(170 \pm 10)$  BLU, respectively.

Both data sets were correlated by either extracting the values at  $t = 0.5$  h, calculating the AUC between  $t = 0-0.75$  h or determining the signal maxima. The results for the impedance (y-axis) were plotted against the data for the luminescence (x-axis) as given in **Figure 87A-C**.

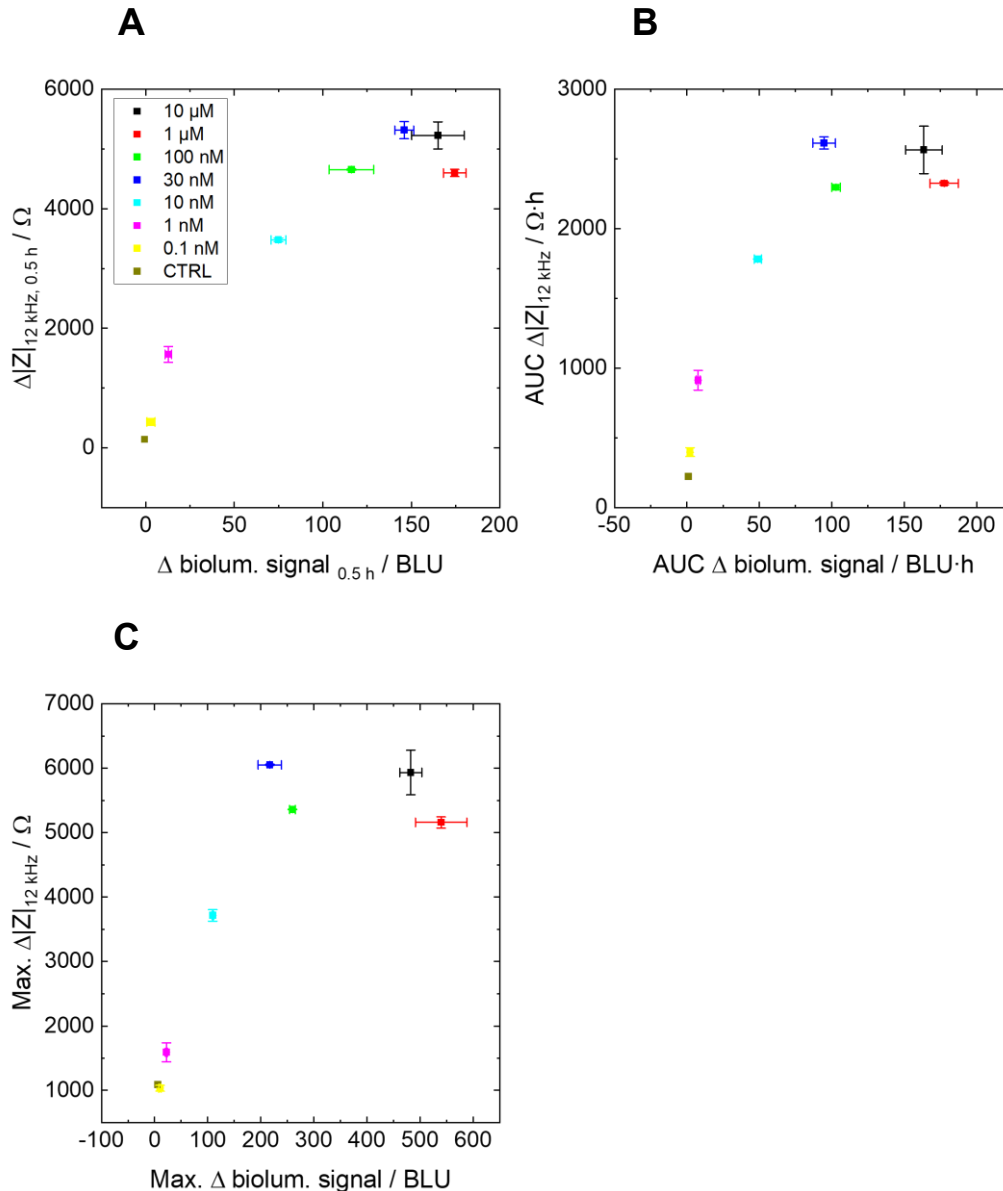


**Figure 87.** Correlation plots for **HEK M1R/mG<sub>q</sub>** cells. The cells were preincubated with **1 μM coelenterazine h** and were stimulated with different concentrations of **iperoxo**. Black **10 μM**, red **1 μM**, green **100 nM**, blue **30 nM**, cyan **10 nM**, pink **1 nM**, yellow **0.1 nM**, brown **CTRL**. (A) The change of impedance at  $t = 0.5$  h is plotted against the change of luminescence at  $t = 0.5$  h. (B) The AUC of impedance and luminescence were calculated for  $t = 0-0.75$  h. Both were plotted against each other. (C) The maxima of impedance and luminescence were determined and plotted against each other. Spearman  $r_s$  from A to C: 0.83, 0.83, 0.76. Mean  $\pm$  SE,  $N = 1-2$ , single experiment. **Manually contacted.** CTRL = vehicle control. BLU = bioluminescence units. Temperature: 37°C.

For all three data evaluation techniques (**Figure 87A-C**), similar results are obtained. The luminescence and impedance signal mostly increase with increasing iperoxo concentration. Independent of the analysis technique, the impedance values for the CTRL and 0.1 nM (**Figure 87A-C, yellow, brown**) as well as for 30 nM, 100 nM, 1  $\mu$ M and 10  $\mu$ M (**Figure 87A-C, black, red, green, blue**) are very similar. The luminescence values for the CTRL and 0.1 nM iperoxo (**Figure 87A-C, yellow, brown**) are similar as well. Furthermore, the luminescence values for 30 nM, 1  $\mu$ M and 10  $\mu$ M at  $t = 0.5$  h (**Figure 87A, black, red, blue**) and the luminescence values for 1  $\mu$ M and 10  $\mu$ M between 0-0.75 h or at the signal maximum (**Figure 87B-C, black, red**) are similar. In contrast to impedance, for concentrations of 0.1 nM and 1 nM iperoxo (**Figure 87A-C, pink, yellow**), the bioluminescence response does not change significantly by increasing the iperoxo concentration. The opposite is true for concentrations above 10 nM (**Figure 87A-C, black, red, green, blue**). Here, impedance is saturated, but luminescence still changes. To determine how well the impedance and luminescence data correlate in a monotone, non-linear fashion, Spearman  $r_s$  correlation coefficients were calculated according to **chapter 3.8.2**. The  $r_s$  values are all positive and range between 0.76 and 0.83 for the different evaluation methods.

In another experiment, impedance and luminescence data for HEK M1R/mG<sub>q</sub> cells stimulated with a different ligand, specifically carbachol, were correlated. They are found in **Figure 88A-H and Figure 89A-C**. Another depiction of the impedance and luminescence time courses and the determined pEC<sub>50</sub> and  $E_{max}$  values is found in **Appendix 31**. After an impedance baseline of  $(8270 \pm 30) \Omega$  was recorded (not shown completely), 1  $\mu$ M coelenterazine h was added at  $t = -0.42$  h and a simultaneous luminescence measurement was started (manually contacted). An average baseline value of  $(11.8 \pm 0.5)$  BLU was found. At  $t = 0$  h, different carbachol concentrations between 100 nM and 1 mM or a CTRL were added and the luminescence measurement was continued.

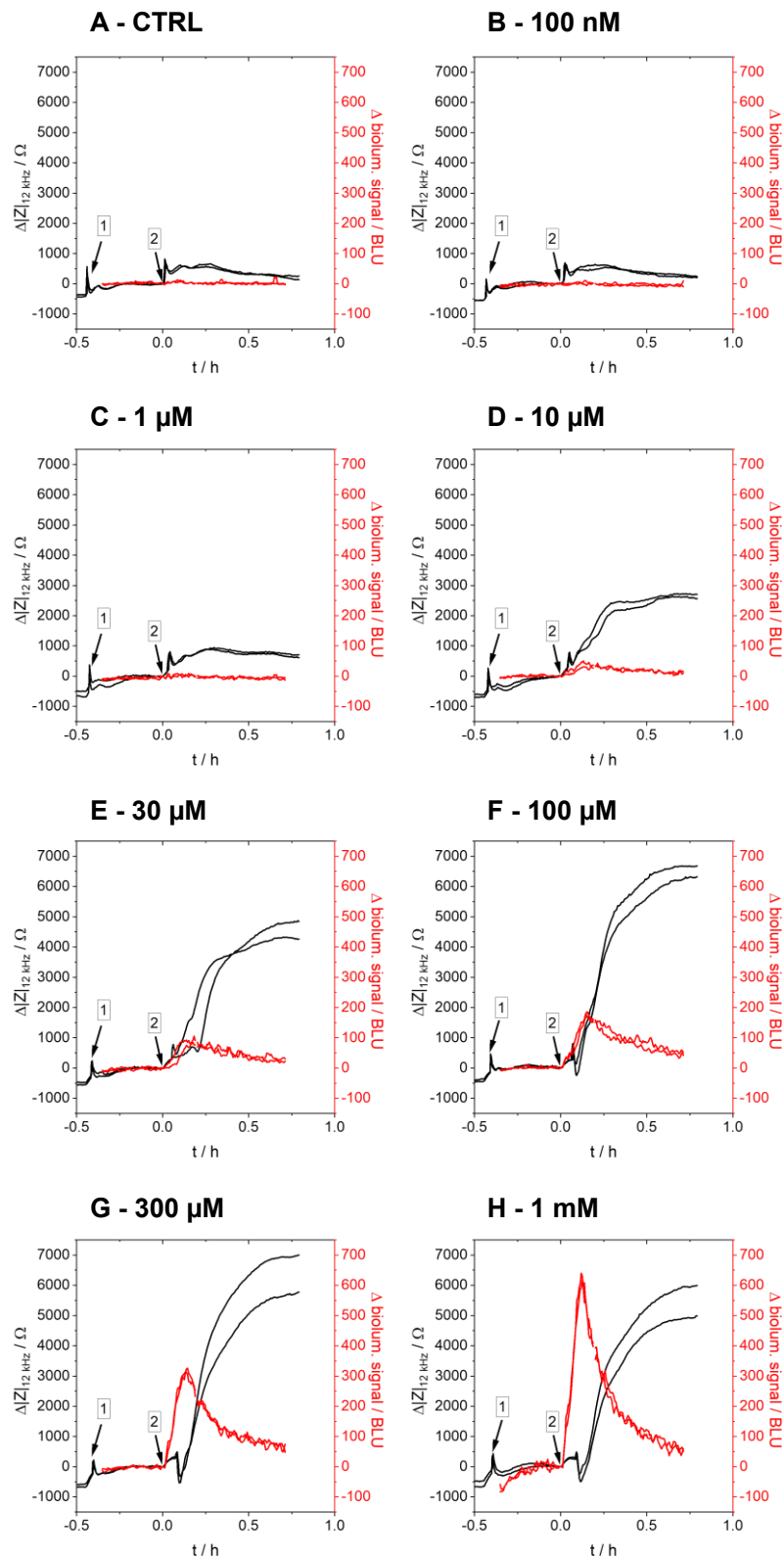


Figure 88. Correlated kinetic data for impedance (black) and luminescence (red) of **HEK M1R/mG<sub>q</sub>** cells that were seeded on transparent 96W1E+ arrays. The cells were preincubated with 1  $\mu\text{M}$  coelenterazine h (arrow 1) and stimulated with **carbachol** (arrow 2). The ligand concentration increases from the CTRL (A) to 100 nM (B), 1  $\mu\text{M}$  (C), 10  $\mu\text{M}$  (D), 30  $\mu\text{M}$  (E), 100  $\mu\text{M}$  (F), 300  $\mu\text{M}$  (G) and 1 mM (H).  $N = 2$ , single experiment. **Manually contacted**. CTRL = vehicle control. BLU = bioluminescence units. Temperature: 37°C.

In impedance, transient peaks with an amplitude of several 100  $\Omega$  are visible after coelenterazine h addition (**Figure 88A-H, black**). Then, impedance slightly increases about 500  $\Omega$  until  $t = 0$  h. After the addition of the CTRL and carbachol, again positive peaks are obtained, which are followed by a decrease in impedance of several 100  $\Omega$  for carbachol concentrations  $\geq 100$   $\mu\text{M}$  (**Figure 88F-H, black**). Then, impedance rises to a maximal value, which is generally larger with increased carbachol concentration, but saturates for concentrations  $\geq 100$   $\mu\text{M}$  (**Figure 88F-H, black**). Only for the highest carbachol concentration of 1 mM (**Figure 88H, black**), a slight decrease in impedance is observed compared to 300  $\mu\text{M}$  carbachol (**Figure 88G, black**). The greatest maximal values lie between 5500-7000  $\Omega$  for concentrations between 100  $\mu\text{M}$  and 1 mM of carbachol (**Figure 88F-H, black**). The impedance curves for the CTRL and 100 nM carbachol (**Figure 88A-B, black**) overlay and remain at a constant level of approximately 500  $\Omega$ .

For the CTRL and small carbachol concentrations up to 1  $\mu\text{M}$  (**Figure 88A-C, red**), no luminescence response is observable. If the carbachol concentration is further increased, luminescence starts to exhibit a maximum after  $t = 0.13$ - $0.15$  h that increases in intensity with larger carbachol concentrations. The absolute luminescence maximum of  $(624 \pm 6)$  BLU is found for 1 mM carbachol (**Figure 88H, red**). For the four highest carbachol concentrations (**Figure 88E-H, red**), the initial slope after compound addition is steeper, the larger the carbachol concentration is. After reaching the maximum of luminescence, it decreases gradually. The luminescence maxima for 300  $\mu\text{M}$  and 1 mM carbachol (**Figure 88G-H, red**) emerge after the same time the transient decrease of impedance after ligand addition is discernable ( $t = 0.13$  h, **Figure 88G-H, black**).

For small carbachol concentrations up to 30  $\mu\text{M}$  (**Figure 88A-E, black**), impedance already shows a distinct response contrary to luminescence. The opposite is true for concentrations  $\geq 100$   $\mu\text{M}$  carbachol, where impedance is already saturated (**Figure 88F-H, black**), while luminescence displays a concentration-wise increase of the signal (**Figure 88F-H, red**).

Both data sets were analyzed at  $t = 0.5$  h to compare the impedance and luminescence data of cells in the same state. The data points were plotted against the logarithmic ligand concentration and fitted with a four-parametric dose-response fit (**equation 15**) to yield  $\text{pEC}_{50}$  and  $E_{\text{max}}$  values (**Appendix 31**). The concentration-response curves reveal  $\text{pEC}_{50}$  values of  $4.8 \pm 0.1$  for impedance and  $4.3 \pm 0.3$  for luminescence. The efficacies amount to  $(6100 \pm 700)$   $\Omega$  and  $(110 \pm 20)$  BLU, correspondingly.

By evaluation of  $t = 0.5$  h, an integral over  $t = 0-0.75$  h (AUC) or the maxima of the impedance and luminescence data, three correlation plots were generated (**Figure 89A-C**). The outcome of impedance (y-axis) was plotted against the outcome of luminescence (x-axis), respectively.

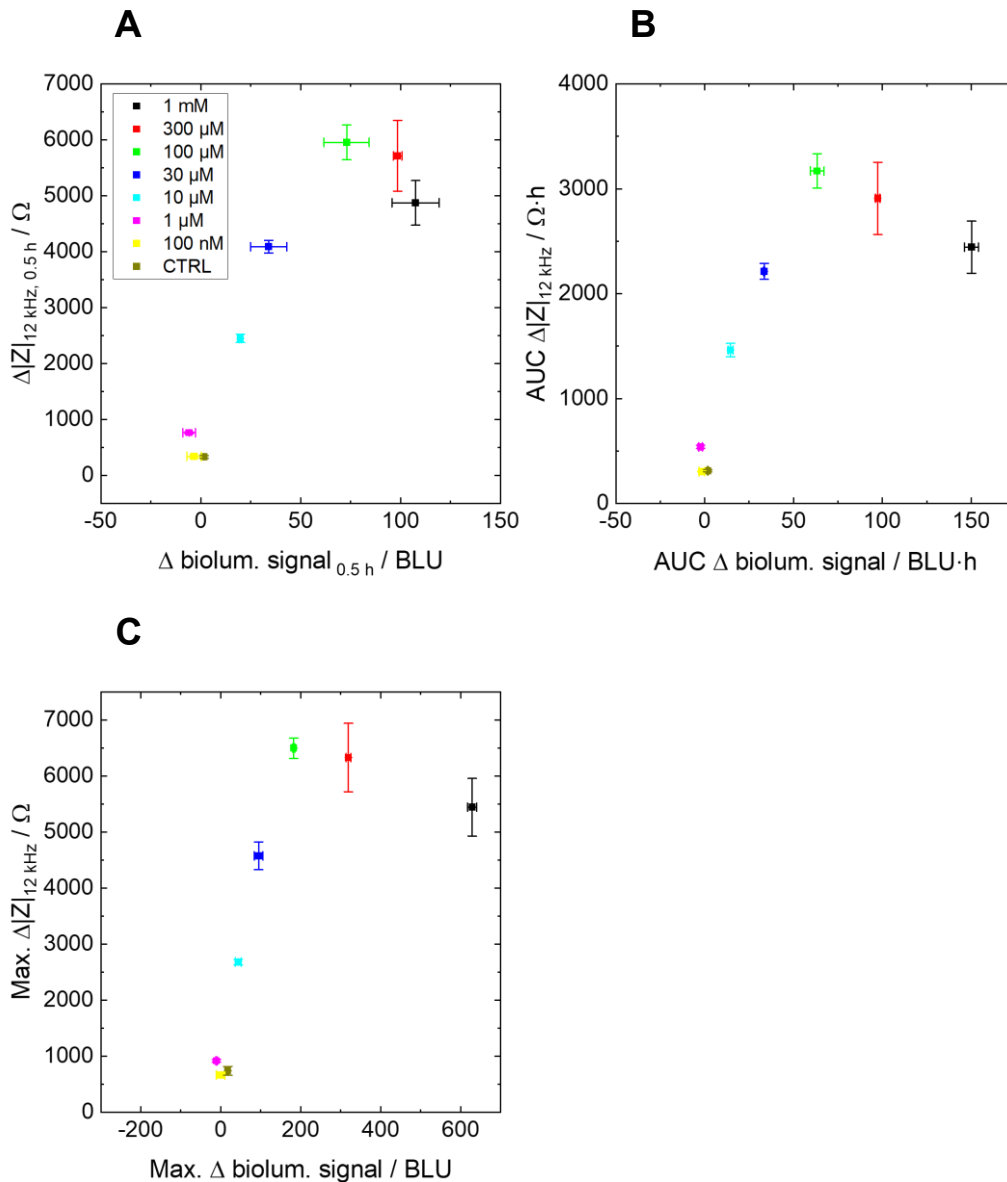


**Figure 89.** Correlation plots for **HEK M1R/mG<sub>q</sub>** cells. The cells were preincubated with  $1 \mu\text{M}$  coelenterazine h and were stimulated with different concentrations of **carbachol**. Black  $1 \text{ mM}$ , red  $300 \mu\text{M}$ , green  $100 \mu\text{M}$ , blue  $30 \mu\text{M}$ , cyan  $10 \mu\text{M}$ , pink  $1 \mu\text{M}$ , yellow  $100 \text{ nM}$ , brown CTRL. (A) The change of impedance at  $t = 0.5$  h is plotted against the change of luminescence at  $t = 0.5$  h. (B) The AUC of impedance and luminescence were calculated for  $t = 0-0.75$  h. Both were plotted against each other. (C) The maxima of impedance and luminescence were determined and plotted against each other. Spearman  $r_s$  from A to C:  $0.81$ ,  $0.83$ ,  $0.83$ . Mean  $\pm$  SE,  $N = 2$ , single experiment. **Manually contacted.** CTRL = vehicle control. BLU = bioluminescence units. Temperature:  $37^\circ\text{C}$ .

The different evaluation methods (time point, AUC, maximum) reveal graphs that show the same behavior. For small carbachol concentrations  $\leq 1 \mu\text{M}$  (**Figure 89A-C, pink, yellow, brown**), neither luminescence nor impedance change significantly. Concentrations between 10-100  $\mu\text{M}$  (**Figure 89A-C, green, blue, cyan**) feature a pronounced change in impedance. The luminescence differences are more distinct for carbachol concentrations between 1-300  $\mu\text{M}$  at  $t = 0.5 \text{ h}$  (**Figure 89A, red, green, blue, cyan, pink**) or between 1  $\mu\text{M}$  and 1 mM for the AUC analysis and evaluation of the maximum (**Figure 89B,C, black, red, green, blue, cyan, pink**). Above concentrations of 30  $\mu\text{M}$  carbachol (**Figure 89A-C, black, red, green**), impedance slightly decreases with increasing carbachol concentration but is not altered significantly. Spearman correlation coefficients of 0.81, 0.83 and 0.83 were determined, which are all greater than zero.

In addition to HEK M1R/mG<sub>q</sub> cells, another GPCR system was investigated. HEK M5R/mG<sub>q</sub> cells were seeded as described above. Following the standard experimental protocol, first an impedance baseline was recorded in L15 buffer. Then, 1  $\mu\text{M}$  coelenterazine h was added and a luminescence baseline was measured (manually contacted). Finally, at  $t = 0 \text{ h}$ , a CTRL or iperoxo in different concentrations (between 0.1 nM and 1  $\mu\text{M}$ ) were added and both signals were traced in real-time. Another depiction of the impedance and luminescence data and the respective concentration-response curves is found in **Appendix 32**. Below the simultaneously measured kinetic data (**Figure 90A-H**) and the correlation plots (**Figure 91A-C**) are depicted. An impedance baseline of  $(7320 \pm 30) \Omega$  was recorded. The average luminescence baseline takes a value of  $(5.9 \pm 0.2) \text{ BLU}$ .

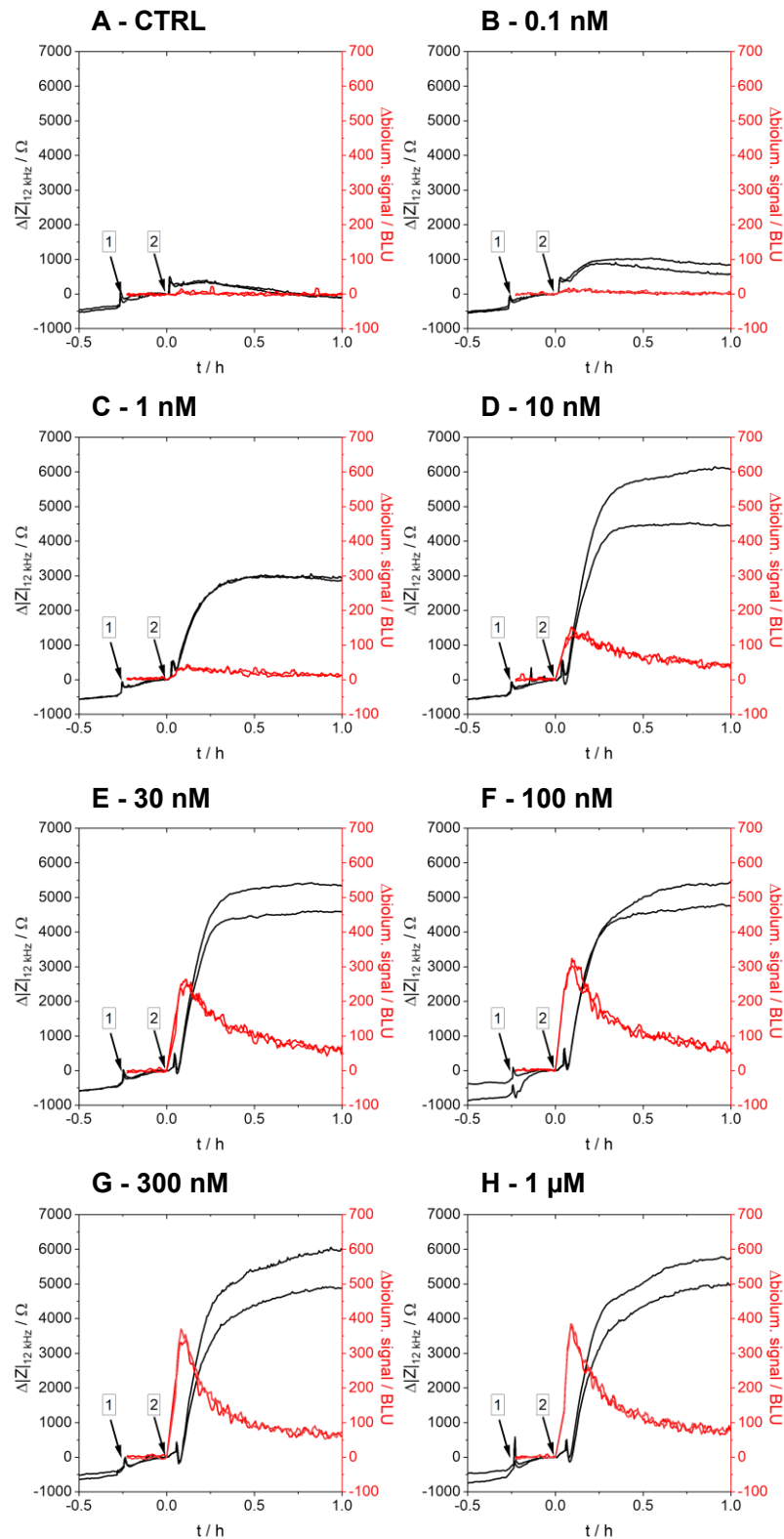


Figure 90. Correlated kinetic data for impedance (black) and luminescence (red) of **HEK M5R/mG<sub>q</sub>** cells that were seeded on transparent 96W1E+ arrays. The cells were preincubated with 1  $\mu\text{M}$  coelenterazine h (arrow 1) and stimulated with **iperoxo** (arrow 2). The ligand concentration increases from the CTRL (A) to 0.1 nM (B), 1 nM (C), 10 nM (D), 30 nM (E), 100 nM (F), 300 nM (G) and 1  $\mu\text{M}$  (H). *N* = 2, single experiment. **Manually contacted**. CTRL = vehicle control. BLU = bioluminescence units. Temperature: 37°C.

A several 100  $\Omega$  increase in impedance is observed after the addition of coelenterazine h and iperoxo, respectively (**Figure 90A-H, black**). Furthermore, impedance shows an initial decrease after the addition of iperoxo concentrations of  $\geq 10$  nM (**Figure 90D-H, black**). Thereafter, impedance rises and reaches a stable plateau after  $t = 0.25-0.5$  h. Only the curves for the CTRL remain at a constant level over time (**Figure 90A, black**). The impedance maxima rise concentration-dependent, but for iperoxo concentrations  $\geq 10$  nM (**Figure 90D-H, black**), impedance is saturated and does not increase further with larger ligand concentration. The maximal impedance values amount to 5000-6000  $\Omega$ .

After compound addition, luminescence increases, reaches a maximum after  $t = 0.08-0.10$  h and drops off again. Below an iperoxo concentration of 10 nM, luminescence fluctuates around zero over the measurement period (**Figure 90A-C, red**). A first distinct luminescence change is observed for a concentration of 10 nM (**Figure 90D, red**). By further increasing the iperoxo concentration, larger luminescence signals are observed. The three highest iperoxo concentrations (100 nM, 300 nM and 1  $\mu$ M) display similar luminescence time courses with maxima between 300-400 BLU (**Figure 90F-H, red**).

By concentration-response analysis of  $t = 0.5$  h according to **chapters 3.5.4 and 3.6.2.1**, potencies of  $9.19 \pm 0.02$  for impedance and  $8.06 \pm 0.10$  for luminescence were determined (**Appendix 32**). The corresponding efficacies are  $(4900 \pm 100) \Omega$  and  $(120 \pm 5)$  BLU. The consideration of the same time point enables a true comparison between impedance and luminescence data since cells in the same stage are investigated.

Data at time point  $t = 0.5$  h, the AUC between  $t = 0-0.75$  h and the maxima of impedance and luminescence were evaluated to find possible correlations between both parameters. The simultaneously measured data was plotted against each other with a color code referring to the iperoxo concentration. The results are given in **Figure 91A-C**.

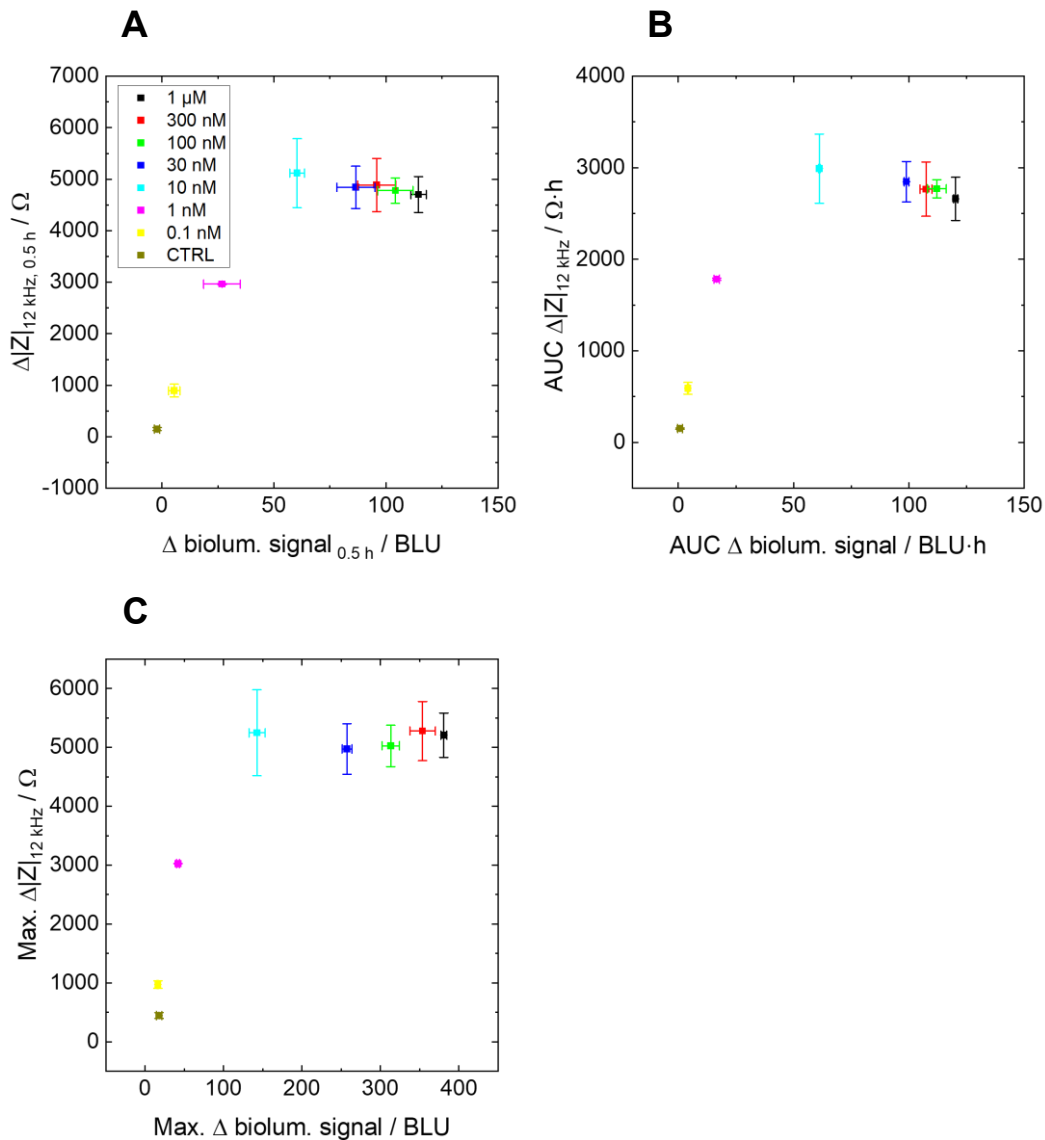


Figure 91. Correlation plots for **HEK M5R/mG<sub>q</sub>** cells. The cells were preincubated with 1  $\mu\text{M}$  coelenterazine *h* and were stimulated with different concentrations of **iperexo**. Black 1  $\mu\text{M}$ , red 300 nM, green 100 nM, blue 30 nM, cyan 10 nM, pink 1 nM, yellow 0.1 nM, brown CTRL. (A) The change of impedance at  $t = 0.5 \text{ h}$  is plotted against the change of luminescence at  $t = 0.5 \text{ h}$ . (B) The AUC of impedance and luminescence were calculated for  $t = 0-0.75 \text{ h}$ . Both were plotted against each other. (C) The maxima of impedance and luminescence were determined and plotted against each other. Spearman  $r_s$  from A to C: 0.55, 0.55, 0.79. Mean  $\pm$  SE,  $N = 2$ , single experiment. **Manually contacted.** CTRL = vehicle control. BLU = bioluminescence units. Temperature: 37°C.

The three data evaluation methods (time point, AUC, maximum) display graphs with similar behavior. Small iperexo concentrations  $\leq 1 \text{ nM}$  (**Figure 91A-C, pink, yellow, brown**) rather have an influence on impedance than on luminescence. With larger iperexo concentrations, the impedance signals increase more drastically than the luminescence. By further increasing the concentration to 10 nM (**Figure 91A-C, cyan**), impedance and luminescence increase. Beyond a concentration of 30 nM (**Figure 91A-C, black, red, green, blue**), the impedance is constant and small

changes in luminescence are observable. Spearman correlation coefficients of 0.55, 0.55 and 0.79 were determined and all target values  $> 0$ . However, they are not as close to unity as the  $r_s$  values determined for HEK M1R/mG<sub>q</sub> cells.

To determine the flexibility and versatility of the dual luminescence-impedance setup, HEK M5R/mG<sub>q</sub> cells were also tested with carbachol as a ligand. Initially, an impedance baseline was recorded ( $6420 \pm 30 \Omega$ ). At  $t = -0.35$  h,  $1 \mu\text{M}$  coelenterazine h was added and a luminescence measurement was started in parallel (baseline:  $5.7 \pm 0.2$  BLU, circuit board contacting). After stimulation with different carbachol concentrations (between 10 nM and 100  $\mu\text{M}$ ) or the addition of a CTRL at  $t = 0$  h, both measurements were monitored for 1 h. The kinetic data is depicted in **Figure 92A-H** for each concentration. An overview of the pooled impedance and luminescence data and the corresponding concentration-response analysis is found in **Appendix 33**.

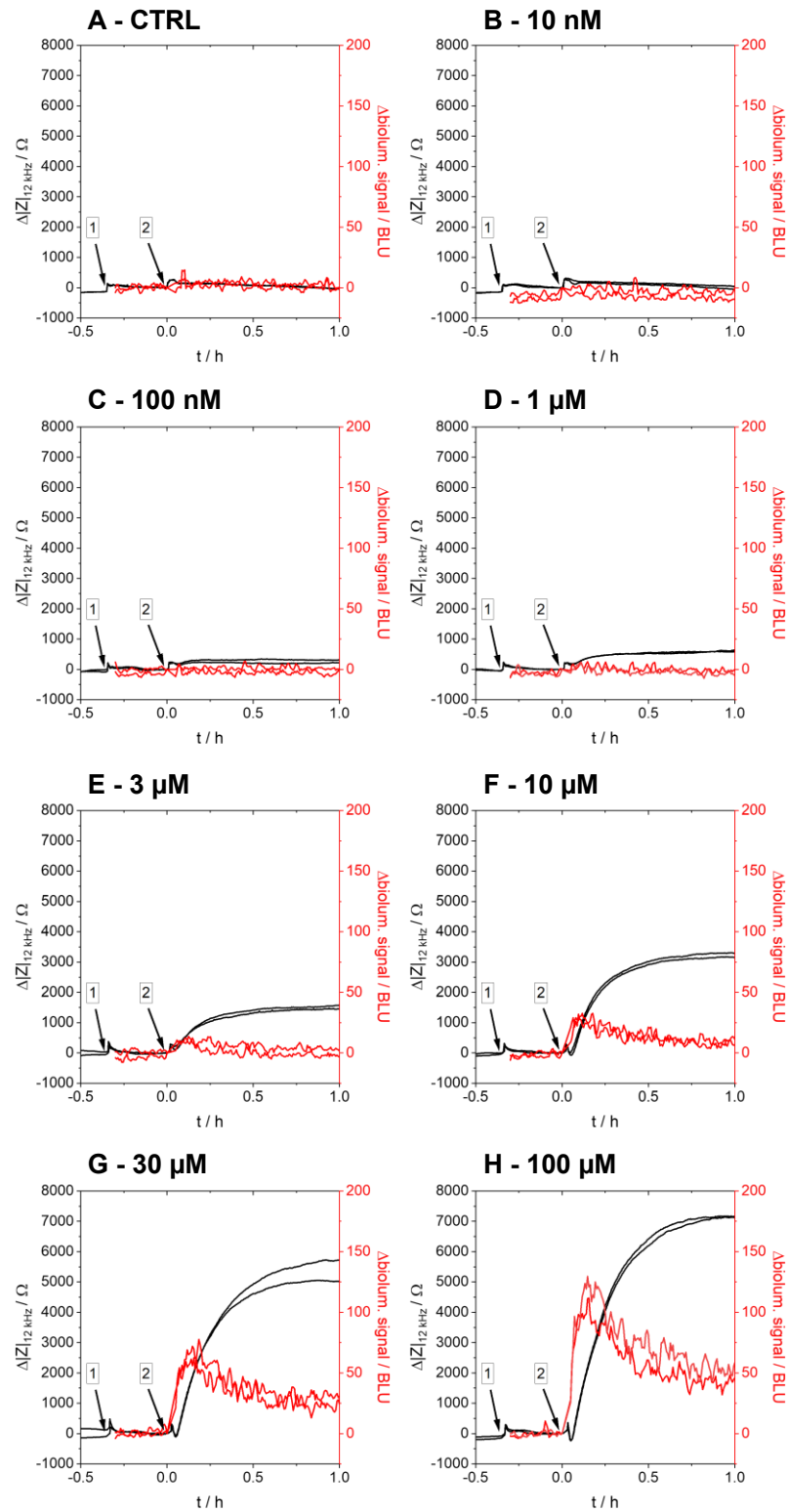


Figure 92. Correlated kinetic data for impedance (black) and luminescence (red) of **HEK M5R/mG<sub>q</sub>** cells that were seeded on 96W1E+ arrays. The cells were preincubated with 1  $\mu\text{M}$  coelenterazine h (arrow 1) and stimulated with **carbachol** (arrow 2). The ligand concentration increases from the CTRL (A) to 10 nM (B), 100 nM (C), 1  $\mu\text{M}$  (D), 3  $\mu\text{M}$  (E), 10  $\mu\text{M}$  (F), 30  $\mu\text{M}$  (G) and 100  $\mu\text{M}$  (H).  $N = 2$ , single experiment. **Circuit board contacting**. CTRL = vehicle control. BLU = bioluminescence units. Temperature: 37°C.

For impedance and luminescence, the typical time courses are observed (cf. **chapters 4.2 and 4.3**). After coelenterazine h and ligand addition, small peaks in impedance are detected (**Figure 92A-H, black**). For concentrations  $\geq 10 \mu\text{M}$  (**Figure 92F-H, black**), a transient impedance decrease becomes visible when carbachol is added. Thereafter, impedance increases concentration-dependently and reaches a maximum at around  $t = 0.5 \text{ h}$ , which is retained until the end of the measurement. Impedance increases with higher concentration but only shows significant signals for concentrations  $\geq 1 \mu\text{M}$  (**Figure 92D-H, black**). The impedance curves for the CTRL, 10 nM and 100 nM carbachol, remain at a constant and very low level of 100-300  $\Omega$  throughout the measurement. Maximal values are found for 100  $\mu\text{M}$  carbachol (**Figure 92H, black**) with values around 7100  $\Omega$ .

For concentrations  $< 10 \mu\text{M}$ , no change in luminescence is visible and luminescence remains at the baseline level (**Figure 92A-E, red**). A first distinct luminescence signal is perceived for 10  $\mu\text{M}$  carbachol (**Figure 92F, red**). Above this concentration, luminescence rises to a maximum at  $t = 0.13 \text{ h}$  and rapidly declines afterward. The signal maximum increases up to carbachol concentrations of 100  $\mu\text{M}$  (**Figure 92F-H, red**). The absolute maximum is found for a concentration of 100  $\mu\text{M}$  at  $(121 \pm 9) \text{ BLU}$  (**Figure 92H, red**).

While the impedance signal already rises for the carbachol concentrations 1  $\mu\text{M}$  and 3  $\mu\text{M}$  (**Figure 92D-E, black**), the luminescence values of these concentrations remain at the baseline level (**Figure 92D-E, red**). For larger carbachol concentrations, both signals increase.

Potencies and efficacies were determined by concentration-response analysis after  $t = 0.5 \text{ h}$  (cf. **chapters 3.5.4 and 3.6.2.1**). The data points were plotted against the logarithmic carbachol concentration and were fitted with a four-parametric dose-response fit (**equation 15**). For impedance,  $\text{pEC}_{50}$  and  $E_{\text{max}}$  values of  $4.83 \pm 0.05$  and  $(7200 \pm 300) \Omega$  were calculated, while luminescence yielded a  $\text{pEC}_{50}$  value of  $4.6 \pm 0.2$  and an  $E_{\text{max}}$  value of  $(70 \pm 20) \text{ BLU}$  (**Appendix 33**).

Three types of luminescence and impedance data were extracted from the time courses: the time point data at  $t = 0.5 \text{ h}$ , the AUC between 0-0.75 h and the maximal data. Correlation graphs were generated as given in **Figure 93A-C** by plotting the impedance results against the luminescence data.

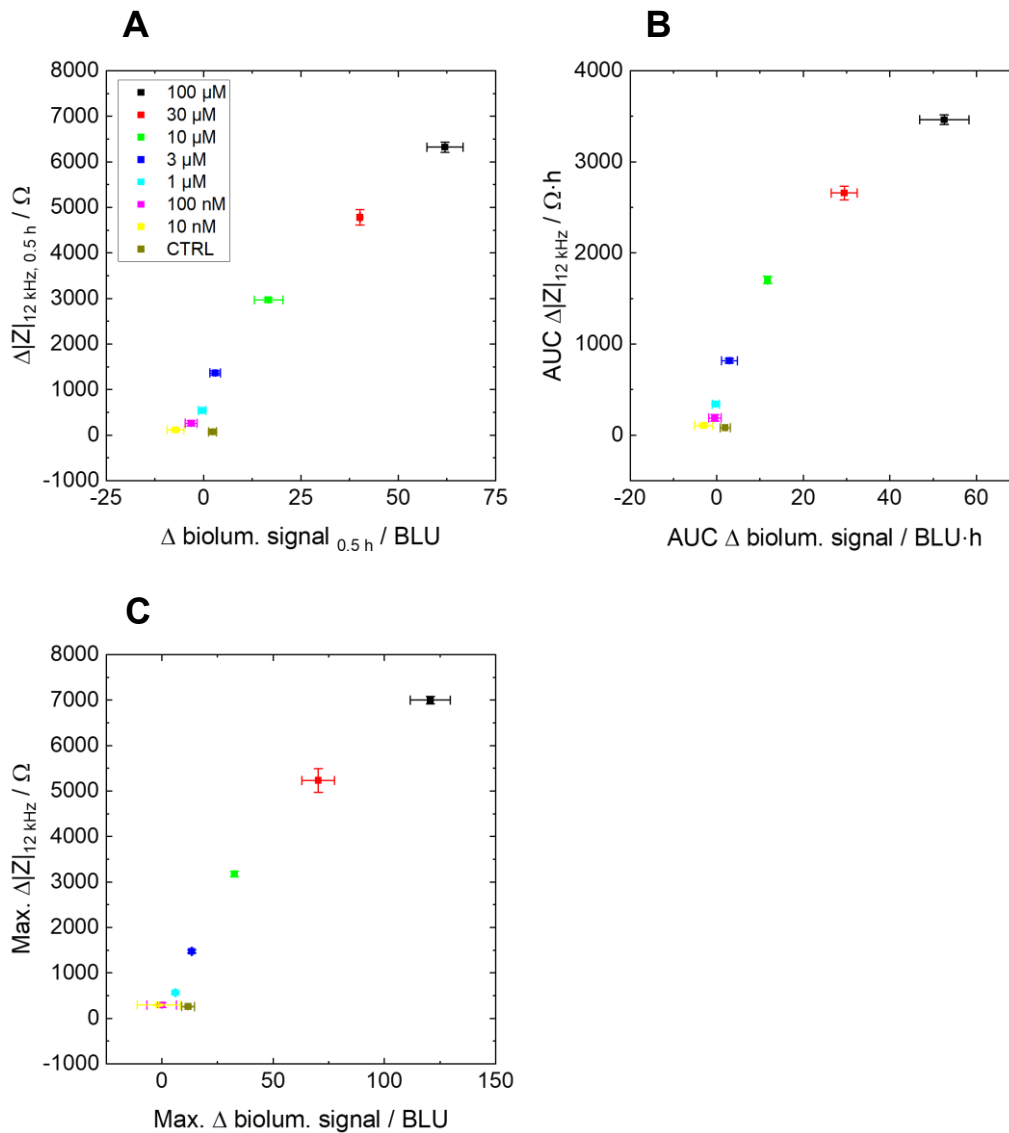


Figure 93. Correlation plots for **HEK M5R/mG<sub>q</sub>** cells. The cells were preincubated with 1  $\mu\text{M}$  coelenterazine *h* and were stimulated with different concentrations of **carbachol**. Black 100  $\mu\text{M}$ , red 30  $\mu\text{M}$ , green 10  $\mu\text{M}$ , blue 3  $\mu\text{M}$ , cyan 1  $\mu\text{M}$ , pink 100 nM, yellow 10 nM, brown CTRL. (A) The change of impedance at  $t = 0.5\text{ h}$  is plotted against the change of luminescence at  $t = 0.5\text{ h}$ . (B) The AUC of impedance and luminescence were calculated for  $t = 0-0.75\text{ h}$ . Both were plotted against each other. (C) The maxima of impedance and luminescence were determined and plotted against each other. Spearman  $r_s$  from A to C: 0.86, 0.86, 0.83. Mean  $\pm$  SE,  $N = 2$ , single experiment. **Circuit board contacting**. CTRL = vehicle control. BLU = bioluminescence units. Temperature: 37°C.

Independent of the data evaluation type, the graphs show the same behavior (Figure 93A-C). For small ligand concentrations  $\leq 1\ \mu\text{M}$  (Figure 93A-C, cyan, pink, yellow, brown), neither luminescence nor impedance changes markedly. The data overlays and no significant difference is observed. At a concentration of 3  $\mu\text{M}$  carbachol (Figure 93A-C, blue), luminescence is still low but impedance is increased compared to smaller concentrations. If the compound concentration is even further increased, both impedance and luminescence show a more pronounced increase and

rise steadily up to a concentration of 100  $\mu\text{M}$  (**Figure 93A-C, black, red, green**). Spearman correlation coefficients were determined. They range between 0.83-0.86 and are all positive.

Ultimately, HEK H2R/mG<sub>s</sub> cells, which favor a completely different coupling pathway than HEK M1R/mG<sub>q</sub> and HEK M5R/mG<sub>q</sub> cells, were investigated. After an impedance baseline was recorded ( $(5240 \pm 30) \Omega$ ), at  $t = -0.19$  h, 1  $\mu\text{M}$  coelenterazine h was added as luciferase substrate and a luminescence baseline was measured simultaneously ( $(279 \pm 5)$  BLU, circuit board contacting). At  $t = 0$  h, a CTRL and different histamine solutions (between 10 nM and 100  $\mu\text{M}$ ) were added and both measurements were continued until  $t = 1$  h. Below the time traces of luminescence and impedance are plotted in one graph for each histamine concentration (**Figure 94A-H**). The correlated data sets are found in **Figure 95A-C**. Another depiction of the impedance and luminescence time courses and the determined pEC<sub>50</sub> and E<sub>max</sub> values is found in **Appendix 34**.

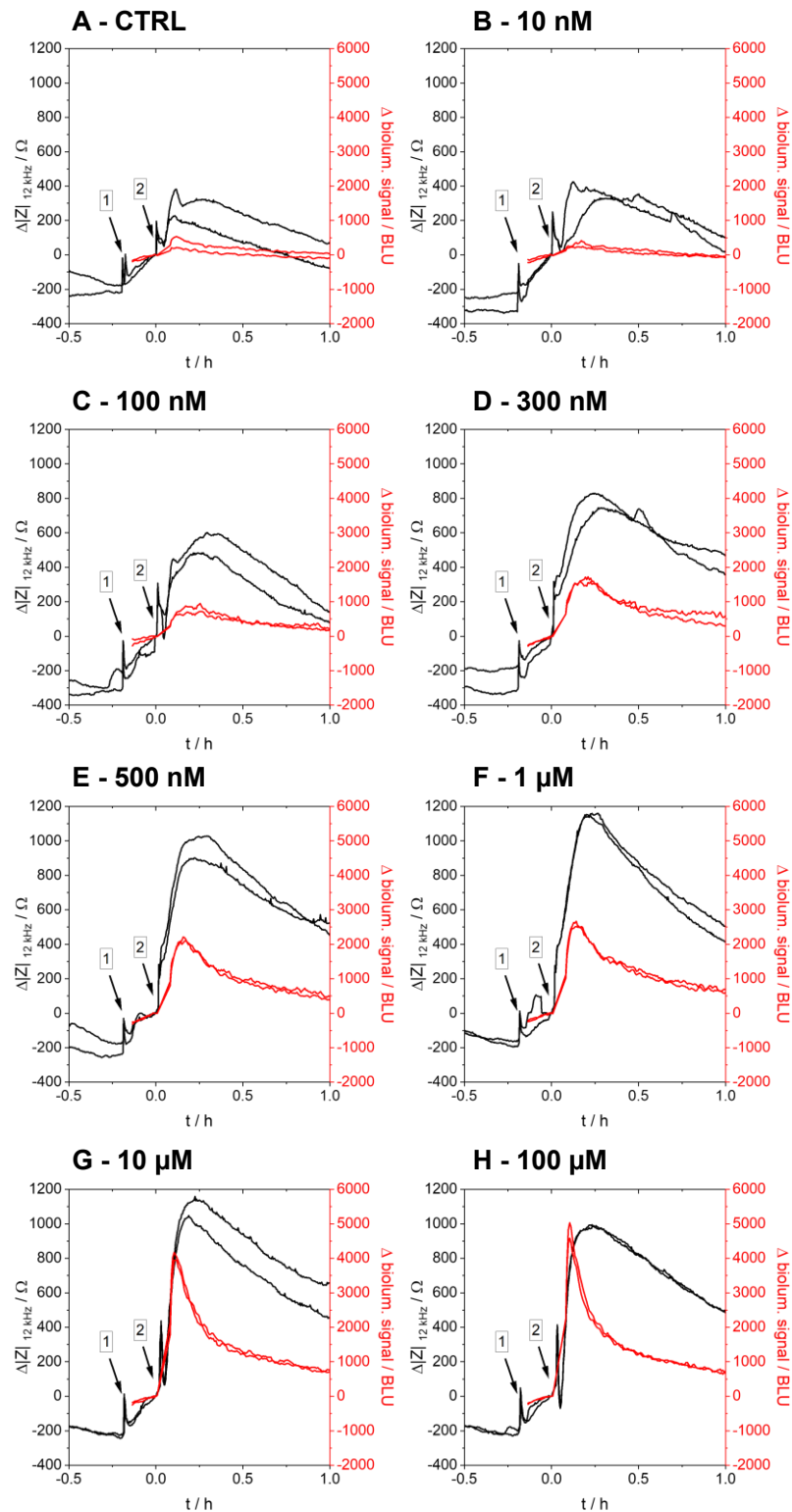


Figure 94. Correlated kinetic data for impedance (black) and luminescence (red) of **HEK H2R/mGs** cells that were seeded on transparent 96W1E+ arrays. The cells were preincubated with 1  $\mu\text{M}$  coelenterazine h (arrow 1) and stimulated with **histamine** (arrow 2). The ligand concentration increases from the CTRL (A) to 10 nM (B), 100 nM (C), 300 nM (D), 500 nM (E), 1  $\mu\text{M}$  (F), 10  $\mu\text{M}$  (G) and 100  $\mu\text{M}$  (H). *N* = 2, single experiment. **Circuit board contacting**. CTRL = vehicle control. BLU = bioluminescence units. Temperature: 37°C.

After substrate and ligand addition, transient peaks caused by liquid handling of up to 400  $\Omega$  are obtained in impedance (**Figure 94A-H, black**). For histamine concentrations of 10  $\mu\text{M}$  and 100  $\mu\text{M}$  (**Figure 94G-H, black**), a rapid decrease of impedance becomes visible after histamine addition. Subsequently, impedance slowly increases with the agonist concentration to reach a maximum at  $t = 0.25$  h and then gradually declines over the measurement period. The curve for 10 nM histamine is similar to the curve of the CTRL (**Figure 94A-B, black**): impedance increases about 200-400  $\Omega$  after compound addition and slowly declines until  $t = 1$  h. For larger histamine concentrations, enhanced impedance signals are observed (**Figure 94C-H, black**). However,  $\geq 500$  nM histamine (**Figure 94E-H, black**), the impedance signal saturates. Only for the highest histamine concentration of 100  $\mu\text{M}$  (**Figure 94H, black**) impedance slightly decreases in comparison to 10  $\mu\text{M}$  of histamine. An absolute maximum is found for 1  $\mu\text{M}$  histamine at  $(1151 \pm 6)$   $\Omega$  after  $t = 0.22$  h (**Figure 94F, black**).

Luminescence remains at the zero line for the CTRL and a histamine concentration of 10 nM (**Figure 94A-B, red**). A first luminescence response is recognized for 100 nM histamine (**Figure 94C, red**): when histamine is added, luminescence rises to a maximum after approximately  $t = 0.25$  h and gradually drops down again. With increased histamine concentrations, the maximum of luminescence increases (**Figure 94C-H, red**). While the signal maximum between concentrations of 100 nM and 1  $\mu\text{M}$  histamine (**Figure 94C-F, red**) is quite broad, for larger concentrations (**Figure 94G-H, red**) it becomes very sharp and peaks at  $t = 0.11$  h. An absolute maximum of luminescence is reached by 100  $\mu\text{M}$  histamine with a value of  $(4800 \pm 200)$  BLU (**Figure 94H, red**).

Potency and efficacy values were identified after concentration-response analysis of time point  $t = 0.5$  h (cf. **chapters 3.5.4 and 3.6.2.1**). For impedance, a pEC<sub>50</sub> value of  $6.7 \pm 0.2$  and for luminescence a value of  $6.69 \pm 0.05$  was determined. The corresponding  $E_{\text{max}}$  values amount to  $(823 \pm 7)$   $\Omega$  and  $(1243 \pm 9)$  BLU.

Both parameters, impedance and bioluminescence, were analyzed regarding the values at  $t = 0.5$  h, the AUC between  $t = 0-0.75$  h and their maxima. Correlation plots were generated by plotting the impedance outcome against the luminescence values, which are depicted in **Figure 95A-C**.

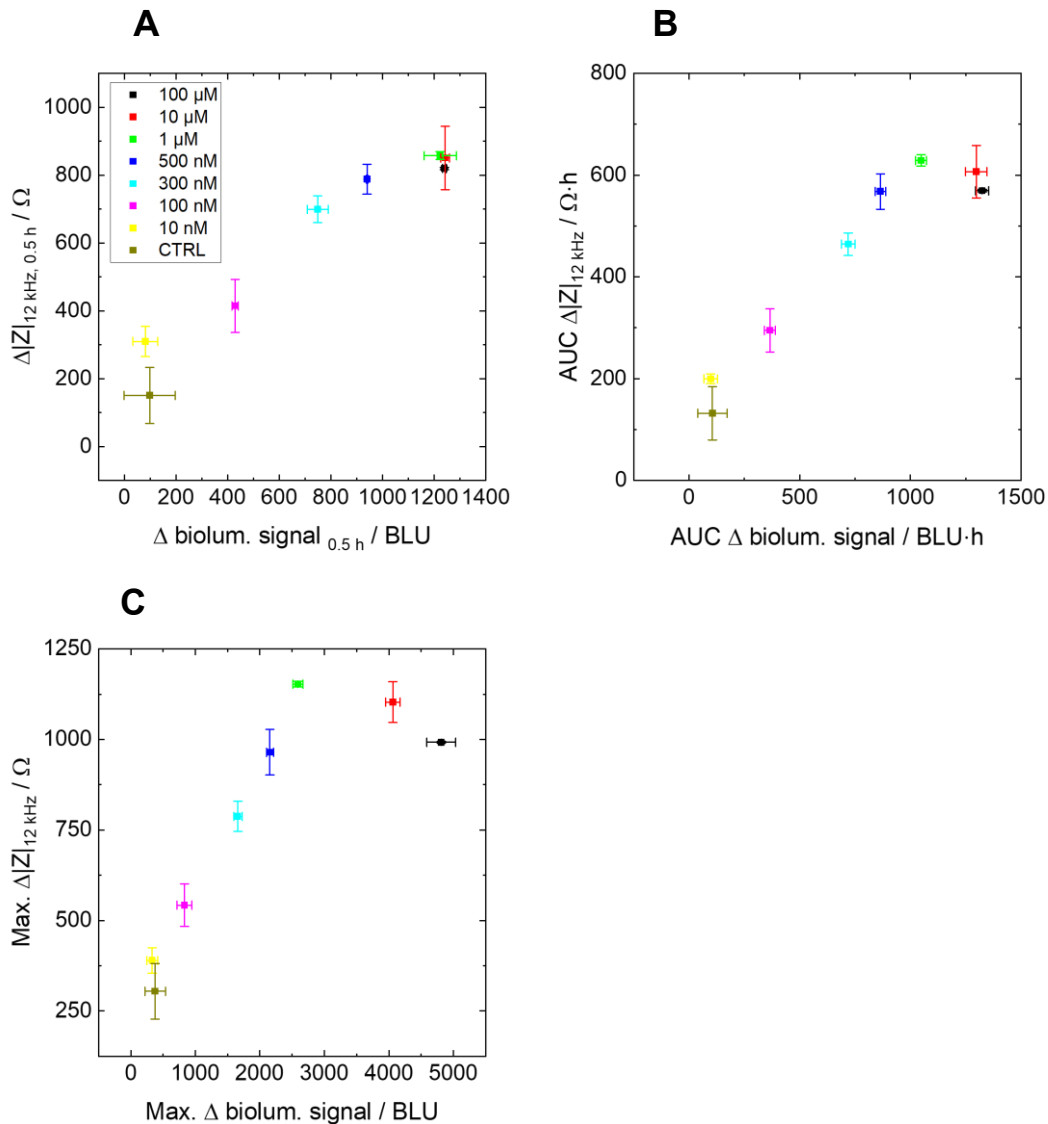


Figure 95. Correlation plots for **HEK H2R/mGs** cells. The cells were preincubated with 1  $\mu\text{M}$  coelenterazine *h* and were stimulated with different concentrations of **histamine**. Black 100  $\mu\text{M}$ , red 10  $\mu\text{M}$ , green 1  $\mu\text{M}$ , blue 500 nM, cyan 300 nM, pink 100 nM, yellow 10 nM, brown CTRL. (A) The change of impedance at  $t = 0.5 \text{ h}$  is plotted against the change of luminescence at  $t = 0.5 \text{ h}$ . (B) The AUC of impedance and luminescence were calculated for  $t = 0-0.75 \text{ h}$ . Both were plotted against each other. (C) The maxima of impedance and luminescence were determined and plotted against each other. Spearman  $r_s$  from A to C: 0.90, 0.88, 0.88. Mean  $\pm$  SE,  $N = 2$ , single experiment. **Circuit board contacting**. CTRL = vehicle control. BLU = bioluminescence units. Temperature: 37°C.

The three correlation plots all depict a similar behavior between impedance and luminescence (**Figure 95A-C**): with increasing histamine concentration, both signals increase. However, for 10 nM histamine and the CTRL, luminescence behaves similarly (**Figure 95A-C, yellow, brown**). Additionally, for concentrations between 1-100  $\mu\text{M}$  histamine, the impedance values either can not be distinguished (**Figure 95A, black, red, green**) or saturate (**Figure 95B-C, black, red, green**). The luminescence after  $t = 0.5 \text{ h}$  for histamine concentrations between 1-100  $\mu\text{M}$

(**Figure 95A, black, red, green**) and the AUC of luminescence between 0-0.75 h for 10-100  $\mu\text{M}$  histamine (**Figure 95B, black, red**) are not distinguishable. In contrast, the maximal luminescence is able to discriminate between histamine concentrations of 1-100  $\mu\text{M}$  (**Figure 95C, black, red green**). Spearman coefficients were calculated to quantify the correlation between impedance and luminescence. They amount to 0.90, 0.88 and 0.88 for the evaluation of the time point  $t = 0.5$  h, the AUC between 0-0.75 h and the signal maxima, respectively.

In the following tables (**Table 19 and Table 20**), all potencies, efficacies, baseline values and maxima for the three systems (HEK M1R/mG<sub>q</sub>, HEK M5R/mG<sub>q</sub>, HEK H2R/mG<sub>s</sub>) and different compounds (iperoxo, carbachol, histamine) are listed and contrasted with the values determined in single impedance or luminescence measurements (cf. **chapters 4.2 and 4.3**).

*Table 19. Comparison of potencies ( $pEC_{50}$ ) and efficacies ( $E_{max}$ ) for HEK M1R/mG<sub>q</sub>, HEK M5R/mG<sub>q</sub> and HEK H2R/mG<sub>s</sub> cells determined in single impedance and luminescence experiments (**chapters 4.2 and 4.3**) or with the dual setup (this chapter). Iperoxo, carbachol and histamine were used as agonists. The values were determined after analysis of the data at  $t = 0.5$  h by a four-parametric dose-response fit (**equation 15**).  $Z$  = impedance,  $BL$  = bioluminescence,  $BLU$  = bioluminescence units. Errors from data fitting. \* =  $E_{max}$  was fixed to value of 30  $\mu\text{M}$  carbachol.*

		$pEC_{50}$		$pEC_{50}$		$E_{max}$		$E_{max}$	
		Single		Dual		Single		Dual	
		$Z$	$BL$	$Z$	$BL$	$Z / \Omega$	$BL / BLU$	$Z / \Omega$	$BL / BLU$
<b>M1R</b>	Iperoxo	8.39 $\pm$ 0.06	8.14 $\pm$ 0.06	8.5 $\pm$ 0.1	8.0 $\pm$ 0.1	5400 $\pm$ 100	2300 $\pm$ 100	4900 $\pm$ 200	170 $\pm$ 10
	Carbachol	5.55 $\pm$ 0.06	4.4 $\pm$ 0.3	4.8 $\pm$ 0.1	4.3 $\pm$ 0.3	5340 $\pm$ 90	1400 $\pm$ 300	6100 $\pm$ 700	110 $\pm$ 20
<b>M5R</b>	Iperoxo	9.0 $\pm$ 0.2	8.3 $\pm$ 0.1	9.19 $\pm$ 0.02	8.06 $\pm$ 0.10	6000 $\pm$ 100	360 $\pm$ 20	4900 $\pm$ 100	120 $\pm$ 5
	Carbachol	5.46 $\pm$ 0.04	4.8 $\pm$ 0.3	4.83 $\pm$ 0.05	4.6 $\pm$ 0.2	6300 $\pm$ 100	90 $\pm$ 10*	7200 $\pm$ 300	70 $\pm$ 20
<b>H2R</b>	Histamine	6.3 $\pm$ 0.2	7.4 $\pm$ 0.2	6.7 $\pm$ 0.2	6.69 $\pm$ 0.05	1400 $\pm$ 100	4100 $\pm$ 400	823 $\pm$ 7	1243 $\pm$ 9

## 4 Simultaneous Measurement of Luminescence and Impedance

Table 20. Comparison of baseline and maximal values for HEK M1R/mG<sub>q</sub>, HEK M5R/mG<sub>q</sub> and HEK H2R/mG<sub>s</sub> cells determined in single impedance and luminescence experiments (chapters 4.2 and 4.3) or with the dual setup (this chapter). Iperoxo, carbachol and histamine were used as agonists. The absolute maxima were determined for the same ligand concentrations, respectively. Z = impedance, BL = bioluminescence, BLU = bioluminescence units. a = 10 μM iperoxo, b = 1 μM iperoxo, c = 100 nM iperoxo, d = 1 mM carbachol, e = 100 μM carbachol, f = 10 μM histamine. Mean ± SE.

		Baseline		Baseline		Maximum		Maximum	
		Single		Dual		Single		Dual	
		Z / Ω	BL / BLU	Z / Ω	BL / BLU	Z / Ω	BL / BLU	Z / Ω	BL / BLU
<b>M1R</b>	Iperoxo	5540 ± 40	22.6 ± 0.5	6640 ± 30	7.5 ± 0.3	5600 ± 200 <sup>b</sup>	3900 ± 100 <sup>a</sup>	5300 ± 100 <sup>b</sup>	470 ± 40 <sup>a</sup>
	Carbachol	5530 ± 40	22.6 ± 0.6	8270 ± 30	11.8 ± 0.5	5600 ± 200 <sup>d</sup>	2700 ± 200 <sup>d</sup>	5500 ± 500 <sup>d</sup>	624 ± 6 <sup>d</sup>
<b>M5R</b>	Iperoxo	5350 ± 10	17.9 ± 0.4	7320 ± 30	5.9 ± 0.2	6400 ± 400 <sup>b</sup>	1050 ± 80 <sup>c</sup>	5400 ± 400 <sup>b</sup>	310 ± 10 <sup>c</sup>
	Carbachol	5180 ± 10	17.6 ± 0.4	6420 ± 30	5.7 ± 0.2	6100 ± 200 <sup>e</sup>	300 ± 50 <sup>e</sup>	7160 ± 10 <sup>e</sup>	121 ± 9 <sup>e</sup>
<b>H2R</b>	Histamine	5810 ± 30	2340 ± 10	5240 ± 30	279 ± 5	1500 ± 100 <sup>f</sup>	21000 ± 4000 <sup>f</sup>	1080 ± 40 <sup>f</sup>	4100 ± 100 <sup>f</sup>

Overall, the potencies determined with the dual setup correspond well to the pEC<sub>50</sub> values determined for the single impedance and luminescence measurements in previous chapters (Table 19, cf. chapters 4.2 and 4.3). Additionally, the efficacy values of impedance are similar between the single and dual setup (Table 19, cf. chapter 4.2). However, the E<sub>max</sub> values of bioluminescence do not match well. In the dual setup, only up to 80% of the E<sub>max</sub> values of the single measurements are achieved.

In contrast to the single measurements, the impedance baseline values of the dual setup are 20-50% larger (Table 20). The only exception is the H2R system, where the impedance baseline of the dual setup is reduced by about 10% in comparison with the baseline value of the single impedance measurement. Furthermore, the bioluminescence baseline values in the dual setup take 10-50% of the values of the single setup. The same trend is identified for the luminescence maxima. In the dual setup, only 12-40% of the luminescence signals for the single measurements are achieved (Table 20). The maximal values of impedance for the dual setup take up to 40% smaller values than for the single measurements. Only the impedance maximum of HEK M5R/mG<sub>q</sub> cells stimulated with carbachol is 20% larger in the dual setup than for the single measurement.

To conclude, for all systems the typical time courses for luminescence and impedance were reproduced as in the single experiments described before (**chapters 4.2 and 4.3**). Both impedance and luminescence increase concentration-dependently and luminescence exhibits maxima at 0.08-0.13 h, respectively. The impedance signal shows maxima between 0.25-0.5 h. It is relatively stable over the measurement period except for the H2R system, while luminescence quickly peaks and drops off again. Impedance, especially for high ligand concentrations, also exhibits an initial decrease of several 100  $\Omega$  right after ligand addition. This phenomenon was already described in literature before for G<sub>q</sub>-coupled systems and might correlate with G<sub>q</sub> protein activation and calcium mobilization (Parviz et al., **2017**, Scott, Peters, **2010**, Verdonk et al., **2006**). Since the maximum luminescence often occurs at the same time as the initial decrease of impedance, the impedance decrease might indeed indicate (mini)G protein activation or calcium mobilization as previously described by Parviz *et al.* (Parviz et al., **2017**).

In contrast to **chapter 4.2**, where no addition peaks of impedance were discerned, addition peaks of impedance are observed in the dual setup (**Figure 86, Figure 88, Figure 90, Figure 92 and Figure 94**). This might be explained by the enhanced vulnerability of the impedance measurement in the dual setup since the thin copper wires, connected to the electrode arrays, must withstand tensile forces during the movement inside the luminescence plate reader, which is not the case in the commercial setup for single impedance measurements (Applied BioPhysics). Furthermore, GPCR-unspecific effects might be the reason for the impedance peaks since they are also observed under CTRL conditions.

When coelenterazine h is added, impedance commonly rises by about 400-500  $\Omega$ , which is negligible compared to the signal after ligand addition. The slight 400-500  $\Omega$  increase was also observed in **chapter 4.2** and is the only identified influence of coelenterazine h on impedance. The increase is explained by changes in the osmolarity of the cells or liquid handling effects. It might also point to an intrinsic activity of the receptors, miniG protein or NanoLuc under study.

In most cases, the initial slope of luminescence is steeper with larger ligand concentration. In addition, its maximum is arriving earlier in time with increasing agonist concentration. These observations are consistent with **chapter 4.3**. More ligand potentially leads to an amplified activation of receptors and, hence, to faster and more miniG protein recruitment. Differences in the kinetic profiles and initial slopes were also described by Hoare *et al.* for several proximal assays, variations of GPCRs and different ligands (Hoare et al., **2020**, Hoare et al., **2021**). Consequently, the kinetics are always system-dependent. This also explains why the impedance of

the H2R (**Figure 94**) does not remain as constant as for the muscarinic systems (**Figure 86, Figure 88, Figure 90 and Figure 92**) after reaching the maximal value. Throughout all studies, impedance is more sensitive for smaller ligand concentrations, while luminescence is more sensitive for high concentrations. This observation reflects the integrative character of impedance. Even at small ligand concentrations a signaling cascade is triggered that is not necessarily detectable in a proximal assay but can be observed in a more sensitive, distal assay such as the impedance assay. In 1991, the ECIS method was already sensitive enough to detect the smallest cellular movements, also called micromotions, used as an indicator for cellular viability and mirroring cytoskeletal rearrangements (Giaever, Keese, **1991**, Lo et al., **1993**, Zinkl, Wegener, **2019**). However, alongside a signaling cascade, more and more processes are triggered, branch out and, hence, lead to an enhancement of distal readout parameters. Consequently, impedance saturates quickly for high ligand concentrations, leading to smaller sensitivities above a certain ligand concentration. For high concentrations, proximal readout parameters such as miniG protein recruitment, mirroring the first functional response after GPCR activation, are more advantageous. Besides that, it is obvious that impedance is a more long-lived process (minutes to hours), while luminescence is very short-lived (< 10 min) (**Figure 86, Figure 88, Figure 90, Figure 92 and Figure 94**). The short-lived miniG protein signal might be explained by deactivation mechanisms such as  $\beta$ -arrestin recruitment and receptor internalization or depletion of the luciferase substrate coelenterazine h. Overall, miniG protein recruitment occurs earlier and faster than morphological changes and cytoskeletal rearrangements detected by impedance measurements. Furthermore, the long-lasting nature of the impedance signal once more confirms its integrative and very distal characteristics. It is suggested that somewhere downstream of the signaling cascade a point of no return is reached at which a deactivation of the signaling cascade is not possible anymore indicated by constant impedance values above a certain ligand concentration.

Since the evaluation of a certain time point ( $t = 0.5$  h), the AUC between 0-0.75 h and the maximum reveals similar results for the correlation of impedance and luminescence (**Figure 87, Figure 89, Figure 91, Figure 93 and Figure 95**), all analysis methods are suitable and valid to characterize diverse cellular systems. Independent of the evaluation method, only positive Spearman correlation coefficients were found for HEK M1R/mG<sub>q</sub>, HEK M5R/mG<sub>q</sub> and HEK H2R/mG<sub>s</sub> cells in combination with iperoxo, carbachol and histamine. Positive correlations ( $r_s > 0$ ) between impedance and luminescence are detected, i.e. both signals increase with the ligand concentration. Furthermore, most Spearman coefficients range between

0.76-0.90, indicating a close to monotonic, non-linear relationship between impedance and luminescence. Only for HEK M5R/mG<sub>q</sub> cells stimulated with iperoxo the  $r_s$  values are smaller and ranged between 0.55-0.79. This is explained by a change of the slope of the correlation plot with larger iperoxo concentration. A changed behavior between luminescence and impedance with larger ligand concentration is suggested and could be explained by unspecific binding effects or a potentially toxic effect of the ligand above a certain working concentration. This can also be deduced from the decreasing impedance signal above an iperoxo concentration of 30-100 nM for HEK M5R/mG<sub>q</sub> cells (cf. **Figure 91A-B and Appendix 32**).

Small ligand concentrations lead to quick changes in impedance but minor changes in luminescence (**Figure 87, Figure 89, Figure 91, Figure 93 and Figure 95**). In contrast, for large ligand concentrations usually a saturation behavior is observed in impedance, while luminescence still varies. For HEK M5R/mG<sub>q</sub> cells stimulated with carbachol (**Figure 93**), an almost linear correlation is found. However, this is attributed to the chosen concentration range. If larger carbachol concentrations were investigated, a saturation behavior would be expected for impedance similar to all other tested systems. This is also confirmed by the concentration-response analysis in **chapter 4.3**, where a fit of the data points was not possible because of an underconstrained upper asymptote (**Figure 55B**).

With the dual luminescence-impedance setup, reliable pEC50 values can be determined as a comparison to values from the single impedance and luminescence measurements confirms (**chapters 4.2 and 4.3; Table 19**). In addition, the efficacies from impedance measurements are reproducible (**Table 19**). However, the basal and maximum luminescence (**Table 20**) as well as the corresponding  $E_{max}$  values (**Table 19**) are lowered in the dual setup in contrast to the single luminescence measurements (**chapter 4.3**). This is mainly attributed to the usage of transparent 96-well arrays in the dual setup, while in **chapter 4.3** white plates were deployed for the luminescence measurements. As investigated in **chapter 4.5.1**, the optimization of the NanoBiT assay revealed that the plate color greatly impacts the luminescence outcome. Because of an enhanced reflectivity, white plates yield larger S/N ratios and overall signals, which is why white plates are recommended for luminescence (Garvin et al., **2021**). But since no white electrode arrays were available within the frame of this work, commercially available transparent 96W1E+ arrays (Applied BioPhysics) were used in the dual setup. As observed in **chapter 4.5.1**, black 96W1E+ delivered similar luminescence results as transparent 96W1E+. Consequently, no benefit of black plates over transparent plates was expected here.

In a further experiment, the performance of manual contacting and circuit board contacting of 96W1E+ arrays was investigated and compared more in-depth with the dual luminescence-impedance setup. Two manually contacted 96W1E+ arrays (C2,3,10,11/D1-12 and G2,3,10,11/H1-12) were compared with the four possibilities to use circuit board contacting of a 96W1E+ array (A/C, B/D, E/G, F/H, cf. **chapter 3.8**). HEK M1R/mG<sub>q</sub> cells were seeded on three crosslinked gelatin-coated arrays (2x96W1E+ manually contacted, 16 wells respectively; 1x96W1E+ for circuit board contacting, 64 wells → 16 wells per circuit board) according to the standard protocol (cf. **chapter 3.8.1**). After a two-day cultivation, the cells were equilibrated to L15 buffer and an impedance baseline read was started. At  $t = -0.2$  h, 1  $\mu$ M coelenterazine h was added and a simultaneous luminescence measurement was initiated in parallel to the impedance reading. Finally, at  $t = 0$  h, a CTRL and different carbachol concentrations (1  $\mu$ M, 30  $\mu$ M, 300  $\mu$ M) were added and stimulation was monitored for 0.25 h with the dual setup. The circuit boards (A/C, B/D, E/G, F/H, cf. **chapter 3.8**) were tested in four successive experiments. The results for the simultaneously recorded impedance and luminescence are depicted in **Figure 96**.

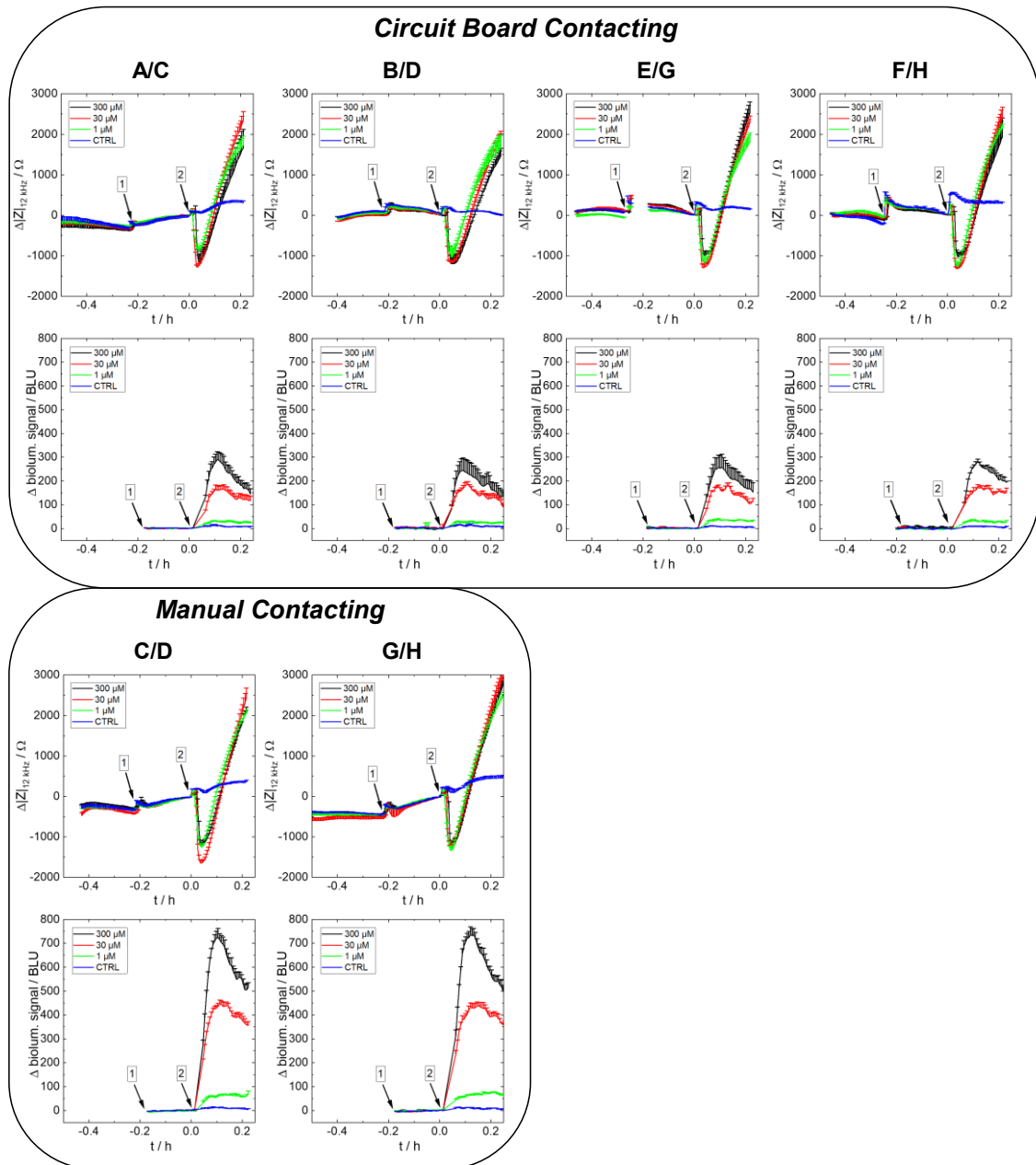


Figure 96. Comparison of simultaneously detected impedance and luminescence data of **HEK M1R/mG<sub>q</sub>** cells on 96W1E+ arrays that were contacted via **four different circuit boards** (top; contacted rows: A/C, B/D, E/G, F/H, cf. **chapter 3.8**) and on **manually contacted 96W1E+** (bottom; contacted rows: C/D, G/H) (dual setup). The arrays were coated with crosslinked gelatin. At  $t = -0.2$  h,  $1 \mu\text{M}$  coelenterazine h was added and a luminescence measurement was started in parallel to the impedance read (arrow 1). Finally, at  $t = 0$  h,  $300 \mu\text{M}$  (black),  $30 \mu\text{M}$  (red) and  $1 \mu\text{M}$  (green) of carbachol or a CTRL (blue) were added (arrow 2). Mean + SE,  $N = 4$ , single experiment. Temperature:  $37^\circ\text{C}$ .

The impedance time courses of the manually contacted arrays (**Figure 96, bottom**) are equal to the ones of the plates contacted via circuit boards (**Figure 96, top**). After a stable baseline recording and the addition of coelenterazine h, a  $200 \Omega$  peak is visible. As soon as carbachol is added, a  $1000 \Omega$  decrease of impedance emerges followed by a steady increase over the measurement period. The impedance curves for the three carbachol concentrations (**Figure 96, black, red, green**) can not be

discriminated within this test period. The curve of the CTRL (**Figure 96, blue**) remains constant and at the baseline level.

Oppositely, luminescence significantly differs depending on the contacting method (**Figure 96, top and bottom**). For circuit board contacting, maximal values between 240-290 BLU are identified for 300  $\mu\text{M}$  carbachol (**Figure 96, top, black**), whereas values of about 730 BLU are detected on manually contacted plates (**Figure 96, bottom, black**). Similar observations are made for 30  $\mu\text{M}$  and 1  $\mu\text{M}$  carbachol (**Figure 96, top and bottom, red, green**): on manually contacted plates, the luminescence values are amplified. For every measurement, the luminescence curve of the CTRL remains at the zero line. The maxima of luminescence emerge after  $t = 0.10\text{-}0.13$  h in all cases. Neither between the four plates contacted via the circuit boards nor for both manually contacted arrays variances in luminescence are detectable.

The results in **Figure 96** indicate that impedance is reproducible among all varying contacting techniques and plates used. However, bioluminescence is negatively influenced when a circuit board is mounted to the 96W1E+ arrays (*circuit board contacting*). This originates from the misplacement of the 96-well plate inside the plate holder. Since not only the circuit board is mounted to the array but also four clamps to fasten the array to the spring contacts and to ensure continuous electrical contact, in total, the plates contacted via circuit boards are larger in size than *manually contacted* plates and do not fit inside the plate holder perfectly. Consequently, the detector no longer aligns with the well centers in case of *circuit board contacting* and, hence, a smaller portion of luminescence is read. Nonetheless, the same kinetic behavior is monitored and reliable and reproducible  $\text{pEC}_{50}$  values are determined for both contacting approaches as demonstrated before (cf. **Table 19**).

Over the course of this work, several advantages and drawbacks with respect to the preparation and handling of manually contacted plates and plates contacted by circuit boards were ascertained. An overview of these is given in **Table 21**.

#### 4 Simultaneous Measurement of Luminescence and Impedance

Table 21. Advantages and shortcomings of manual and circuit board contacting of 96W1E+ arrays with respect to preparation, handling and the signal outcome measured with the dual luminescence-impedance setup.

Manual Contacting		Circuit Board Contacting	
Pros	Cons	Pros	Cons
Custom-made black plates measurable	Sterilized far in advance by UV light exposure and hard to examine under microscope	Standard cultivation possible, i.e. Argon plasma sterilization and investigation under microscope	Custom-made black 96W1E+ plates <b>not</b> measurable because bad alignment with circuit boards
<b>No</b> misplacement inside the plate reader	Copper wires <b>not</b> reversibly detachable	Reversible contacting	Misplacement inside the plate reader and signal loss
Fabrication does <b>not</b> require expertise	Time-consuming contacting	Time-saving contacting	Fabrication of circuit boards and soldering requires expertise
	16 wells per plate per day measurable; after 3-5 experiments with same wells: repeated contacting	64 wells per plate and per day measurable (four circuit boards)	Larger evaporation effects if four successive experiments with four circuit boards on one plate
	Contact loss <b>not</b> easy to fix	Contact loss easy to fix	Contact loss only discernable when measurement is started
	Contact loss only discernable when measurement is started	More economical	

Using *circuit board contacting*, a misplacement of the 96W1E+ array inside the plate reader and a concomitant signal loss (cf. **Figure 96**) is observed. However, it is time-saving and more economical than manual contacting since the array is simply mounted to the circuit board and no additional components like copper wires or silver conductive paint are necessary, implying less consumption of materials. Furthermore, the handling of circuit board contacted plates is easier because no wires or silver conductive paint interfere during the preparation, sterilization and microscopy of the substrates. The plates are operated as usual culture substrates. In addition, 64 wells can be measured per plate and day by utilizing the four circuit boards (cf. **chapter 3.8**). If successive experiments are performed on one plate with the four circuit boards, stronger evaporation effects must be considered compared to manual contacting where only one experiment per plate per day is possible. Loss of contact usually is due to a deficiency of the circuit board and, thus, can be fixed easily. Nonetheless, it becomes only apparent as soon as the measurement is started, which leads to an experimental time lag. Moreover, black 96W1E+ arrays do not always

perfectly align with the contact springs of the circuit board since they are custom-made, potentially leading to a decreased throughput. Moreover, manufacturing circuit boards is not trivial and requires the expertise of an electrical engineer and soldering experience.

On behalf of *manually contacted* arrays, all 96 wells can be used bit by bit after reconfiguring the contacted wells, while max. 64 wells can be measured with the circuit boards designated to 16 different wells, respectively (cf. **chapter 3.8**). Furthermore, no soldering is necessary, rendering the contacting procedure less complex, yet, more time-consuming. The general handling of manually contacted plates is very unpleasant. Just before attaching the wires to the contact pads, the plate is sterilized in the Argon plasmalizer. Thereafter, UV sterilization is harnessed, taking place under semi-sterile conditions. In addition, the copper wires are very difficult to manage inside the sterile hood or incubators and easily entangle or tear. Phase contrast microscopy also raises problems with respect to the cables and non-transparent well bottoms due to the silver conductive paint applied on the backside of the array. Additionally, the manually contacted wells can only be used 3-5 times at maximum after trypsinization and regeneration of the electrodes. Thereafter, either other wells or a new electrode array need(s) to be contacted, which demands copper wires and other materials. The throughput per plate is restricted to 16 wells per day or experiment. In case of contact loss, it is mostly discerned at the beginning of or during a measurement. At this point in time, it is very difficult to reestablish electrical contact since the cells and solutions are already filled inside the wells and the plate can not be inverted to get better access to the points of contact.

Concludingly, the contacting technique must be chosen depending on the system under investigation. In general, arrays contacted via circuit boards are easier to cultivate and operate. However, if cells with a weakly pronounced luminescence are investigated, manual contacting is recommended. In all cases, the experimental parameters should be adjusted and optimized as described in **chapters 4.4 and 4.5**.

### 4.7 Summary and Outlook

In **chapter 4.1**, HEK and CHO cells were characterized with the impedance technique ECIS. Adhesion measurements revealed that a seeding density of  $3 \cdot 10^5$  c/cm<sup>2</sup> and a coating with crosslinked gelatin enhance the cellular impedance response of HEK cells on 8W1E and 96W1E+ arrays and lead to a better discrimination between cell-covered and cell-free electrodes. For CHO cells, crosslinked gelatin results in faster adhesion but medium serum proteins lead to stronger adhesion, indicated by

increased impedance values. Gelatin displayed the smallest change in impedance over the measurement period. Consequently, medium preincubation was the method of choice for CHO cells in following experiments to avoid the time-consuming crosslinking procedure and obtain satisfactory impedance results. A sensitive frequency of 12 kHz was identified for HEK and CHO cells, respectively. After a cultivation time of two days, raw impedance values of  $\geq 5000 \Omega$  are observed. This value served as a reference point for the baseline impedance of successive experiments.

In **chapters 4.2 and 4.3**, HEK M1R/mG<sub>q</sub>, HEK M5R/mG<sub>q</sub> and HEK H2R/mG<sub>s</sub> cells, all expressing a NanoBiT system to study miniG protein recruitment, were investigated with respect to their stimulative response. Impedance and bioluminescence were monitored after the addition of the luciferin coelenterazine h and an activating ligand. Carbachol and iperoxo were utilized as M1R and M5R agonists, whereas histamine was used as H2R stimulus. The impact of coelenterazine h on impedance was studied by comparing the time courses in the presence and absence of the luciferin. The addition of coelenterazine h leads to a 400-500  $\Omega$  increase in impedance but no impact of coelenterazine h on the impedance response after GPCR stimulation was observed. All time courses illustrated an agonist concentration dependency. Whereas a concentration-correlated transient decrease and a subsequent long-lasting rise are identified for impedance (time scale: minutes to hours), the luminescence signal is very transient and short-lived (time scale: < 10 min).

Both signals were compared to HEK wt cells and cell lines engineered to overexpress the same receptor but without a luciferase system. The latter did display similar impedance responses but no luminescence response. HEK wt cells neither showed a significant impedance outcome nor any change in luminescence. These control experiments proved that the observed impedance responses for HEK M1R/mG<sub>q</sub>, HEK M5R/mG<sub>q</sub> and HEK H2R/mG<sub>s</sub> cells are ascribed to the overexpressed GPCRs and miniG proteins and that luminescence can only be read if a luciferase is present and catalyzes the oxidation of its substrate.

The change of impedance is explained by downstream processes impacting the cytoskeletal architecture of the cells, for instance by rearrangement of the actin filaments (Dutt et al., **2002**, Yan, Jin, **2012**). Consequently, cell-substrate- and cell-cell-contacts are influenced and the membrane composition and topography might change, affecting the parameters  $\alpha$ ,  $R_b$  and  $C_m$  and, hence, the overall impedance. For large ligand concentrations, the impedance signal saturates. This is explained by signal amplification along the triggered cascade and the very distal and integrative nature of impedance.

Luminescence remains at a relatively constant level when coelenterazine h but no agonist is added, giving proof of insignificant intrinsic recruitment of freely diffusing miniG protein to the receptor. Once the cells are stimulated with an agonistic ligand, luminescence quickly rises, which suggests that miniG proteins are recruited to the receptor immediately. Then, NanoLuc re-complements and oxidizes its luciferin coelenterazine h. This process is enhanced and the faster, the bigger the ligand concentration is. The subsequent decline of luminescence is explained by desensitization processes and a depletion of coelenterazine h itself.

Luminescence and impedance data were analyzed at  $t = 0.5$  h. This time point was chosen since after this time, impedance reaches its maximum and saturates. For better comparison of cells in the same state, the same time point was chosen for the evaluation of the luminescence data. An analysis of time point  $t = 0.5$  h yields potency and efficacy values similar between experiments and similar to literature. The evaluation of a single time point proved sufficient and delivered similar results as AUC and maximum signal analysis, which is confirmed by **Figure 27** for impedance and in **Appendix 18** for luminescence. In **Appendix 18**, similar  $pEC_{50}$  values of  $4.4 \pm 0.3$  (time point  $t = 0.5$  h),  $4.6 \pm 0.1$  (AUC analysis between  $t = 0-0.75$  h) and  $4.3 \pm 0.2$  (maximum of luminescence) for the three analysis techniques were found. Nonetheless, considering a time interval instead of a time point, e.g. by AUC analysis, is recommended in future perspective to incorporate kinetic effects (e.g. if luminescence is already leveled off after 0.5 h) and would lead to more profound insights and a better understanding of the signaling processes.

**Chapters 4.4 and 4.5** dealt with the optimization of the measurement parameters of impedance and luminescence. Studies regarding the plate coating, plate color, coelenterazine h aging, seeding density, growth time, measurement buffer, integration time, gain, coelenterazine h concentration and an additional washing step were conducted with HEK M1R/mG<sub>q</sub> cells as a model cell line.

The coating of the substrate greatly influences the adhesiveness of cells to their substrate. Consequently, three coating procedures, namely a preincubation with medium (containing serum), a gelatin coating and a crosslinked gelatin coating (crosslinking with glutardialdehyde), were compared. Crosslinked gelatin was identified as the best option for adhesion and stimulation measurements of HEK cells and ensures that the cells remain constantly attached to the substrate even after substance addition. No influence of the coating on luminescence was detected.

However, the plate color affects luminescence. White plates feature enhanced maximal values, efficacies and S/N ratios of luminescence in contrast to black and transparent plates. But since no white electrode arrays were available for the ECIS

setup, measurements with the dual luminescence-impedance setup were performed with commercial transparent 96W1E+ arrays, leading to a slight signal loss of luminescence.

The luciferin aging study revealed that coelenterazine h is prone to oxidation and hydrolysis. Furthermore, elevated temperatures and light exposure lead to its degradation. Consequently, the stock solution should be stored at  $-20^{\circ}\text{C}$  and must always be diluted freshly on the day of the experiment and stored in the dark at low temperatures ( $4^{\circ}\text{C}$ ) until use. An influence on impedance was not observed, which is hardly surprising since a freshly prepared coelenterazine h solution did not have any significant impact on impedance either.

Since the seeding density showed an influence on the adhesion behavior of HEK cells measured by impedance, its impact was also tested in terms of GPCR stimulation. The results demonstrated that larger seeding densities generate increased impedance responses because more cells are attached to the electrodes. A seeding density of  $3 \cdot 10^5 \text{ c/cm}^2$  is favored and recommended for HEK cells.

If  $3 \cdot 10^5 \text{ c/cm}^2$  are seeded and grown for one, two (standard) or three days on 96-well plates, differences in the receptor activation after ligand addition are recognized in luminescence, while impedance is quite unaltered. With increased cultivation time, the impedance signals only slightly increase but become more instable. The loss of signal stability might be due to stronger desensitization mechanisms or a change of the ECM composition with longer cultivation. In contrast, the luminescence signals decrease significantly with increased cultivation time, which must be attributed to a flattened expression of the NanoBiT system. This might be due to degradation of the receptor, luciferase or miniG proteins. Consequently, the relatively constant impedance signal is rather explained by the detection of a signaling mechanism (e.g. second messenger release) being amplified along the signaling cascade. In further experiments, a growth time of two days was chosen as the best practice parameter to ensure a high luminescence as well as strong adherence, which is essential for impedance measurements.

Since there are several buffer systems and formulations available for cell culture, the dependency of GPCR activation on the buffer composition was investigated. L15, PBS and HBSS were used as measurement buffers in the luminescence and impedance assay. No huge impact was detected in impedance, whereas luminescence varied depending on the three buffers. Luminescence diminished in the following order: HBSS > PBS > L15. This is not trivial and can only be explained by the buffer composition and a changed receptor activation or metabolism of the cells in the respective medium. L15 was chosen as measurement buffer in most

experiments since it not only provides physiologically and osmotically relevant salts and buffer systems but also a carbon and nitrogen source to guarantee the long-term viability of the cells. Additionally, in HBSS the mechanosensitivity of the GPCRs must be considered.

The integration time and gain should always be selected with respect to the system under investigation. The larger the integration time, the better the S/N but the poorer the time resolution. If the gain is increased too much, noise prevails and exceeds the actual signal. In case both parameters are set to too small values, signals and noise can not be discriminated anymore. In this work, a gain of 150 and an integration time of 1000 ms yielded the best results for HEK M1R/mG<sub>q</sub> cells. In the case of HEK H2R/mG<sub>s</sub> cells, 100 ms rendered optimal luminescence results.

Two factors must be considered when selecting the coelenterazine h concentration: first, the signal height and second, the expenses (0.484 € per 1 µg coelenterazine h; promega.de #3; **August 10, 2024**). With respect to the determined S/N ratios, signal amplitudes of luminescence and expenses, a concentration of 0.5 µM coelenterazine h is recommended and delivers satisfactory results using HEK M1R/mG<sub>q</sub> cells.

Introducing a washing step to remove phenol red remnants before luminescence measurements is not necessary. Indeed, the NanoLuc emission interferes with the absorption of the fluorophore phenol red. Nonetheless, no significant change in the S/N, pEC50 or signal intensities of luminescence was identified when the culture medium was directly exchanged with L15 buffer. Therefore, omitting the washing step saves materials, costs and time and still yields adequate results.

Ultimately, in **chapter 4.6**, the impedance assay was combined with the NanoBiT assay in a self-built setup. On that account, 96W1E+ arrays were either *manually contacted* or *contacted by circuit boards* to an impedance analyzer to enable a simultaneous measurement inside a luminescence plate reader. In the former case, copper wires were manually attached to the contact points of a 96W1E+ array and joined together in a RS232 plug to connect the array to an impedance reader. In the latter case, four different circuit boards, each contacting 16 wells, were designed and linked to the impedance analyzer by soldering them to copper wires. The array is simply mounted to the circuit board by screwing on four clamps. Both measurement techniques show good performance but also have their deficits. A manually contacted array is more difficult to handle during the cultivation of the cells and can only be used 3-5 times, which means a new plate needs to be contacted recurrently. This is very time-consuming and cost-intensive. Nonetheless, manually contacted plates benefit from larger signal outcomes because the plate is not misplaced inside the

luminescence reader. This is not true for arrays contacted via the circuit boards. Here, the big downside is the misplacement inside the plate reader because of an overall increase in the size of the array (clamps), leading to a signal loss of luminescence. Moreover, soldering and creating the circuit board demands expertise. On a positive note, contacting the array is quicker and easier. Furthermore, the cultivation of cells can be performed as usual. Concludingly, manual contacting is recommended for weakly luminescent systems whereas circuit board contacting is advised when higher experimental throughput is required.

With both contacting techniques, a simultaneous measurement of luminescence and impedance for one cell population is possible. Three cellular systems, in particular HEK M1R/mG<sub>q</sub>, HEK M5R/mG<sub>q</sub> and HEK H2R/mG<sub>s</sub>, were analyzed. Iperoxo and carbachol were used as agonists for the muscarinic acetylcholine receptors M1R and M5R and histamine served as agonist for the H2R. All systems revealed positive correlation coefficients (Spearman  $r_s > 0$ , mostly between 0.76-0.90) between impedance and luminescence, suggesting a monotonic, non-linear increase of both measures with increasing ligand concentrations. The three evaluation methods (time point, AUC and maximum) yielded similar correlation plots. Impedance proved to be more sensitive for smaller ligand concentrations and saturated for large ligand concentrations, while luminescence behaved *vice versa*. This was also observed for the kinetic correlations and is ascribed to the proximal character of the miniG protein recruitment and the distal nature of impedance. If the readout parameter is more downstream, the signal saturates quicker because of signal amplification along the triggered cascade. Added to this, the transient decrease of impedance immediately after ligand addition kinetically correlates with the maximum in luminescence. In literature, the quick decrease in impedance is often ascribed to G<sub>q</sub>- and subsequent Ca<sup>2+</sup>-signaling (Parviz et al., **2017**). But since HEK H2R/mG<sub>s</sub> cells also exhibit an initial decrease of impedance after histamine addition, although the G<sub>s</sub>-pathway should be favored (canonical pathway and statistics because mG<sub>s</sub> is overexpressed), it is suggested that the decrease of impedance in HEK H2R/mG<sub>s</sub> cells could also indicate G<sub>q</sub> protein recruitment. This will be further investigated in **chapter 5**.

The different ligand-receptor combinations yielded pEC50 and E<sub>max</sub> values close to the values determined with the single experimental setups. Only the E<sub>max</sub> values of bioluminescence were lowered in the dual setup. This is because the single luminescence measurements were performed with white plates, whereas the dual measurements could only be conducted with transparent plates, displaying a smaller reflectivity and lower S/N ratios.

Overall, the dual luminescence-impedance technique is well suited to in-depth characterize GPCR systems and their signaling behavior in real-time. It is possible to study different GPCRs (M1R, M5R, H2R) with varying coupling behavior ( $G_q$ ,  $G_s$ ). Furthermore, several agonists (iperoxo, carbachol, histamine) and antagonists (data not shown) can be investigated and compared regarding their signaling. The order and time scale of events along the signaling cascade can be compared (first miniG protein recruitment, then morphological changes) and correlated. Furthermore, potencies and efficacies can be determined in parallel to further characterize the investigated system. The greatest advantage, however, is that one single cell population is studied in two simultaneous measurements, providing different pieces of information (proximal, distal), which is not trivial. As all cell biologists know, cells vary from passage to passage and with thawing cycles and, therefore, often show varying behavior over a multitude of experiments. Only very robust cell lines display reproducible results over time. Accordingly, results from two functional assays recorded one after another are not necessarily comparable. In this work, this problem was overcome by a combination of two functional assays performed in parallel for one and the same cell population. All in all, a very monotonic, non-linear correlation between luminescence and impedance was found, which demonstrates how well two profoundly different parameters complement each other.

In future work, problems induced by circuit board contacting, leading to a misplacement inside the luminescence plate reader, must be addressed. This could be done by narrowing the width of the clamps necessary for mounting the plate to the circuit board. Another option is designing a wireless circuit board for impedance analysis by which increasing the throughput to 96 wells is conceivable (Ozdalğic et al., **2022**, Tenreiro et al., **2022**).

The impedance and luminescence measurement parameters must be further optimized with respect to the electrode arrays. By manufacturing custom-made white 96W1E+ arrays, luminescence could be boosted. Consequently, less luciferin and smaller integration and, hence, measurement times would be sufficient, offering the opportunity to test weakly expressed systems or more short-lived kinetics.

The influence of the measurement buffers on luminescence is hard to interpret and must be further investigated. By modification of the concentration of single buffer components, especially riboflavin 5'-phosphate (R5P), the reason for the change of luminescence might be elucidated. Hereby, the pH and osmolarity must remain constant.

The dual luminescence-impedance setup is easily adaptable to other luminescence techniques such as fluorescence. Since fluorescence often is the readout parameter for intracellular calcium detection with Fura-2 or Fluo-4, the dual setup offers whole new options to unravel GPCR signaling and underlying mechanisms. However, the very transient nature (seconds time scale) of calcium signaling must be taken into consideration with respect to the time resolution of the plate reader. Furthermore, the circuit board contacting method might be problematic because the excitation light is quite certainly reflected to the detector (reflective metal surface of circuit boards), leading to artificial signals and a quick transgression of the device's threshold.

Another imaginable modification of the dual setup is measuring dynamic mass redistribution (DMR) and impedance simultaneously. This system would allow for the comparison of two distal readout parameters to investigate if they are complementary or rather yield different pieces of information. If they are not complementary, the combination of both might help to resolve morphological changes more in-depth. Since impedance is a non-optical, label-free method, it should not interfere with the optical readout of DMR. Nevertheless, creating a surface to measure both parameters (gold-film electrode and optical waveguide grating) is very complex and demands sophisticated technologies.

With the developed setup, miniG protein recruitment was measured in parallel to impedance. But there are also systems expressing full NanoLuc to study the binding kinetics of a GPCR ligand with bioluminescence resonance energy transfer (BRET) (Grätz, **2023**). This opens up a new perspective and allows not only functional characterization of a ligand-GPCR system but at the same time reveals binding information of the ligand.

So far, it was not possible to investigate  $G_i$ -coupled HEK systems with the dual luminescence-impedance assay because of low impedance responses (data not shown). However, dual luminescence-impedance measurements of other  $G_i$ -coupled cell lines expressing a NanoBiT system might be possible. A potential candidate could be CHO cells, which often display an impedance response after  $G_i$ -stimulation. In addition to miniG protein recruitment studies, the investigation of e.g.  $\beta$ -arrestin recruitment with the NanoBiT approach could help to further elucidate other underlying signaling mechanisms and might broaden the spectrum of the applicability of the dual setup.

Since ECIS is a very sensitive technique and can monitor the activation of natively expressed GPCRs, as was shown in literature by stimulation of the  $\beta$ -adrenoceptor of bovine aortic endothelial cells (BAEC) cells (Wegener et al., **1999**) or activation of the H1R in the human glioblastoma cell line U-373 MG (Stolwijk et al., **2019**), it is

conceivable to investigate endogenously expressed GPCRs with the dual luminescence-impedance technique as well if genetic engineering allows the introduction of luminescent transducers. In most cases, overexpressed systems are in the focus of pharmacological research. However, these test systems often are artificial and do not depict physiologically relevant environments. By knocking in fluorescent or bioluminescent reporters such as NanoLuc with the CRISPR/Cas9 technology, these problems can be overcome (Soave et al., **2021**). Since NanoLuc is a very bright and sensitive luciferase, natively expressed receptor activation and internalization can be resolved as proved by Boursier *et al.* in split luciferase complementation and NanoBRET assays (Boursier et al., **2020**). In combination with impedance spectroscopy, this might pave the way for extensive studies of physiologically relevant systems to improve our understanding of tissue-selective actions, pathophysiological processes and diseases (Soave et al., **2021**).

## 5 Unraveling the Impedance Signal After GPCR Stimulation

Impedance measurements as a technique to monitor G protein-coupled receptor (GPCR) responses in real-time are often referred to as “black box system”. Since impedance integrates the entire cell response, one particular impedance profile can not be assigned to one certain GPCR signaling process (Doijen et al., **2019**, Scott, Peters, **2010**). Impedance signals are more complicated to interpret and, thus, need to be deconvolved with the help of further functional assays, for example by using second messenger assays. Another possibility is the activation or blockage of certain signaling pathways with pathway-specific but GPCR-independent activators and inhibitors. Furthermore, it is essential to consider alternative pathways such as arrestin signaling since arrestins play an important role in the desensitization process of many GPCRs and, thus, might contribute to the impedance signal as well. In the following, the impedance profile of HEK M1R/mG<sub>q</sub> cells after stimulation with carbachol and the impedance response of HEK H2R cells after stimulation with histamine are further elucidated. In **chapter 5.1**, different pathway-specific activators are used to compare the agonist-induced GPCR impedance response with a GPCR-independent activation of the same pathway. Furthermore, pathway inhibitors are utilized to disable certain signaling pathways. From the impedance responses in the presence and absence of pathway inhibitors, it is inferred whether other than the designated pathways contribute to the impedance signal. In **chapter 5.2**, a fluorescence-based calcium mobilization assay is used to find out whether a second messenger activation might contribute to the impedance outcome. Lastly, in **chapter 5.3**, the Nanoluciferase (NanoLuc) Binary Technology (NanoBiT) was used to investigate  $\beta$ -arrestin2 recruitment to the M1R and H2R.

### 5.1 Pathway-Specific Inhibitors and Activators

GPCRs are well known to transduce signals from the extracellular to the intracellular site by coupling to transducers like G proteins or  $\beta$ -arrestins. However, in whole-cell methods like impedance assays, the exact underlying signaling mechanisms and coupling pathways can not be distinguished. Thus, pathway-specific inhibitors such as pertussis toxin (PTX), cholera toxin (CTX), 3-isobutyl-1-methylxanthine (IBMX), YM-254890 (YM) and FR900359 (FR) are often utilized to unravel GPCR responses (Bharati, Ganguly, **2011**, Campbell, Smrcka, **2018**, Seibel-Ehlert et al., **2021**).

Agonist-induced impedance responses compared to the impedance response of GPCR-independent activators of second messengers, such as cyclic adenosine monophosphate (cAMP) or calcium, can be used as well to further elucidate the signaling cascade following GPCR activation. In this chapter, the impedance of HEK H2R cells was investigated under the influence of the GPCR-independent cAMP activator forskolin (FSK), the cAMP-analog 8-(4-chlorophenylthio) adenosine 3',5'-cyclic monophosphate (8-CPT-cAMP) (**chapter 5.1.1**) and the  $G_s$ -pathway inhibitor CTX (**chapter 5.1.2**). Furthermore, the impedance response of HEK M1R/mG<sub>q</sub> cells after stimulation with carbachol was compared to calcimycin addition, which leads to calcium ion increases in the cell interior (**chapter 5.1.3**).

### 5.1.1 Imitation of the $G_s$ -Pathway and cAMP Signaling with Forskolin and 8-CPT-cAMP

FSK and 8-CPT-cAMP both lead to increases in cAMP levels (Insel, Ostrom, **2003**, Seamon et al., **1981**, Wernick et al., **2010**). While FSK directly activates adenylate cyclases (ACs), 8-CPT-cAMP acts as an analog of cAMP. Both are readily membrane-permeable (Xu et al., **2022b**) and mimic  $G_s$  downstream signaling. Since no significant impedance response for  $G_i$ -coupled HEK cells was observed after agonist addition (data not shown), a previous enhancement of the cAMP concentration with FSK or 8-CPT-cAMP treatment was investigated to find out whether these pretreatments improve the impedance signal quality as previously observed for  $G_i$ -coupled Chinese hamster ovary (CHO) cells (cf. **chapter 6**, (Skiba et al., **2022**, Skiba, **2022**)) and other cell lines (Hill et al., **2010**). However, neither the GPCR-independent AC activator FSK nor the cAMP derivative 8-CPT-cAMP could enhance the impedance response of  $G_i$ -coupled HEK cells upon stimulation of  $G_i$ -coupled GPCRs. Consequently, in another experiment, it was examined whether this is a phenomenon typical for HEK cells by comparing the impedance response of HEK H2R cells after the addition of the endogenous ligand histamine with the impedance responses of FSK and 8-CPT-cAMP. Since histamine activates the  $G_s$ -pathway, leading to increased cAMP levels, it should present a similar impedance profile as FSK and 8-CPT-cAMP (Höring, **2022**, Seibel-Ehlert et al., **2021**, Wellner-Kienitz et al., **2003**).

HEK H2R cells were seeded on a crosslinked gelatin-coated 96W1E+ array according to the standard protocol (see **chapter 3.5.3.1**). After a two-day cultivation, the cells were equilibrated in Leibovitz' 15 (L15) buffer for 2-2.5 h. Then, a baseline of

impedance was recorded at a frequency of 12 kHz (ECIS Z $\theta$ ). At  $t = 0$  h, a vehicle control (CTRL) and different concentrations of FSK (between 10 nM and 10  $\mu$ M) or 8-CPT-cAMP (between 1  $\mu$ M and 500  $\mu$ M) were added to increase intracellular cAMP levels. After a recording time of 0.25-0.33 h, an EC80 concentration of 2  $\mu$ M histamine was added to find out whether the impedance response of histamine provokes the same or a different impedance response as FSK and 8-CPT-cAMP. The impedance time course data is given in **Figure 97A-D**. Please note that the following data is normalized to the addition of FSK and 8-CPT-cAMP.

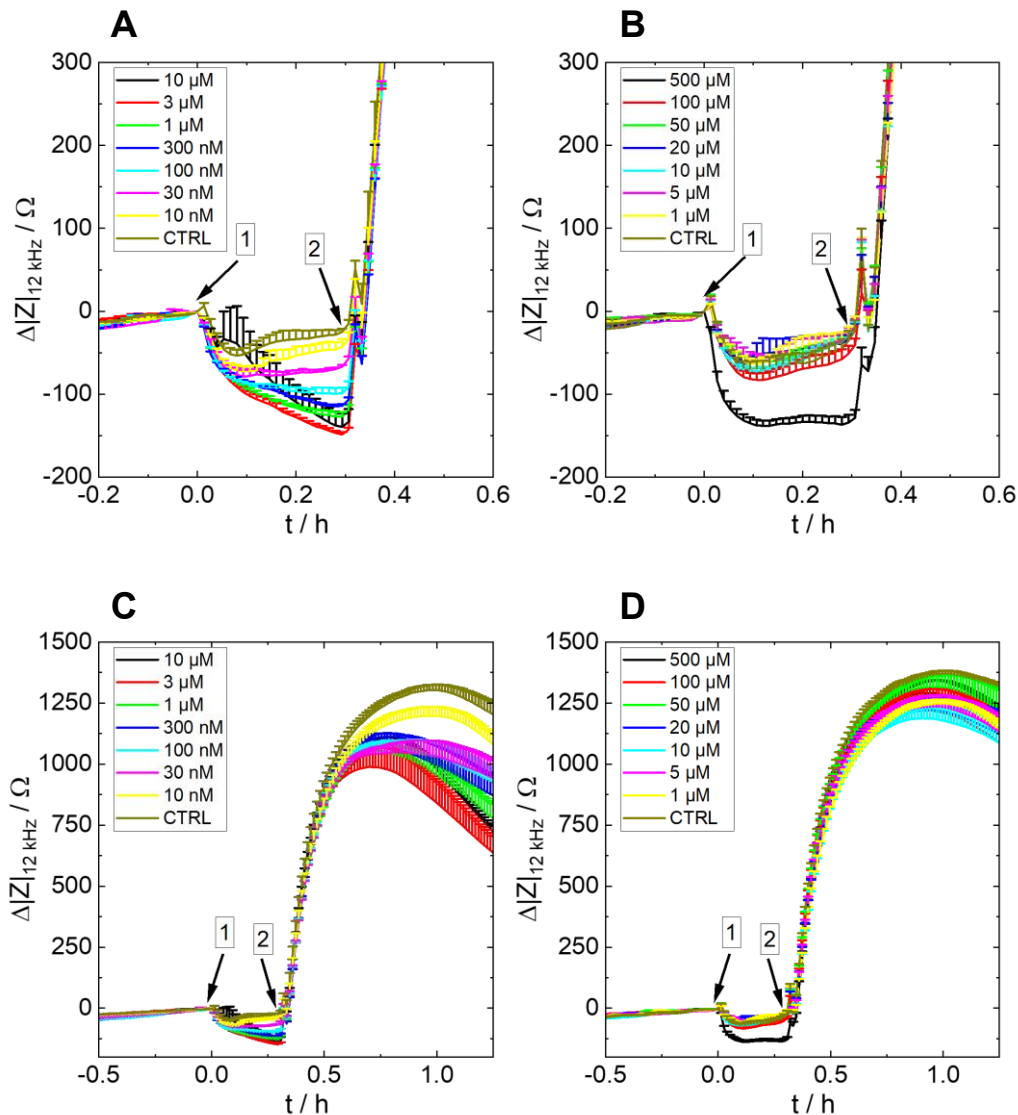


**Figure 97.** Impedance change over time of **HEK H2R** cells at a frequency of 12 kHz. The cells were cultivated on a 96W1E+ electrode array that was coated with crosslinked gelatin. At  $t = 0$  h (arrow 1), different concentrations of **FSK (A,C)** or **8-CPT-cAMP (B,D)** were added. A,C: black 10  $\mu$ M, red 3  $\mu$ M, green 1  $\mu$ M, blue 300 nM, cyan 100 nM, pink 30 nM, yellow 10 nM, brown CTRL. B,D: black 500  $\mu$ M, red 100  $\mu$ M, green 50  $\mu$ M, blue 20  $\mu$ M, cyan 10  $\mu$ M, pink 5  $\mu$ M, yellow 1  $\mu$ M, brown CTRL. At  $t = 0.3$  h (arrow 2), the cells were stimulated with **2  $\mu$ M histamine**. A and B are magnifications of C and D, respectively. Baseline A,C: ( $3328 \pm 3$ )  $\Omega$ , baseline B,D: ( $3371 \pm 5$ )  $\Omega$ . Mean + SE,  $N = 4$ , single experiment. CTRL = vehicle control. Temperature: 37°C.

After the addition of FSK (**Figure 97A**), impedance decreases in a concentration-dependent manner. The greater the FSK concentration, the more pronounced the impedance decrease. Only the largest FSK concentration (**Figure 97A, black**) behaves differently and displays two minima: a first minimum at  $t = 0.04$  h and a second minimum at  $t = 0.29$  h. For  $3 \mu\text{M}$  FSK (**Figure 97A, red**), the largest change in impedance is detected with a minimum of about  $-150 \Omega$  at  $t = 0.29$  h. Before histamine addition, impedance plateaus for concentrations between the CTRL and  $1 \mu\text{M}$  FSK (**Figure 97A, green, blue, cyan, pink, yellow, brown**). Immediately after histamine addition, impedance peaks and strongly increases to reach a maximum between  $t = 0.8$ - $1$  h (**Figure 97C**). The maxima are more pronounced and time-delayed as the FSK concentration decreases. For instance, the vehicle-treated cells show a maximum of  $(1300 \pm 20) \Omega$  after  $t = 0.98$  h (**Figure 97C, brown**) and for  $10 \text{ nM}$  FSK, a maximum of  $(1200 \pm 40) \Omega$  after  $t = 0.97$  h is observed (**Figure 97C, yellow**). In contrast, the maximum for the highest concentration of  $10 \mu\text{M}$  FSK amounts to  $(1090 \pm 20) \Omega$  at  $t = 0.81$  h (**Figure 97C, black**). The curves between  $30 \text{ nM}$  and  $10 \mu\text{M}$  FSK mostly overlay after histamine addition (**Figure 97C, black, red, green, blue, cyan, pink**).

The curves for 8-CPT-cAMP behave differently (**Figure 97B**). After addition of the 8-CPT-cAMP dilutions, a  $50$ - $80 \Omega$  decrease in impedance is observed for concentrations between the CTRL and  $100 \mu\text{M}$  8-CPT-cAMP (**Figure 97B red, green, blue, cyan, pink, yellow, brown**). For the largest concentration of  $500 \mu\text{M}$  8-CPT-cAMP (**Figure 97B, black**), a more pronounced decrease of about  $140 \Omega$  is observed. For all concentrations, impedance plateaus after  $t = 0.1$  h. When a histamine concentration of  $2 \mu\text{M}$  is added, a small positive peak is visible for each condition followed by a steady increase of impedance until a maximum is reached after  $t = 0.9$ - $1$  h (**Figure 97D**). All maximal values vary between  $1125$ - $1375 \Omega$  with an average impedance maximum of about  $1300 \Omega$ .

A small concentration-dependent decrease of impedance is observed after the addition of different FSK concentrations (**Figure 97A**), while for 8-CPT-cAMP (**Figure 97B**), the impedance decrease was similar for all investigated concentrations. Only the largest FSK and 8-CPT-cAMP concentrations behaved differently (**Figure 97A-B, black**). This might be attributed to effects, occurring above a certain limiting concentration. For instance, FSK is known to also indirectly mediate AC activation by  $G_s$ -coupled receptors (Hill et al., **2010**, Insel, Ostrom, **2003**), which could lead to a different impedance outcome at high FSK concentrations. 8-CPT-cAMP was identified as a ligand for epithelial sodium channels (Ji et al., **2016**) and, thus, might

trigger different mechanisms depending on the utilized concentration as well. However, the impedance change after FSK and 8-CPT-cAMP addition was not significant in contrast to the histamine addition (**Figure 97C-D**). The slight decrease in impedance after FSK and 8-CPT-cAMP addition is explained by morphological changes (Wolf et al., **2008**). FSK has previously been described as a substance that leads to a rounder shape of an interconverted neuroblastoma cell line (Dong et al., **1998**). Moreover, similar impedance responses were detected for CHO cells in previous studies (cf. **chapter 6**, (Skiba et al., **2022**, Skiba, **2022**)), leading to the conclusion that the  $G_s$ -pathway leads to a decrease in impedance by actin depolymerization (Vázquez-Victorio et al., **2016**). This was confirmed by impedance measurements of several other GPCRs that are predominantly  $G_s$ -coupled (Scott, Peters, **2010**, Skiba, **2022**, Verdonk et al., **2006**) but gives rise to the question which signaling pattern is induced by histamine. Contrary to FSK and 8-CPT-cAMP, a huge impedance increase, which is comparable to values obtained in another experiment without FSK or 8-CPT-cAMP addition (**Appendix 25**), is observed after histamine addition and presumably AC activation (**Figure 97C-D**). One possible explanation could be that other pathways but the  $G_s$ -pathway might influence the impedance response of histamine acting at the H2R. Since an increase in the cAMP concentration provokes a negative impedance change as shown by FSK and 8-CPT-cAMP (**Figure 97A-B**), the contribution of the  $G_s$ -pathway to the impedance signal after histamine addition might be suppressed and overlaid by another pathway with an opposite and much greater impact on the cells' morphology. Potential pathways that were identified for the H2R in literature before are the  $G_q$ -,  $G_i$  and  $\beta$ -arrestin pathways (Felixberger, **2016**, Hörung et al., **2021**, Kühn et al., **1996**, Tropmann et al., **2020**, Wellner-Kienitz et al., **2003**). They will be further investigated in **chapters 5.1.2, 5.2 and 5.3**.

### 5.1.2 Inhibition of the $G_s$ -Pathway with Cholera Toxin

CTX leads to irreversible adenosine diphosphate (ADP) ribosylation of the  $G_s$  protein, forcing the protein to remain in its active state (Wernick et al., **2010**). Therefore, the  $G_s$ -pathway is entirely blocked. To clarify whether the impedance response of HEK H2R cells after histamine addition potentially refers to the activation of other GPCR signaling pathways (cf. **chapter 5.1.1**), an experiment with the  $G_s$ -pathway inhibitor CTX was performed. HEK H2R cells were seeded on a crosslinked gelatin-coated 96W1E+ array as described in **chapter 3.5.3.1**. On the day of the experiment, the medium was exchanged with L15 buffer, the cells were equilibrated at 0% (v/v)  $CO_2$

and 37°C for 2-2.5 h and an impedance baseline was recorded at a frequency of 12 kHz (ECIS Z $\theta$ ). At  $t = -0.2$  h, a CTX control and three different CTX concentrations between 1-100 ng/mL were added and incubated with the cells for 0.2 h. Then, a histamine vehicle control CTRL and seven histamine concentrations between 10 nM and 100  $\mu$ M were added and impedance was monitored for 1 h. The results are given in **Figure 98A-D** for the different CTX concentrations.

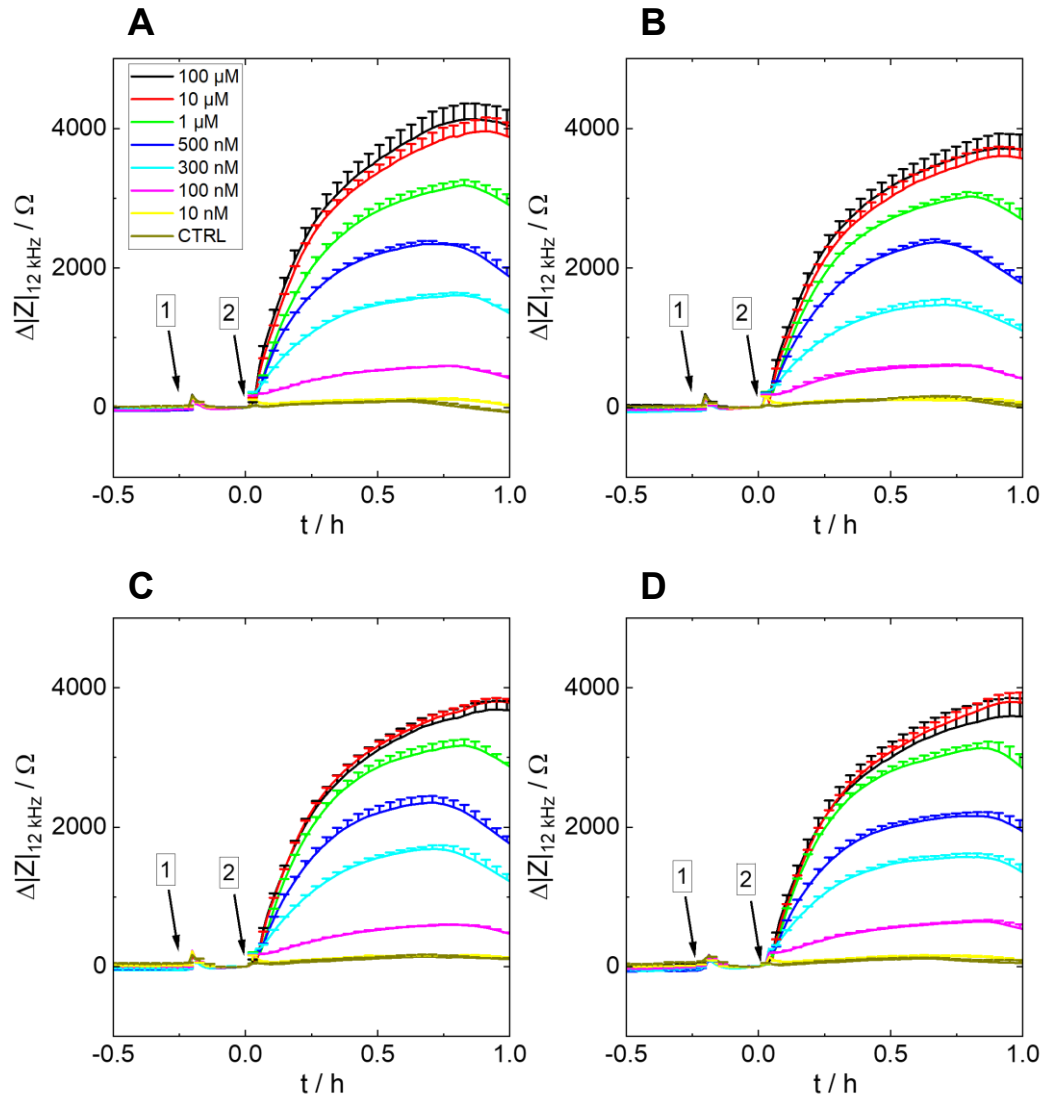


**Figure 98.** Impedance change over time of **HEK H2R** cells at a frequency of 12 kHz. The cells were cultivated on a 96W1E+ electrode array that was coated with crosslinked gelatin. At  $t = -0.2$  h (arrow 1), the cells were incubated with **different CTX concentrations (A: CTX control, B: 1 ng/mL, C: 10 ng/mL, D: 100 ng/mL)**. Subsequently, at  $t = 0$  h (arrow 2), the cells were stimulated with different **histamine concentrations**. Black 100  $\mu$ M, red 10  $\mu$ M, green 1  $\mu$ M, blue 500 nM, cyan 300 nM, pink 100 nM, yellow 10 nM, brown CTRL. Baseline from A to D:  $(4304 \pm 7) \Omega$ ,  $(4158 \pm 6) \Omega$ ,  $(4192 \pm 6) \Omega$ ,  $(4229 \pm 7) \Omega$ . Mean + SE,  $N = 3$ , single experiment. CTRL = histamine vehicle control. Temperature: 37°C.

After the addition of increasing concentrations of CTX (CTX control, 1 ng/mL, 10 ng/mL, 100 ng/mL), a small positive peak of about 160  $\Omega$  emerges in all four cases but rapidly returns to the baseline level within 0.1 h (**Figure 98A-D**). When histamine is added, no significant differences in the time courses are observed between the four CTX treatment conditions. Impedance rises in a concentration-dependent manner and reaches a maximum after  $t = 0.5-0.75$  h after which impedance slowly drops off again for histamine concentrations between 100 nM and 1  $\mu$ M (**Figure 98A-D, green, blue, cyan, pink**). Only the curves for the CTRL and 10 nM histamine remain at the baseline level throughout the experiment (**Figure 98A-D, yellow, brown**). The curves for 100  $\mu$ M and 10  $\mu$ M histamine overlay and display the largest impedance values (**Figure 98A-D, black, red**).

Concentration-response curves were generated by evaluation of the time point  $t = 0.5$  h. The impedance data at this time point was plotted against the logarithmic histamine concentration and fitted by a four-parametric dose-response fit (**equation 15**).  $pEC_{50}$  and  $E_{max}$  values were determined from the point of inflection and upper asymptote. The fit data is depicted in **Figure 99** for the different CTX treatment conditions.

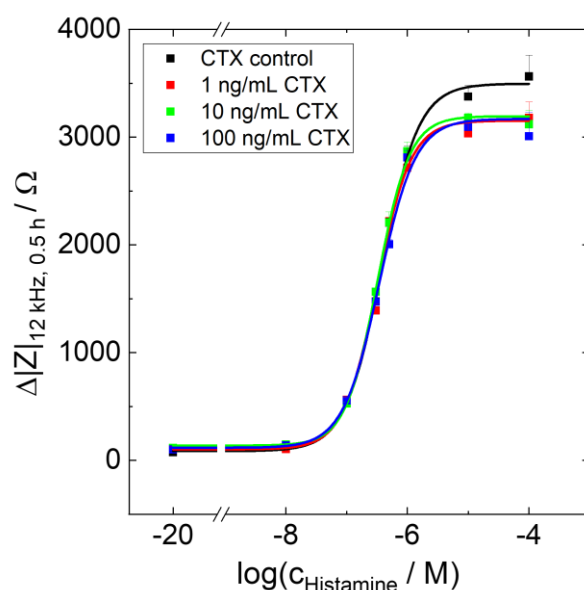


**Figure 99.** Concentration-response curves of **HEK H2R** cells after incubation with a **CTX control (black) or with 1 ng/mL (red), 10 ng/mL (green) or 100 ng/mL (blue) CTX** and subsequent stimulation with different concentrations of **histamine**. The impedance data at a frequency of 12 kHz and 0.5 h after stimulation (squares) is plotted as a function of the histamine concentration and was extracted from **Figure 98A-D**. The dose-response fits (solid lines) reveal  $pEC_{50}$  values of  $6.42 \pm 0.03$  for the CTX control,  $6.50 \pm 0.04$  for 1 ng/mL CTX,  $6.49 \pm 0.01$  for 10 ng/mL CTX and  $6.46 \pm 0.03$  for 100 ng/mL CTX. The  $E_{max}$  values lie at  $(3500 \pm 100) \Omega$ ,  $(3200 \pm 100) \Omega$ ,  $(3190 \pm 30) \Omega$  and  $(3200 \pm 100) \Omega$  in the same order. Mean + SE,  $N = 3$ , single experiment. Temperature: 37°C.

In general, the impedance at  $t = 0.5$  h increases with increasing histamine concentration, independent of the used CTX concentration (**Figure 99**). The values for 10 nM histamine are at the same level as the values of the histamine CTRL. Furthermore, the values for 100  $\mu$ M and 10  $\mu$ M histamine are similar and saturation is observed. There are no differences between the concentration-response curves in the presence of increasing concentrations of CTX (**Figure 99, red, green, blue**). Only the curve for the CTX control shows higher impedance values for 10-100  $\mu$ M histamine compared to the curves in the presence of CTX. However, the differences are not significant as was confirmed by Tukey's significance test (**Figure 99, black**). With increasing CTX concentration, pEC<sub>50</sub> values of  $6.42 \pm 0.03$  (control, **Figure 99, black**),  $6.50 \pm 0.04$  (1 ng/mL, **Figure 99, red**),  $6.49 \pm 0.01$  (10 ng/mL, **Figure 99, green**) and  $6.46 \pm 0.03$  (100 ng/mL, **Figure 99, blue**) were determined. The  $E_{\max}$  values lie at  $(3500 \pm 100)$   $\Omega$ ,  $(3200 \pm 100)$   $\Omega$ ,  $(3190 \pm 30)$   $\Omega$  and  $(3200 \pm 100)$   $\Omega$  in the same order. Consequently, both the pEC<sub>50</sub> as well as the  $E_{\max}$  values are comparable between the four CTX treatment conditions.

Compared to the impedance time courses observed in **chapter 5.1.1** and **Appendix 25**, 3-4 times larger impedance changes are observed in **Figure 98A-D** after stimulation of HEK H2R cells with 1-2  $\mu$ M histamine. Furthermore, no initial impedance decrease is observed after histamine addition in **Figure 98A-D**. These findings are hard to interpret but might be attributed to variances in the seeding density as observed by the values of the baseline impedance. Furthermore, the cellular behavior might change with the passage number and thawing cycle and the coherent receptor expression, which is often declared as system bias (Kolb et al., **2022**).

As no significant effect on impedance was observed in the presence of different CTX concentrations (**Figure 98A-D**), it is suggested that the impedance profile of HEK H2R cells after histamine addition is not generated by G<sub>s</sub>-signaling but by other downstream processes. This is also confirmed by the unchanged pEC<sub>50</sub> and  $E_{\max}$  values. In contrast, a dynamic mass redistribution (DMR) assay of HEK H2R cells, which were pretreated with the same CTX concentrations as in **Figure 98A-D** and stimulated with 10  $\mu$ M histamine, revealed an impact of CTX on the DMR response (Seibel-Ehlert et al., **2021**). Nonetheless, the suppression of the DMR response of HEK H2R cells by CTX (compared to other histaminergic receptors) was lower than expected. The authors suggest an involvement of other signaling pathways such as the G $\alpha_z$ - and G $\alpha_{12/13}$ -pathway and could exclude an impact of the G<sub>q</sub>-pathway on the DMR response by using the G<sub>q</sub>-inhibitor FR.

As further literature suggests,  $G_q$ -,  $G_i$ - or  $\beta$ -arrestin2-signaling (Felixberger, **2016**, Fernández et al., **2017**, Höring et al., **2021**, Kühn et al., **1996**, Tropmann et al., **2020**, Wellner-Kienitz et al., **2003**) or mechanisms mediated by extracellular signal-regulated kinases 1/2 (ERK1/2) (Fernández et al., **2017**) might be the explanation for the change of the impedance of HEK H2R cells after histamine addition. The impact of the  $G_q$ -pathway (in terms of calcium mobilization) and  $\beta$ -arrestin2 recruitment on the impedance signal of HEK H2R cells will be further investigated in the **chapters 5.2 and 5.3**.

### 5.1.3 Imitation of the $G_q$ -Pathway and Calcium Ion Signaling with Calcimycin

Calcimycin (also called A23187) is a calcium ionophore that leads to increased intracellular calcium ion levels by transporting calcium ions across the plasma membrane and, hence, mimics  $G_q$  downstream signaling (Hutchinson et al., **2008**, Kao et al., **2010**, Sobotka et al., **1987**). In this chapter, the impedance signal of the cell line HEK M1R/ $mG_q$  after stimulation with carbachol was compared to the impedance signal after the addition of the calcium ionophore calcimycin. Since the M1R predominantly couples to  $G_q$  proteins (Maeda et al., **2019**), phospholipase C (PLC) is activated, triggering a calcium ion release from the endoplasmic reticulum (ER). Increased intracellular calcium ion concentrations are often described as the reason for impedance changes after GPCR stimulation since calcium modifies actin filament polymerization (Bennett, Weeds, **1986**, Lehne, Bogdan, **2023**, Pollard, **2016**, Vázquez-Victorio et al., **2016**). Calcimycin also leads to increased intracellular calcium ion levels by binding extracellular calcium ions in a 2:1 ratio (2  $Ca^{2+}$  ions per calcimycin molecule) and transporting them across the plasma membrane.

In the following experiment, HEK M1R/ $mG_q$  cells were seeded with a density of  $3 \cdot 10^5$  c/cm<sup>2</sup> on a crosslinked gelatin-coated 96W1E+ array. After a cultivation time of two days, the medium was exchanged with L15 buffer and the cells were equilibrated to the new conditions for 2-2.5 h. An impedance baseline was recorded at 12 kHz for 0.15 h (ECIS Z). Subsequently, 10  $\mu$ M and 1  $\mu$ M carbachol and 10  $\mu$ M and 1  $\mu$ M calcimycin were added. Impedance was measured for 1 h and is given in **Figure 100**.

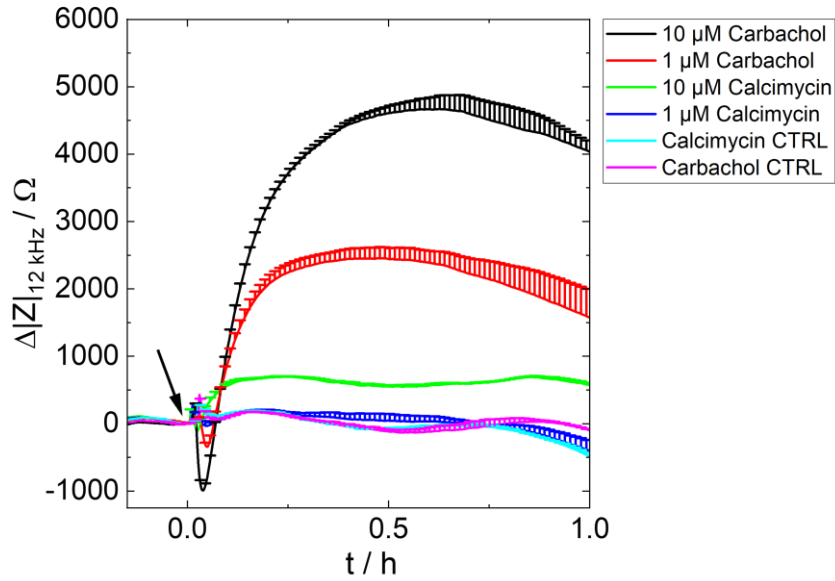


Figure 100. Impedance change of **HEK M1R/mG<sub>q</sub>** cells on a crosslinked gelatin-coated 96W1E+ array. After a baseline recording for 0.15 h, different concentrations of **carbachol** and **calcimycin** were added at  $t = 0$  h. Black 10  $\mu\text{M}$  carbachol, red 1  $\mu\text{M}$  carbachol, green 10  $\mu\text{M}$  calcimycin, blue 1  $\mu\text{M}$  calcimycin, cyan calcimycin CTRL, pink carbachol CTRL. Baseline:  $(7260 \pm 20)$   $\Omega$ . Mean + SE,  $N = 2-3$ , single experiment. CTRL = vehicle control. Temperature: 37°C.

For both vehicle controls and 1  $\mu\text{M}$  calcimycin (**Figure 100, blue, cyan, pink**), impedance remains at the baseline level over a period of 1 h. Upon the addition of 10  $\mu\text{M}$  and 1  $\mu\text{M}$  carbachol (**Figure 100, black, red**) and 10  $\mu\text{M}$  calcimycin (**Figure 100, green**), impedance immediately decreases with a concentration-dependent decrease in impedance observed for carbachol. The decrease in impedance for 10  $\mu\text{M}$  calcimycin amounts to about 100  $\Omega$  (**Figure 100, green**) while the same concentration of carbachol generates a reduction of about 900  $\Omega$  (**Figure 100, black**). Thereafter, impedance increases for 10  $\mu\text{M}$  and 1  $\mu\text{M}$  carbachol and 10  $\mu\text{M}$  calcimycin. The curve for 10  $\mu\text{M}$  calcimycin reaches a stable level of  $(630 \pm 30)$   $\Omega$  after 0.13 h (**Figure 100, green**). This value is kept over a measurement period of 1 h. Compared to calcimycin, carbachol concentrations of 10  $\mu\text{M}$  and 1  $\mu\text{M}$  evoke larger maximal values of  $(4700 \pm 200)$   $\Omega$  for 10  $\mu\text{M}$  carbachol and  $(2500 \pm 200)$   $\Omega$  for 1  $\mu\text{M}$  carbachol after  $t = 0.62$  h and  $t = 0.49$  h, respectively (**Figure 100, black, red**). Here, the impedance signal shows a slow decline over the measurement period.

For a better comparison between carbachol and calcimycin, the impedance data points after  $t = 0.5$  h were extracted and compared in **Figure 101**.

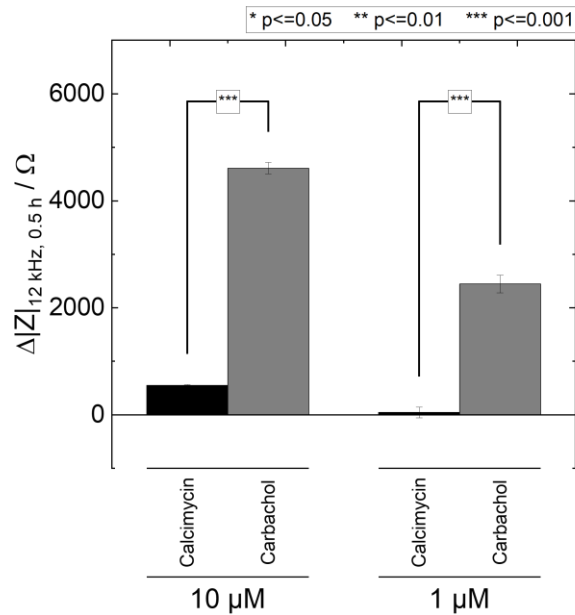


Figure 101. Impedance change of **HEK M1R/mG<sub>q</sub>** cells seeded on a crosslinked gelatin-coated 96W1E+ array 0.5 h after stimulation with 10 μM and 1 μM of **calcimycin (black)** and 10 μM and 1 μM of **carbachol (grey)**. The data was extracted from **Figure 100**. Statistical significance (\*) was assessed with Tukey's range test. Mean ± SE, N = 2-3, single experiment. Temperature: 37°C.

The impedance values at t = 0.5 h of calcimycin and carbachol are significantly different (**Figure 101**, \*\*\*,  $p \leq 0.001$ ). A concentration of 10 μM carbachol ((4600 ± 100) Ω) exhibits 8-fold larger values than 10 μM calcimycin ((550 ± 20) Ω). For a concentration of 1 μM, even 56-fold larger impedance values are observed for carbachol ((2400 ± 200) Ω) compared to calcimycin ((44 ± 99) Ω).

The impedance decrease after GPCR ligand addition is often justified by the activation of the G<sub>q</sub>-pathway and subsequent calcium ion immobilization (Denelavas et al., **2011**, Scott, Peters, **2010**, Verdonk et al., **2006**). Since calcimycin, which increases intracellular calcium levels, also provokes a decrease in impedance immediately after addition (**Figure 100**), this hypothesis is further substantiated.

Equal concentrations of the predominantly G<sub>q</sub>-coupled ligand carbachol and the calcium ionophore calcimycin do not show similar impedance magnitudes with respect to the initial decrease of impedance or the impedance maximum. However, it must be noted that both molecules induce different mechanisms. While carbachol leads to a calcium burst out of the ER after G<sub>q</sub> activation, calcimycin generates a calcium influx from the extracellular space until the intracellular and extracellular calcium concentrations are equilibrated (ie.vwr.com; **August 10, 2024**).

Consequently, equal concentrations of carbachol and calcimycin are not expected to lead to the same impedance outcome.

Nonetheless, according to the similar impedance profiles of HEK M1R/mG<sub>q</sub> cells after carbachol and calcimycin addition, it is possible that part of the impedance signal after carbachol addition indeed arises from (m)G<sub>q</sub>- and calcium ion signaling (Grogan et al., **2023**). Nonetheless, other signaling pathways can not be excluded and must be studied more profoundly to unravel the carbachol-induced impedance signal. For instance, calcium ion signaling of HEK M1R/mG<sub>q</sub> after carbachol addition will be further investigated in **chapter 5.2** to confirm the results found here. In addition,  $\beta$ -arrestin2 recruitment is assayed in **chapter 5.3** since it is considered another important signaling pathway for the M1R (Wang et al., **2023**).

## 5.2 Calcium Second Messenger Assay

Second messengers are small ions or molecules that are released inside a cell after ligand-receptor interactions at the cell surface (ligand = first messenger). In resting cells, the second messenger concentration is usually low but quickly rises if an external stimulus is present. Typical second messengers are cAMP, calcium ions (Ca<sup>2+</sup>), inositol 1,4,5-trisphosphate (IP<sub>3</sub>) and diacylglycerol (DAG) (Guo et al., **2022**, Newton et al., **2016**). Since second messengers are often released after GPCR stimulation, they are of major importance for medicinal chemistry and are deployed as analytes in several functional assays to clarify underlying GPCR signaling patterns and mechanisms. In this work, a fluorescence-based calcium ion assay was utilized to elucidate the previously described impedance signals of HEK M1R/mG<sub>q</sub> and HEK H2R (see **chapter 5.1**).

As described in **chapter 3.7.1**, both HEK cell lines were seeded with a density of  $1.18 \cdot 10^5$  c/cm<sup>2</sup> on poly-D-lysine coated black 96-well plates with transparent bottom. After a cultivation time of one day, the cells were loaded with the calcium ion-sensitive fluorophore fluo-4 AM for (45 ± 5) min. Then the plate was washed with HEPES-buffered saline (HBS) containing bovine serum albumin (BSA) and probenecid and was equilibrated in the same buffer for 10-20 min. After a 15 s baseline recording with the Flexstation 3 fluorescence reader, different ligands in the respective buffer were added and fluorescence was recorded for 90 s. The fluorescence time courses for HEK M1R/mG<sub>q</sub> and HEK H2R cells are given in **Figure 102A-D** and **Figure 104A-D**, respectively. For comparison, the same ligands were tested on HEK wt cells known

to endogenously express G<sub>q</sub>-coupled histaminergic and muscarinic receptors (cf. **Figure 106** and **Figure 107**) (Atwood et al., 2011, Meisenberg et al., 2015).

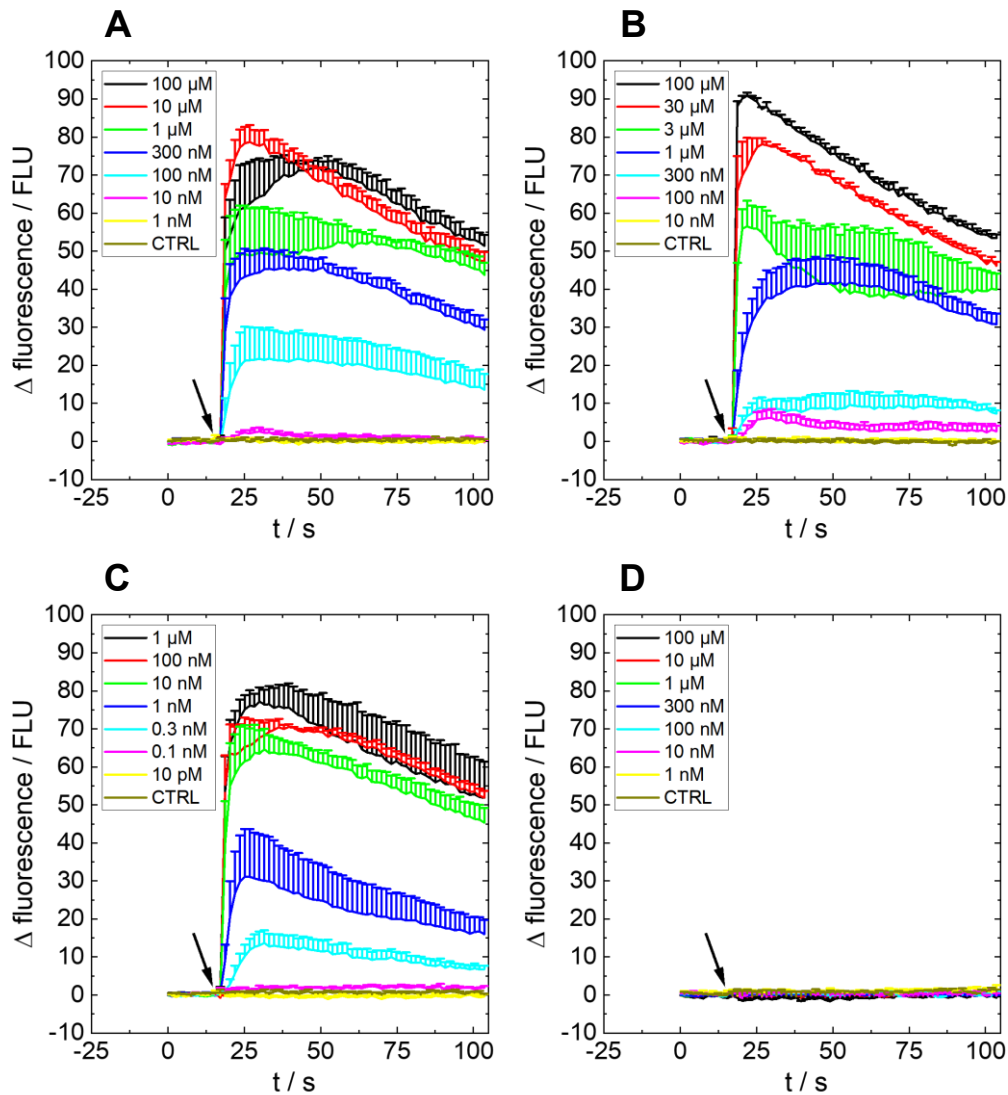


**Figure 102.** Calcium-induced fluorescence change of **HEK M1R/mG<sub>q</sub>** cells over time after incubation with the fluo-4 AM dye and stimulation with different concentrations of **acetylcholine (A)**, **carbachol (B)**, **iperoxo (C)** and **histamine (D)**. A and D: black 100 μM, red 10 μM, green 1 μM, blue 300 nM, cyan 100 nM, pink 10 nM, yellow 1 nM, brown CTRL. B: black 100 μM, red 10 μM, green 1 μM, blue 300 nM, cyan 100 nM, pink 10 nM, yellow 1 nM, brown CTRL. C: black 1 μM, red 100 nM, green 10 nM, blue 1 nM, cyan 0.3 nM, pink 0.1 nM, yellow 10 pM, brown CTRL. Mean + SE, N = 3-4, single experiment. CTRL = vehicle control. FLU = fluorescence units. Temperature: 37°C.

For HEK M1R/mG<sub>q</sub> cells, fluorescence rises from a baseline that fluctuates around zero to a maximum immediately after the addition of acetylcholine (1 nM to 100 μM, **Figure 102A**), carbachol (10 nM to 100 μM, **Figure 102B**) and iperoxo (10 pM to 1 μM, **Figure 102C**) in a concentration-dependent manner. After reaching the maximum, fluorescence gradually decreases over a time span of 75 s. For a concentration of 1 μM, the fluorescence maxima amount to (50 ± 10) FLU for

acetylcholine (**Figure 102A, green**), ( $34 \pm 7$ ) FLU for carbachol (**Figure 102B, blue**) and ( $76 \pm 4$ ) FLU for iperoxo (**Figure 102C, black**). The curves for 1-10 nM acetylcholine (**Figure 102A, pink, yellow**), 10 nM carbachol (**Figure 102B, yellow**) and 10 pM and 0.1 nM iperoxo (**Figure 102C, pink, yellow**) superimpose with the curves of the vehicle controls (CTRL) (**Figure 102A-C, brown**), which remain at the baseline level. If histamine (1 nM to 100  $\mu$ M, **Figure 102D**) is added to HEK M1R/mG<sub>q</sub> cells, no response is visible and fluorescence remains close to zero.

From the time courses, concentration-response curves were generated by analyzing the fluorescence maxima relative to the fluorescence maximum of 100  $\mu$ M acetylcholine. The concentration-response plots of acetylcholine, carbachol, iperoxo and histamine are depicted in **Figure 103**.

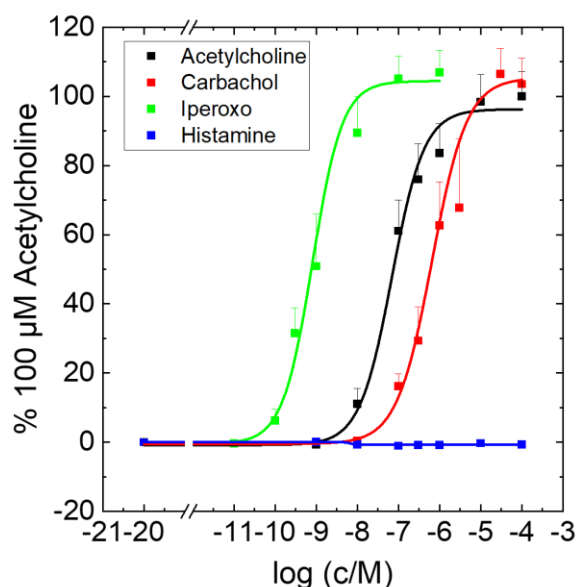


*Figure 103. Concentration-response curves of HEK M1R/mG<sub>q</sub> cells after stimulation with different ligands (black acetylcholine, red carbachol, green iperoxo, blue histamine). The fluorescence data at the maximum relative to the fluorescence maximum of 100  $\mu$ M acetylcholine (squares) is plotted as a function of the ligand concentration. The dose-response fits (solid lines) reveal pEC<sub>50</sub> values of  $7.2 \pm 0.1$  for acetylcholine,  $6.2 \pm 0.1$  for carbachol and  $9.1 \pm 0.1$  for iperoxo. The respective  $R_{max}$  values are  $(96 \pm 4)\%$  for acetylcholine,  $(105 \pm 5)\%$  for carbachol and  $(104 \pm 4)\%$  for iperoxo. For histamine, no pEC<sub>50</sub> or  $R_{max}$  value could be determined. Mean + SE, N = 9-14, three or four independent experiments. Temperature: 37°C.*

Histamine does not show any response (**Figure 103, blue**). All other ligands feature well-fitted concentration-response curves with iperoxo (**Figure 103, green**) being the most potent ligand followed by acetylcholine (**Figure 103, black**) and carbachol (**Figure 103, red**). The fluorescence signals increase with increasing ligand concentrations and saturate above 10  $\mu$ M acetylcholine, 30  $\mu$ M carbachol and 100 nM iperoxo, respectively. Potencies, in the form of pEC<sub>50</sub> values, of  $7.2 \pm 0.1$  for acetylcholine,  $6.2 \pm 0.1$  for carbachol and  $9.1 \pm 0.1$  for iperoxo were determined. The

$R_{\max}$  values are  $(96 \pm 4)\%$ ,  $(105 \pm 5)\%$  and  $(104 \pm 4)\%$  in the same order. In **chapter 4.2.1**, smaller  $pEC_{50}$  values of  $5.55 \pm 0.06$  and  $8.39 \pm 0.06$  were determined for carbachol and iperoxo in an impedance assay. The  $E_{\max}$  values of impedance were very similar for both ligands with values of  $(5340 \pm 90) \Omega$  for carbachol and  $(5400 \pm 100) \Omega$  for iperoxo. In the miniG recruitment assay (cf. **chapter 4.3**),  $pEC_{50}$  values of  $4.4 \pm 0.3$  for carbachol and  $8.14 \pm 0.06$  for iperoxo were found. The  $E_{\max}$  values showed larger differences here with  $(1400 \pm 300)$  BLU for carbachol and  $(2300 \pm 100)$  BLU for iperoxo.

In an equivalent experiment, the calcium-induced fluo-4 signals of HEK H2R cells after the addition of acetylcholine, carbachol, iperoxo and histamine were investigated. They are given in **Figure 104A-D**.

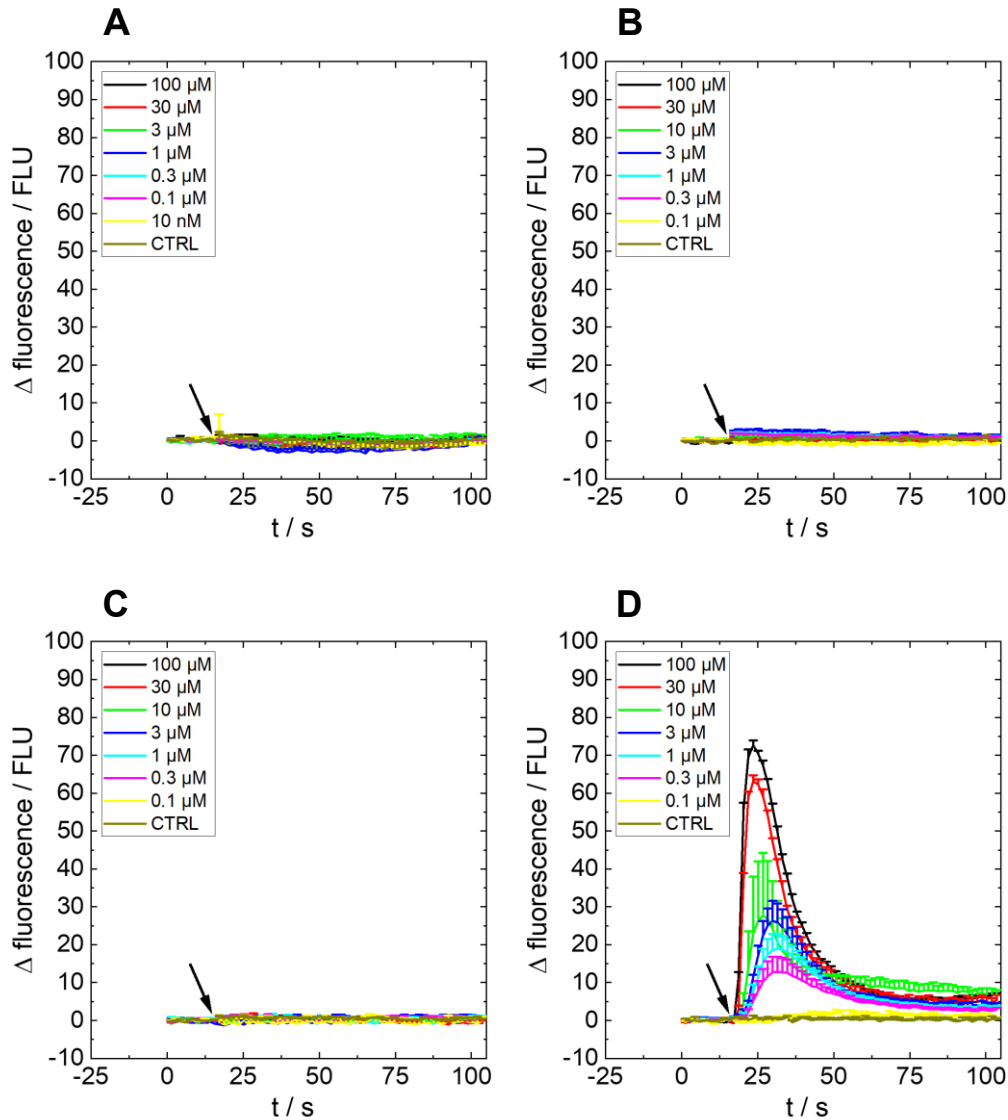
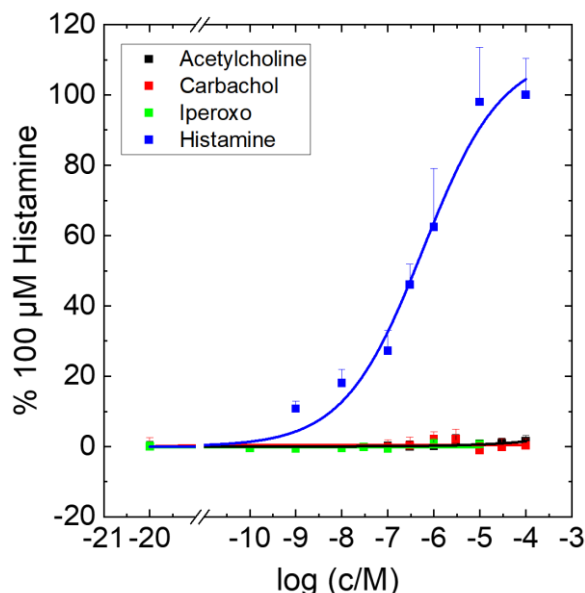


Figure 104. Calcium-induced fluorescence change of **HEK H2R** cells over time after incubation with the fluo-4 AM dye and stimulation with different concentrations of **acetylcholine (A)**, **carbachol (B)**, **iperoxo (C)** and **histamine (D)**. A: black 100 μM, red 30 μM, green 3 μM, blue 1 μM, cyan 0.3 μM, pink 0.1 μM, yellow 10 nM, brown CTRL. B, C and D: black 100 μM, red 30 μM, green 10 μM, blue 3 μM, cyan 1 μM, pink 0.3 μM, yellow 0.1 μM, brown CTRL. Mean + SE, N = 3, single experiment. CTRL = vehicle control. FLU = fluorescence units. Temperature: 37°C.

In the case of HEK H2R cells, only histamine (0.1-100 μM, **Figure 104D**) shows a significant and concentration-dependent fluorescence increase compared to the baseline level (around zero). Neither acetylcholine (10 nM to 100 μM, **Figure 104A**) nor carbachol (0.1-100 μM, **Figure 104B**) or iperoxo (0.1-100 μM, **Figure 104C**) leads to an increased fluorescence of HEK H2R cells. In contrast to HEK M1R/mG<sub>q</sub> cells (**Figure 102A-C**), the fluorescence profile for HEK H2R cells after histamine addition is more transient: fluorescence quickly increases to a maximal value but rapidly decreases again within 25-30 s. The greatest fluorescence value is observed for 100 μM histamine with a maximum of (73 ± 1) FLU (**Figure 104D, black**).

Concentration-response curves were created by using relative maximal fluorescence values compared to the maximum fluorescence of 100  $\mu\text{M}$  histamine. The relative fluorescence data is plotted against the logarithmic ligand concentration and is fitted with a four-parametric dose-response fit (**equation 15**). The curves are given in **Figure 105** below.



*Figure 105. Concentration-response curves of HEK H2R cells after stimulation with different ligands (black acetylcholine, red carbachol, green iperoxo, blue histamine). The fluorescence data at the maximum relative to the fluorescence maximum of 100  $\mu\text{M}$  histamine (squares) is plotted as a function of the ligand concentration. The dose-response fit (solid line) reveals a  $p\text{EC}_{50}$  value of  $6.2 \pm 0.2$  for histamine. The respective  $R_{\text{max}}$  value of histamine is  $(110 \pm 10)\%$ . For acetylcholine, carbachol and iperoxo, no  $p\text{EC}_{50}$  or  $R_{\text{max}}$  value could be determined. Mean + SE,  $N = 9-13$ , three or four independent experiments. Temperature:  $37^\circ\text{C}$ .*

No concentration-response relationship was found for acetylcholine, carbachol or iperoxo (**Figure 105, black, red, green**). In contrast, histamine demonstrates a concentration-dependent response with a  $p\text{EC}_{50}$  of  $6.2 \pm 0.2$  and a  $R_{\text{max}}$  value of  $(110 \pm 10)\%$  (**Figure 105, blue**). Here, the relative fluorescence increases with increasing histamine concentration and saturates above 10  $\mu\text{M}$  of histamine. A sigmoidal curve shape is observed. A  $p\text{EC}_{50}$  of  $6.70 \pm 0.04$  was found in an impedance measurement of the same cell line stimulated with histamine as given in **Appendix 25**.

To exclude that the signals originate from endogenously expressed muscarinic and histaminergic receptors (Atwood et al., 2011, Meisenberg et al., 2015), HEK wt cells were tested with the four ligands as well. The time course and concentration-response data is given in **Figure 106** and **Figure 107**, respectively.

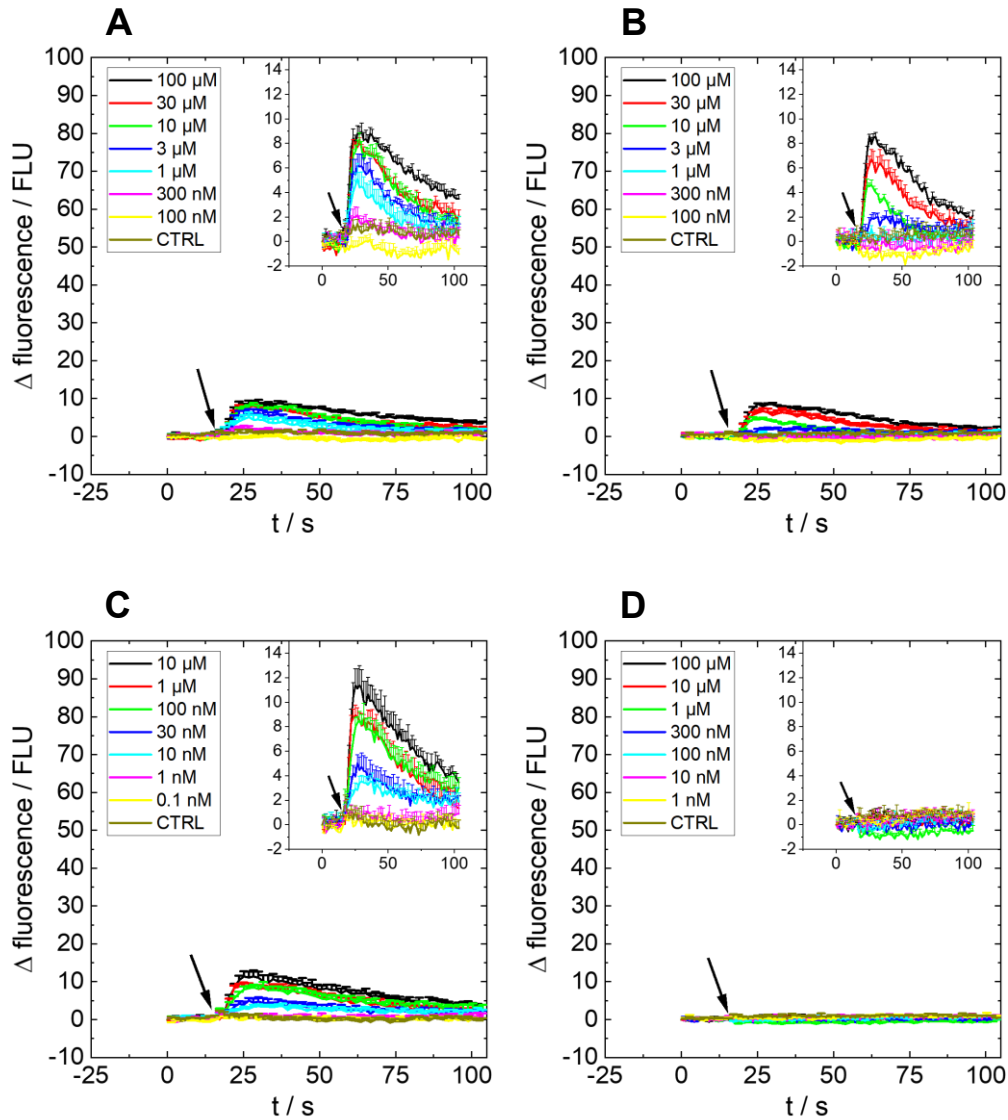
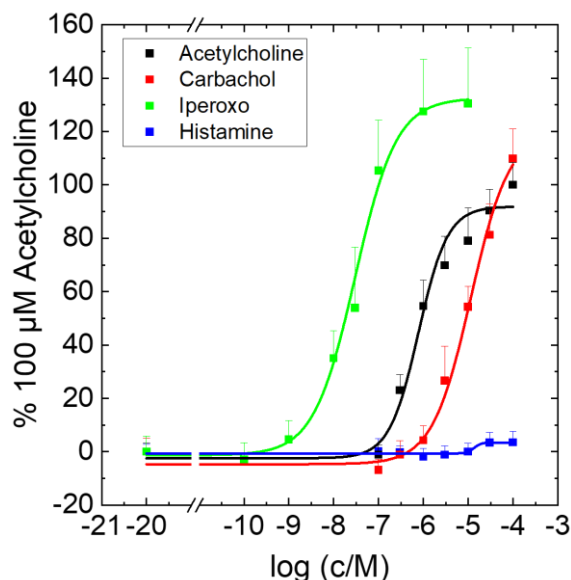


Figure 106. Calcium-induced fluorescence change of **HEK wt** cells over time after incubation with the fluo-4 AM dye and stimulation with different concentrations of **acetylcholine (A)**, **carbachol (B)**, **iperoxo (C)** and **histamine (D)**. A and B: black 100  $\mu\text{M}$ , red 30  $\mu\text{M}$ , green 10  $\mu\text{M}$ , blue 3  $\mu\text{M}$ , cyan 1  $\mu\text{M}$ , pink 300 nM, yellow 100 nM, brown CTRL. C: black 10  $\mu\text{M}$ , red 1  $\mu\text{M}$ , green 100 nM, blue 30 nM, cyan 10 nM, pink 1 nM, yellow 0.1 nM, brown CTRL. D: black 100  $\mu\text{M}$ , red 10  $\mu\text{M}$ , green 1  $\mu\text{M}$ , blue 300 nM, cyan 100 nM, pink 10 nM, yellow 1 nM, brown CTRL. Mean + SE,  $N = 4$ , single experiment. CTRL = vehicle control. FLU = fluorescence units. Temperature: 37°C.

As apparent from **Figure 106A-D**, concentration-dependent signals with maxima around 10 FLU are obtained for acetylcholine (100 nM to 100  $\mu\text{M}$ , **Figure 106A**), carbachol (100 nM to 100  $\mu\text{M}$ , **Figure 106B**) and iperoxo (0.1 nM to 10  $\mu\text{M}$ , **Figure 106C**), whereas histamine (1 nM to 100  $\mu\text{M}$ , **Figure 106D**) does not show any response. In comparison, HEK M1R/mG<sub>q</sub> cells exhibit about 9-fold larger fluorescence signals for acetylcholine, carbachol and iperoxo (**Figure 102A-C**). After reaching the maxima, fluorescence slowly decreases akin to HEK M1R/mG<sub>q</sub> cells.

Concentration-response curves were generated by calculating the ratio of the maximal fluorescence relative to the maximal fluorescence of 100  $\mu\text{M}$  acetylcholine. The data was plotted against the logarithmic ligand concentration and fitted by a four-parametric dose-response fit (**equation 15**). The corresponding results are given in **Figure 107**.



*Figure 107. Concentration-response curves of HEK wt cells after stimulation with different ligands (black acetylcholine, red carbachol, green iperoxo, blue histamine). The fluorescence data at the maximum relative to the fluorescence maximum of 100  $\mu\text{M}$  acetylcholine (squares) is plotted as a function of the ligand concentration. The dose-response fits (solid lines) reveal  $p\text{EC}_{50}$  values of  $6.1 \pm 0.1$  for acetylcholine,  $4.9 \pm 0.1$  for carbachol and  $7.52 \pm 0.08$  for iperoxo. The respective  $R_{\text{max}}$  values lie at  $(92 \pm 6)\%$ ,  $(120 \pm 10)\%$  and  $(133 \pm 6)\%$  in the same order. For histamine, no dose-response analysis was possible. Mean + SE,  $N = 9-15$ , three or four independent experiments. Temperature:  $37^\circ\text{C}$ .*

For acetylcholine (**Figure 107, black**), carbachol (**Figure 107, red**) and iperoxo (**Figure 107, green**), an increase in fluorescence with larger ligand concentration is observed. The only exceptions are the fluorescence values of 100 nM acetylcholine, 100 nM carbachol and 0.1 nM iperoxo, which resemble the values of the CTRL, respectively. Furthermore, saturation is observed for iperoxo concentrations above 1  $\mu\text{M}$ . In contrast, the curves for acetylcholine and carbachol constantly rise with increasing ligand concentration and no saturation behavior is observed. The concentration-response curve of histamine (**Figure 107, blue**) remains close to 0% over the entire concentration range. For histamine, neither a potency- nor an efficacy-determination was possible. The concentration-response curves of the other ligands reveal  $p\text{EC}_{50}$  values of  $6.1 \pm 0.1$  for acetylcholine,  $4.9 \pm 0.1$  for carbachol and  $7.52 \pm 0.08$  for iperoxo. The  $R_{\text{max}}$  values relative to the maximal fluorescence response of 100  $\mu\text{M}$  acetylcholine amount to  $(92 \pm 6)\%$ ,  $(120 \pm 10)\%$  and  $(133 \pm 6)\%$

in the same order. All three pEC<sub>50</sub> values are at least one order of magnitude smaller for HEK wt cells compared with HEK M1R/mG<sub>q</sub> cells.

Overall, four ligands were tested in the fluo-4 assay detecting changes in the intracellular calcium concentration (**Figure 102A-D** and **Figure 104A-D**). Since in HEK wt cells (**Figure 106A-C**) the muscarinic acetylcholine receptor agonists only caused a 10-15% response of the signals compared to HEK M1R/mG<sub>q</sub> cells (**Figure 102A-C**) and displayed smaller pEC<sub>50</sub> values, it is concluded that the endogenous M3R receptors do not have a significant impact on calcium ion signaling of HEK M1R/mG<sub>q</sub> cells (Atwood et al., **2011**, Meisenberg et al., **2015**). Likewise, this observation is confirmed by the stimulation of HEK H2R cells with muscarinic acetylcholine ligands (**Figure 104A-C**). Here, the fluorescence signals after acetylcholine, carbachol and iperoxo addition might be suppressed because of the overexpression of the H2R. This was also observed in literature before. Tubio *et al.* overexpressed the H2R in CHO cells and found less G<sub>s</sub>-coupling of endogenously expressed G<sub>s</sub>-coupled receptors in cAMP assays (Tubio et al., **2010**). It is suggested that histaminergic receptors neither play a role for HEK wt nor HEK M1R/mG<sub>q</sub> cells since no histamine response was detectable. Consequently, the histamine-induced calcium response of HEK H2R cells (**Figure 104D**) is fully attributed to the stimulation of H2R receptors instead of endogenously expressed H1R, H3R or H4R.

All other ligand-receptor combinations rendered signals that are explained by an increase in the endoplasmic calcium ion concentration (Mizuno, Itoh, **2009**). Whilst the G<sub>q</sub>-coupling of the M1R has been extensively studied and represents the canonical signaling pathway (**Figure 102A-C**) (Maeda et al., **2019**), the H2R is known to couple predominantly to G<sub>s</sub> proteins (Höring, **2022**, Seibel-Ehlert et al., **2021**). Still, an increase of the calcium concentration in HEK H2R cells after stimulation with the endogenous ligand histamine is observed (**Figure 104D**). This indicates that the H2R is partly G<sub>q</sub>-coupled (Höring et al., **2021**, Kühn et al., **1996**, Wellner-Kienitz et al., **2003**) or that downstream of the G<sub>s</sub>-pathway or other activated pathways, calcium ions transiently accumulate within the cytoplasm as was shown in literature before for G<sub>s</sub>- and G<sub>i</sub>-coupled systems (Dhyani et al., **2020**).

Comparing the potencies and efficacies at the M1R (**Figure 103**), iperoxo is most potent with a pEC<sub>50</sub> of  $9.1 \pm 0.1$ , followed by acetylcholine with  $7.2 \pm 0.1$  and carbachol with  $6.2 \pm 0.1$ . The value for iperoxo is larger compared to the ones determined in **chapters 4.2 and 4.3** ( $8.39 \pm 0.06$  and  $8.14 \pm 0.06$ ). The same is true for carbachol ( $5.55 \pm 0.06$  and  $4.4 \pm 0.3$ ). However, a similar value of 6.96 was found for carbachol acting at M1R transfected CHO K1 cells in a calcium assay (Pronin et

al., 2017). Moreover, the pEC50 of acetylcholine is similar to a value of  $7.1 \pm 0.1$  determined with an IP1 accumulation assay in CHO cells expressing an M1R modification (Bradley et al., 2018). The pEC50 of histamine at the H2R (**Figure 105**) takes values of  $6.2 \pm 0.2$  in the calcium assay,  $6.3 \pm 0.2$  in the impedance assay (**chapter 4.2**) and  $7.4 \pm 0.2$  in the miniG protein recruitment assay (**chapter 4.3**). Consequently, all pEC50 values vary depending on the utilized assay format and whether the readout parameter is at the receptor level (proximal) or more downstream of receptor activation (Schröder et al., 2010). The  $R_{\max}$  of iperoxo, carbachol and acetylcholine for HEK M1R/mG<sub>q</sub> cells are close to 100%. Thus, all ligands are considered full agonists in the calcium assay (**Figure 103**). When the efficacy values of iperoxo and carbachol from previous **chapters 4.2 and 4.3** are brought into the equation, it becomes obvious that more distal readouts (calcium, impedance) show similar efficacy values for carbachol and iperoxo. By contrast, in the proximal miniG protein recruitment assay, carbachol showed a 40% reduced  $E_{\max}$  compared to iperoxo. This can be explained by signal amplification along the triggered cascade and, in case of impedance, its integrative nature and has already been observed in resembling G protein and impedance assays with photochromic GPCR ligands before (Wirth et al., 2023).

At the M1R and H2R, the calcium signaling proceeds within seconds (**Figure 102A-C and Figure 104D**). This is in good agreement with the time scales found in literature, which vary between a few hundred milliseconds to seconds (Ma et al., 2017, Saxena et al., 2012). While the fluorescence signal at the M1R is more sustained (**Figure 102A-C**), the histamine response at the H2R is very transient (**Figure 104D**). This points towards varying kinetics at both receptors but is difficult to interpret. However, in both cases, a rise and fall of fluorescence to the baseline level is observed, indicating calcium mobilization and subsequent desensitization and signal degradation (Hoare et al., 2021). Comparing the kinetics of calcium mobilization with miniG protein recruitment and the impedance assay (**chapters 4.2 and 4.3**), the maximum calcium signal is reached approximately 10 s after ligand addition, while it takes about 0.13 h (468 s) to acquire the luminescence maximum in miniG protein recruitment and 0.025-0.075 h (90-270 s) to observe the first change of impedance (transient decrease). However, it should be noted that the miniG protein recruitment assay is the only assay without online addition of the ligand solutions. Furthermore, the time resolution of the miniG protein recruitment assay and the impedance assay are in a range of 50-56 s. If the miniG protein recruitment assay could be implemented in an online format and if the time resolutions of the miniG protein recruitment and impedance assay could be improved to reach a value  $\leq 10$  s, a potential superposition

of the calcium signal with the miniG protein signal and transient impedance increase could be unveiled allowing further insights into the sequence of signaling processes. In general, all agonist ligands that were investigated at the M1R (iperoxo, carbachol, acetylcholine) and H2R (histamine) provoked concentration-dependent calcium ion responses. Therefore, calcium mobilization is a possible explanation for the observed impedance signals (cf. **chapter 5.1**). Nonetheless, it is impossible to assign one particular G protein pathway to the respective ligand-GPCR system since increased calcium ion concentrations are generally observed for  $G_q$ -,  $G_i$ - and  $G_s$ -coupled systems (Dhyani et al., **2020**). Further to  $G_s$ - and  $G_q$ -signaling, arrestin recruitment may also contribute to the impedance response and will be addressed in **chapter 5.3**.

### 5.3 $\beta$ -Arrestin2 Recruitment Assay

Besides G protein-dependent signaling, there is also G protein-independent signaling often associated with GPCR kinases (GRK) or  $\beta$ -arrestin (Gurevich, Gurevich, **2019**, Jean-Charles et al., **2017**). The two ubiquitously expressed arrestins,  $\beta$ -arrestin1 and  $\beta$ -arrestin2, facilitate receptor desensitization and internalization after phosphorylation by GRKs in non-visual systems but also promote autonomous signaling. In this chapter, the impedance response of cells expressing the M1R or H2R was further clarified by a luminescence-based  $\beta$ -arrestin2 recruitment assay. Like the previously described miniG recruitment assay (see **chapter 4.3**), the  $\beta$ -arrestin2 assay uses the NanoBiT technology with LgBiT fused to the C-terminus of the receptor (M1R, H2R) and SmBiT linked to the N-terminus of  $\beta$ -arrestin2. If  $\beta$ -arrestin2 is recruited to the receptor, both NanoLuc fragments complement, NanoLuc oxidizes its luciferin furimazine and creates a bioluminescent signal.

To study  $\beta$ -arrestin2 recruitment at the M1R and H2R, HEK SmBiT  $\beta$ -Arr.2 cells were transiently transfected with plasmids encoding for the SNAP-M1R-LgBiT or SNAP-H2R-LgBiT according to **chapter 3.2.5**. One day before the experiment, the transfected cells were seeded with a density of  $1.18 \cdot 10^5$  c/cm<sup>2</sup> on white 96-well plates with transparent bottom that were coated with poly-D-lysine (for details see **chapter 3.6.1.2**). Before the measurement, the cells were washed with HBS containing BSA once and, subsequently, were equilibrated in the same buffer (agonist mode) or were incubated with antagonist solution (antagonist mode, M1R: pirenzepine, H2R: cimetidine). A 1/100 dilution of furimazine was added (final dilution of 1/600 relative to the stock solution; no molar concentration given by the manufacturer) and a luminescence baseline was recorded at the PHERAstar FS luminescence reader. Then, different agonist concentrations, i.e. carbachol (M1R)

and histamine (H2R), were added and the kinetic progress of bioluminescence was monitored for 0.5-1 h. As a control, the transfection with the SNAP-H2R-LgBiT construct was compared to a transfection with the precursor DNA (SNAP- $\beta$ 2AR-LgBiT) that is well studied in the group of Prof. Holliday (University of Nottingham, UK) and was kindly provided by Dr. Nicola Dijon (University of Nottingham, UK) (Dijon, **2022**).

In the following experiment (agonist mode), the transfected HEK  $\beta$ 2AR/ $\beta$ -Arr.2 and HEK H2R/ $\beta$ -Arr.2 cells were treated with a vehicle control (CTRL) or stimulated with the  $\beta$ 2AR agonist isoprenaline (also called isoproterenol, 1 nM to 10  $\mu$ M) and the endogenous H2R ligand histamine (1 nM to 10  $\mu$ M) to identify whether the obtained H2R construct still contains  $\beta$ 2AR DNA. The results are given in **Figure 108A-C** for HEK  $\beta$ 2AR/ $\beta$ -Arr.2 cells and in **Figure 109A-C** for HEK H2R/ $\beta$ -Arr.2 cells.

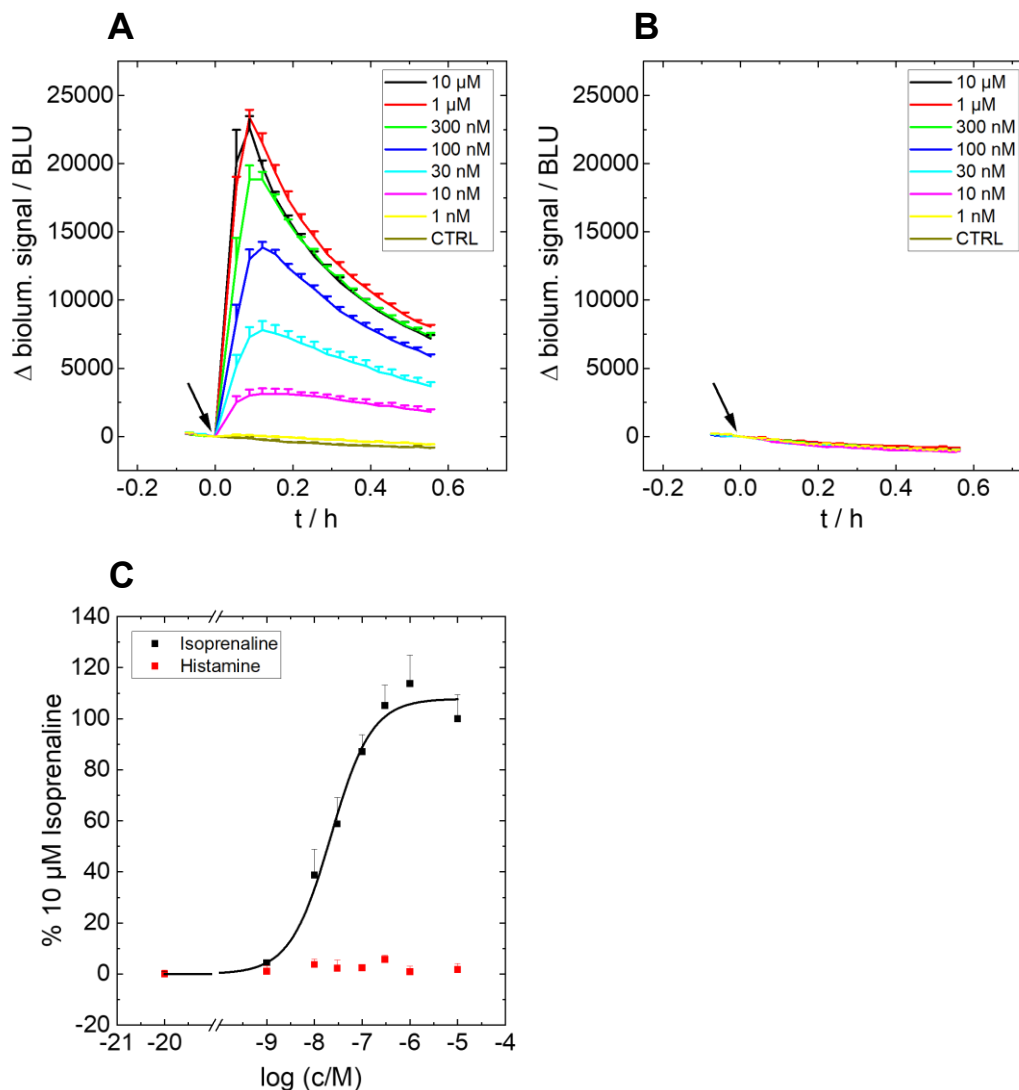


Figure 108. Luminescence change of transiently transfected **HEK  $\beta 2AR/\beta\text{-Arr.2}$**  cells. After a baseline recording with **furimazine** (final dilution of 1/600 relative to the stock solution; no molar concentration given by the manufacturer), at  $t = 0$  h, different concentrations of **isoprenaline (A)** or **histamine (B)** were added. Black 10  $\mu\text{M}$ , red 1  $\mu\text{M}$ , green 300 nM, blue 100 nM, cyan 30 nM, pink 10 nM, yellow 1 nM, brown CTRL. From the data at  $t = 0.5$  h relative to the data of 10  $\mu\text{M}$  isoprenaline at  $t = 0.5$  h, concentration-response curves were extracted (C). A four-parametric dose-response fit was applied (equation 15). A  $pEC_{50}$  value of  $7.66 \pm 0.09$  was determined for isoprenaline (black). For histamine (red), no  $pEC_{50}$  could be determined. Baseline A and B:  $(3110 \pm 40)$  BLU,  $(2970 \pm 40)$  BLU. Mean + SE,  $N = 3$ , single experiment. CTRL = vehicle control. BLU = bioluminescence units. Temperature:  $37^\circ\text{C}$ .

The HEK  $\beta 2AR/\beta\text{-Arr.2}$  cells show a distinct luminescence signal after isoprenaline stimulation (**Figure 108A**) but remain at the zero line when histamine is added (**Figure 108B**). The time course for isoprenaline reveals a concentration-dependent luminescence: the curves for the CTRL and 1 nM isoprenaline stay at the baseline level throughout the experiment (**Figure 108A**, yellow, brown). For larger isoprenaline concentrations (**Figure 108A**, black, red, green, blue, cyan, pink), luminescence increases concentration-wise and displays maxima between 0.08-

0.12 h. Thereafter, the signal decreases gradually. The curves for the two highest isoprenaline concentrations of 1  $\mu$ M and 10  $\mu$ M superimpose (**Figure 108, black, red**).

By analysis of the luminescence at  $t = 0.5$  h relative to the luminescence response of 10  $\mu$ M isoprenaline, concentration-response curves were extracted (**Figure 108C**). For histamine, no change of luminescence is observed over the investigated concentration range (**Figure 108C, red**). Consequently, no concentration-response analysis was possible. The luminescence after stimulation with isoprenaline first shows a constant behavior up to 1 nM, increases for concentrations up to 1  $\mu$ M and slightly decreases for the maximal concentration of 10  $\mu$ M isoprenaline (**Figure 108C, black**). A sigmoidal curve shape is observed, which reveals a pEC<sub>50</sub> of  $7.66 \pm 0.09$  and a R<sub>max</sub> of  $(108 \pm 5)\%$  for isoprenaline.

Below, the data for HEK H2R/ $\beta$ -Arr.2 cells after stimulation with isoprenaline and histamine is depicted (**Figure 109A-C**).

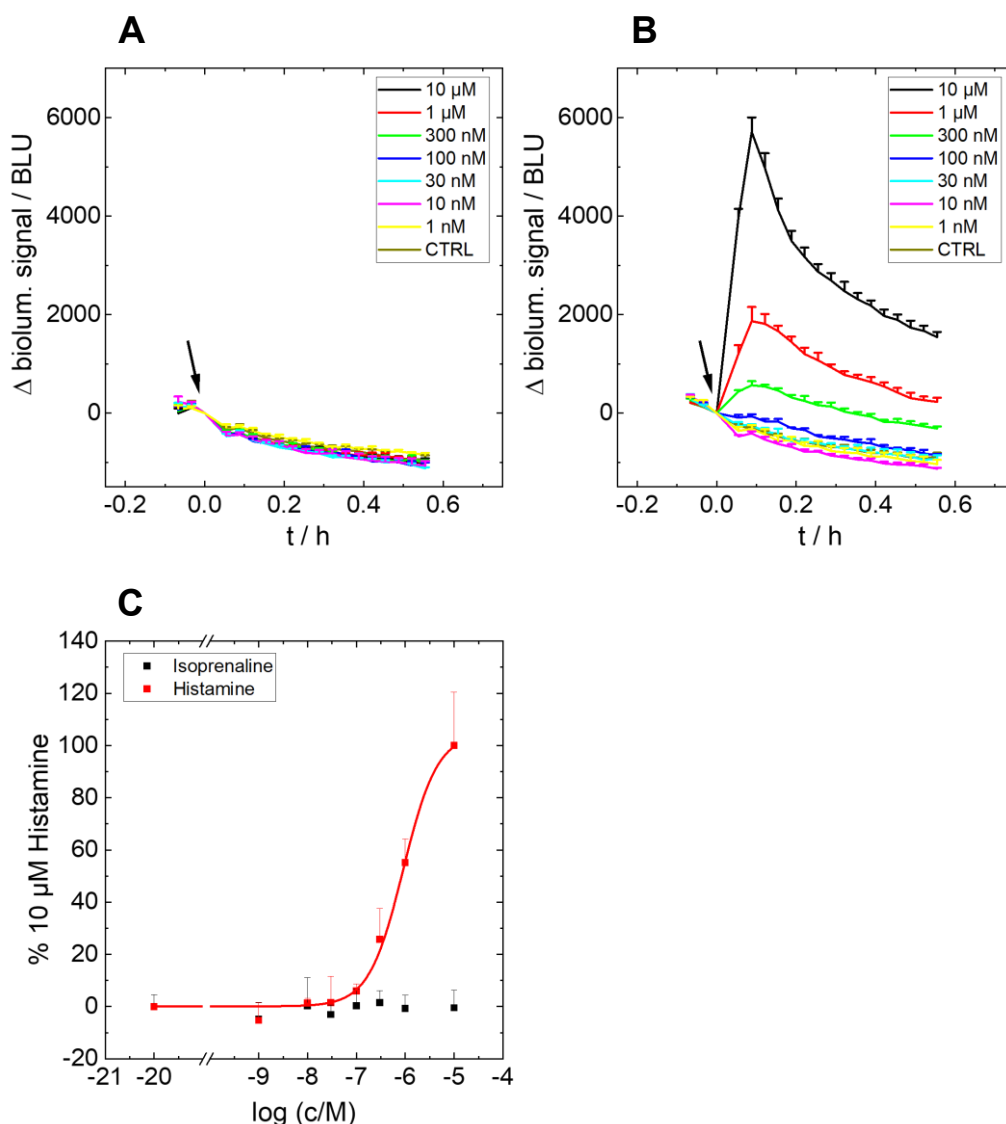


Figure 109. Luminescence change of transiently transfected **HEK H2R/β-Arr.2** cells. After a baseline recording with **furimazine** (final dilution of 1/600 relative to the stock solution; no molar concentration given by the manufacturer), at  $t = 0$  h, different concentrations of **isoprenaline** (A) or **histamine** (B) were added. Black 10  $\mu\text{M}$ , red 1  $\mu\text{M}$ , green 300 nM, blue 100 nM, cyan 30 nM, pink 10 nM, yellow 1 nM, brown CTRL. From the data at  $t = 0.5$  h relative to the data of 10  $\mu\text{M}$  histamine at  $t = 0.5$  h, concentration-response curves were extracted (C). A four-parametric dose-response fit was applied (equation 15). A  $p\text{EC}_{50}$  value of  $6.0 \pm 0.1$  was determined for histamine (red). For isoprenaline (black), no  $p\text{EC}_{50}$  could be determined. Baseline A and B:  $(2510 \pm 30)$  BLU,  $(2780 \pm 30)$  BLU. Mean + SE,  $N = 3$ , single experiment. CTRL = vehicle control. BLU = bioluminescence units. Temperature: 37°C.

For HEK H2R/β-Arr.2 cells (Figure 109A-C), the opposite behavior compared with HEK β2AR/β-Arr.2 cells (Figure 108A-C) is observed. For isoprenaline, no luminescence signal is obtained independent of the utilized concentration (Figure 109A). However, histamine shows a concentration-dependent increase of the luminescence intensity with a maximum after 0.08 h and a subsequent decline (Figure 109B). Only the curves up to a histamine concentration of 30 nM superimpose and remain at the baseline level (Figure 109B, cyan, pink, yellow,

**brown**). A maximal luminescence value of  $(5700 \pm 300)$  BLU is found for  $10 \mu\text{M}$  histamine (**Figure 109B, black**). No saturation is observed for high histamine concentrations.

By analysis of the data at  $t = 0.5$  h relative to the data of  $10 \mu\text{M}$  histamine, concentration-response curves are generated (**Figure 109C**). For isoprenaline, the relative luminescence fluctuates around zero for all investigated concentrations (**Figure 109C, black**). No concentration-response analysis was feasible for isoprenaline. The relative luminescence of histamine remains at the level of the CTRL up to a concentration of  $100 \text{ nM}$  and gradually increases for larger concentrations (**Figure 109C, red**). However, no saturation behavior is observed for large histamine concentrations. The concentration-response analysis yields a  $\text{pEC}_{50}$  of  $6.0 \pm 0.1$  and a relative efficacy of  $R_{\text{max}} = (110 \pm 10)\%$  for histamine.

Further studies with the SNAP-H2R-LgBiT construct and an analogous vector, encoding the M1R (SNAP-M1R-LgBiT, see below), were performed in antagonist mode to investigate if the obtained  $\beta$ -arrestin2 signals are receptor-specific. First, HEK H2R/ $\beta$ -Arr.2 cells were generated by transient transfection of HEK SmBiT  $\beta$ -Arr.2 with SNAP-H2R-LgBiT DNA according to **chapter 3.2.5** and were seeded on white 96-well plates as described in **chapter 3.6.1.2**. On the day of the experiment, the cells were washed with HBS containing 0.1% BSA and incubated with  $1$ - $100 \mu\text{M}$  cimetidine or a cimetidine control for  $0.25$ - $0.33$  h. Cimetidine is a selective H2R antagonist and, therefore, reduces the action of histamine at the H2R (Finkelstein, Isselbacher, **1978**). After furimazine addition (final dilution of  $1/600$  relative to the stock solution; no molar concentration given by the manufacturer), a luminescence baseline was recorded for  $0.08$  h at the PHERAstar FS and, subsequently, a CTRL or different histamine concentrations between  $100 \text{ nM}$  and  $1 \text{ mM}$  were added at  $t = 0$  h. Luminescence was monitored for  $1$  h and is depicted in **Figure 110A-F**. An empty vector (ev) control was used for comparison reasons.

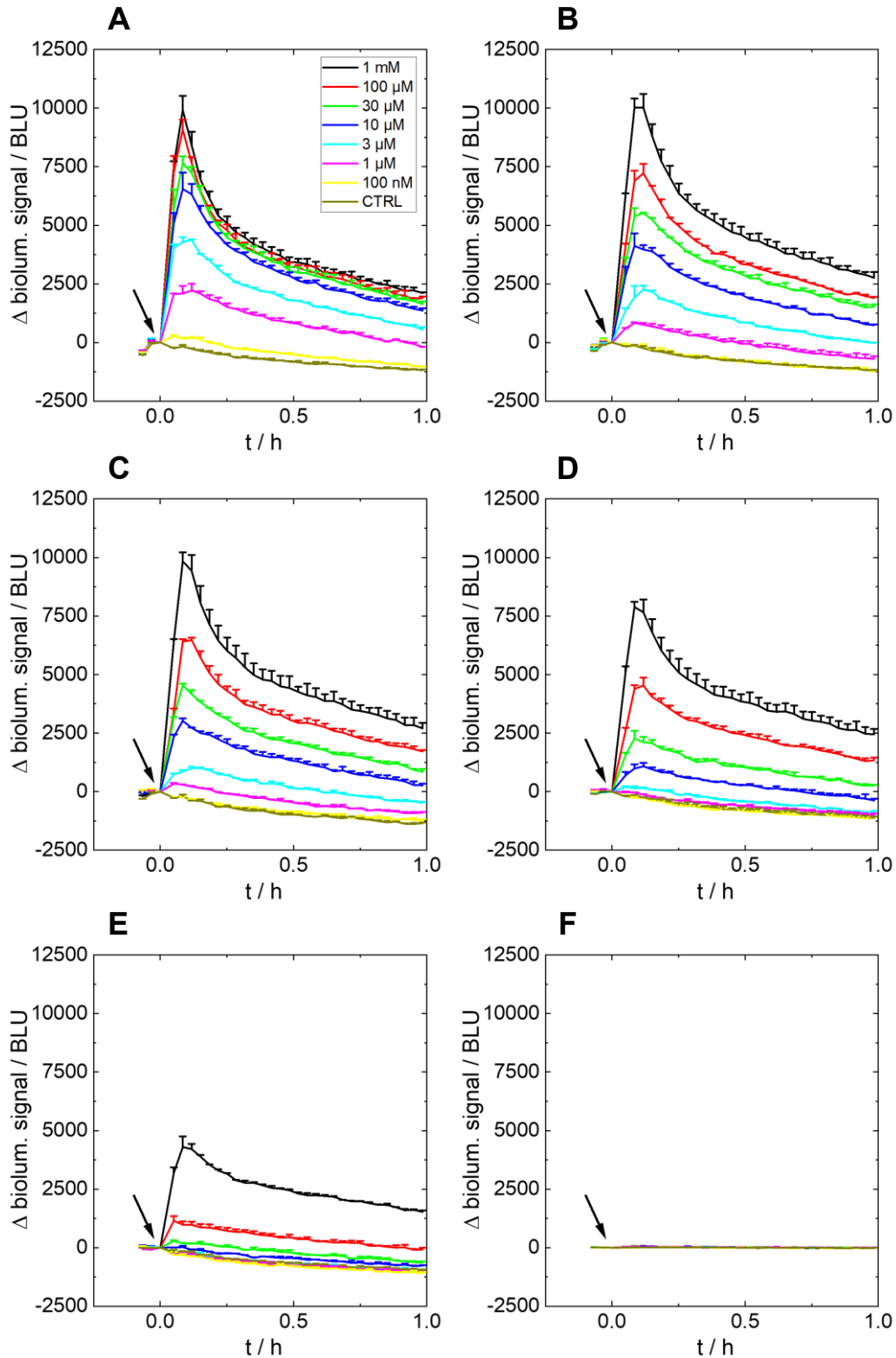


Figure 110. Luminescence change of transiently transfected **HEK H2R/β-Arr.2** cells. After preincubation with different cimetine concentrations for 0.25-0.33 h (**A: cimetine control**, **B: 1 μM**, **C: 3 μM**, **D: 10 μM**, **E: 100 μM**, **F: ev**) and a baseline recording with **furimazine** (final dilution of 1/600 relative to the stock solution; no molar concentration given by the manufacturer), at  $t = 0$  h, different concentrations of **histamine** were added. Black 1 mM, red 100 μM, green 30 μM, blue 10 μM, cyan 3 μM, pink 1 μM, yellow 100 nM, brown CTRL. Baseline from A to F:  $(2250 \pm 40)$  BLU,  $(2480 \pm 40)$  BLU,  $(2590 \pm 20)$  BLU,  $(2370 \pm 30)$  BLU,  $(2110 \pm 20)$  BLU,  $(73 \pm 2)$  BLU. Mean + SE,  $N = 2$ , single experiment. CTRL = histamine vehicle control. BLU = bioluminescence units. ev = empty vector control. Temperature: 37°C.

After a luminescence baseline of approximately 2400 BLU (SNAP-H2R-LgBiT, **Figure 110A-E**) was recorded, luminescence increases in a concentration-dependent manner when histamine is added. Maxima are developed after  $t = 0.08-0.12$  h followed by a slow decay of luminescence over the measurement period. Considering the cimetidine control condition, the curves for 1 mM and 100  $\mu$ M histamine (**Figure 110A, black, red**) and the curves for 100 nM histamine and the CTRL (**Figure 110A, yellow, brown**) overlay. However, increasing cimetidine concentrations considerably suppress the luminescence signals. For an intermediate histamine concentration of 10  $\mu$ M (**Figure 110A-E, blue**), the maxima decrease from  $(6500 \pm 700)$  BLU to  $(4100 \pm 500)$  BLU,  $(3000 \pm 100)$  BLU,  $(1000 \pm 200)$  BLU and  $(20 \pm 50)$  BLU with increasing cimetidine concentration. The empty vector (ev) control does not show any response and remains at the baseline level  $((73 \pm 2)$  BLU) independent of the added histamine concentration (**Figure 110F**).

To better quantify the antagonistic effect of cimetidine, concentration-response curves were generated. The luminescence data after  $t = 0.5$  h was divided by the luminescence data of 1 mM histamine after  $t = 0.5$  h and plotted against the histamine concentration. The curves determined for the different cimetidine concentrations are shown in **Figure 111A**. The corresponding Schild analysis is depicted in **Figure 111B**. In that instance, dose ratios  $DR_x = \frac{EC50(\text{in presence of } x \frac{\text{mol}}{\text{L}} \text{ antagonist})}{EC50(\text{in absence of antagonist})}$  are calculated and plotted as  $\log(DR_x - 1)$  against the logarithm of the molar antagonist concentration  $\log x$ .

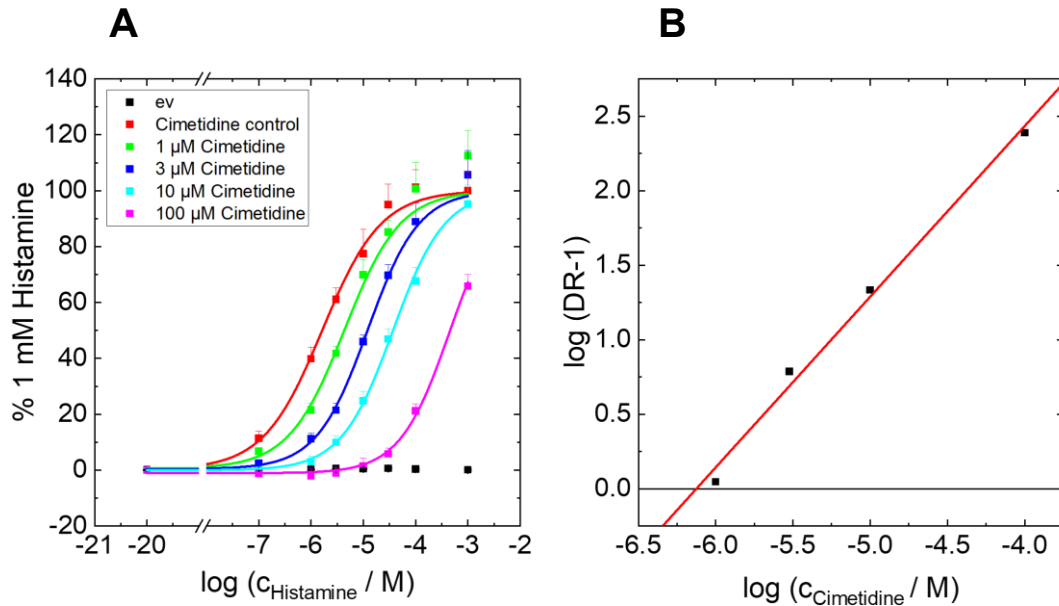


Figure 111. Concentration-response curves for transiently transfected **HEK H2R/β-Arr.2** cells (A). After preincubation with different cimetidine concentrations (**black ev**, **red cimetidine control**, **green 1 μM**, **blue 3 μM**, **cyan 10 μM**, **pink 100 μM**) for 0.25-0.33 h, the cells were stimulated with different **histamine** concentrations.  $R_{max}$  was set to 100%.  $pEC_{50}$  values of  $5.79 \pm 0.03$ ,  $5.36 \pm 0.06$ ,  $4.92 \pm 0.02$ ,  $4.43 \pm 0.02$  and  $3.35 \pm 0.04$  were calculated for increasing cimetidine concentrations. For the ev, no  $pEC_{50}$  value could be determined. Corresponding Schild analysis (B). Black: experimental data, red: linear regression. The slope takes a value of  $1.15 \pm 0.07$ . An affinity of  $(570 \pm 70)$  nM was determined for cimetidine. Mean + SE,  $N = 8$ , four independent experiments. DR = dose ratio. ev = empty vector control. Temperature: 37°C.

Since cimetidine is classified as a competitive or surmountable antagonist (Schunack, 1987), the  $R_{max}$  value was set to 100% for fitting the concentration-response curves (Figure 111A). The relative luminescence data generally increases with larger histamine concentrations and saturates for concentrations  $\geq 100$  μM histamine. Only the empty vector (ev) control does not exhibit any luminescence signal. Besides that, the fits describe the data very well. Only the upper asymptotes for cimetidine concentrations of 10-100 μM are not well described (Figure 111A, cyan, pink). With increasing cimetidine concentration, a shift towards larger histamine concentrations is observed.  $pEC_{50}$  values of  $5.79 \pm 0.03$  for the cimetidine control (Figure 111A, red),  $5.36 \pm 0.06$  for 1 μM cimetidine (Figure 111A, green),  $4.92 \pm 0.02$  for 3 μM cimetidine (Figure 111A, blue),  $4.43 \pm 0.02$  for 10 μM cimetidine (Figure 111A, cyan) and  $3.35 \pm 0.04$  for 100 μM cimetidine (Figure 111A, pink) were identified. Schild analysis was performed by comparing the  $EC_{50}$  values in the presence and absence of cimetidine (Figure 111B, see chapter 3.6.2.2). The  $\log(DR_x - 1)$  values increase linearly by increasing the logarithmic cimetidine concentration. A slope of  $1.15 \pm 0.07$  is observed for the linear regression of the data. From the x-intercept, an affinity of  $(570 \pm 70)$  nM was determined for cimetidine. This value is in the same

range as the  $K_i$  value ( $0.60 \pm 0.43$ )  $\mu\text{M}$  found in a cAMP assay of Sf9 cells in literature (Beukers et al., **1997**).

In a second experiment, the same protocol was applied for HEK M1R/ $\beta$ -Arr.2 cells but the subtype-selective M1R antagonist pirenzepine (between 100 pM and 1  $\mu\text{M}$ ) was used (Calcutt et al., **2017**). After an incubation time of 0.25-0.33 h with different pirenzepine solutions or a pirenzepine control, furimazine (final dilution of 1/600 relative to the stock solution; no molar concentration given by the manufacturer) was added as NanoLuc substrate and a baseline of luminescence was recorded for 0.08 h at the PHERAstar FS. Subsequently, carbachol (10 nM to 100  $\mu\text{M}$ ) was added as an agonist at  $t = 0$  h. The respective assay buffer was used as CTRL. Luminescence was measured for 1 h and is depicted in **Figure 112A-F** for the different pirenzepine concentrations. An average luminescence baseline of 5200 BLU was recorded.

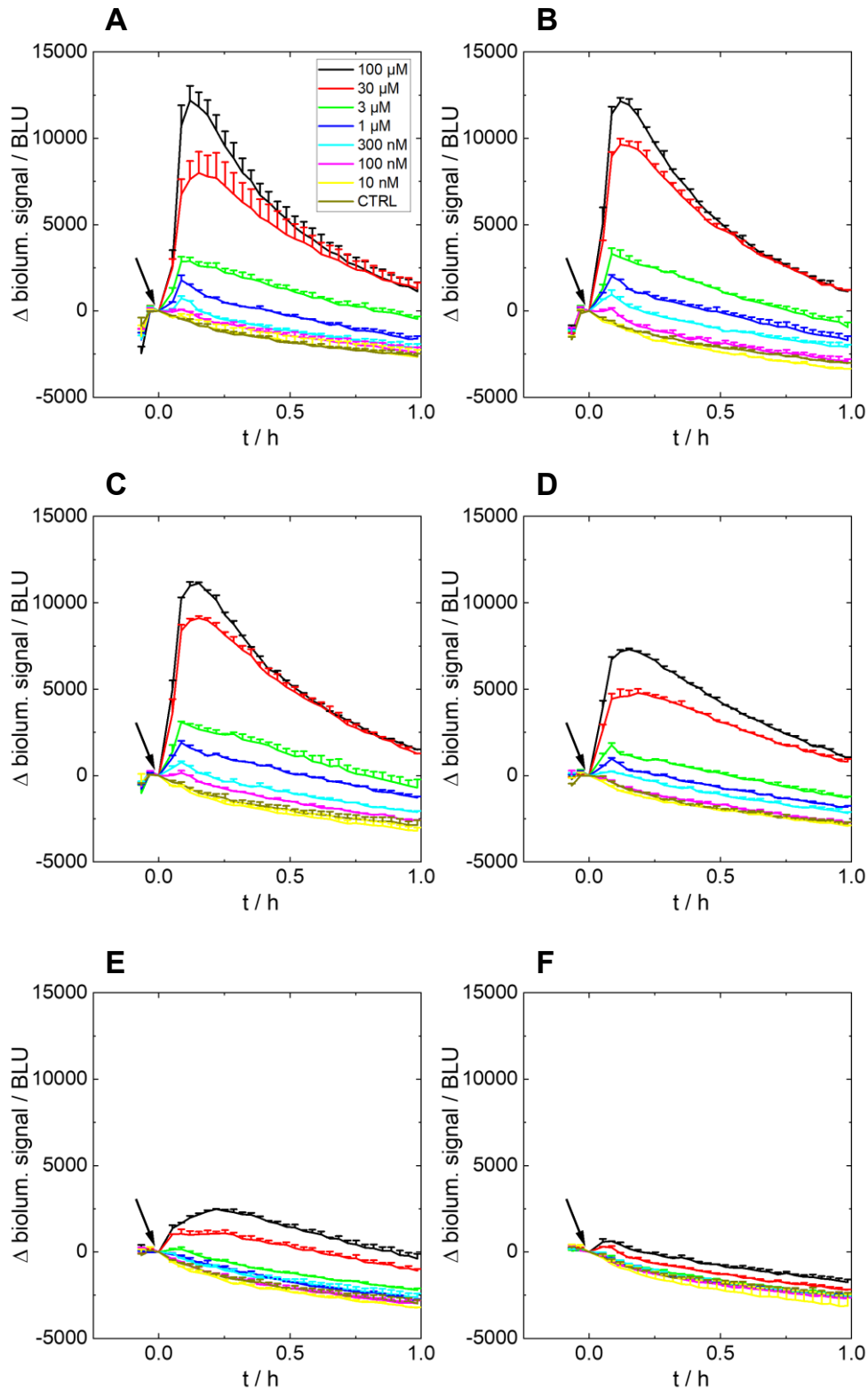


Figure 112. Luminescence change of transiently transfected **HEK M1R/β-Arr.2** cells. After preincubation with different pirenzepine concentrations (**A: pirenzepine vehicle control**, **B: 100 pM**, **C: 1 nM**, **D: 10 nM**, **E: 100 nM**, **F: 1 μM**) for 0.25-0.33 h and a baseline recording with **furimazine** (final dilution of 1/600 relative to the stock solution; no molar concentration given by the manufacturer), at  $t = 0$  h, different concentrations of **carchamol** were added. Black 100 μM, red 30 μM, green 3 μM, blue 1 μM, cyan 300 nM, pink 100 nM, yellow 10 nM, brown CTRL. Baseline from A to F:  $(4600 \pm 100)$  BLU,  $(5400 \pm 100)$  BLU,  $(5440 \pm 90)$  BLU,  $(5300 \pm 60)$  BLU,  $(5340 \pm 60)$  BLU,  $(4900 \pm 80)$  BLU. Mean + SE,  $N = 2$ , single experiment. CTRL = carchamol vehicle control. BLU = bioluminescence units. Temperature: 37°C.

For the pirenzepine vehicle control (**Figure 112A**), luminescence rises concentration-dependently after carbachol addition, reaches a maximum after  $t = 0.08-0.15$  h and slowly declines until  $t = 1$  h. The curves for the CTRL, 10 nM and 100 nM carbachol (**Figure 112A, pink, yellow, brown**) overlay and remain at the lowest luminescence level. The curves for 100  $\mu$ M and 30  $\mu$ M carbachol (**Figure 112A, black, red**) superimpose for  $t \geq 0.5$  h. In general, the same kinetics are observed for all pirenzepine concentrations. However, concentration-dependent antagonism of the carbachol activation and subsequent  $\beta$ -arrestin2 recruitment was observed upon the treatment with pirenzepine. This means that the luminescence signals are more suppressed, the larger the pirenzepine concentration is. For instance, at a carbachol concentration of 100  $\mu$ M (**Figure 112A-F, black**), the maxima lose intensity from  $(12200 \pm 900)$  BLU for the pirenzepine control to  $(12100 \pm 200)$  BLU for 100 pM pirenzepine,  $(11130 \pm 60)$  BLU for 1 nM pirenzepine,  $(7300 \pm 70)$  BLU for 10 nM pirenzepine,  $(2160 \pm 80)$  BLU for 100 nM pirenzepine and  $(619 \pm 9)$  BLU for 1  $\mu$ M pirenzepine. In contrast to HEK H2R/ $\beta$ -Arr.2 cells (**Figure 110A-F**), the kinetics are more long-lived, which is perceptible by the elongated  $t_{1/2} = 0.4-0.5$  h and a less transient maximal response.

By analyzing the luminescence at  $t = 0.5$  h relative to the response of 100  $\mu$ M carbachol, concentration-response curves were generated for the different pirenzepine concentrations (**Figure 113A**). The corresponding Schild analysis is depicted in **Figure 113B**.

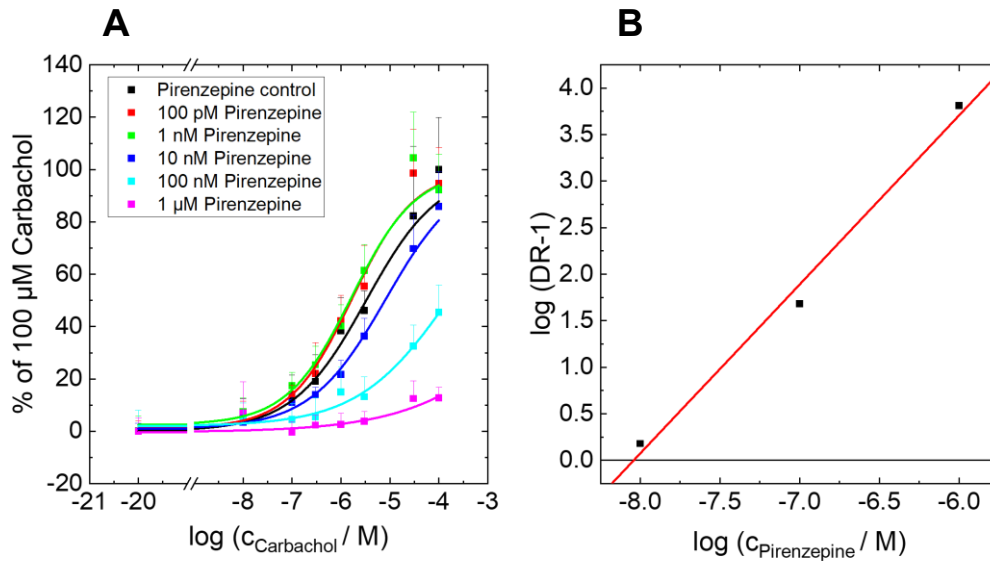


Figure 113. Concentration-response curves for transiently transfected **HEK M1R/ $\beta$ -Arr.2** cells (A). After preincubation for 0.25-0.33 h with different pirenzepine concentrations (**black pirenzepine control, red 100 pM, green 1 nM, blue 10 nM, cyan 100 nM, pink 1  $\mu\text{M}$** ), the cells were stimulated with different **carbachol** concentrations.  $R_{\max}$  was set to 100%.  $pEC_{50}$  values of  $5.49 \pm 0.08$ ,  $5.78 \pm 0.08$ ,  $5.79 \pm 0.09$ ,  $5.09 \pm 0.08$ ,  $3.8 \pm 0.1$  and  $1.7 \pm 0.8$  for increasing pirenzepine concentrations were calculated. Corresponding Schild analysis (B). Black: experimental data, red: linear regression. The slope takes a value of  $1.8 \pm 0.2$ . An affinity of 9 nM was determined for pirenzepine. Mean + SE,  $N = 2$ , single experiment. DR = dose ratio. Temperature: 37°C.

The  $R_{\max}$  values were constrained to 100% under the assumption that pirenzepine acts as a competitive antagonist (**Figure 113A**), which was demonstrated by *in vivo* experiments before, where pirenzepine was compared to the non-selective antagonist atropine to reduce possible side effects of the latter (Ostrin et al., 2004). For the CTRL and 10 nM carbachol, relative luminescence values of 0-10% are observed. Above these concentrations, the relative luminescence generally increases with increasing carbachol concentrations. However, no saturation is detected at the high-concentration end. The concentration-response curves for 100 pM and 1 nM pirenzepine (**Figure 113A, red, green**) are not distinguishable and are shifted to lower carbachol concentrations in comparison to the control conditions (**Figure 113A, black**). The curves for larger pirenzepine concentrations (**Figure 113, blue, cyan, pink**) are shifted to higher carbachol concentrations with increasing antagonist concentrations. The curve for 1  $\mu\text{M}$  pirenzepine is very flat and remains close to the level of the CTRL independent of the carbachol concentration (**Figure 113A, pink**).  $pEC_{50}$  values of  $5.49 \pm 0.08$  for the pirenzepine control,  $5.78 \pm 0.08$  for 100 pM pirenzepine,  $5.79 \pm 0.09$  for 1 nM pirenzepine,  $5.09 \pm 0.08$  for 10 nM pirenzepine,  $3.8 \pm 0.1$  for 100 nM pirenzepine and  $1.7 \pm 0.8$  for 1  $\mu\text{M}$  pirenzepine were determined. Since only the curves for 10 nM, 100 nM and 1  $\mu\text{M}$  pirenzepine displayed a shift to larger carbachol concentrations relative to the curve of the pirenzepine control, the

Schild plot only consists of 3 data points (**Figure 113B**). This might be attributed to the analysis of a single time point and potentially could be improved by analysis of a certain time interval (e.g. area under the curve (AUC) analysis) or the signal maximum of luminescence. With increasing pirenzepine concentration, the  $\log(DR_x-1)$  values increase linearly with the logarithmic antagonist concentration. A slope of  $1.8 \pm 0.2$  is detected for the linear regression. Analysis of the x-intercept reveals an affinity of 9 nM for pirenzepine. No error is given since only one single experiment was performed. In a radioligand displacement assay, a  $K_i$  value of  $8.29 \pm 0.12$  (corresponding to approximately 4-7 nM) was found for pirenzepine at the M1R (Huang et al., **2001**).

From the first experiments (**Figure 108A-C** and **Figure 109A-C**), it is concluded that the transfection of the SNAP-H2R-LgBiT DNA (see **chapter 3.2.1**) is possible and comparable to the well-studied transfection of the SNAP- $\beta$ 2AR-LgBiT vector (Dijon, **2022**). Furthermore, it was proven that the generated SNAP-H2R-LgBiT construct indeed contains the H2R DNA and not the  $\beta$ 2AR DNA as in the starting material because the isoprenaline response is specific for the  $\beta$ 2AR (**Figure 108A-C**) and a histamine response only occurs at the H2R (**Figure 109A-C**). At the  $\beta$ 2AR and H2R, concentration-dependent  $\beta$ -arrestin2 recruitment is observed with similar kinetics. The maxima are acquired after  $t = 0.08-0.12$  h and the signal is halved after  $t_{1/2} = 0.25-0.32$  h, respectively.

The pEC50 value determined for histamine ( $6.0 \pm 0.1$ , **Figure 109C, red**) is similar to  $6.3 \pm 0.2$  obtained in **chapter 4.2** and to 5.42 found in literature in another  $\beta$ -arrestin2 recruitment assay (Felixberger, **2016**). The pEC50 determined in **chapter 4.3** ( $7.4 \pm 0.2$ ) shows the biggest discrepancy to the value determined in this chapter. This potentially could be explained by differences in the cell behavior of HEK H2R cells (this chapter) and HEK H2R/mG<sub>s</sub> cells (**chapters 4.2 and 4.3**) but also might be attributed to the readout parameter. The pEC50 values for more distal readout parameters (impedance: **chapter 4.2** and  $\beta$ -arrestin2: this chapter) might resemble each other, while the proximal miniG protein recruitment assay (**chapter 4.3**) displays a higher potency of histamine at the H2R. Spillmann *et al.* detected a pEC50 of approximately 6.82 for isoprenaline at the  $\beta$ 2AR in a  $\beta$ -arrestin2 recruitment assay, which is about one order of magnitude smaller than the here determined value ( $7.66 \pm 0.09$ ) (Spillmann et al., **2020**) but still in the same range (nM).

At the H2R and M1R,  $\beta$ -arrestin2 recruitment is observed after stimulation with histamine (**Figure 110A-E**) and carbachol (**Figure 112A-F**). Specificity was proved

by the use of the selective antagonists cimetidine and pirenzepine, i.e. no other endogenously expressed receptor accounts for the observed bioluminescence. This was also confirmed by the empty vector (ev) control (**Figure 110F**). The increased baseline values of HEK H2R/ $\beta$ -Arr.2 and HEK M1R/ $\beta$ -Arr.2 cells compared to the ev control are ascribed to constitutively active luciferase and no occurrence of luciferase in the empty vector (ev) cells. The antagonists suppressed the agonist-stimulated bioluminescent signals and led to shifts of the pEC50 values to larger agonist concentrations (**Figure 111A and Figure 113A**). But since an increase of the agonist concentration can be used to generate the same  $R_{max}$ , cimetidine and pirenzepine are considered as competitive or surmountable antagonists (Ostrin et al., **2004**, Schunack, **1987**). Affinities  $K_B$  of  $(570 \pm 70)$  nM for cimetidine and 9 nM for pirenzepine were determined by Schild analysis (**Figure 111B and Figure 113B**). Similar binding affinities of cimetidine and pirenzepine have been previously observed in cAMP assays of H2R-expressing Sf9 cells or radioligand binding experiments of membrane preparations with the M1R (Beukers et al., **1997**, Huang et al., **2001**). The kinetics at both receptors differed sparsely with somewhat faster kinetics at the H2R with  $t_{1/2}$  being 0.25-0.32 h (**Figure 109B and Figure 110A-E**) compared to  $t_{1/2} = 0.4$ -0.5 h at the M1R (**Figure 112A-F**). Both receptors as well as the  $\beta$ 2AR (**Figure 108A**) present rise and fall to steady-state conditions of the bioluminescence. Similar results were obtained by Hoare *et al.* in  $\beta$ -arrestin recruitment assays at the  $\beta$ 2AR (Hoare et al., **2020**, Hoare et al., **2021**). They observed changes in  $\beta$ -arrestin signaling kinetics dependent on the receptor type and the receptor complex formation during the receptor recycling process. Since HEK cells expressing the M1R and H2R both display  $\beta$ -arrestin2 signaling,  $\beta$ -arrestin2 recruitment could be a further explanation for the impedance signals after carbachol and histamine addition (cf. **chapters 5.1 and 5.2**).

## 5.4 Summary and Outlook

Previous experiments demonstrated that  $G_i$ -coupled HEK cells do not display a significant impedance response after stimulation with an agonist (data not shown), despite a preincubation with the AC activator FSK to enhance the signal readout (Hill et al., **2010**). However,  $G_s$ -coupled HEK H2R cells did exhibit a distinct impedance increase after histamine addition (cf. **Appendix 25**). Consequently, **chapter 5.1.1** aimed to find out whether increases and decreases of the cAMP concentration inside HEK cells are measurable with impedance or whether the impedance response of HEK H2R cells originates from different mechanisms. The impedance outcome of

HEK H2R cells after the addition of FSK and 8-CPT-cAMP was compared to the impedance signal after stimulation with histamine (**Figure 97A-D**). While FSK and 8-CPT-cAMP provoked a slight decrease of impedance with a concentration dependency for FSK (**Figure 97A-B**), 2  $\mu$ M histamine caused a significant impedance increase (**Figure 97C-D**). This indicates that (i) histamine does not lead to cAMP level increases but triggers other signaling pathways, which are detectable with impedance readings or (ii) histamine triggers other signaling pathways that overlay with the impedance signal resulting from cAMP concentration increases or (iii) the cAMP increases of HEK H2R cells after histamine addition are not detectable with impedance measurements but different competing signaling pathways are detected. The former (i) is highly unlikely as the canonical coupling pathway of the H2R is the  $G_s$ -pathway, which is well documented in the literature (Levick, **2022**). To investigate whether the  $G_s$ -pathway contributes to the impedance signal of HEK H2R cells after histamine addition and potentially overlays with other signaling pathways, the impact of CTX was studied in **chapter 5.1.2**. Assuming that (ii) is true, increasing concentrations of CTX should lead to increasing impedance values since the decrease of impedance after cAMP activation (cf. FSK and 8-CPT-cAMP) is reduced. Nonetheless, no impact of CTX on the impedance signals of HEK H2R cells was identified (**Figure 98A-D**). This means that the cAMP-induced impedance decreases of HEK H2R cells are not measurable and too insignificant, which means (iii) is supposedly true. This yields the impedance response of HEK cells rather insensitive to changes in the cAMP concentration. If the impedance technique is compared to the DMR method, in particular for HEK cells, DMR is capable of unveiling  $G_q$ ,  $G_i$ ,  $G_{12/13}$  and  $G_s$  responses (Schrage et al., **2015**, Schröder et al., **2010**, Seibel-Ehlert et al., **2021**) while the impedance response of HEK cells often appears insensitive for  $G_i$ - and  $G_s$ -coupling. In addition, DMR is able to discern cAMP level increases induced by FSK in HEK cells (Schröder et al., **2010**) while impedance shows opposite effects for FSK and  $G_s$ -activating ligands (**Figure 97A,C**). Consequently, the impedance assay of  $G_s$ - or  $G_i$ -coupled HEK cells poses a challenge. Other functional assays are recommended to unravel  $G_s$ - and  $G_i$ -coupling of HEK cells.

In **chapter 5.1.3**, the impedance signal of HEK M1R/ $mG_q$  cells after stimulation with the agonist carbachol was compared to the addition of the calcium ionophore calcimycin (**Figure 100**). Both compounds either activate or imitate the  $G_q$  signaling pathway and subsequent increases of the intracellular calcium ion concentration. In a previous study, equal concentrations of calcimycin and histamine, activating the  $G_q$ -coupled H1R, led to comparable SPR and impedance results (Parić, **2021**). However, this was not the case for HEK M1R/ $mG_q$  cells. Carbachol provoked significantly larger

impedance outcomes compared to calcimycin used in the same concentration (**Figure 100 and Figure 101**). This might be attributed to the varying mechanisms both molecules activate. Calcimycin leads to a calcium influx from the extracellular side along the calcium ion gradient. Instead, carbachol provokes a calcium ion release from the ER. Nonetheless, since the impedance profiles of carbachol and calcimycin are similar, it is highly probable that HEK M1R/mG<sub>q</sub> cells activate calcium as a second messenger. For instance, the initial decrease of impedance after compound addition (**Figure 100**) indicates calcium mobilization as often mentioned in literature (Denelavas et al., **2011**, Parviz et al., **2017**, Scott, Peters, **2010**, Verdonk et al., **2006**). To confirm that carbachol induces calcium mobilization in HEK M1R/mG<sub>q</sub> cells and to find out whether the G<sub>q</sub>-pathway potentially contributes to the impedance signal of HEK H2R cells after histamine addition as well, fluorescence-based calcium assays were performed (**chapter 5.2**). HEK wt cells were used as a control for endogenous receptor expression. While HEK M1R/mG<sub>q</sub> cells displayed calcium signals for acetylcholine, carbachol and iperoxo but not for histamine (**Figure 102 and Figure 103**), HEK H2R showed a calcium response after histamine addition but no response for acetylcholine, carbachol and iperoxo (**Figure 104 and Figure 105**). HEK wt cells also featured a calcium response after acetylcholine, carbachol and iperoxo addition but the responses were significantly decreased compared to HEK M1R/mG<sub>q</sub> cells (**Figure 106 and Figure 107**). This confirms that HEK cells do not express histaminergic receptors but muscarinic acetylcholine receptors, e.g. the M3R, endogenously (Atwood et al., **2011**, Meisenberg et al., **2015**). Since HEK H2R cells did not respond to the muscarinic acetylcholine receptor ligands, the expression of the endogenous M3R must be repressed in HEK H2R cells, which can be explained by an overexpression of the H2R (Tubio et al., **2010**). HEK M1R/mG<sub>q</sub> cells and HEK H2R cells usually display a transient decrease of impedance after ligand addition, which is often associated with G<sub>q</sub> or calcium ion signaling (cf. **Figure 100 and Appendix 25**) (Denelavas et al., **2011**, Scott, Peters, **2010**, Verdonk et al., **2006**). This statement is confirmed by the fluorescence measurements since both cell lines demonstrate calcium mobilization and G<sub>q</sub> recruitment also observed in miniG protein recruitment assays before (Höring, **2022**). Nonetheless, it is well known that other pathways such as the G<sub>s</sub>- or G<sub>i</sub>-pathway also trigger intracellular calcium ion increases further downstream of the signaling cascade (Dhyani et al., **2020**). One example are β-adrenergic receptors. After stimulation of these G<sub>s</sub>-coupled receptors, calcium mobilization is frequently observed. In literature, this phenomenon is often explained by cAMP-driven calcium channels. When cAMP levels increase and PKA is activated and starts to phosphorylate its substrates, an increased activity of L-type

voltage-dependent calcium channels is observed (Charnet et al., **1995**, Cserne Szappanos et al., **2017**, Gao et al., **1997**). In summary, the impedance response of HEK M1R/mG<sub>q</sub> cells might indeed be explained by G<sub>q</sub>-coupling and subsequent calcium mobilization from the ER, while the impedance response of HEK H2R cells had to be investigated more in-depth since the calcium signal after histamine addition could either arise after G<sub>q</sub>- or G<sub>s</sub>-stimulation.

In **chapter 5.3**, both receptors were analyzed in terms of  $\beta$ -arrestin2 signaling by using the NanoBiT technology (cf. **chapter 3.2.5**). A first experiment confirmed the correct formation of SNAP-H2R-LgBiT DNA (cf. **chapter 3.2.1**) out of the original vector (cf. **Figure 108A-C**) and a successful transient transfection of the H2R vector into HEK SmBiT  $\beta$ -Arr.2 cells (**Figure 109A-C**). Subsequent experiments with SNAP-H2R-LgBiT and a derived SNAP-M1R-LgBiT vector revealed  $\beta$ -arrestin2 recruitment to the H2R (**Figure 110A-F**) and M1R (**Figure 112A-F**) after histamine and carbachol stimulation. Both luminescence signals were receptor-specific as approved by the reduction of signals in the presence of the antagonists cimetidine and pirenzepine. Both antagonists were identified as surmountable or competitive antagonists by Schild analysis with an affinity in good agreement with the literature. These results offer a further explanation for the changes in impedance of HEK M1R/mG<sub>q</sub> and HEK H2R cells.  $\beta$ -arrestins lead to the desensitization and internalization of GPCRs and trigger processes such as extracellular signal-regulated kinase (ERK1/2) and mitogen-activated protein kinase (MAPK) signaling. Accordingly, cytoskeletal components are phosphorylated and thereby modified and rearranged (Guo et al., **2020**) potentially identifiable by impedance measurements. In contrast, Grundmann *et al.*, who studied the dynamic mass redistribution (DMR) response of various class A GPCRs under the influence of different G protein inhibitors in G protein or  $\beta$ -arrestin1/2 depleted HEK cells, claim that all detected cytoskeletal changes are solely attributed to G protein signaling but not  $\beta$ -arrestin signaling (Grundmann et al., **2018**). However, it must be noted that the used DMR technique only considers the basal side of the cells and, hence, might be less sensitive than impedance readings.

Overall, at the M1R, (m)G<sub>q</sub> recruitment (**chapter 4.3**), calcium ion signaling (**chapter 5.2**) and  $\beta$ -arrestin2 recruitment (**chapter 5.3**) were observed while at the H2R, (m)G<sub>s</sub> recruitment (**chapter 4.3**), intracellular calcium ion release (**chapter 5.2**) and  $\beta$ -arrestin2 recruitment (**chapter 5.3**) were detected. All these pathways might contribute to the impedance signals of HEK M1R/mG<sub>q</sub> and HEK H2R cells after GPCR stimulation. Nonetheless, these results prove that a single functional assay can not fully unravel the underlying signaling pathways of impedance. Elucidating the exact mechanisms is exceedingly complex and requires a repertoire of several functional

assays that must be combined and correlated. In addition, researchers should reflect on their results more in-depth to find potential false negatives and prevent overlooking pathways that potentially cancel out. The major issue with respect to resolving GPCR signaling is that plenty of signaling pathways and mechanisms intertwine, which complicates a distinct categorization into  $G_q$ ,  $G_i$ ,  $G_s$  or  $\beta$ -arrestin2 signaling and should be deliberated with caution.

In future perspective, knockdown and knockout of certain signaling pathways by utilizing CRISPR/Cas9 techniques or small interfering RNA (siRNA), which can easily be imported inside the cells by electroporation techniques using the previously described impedance setup (Stolwijk, Wegener, **2020**), will become more relevant to clarify GPCR signaling patterns (Gurevich, Gurevich, **2019**, Luttrell et al., **2018**). These techniques also offer the possibility to elucidate signaling patterns of endogenously expressed receptors by modification of the target allowing for the study of primary cells and disease models (Soave et al., **2021**). However, this requires expertise in molecular biology and is not always easy to control (e.g. off-target gene editing) (Milligan, Inoue, **2018**). Furthermore, the modified system might diverge from the native one and, hence, might display less physiological behavior.

In addition, impedance spectroscopists need to combine functional assays with more proximal readouts to fully understand where impedance changes originate from. Not only  $G_q$ ,  $G_i$ ,  $G_s$  and  $\beta$ -arrestin signaling should be considered but also  $G_{12/13}$ -signaling and the impact of GRKs, MAPKs and the ERK1/2 pathway. Only the combination of several assays with different readouts allows for a more comprehensive understanding of GPCR signaling detected by impedance or any other GPCR readout.

Furthermore, performing the impedance assay in MFT-mode and making use of the ECIS model to determine  $\alpha$ ,  $R_b$  and  $C_m$  before, during and after GPCR stimulation would give further insights into the signaling processes over time (e.g. change of membrane topography or rearrangement of filaments impacting cell-cell or cell-matrix contacts). Nonetheless, an alteration of the parameters  $\alpha$ ,  $R_b$  and  $C_m$  would still be hard to interpret on a molecular level and would need further elucidation, e.g. by fluorescence stainings of filaments or additional functional assays.

## 6 Monitoring the Bioactivity of Photochromic Ligands Using Impedance Assays

*In this chapter, the following nomenclature is used for all photoswitchable ligands: when a certain ligand isoform is mentioned, the ligand was illuminated with the corresponding switching wavelength for 3 min to obtain a certain photostationary state (PSS), i.e. equilibrium concentrations of both ligand isoforms. It is not possible to generate the pure isoforms.*

Photochromic ligands (also photoswitchable ligands) consist of a bioactive pharmacophore and a photoswitchable moiety (Kobauri et al., **2023**). Their bioactivity is tuned by changing the conformation of the photoswitchable part after irradiation with light of varying wavelengths. In the ideal case, one of the two isomers exhibits an enhanced bioactivity while the second one does not show any activity at all. This allows for temporal and spatial control of the operation of pharmacological compounds inside the body to treat certain diseases or prevent adverse side effects by selective activation (Kienzler, Isacoff, **2017**). Frequent targets of photochromic ligands are ion channels, enzymes, cytoskeletal components and G protein-coupled receptors (GPCRs) (Broichhagen et al., **2015**). The most extensively studied photoswitchable ligands are reversible ones. They either can be switched between a *cis*- and *trans*-isoform (e.g. azobenzene, azopyrazole or stilbene) or an *open* and *closed* isoform (e.g. diarylethene or fulgide) (Ricart-Ortega et al., **2019**). In this work, two photoswitchable ligands for the neuropeptide Y4 receptor (Y4R) and the dopamine 2 receptor (long splicing variant, D2L) were studied in a whole-cell impedance assay. The Y4R ligand consists of an azobenzene moiety and a cyclic peptide, whereas the D2L ligand is a dithienylethene-based photoswitchable ligand (for structures see **chapter 3.5.3.2**). Both can be switched by irradiation with UV/Vis light to generate the *cis/trans*- or *open/closed* form, respectively. In the following, the investigated Chinese hamster ovary (CHO) cell lines either expressing the Y4R or D2L are first characterized with the CardioExcyte 96 (CE96, Nanion Technologies, see **chapter 3.5.3.2**) setup regarding their adhesion behavior and the most sensitive frequency for impedance-based analysis (**chapter 6.1**). In a subsequent experiment, the photoswitchable ligands **1**, acting at the D2L, and **2**, acting at the Y4R, are tested in concentration-response measurements for both isomers to find the optimal concentration for switching (**chapter 6.2**). Lastly, switching and toggling experiments are performed to modulate the substances' bioactivity (**chapter 6.3**) and a first switching mechanism is postulated (**chapter 6.4**).

## 6.1 Characterization of Chinese Hamster Ovary Cells

CHO cells expressing the D2L or Y4R were used to investigate the biological activity and switching behavior of the photoswitchable ligands **1** and **2** with impedance measurements (see **chapter 3.5.3.2**). Prior to that, both cell lines (CHO D2L, CHO NPY) were characterized in adhesion measurements by impedance spectroscopy. The cells were seeded with a density of  $10^5$  c/cm<sup>2</sup> on medium preincubated CE96 electrode arrays (working electrode diameter: 0.6 mm). The plates were mounted to the CE96 device and impedance spectra were recorded for 21 evenly distributed frequencies between 1-100 kHz over 30-44 h. 24 h after seeding, a medium exchange took place to provide the cells with fresh nutrients. The impedance spectra 0 h and 30 h (CHO D2L) or 0 h and 44 h (CHO NPY) after seeding are given in **Figure 114A-B**.

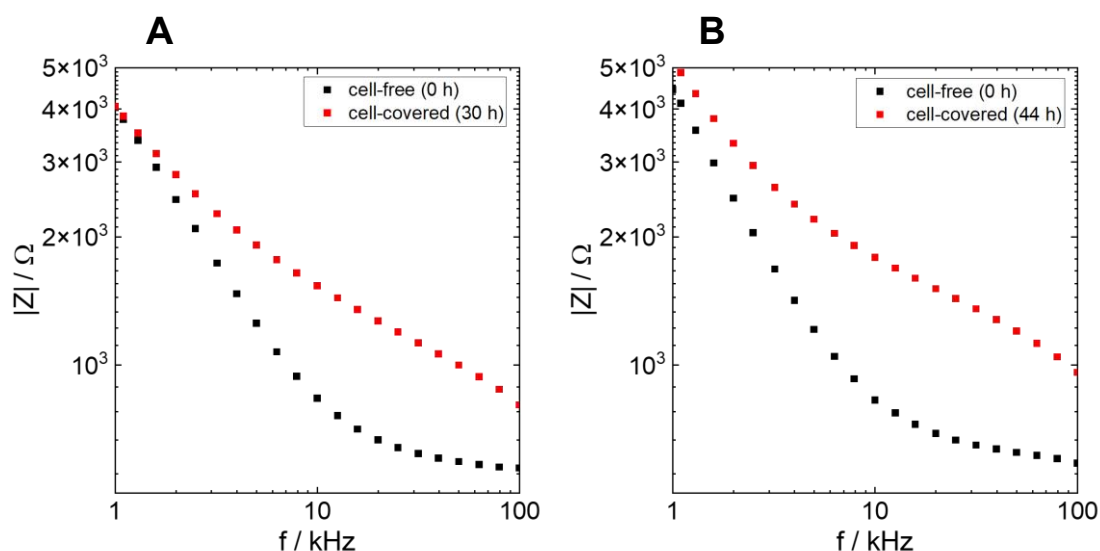


*Figure 114. Impedance spectra of **CHO D2L (A)** and **CHO NPY (B)** cells 0 h (black) and 30 h (A, red) or 44 h (B, red) after seeding on CE96 electrode arrays (0.6 mm). Impedance was measured for 21 evenly distributed frequencies between 1 kHz and 100 kHz with the CE96 device. Before seeding, the electrode arrays were preincubated with medium. Mean + SE, N = 95, single experiment. Temperature: 37°C.*

The impedance spectra at  $t = 0$  h are very similar for CHO D2L (**Figure 114A, black**) and CHO NPY (**Figure 114B, black**) cells. Starting at 1 kHz (4000-5000  $\Omega$ ), impedance decreases linearly for increasing frequencies. Above an intermediate frequency of approximately 10 kHz, the curves level off and approach a constant impedance value of about 600  $\Omega$ . After a cultivation time of 30 h (**Figure 114A, red**) or 44 h (**Figure 114B, red**), both curves reach an elevated impedance level in comparison to the curves after 0 h. At the low-frequency end ( $\leq 2$  kHz), the impedance

spectra after 0 h and 30 h or 44 h display small differences (**Figure 114B**) or even overlay (**Figure 114A**). For intermediate frequencies between 2-30 kHz, the curves for 30 h (**Figure 114A, red**) and 44 h (**Figure 114B, red**) show higher impedance values compared to the curves after 0 h and somewhat flatten out with increasing frequency. When the measurement frequency is increased even further ( $\geq 30$  kHz), impedance drops off again and approaches the values of the curves at  $t = 0$  h again. The largest difference between the curves after 0 h and 30 h or 44 h is found for intermediate frequencies between 10-30 kHz.

Since the spectra at  $t = 0$  h were recorded for cell-free electrodes (**Figure 114A-B, black**), no cellular contribution to the impedance signal is expected. Therefore, the curve shape is only dependent on the electrode-electrolyte interface (constant phase element, CPE) and the medium resistance ( $R_{\text{bulk}}$ ) (cf. **chapter 3.5.2**) (Stolwijk et al., **2015**). While the CPE determines the linearly descending part of the spectrum, the bulk resistance defines the impedance at the high-frequency end. When cells are attached and adhered to the electrodes, the current is forced to flow around and couple through the insulating cell bodies by which impedance at intermediate frequencies of 2-30 kHz increases. This is observed after 30 h and 44 h for CHO D2L (**Figure 114A, red**) and CHO NPY (**Figure 114B, red**) cells, respectively. Contrary to **chapter 4.1**, this could not be confirmed by phase contrast microscopy since the CE96 electrode arrays were non-transparent. However, routine cultivation of CHO D2L and CHO NPY cells as well as adhesion measurements of a different CHO cell line (**Appendix 20**) confirmed a strong attachment of the cells after 30-44 h. The largest cellular contribution to impedance is observed between frequencies of 10-30 kHz. Consequently, an intermediate frequency of 12 kHz was chosen as the sensitive measurement frequency for all further experiments. After a two-day cultivation, an impedance value of at least 1000  $\Omega$  is expected at 12 kHz as discerned by the spectra after 30-44 h (**Figure 114A-B, red**).

## 6.2 Characterization of Photoswitchable Ligands with Impedance Spectroscopy

Both photoswitchable ligands **1** and **2** are derived from dopamine 2 receptor (D2R) (Lachmann et al., **2017**) and Y4R (Wirth et al., **2023**) agonists (see **chapter 3.5.3.2**) and activate  $G_i$  proteins, i.e. inhibit cyclic adenosine monophosphate (cAMP) production. Ligand **1** has proven GPCR activity at the D2S (short splicing variant of the D2R) in IP1 accumulation and  $\beta$ -arrestin2 recruitment assays (Lachmann et al.,

**2017**). However, the efficacies of both ligand isoforms were very similar independent of the utilized concentration. Ligand **2** showed activity in a luminescence-based minimal G protein (miniG, mG) recruitment assay with distinct concentration-response curves and selective binding to the Y4R (Wirth et al., **2023**).

To investigate the ligands' bioactivity with the CE96 impedance assay, CHO NPY and CHO D2L cells were seeded with a density of  $10^5$  c/cm<sup>2</sup> on CE96 electrode arrays (0.6 mm) that were preincubated with medium. After a cultivation time of two days, the medium was exchanged with Leibovitz' 15 (L15) buffer and the cells were equilibrated at 0% (v/v) CO<sub>2</sub> and 37°C for 4 h inside the CE96 device. During equilibration, impedance was recorded at 12 kHz until reaching a stable baseline. Then, the cells were prestimulated with the adenylate cyclase (AC) activator forskolin (FSK, 0.4  $\mu$ M) to enhance the sensitivity after G<sub>i</sub>-activation (Hill et al., **2010**). Finally, both isoforms of ligands **1** and **2** were added in concentrations of 200 nM (ligand **1**) and 50 nM (ligand **2**). The photoactive states were obtained by irradiating the respective stock solutions with the corresponding wavelengths for 3 min (cf. **chapter 3.5.3.2**). Besides a negative control (CTRL), human pancreatic polypeptide (hPP) and quinpirole were utilized as positive controls. The results are given in **Figure 115A** for CHO D2L stimulation with ligand **1** and in **Figure 115B** for CHO NPY stimulation with ligand **2**.

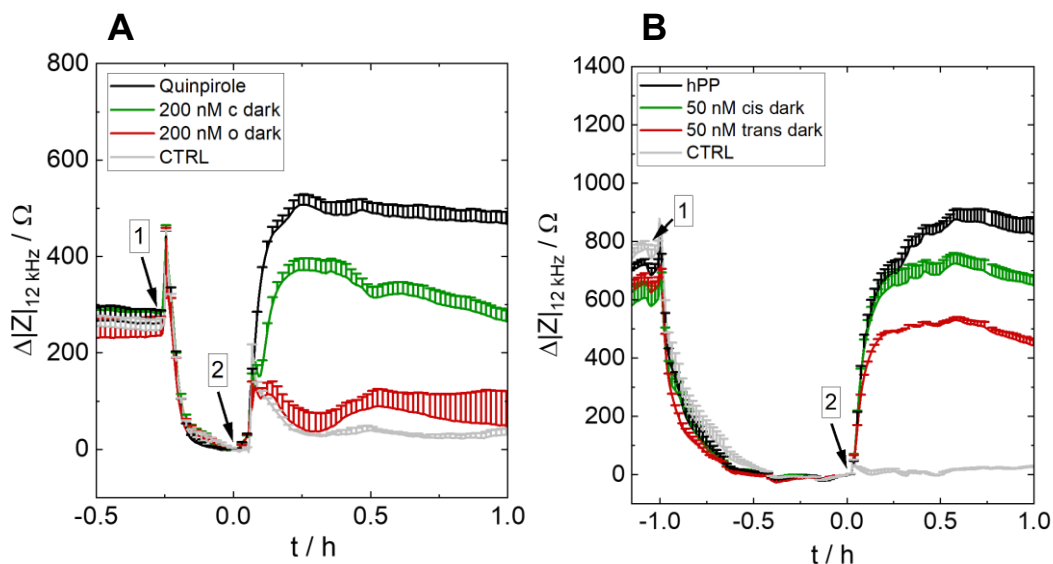


**Figure 115.** Impedance change over time of **CHO D2L (A)** and **CHO NPY (B)** cells after incubation with 0.4  $\mu$ M **FSK** (arrow 1) and stimulation with 200 nM of **ligand 1 (A, green closed, red open)** and 50 nM of **ligand 2 (B, green cis, red trans)** (arrow 2). 100 nM quinpirole (A, black) and 50 nM hPP (B, black) served as positive controls. The negative control (CTRL) is shown in grey. The cells were seeded on a black CE96 electrode array (0.6 mm) that was preincubated with medium. CTRL = negative control. c = closed, o = open. hPP = human pancreatic polypeptide. Baseline A and B: ( $3100 \pm 400$ )  $\Omega$ , ( $2100 \pm 70$ )  $\Omega$ . Mean + SE, N = 3, single experiment. Temperature: 37°C.

After recording an impedance baseline of  $(3100 \pm 400) \Omega$  for CHO D2L cells and addition of FSK, a  $160 \Omega$  peak is observed before impedance drops down about  $300 \Omega$  (**Figure 115A**). Impedance stabilizes 0.25 h after FSK addition. When quinpirole is added (**Figure 115A, black**), the curve increases within 0.25 h to a maximum of about  $500 \Omega$  and keeps a constant level over the measurement period. The *open* and *closed* ligand isomers of **1** show different behavior. While the *closed* isoform (**Figure 115A, green**) behaves similarly to quinpirole but only reaches a level of  $370 \Omega$  that slowly decreases over time, the *open* isoform (**Figure 115A, red**) runs with the curve of the CTRL (**Figure 115A, grey**). For the latter, impedance rises about  $130\text{--}200 \Omega$  at  $t = 0$  h but flattens out again over time to approach the impedance level before the addition of the CTRL.

CHO NPY cells exhibit an impedance baseline of  $(2100 \pm 70) \Omega$  at 12 kHz (**Figure 115B**). When FSK is added, impedance drops down about  $750 \Omega$  over a time of 0.75-1 h. Then, a constant impedance level is observed and hPP, 50 nM of the two ligand isoforms of **2** and a CTRL are added. While the curve of the CTRL remains at the same level over time (**Figure 115B, grey**), the curves for hPP and ligand **2** rise to reach maximal values of about  $900 \Omega$  for hPP (**Figure 115B, black**),  $700 \Omega$  for the *cis*-isoform of **2** (**Figure 115B, green**) and  $500 \Omega$  for the *trans*-isomer of **2** (**Figure 115B, red**) after  $t = 0.25\text{--}0.5$  h. After that, impedance remains unchanged over time.

In a subsequent experiment, the optimal switching concentration was investigated by recording concentration-response curves of ligands **1** and **2** and their respective ligand isoforms. To generate concentration-response curves, CHO D2L and CHO NPY cells were seeded on CE96 electrode arrays (0.6 mm) as described in **chapter 3.5.3.2**. On the day of the experiment, an impedance measurement at the CE96 was started and the cells were prestimulated with  $0.4 \mu\text{M}$  FSK before stimulation with different ligand concentrations ( $2.5\text{--}300$  nM for ligand **1**,  $0.25\text{--}250$  nM for ligand **2**) that were preirradiated with the respective wavelengths for 3 min (see **chapter 3.5.3.2**). For ligand **1**, the impedance data 0.33 h after stimulation relative to the data of  $300$  nM ligand **1** in its *closed* isoform was extracted and plotted against the logarithmic ligand concentration. For ligand **2**, the area under the curve (AUC) between 0.33-0.67 h after stimulation relative to the AUC of  $250$  nM of ligand **2** in its *cis*-isoform was analyzed and plotted against the logarithmic ligand concentration. To obtain concentration-response curves, the data was fitted with a four-parametric dose-response fit (**equation 15**). The results are depicted in **Figure 116A** for CHO D2L and **Figure 116B** for CHO NPY cells.

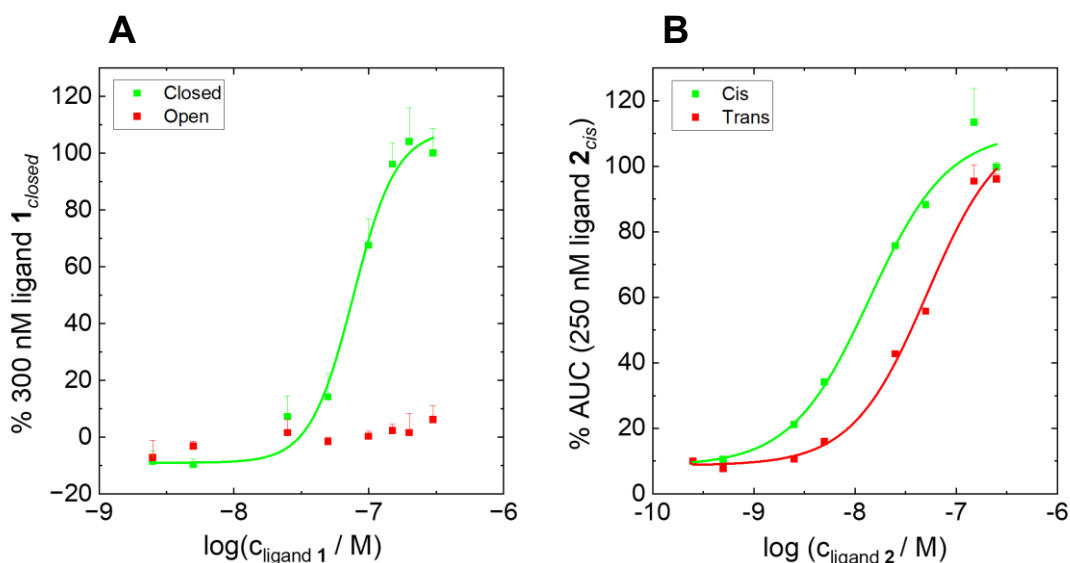


Figure 116. Concentration-response curves for the two ligand isoforms of the **D2L ligand 1** (A, green closed, red open) and **Y4R ligand 2** (B, green cis, red trans). While in (A) the impedance change 0.33 h after stimulation was evaluated relative to the impedance change of 300 nM ligand 1 in its closed isoform, in (B) the area under the curve (AUC) of impedance between 0.33-0.67 h relative to the AUC of 250 nM of ligand 2 in its cis-isoform is plotted. For ligand 1, a  $pEC_{50}$  of  $7.11 \pm 0.05$  and an  $R_{max}$  of  $(100 \pm 10)$  % was determined in its closed isoform. For the open isoform of 1, no  $pEC_{50}$  or  $R_{max}$  value could be determined. The cis- and trans-isomer of ligand 2 reveal  $pEC_{50}$  values of  $7.9 \pm 0.1$  (cis) and  $7.3 \pm 0.1$  (trans). The  $R_{max}$  values are  $(111 \pm 7)$ % for the cis-isoform and  $(110 \pm 10)$ % for the trans-isoform. Mean + SE,  $N = 3$ , four (A) or three (B) independent experiments. Temperature: 37°C.

For ligand 1 in its *open* isoform, constant relative impedance values are detected over the full concentration range (Figure 116A, red). Relative impedance changes around zero are observed. In contrast, the relative impedance of the *closed* isoform of 1 is constant up to a concentration of 25 nM, then increases with increasing ligand concentration and saturates above 150 nM (Figure 116A, green). The relative impedance of the *trans*-isoform of ligand 2 is close to 10% up to a concentration of 2.5-5 nM, increases gradually for larger concentrations and saturates above 150 nM (Figure 116B, red). In comparison, the curve of the *cis*-isoform of ligand 2 is shifted to lower ligand concentrations (Figure 116B, green). For concentrations of 0.25-0.5 nM for the *cis*-isomer of 2, relative values of about 10% are observed. With larger ligand concentrations, the relative AUC of impedance increases and shows a maximum at 150 nM with a significantly larger error bar compared to all other concentrations (up to 700-fold larger). By further increasing the concentration to 250 nM, the relative AUC of impedance is lowered again. The curve for the *cis*-isomer of 2 is not well-fitted for concentrations of 150-250 nM. The largest impedance difference between the two isoforms is observed at 200 nM for ligand 1 and 25-50 nM for ligand 2.

The fits reveal a pEC50 value of  $7.11 \pm 0.05$  and an  $R_{\max}$  (relative  $E_{\max}$ ) of  $(100 \pm 10) \%$  for the *closed* form of ligand **1**, a pEC50 value of  $7.9 \pm 0.1$  for the *cis*-isomer of ligand **2** and  $7.3 \pm 0.1$  for the *trans*-isomer of ligand **2**. The  $R_{\max}$  values for ligand **2** are  $(111 \pm 7) \%$  for the *cis*-isoform and  $(110 \pm 10) \%$  for the *trans*-isoform. For the *open* form of ligand **1**, no sigmoidal fit of the experimental data and, hence, no pEC50 determination was possible.

CHO D2L and CHO NPY cells canonically couple to  $G_i$  proteins (Beaulieu et al., **2015**, Brothers, Wahlestedt, **2010**, Czarnecka et al., **2019**, Polit et al., **2020**). This means downstream of the signaling cascade ACs are inhibited, which leads to decreased cAMP levels. Since it is very hard to detect reductions in the physiological cAMP concentration, the GPCR-independent AC activator FSK is applied before activation of the  $G_i$ -pathway (Hill et al., **2010**, Storch et al., **2017**). This eventually leads to a larger dynamic range of the agonist response (Insel, Ostrom, **2003**). For both CHO D2L (**Figure 115A**) as well as CHO NPY cells (**Figure 115B**), impedance drops down after FSK addition. For CHO D2L cells, a  $300 \Omega$  decrease over 0.25 h and for CHO NPY cells, a  $750 \Omega$  decrease over 0.75-1 h is observed before a stable impedance plateau is reached. Similar observations have been made before (Skiba, **2022**). However, the differences between the FSK-induced time courses of CHO D2L and CHO NPY cells could be attributed to varying activity of the ACs upon FSK addition (Qi et al., **2022**). Furthermore, a more downstream effect could be responsible for the different reactions to FSK. Overall, FSK stimulation or cAMP level increases lead to a decrease in the impedance of  $G_i$ -coupled CHO D2L and CHO NPY cells, indicating morphological changes such as shrinkage of the cells (Kim et al., **2015**, Zor, **1983**).

The opposite effect is observed after  $G_i$  protein activation and a concomitant decrease of intracellular cAMP concentrations (**Figure 115A-B**). After the addition of the full agonists quinpirole and hPP (**Figure 115A-B, black**), impedance rises and reaches maxima of about  $500 \Omega$  (quinpirole) or  $900 \Omega$  (hPP), which are maintained over time. As compared with the FSK response, the increase of impedance after quinpirole and hPP addition indicates cAMP level decreases after  $G_i$  activation. Quinpirole and hPP concentrations are  $\geq EC_{80}$  and, thus, saturate the signals (Boeckler, Gmeiner, **2007**, van der Kolk et al., **2022**).

The photoswitchable ligands exhibit different bioactivities detected by impedance spectroscopy. While ligand **1** shows a distinct impedance increase (referred to as “more active”) in its *closed* isoform (**Figure 115A, green**), its *open* isoform does not show any bioactivity indicated by impedance values comparable to the CTRL

(**Figure 115A, red, grey**). Furthermore, both isomers of ligand **2** show an impedance increase with the *cis*-isomer (**Figure 115B, green**) displaying higher values (“more active”) compared to the *trans*-isoform (**Figure 115B, red**). Since the *closed* isoform of **1** and both isoforms of **2** exhibit an impedance increase after ligand addition, which is similar to the impedance profile of the positive controls quinpirole and hPP, it is straightforward to conclude that cAMP levels decrease after ligand exposure. However, the *open* isoform of **1** does not show any impedance response. This suggests that the *open* isomer of **1** does not display any G<sub>i</sub>-activity with subsequent reduction of cAMP concentrations. Another rather hypothetical explanation could be the activation of an additional pathway, which overlays with the impedance response after G<sub>i</sub>-activation, leading to a compensation of the impedance readout.

These observations are also confirmed by the concentration-response curves (**Figure 116A-B**). For the D2L ligand **1**, bioactivity detected by a concentration-dependent impedance signal is only observed for the *closed* isoform (**Figure 116A, green**). The *open* isoform of **1** does not display any impedance change with increasing ligand concentrations (**Figure 116A, red**). Virtually, a “full on/off” behavior is observed since concentrations of 150 nM and larger either display no impedance response (*open*, **1**) or about 60% of the impedance response of quinpirole (*closed*, **1**). In IP accumulation and β-arrestin recruitment assays, efficacy values relative to the positive control quinpirole have been determined for both isoforms of **1** before (Lachmann et al., **2017**). In contrast to the impedance data, both isoforms displayed similar efficacy values in the IP accumulation and β-arrestin recruitment assay and only showed weak β-arrestin recruitment. Since the IP accumulation, indicating G<sub>q</sub>-protein activation (Trinquet et al., **2011**), and the β-arrestin signaling revealed similar results for both isomers of **1**, neither can be used as an explanation for the differing impedance values. Further studies are necessary to clarify the impedance signaling patterns of the *closed* and *open* isoform of **1**, e.g. regarding G<sub>s</sub>- or G<sub>12/13</sub>-activation and other mechanisms.

Ligand **2** displays a bioactivity for both isomers given by increased impedance values compared to the CTRL (**Figure 116B**). No “full on/off” behavior is observed here. However, the *cis*-form (**Figure 116B, green**) is more potent than its *trans*-isomer (**Figure 116B, red**). The impedance decrease observed for 250 nM of the *cis*-form can be explained by a toxic or hook effect, i.e. unspecific binding effect (Ross et al., **2020**). The pEC<sub>50</sub> values of  $7.9 \pm 0.1$  for the *cis*-isomer and  $7.3 \pm 0.1$  for the *trans*-isomer of ligand **2** are in good agreement with values determined in a split luciferase complementation assay. There, values of  $7.79 \pm 0.04$  for the *cis*-isomer and  $7.08 \pm 0.02$  for the *trans*-isomer were reported (Wirth et al., **2023**). The R<sub>max</sub> values

for ligand **2** determined by impedance spectroscopy are  $(111 \pm 7)\%$  for the *cis*-isoform and  $(110 \pm 10)\%$  for the *trans*-isoform. These values are larger compared to the values found in the split luciferase assay (83% for the *cis*- and 62% for the *trans*-isomer) (Wirth et al., **2023**), which is attributed to the distal nature of the impedance readout compared to the proximal measurement of G protein activation. In the case of impedance, the signals along the cascade are integrated and, hence, already saturate for smaller ligand concentrations. This might also explain why the difference between both  $R_{\max}$  values is smaller for impedance than for the G protein recruitment (Schröder et al., **2010**, Wirth et al., **2023**).

From the largest difference between the concentration-response curves of two ligand isoforms (**Figure 116A-B**), the optimal concentration for switching experiments is determined. The larger the differences between the two curves, the more distinguishable the two impedance profiles and the more evident will the switch between isoforms be. Subsequently, in further experiments, concentrations of 200 nM (ligand **1**) and 50 nM (ligand **2**) were chosen as suitable concentrations in switching assays.

### 6.3 Switching and Toggling of Photoswitchable Ligands

After the determination of the optimal switching concentrations for ligands **1** and **2** in **chapter 6.2**, the switching and toggling behavior is investigated. For that purpose, impedance analysis is considered a suitable detection method because of its non-optical, real-time readout.

CHO D2L and CHO NPY cells were seeded according to **chapter 3.5.3.2** on CE96 electrode arrays (0.6 mm) that were preincubated with medium. On the day of the experiment, the culture medium was removed and exchanged with L15 buffer and an impedance baseline was recorded at the CE96 impedance device. As usual, cells were pretreated with 0.4  $\mu\text{M}$  FSK until a stable impedance level was reached. Subsequently, the cells were stimulated with preirradiated ligand solutions (200 nM ligand **1**, 50 nM ligand **2**). At least 0.33 h after stimulation, a part of the 96-well plate was irradiated with LEDs of appropriate wavelengths to switch from one ligand isoform to another (ligand **1** 395 nm: *o*→*c*, 505 nm: *c*→*o*; ligand **2** 340 nm: *trans*→*cis*, 451 nm: *cis*→*trans*). The respective wells were irradiated for 3 min. Non-irradiated wells were covered with aluminum foil to prevent unintentional switching (dark controls, quinpirole, hPP and negative control (CTRL)). The results for CHO D2L cells and ligand **1** are given in **Figure 117A-B**.

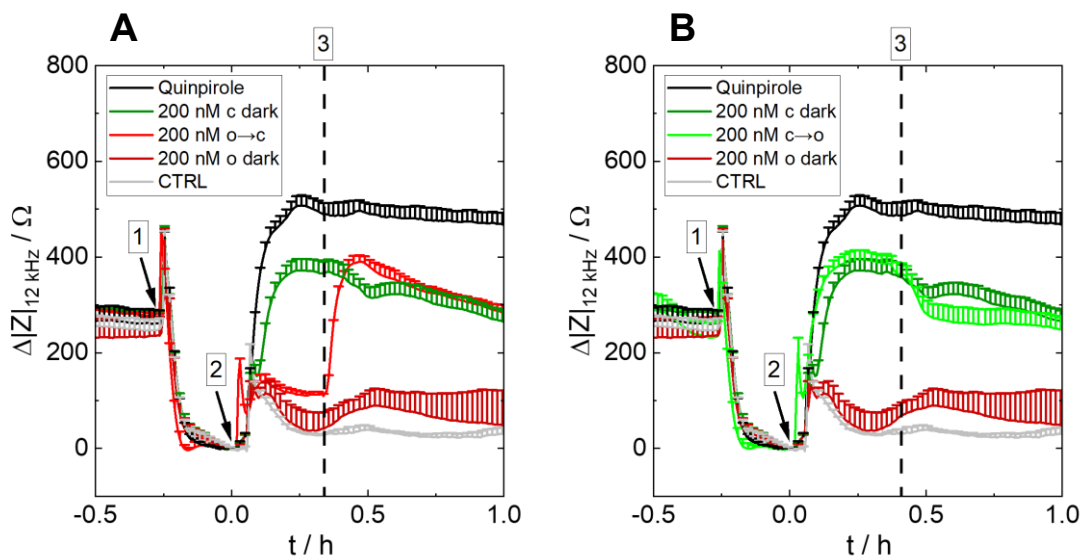


Figure 117. Impedance change over time of **CHO D2L** cells after incubation with  $0.4 \mu\text{M}$  **FSK** (arrow 1) and stimulation with 200 nM of **ligand 1** (arrow 2). 0.33 h after stimulation, the open isoform of **1** was irradiated with a 395 nm LED for 3 min to create the closed isoform (A, light red) and 0.42 h after stimulation, the closed isoform of **1** was illuminated with a wavelength of 505 nm for 3 min to switch to the open isoform (B, light green) (dashed vertical line 3). 100 nM quinpirole served as a positive control (black), while the grey curve describes the negative control (CTRL). In addition, non-illuminated controls are depicted (dark green: non-illuminated closed isoform “c dark”, dark red: non-illuminated open isoform “o dark”). The cells were seeded on a black CE96 electrode array (0.6 mm) that was preincubated with medium. CTRL = negative control. c = closed, o = open. Baseline:  $(3100 \pm 400) \Omega$ . Mean + SE,  $N = 3$ , single experiment. Temperature:  $37^\circ\text{C}$ .

For a detailed description and explanation of the impedance curves of quinpirole (Figure 117A-B, black), the non-illuminated closed (Figure 117A-B, dark green) and open (Figure 117A-B, dark red) isoforms of ligand **1** and the CTRL (Figure 117A-B, grey), please refer to chapter 6.2. In brief, after the addition of FSK, an impedance decrease of about 300  $\Omega$  is discerned. As impedance stabilizes after 0.25 h, the different compounds are added. While the curves of the CTRL and non-illuminated open isoform of **1** remain at a similar impedance level as before compound addition, the curves for quinpirole and the closed isoform of **1** increase to levels of 500  $\Omega$  and 370  $\Omega$ , respectively.

Considering the light red and light green curves in Figure 117A-B, the wells were treated like the non-illuminated open (Figure 117A-B, dark red) and closed (Figure 117A-B, dark green) isomers. However, at the time points  $t = 0.33$  h and  $t = 0.42$  h, the respective wells were illuminated to switch from the open to the closed (o  $\rightarrow$  c, Figure 117A, light red) or from the closed to the open (c  $\rightarrow$  o, Figure 117B, light green) isomer. After an irradiation time of 3 min with a wavelength of 395 nm, the impedance of the open isoform of **1** increases from the level of the non-illuminated open isomer (Figure 117A, dark red) to a maximum of  $(390 \pm 10) \Omega$  within 0.13 h (Figure 117A, light red). Then, impedance stabilizes around the level of the non-

irradiated *closed* isoform (**Figure 117A, dark green**). The curves for the  $o \rightarrow c$  switch and the non-illuminated *closed* isomer are indistinguishable until the end of the measurement (**Figure 117A, light red, dark green**). When the *closed* isoform of **1** is irradiated with a wavelength of 505 nm for 3 min, impedance decreases from the impedance level of the non-illuminated *closed* isoform (**Figure 117B, dark green**) and reaches a constant impedance value of approximately 260  $\Omega$  within 0.17 h (**Figure 117B, light green**). This level is kept constant over the measurement period. The level of the non-illuminated *open* isomer of **1** (**Figure 117A-B, dark red**) is not reached.

In a second experiment, the switching behavior of the two ligand isoforms of **2** was analyzed with the CHO NPY system by impedance measurements at the CE96 device. The time courses are depicted in **Figure 118A-B**.

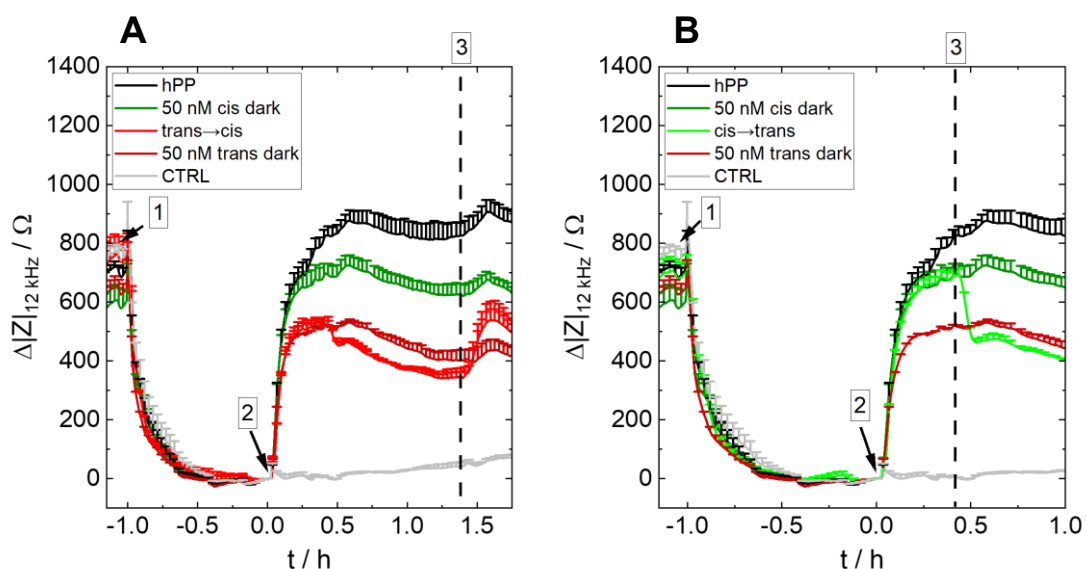


**Figure 118.** Impedance change over time of **CHO NPY** cells after incubation with 0.4  $\mu\text{M}$  **FSK** (arrow 1) and stimulation with 50 nM of **ligand 2** (arrow 2). 1.4 h after stimulation, the *trans*-isoform of **2** was irradiated with a 340 nm LED for 3 min to create the *cis*-isoform (A, light red) and 0.4 h after stimulation the *cis*-isoform of **2** was illuminated with a wavelength of 451 nm for 3 min to switch it to the *trans*-isoform (B, light green) (dashed vertical line 3). 50 nM hPP served as a positive control (black), while the grey curve displays the negative control (CTRL). In addition, not-illuminated controls are depicted (dark green: non-illuminated *cis*-isoform “*cis* dark”, dark red: non-illuminated *trans*-isoform “*trans* dark”). The cells were seeded on a black CE96 electrode array (0.6 mm) that was preincubated with medium. CTRL = negative control. hPP = human pancreatic polypeptide. Baseline:  $(2100 \pm 70) \Omega$ . Mean + SE,  $N = 3$ , single experiment. Temperature: 37°C.

For a detailed description and explanation of the impedance curves of hPP (**Figure 118A-B, black**), the non-illuminated *cis*- (**Figure 118A-B, dark green**) and *trans*- (**Figure 118A-B, dark red**) isoforms of ligand **2** and the CTRL (**Figure 118A-**

**B, grey**), please refer to **chapter 6.2**. Very briefly, the addition of FSK leads to a 750  $\Omega$  impedance decrease within 0.75-1 h. After compound addition, the impedance of the CTRL remains at the same level as before, while the impedance of the *cis*- and *trans*-isomer of **2** as well as of the hPP control rises until a stable impedance level is observed. The plateaued values amount to 900  $\Omega$  (hPP), 700  $\Omega$  (*cis*-isoform) and 500  $\Omega$  (*trans*-isoform).

In the following, the impedance courses of the irradiated isoforms of **2** (**Figure 118A, light red** and **Figure 118B, light green**) will be described. The curve of the irradiated *trans*-isomer (**Figure 118A, light red**) predominantly superimposes with the corresponding non-illuminated *trans*-control (**Figure 118A, dark red**). Only after  $t = 0.4$  h, an effect on impedance is visible: it decreases by about 100  $\Omega$ . At this time point, the *trans*-isomer was illuminated with 451 nm to convert the remaining *cis*-isomer to the *trans*-form (**Figure 118A, light red**). When the same wells are illuminated with a wavelength of 340 nm for 3 min at  $t = 1.4$  h, an impedance increase of approximately 190  $\Omega$  is observed (*trans*→*cis*, **Figure 118A, light red**). This impedance change is in accordance with the impedance difference between both non-illuminated controls of ligand **2** (**Figure 118A, dark red, dark green**). **Figure 118B, light green** depicts the equivalent results for the illuminated *cis*-isomer of ligand **2**. Its impedance progress over time can not be discriminated from the respective non-illuminated *cis*-control (**Figure 118B, dark green**). Only after illumination with a wavelength of 451 nm for 3 min, impedance decreases from  $(690 \pm 20)$   $\Omega$  to  $(480 \pm 10)$   $\Omega$  within 0.07-0.08 h (*cis*→*trans*, **Figure 118B, light green**). Thereafter, the impedance values are similar to those of the unperturbed *trans*-isoform (**Figure 118B, dark red**).

In a consecutive experiment, repeated switching between the two isoforms of ligand **2** was examined. The experimental protocol is the same as described above. After prestimulation with 0.4  $\mu$ M FSK and stimulation with 50 nM of the *cis*- and *trans*-isomer of ligand **2** (cf. **Figure 118A-B**), the *trans*-isoform was illuminated with 451 nm at  $t = 0.4$  h and the *cis*-form was irradiated with a wavelength of 340 nm after  $t = 0.55$  h. In either case, the isoforms are switched towards the same isoform again to explore whether the PSS are in a range of 78-92% as determined by HPLC measurements and UV/Vis detection at the isosbestic points (Wirth et al., **2023**). Thereafter, the isoforms were alternately irradiated with both wavelengths to toggle between the *cis*- and *trans*-state and the corresponding bioactivity. The illumination time was set to 3 min in every case. The change of impedance over time in

comparison to 50 nM hPP, a CTRL and non-illuminated controls is depicted in **Figure 119A-B**.

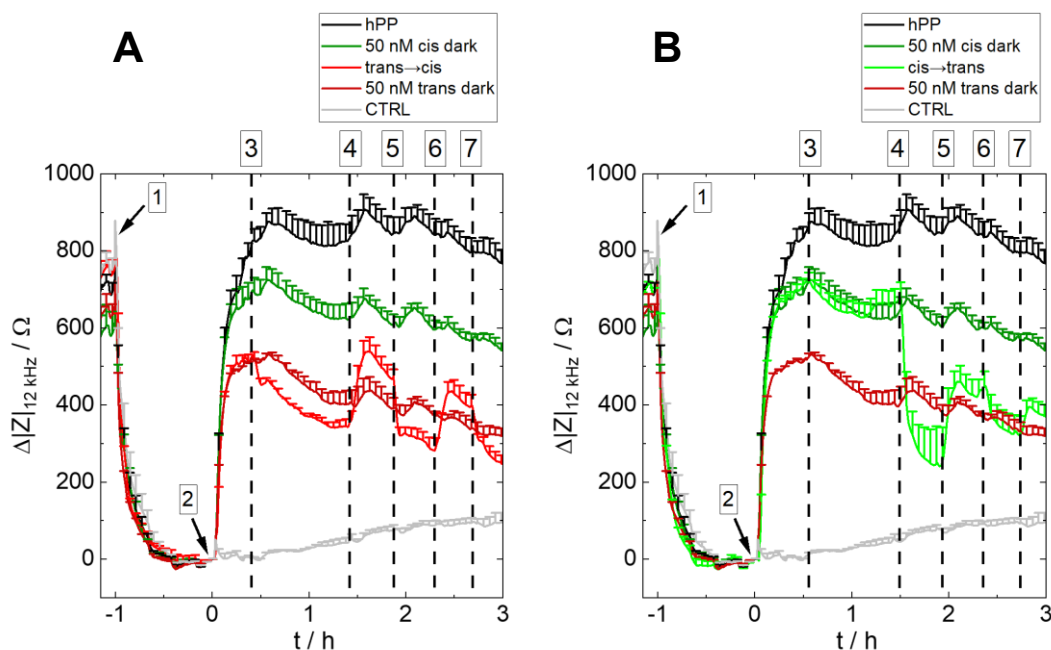


**Figure 119.** Impedance change over time of **CHO NPY** cells after incubation with  $0.4 \mu\text{M}$  **FSK** (arrow 1) and compound addition (arrow 2, black hPP, dark green non-illuminated *cis*-isoform of ligand **2**, dark red non-illuminated *trans*-isoform of ligand **2**, light red toggling of ligand **2** starting with *trans*-isomer, light green toggling of ligand **2** starting with *cis*-isomer, grey negative control (CTRL)). (A) The *trans*-isoform of **2** (light red) is first illuminated with a wavelength of 451 nm to transfer all remaining *cis*-isomers into the *trans*-form (vertical line 3). Then, the respective wells are alternately illuminated with 340 nm and 451 nm to toggle between both isoforms (vertical lines 4-7). (B) The *cis*-isomer of **2** (light green) is first illuminated with 340 nm to ensure that only the *cis*-isomer is present in the wells (vertical line 3). Subsequently, an alternating illumination with 451 nm and 340 nm is performed to toggle between the two isoforms (vertical lines 4-7). The irradiation time is 3 min in all cases. All utilized concentrations are 50 nM. The cells were seeded on a black CE96 electrode array (0.6 mm) that was preincubated with medium. CTRL = negative control. hPP = human pancreatic polypeptide. Baseline:  $(2100 \pm 70) \Omega$ . Mean + SE,  $N = 3$ , single experiment. Temperature:  $37^\circ\text{C}$ .

The impedance responses after FSK and compound addition (hPP, *cis*- and *trans*-isoform of **2**, CTRL) have been described before and are similar to **chapter 6.2**. Therefore, only the toggling behavior of both isoforms of ligand **2** will be considered in the following (**Figure 119A-B**).

Once the *trans*-isoform is illuminated with 451 nm to switch towards the same isoform (**Figure 119A**, light red, vertical line 3), impedance quickly decreases by about 100  $\Omega$ . Then, a slow impedance decrease over time is observed as for the non-illuminated controls and hPP (**Figure 119A-B**, black, dark green, dark red). After  $t = 1.4$  h, illumination of the same wells with 340 nm leads to a 190  $\Omega$  impedance increase (*trans*→*cis*, **Figure 119A**, light red, vertical line 4). A local maximum is reached followed by a slow and gradual decrease of impedance as for hPP and the

dark controls of ligand **2**. Subsequent alternate irradiation with 451 nm, 340 nm and 451 nm (**Figure 119A, light red, vertical lines 5, 6 and 7**) leads to an alternate decrease and increase of impedance.  $\Delta|Z|_{12\text{ kHz}}$  diminishes from 150  $\Omega$  to 90  $\Omega$  with each switching cycle. The curve consistently fluctuates around the curve of the non-illuminated *trans*-control (**Figure 119A, dark red**). Overall, impedance gradually decreases for the hPP control, the non-illuminated controls and the toggled sample (**Figure 119A, black, dark green, dark red, light red**). Furthermore, the impedance time courses of the non-irradiated wells (**Figure 119A, black, dark green, dark red**) show small perturbations as soon as the toggled wells are exposed to light and switched from one isomer to another. Only the CTRL curve shows a slight impedance increase over a measurement time of 3 h (**Figure 119A, grey**).

If the *cis*-isomer of ligand **2** is illuminated with 340 nm to convert the remaining *trans*-isomer to the *cis*-form (**Figure 119B, light green, vertical line 3**), impedance does not change but remains at the same level as the curve for the dark *cis*-control (**Figure 119B, dark green**). After switching with 451 nm at  $t = 1.5$  h, impedance decreases about 435  $\Omega$  and reaches values between 250-350  $\Omega$  (*cis*→*trans*, **Figure 119B, light green, vertical line 4**), which lie below the values of the non-irradiated *trans*-control (**Figure 119B, dark red**). When the wavelength is changed to 340 nm again after  $t = 1.9$  h, impedance rises about 220  $\Omega$  (**Figure 119B, light green, vertical line 5**), which is similar to the difference between both non-illuminated controls (**Figure 119B, dark green, dark red**). At  $t = 2.4$  h, further illumination with 451 nm leads to a 130  $\Omega$  decrease of impedance (**Figure 119B, light green, vertical line 6**), which is less pronounced than the one observed before (**Figure 119B, light green, vertical line 4**). Another illumination step with 340 nm increases impedance but only about 60  $\Omega$  (**Figure 119B, light green, vertical line 7**), which is also less marked compared to 220  $\Omega$  after the third switch (**Figure 119B, light green, vertical line 5**). It is noticed that the curve for the alternately switched *cis*-isomer fluctuates around the values of the dark *trans*-control (**Figure 119B, dark red**) starting after the second illumination step. In contrast, the impedance level of the non-illuminated *cis*-control (**Figure 119B, dark green**) is not reached anymore. Moreover, the impedance curves of the hPP control and the non-illuminated controls (**Figure 119B, black, dark green, dark red**) display minor fluctuations once the *cis*-isomer is illuminated and gradually decrease over a measurement time of 3 h. Only the impedance of the CTRL gradually increases over time (**Figure 119B, grey**).

Ligand **1** fully switches from the *open* to the *closed* isomer and, hence, portrays a textbook example because a regulation between an inactive (impedance close to

CTRL values) and an almost fully active state (impedance close to the values of the positive control) is possible (**Figure 117A, light red**). However, switching of ligand **1** from the *closed* to its less active *open* isomer is poorly developed (**Figure 117B, light green**). Only a 140  $\Omega$  decrease in impedance is observed while the impedance difference between both non-illuminated isoforms of ligand **1** takes a value of about 300  $\Omega$ . This can be explained by the nature of GPCR signaling: it is more difficult to imagine switching off a signaling cascade composed of a variety of processes once it has been triggered than initiating a series of reactions to trigger a signaling cascade. Nonetheless, it should be kept in mind that an impedance decrease might imply the activation of ACs and an increase in the cAMP formation (Leung et al., **2005**).

The switch from the *cis*- to the less active *trans*-form of ligand **2** is very efficient (**Figure 118B, light green**). Additionally, ligand **2** shows an impedance change from the *trans*- to the *cis*-isoform that is similar to the impedance difference between the non-illuminated controls (**Figure 118A, light red**). Still, the impedance level of the non-irradiated *cis*-isoform (**Figure 118A, dark green**) is not achieved. This is attributed to the illumination of the *trans*-isomer with 451 nm at  $t = 0.4$  h to convert remaining *cis*-isomers to their *trans*-form and yielded a 100  $\Omega$  decrease of impedance in comparison to the dark *trans*-control of **2** (**Figure 118A, light red**). This impedance decrease indicates that the PSS of the *trans*-isomer of **2** (78%) was not achieved by preirradiating the ligand solution with 451 nm for 3 min. Consequently, the preirradiation time for the *trans*-isomer might be too short. Another explanation could be the modification of the PSS attributed to the change of the environment of the photoswitchable ligand: the peptide-derived *cis*-isoform might be stabilized better in the cellular and GPCR environment compared to the conditions in solution. In the opposite case, i.e. illuminating the *cis*-isomer with 340 nm to switch the remaining *trans*-isomer to the *cis*-isoform, no alterations in impedance are observed (**Figure 119B, light green, vertical line 3**). Presumably, the PSS of 92% is obtained for the *cis*-isoform of **2**. No back-isomerization to the thermally more stable *trans*-isomer is observed within the framework of the experiment with a total measurement time of 5 h. This corresponds well to the thermal half-life of 23.7 d detected in aqueous buffer (Wirth et al., **2023**).

Generally, decreases in impedance indicate an increase in the cAMP concentration in the cell interior as observed for the FSK prestimulation step (Leung et al., **2005**, Scott, Peters, **2010**). The opposite effect, i.e. cAMP level decreases, is suggested when increases in impedance are detected. Consequently, photoswitching and subsequent increases and decreases of the impedance are correlated with the modification of intracellular cAMP concentrations. Accordingly, regulation of cAMP

levels and the associated bioactivity by light is possible and can be detected with impedance measurements. This offers whole new methods for medical near-surface applications like tumor treatment where a spatiotemporal control of the destruction of malignant cells is inevitable. In 2020, Reynders *et al.* developed a new family of photoswitchable ligands called photochemically targeted chimeras (PHOTACs) for cancer therapy (Reynders *et al.*, **2020**). PHOTACs are derived from the previously described proteolysis targeting chimeras (PROTACs), which consist of two binding domains, one for an E3 ubiquitin ligase and another for a protein of interest, both connected by a linker. After the formation of a ternary ligase-PROTAC-protein complex, the bound protein of interest is degraded. PHOTACs, however, incorporate a photoswitchable moiety. Thus, protein degradation is controlled by light of a certain wavelength. PHOTACs have been used to destroy different proteins implicated in cancer close to the surface (Reynders *et al.*, **2020**, Wang *et al.*, **2022**).

Considering the toggling behavior of ligand **2**, switching between the two isoforms is most effective after the first illumination (**Figure 119A-B, light red, light green**). Here, the impedance change is similar to the difference between both non-illuminated controls (**Figure 119A-B, dark red, dark green**). With an increasing number of illuminations and alternate switching, the switching efficiency and, thus, the impedance change is reduced. Furthermore, an overall downward drift to smaller impedance values is observed for all curves (but the CTRL curve (**Figure 119A-B, grey**)). This suggests that over time the cells lose their sensitivity towards the (photoswitchable) ligands, which might be attributed to desensitization and internalization of the GPCRs (Doijen *et al.*, **2019**, Rajagopal, Shenoy, **2018**). Furthermore, a lack of serum proteins in the L15 buffer and the prolonged measurement time might lead to cellular fatigue behavior (Wirth *et al.*, **2023**).

Non-irradiated wells show fluctuations in the impedance if different wells on the same 96-well plate are illuminated (**Figure 119A-B**). This is attributed to small changes in the temperature, humidity or CO<sub>2</sub> content inside the measurement chamber. When a certain number of wells is illuminated, the chamber lid must be removed, the non-illuminated wells are covered with aluminum foil and the remaining wells are exposed to light for 3 min. Accordingly, an effect on impedance by the light itself is ruled out. However, during the illumination process, a temperature of 37°C and a humidity of 100% can not be held constant. The impact of varying CO<sub>2</sub> concentrations on impedance measurements should not be underestimated either. Changes in the CO<sub>2</sub> content potentially result in the modification of the pH value of the assay medium, which leads to altered impedance values (Lo *et al.*, **1994**). But since the measurement was performed at 0% (v/v) CO<sub>2</sub>, which corresponds to ambient air conditions,

temperature or humidity variations are suggested to account for the small impedance changes.

In summary, switching between the two isoforms of ligands **1** and **2** can be monitored with the CE96 impedance assay. A change in bioactivity after an illumination time of 3 min with light of different wavelengths is highly distinctive for switching ligand **1** from the *open* to the *closed* isomer (**Figure 117A, light red**) and ligand **2** from the *trans*- to the *cis*-form (**Figure 118A, light red**). In addition, switching ligand **2** from the *cis*-isoform to its *trans*-isoform (**Figure 118B, light green**) is detectable. Maximal switching is observed in these cases since the impedance changes correspond well to the impedance differences between the curves of the non-illuminated isoforms of ligands **1** and **2**. This confirms the choice of the LEDs, their wavelengths, the selected illumination time of 3 min and the choice of the switching concentrations (200 nM for ligand **1** and 50 nM for ligand **2**). The light intensity of the diodes is large enough to switch highly diluted (nM) solutions of both ligands from one isoform to another. Furthermore, an illumination time of 3 min results in a maximal conversion of all photoswitchable ligands. This illumination time was also sufficient for the preirradiation of the ligand stock solutions to generate the single isoforms before dilution and subsequent stimulation of the cells. The only exception is the *trans*-isoform of ligand **2**. Here, longer preirradiation times are recommended to obtain the respective PSS. Moreover, the impedance values of both ligand isoforms of **1** and **2** at the respective switching concentrations were well distinguishable. Accordingly, switching and toggling between the isoforms was detectable by the impedance assay as well (**Figure 117A, Figure 118A-B and Figure 119A-B**).

The question arises whether the switching and toggling between two isoforms of one photoswitchable ligand take place within the binding pocket of the GPCR or in the bulk solution. This issue will be addressed in the following **chapter 6.4**.

## 6.4 Insights Into the Switching Mechanism

To clarify whether switching takes place in the binding pocket of the GPCR or in solution, a washing experiment was performed with CHO NPY cells and ligand **2**. The cells were cultivated as described in **chapter 3.5.3.2**. After the exchange of the culture medium on the day of the experiment, an impedance baseline in L15 buffer was recorded at the CE96 device. Then, the cells were prestimulated with 0.4  $\mu\text{M}$  FSK and stimulated with 50 nM of the preirradiated *cis*- and *trans*-isoform of ligand **2**. In addition, positive (hPP) and negative controls (CTRL) were investigated. 0.3-0.4 h

after stimulation the impedance measurement was paused and multiple wells were washed with L15 buffer once to remove non-bound ligand. The measurement was continued in L15 buffer and switching between both ligand isomers of **2** was implemented to elucidate the switching mechanism (**Figure 120A-B**).

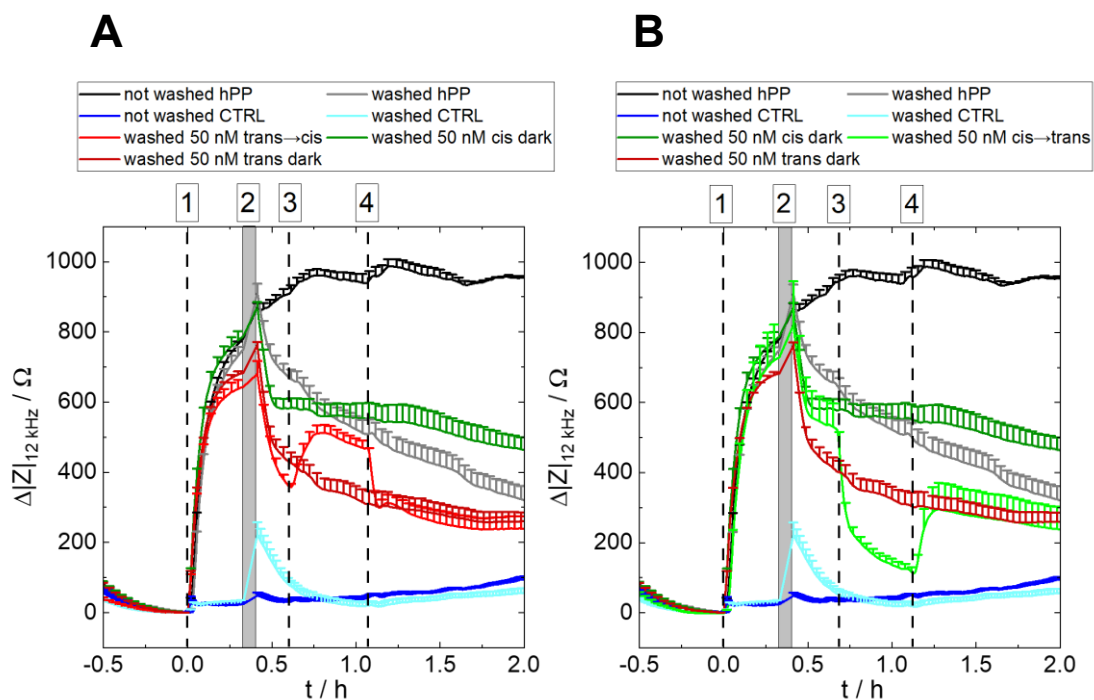


**Figure 120.** Impedance change over time of **CHO NPY** cells after incubation with  $0.4 \mu\text{M}$  **FSK** (not shown) and addition of  $100 \text{ nM}$  hPP (black, grey), a negative control (CTRL, blue, cyan) or  $50 \text{ nM}$  of the *cis*- (dark green, light green) or *trans*-isomer (dark red, light red) of ligand **2** (vertical line 1). During time interval 2, indicated by the grey bar, the cells were either washed with L15 buffer once (grey, dark green, dark red, light green, light red, cyan) or were not influenced (black, blue). Subsequently, the wells were irradiated alternately with wavelengths of  $340 \text{ nm}$  and  $451 \text{ nm}$  (A, light red) or  $451 \text{ nm}$  and  $340 \text{ nm}$  (B, light green) (vertical lines 3 and 4). The cells were seeded on a black CE96 electrode array ( $0.6 \text{ mm}$ ) that was preincubated with medium. CTRL = negative control. hPP = human pancreatic polypeptide. Baseline:  $(1700 \pm 6) \Omega$ . Mean + SE,  $N = 2-3$ , single experiment. Temperature:  $37^\circ\text{C}$ .

After prestimulation with FSK, impedance decreases as observed in **chapter 6.2** (not fully shown). Once hPP, the *cis*- or *trans*-isoform of ligand **2** or the CTRL is added, impedance remains at the same impedance level (CTRL) or quickly rises to an impedance level of about  $800 \Omega$  (hPP and *cis*-isoform of **2**) or  $650 \Omega$  (*trans*-isoform of **2**). Between  $t = 0.3-0.4 \text{ h}$ , the measurement was paused and part of the wells containing hPP, the CTRL or the *cis*- or *trans*-isoform of **2** were washed (**Figure 120A-B**, grey, dark green, dark red, light green, light red, cyan) while some wells containing hPP and the CTRL were kept unaffected (**Figure 120A-B**, black, blue). Immediately after washing, the impedance of the washed wells is increased by about  $100 \Omega$  and, subsequently, continuously recedes over the measurement period. Only for the washed CTRL (**Figure 120A-B**, cyan), impedance

levels off within 0.25 h and reaches a plateau with values similar to the values of the unperturbed CTRL (**Figure 120A-B, blue**). The impedance values of all other washed wells diminish in the following order: hPP > *cis*-isoform of **2** > *trans*-isoform of **2** > CTRL. Thereby, both curves of the *trans*-isomer superimpose (**Figure 120A, light red, dark red**), while one curve of the *cis*-isomer of **2** is lowered about 50-100  $\Omega$  in comparison to the other (**Figure 120B, light green, dark green**). It must be noted that up to this point, both curves of the *cis*-isomer (**Figure 120B, light green, dark green**) should overlay since no illumination was conducted. However, it is obvious that the error bars of the light green curve in **Figure 120B** are at least twice as big as for the dark green curve. The non-influenced wells (**Figure 120A-B, black, blue**) display an impedance progression similar to **chapter 6.2**. At  $t = 0.6-0.7$  h, the *trans*-isoform of **2** is illuminated with 340 nm (**Figure 120A, light red**) and the *cis*-form of **2** is irradiated with a wavelength of 451 nm (**Figure 120B, light green**) to isomerize the remaining ligands and obtain the respective opposing isomer. In the former case, impedance increases from the level of the non-illuminated but washed *trans*-isomer (**Figure 120A, dark red**) and approaches the level of the non-irradiated but washed *cis*-isomer (**Figure 120A, dark green**). If the *cis*-isomer is illuminated to obtain the *trans*-isomer (**Figure 120B, light green**), impedance drops about 300-400  $\Omega$  and reaches an impedance level that is about 200  $\Omega$  smaller than the level of the non-irradiated but washed *trans*-control (**Figure 120B, dark red**). Back-isomerization after  $t = 1.07$  h (451 nm, **Figure 120A, light red**) and  $t = 1.12$  h (340 nm, **Figure 120B, light green**) causes the opposite effects. In **Figure 120A, light red**, impedance falls back to the level of the washed but non-illuminated *trans*-isomer (**Figure 120A, dark red**). Both curves superimpose until the end of the measurement (**Figure 120A, light red, dark red**) but continuously decline. In **Figure 120B, light green**, impedance rises about 200  $\Omega$  when illuminated with 340 nm light to obtain the *cis*-isoform of **2**. However, only the impedance level of the *trans*-isomer of **2** (**Figure 120B, dark red**) is reached and kept over the measurement period while impedance gradually decreases.

The impedance decrease after FSK addition and the impedance increase after stimulation with hPP and both ligand isoforms of **2** are explained by morphological changes resulting from cAMP level increases and decreases and have been discussed and illustrated in **chapter 6.2** before. In **Figure 120A-B**, it is noted that the curves for hPP and the *cis*-isomer of **2** fully overlay up to the time interval of washing starting at  $t = 0.3$  h. This has also been observed in **Figure 115B, black, dark green** before for a similar acquisition time of  $t = 0.25-0.3$  h. Just after 0.3 h, the curve for the

*cis*-isomer of **2** levels off and remains at an impedance level of about 700  $\Omega$ , while the curve for hPP continues to increase to an impedance value of 900  $\Omega$  (**Figure 115B, black, dark green**). The latter is also observed in this chapter (**Figure 120A-B, black, dark green**). However, the impedance values of 650-700  $\Omega$  obtained for the *trans*-isomer of **2** after 0.3 h (**Figure 120A-B, light red, dark red**) are 150-200  $\Omega$  larger compared to **chapters 6.2 and 6.3**. Since the ligand concentrations were the same, this might be attributed to an enhanced sensitivity of the cells towards the *trans*-ligand depending on the passage number and expression level of the GPCR (Eiger et al., **2022**). Another explanation could be that the PSS of the *trans*-isomer (Wirth et al., **2023**) is not fully achieved as was anticipated in **chapter 6.3** for the same ligand isomer of **2** before.

When the impedance measurement is continued after washing with L15, impedance gradually declines over time. The impedance decrease is explained by the washing procedure itself, stressing the cells and potentially leading to desensitization and internalization mechanisms (Bagnato, Rosanò, **2019**, DeFea, **2013**, Szénási et al., **2023**). Since the impedance of the washed CTRL (**Figure 120A-B, cyan**) only takes about 0.25 h until a stable impedance plateau similar to the non-washed CTRL (**Figure 120A-B, blue**) is reached again, the observed impedance decrease after  $t = 0.75$  h can not be explained by the washing procedure itself but must be attributed to desensitization processes.

Once the two isomers are illuminated with 340 nm (**Figure 120A, light red, vertical line 3**) or 451 nm (**Figure 120B, light green, vertical line 3**) light to isomerize them, impedance increases to the level of the non-illuminated *cis*-control (**Figure 120A, light red, dark green**) or decreases and reaches a level below the level of the non-illuminated *trans*-control (**Figure 120B, light green, dark red**). This indicates that the photoswitching after a washing step is possible, detectable with impedance readings and similar to the results observed in previous chapters where no washing took place (cf. **chapter 6.3**). According to **Figure 118A-B, light red, light green**, an impedance change of 200  $\Omega$  was observed for switching ligand **2** in either direction. The amplified decrease of impedance in **Figure 120B, light green** might be referred to the superposition of washing and desensitization effects.

When the ligands are back-isomerized (**Figure 120A-B, vertical line 4**), again an impedance change of 200  $\Omega$  is expected (see **Figure 119A-B, vertical line 5**). This is confirmed by the results found in this chapter (**Figure 120A-B, light red, light green**). Nonetheless, the light green curve in **Figure 120B** does not reach the same impedance plateau as the non-illuminated *cis*-control (**Figure 120B, dark green**) because of the previously observed enhanced decrease of impedance. Similar

observations were made in **chapter 6.3**, where the switching efficiency was reduced with increasing switching cycles.

Under the assumption that all non-bound diffusible ligand molecules are removed in the washing step, switching between the two isomers of **2** should only be discerned by impedance measurements if it takes place within the binding pocket of the GPCRs (**Figure 121A,C**). If photoswitching took place in the bulk medium (**Figure 121B,D**), the ligand solution would be highly diluted after a washing step. This implies that a rebinding of the switched ligand to the GPCR is very unlikely and might not be detectable by the impedance assay. Since a switch is observed for both isoforms of **2** even after a washing step (**Figure 120A-B, light green, light red**), it is assumed that the photoswitching mechanism proceeds inside the GPCR binding pocket.

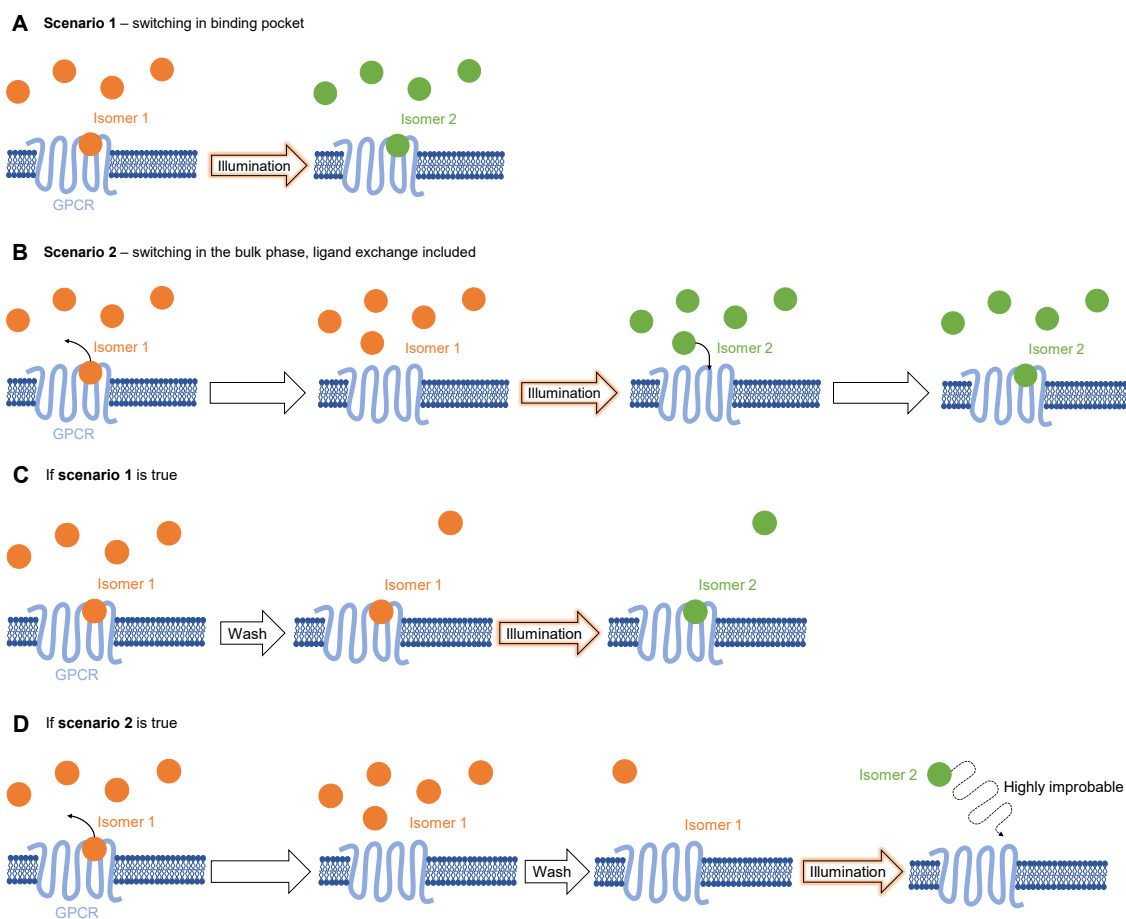


**Figure 121.** Proposed switching mechanisms of photoswitchable ligand **2** at the Y4R. (A) Switching inside the GPCR binding pocket. (B) Switching in the bulk phase and subsequent ligand exchange. (C) If the first switching mechanism holds true and photoswitching takes place inside the binding pocket, photoswitching and subsequent impedance changes can be detected after washing since the ligand is assumed to remain bound to the GPCR. (D) If the second switching mechanism is true and switching takes place in the bulk phase, ligand reassociation with the GPCR is highly unlikely because the ligand solution above the cells is highly diluted after washing. Please note that all depicted mechanisms are equilibria and are only drawn schematically under the assumption that all ligands are isomerized.

## 6.5 Summary and Outlook

Spatiotemporal control and regulation of the bioactivity is a major issue in drug development (Kobauri et al., **2023**). An approach for tuning the biological activity of nucleic acids, amino acids and peptides, enzymes and receptors (Szymański et al., **2013**) is to introduce a light-controllable photoswitchable moiety. The regulation of the action of GPCRs is often addressed by the utilization of photochromic diffusible ligands. In this chapter, two photoswitchable GPCR ligands were investigated with the help of label-free, non-optical and time-resolved impedance measurements. Ligand **1** targets the D2R and is based on a dithienylethene-moiety, which can be switched between an *open* and a *closed* isoform. Ligand **2** is a Y4R agonist and structurally consists of a cyclic peptide with an integrated azobenzene-moiety, which can be switched between a *cis*- and a *trans*-isomer. Initially, CHO D2L and CHO NPY cells were characterized in adhesion measurements by impedance spectroscopy (**chapter 6.1**). A sensitive frequency of 12 kHz was determined for both cell lines, which was used in consecutive impedance experiments. Subsequently, the ligand isoforms were examined in the impedance assay to find out if they possess different bioactivities (**chapter 6.2**). Before ligand addition, ligands **1** and **2** were preirradiated for 3 min with the respective wavelengths to receive the “single” isomers in their PSS. Contrary to FSK, which was used to enhance the signal induced by the G<sub>i</sub>-coupled agonists **1** and **2**, the ligand isomers induced a rise in impedance. Only the *open* isoform of ligand **1** did not display any impedance response or bioactivity (**Figure 116A, red**). The impedance increase after ligand addition suggests that G<sub>s</sub>-coupling mimicked by FSK addition and G<sub>i</sub>-coupling triggered by the photoswitchable ligands generate opposite effects in the impedance of CHO D2L and CHO NPY cells. For both ligands **1** and **2**, concentration-response curves were recorded to determine the optimum switching concentrations between the isomers. Values of 200 nM for ligand **1** and 50 nM for ligand **2** were found. These concentrations were eventually used in switching and toggling experiments (**chapter 6.3**). Ligand **1** is classified as a near “full on/off” switch since its *closed* isoform provoked a close to maximal impedance value and its *open* form barely showed any bioactivity. In contrast, both isomers of ligand **2** demonstrated increased impedance values compared to the negative control (CTRL) with the *cis*-isomer exhibiting a larger impedance change than the *trans*-isomer. Switching took place earliest 0.33 h after stimulation and worked effectively for the switch from the *open* to the *closed* form of ligand **1** and in both directions for ligand **2**. In the latter case, even toggling behavior over several illumination cycles was observed. Nonetheless, the switching efficiency decreased

with the cycle number correlated to receptor desensitization and cell fatigue in the serum-free medium. Lastly, the switching mechanism at the Y4R was further elucidated by a washing experiment (**chapter 6.4**). Switching of ligand **2** was still possible after washing stimulated CHO NPY cells with measurement buffer. This indicates that switching takes place without ligand exchange but within the orthosteric binding pocket of the GPCR.

In summary, non-invasive and time-resolved impedance measurements are a great method to study the light-controlled bioactivity of GPCR ligands. Since it is a non-optical technique, it does not interfere with the photoswitching process itself. However, impedance might overestimate ligands and ligand isomers with varying bioactivity because of its integrative behavior giving rise to false-positive results (Stolwijk et al., **2012**). On the other hand, different ligands and ligand isomers might show distinct bioactivities in the impedance assay but not in more proximal assays as observed for ligand **1** in IP accumulation and arrestin recruitment assays (Lachmann et al., **2017**).

In future work and depending on the ligand, receptor and cell line under study, the switching mechanism of photoswitchable GPCR ligands can be further clarified to either confirm that switching occurs inside the ligand binding pocket or in the bulk medium. This could be implemented by using *in silico* techniques and molecular dynamics simulations (Kobauri et al., **2023**, Ricart-Ortega et al., **2019**) but requires expertise and time to generate an appropriate model that mirrors the physiological situation at the receptor well. Another possibility is to determine the retention time and dissociation kinetics of the photoswitchable ligand at the receptor (Ricart-Ortega et al., **2020**) or to bioimage the ligand locomotion (Acosta-Ruiz et al., **2020**). However, if fluorescent labels are used, attention must be given to unintended switching. Additionally, the molecular properties might be changed.

Since impedance is a very sensitive technique (Stolwijk et al., **2019**), it is well-suited to detect the regulation of the bioactivity of endogenous GPCRs with light. Furthermore, it might be of interest to equip GPCRs themselves with a photoswitchable moiety (e.g. covalent ligands) to control their activity ligand-independently and to prevent unspecific binding effects (Kienzler, Isacoff, **2017**).

For a broader *in vivo* applicability of photoswitchable ligands, their absorbances must be shifted from the UV and short-wavelength visible light to longer wavelengths to guarantee higher tissue penetration depths. This already is an important research topic in the field of photopharmacology and is implemented by modifying the substituents at the photoswitchable moiety or by using two-photon-excitation

(Wijtmans et al., **2022**). For instance, introducing electron-withdrawing substituents in the para-position of an azobenzene switch has proven to red-shift the absorption wavelength of certain ligands (Dong et al., **2015**). Nevertheless, designated ligand isoforms are thermally less stable due to the substitution of the aryl rings and quickly interconvert again. Optimized strategies for shifting the absorption wavelengths of photochromic ligands are still necessary.

Besides tuning the GPCR activity by photoswitchable ligands, it might also be possible to directly intervene with cellular processes to regulate second messenger concentrations and other effector proteins. For instance, by integrating a photoswitchable moiety into cAMP or diacylglycerol (DAG), downstream effector proteins like protein kinases could be activated with better temporal control (Frank et al., **2016**, Xu et al., **2022a**). In this way, fewer unintended pathways and, accordingly, fewer side effects could be triggered compared to photoswitchable ligands. This might facilitate new options for drug development processes and the control of microphysiometry by changing the cells' metabolism (Brischwein, Wiest, **2018**).

Since photopharmacology enables great spatiotemporal control over the biological activity, photoswitchable molecules will play a pivotal role in biomedical applications and future aspects (Cheng et al., **2018**). As recent studies have shown, photoswitchable GPCR ligands offer great control of the cardiac rhythm by targeting  $\beta$ 1-adrenoceptors (Duran-Corbera et al., **2022**) and new possibilities for tumor therapy and cancer treatment by utilizing protein degradation strategies (Negi et al., **2022**).

## 7 Summary

A large number of functional assays to characterize G protein-coupled receptor (GPCR) signaling is based on the readout of a single time point and does not consider signaling dynamics. In addition, many researchers solely orientate on one certain assay format and do not utilize different readout parameters to elucidate the exact molecular mechanisms of GPCR signaling. If two or more functional assays are used, experimental variations need to be taken into account. To tackle these problems, a novel setup for the simultaneous measurement of two functional parameters was developed (**chapter 4**). Label-free and time-resolved electric cell-substrate impedance sensing (ECIS) was combined with a kinetic bioluminescence readout of human embryonic kidney (HEK) cells expressing a NanoLuc Binary Technology (NanoBiT) system for the investigation of minimal G protein (miniG, mG) activation. 96W1E+ electrode arrays were electrically contacted in a way that enables simultaneous impedance and bioluminescence measurements inside a commercial 96-well plate reader. First, the cell lines HEK M1R/mG<sub>q</sub>, HEK M5R/mG<sub>q</sub> and HEK H2R/mG<sub>s</sub> were characterized in individual impedance and luminescence measurements using the receptor agonists carbachol, iperoxo (M1R and M5R) and histamine (H2R). Based on the model cell line HEK M1R/mG<sub>q</sub>, the following assay parameters were optimized: (a) coating of the culture substrate to enhance cellular adhesion, (b) stability and concentration of the luciferin coelenterazine h, (c) the impact of the seeding density, (d) the assay buffer, (e) the reflectivity of the culture substrate, (f) the integration time and optical gain and (g) the cultivation time. With the optimized parameters in hand, all three cell lines were investigated in the dual luminescence-impedance setup. The results indicate that time-resolved and correlated data of one single cell population enable greater insights into the underlying molecular mechanisms of GPCR activation. Additionally, the recorded impedance data is more sensitive for small agonist concentrations, while luminescence displayed a higher sensitivity for large agonist concentrations, where impedance already saturates. The combination of a distal and proximal readout for one and the same cell population is a novel approach that should be considered in future work to clarify the complex signaling machinery of the medically highly relevant GPCRs.

Impedance spectroscopy is a holistic technique and integrates all processes inducing morphological changes and impacting cellular junctions without being molecularly specific. The exact clarification of its underlying mechanisms was part of this work. In **chapter 5**, the impedance responses of HEK M1R/mG<sub>q</sub> and HEK H2R cells after stimulation with carbachol and histamine were elucidated by using pathway-specific

activators and inhibitors and additional functional assays. For the muscarinic acetylcholine receptor 1 (M1R), not only canonical  $G_q$ -coupling was observed but also  $\beta$ -arrestin2 recruitment could be an explanation for the impedance signal after carbachol addition. The canonically  $G_s$ -coupled histamine 2 receptor (H2R) also showed calcium ion mobilization ( $G_q$ ) and  $\beta$ -arrestin2 recruitment after agonist addition. Additionally, impedance measurements of HEK cells (compared to other cell lines, i.e. CHO cells) were insensitive towards intracellular cAMP level changes. To clarify the exact signaling pathways of impedance-based assays, it is of major importance to utilize different independent assays and measurement techniques as well as specific pathway inhibitors and activators.

*Photoswitchable ligands* can be switched between two isoforms upon illumination with UV or visible light. Ideally, both isomers exhibit different bioactivity and can be switched between a “full on/off” behavior. This enables better spatiotemporal control of the bioactivity. In **chapter 6**, two photochromic ligands for the neuropeptide Y4 receptor (Y4R) and the dopamine 2 receptor in its long splicing variant (D2R, D2L) were characterized with impedance measurements. After illumination, CHO cells overexpressing the respective GPCR (CHO D2L or CHO NPY) were incubated with the different ligand isoforms. After determination of the potencies ( $pEC_{50}$ ) and the optimal switching concentrations, first switching experiments were conducted. Ligand **1** (D2R, D2L) nearly resembled a “full on/off” behavior. Both isoforms of ligand **2** (Y4R) showed individual impedance profiles but not a “full on/off” behavior. A washing step conducted after ligand incubation and previous to illumination gave mechanistic insights into the switching process of ligand **2**. The results suggest that switching occurs within the receptor binding pocket and not by ligand exchange. Overall, the results prove that impedance spectroscopy in combination with photoswitchable ligands is a valuable tool to study GPCR signaling, tune the bioactivity and clarify underlying mechanisms.

## 8 Zusammenfassung

Eine Vielzahl funktioneller Assays zur Charakterisierung G Protein gekoppelter Rezeptoren (GPCRs) basiert auf der Messung eines einzelnen Zeitpunktes und lässt die Kinetik der Signalübertragung unberücksichtigt. Zudem fokussieren sich viele Forschende ausschließlich auf ein Assay Format und ziehen keine weiteren Ausleseparameter heran, um die exakten molekularen Mechanismen der GPCR-Aktivierung aufzuklären. Werden zwei oder mehr funktionelle Assays genutzt, müssen experimentelle Variationen berücksichtigt werden. Um diese Probleme zu überwinden, wurde ein neuartiger, dualer Assay entwickelt mit welchem zwei unterschiedliche funktionelle Parameter simultan gemessen werden können (**Kapitel 4**). Die Label-freie und zeitaufgelöste Methode *Electric Cell-Substrate Impedance Sensing* (ECIS) wurde mit einem kinetischen Biolumineszenz Assay kombiniert. Mithilfe der *NanoLuc Binary Technology* (NanoBiT), welche stabil in humane embryonale Nierenzellen (HEK) transfiziert wurde, kann die Aktivierung von minimalen G Proteinen (miniG, mG) luminometrisch erfasst werden. Für den dualen Assay wurden die Elektroden eines 96W1E+ Elektrodenarrays rückseitig elektrisch kontaktiert, so dass eine simultane Detektion von Impedanz und Lumineszenz innerhalb eines kommerziellen Lumineszenz-Plattenlesers möglich war. Zu Beginn wurden die Zelllinien HEK M1R/mG<sub>q</sub>, HEK M5R/mG<sub>q</sub> und HEK H2R/mG<sub>s</sub> in individuellen Impedanz- und Lumineszenz-Messungen charakterisiert. Als Rezeptor Agonisten wurden Carbachol, Iperoxo (M1R, M5R) und Histamin (H2R) eingesetzt. Anhand der Modellzelllinie HEK M1R/mG<sub>q</sub> wurden für den dualen Assay die folgenden experimentellen Bedingungen optimiert: (a) Substratbeschichtung mit adhäsions-fördernden Proteinen, (b) Stabilität und Konzentration des Luziferins Coelenterazin h, (c) Einfluss der Aussaatdichte, (d) Messpuffer, (e) Reflektivität des Substrates, (f) Integrationszeit und faktorielle Verstärkung der Lumineszenz und (g) Zelldichte. Mit den optimierten Parametern konnten Populationen der drei Zelllinien schließlich erstmalig und quasi-simultan im dualen Impedanz-Lumineszenz-Setup untersucht werden. Die Ergebnisse zeigen, dass zeitaufgelöste und korrelierte Daten einer einzelnen Zellpopulation einen besseren Einblick in die grundlegenden molekularen Mechanismen der GPCR-Aktivierung ermöglichen. Die Impedanz Daten zeigten außerdem eine höhere Sensitivität gegenüber kleineren Agonist Konzentrationen, wohingegen die Biolumineszenz sensitiver gegenüber größeren Konzentrationen ist, bei welchen die Impedanz bereits eine Sättigung vorweist. Die Kombination eines distalen und proximalen Assays für ein und dieselbe Zellpopulation ist ein neuartiger Ansatz, der in Zukunft weiter an Bedeutung gewinnen

sollte, um die komplexe Signaltransduktion der medizinisch hochrelevanten GPCRs aufzuklären und die Wirkstoffentwicklung voranzutreiben.

Impedanzspektroskopie ist eine holistische Technik und integriert über alle Prozesse, die zellmorphologische Änderungen induzieren und zelluläre Kontakte beeinflussen, ohne molekulare Spezifität zu besitzen. Die genaue Aufklärung der zugrundeliegenden molekularen Mechanismen war Teil dieser Arbeit. In **Kapitel 5** wurden die Impedanz Profile der Zelllinien HEK M1R/mG<sub>q</sub> und HEK H2R nach Stimulation mit Carbachol und Histamin entschlüsselt. Dazu wurden sowohl weitere funktionelle Assays als auch Signalweg-spezifische Aktivatoren und Inhibitoren hinzugezogen. Für den muskarinischen Acetylcholin Rezeptor 1 (M1R) konnte gefolgert werden, dass das Impedanz Profil nach Carbachol Zugabe nicht ausschließlich auf einer Signalübertragung auf G<sub>q</sub> Proteine, sondern auch auf der Rekrutierung von  $\beta$ -Arrestin2 basiert. Auch für den kanonisch G<sub>s</sub>-gekoppelten Histamin 2 Rezeptor (H2R) konnte die Aktivierung weiterer Signalwege (Calcium bzw. G<sub>q</sub>,  $\beta$ -Arrestin2) durch den Agonisten nachgewiesen werden. Weiterhin zeigen die Untersuchungen, dass Impedanz-Messungen von HEK-Zellen im Gegensatz zu anderen Zelllinien (wie CHO-Zellen) nicht sensitiv gegenüber Veränderungen der intrazellulären cAMP-Konzentration sind. Eine eindeutige Aufklärung von Signalwegen über Impedanz-basierte Assays verlangt zwingend die Durchführung unabhängiger funktioneller Assays sowie die Nutzung Signalweg-spezifischer Aktivatoren und Inhibitoren.

*Photoschaltbare Liganden* verändern nach Belichtung mit UV-Strahlen oder sichtbarem Licht ihre räumliche Anordnung. Üblicherweise lassen sie sich zwischen zwei Isomeren hin- und herschalten. Idealerweise besitzen die beiden Isomere eine unterschiedliche Bioaktivität und können mittels Belichtung zwischen einem vollständigen AN/AUS Zustand wechseln. Dies erlaubt eine bessere lokal und temporär aufgelöste Kontrolle der Aktivierung von GPCRs. In **Kapitel 6** wurden zwei photochrome Liganden für den Neuropeptid Y4 Rezeptor (Y4R) und für den Dopamin 2 Rezeptor (D2R, D2L) mittels Impedanz-Messungen charakterisiert. Nach Belichtung wurden CHO-Zellen, die die entsprechenden Rezeptoren überexprimieren (CHO D2L, CHO NPY), mit den verschiedenen Ligand-Isomeren inkubiert. Nach Bestimmung der Potenzen (pEC<sub>50</sub>) und Ermittlung der optimalen Konzentrationen zum Photoschalten, wurden erste Schaltexperimente durchgeführt. Ligand **1** (D2R, D2L) wies ein nahezu vollständiges AN/AUS Verhalten auf. Beide Isomere des Liganden **2** (Y4R) zeigten individuelle Änderungen des zeitabhängigen Impedanz Profils, ohne jedoch wie ein EIN/AUS-Schalter zu funktionieren. Durch Waschexperimente nach Ligand-Inkubation und vor Belichtung mit Ligand **2** konnten

erste mechanistische Einblicke in den Schaltprozess erhalten werden. Die Ergebnisse deuten darauf hin, dass der Schaltprozess nicht über einen Ligand Austausch stattfindet, sondern innerhalb der Bindungstasche des GPCRs. Diese Resultate zeigen wie wertvoll und nützlich die Impedanzspektroskopie in Kombination mit photoschaltbaren Molekülen ist, um die Signalübertragung von GPCRs und sogar mechanistische Prozesse auf molekularer Ebene aufzuklären.

## 9 References

- 1 Abasi, S.; Aggas, J. R.; Garayar-Leyva, G. G.; Walther, B. K.; Guiseppi-Elie, A. Bioelectrical Impedance Spectroscopy for Monitoring Mammalian Cells and Tissues under Different Frequency Domains: A Review. *ACS Measurement Science Au* **2022**, 2 (6), 495–516.
- 2 Acosta-Ruiz, A.; Gutzeit, V. A.; Skelly, M. J.; Meadows, S.; Lee, J.; Parekh, P.; Orr, A. G.; Liston, C.; Pleil, K. E.; Broichhagen, J.; Levitz, J. Branched Photoswitchable Tethered Ligands Enable Ultra-efficient Optical Control and Detection of G Protein-Coupled Receptors In Vivo. *Neuron* **2020**, 105 (3), 1-18.
- 3 Adam, Gerold, Läuger, Peter, Stark, Günther. *Physikalische Chemie und Biophysik*; Springer Berlin Heidelberg: Berlin, Heidelberg, **2009**.
- 4 Adamiak, K.; Sionkowska, A. Current methods of collagen cross-linking: Review. *International journal of biological macromolecules* **2020**, 161, 550–560.
- 5 Addis, P.; Bali, U.; Baron, F.; Campbell, A.; Harborne, S.; Jagger, L.; Milne, G.; Pearce, M.; Rosethorne, E. M.; Satchell, R.; Swift, D.; Young, B.; Unitt, J. F. Key aspects of modern GPCR drug discovery. *SLAS discovery : advancing life sciences R & D* **2023**, 1–22.
- 6 Altamash, T.; Ahmed, W.; Rasool, S.; Biswas, K. H. Intracellular Ionic Strength Sensing Using NanoLuc. *International journal of molecular sciences* **2021**, 22 (2), 1–11.
- 7 Arndt, S.; Seebach, J.; Psathaki, K.; Galla, H.-J.; Wegener, J. Bioelectrical impedance assay to monitor changes in cell shape during apoptosis. *Biosensors and Bioelectronics* **2004**, 19 (6), 583–594.
- 8 Attwood, T. K.; Findlay, J. B. Fingerprinting G-protein-coupled receptors. *Protein engineering* **1994**, 7 (2), 195–203.
- 9 Atwood, B. K.; Lopez, J.; Wager-Miller, J.; Mackie, K.; Straiker, A. Expression of G protein-coupled receptors and related proteins in HEK293, AtT20, BV2, and N18 cell lines as revealed by microarray analysis. *BMC Genomics* **2011**, 12, 14.
- 10 Bachmann, M.; Kukkurainen, S.; Hytönen, V. P.; Wehrle-Haller, B. Cell Adhesion by Integrins. *Physiological Reviews* **2019**, 99 (4), 1655–1699.
- 11 Bagnato, A.; Rosanò, L. New Routes in GPCR/ $\beta$ -Arrestin-Driven Signaling in Cancer Progression and Metastasis. *Front. Pharmacol.* **2019**, 10, 114.
- 12 Beaulieu, J.-M.; Espinoza, S.; Gainetdinov, R. R. Dopamine receptors - IUPHAR Review 13. *British journal of pharmacology* **2015**, 172 (1), 1–23.
- 13 Bellotti, M.; Bast, W.; Berra, A.; Bonetto, F. J. Effects of osmolarity on human epithelial conjunctival cells using an electrical technique. *Graefe's archive for*

- clinical and experimental ophthalmology = Albrecht von Graefes Archiv fur klinische und experimentelle Ophthalmologie* **2011**, 249 (12), 1875–1882.
- 14 Belly, H. de; Paluch, E. K.; Chalut, K. J. Interplay between mechanics and signalling in regulating cell fate. *Nat Rev Mol Cell Biol* **2022**, 23 (7), 465–480.
- 15 Bennett, J.; Weeds, A. Calcium and the cytoskeleton. *British medical bulletin* **1986**, 42 (4), 385–390.
- 16 Beukers, M. W.; Klaassen, C. H.; Grip, W. J. de; Verzijl, D.; Timmerman, H.; Leurs, R. Heterologous expression of rat epitope-tagged histamine H<sub>2</sub> receptors in insect Sf9 cells. *British journal of pharmacology* **1997**, 122 (5), 867–874.
- 17 Bharati, K.; Ganguly, N. K. Cholera toxin: a paradigm of a multifunctional protein. *The Indian Journal of Medical Research* **2011**, 133 (2), 179–187.
- 18 biophysics.com #1: <https://www.biophysics.com/cultureware.php#8W1E>; **August 10, 2024**.
- 19 biophysics.com #2: <https://www.biophysics.com/cultureware.php#96W1E>; **August 10, 2024**.
- 20 Black, J. W.; Duncan, W. A. M.; Durant, C. J.; Ganellin, C. R.; Parsons, E. M. Definition and antagonism of histamine H<sub>2</sub>-receptors. *Nature* **1972**, 236 (5347), 385–390.
- 21 bmglabtech.com: <https://www.bmglabtech.com/en/luminescence/>; **August 10, 2024**.
- 22 Boeckler, F.; Gmeiner, P. Dopamine D<sub>3</sub> receptor ligands: recent advances in the control of subtype selectivity and intrinsic activity. *Biochimica et biophysica acta* **2007**, 1768 (4), 871–887.
- 23 Bongers, G.; Esch, I. de; Leurs, R. Molecular Pharmacology of the Four Histamine Receptors. In *Histamine in inflammation*; Thurmond, R. L., Ed.; Advances in experimental medicine and biology 709; Landes Bioscience: Austin, Tex., **2010**; pp 11–19.
- 24 Boursier, M. E.; Levin, S.; Zimmerman, K.; Machleidt, T.; Hurst, R.; Butler, B. L.; Eggers, C. T.; Kirkland, T. A.; Wood, K. V.; Friedman Ohana, R. The luminescent HiBiT peptide enables selective quantitation of G protein-coupled receptor ligand engagement and internalization in living cells. *Journal of Biological Chemistry* **2020**, 295 (15), 5124–5135.
- 25 Bradley, S. J.; Molloy, C.; Bundgaard, C.; Mogg, A. J.; Thompson, K. J.; Dwomoh, L.; Sanger, H. E.; Crabtree, M. D.; Brooke, S. M.; Sexton, P. M.; Felder, C. C.; Christopoulos, A.; Broad, L. M.; Tobin, A. B.; Langmead, C. J. Bitopic Binding Mode of an M<sub>1</sub> Muscarinic Acetylcholine Receptor Agonist Associated with Adverse Clinical Trial Outcomes. *Molecular pharmacology* **2018**, 93 (6), 645–656.

- 26 Brischwein, M.; Wiest, J. Microphysiometry. *Label-Free Monitoring of Cells in vitro*; Springer, Cham, **2018**; pp 163–188.
- 27 Broichhagen, J.; Frank, J. A.; Trauner, D. A roadmap to success in photopharmacology. *Accounts of chemical research* **2015**, *48* (7), 1947–1960.
- 28 Brothers, S. P.; Wahlestedt, C. Therapeutic potential of neuropeptide Y (NPY) receptor ligands. *EMBO Molecular Medicine* **2010**, *2* (11), 429–439.
- 29 Cai, S.; Wu, C.; Yang, W.; Liang, W.; Yu, H.; Liu, L. Recent advance in surface modification for regulating cell adhesion and behaviors. *Nanotechnology Reviews* **2020**, *9* (1), 971–989.
- 30 Calcutt, N. A.; Smith, D. R.; Frizzi, K.; Sabbir, M. G.; Chowdhury, S. K. R.; Mixcoatl-Zecuatl, T.; Saleh, A.; Muttalib, N.; van der Ploeg, R.; Ochoa, J.; Gopaul, A.; Tessler, L.; Wess, J.; Jolival, C. G.; Fernyhough, P. Selective antagonism of muscarinic receptors is neuroprotective in peripheral neuropathy. *J Clin Invest* **2017**, *127* (2), 608–622.
- 31 Campbell, A. P.; Smrcka, A. V. Targeting G protein-coupled receptor signalling by blocking G proteins. *Nature reviews. Drug discovery* **2018**, *17* (11), 789–803.
- 32 Caniceiro, A. B.; Bueschbell, B.; Schiedel, A. C.; Moreira, I. S. Class A and C GPCR Dimers in Neurodegenerative Diseases. *Current Neuropharmacology* **2022**, *20* (11), 2081–2141.
- 33 Carpenter, B. Current applications of mini G proteins to study the structure and function of G protein-coupled receptors. *AIMSBOA* **2018**, *5* (4), 209–225.
- 34 Carpenter, B.; Tate, C. G. Engineering a minimal G protein to facilitate crystallisation of G protein-coupled receptors in their active conformation. *Protein engineering, design & selection : PEDS* **2016**, *29* (12), 583–594.
- 35 cdna.org: <https://www.cdna.org/home.php?cat=177>; **August 10, 2024**.
- 36 Charnet, P.; Lory, P.; Bourinet, E.; Collin, T.; Nargeot, J. cAMP-dependent phosphorylation of the cardiac L-type Ca channel: a missing link? *Biochimie* **1995**, *77* (12), 957–962.
- 37 Chaudhary, P. K.; Kim, S. An Insight into GPCR and G-Proteins as Cancer Drivers. *Cells* **2021**, *10* (12), 3288–3329.
- 38 Cheng, H.; Yoon, J.; Tian, H. Recent advances in the use of photochromic dyes for photocontrol in biomedicine. *Coordination Chemistry Reviews* **2018**, *372*, 66–84.
- 39 Cherezov, V.; Rosenbaum, D. M.; Hanson, M. A.; Rasmussen, S. G. F.; Thian, F. S.; Kobilka, T. S.; Choi, H.-J.; Kuhn, P.; Weis, W. I.; Kobilka, B. K.; Stevens, R. C. High-resolution crystal structure of an engineered human beta2-adrenergic G protein-coupled receptor. *Science (New York, N. Y.)* **2007**, *318* (5854), 1258–1265.

- 40 Cobbold, P. H.; Rink, T. J. Fluorescence and bioluminescence measurement of cytoplasmic free calcium. *Biochem J* **1987**, *248* (2), 313–328.
- 41 Cong, X.; Topin, J.; Golebiowski, J. *Class A GPCRs: Structure, Function, Modeling and Structure-based Ligand Design 23*; Bentham Science Publishers, **2017**.
- 42 Congreve, M.; Graaf, C. de; Swain, N. A.; Tate, C. G. Impact of GPCR Structures on Drug Discovery. *Cell* **2020**, *181* (1), 81–91.
- 43 Conte, F.; van Buuringen, N.; Voermans, N. C.; Lefeber, D. J. Galactose in human metabolism, glycosylation and congenital metabolic diseases: Time for a closer look. *Biochimica et biophysica acta. General subjects* **2021**, *1865* (8), 129898.
- 44 Cordeau, P.; Kriz, J. Chapter seven - Real-Time Imaging After Cerebral Ischemia: Model Systems for Visualization of Inflammation and Neuronal Repair. In *Methods in Enzymology : Imaging and Spectroscopic Analysis of Living Cells*; Conn, P. M., Ed.; Academic Press, **2012**; pp 117–133.
- 45 corning.com: <https://www.lms-lab.de/de-de/corning-96-well-white-flat-bottom-polystyrene-nbs-microplate-5-per-bag-without-lid-nonsterile-3990>; **August 10, 2024**.
- 46 Coutant, E. P.; Gagnot, G.; Hervin, V.; Baatallah, R.; Goyard, S.; Jacob, Y.; Rose, T.; Janin, Y. L. Bioluminescence Profiling of NanoKAZ/NanoLuc Luciferase Using a Chemical Library of Coelenterazine Analogues. *Chemistry – A European Journal* **2020**, *26* (4), 948–958.
- 47 Croset, A.; Delafosse, L.; Gaudry, J.-P.; Arod, C.; Glez, L.; Losberger, C.; Begue, D.; Krstanovic, A.; Robert, F.; Vilbois, F.; Chevalet, L.; Antonsson, B. Differences in the glycosylation of recombinant proteins expressed in HEK and CHO cells. *Journal of biotechnology* **2012**, *161* (3), 336–348.
- 48 Cserne Szappanos, H.; Muralidharan, P.; Ingley, E.; Petereit, J.; Millar, A. H.; Hool, L. C. Identification of a novel cAMP dependent protein kinase A phosphorylation site on the human cardiac calcium channel. *Sci Rep* **2017**, *7* (1), 15118.
- 49 Czarnecka, M.; Lu, C.; Pons, J.; Maheswaran, I.; Ciborowski, P.; Zhang, L.; Cheema, A.; Kitlinska, J. Neuropeptide Y receptor interactions regulate its mitogenic activity. *Neuropeptides* **2019**, *73*, 11–24.
- 50 DeFea, K. A. Arrestins in actin reorganization and cell migration. *Progress in molecular biology and translational science* **2013**, *118*, 205–222.
- 51 Denelavas, A.; Weibel, F.; Prummer, M.; Imbach, A.; Clerc, R. G.; Apfel, C. M.; Hertel, C. Real-time cellular impedance measurements detect Ca(2+) channel-dependent oscillations of morphology in human H295R adenoma cells. *Biochimica et biophysica acta* **2011**, *1813* (5), 754–762.

- 52 Dhyani, V.; Gare, S.; Gupta, R. K.; Swain, S.; Venkatesh, K. V.; Giri, L. GPCR mediated control of calcium dynamics: A systems perspective. *Cellular Signalling* **2020**, *74*, 109717.
- 53 Didiot, M.-C.; Serafini, S.; Pfeifer, M. J.; King, F. J.; Parker, C. N. Multiplexed reporter gene assays: monitoring the cell viability and the compound kinetics on luciferase activity. *Journal of biomolecular screening* **2011**, *16* (7), 786–793.
- 54 Dijon, N. Novel complementation biosensors to investigate G protein-coupled receptor kinetics and signalling bias., **2022**.
- 55 Dijon, N. C.; Nesheva, D. N.; Holliday, N. D. Luciferase Complementation Approaches to Measure GPCR Signaling Kinetics and Bias. *G Protein-Coupled Receptor Screening Assays*; Humana, New York, NY, **2021**; pp 249–274.
- 56 Dixon, A. S.; Schwinn, M. K.; Hall, M. P.; Zimmerman, K.; Otto, P.; Lubben, T. H.; Butler, B. L.; Binkowski, B. F.; Machleidt, T.; Kirkland, T. A.; Wood, M. G.; Eggers, C. T.; Encell, L. P.; Wood, K. V. NanoLuc Complementation Reporter Optimized for Accurate Measurement of Protein Interactions in Cells. *ACS chemical biology* **2016**, *11* (2), 400–408.
- 57 Doijen, J.; van Loy, T.; Haes, W. de; Landuyt, B.; Luyten, W.; Schoofs, L.; Schols, D. Signaling properties of the human chemokine receptors CXCR4 and CXCR7 by cellular electric impedance measurements. *PLOS ONE* **2017**, *12* (9), e0185354.
- 58 Doijen, J.; van Loy, T.; Landuyt, B.; Luyten, W.; Schols, D.; Schoofs, L. Advantages and shortcomings of cell-based electrical impedance measurements as a GPCR drug discovery tool. *Biosensors & bioelectronics* **2019**, *137*, 33–44.
- 59 Dong, J. M.; Leung, T.; Manser, E.; Lim, L. cAMP-induced morphological changes are counteracted by the activated RhoA small GTPase and the Rho kinase ROK $\alpha$ . *Journal of Biological Chemistry* **1998**, *273* (35), 22554–22562.
- 60 Dong, M.; Babalhavaeji, A.; Samanta, S.; Beharry, A. A.; Woolley, G. A. Red-Shifting Azobenzene Photoswitches for in Vivo Use. *Accounts of chemical research* **2015**, *48* (10), 2662–2670.
- 61 Dorsam, R. T.; Gutkind, J. S. G-protein-coupled receptors and cancer. *Nat Rev Cancer* **2007**, *7* (2), 79–94.
- 62 dsmz.de: <https://www.dsmz.de/collection/catalogue/details/culture/ACC-635>; **August 10, 2024**.
- 63 DuBridge, R. B.; Tang, P.; Hsia, H. C.; Leong, P. M.; Miller, J. H.; Calos, M. P. Analysis of mutation in human cells by using an Epstein-Barr virus shuttle system. *Mol. Cell. Biol.* **1987**, *7* (1), 379–387.
- 64 Duebel, J.; Marazova, K.; Sahel, J.-A. Optogenetics. *Current opinion in ophthalmology* **2015**, *26* (3), 226–232.

- 65 Duran-Corbera, A.; Faria, M.; Ma, Y.; Prats, E.; Dias, A.; Catena, J.; Martinez, K. L.; Raldua, D.; Llebaria, A.; Rovira, X. A. Photoswitchable Ligand Targeting the  $\beta$ 1-Adrenoceptor Enables Light-Control of the Cardiac Rhythm. *Angewandte Chemie (International ed. in English)* **2022**, *61* (30), e202203449.
- 66 Dutt, P.; Kjoller, L.; Giel, M.; Hall, A.; Toksoz, D. Activated Galphaq family members induce Rho GTPase activation and Rho-dependent actin filament assembly. *FEBS Letters* **2002**, *531* (3), 565–569.
- 67 Dwomoh, L.; Tejada, G. S.; Tobin, A. B. Targeting the M1 muscarinic acetylcholine receptor in Alzheimer's disease. *Neuronal signaling* **2022**, *6* (1), NS20210004.
- 68 Ebrahim, A. S.; Ebrahim, T.; Kani, H.; Ibrahim, A. S.; Carion, T. W.; Berger, E. A. Functional optimization of electric cell-substrate impedance sensing (ECIS) using human corneal epithelial cells. *Sci Rep* **2022**, *12* (1), 14126.
- 69 Eiger, D. S.; Pham, U.; Gardner, J.; Hicks, C.; Rajagopal, S. GPCR systems pharmacology: a different perspective on the development of biased therapeutics. *American journal of physiology. Cell physiology* **2022**, *322* (5), C887-C895.
- 70 England, C. G.; Ehlerding, E. B.; Cai, W. NanoLuc: A Small Luciferase Is Brightening Up the Field of Bioluminescence. *Bioconjugate chemistry* **2016**, *27* (5), 1175–1187.
- 71 Ettinger, A.; Wittmann, T. Fluorescence live cell imaging. *Methods in cell biology* **2014**, *123*, 77–94.
- 72 Farris, S.; Song, J.; Huang, Q. Alternative reaction mechanism for the cross-linking of gelatin with glutaraldehyde. *Journal of agricultural and food chemistry* **2010**, *58* (2), 998–1003.
- 73 Faussner, A.; Deininger, M. M.; Weber, C.; Steffens, S. Direct addition of polylysine or poly-ethylenimine to the medium: A simple alternative to plate pre-coating. *PLOS ONE* **2022**, *17* (7), e0260173.
- 74 Feeney, K. A.; Putker, M.; Brancaccio, M.; O'Neill, J. S. In-depth Characterization of Firefly Luciferase as a Reporter of Circadian Gene Expression in Mammalian Cells. *Journal of Biological Rhythms* **2016**, *31* (6), 540–550.
- 75 Felder, C. C. Muscarinic acetylcholine receptors: signal transduction through multiple effectors. *FASEB j.* **1995**, *9* (8), 619–625.
- 76 Felixberger, J. Luciferase complementation for the determination of arrestin recruitment: Investigations at histamine and NPY receptors, **2016**.
- 77 Fernandez, T. J.; Maria, M. de; Lobingier, B. T. A cellular perspective of bias at G protein-coupled receptors. *Protein Science* **2020**, *29* (6), 1345–1354.

- 78 Fernández, N. C.; Shayo, C.; Davio, C.; Monczor, F. Histamine H<sub>2</sub> Receptor Biased Signaling Methods. In *Histamine Receptors as Drug Targets*; Ennis, M., Tiligada, E., Eds.; SpringerLink Bücher; Humana Press: New York, NY, **2017**; pp 67–114.
- 79 Fields, S.; Song, O. A novel genetic system to detect protein-protein interactions. *Nature* **1989**, *340* (6230), 245–246.
- 80 Finkelstein, W.; Isselbacher, K. J. Drug therapy: Cimetidine. *The New England journal of medicine* **1978**, *299* (18), 992–996.
- 81 Finlay, D. B.; Duffull, S. B.; Glass, M. 100 years of modelling ligand-receptor binding and response: A focus on GPCRs. *British journal of pharmacology* **2020**, *177* (7), 1472–1484.
- 82 Frank, J. A.; Yushchenko, D. A.; Hodson, D. J.; Lipstein, N.; Nagpal, J.; Rutter, G. A.; Rhee, J.-S.; Gottschalk, A.; Brose, N.; Schultz, C.; Trauner, D. Photoswitchable diacylglycerols enable optical control of protein kinase C. *Nature chemical biology* **2016**, *12* (9), 755–762.
- 83 Fredriksson, R.; Lagerström, M. C.; Lundin, L.-G.; Schiöth, H. B. The G-Protein-Coupled Receptors in the Human Genome Form Five Main Families: Phylogenetic Analysis, Paralogon Groups, and Fingerprints. *Molecular pharmacology* **2003**, *63* (6), 1256–1272.
- 84 Gao, T.; Yatani, A.; Dell'Acqua, M. L.; Sako, H.; Green, S. A.; Dascal, N.; Scott, J. D.; Hosey, M. M. cAMP-dependent regulation of cardiac L-type Ca<sup>2+</sup> channels requires membrane targeting of PKA and phosphorylation of channel subunits. *Neuron* **1997**, *19* (1), 185–196.
- 85 Gao, Z.-G.; Auchampach, J. A.; Jacobson, K. A. Species dependence of A<sub>3</sub> adenosine receptor pharmacology and function. *Purinergic Signalling* **2022**, 1–28.
- 86 García-Nafria, J.; Tate, C. G. Structure determination of GPCRs: cryo-EM compared with X-ray crystallography. *Biochemical Society transactions* **2021**, *49* (5), 2345–2355.
- 87 Garrison, A. T.; Orsi, D. L.; Capstick, R. A.; Whomble, D.; Li, J.; Carter, T. R.; Felts, A. S.; Vinson, P. N.; Rodriguez, A. L.; Han, A.; Hajari, K.; Cho, H. P.; Teal, L. B.; Ragland, M. G.; Ghamari-Langroudi, M.; Bubser, M.; Chang, S.; Schnetz-Boutaud, N. C.; Boutaud, O.; Blobaum, A. L.; Foster, D. J.; Niswender, C. M.; Conn, P. J.; Lindsley, C. W.; Jones, C. K.; Han, C. Development of VU6019650: A Potent, Highly Selective, and Systemically Active Orthosteric Antagonist of the M<sub>5</sub> Muscarinic Acetylcholine Receptor for the Treatment of Opioid Use Disorder. *Journal of medicinal chemistry* **2022**, *65* (8), 6273–6286.
- 88 Garvin, D.; Stecha, P.; Gilden, J.; Wang, J.; Grailer, J.; Hartnett, J.; Fan, F.; Cong, M.; Cheng, Z. J. Determining ADCC Activity of Antibody-Based Therapeutic

- Molecules using Two Bioluminescent Reporter-Based Bioassays. *Current Protocols* **2021**, 1 (11), e296.
- 89 Gaspar, N.; Walker, J. R.; Zambito, G.; Marella-Panth, K.; Lowik, C.; Kirkland, T. A.; Mezzanotte, L. Evaluation of NanoLuc substrates for bioluminescence imaging of transferred cells in mice. *Journal of photochemistry and photobiology. B, Biology* **2021**, 216, 112128.
- 90 Gee, K. R.; Brown, K. A.; Chen, W. N.; Bishop-Stewart, J.; Gray, D.; Johnson, I. Chemical and physiological characterization of fluo-4 Ca(2+)-indicator dyes. *Cell calcium* **2000**, 27 (2), 97–106.
- 91 Giaever, I.; Keese, C. R. Monitoring fibroblast behavior in tissue culture with an applied electric field. *Proceedings of the National Academy of Sciences of the United States of America* **1984**, 81 (12), 3761–3764.
- 92 Giaever, I.; Keese, C. R. Use of electric fields to monitor the dynamical aspect of cell behavior in tissue culture. *IEEE Trans. Biomed. Eng.* **1986**, 33 (2), 242–247.
- 93 Giaever, I.; Keese, C. R. Micromotion of mammalian cells measured electrically. *Proceedings of the National Academy of Sciences of the United States of America* **1991**, 88 (17), 7896–7900.
- 94 Giaever, I.; Keese, C. R. Electric Cell-Substrate Impedance Sensing Concept to Commercialization. *Electric Cell-Substrate Impedance Sensing and Cancer Metastasis*; Springer, Dordrecht, **2012**; pp 1–19.
- 95 Giuliani, G.; Merolla, A.; Paolino, M.; Reale, A.; Saletti, M.; Blancafort, L.; Cappelli, A.; Benfenati, F.; Cesca, F. Stability Studies of New Caged bis-deoxy-coelenterazine Derivatives and Their Potential Use as Cellular pH Probes. *Photochemistry and photobiology* **2021**, 97 (2), 343–352.
- 96 Goerke, A. R.; Loening, A. M.; Gambhir, S. S.; Swartz, J. R. Cell-free metabolic engineering promotes high-level production of bioactive Gaussia princeps luciferase. *Metabolic engineering* **2008**, 10 (3-4), 187–200.
- 97 Good, N. E.; Winget, G. D.; Winter, W.; Connolly, T. N.; Izawa, S.; Singh, R. M. Hydrogen ion buffers for biological research. *Biochemistry* **1966**, 5 (2), 467–477.
- 98 Graham, F. L.; Smiley, J.; Russell, W. C.; Nairn, R. Characteristics of a human cell line transformed by DNA from human adenovirus type 5. *The Journal of general virology* **1977**, 36 (1), 59–74.
- 99 Grätz, L. Luminescence-based methods for the investigation of ligand binding and GRK2 recruitment to GPCRs, **2023**.
- 100 Grogan, A.; Lucero, E. Y.; Jiang, H.; Rockman, H. A. Pathophysiology and pharmacology of G protein-coupled receptors in the heart. *Cardiovasc Res* **2023**, 119 (5), 1117–1129.

- 101 Grundmann, M. Label-Free Dynamic Mass Redistribution and Bio-Impedance Methods for Drug Discovery. *Current Protocols in Pharmacology* **2017**, 77 (1), 9.24.1-9.24.21.
- 102 Grundmann, M.; Merten, N.; Malfacini, D.; Inoue, A.; Preis, P.; Simon, K.; Rüttiger, N.; Ziegler, N.; Benkel, T.; Schmitt, N. K.; Ishida, S.; Müller, I.; Reher, R.; Kawakami, K.; Inoue, A.; Rick, U.; Kühn, T.; Imhof, D.; Aoki, J.; König, G. M.; Hoffmann, C.; Gomeza, J.; Wess, J.; Kostenis, E. Lack of beta-arrestin signaling in the absence of active G proteins. *Nat Commun* **2018**, 9 (1), 341.
- 103 Guo, S.; Zhao, T.; Yun, Y.; Xie, X. Recent progress in assays for GPCR drug discovery. *American journal of physiology. Cell physiology* **2022**, 323 (2), C583-C594.
- 104 Guo, Y.-J.; Pan, W.-W.; Liu, S.-B.; Shen, Z.-F.; Xu, Y.; Hu, L.-L. ERK/MAPK signalling pathway and tumorigenesis. *Experimental and therapeutic medicine* **2020**, 19 (3), 1997–2007.
- 105 Gurevich, V. V.; Gurevich, E. V. Molecular Mechanisms of GPCR Signaling: A Structural Perspective. *International journal of molecular sciences* **2017**, 18 (12), 2519.
- 106 Gurevich, V. V.; Gurevich, E. V. GPCR Signaling Regulation: The Role of GRKs and Arrestins. *Frontiers in pharmacology* **2019**, 10, 125.
- 107 Gutiérrez-de-Terán, H.; Massink, A.; Rodríguez, D.; Liu, W.; Han, G. W.; Joseph, J. S.; Katritch, I.; Heitman, L. H.; Xia, L.; IJzerman, A. P.; Cherezov, V.; Katritch, V.; Stevens, R. C. The role of a sodium ion binding site in the allosteric modulation of the A(2A) adenosine G protein-coupled receptor. *Structure (London, England : 1993)* **2013**, 21 (12), 2175–2185.
- 108 Haddock, S. H. D.; Moline, M. A.; Case, J. F. Bioluminescence in the sea. *Annual review of marine science* **2010**, 2, 443–493.
- 109 Haga, T. Molecular properties of muscarinic acetylcholine receptors. *Proceedings of the Japan Academy. Series B, Physical and Biological Sciences* **2013**, 89 (6), 226–256.
- 110 Hall, M. P.; Unch, J.; Binkowski, B. F.; Valley, M. P.; Butler, B. L.; Wood, M. G.; Otto, P.; Zimmerman, K.; Vidugiris, G.; Machleidt, T.; Robers, M. B.; Benink, H. A.; Eggers, C. T.; Slater, M. R.; Meisenheimer, P. L.; Klaubert, D. H.; Fan, F.; Encell, L. P.; Wood, K. V. Engineered luciferase reporter from a deep sea shrimp utilizing a novel imidazopyrazinone substrate. *ACS chemical biology* **2012**, 7 (11), 1848–1857.

- 111 Ham, R. G. Clonal Growth of Mammalian Cells in a Chemically Defined, Synthetic Medium. *Proceedings of the National Academy of Sciences of the United States of America* **1965**, *53* (2), 288–293.
- 112 Ham, R. G.; McKeehan, W. L. Media and growth requirements. *Methods in Enzymology* **1979**, *58*, 44–93.
- 113 Hao, Y.; Tatonetti, N. P. Predicting G protein-coupled receptor downstream signaling by tissue expression. *Bioinformatics* **2016**, *32* (22), 3435–3443.
- 114 Hauser, A. S.; Attwood, M. M.; Rask-Andersen, M.; Schiöth, H. B.; Gloriam, D. E. Trends in GPCR drug discovery: new agents, targets and indications. *Nature reviews. Drug discovery* **2017**, *16* (12), 829–842.
- 115 Hayes, G.; Biden, T. J.; Selbie, L. A.; Shine, J. Structural subtypes of the dopamine D2 receptor are functionally distinct: expression of the cloned D2A and D2B subtypes in a heterologous cell line. *Mol Endocrinol* **1992**, *6* (6), 920–926.
- 116 He, S.; Wang, J.; Li, Z.; Cao, Y.; Ning, X.; Sun, J.; Chen, Q.; Ling, M. Reversible cross-linking of gelatin by a disulphide-containing bis-succinimide for tunable degradation and release. *2590-1575* **2023**, *18*, 100699.
- 117 Heitmann, V.; Reiß, B.; Wegener, J. The Quartz Crystal Microbalance in Cell Biology: Basics and Applications. In *Piezoelectric sensors*; Steinem, C., Janshoff, A., Cooper, M. A., Cooper, M. A., Eds.; Springer Series on Chemical Sensors and Biosensors 5; Springer: Berlin, Heidelberg, **2007**; pp 303–338.
- 118 Hill, S. J.; Baker, J. G.; Rees, S. Reporter-gene systems for the study of G-protein-coupled receptors. *Current Opinion in Pharmacology* **2001**, *1* (5), 526–532.
- 119 Hill, S. J.; Williams, C.; May, L. T. Insights into GPCR pharmacology from the measurement of changes in intracellular cyclic AMP; advantages and pitfalls of differing methodologies. *British journal of pharmacology* **2010**, *161* (6), 1266–1275.
- 120 Hoare, S. R.; Tewson, P. H.; Quinn, A. M.; Hughes, T. E.; Bridge, L. J. *Analyzing kinetic signaling data for G-protein-coupled receptors*; Cold Spring Harbor Laboratory, **2020**.
- 121 Hoare, S. R. J.; Tewson, P. H.; Sachdev, S.; Connor, M.; Hughes, T. E.; Quinn, A. M. Quantifying the Kinetics of Signaling and Arrestin Recruitment by Nervous System G-Protein Coupled Receptors. *Frontiers in cellular neuroscience* **2021**, *15*, 814547.
- 122 Höring, C. Split-Luciferase Complementation and Molecular Dynamics Studies for the Mini-G Protein-Based Functional Characterization of GPCRs, **2022**.
- 123 Höring, C.; Conrad, M.; Söldner, C. A.; Wang, J.; Sticht, H.; Strasser, A.; Miao, Y. Specific Engineered G Protein Coupling to Histamine Receptors Revealed from

- Cellular Assay Experiments and Accelerated Molecular Dynamics Simulations. *International journal of molecular sciences* **2021**, *22* (18), 10047.
- 124 Huang, F.; Buchwald, P.; Browne, C. E.; Farag, H. H.; Wu, W. M.; Ji, F.; Hochhaus, G.; Bodor, N. Receptor binding studies of soft anticholinergic agents. *AAPS pharmSci* **2001**, *3* (4), E30.
- 125 Huang, Y.; Todd, N.; Thathiah, A. The role of GPCRs in neurodegenerative diseases: avenues for therapeutic intervention. *Current Opinion in Pharmacology* **2017**, *32*, 96–110.
- 126 Hutchinson, D. S.; Summers, R. J.; Bengtsson, T. Regulation of AMP-activated protein kinase activity by G-protein coupled receptors: potential utility in treatment of diabetes and heart disease. *Pharmacology & Therapeutics* **2008**, *119* (3), 291–310.
- 127 ie.vwr.com: <https://ie.vwr.com/store/product/25929652/calcimycin-a23187-free-acid-98-by-tlc-ionophore>; **August 10, 2024**.
- 128 Inouye, S.; Watanabe, K.; Nakamura, H.; Shimomura, O. Secretional luciferase of the luminous shrimp *Oplophorus gracilirostris*: cDNA cloning of a novel imidazopyrazinone luciferase(1). *FEBS Letters* **2000**, *481* (1), 19–25.
- 129 Insel, P. A.; Ostrom, R. S. Forskolin as a tool for examining adenylyl cyclase expression, regulation, and G protein signaling. *Cell Mol Neurobiol* **2003**, *23* (3), 305–314.
- 130 Irvine, J. T. S.; Sinclair, D. C.; West, A. R. Electroceramics: Characterization by Impedance Spectroscopy. *Adv. Mater.* **1990**, *2* (3), 132–138.
- 131 Isberg, V.; Vroling, B.; van der Kant, R.; Li, K.; Vriend, G.; Gloriam, D. GPCRDB: an information system for G protein-coupled receptors. *Nucleic acids research* **2014**, *42* (Database issue), D422-5.
- 132 Ishii, M.; Kurachi, Y. Muscarinic acetylcholine receptors. *Current pharmaceutical design* **2006**, *12* (28), 3573–3581.
- 133 Jaluria, P.; Chu, C.; Betenbaugh, M.; Shiloach, J. Cells by design: a mini-review of targeting cell engineering using DNA microarrays. *Mol Biotechnol* **2008**, *39* (2), 105–111.
- 134 Janshoff, A.; Kunze, A.; Michaelis, S.; Heitmann, V.; Reiss, B.; Wegener, J. Cell Adhesion Monitoring Using Substrate-Integrated Sensors. *Journal of Adhesion Science and Technology* **2010**, *24* (13-14), 2079–2104.
- 135 Janshoff, A.; Wegener, J.; Steinem, C.; Sieber, M.; Galla, H. J. Applications of impedance spectroscopy in biochemistry and biophysics. *Acta Biochim Pol* **1996**, *43* (2), 339–348.

- 136 Jayakumar, J. A. K. J.; Panicker, M. M.; Basu, B. Serotonin 2A (5-HT<sub>2A</sub>) receptor affects cell-matrix adhesion and the formation and maintenance of stress fibers in HEK293 cells. *Sci Rep* **2020**, *10* (1), 21675.
- 137 Jean-Charles, P.-Y.; Kaur, S.; Shenoy, S. K.G Protein-Coupled Receptor Signaling Through  $\beta$ -Arrestin-Dependent Mechanisms. *Journal of cardiovascular pharmacology* **2017**, *70* (3), 142–158.
- 138 Ji, H.-L.; Nie, H.-G.; Chang, Y.; Lian, Q.; Liu, S.-L. CPT-cGMP Is A New Ligand of Epithelial Sodium Channels. *International journal of biological sciences* **2016**, *12* (4), 359–366.
- 139 Jiang, T.; Du, L.; Li, M. Lighting up bioluminescence with coelenterazine: strategies and applications. *Photochem Photobiol Sci* **2016**, *15* (4), 466–480.
- 140 Kanie, S.; Komatsu, M.; Mitani, Y. Luminescence of Cypridina Luciferin in the Presence of Human Plasma Alpha 1-Acid Glycoprotein. *International journal of molecular sciences* **2020**, *21* (20), 7516.
- 141 Kao, F. T.; Puck, T. T. Genetics of somatic mammalian cells, VII. Induction and isolation of nutritional mutants in Chinese hamster cells. *Proceedings of the National Academy of Sciences of the United States of America* **1968**, *60* (4), 1275–1281.
- 142 Kao, J. P. Y.; Li, G.; Auston, D. A. Practical aspects of measuring intracellular calcium signals with fluorescent indicators. *Methods in cell biology* **2010**, *99*, 113–152.
- 143 Kaskova, Z. M.; Tsarkova, A. S.; Yampolsky, I. V. 1001 lights: luciferins, luciferases, their mechanisms of action and applications in chemical analysis, biology and medicine. *Chemical Society reviews* **2016**, *45* (21), 6048–6077.
- 144 Katritch, V.; Fenalti, G.; Abola, E. E.; Roth, B. L.; Cherezov, V.; Stevens, R. C. Allosteric sodium in class A GPCR signaling. *Trends in Biochemical Sciences* **2014**, *39* (5), 233–244.
- 145 Kenakin, T. The Nature of Constitutive Activity and Inverse Agonism. In *G Protein-Coupled Receptors as Drug Targets: Analysis of Activation and Constitutive Activity, Volume 24*; Seifert, R., Wieland, T., Mannhold, R., Kubinyi, H., Folkers, G., Eds.; Methods and Principles in Medicinal Chemistry v.24; Wiley: Hoboken, **2006**; pp 11–26.
- 146 Kienzler, M. A.; Isacoff, E. Y. Precise modulation of neuronal activity with synthetic photoswitchable ligands. *Current opinion in neurobiology* **2017**, *45*, 202–209.
- 147 Kim, M. O.; Ryu, J. M.; Suh, H. N.; Park, S. H.; Oh, Y.-M.; Lee, S. H.; Han, H. J. cAMP Promotes Cell Migration Through Cell Junctional Complex Dynamics and

- Actin Cytoskeleton Remodeling: Implications in Skin Wound Healing. *Stem cells and development* **2015**, *24* (21), 2513–2524.
- 148 Kloeckner, J.; Schmitz, J.; Holzgrabe, U. Convergent, short synthesis of the muscarinic superagonist iperoxo. *Tetrahedron Letters* **2010**, *51* (27), 3470–3472.
- 149 Kobauri, P.; Dekker, F. J.; Szymanski, W.; Feringa, B. L. Rational Design in Photopharmacology with Molecular Photoswitches. *Angewandte Chemie* **2023**, *135* (30), e202300681.
- 150 Kolakowski, L. F. GCRDb: a G-protein-coupled receptor database. *Receptors & channels* **1994**, *2* (1), 1–7.
- 151 Kolb, P.; Kenakin, T.; Alexander, S. P. H.; Bermudez, M.; Bohn, L. M.; Breinholt, C. S.; Bouvier, M.; Hill, S. J.; Kostenis, E.; Martemyanov, K. A.; Neubig, R. R.; Onaran, H. O.; Rajagopal, S.; Roth, B. L.; Selent, J.; Shukla, A. K.; Sommer, M. E.; Gloriam, D. E. Community guidelines for GPCR ligand bias: IUPHAR review 32. *British journal of pharmacology* **2022**, *179* (14), 3651–3674.
- 152 Kostrzewa, R. M.; Wydra, K.; Filip, M.; Crawford, C. A.; McDougall, S. A.; Brown, R. W.; Borroto-Escuela, D. O.; Fuxe, K.; Gainetdinov, R. R. Dopamine D2 Receptor Supersensitivity as a Spectrum of Neurotoxicity and Status in Psychiatric Disorders. *The Journal of pharmacology and experimental therapeutics* **2018**, *366* (3), 519–526.
- 153 Krasitskaya, V. V.; Bashmakova, E. E.; Frank, L. A. Coelenterazine-Dependent Luciferases as a Powerful Analytical Tool for Research and Biomedical Applications. *International journal of molecular sciences* **2020**, *21* (20), 7465.
- 154 Kricka, L. J.; Thorpe, G. H. G. Chemiluminescent and bioluminescent methods in Analytical Chemistry. A review. *Analyst* **1983**, *108* (1292), 1274.
- 155 Kroning, K. E.; Wang, W. Genetically encoded tools for in vivo G-protein-coupled receptor agonist detection at cellular resolution. *Clinical and translational medicine* **2022**, *12* (12), e1124.
- 156 Krukiewicz, K. Electrochemical impedance spectroscopy as a versatile tool for the characterization of neural tissue: A mini review. *Electrochemistry Communications* **2020**, *116*, 106742.
- 157 Kühn, B.; Schmid, A.; Harteneck, C.; Gudermann, T.; Schultz, G. G proteins of the Gq family couple the H2 histamine receptor to phospholipase C. *Mol Endocrinol* **1996**, *10* (12), 1697–1707.
- 158 Kumari, P.; Ghosh, E.; Shukla, A. K. Emerging Approaches to GPCR Ligand Screening for Drug Discovery. *Trends in Molecular Medicine* **2015**, *21* (11), 687–701.

- 159 Lachmann, D.; Studte, C.; Männel, B.; Hübner, H.; Gmeiner, P.; König, B. Photochromic Dopamine Receptor Ligands Based on Dithienylethenes and Fulgides. *Chemistry – A European Journal* **2017**, *23* (54), 13423–13434.
- 160 Lagerström, M. C.; Schiöth, H. B. Structural diversity of G protein-coupled receptors and significance for drug discovery. *Nat Rev Drug Discov* **2008**, *7* (4), 339–357.
- 161 Lämmermann, T.; Kastenmüller, W. Concepts of GPCR-controlled navigation in the immune system. *Immunological reviews* **2019**, *289* (1), 205–231.
- 162 Lan, T.-H.; Liu, Q.; Li, C.; Wu, G.; Steyaert, J.; Lambert, N. A. BRET evidence that  $\beta$ 2 adrenergic receptors do not oligomerize in cells. *Sci Rep* **2015**, *5* (1), 10166.
- 163 Lebkowski, J. S.; Clancy, S.; Calos, M. P. Simian virus 40 replication in adenovirus-transformed human cells antagonizes gene expression. *Nature* **1985**, *317* (6033), 169–171.
- 164 Lefkowitz, R. J. A brief history of G-protein coupled receptors (Nobel Lecture). *Angewandte Chemie (International ed. in English)* **2013**, *52* (25), 6366–6378.
- 165 Lehne, F.; Bogdan, S. Getting cells into shape by calcium-dependent actin cross-linking proteins. *Frontiers in cell and developmental biology* **2023**, *11*, 1171930.
- 166 Leibovitz, A. The growth and maintenance of tissue-cell cultures in free gas exchange with the atmosphere. *American Journal of Hygiene* **1963**, No. 78, 173–180.
- 167 Leitinger, B.; McDowall, A.; Stanley, P.; Hogg, N. The regulation of integrin function by  $Ca^{2+}$ . *Biochimica et biophysica acta* **2000**, *1498* (2-3), 91–98.
- 168 Leung, G.; Tang, H. R.; McGuinness, R.; Verdonk, E.; Michelotti, J. M.; Liu, V. F. Cellular Dielectric Spectroscopy: A Label-Free Technology for Drug Discovery. *JALA: Journal of the Association for Laboratory Automation* **2005**, *10* (4), 258–269.
- 169 Levick, S. P. Histamine receptors in heart failure. *Heart Fail Rev* **2022**, *27* (4), 1355–1372.
- 170 Li, J.; Tian, Y.; Wu, A. Neuropeptide Y receptors: a promising target for cancer imaging and therapy. *Regenerative biomaterials* **2015**, *2* (3), 215–219.
- 171 Liang, Y.-L.; Khoshouei, M.; Radjainia, M.; Zhang, Y.; Glukhova, A.; Tarrasch, J.; Thal, D. M.; Furness, S. G. B.; Christopoulos, G.; Coudrat, T.; Danev, R.; Baumeister, W.; Miller, L. J.; Christopoulos, A.; Kobilka, B. K.; Wootten, D.; Skiniotis, G.; Sexton, P. M. Phase-plate cryo-EM structure of a class B GPCR-G-protein complex. *Nature* **2017**, *546* (7656), 118–123.
- 172 Lieb, S.; Littmann, T.; Plank, N.; Felixberger, J.; Tanaka, M.; Schäfer, T.; Krief, S.; Elz, S.; Friedland, K.; Bernhardt, G.; Wegener, J.; Ozawa, T.; Buschauer,

- A. Label-free versus conventional cellular assays: Functional investigations on the human histamine H1 receptor. *Pharmacological Research* **2016a**, *114*, 13–26.
- 173 Lieb, S.; Michaelis, S.; Plank, N.; Bernhardt, G.; Buschauer, A.; Wegener, J. Label-free analysis of GPCR-stimulation: The critical impact of cell adhesion. *Pharmacological Research* **2016b**, *108*, 65–74.
- 174 Littmann, T.; Ozawa, T.; Hoffmann, C.; Buschauer, A.; Bernhardt, G. A split luciferase-based probe for quantitative proximal determination of Gαq signalling in live cells. *Scientific reports* **2018**, *8* (17179), 1–10.
- 175 Liu, K.; Southall, N.; Titus, S. A.; Inglese, J.; Eskay, R. L.; Shinn, P.; Austin, C. P.; Heilig, M. A.; Zheng, W. A multiplex calcium assay for identification of GPCR agonists and antagonists. *Assay and drug development technologies* **2010**, *8* (3), 367–379.
- 176 Lo, C. M.; Keese, C. R.; Giaever, I. Monitoring motion of confluent cells in tissue culture. *Experimental cell research* **1993**, *204* (1), 102–109.
- 177 Lo, C. M.; Keese, C. R.; Giaever, I. pH changes in pulsed CO<sub>2</sub> incubators cause periodic changes in cell morphology. *Experimental cell research* **1994**, *213* (2), 391–397.
- 178 Lundstrom, K. Cell-impedance-based label-free technology for the identification of new drugs. *Expert opinion on drug discovery* **2017**, *12* (4), 335–343.
- 179 Luttrell, L. M.; Wang, J.; Plouffe, B.; Smith, J. S.; Yamani, L.; Kaur, S.; Jean-Charles, P.-Y.; Gauthier, C.; Lee, M.-H.; Pani, B.; Kim, J.; Ahn, S.; Rajagopal, S.; Reiter, E.; Bouvier, M.; Shenoy, S. K.; Laporte, S. A.; Rockman, H. A.; Lefkowitz, R. J. Manifold roles of β-arrestins in GPCR signaling elucidated with siRNA and CRISPR/Cas9. *Science signaling* **2018**, *11* (549), 7650.
- 180 Ma, Q.; Ye, L.; Liu, H.; Shi, Y.; Zhou, N. An overview of Ca<sup>2+</sup> mobilization assays in GPCR drug discovery. *Expert opinion on drug discovery* **2017**, *12* (5), 511–523.
- 181 Macdonald, J.; Johnson, W. B. Fundamentals of Impedance Spectroscopy. *Impedance Spectroscopy*; John Wiley & Sons, Ltd, **2018**; pp 1–20.
- 182 Maeda, S.; Qu, Q.; Robertson, M. J.; Skiniotis, G.; Kobilka, B. K. Structures of the M1 and M2 muscarinic acetylcholine receptor/G-protein complexes. *Science (New York, N.Y.)* **2019**, *364* (6440), 552–557.
- 183 Markova, S. V.; Larionova, M. D.; Vysotski, E. S. Shining Light on the Secreted Luciferases of Marine Copepods: Current Knowledge and Applications. *Photochemistry and photobiology* **2019**, *95* (3), 705–721.
- 184 Martel, J. C.; Gatti McArthur, S. Dopamine Receptor Subtypes, Physiology and Pharmacology: New Ligands and Concepts in Schizophrenia. *Frontiers in pharmacology* **2020**, *11*, 1003.

- 185 Martins, S. A. M.; Prazeres, D. M. F. *G protein-coupled receptor screening assays. Methods and protocols*, Second edition; Springer protocols 2268; Humana Press: New York, NY, **2021**.
- 186 Maziarz, M.; Park, J.-C.; Leyme, A.; Marivin, A.; Garcia-Lopez, A.; Patel, P. P.; Garcia-Marcos, M. Revealing the Activity of Trimeric G-proteins in Live Cells with a Versatile Biosensor Design. *Cell* **2020**, *182* (3), 770-785.e16.
- 187 McGuinness, R. P.; Proctor, J. M.; Gallant, D. L.; van Staden, C. J.; Ly, J. T.; Tang, F. L.; Lee, P. H. *Enhanced selectivity screening of GPCR ligands using a label-free cell based assay technology 12*; Bentham Science Publishers, **2009**.
- 188 Meisenberg, A.; Kaschuba, D.; Balfanz, S.; Jordan, N.; Baumann, A. Molecular and functional profiling of histamine receptor-mediated calcium ion signals in different cell lines. *Analytical biochemistry* **2015**, *486*, 96–101.
- 189 Michaelis, L.; Menten, M. L. Die Kinetik der Invertinwirkung. *Biochemische Zeitschrift* **1913**, No. 49, 333–369.
- 190 Michaelis, L.; Menten, M. L.; Johnson, K. A.; Goody, R. S. The original Michaelis constant: translation of the 1913 Michaelis-Menten paper. *Biochemistry* **2011**, *50* (39), 8264–8269.
- 191 Michelotti, G. A.; Price, D. T.; Schwinn, D. A. Alpha 1-adrenergic receptor regulation: basic science and clinical implications. *Pharmacology & Therapeutics* **2000**, *88* (3), 281–309.
- 192 microscopyu.com:  
<https://www.microscopyu.com/techniques/stereomicroscopy/introduction-to-stereomicroscopy>; **August 10, 2024**.
- 193 Miller, E. J.; Lappin, S. L. Physiology, Cellular Receptor. In *StatPearls [Internet]*; Miller, E. J., Lappin, S. L., Eds.; StatPearls Publishing, **2022**.
- 194 Milligan, G. Constitutive activity and inverse agonists of G protein-coupled receptors: a current perspective. *Molecular pharmacology* **2003**, *64* (6), 1271–1276.
- 195 Milligan, G.; Inoue, A. Genome Editing Provides New Insights into Receptor-Controlled Signalling Pathways. *Trends in pharmacological sciences* **2018**, *39* (5), 481–493.
- 196 Mizuno, N.; Itoh, H. Functions and regulatory mechanisms of Gq-signaling pathways. *Neurosignals* **2009**, *17* (1), 42–54.
- 197 Mohammadi-Farani, A.; Ghazi-Khansari, M.; Sahebgharani, M. Glucose concentration in culture medium affects mRNA expression of TRPV1 and CB1 receptors and changes capsaicin toxicity in PC12 cells. *Iranian Journal of Basic Medical Sciences* **2014**, *17* (9), 673-378.

- 198 Monczor, F.; Fernandez, N. Current Knowledge and Perspectives on Histamine H1 and H2 Receptor Pharmacology: Functional Selectivity, Receptor Crosstalk, and Repositioning of Classic Histaminergic Ligands. *Molecular pharmacology* **2016**, *90* (5), 640–648.
- 199 Munk, C.; Isberg, V.; Mordalski, S.; Harpsøe, K.; Rataj, K.; Hauser, A. S.; Kolb, P.; Bojarski, A. J.; Vriend, G.; Gloriam, D. E. GPCRdb: the G protein-coupled receptor database - an introduction. *British journal of pharmacology* **2016**, *173* (14), 2195–2207.
- 200 Murthy, K.; Virk, H. S. Luminescence Phenomena: An Introduction. *DDF* **2013**, *347*, 1–34.
- 201 Nakajima, K.; Hamada, K.; Ito, R.; Yoshida, Y.; Sutherland, K.; Ishikawa, M.; Ozaki, M.; Shirato, H.; Hamada, T. Stability of d-luciferin for bioluminescence to detect gene expression in freely moving mice for long durations. *Luminescence : the journal of biological and chemical luminescence* **2021**, *36* (1), 94–98.
- 202 nanion.de: [https://www.nanion.de/wp-content/uploads/2023/02/Nanion\\_Product\\_Flyer\\_CE\\_FL\\_Plates.pdf?1677675933](https://www.nanion.de/wp-content/uploads/2023/02/Nanion_Product_Flyer_CE_FL_Plates.pdf?1677675933) ; **August 10, 2024.**
- 203 Negi, A.; Kesari, K. K.; Voisin-Chiret, A. S. Light-Activating PROTACs in Cancer: Chemical Design, Challenges, and Applications. *Applied Sciences* **2022**, *12* (19), 9674.
- 204 Nehmé, R.; Carpenter, B.; Singhal, A.; Strege, A.; Edwards, P. C.; White, C. F.; Du, H.; Grisshammer, R.; Tate, C. G. Mini-G proteins: Novel tools for studying GPCRs in their active conformation. *PloS one* **2017**, *12* (4), e0175642.
- 205 Newton, A. C.; Bootman, M. D.; Scott, J. D. Second Messengers. *Cold Spring Harbor perspectives in biology* **2016**, *8* (8), a005926.
- 206 Ngoc Le, H. T.; Kim, J.; Park, J.; Cho, S. A Review of Electrical Impedance Characterization of Cells for Label-Free and Real-Time Assays. *BioChip J* **2019**, *13* (4), 295–305.
- 207 Nguyen, V. T.; Morange, M.; Bensaude, O. Firefly luciferase luminescence assays using scintillation counters for quantitation in transfected mammalian cells. *Analytical biochemistry* **1988**, *171* (2), 404–408.
- 208 Nieto Gutierrez, A.; McDonald, P. H. GPCRs: Emerging anti-cancer drug targets. *Cellular Signalling* **2018**, *41*, 65–74.
- 209 Nogués, L.; Palacios-García, J.; Reglero, C.; Rivas, V.; Neves, M.; Ribas, C.; Penela, P.; Mayor, F. G protein-coupled receptor kinases (GRKs) in tumorigenesis and cancer progression: GPCR regulators and signaling hubs. *Seminars in cancer biology* **2018**, *48*, 78–90.

- 210 Oheim, M.; van 't Hoff, M.; Feltz, A.; Zamaleeva, A.; Mallet, J.-M.; Collot, M. New red-fluorescent calcium indicators for optogenetics, photoactivation and multi-color imaging. *Biochimica et biophysica acta* **2014**, *1843* (10), 2284–2306.
- 211 Olsen, R. H. J.; DiBerto, J. F.; English, J. G.; Glaudin, A. M.; Krumm, B. E.; Slocum, S. T.; Che, T.; Gavin, A. C.; McCorvy, J. D.; Roth, B. L.; Strachan, R. T. TRUPATH, an open-source biosensor platform for interrogating the GPCR transducerome. *Nature chemical biology* **2020**, *16* (8), 841–849.
- 212 Olsen, R. H. J.; English, J. G. Advancements in G protein-coupled receptor biosensors to study GPCR-G protein coupling. *British journal of pharmacology* **2023**, *180* (11), 1433–1443.
- 213 O'Mahony, L.; Akdis, M.; Akdis, C. A. Regulation of the immune response and inflammation by histamine and histamine receptors. *The Journal of allergy and clinical immunology* **2011**, *128* (6), 1153–1162.
- 214 Oryan, A.; Kamali, A.; Moshiri, A.; Baharvand, H.; Daemi, H. Chemical crosslinking of biopolymeric scaffolds: Current knowledge and future directions of crosslinked engineered bone scaffolds. *International journal of biological macromolecules* **2018**, *107* (Pt A), 678–688.
- 215 Ostrin, L. A.; Frishman, L. J.; Glasser, A. Effects of pirenzepine on pupil size and accommodation in rhesus monkeys. *Investigative ophthalmology & visual science* **2004**, *45* (10), 3620–3628.
- 216 Ozdalğic, B.; Gul, M.; Uygun, Z. O.; Atçeken, N.; Tasoglu, S. Emerging Applications of Electrochemical Impedance Spectroscopy in Tear Film Analysis. *Biosensors* **2022**, *12* (10), 827.
- 217 Palczewski, K.; Kumasaka, T.; Hori, T.; Behnke, C. A.; Motoshima, H.; Fox, B. A.; Le Trong, I.; Teller, D. C.; Okada, T.; Stenkamp, R. E.; Yamamoto, M.; Miyano, M. Crystal structure of rhodopsin: A G protein-coupled receptor. *Science (New York, N.Y.)* **2000**, *289* (5480), 739–745.
- 218 Parić, Z. Development of a dual ECIS-SPR sensor platform for cell-based assays: Label-free analysis of g-protein coupled receptor signal transduction, **2021**.
- 219 Parviz, M.; Gaus, K.; Gooding, J. J. Simultaneous impedance spectroscopy and fluorescence microscopy for the real-time monitoring of the response of cells to drugs. *Chemical science* **2017**, *8* (3), 1831–1840.
- 220 Peterson, S. M.; Hutchings, C. J.; Hu, C. F.; Mathur, M.; Salameh, J. W.; Axelrod, F.; Sato, A. K. Discovery and design of G protein-coupled receptor targeting antibodies. *Expert opinion on drug discovery* **2023**, 1–12.

- 221 Pockes, S.; Wifling, D.; Keller, M.; Buschauer, A.; Elz, S. Highly Potent, Stable, and Selective Dimeric Hetarylpropylguanidine-Type Histamine H<sub>2</sub> Receptor Agonists. *ACS omega* **2018**, 3 (3), 2865–2882.
- 222 Polit, A.; Rysiewicz, B.; Mystek, P.; Błasiak, E.; Dziedzicka-Wasylewska, M. The Gai protein subclass selectivity to the dopamine D<sub>2</sub> receptor is also decided by their location at the cell membrane. *Cell communication and signaling : CCS* **2020**, 18 (1), 189.
- 223 Pollard, T. D. Actin and Actin-Binding Proteins. *Cold Spring Harb Perspect Biol* **2016**, 8 (8), a018226.
- 224 promega.de #3: <https://www.promega.de/products/biochemicals-and-labware/biochemical-buffers-and-reagents/coelenterazines/?catNum=S2011>; **August 10, 2024.**
- 225 promega.de #2: <https://www.promega.de/products/biochemicals-and-labware/biochemical-buffers-and-reagents/coelenterazines/?catNum=S2001>; **August 10, 2024.**
- 226 promega.de #1: <https://www.promega.de/resources/pubhub/which-plates-to-choose-for-fluorescence-and-luminescence-measurements/>; **August 10, 2024.**
- 227 Pronin, A. N.; Wang, Q.; Slepak, V. Z. Teaching an Old Drug New Tricks: Agonism, Antagonism, and Biased Signaling of Pilocarpine through M<sub>3</sub> Muscarinic Acetylcholine Receptor. *Molecular pharmacology* **2017**, 92 (5), 601–612.
- 228 Puck, T. T.; Cieciora, S. J.; Robinson, A. Genetics of somatic mammalian cells. III. Long-term cultivation of euploid cells from human and animal subjects. *The Journal of Experimental Medicine* **1958**, 945–959.
- 229 Qi, C.; Lavriha, P.; Mehta, V.; Khanppnavar, B.; Mohammed, I.; Li, Y.; Lazaratos, M.; Schaefer, J. V.; Dreier, B.; Plückthun, A.; Bondar, A.-N.; Dessauer, C. W.; Korkhov, V. M. Structural basis of adenylyl cyclase 9 activation. *Nat Commun* **2022**, 13 (1), 1045.
- 230 Rajagopal, S.; Shenoy, S. K. GPCR desensitization: Acute and prolonged phases. *Cellular Signalling* **2018**, 41, 9–16.
- 231 Randáková, A.; Nelic, D.; Hochmalová, M.; Zimčík, P.; Mulenga, M. J.; Boulos, J.; Jakubík, J. Fusion with Promiscuous G $\alpha$ <sub>16</sub> Subunit Reveals Signaling Bias at Muscarinic Receptors. *International journal of molecular sciences* **2021**, 22 (18), 10089.
- 232 Randáková, A.; Nelic, D.; Ungerová, D.; Nwokoye, P.; Su, Q.; Doležal, V.; El-Fakahany, E. E.; Boulos, J.; Jakubík, J. Novel M<sub>2</sub>-selective, G<sub>i</sub>-biased agonists of muscarinic acetylcholine receptors. *British journal of pharmacology* **2020**, 177 (9), 2073–2089.

- 233 Redmond, R. W.; Kochevar, I. E. Medical Applications of Rose Bengal- and Riboflavin-Photosensitized Protein Crosslinking. *Photochemistry and photobiology* **2019**, *95* (5), 1097–1115.
- 234 Reichmann, F.; Holzer, P. Neuropeptide Y: A stressful review. *Neuropeptides* **2016**, *55*, 99–109.
- 235 Reiss, B.; Wegener, J. Impedance analysis of different cell monolayers grown on gold-film electrodes. In *2015 37th Annual International Conference of the IEEE Engineering in Medicine and Biology Society (EMBC)*; IEEE, **2015**.
- 236 Reyes-Alcaraz, A.; Lucero Garcia-Rojas, E. Y.; Merlinsky, E. A.; Seong, J. Y.; Bond, R. A.; McConnell, B. K. A NanoBiT assay to monitor membrane proteins trafficking for drug discovery and drug development. *Communications biology* **2022**, *5* (1), 212.
- 237 Reynders, M.; Matsuura, B. S.; Bérouti, M.; Simoneschi, D.; Marzio, A.; Pagano, M.; Trauner, D. PHOTACs enable optical control of protein degradation. *Science Advances* **2020**, *6* (8), eaay5064.
- 238 Ricart-Ortega, M.; Berizzi, A. E.; Pereira, V.; Malhaire, F.; Catena, J.; Font, J.; Gómez-Santacana, X.; Muñoz, L.; Zussy, C.; Serra, C.; Rovira, X.; Goudet, C.; Llebaria, A. Mechanistic Insights into Light-Driven Allosteric Control of GPCR Biological Activity. *ACS Pharmacol. Transl. Sci.* **2020**, *3* (5), 883–895.
- 239 Ricart-Ortega, M.; Font, J.; Llebaria, A. GPCR photopharmacology. *Molecular and cellular endocrinology* **2019**, *488*, 36–51.
- 240 Rio, D. C.; Clark, S. G.; Tjian, R. A mammalian host-vector system that regulates expression and amplification of transfected genes by temperature induction. *Science (New York, N.Y.)* **1985**, *227* (4682), 23–28.
- 241 Rodionova, N. S.; Petushkov, V. N. Effect of different salts and detergents on luciferin-luciferase luminescence of the enchytraeid *Fridericia heliota*. *Journal of photochemistry and photobiology. B, Biology* **2006**, *83* (2), 123–128.
- 242 Ross, G. M. S.; Filippini, D.; Nielen, M. W. F.; Salentijn, G. I. Unraveling the Hook Effect: A Comprehensive Study of High Antigen Concentration Effects in Sandwich Lateral Flow Immunoassays. *Analytical chemistry* **2020**, *92* (23), 15587–15595.
- 243 Rovati, L.; Fabbri, P.; Ferrari, L.; Pilati, F. Plastic Optical Fiber pH Sensor Using a Sol-Gel Sensing Matrix. In *Fiber Optic Sensors*; Yasin, M., Harun, S. W., Arof, H., Eds.; IntechOpen: Erscheinungsort nicht ermittelbar, **2012**.
- 244 Saffioti, N. A.; Cavalcanti-Adam, E. A.; Pallarola, D. Biosensors for Studies on Adhesion-Mediated Cellular Responses to Their Microenvironment. *Frontiers in bioengineering and biotechnology* **2020**, *8*, 597950.

- 245 Salama, K.; Eltoukhy, H.; Hassibi, A.; El-Gamal, A. Modeling and simulation of luminescence detection platforms. *Biosensors and Bioelectronics* **2004**, *19* (11), 1377–1386.
- 246 Sánchez, M. L.; Rodríguez, F. D.; Coveñas, R. Neuropeptide Y Peptide Family and Cancer: Antitumor Therapeutic Strategies. *International journal of molecular sciences* **2023**, *24* (12).
- 247 Saxena, R.; Ganguly, S.; Chattopadhyay, A. Comparative analysis of calcium spikes upon activation of serotonin(1A) and purinergic receptors. *PLOS ONE* **2012**, *7* (12), e51857.
- 248 Schiffmann, A.; Gimpl, G. Sodium functions as a negative allosteric modulator of the oxytocin receptor. *Biochimica et biophysica acta. Biomembranes* **2018**, *1860* (6), 1301–1308.
- 249 Schiöth, H. B.; Fredriksson, R. The GRAFS classification system of G-protein coupled receptors in comparative perspective. *General and comparative endocrinology* **2005**, *142* (1-2), 94–101.
- 250 Schlie-Wolter, S.; Ngezahayo, A.; Chichkov, B. N. The selective role of ECM components on cell adhesion, morphology, proliferation and communication in vitro. *Experimental cell research* **2013**, *319* (10), 1553–1561.
- 251 Schrage, R.; Min, A. de; Hochheiser, K.; Kostenis, E.; Mohr, K. Superagonism at G protein-coupled receptors and beyond. *British journal of pharmacology* **2016**, *173* (20), 3018–3027.
- 252 Schrage, R.; Schmitz, A.-L.; Gaffal, E.; Annala, S.; Kehraus, S.; Wenzel, D.; Büllsbach, K. M.; Bald, T.; Inoue, A.; Shinjo, Y.; Galandrin, S.; Shridhar, N.; Hesse, M.; Grundmann, M.; Merten, N.; Charpentier, T. H.; Martz, M.; Butcher, A. J.; Slodczyk, T.; Armando, S.; Effern, M.; Namkung, Y.; Jenkins, L.; Horn, V.; Stöbel, A.; Dargatz, H.; Tietze, D.; Imhof, D.; Galés, C.; Drewke, C.; Müller, C. E.; Hölzel, M.; Milligan, G.; Tobin, A. B.; Gomeza, J.; Dohlman, H. G.; Sondek, J.; Harden, T. K.; Bouvier, M.; Laporte, S. A.; Aoki, J.; Fleischmann, B. K.; Mohr, K.; König, G. M.; Tüting, T.; Kostenis, E. The experimental power of FR900359 to study Gq-regulated biological processes. *Nat Commun* **2015**, *6* (1), 10156.
- 253 Schrage, R.; Seemann, W. K.; Klöckner, J.; Dallanoce, C.; Racké, K.; Kostenis, E.; Amici, M. de; Holzgrabe, U.; Mohr, K. Agonists with supraphysiological efficacy at the muscarinic M2 ACh receptor. *British journal of pharmacology* **2013**, *169* (2), 357–370.
- 254 Schröder, R.; Janssen, N.; Schmidt, J.; Kebig, A.; Merten, N.; Hennen, S.; Müller, A.; Blättermann, S.; Mohr-Andrä, M.; Zahn, S.; Wenzel, J.; Smith, N. J.; Gomeza, J.; Drewke, C.; Milligan, G.; Mohr, K.; Kostenis, E. Deconvolution of complex G

- protein-coupled receptor signaling in live cells using dynamic mass redistribution measurements. *Nat Biotechnol* **2010**, 28 (9), 943–949.
- 255 Schunack, W. What are the differences between the H<sub>2</sub>-receptor antagonists? *Alimentary pharmacology & therapeutics* **1987**, 1 Suppl 1, 493S-503S.
- 256 Scott, C. W.; Peters, M. F. Label-free whole-cell assays: expanding the scope of GPCR screening. *Drug Discovery Today* **2010**, 15 (17-18), 704–716.
- 257 Seamon, K. B.; Padgett, W.; Daly, J. W. Forskolin: unique diterpene activator of adenylate cyclase in membranes and in intact cells. *Proceedings of the National Academy of Sciences of the United States of America* **1981**, 78 (6), 3363–3367.
- 258 Seeman, P.; van Tol, H. H. Dopamine receptor pharmacology. *Trends in pharmacological sciences* **1994**, 15 (7), 264–270.
- 259 Seibel-Ehlert, U.; Plank, N.; Inoue, A.; Bernhardt, G.; Strasser, A. Label-Free Investigations on the G Protein Dependent Signaling Pathways of Histamine Receptors. *International journal of molecular sciences* **2021**, 22 (18), 9739.
- 260 Seibert, E.; Tracy, T. S. Fundamentals of Enzyme Kinetics. *Enzyme Kinetics in Drug Metabolism*; Humana Press, Totowa, NJ, **2014**; pp 9–22.
- 261 Seifert, R.; Wenzel-Seifert, K. Constitutive activity of G-protein-coupled receptors: cause of disease and common property of wild-type receptors. *Naunyn-Schmiedeberg's Arch Pharmacol* **2002**, 366 (5), 381–416.
- 262 Senisterra, G. A.; Finerty, P. J. High throughput methods of assessing protein stability and aggregation. *Mol. BioSyst.* **2009**, 5 (3), 217–223.
- 263 Shimomura, O. Membrane permeability of coelenterazine analogues measured with fish eggs. *Biochem J* **1997**, 326 (Pt 2) (Pt 2), 297–298.
- 264 Shimomura, O.; Flood, P. R.; Inouye, S.; Bryan, B.; Shimomura, A. Isolation and properties of the luciferase stored in the ovary of the scyphozoan medusa *Periphylla periphylla*. *The Biological Bulletin* **2001**, 201 (3), 339–347.
- 265 Siehler, S. G<sub>12/13</sub>-dependent signaling of G-protein-coupled receptors: disease context and impact on drug discovery. *Expert opinion on drug discovery* **2007**, 2 (12), 1591–1604.
- 266 Siehler, S. Cell-based assays in GPCR drug discovery. *Biotechnology Journal* **2008**, 3 (4), 471–483.
- 267 sigmaaldrich.com #6: <https://www.sigmaaldrich.com/DE/de/products/cell-culture-and-analysis/cell-culture-media-and-buffers/classical-media-and-buffers/dulbeccos-modified-eagle-medium>; **August 10, 2024**.
- 268 sigmaaldrich.com #10: <https://www.sigmaaldrich.com/DE/en/specification-sheet/SIGMA/D5671>; **August 10, 2024**.

- 269 sigmaaldrich.com #3:  
<https://www.sigmaaldrich.com/deepweb/assets/sigmaaldrich/product/documents/107/900/h4891for.pdf>; **August 10, 2024.**
- 270 sigmaaldrich.com #9: <https://www.sigmaaldrich.com/specification-sheets/237/973/55037C-1000ML.pdf>; **August 10, 2024.**
- 271 sigmaaldrich.com #4: <https://www.sigmaaldrich.com/specification-sheets/237/973/55037C-1000ML.pdf>; **August 10, 2024.**
- 272 sigmaaldrich.com #5: <https://www.sigmaaldrich.com/DE/de/products/chemistry-and-biochemicals/biochemicals/biological-buffers/hepes-buffer>; **August 10, 2024.**
- 273 sigmaaldrich.com #7: <https://www.sigmaaldrich.com/specification-sheets/197/070/L5520-500ML.pdf>; **August 10, 2024.**
- 274 sigmaaldrich.com #1: <https://www.sigmaaldrich.com/specification-sheets/197/070/L5520-500ML.pdf>; **August 10, 2024.**
- 275 sigmaaldrich.com #8: <https://www.sigmaaldrich.com/DE/en/specification-sheet/SIGMA/D8662>; **August 10, 2024.**
- 276 sigmaaldrich.com #2: <https://www.sigmaaldrich.com/DE/de/specification-sheet/SIGMA/D8662>; **August 10, 2024.**
- 277 Skiba, M. The Impact of Heterogenous Cell Populations on Impedance-Based Cell Analysis, **2022.**
- 278 Skiba, M.; Stolwijk, J. A.; Wegener, J. Label-free impedance measurements to unravel biomolecular interactions involved in G protein-coupled receptor signaling. *Methods in cell biology* **2022**, 169, 221–236.
- 279 Sloop, K. W.; Emmerson, P. J.; Statnick, M. A.; Willard, F. S. The current state of GPCR-based drug discovery to treat metabolic disease. *British journal of pharmacology* **2018**, 175 (21), 4060–4071.
- 280 Soave, M.; Stoddart, L. A.; White, C. W.; Kilpatrick, L. E.; Goulding, J.; Briddon, S. J.; Hill, S. J. Detection of genome-edited and endogenously expressed G protein-coupled receptors. *The FEBS Journal* **2021**, 288 (8), 2585–2601.
- 281 Sobotka, T. J.; Brodie, R. E.; Quander, Y.; O'Donnell, M.; West, G. L. Neurobehavioral effects of the calcium ionophore A23187. *Neurotoxicology and teratology* **1987**, 9 (2), 99–106.
- 282 Spalding, T. A.; Burstein, E. S. Constitutive activity of muscarinic acetylcholine receptors. *Journal of receptor and signal transduction research* **2006**, 26 (1-2), 61–85.
- 283 Spillmann, M.; Thurner, L.; Romantini, N.; Zimmermann, M.; Meger, B.; Behe, M.; Waldhoer, M.; Schertler, G. F. X.; Berger, P. New Insights into Arrestin Recruitment to GPCRs. *International journal of molecular sciences* **2020**, 21 (14), 4949.

- 284 Stadtfeld, M.; Varas, F.; Graf, T. Fluorescent Protein-Cell Labeling and Its Application in Time-Lapse Analysis of Hematopoietic Differentiation. *Developmental Hematopoiesis*; Humana Press, Totowa, NJ, **2005**; pp 395–412.
- 285 Stephenson, R. P. A modification of receptor theory. *British Journal of Pharmacology and Chemotherapy* **1956**, *11* (4), 379–393.
- 286 Stolwijk, J. A.; Matrougui, K.; Renken, C. W.; Trebak, M. Impedance analysis of GPCR-mediated changes in endothelial barrier function: overview, and fundamental considerations for stable and reproducible measurements. *Pflugers Archiv : European journal of physiology* **2015**, *467* (10), 2193–2218.
- 287 Stolwijk, J. A.; Michaelis, S.; Wegener, J. Cell Growth and Cell Death Studied by Electric Cell-Substrate Impedance Sensing. In *Electric Cell-Substrate Impedance Sensing and Cancer Metastasis*; Jiang, W. G., Ed.; SpringerLink Bücher 17; Springer: Dordrecht, **2012**; pp 85–117.
- 288 Stolwijk, J. A.; Skiba, M.; Kade, C.; Bernhardt, G.; Buschauer, A.; Hübner, H.; Gmeiner, P.; Wegener, J. Increasing the throughput of label-free cell assays to study the activation of G-protein-coupled receptors by using a serial agonist exposure protocol. *Integrative biology : quantitative biosciences from nano to macro* **2019**, *11* (3), 99–108.
- 289 Stolwijk, J. A.; Wegener, J. Impedance-Based Assays Along the Life Span of Adherent Mammalian Cells In Vitro: From Initial Adhesion to Cell Death. *Label-Free Monitoring of Cells in vitro*; Springer, Cham, **2019**; pp 1–75.
- 290 Stolwijk, J. A.; Wegener, J. Impedance analysis of adherent cells after in situ electroporation-mediated delivery of bioactive proteins, DNA and nanoparticles in  $\mu$ L-volumes. *Sci Rep* **2020**, *10* (1), 21331.
- 291 Storch, U.; Straub, J.; Erdogmus, S.; Gudermann, T.; Mederos Y Schnitzler, M. Dynamic monitoring of Gi/o-protein-mediated decreases of intracellular cAMP by FRET-based Epac sensors. *Pflugers Archiv : European journal of physiology* **2017**, *469* (5-6), 725–737.
- 292 Strange, P. G. Agonist binding, agonist affinity and agonist efficacy at G protein-coupled receptors. *British journal of pharmacology* **2008**, *153* (7), 1353–1363.
- 293 Sykes, D. A.; Stoddart, L. A.; Kilpatrick, L. E.; Hill, S. J. Binding kinetics of ligands acting at GPCRs. *Molecular and cellular endocrinology* **2019**, *485*, 9–19.
- 294 Szénási, T.; Turu, G.; Hunyady, L. Interactions between  $\beta$ -arrestin proteins and the cytoskeletal system, and their relevance to neurodegenerative disorders. *Front. Endocrinol.* **2023**, *14*, 957981.
- 295 Szulcek, R.; Bogaard, H. J.; van Nieuw Amerongen, G. P. Electric cell-substrate impedance sensing for the quantification of endothelial proliferation, barrier

- function, and motility. *Journal of Visualized Experiments : JoVE* **2014**, No. 85, 51300.
- 296 Szymański, W.; Beierle, J. M.; Kistemaker, H. A. V.; Velema, W. A.; Feringa, B. L. Reversible photocontrol of biological systems by the incorporation of molecular photoswitches. *Chemical Reviews* **2013**, *113* (8), 6114–6178.
- 297 Takeda, S.; Kadowaki, S.; Haga, T.; Takaesu, H.; Mitaku, S. Identification of G protein-coupled receptor genes from the human genome sequence. *FEBS Letters* **2002**, *520* (1-3), 97–101.
- 298 Tenreiro, A. F. G.; Lopes, A. M.; Da Silva, L. F. M. A review of structural health monitoring of bonded structures using electromechanical impedance spectroscopy. *Structural Health Monitoring* **2022**, *21* (2), 228–249.
- 299 thermofisher.com: [https://www.thermofisher.com/document-connect/document-connect.html?url=https://assets.thermofisher.com/TFS-Assets%2Fcertificate%2FGRIS%2FCOA%2FCOA\\_21083027\\_2890236\\_1.pdf](https://www.thermofisher.com/document-connect/document-connect.html?url=https://assets.thermofisher.com/TFS-Assets%2Fcertificate%2FGRIS%2FCOA%2FCOA_21083027_2890236_1.pdf);  
**August 10, 2024.**
- 300 Thomsen, W.; Frazer, J.; Unett, D. Functional assays for screening GPCR targets. *Current Opinion in Biotechnology* **2005**, *16* (6), 655–665.
- 301 Threlfell, S.; Exley, R.; Cragg, S. J.; Greenfield, S. A. Constitutive histamine H<sub>2</sub> receptor activity regulates serotonin release in the substantia nigra. *Journal of Neurochemistry* **2008**, *107* (3), 745–755.
- 302 Trinquet, E.; Bouhelal, R.; Dietz, M. Monitoring Gq-coupled receptor response through inositol phosphate quantification with the IP-One assay. *Expert opinion on drug discovery* **2011**, *6* (10), 981–994.
- 303 Tropmann, K.; Höring, C.; Plank, N.; Pockes, S. Discovery of a G Protein-Biased Radioligand for the Histamine H<sub>2</sub> Receptor with Reversible Binding Properties. *Journal of medicinal chemistry* **2020**, *63* (21), 13090–13102.
- 304 Tubio, M. R.; Fernandez, N.; Fitzsimons, C. P.; Copsel, S.; Santiago, S.; Shayo, C.; Davio, C.; Monczor, F. Expression of a G protein-coupled receptor (GPCR) leads to attenuation of signaling by other GPCRs: experimental evidence for a spontaneous GPCR constitutive inactive form. *Journal of Biological Chemistry* **2010**, *285* (20), 14990–14998.
- 305 Tuteja, N. Signaling through G protein coupled receptors. *Plant Signaling & Behavior* **2009**, *4* (10), 942–947.
- 306 van der Kolk, M. R.; Janssen, M. A. C. H.; Rutjes, F. P. J. T.; Blanco-Ania, D. Cyclobutanes in Small-Molecule Drug Candidates. *ChemMedChem* **2022**, *17* (9), e202200020.

- 307 Vázquez-Victorio, G.; González-Espinosa, C.; Espinosa-Riquer, Z. P.; Macías-Silva, M. GPCRs and actin-cytoskeleton dynamics. *Methods in cell biology* **2016**, *132*, 165–188.
- 308 Verdonk, E.; Johnson, K.; McGuinness, R.; Leung, G.; Chen, Y.-W.; Tang, H. R.; Michelotti, J. M.; Liu, V. F. Cellular dielectric spectroscopy: a label-free comprehensive platform for functional evaluation of endogenous receptors. *Assay and drug development technologies* **2006**, *4* (5), 609–619.
- 309 Vilardaga, J.-P. Theme and variations on kinetics of GPCR activation/deactivation. *Journal of receptor and signal transduction research* **2010**, *30* (5), 304–312.
- 310 Voiculescu, I.; Li, F.; Nordin, A. N. Impedance Spectroscopy of Adherent Mammalian Cell Culture for Biochemical Applications: A Review. *IEEE Sensors J.* **2021**, *21* (5), 5612–5627.
- 311 Volpato, D.; Holzgrabe, U. Designing Hybrids Targeting the Cholinergic System by Modulating the Muscarinic and Nicotinic Receptors: A Concept to Treat Alzheimer's Disease. *Molecules* **2018**, *23* (12), 3230.
- 312 Volpato, D.; Kauk, M.; Messerer, R.; Bermudez, M.; Wolber, G.; Bock, A.; Hoffmann, C.; Holzgrabe, U. The Role of Orthosteric Building Blocks of Bitopic Ligands for Muscarinic M1 Receptors. *ACS omega* **2020**, *5* (49), 31706–31715.
- 313 Voss, J. H.; Müller, C. E. *Heterotrimeric G Protein  $\alpha$ -Subunits - Structures, Peptide-Derived Inhibitors, and Mechanisms* 29; Bentham Science Publishers, **2022**.
- 314 Walter, M.; Stark, H. Histamine receptor subtypes: a century of rational drug design. *Frontiers in bioscience (Scholar edition)* **2012**, *4* (2), 461–488.
- 315 Wan, Q.; Okashah, N.; Inoue, A.; Nehmé, R.; Carpenter, B.; Tate, C. G.; Lambert, N. A. Mini G protein probes for active G protein-coupled receptors (GPCRs) in live cells. *The Journal of biological chemistry* **2018**, *293* (19), 7466–7473.
- 316 Wang, C.; Zhang, Y.; Yang, S.; Chen, W.; Xing, D. PROTACs for BRDs proteins in cancer therapy: a review. *Journal of Enzyme Inhibition and Medicinal Chemistry* **2022**, *37* (1), 1694–1703.
- 317 Wang, C.-J.; Hsu, S.-H.; Hung, W.-T.; Luo, C.-W. Establishment of a chimeric reporting system for the universal detection and high-throughput screening of G protein-coupled receptors. *Biosensors & bioelectronics* **2009**, *24* (7), 2298–2304.
- 318 Wang, D.; Yao, Y.; Wang, S.; Hou, Y.; Zhao, L.; Wang, H.; Chen, H.; Xu, J. Structural Insights into M1 Muscarinic Acetylcholine Receptor Signaling Bias between G $\alpha_q$  and  $\beta$ -Arrestin through BRET Assays and Molecular Docking. *International journal of molecular sciences* **2023**, *24* (8), 7356.

- 319 Webster, J. J.; Chang, J. C.; Manley, E. R.; Spivey, H. O.; Leach, F. R. Buffer effects on ATP analysis by firefly luciferase. *Analytical biochemistry* **1980**, *106* (1), 7–11.
- 320 Wegener, J.; Hakvoort, A.; Galla, H. J. Barrier function of porcine choroid plexus epithelial cells is modulated by cAMP-dependent pathways in vitro. *Brain Research* **2000a**, *853* (1), 115–124.
- 321 Wegener, J.; Keese, C. R.; Giaever, I. Electric cell-substrate impedance sensing (ECIS) as a noninvasive means to monitor the kinetics of cell spreading to artificial surfaces. *Experimental cell research* **2000b**, *259* (1), 158–166.
- 322 Wegener, J.; Zink, S.; Rösen, P.; Galla, H. Use of electrochemical impedance measurements to monitor beta-adrenergic stimulation of bovine aortic endothelial cells. *Pflügers Archiv : European journal of physiology* **1999**, *437* (6), 925–934.
- 323 Wellner-Kienitz, M. C.; Bender, K.; Meyer, T.; Pott, L. Coupling to G<sub>s</sub> and G<sub>q/11</sub> of histamine H<sub>2</sub> receptors heterologously expressed in adult rat atrial myocytes. *Biochimica et biophysica acta* **2003**, *1642* (1-2), 67–77.
- 324 Wernick, N. L. B.; Chinnapen, D. J.-F.; Cho, J. A.; Lencer, W. I. Cholera toxin: an intracellular journey into the cytosol by way of the endoplasmic reticulum. *Toxins* **2010**, *2* (3), 310–325.
- 325 White, E. H.; McCapra, F.; Field, G. F.; McElroy, W. D. The structure and synthesis of firefly luciferin. *J. Am. Chem. Soc.* **1961**, *83* (10), 2402–2403.
- 326 Wijtman, M.; Josimovic, I.; Vischer, H. F.; Leurs, R. Optical control of Class A G protein-coupled receptors with photoswitchable ligands. *Current Opinion in Pharmacology* **2022**, *63*, 102192.
- 327 Wilde, C.; Mitgau, J.; Suchý, T.; Schöneberg, T.; Liebscher, I. Translating the force-mechano-sensing GPCRs. *American journal of physiology. Cell physiology* **2022**, *322* (6), C1047-C1060.
- 328 Wilson, E. E.; Chambers, W.; Pelc, R.; Nothnagle, P.; Davidson, M. W. Stereomicroscopy in Neuroanatomy. *Neurohistology and Imaging Techniques*; Humana, New York, NY, **2020**; pp 245–274.
- 329 Wirth, U.; Erl, J.; Azzam, S.; Hoering, C.; Skiba, M.; Singh, R.; Hochmuth, K.; Keller, M.; Wegener, J.; Koenig, B. Monitoring the Reversibility of GPCR Signaling by Combining Photochromic Ligands with Label-free Impedance Analysis. *Angew. Chem.* **2023**, e202215547.
- 330 Wolf, P.; Rothermel, A.; Beck-Sickinger, A. G.; Robitzki, A. A. Microelectrode chip based real time monitoring of vital MCF-7 mamma carcinoma cells by impedance spectroscopy. *Biosensors and Bioelectronics* **2008**, *24* (2), 253–259.

- 331 Wong, T.-S.; Li, G.; Li, S.; Gao, W.; Chen, G.; Gan, S.; Zhang, M.; Li, H.; Wu, S.; Du, Y. G protein-coupled receptors in neurodegenerative diseases and psychiatric disorders. *Sig Transduct Target Ther* **2023**, *8* (1), 177.
- 332 Wouters, E.; Vasudevan, L.; Crans, R. A. J.; Saini, D. K.; Stove, C. P. Luminescence- and Fluorescence-Based Complementation Assays to Screen for GPCR Oligomerization: Current State of the Art. *International journal of molecular sciences* **2019**, *20* (12), 2958.
- 333 Wright, S. C.; Bouvier, M. Illuminating the complexity of GPCR pathway selectivity - advances in biosensor development. *Current opinion in structural biology* **2021**, *69*, 142–149.
- 334 Xu, J.; Koizumi, N.; Morimoto, Y. V.; Ozuru, R.; Masuzawa, T.; Nakamura, S. Light dependent synthesis of a nucleotide second messenger controls the motility of a spirochete bacterium. *Sci Rep* **2022a**, *12* (1), 6825.
- 335 Xu, W.; Dahlke, S. P.; Sung, M.; Samal, B.; Emery, A. C.; Elkahlon, A.; Eiden, L. E. ERK-dependent induction of the immediate-early gene *Egr1* and the late gene *Gpr50* contribute to two distinct phases of PACAP Gs-GPCR signaling for neurogenesis. *Journal of Neuroendocrinology* **2022b**, *34* (9), e13182.
- 336 Yan, J.; Jin, T. Signaling network from GPCR to the actin cytoskeleton during chemotaxis. *Bioarchitecture* **2012**, *2* (1), 15–18.
- 337 Zernike, F. Phase contrast, a new method for the microscopic observation of transparent objects. *Physica* **1942**, *9* (7), 686–698.
- 338 Zernike, F. How I discovered phase contrast. *Science (New York, N. Y.)* **1955**, *121* (3141), 345–349.
- 339 Zhang, R.; Xie, X. Tools for GPCR drug discovery. *Acta Pharmacol Sin* **2012**, *33* (3), 372–384.
- 340 Zhao, P.; Furness, S. G. B. The nature of efficacy at G protein-coupled receptors. *Biochemical pharmacology* **2019**, *170*, 113647.
- 341 Zhou, Y.; Meng, J.; Xu, C.; Liu, J. Multiple GPCR Functional Assays Based on Resonance Energy Transfer Sensors. *Frontiers in cell and developmental biology* **2021**, *9*, 611443.
- 342 Zhu, W.; Taday, N.; Flatt, P. R.; Irwin, N. Pancreatic polypeptide revisited: Potential therapeutic effects in obesity-diabetes. *Peptides* **2023**, *160*, 170923.
- 343 Ziemek, R.; Schneider, E.; Kraus, A.; Cabrele, C.; Beck-Sickinger, A. G.; Bernhardt, G.; Buschauer, A. Determination of affinity and activity of ligands at the human neuropeptide Y Y4 receptor by flow cytometry and aequorin luminescence. *Journal of receptor and signal transduction research* **2007**, *27* (4), 217–233.

- 344 Zinkl, M.; Wegener, J. Using animal cells as sensors for xenobiotics: monitoring phenotypic changes by multimodal impedance assays. *Current Opinion in Environmental Science & Health* **2019**, *10*, 30–37.
- 345 Zor, U. Role of cytoskeletal organization in the regulation of adenylate cyclase-cyclic adenosine monophosphate by hormones. *Endocrine reviews* **1983**, *4* (1), 1–21.

# Appendix

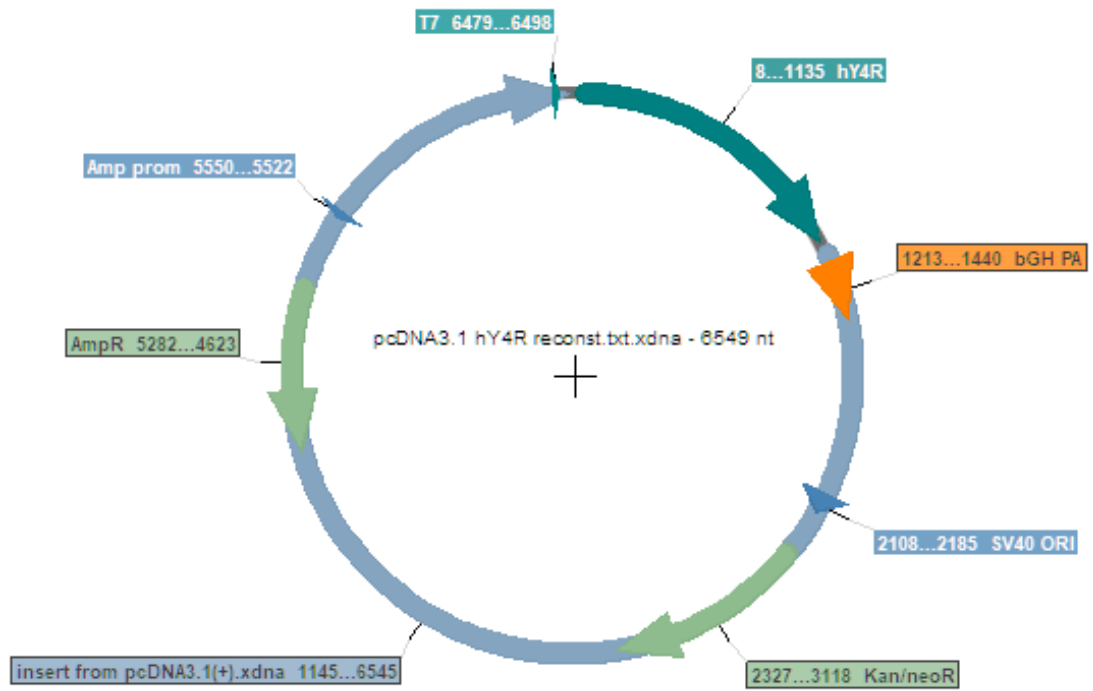
## 9.1 Supplementary Figures

```
GCTAGCGTTTAAACTTAAGCTTGGTACCGAGCTCGGATCCACCATGAACACTTCAGCCCCACCTGCTGTCAGCCCCAACATC
ACCGTCCTGGCACCAGGAAAGGGTCCCTGGCAAGTGGCCTTCATTGGGATCACCACGGGCCTCCTGTCGCTAGCCACAGT
GACAGGCAACCTGCTGGTACTCATCTCTTTCAAGGTCAACACGGAGCTCAAGACAGTCAATAACTACTTCTGCTGAGCCTG
GCCTGTGCTGACCTCATCATCGGTACCTTCTCCATGAACCTCTATACCACGTACCTGCTCATGGGCCACTGGGCTCTGGGC
ACGCTGGCTTGTGACCTCTGGCTGGCCCTGGACTATGTGGCCAGCAATGCCTCCGTCATGAATCTGCTGCTCATCAGCTTT
GACCGTACTTCTCCGTGACTCGGCCCTGAGTACCCTGCAAGCGCACACCCCGCCGGGACGCTCTGATGATCGGCCT
GGCCTGGCTGGTTTCTTTGTGCTCTGGGCCCCAGCCATCCTCTTCTGGCAGTACCTGGTAGGGGAGCGGACAGTGTAG
CTGGGCAGTGCTACATCCAGTTCTCTCCAGCCCATCATCACCTTTGGCACAGCCATGGCTGCCTTCTACCTCCCTGTCAC
AGTCATGTGCACGCTCTACTGGCGCATCTACCGGGAGACAGAGAACCAGACACGGGAGCTGGCAGCCCTTCAGGGCTCCG
AGACGCCAGGCAAAGGGGTGGCAGCAGCAGCAGCTCAGAGAGGTCTCAGCCAGGGGCTGAGGGCTCACCAGAGACTCC
TCCAGGCCGCTGCTGTCGCTGCTGCCGGGCCCCAGGCTGCTGCAGGCCTACAGCTGGAAGGAAGAAGAGGAAGAGGAC
GAAGGCTCCATGGAGTCCCTCACATCCTCAGAGGGAGAGGAGCTGGCTCCGAAGTGGTATCAAGATGCCAATGGTGA
CCCCGAGGCACAGGCCCCCAAGCAGCCCCACGGAGCTCCCCAAATACAGTCAAGAGGCCGACTAAGAAAGGGCGT
GATCGAGCTGGCAAGGGCCAGAAGCCCGTGGAAAGGAGCAGCTGGCCAAGCGGAAGACCTTCTCGTGGTCAAGGAGA
AGAAGGGCGCTCGGACCCTGAGTGCCATCCTCCTGGCCTTATCCTCACCTGGACCCGTACAACATCATGGTGTGGTGT
CCACCTTCTGCAAGGACTGTGTTCCCGAGACCCTGTGGGAGCTGGGCTACTGGCTGTGCTACGTC AACAGCACCATCAACC
CCATGTGCTACGCACTCTGCAACAAAGCCTTCCGGGACACCTTTCGCTGCTGCTGCTTTGCCGCTGGGACAAGAGACGCT
GGCGCAAGATCCCAAGCGCCTGGCTCCGTGCACCGCACTCCCTCCCGCAATGCTGACTCGAGTCTAGAGGGCCCGTT
TAAAC
```

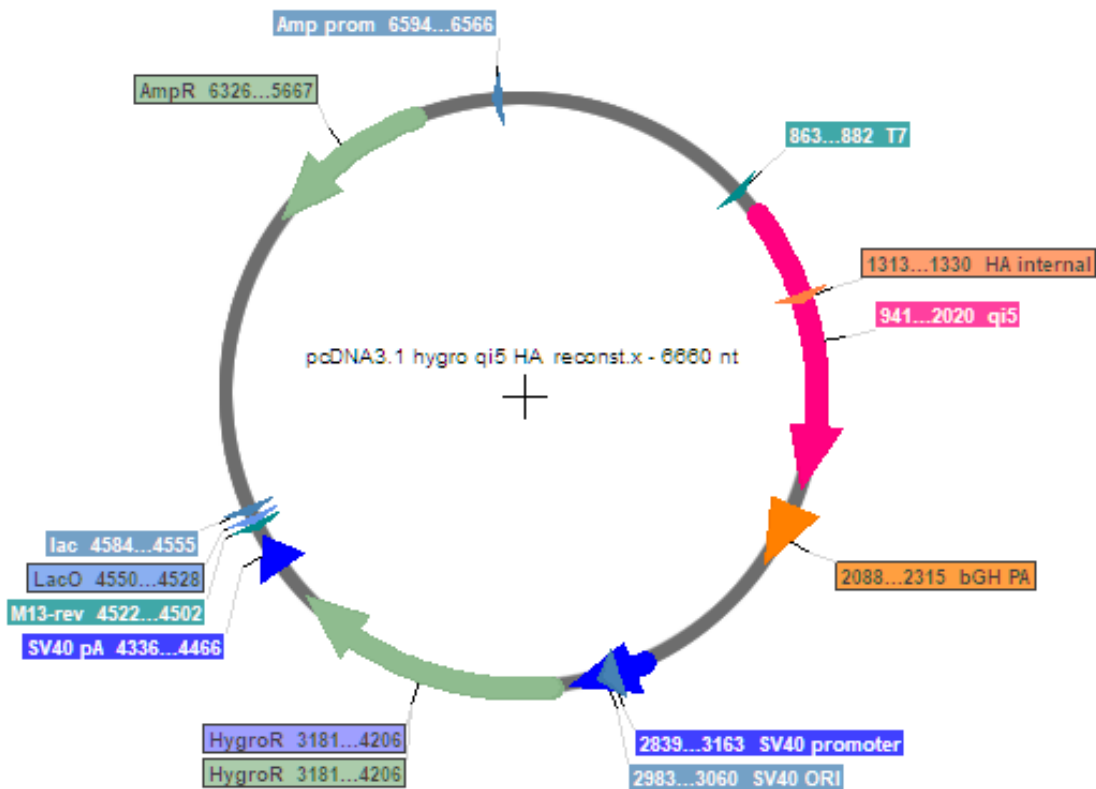
Appendix 1. DNA sequence encoding for the M1R used in the pcDNA3.1/M1R vector for the generation of CHO M1R cells (cdna.org; August 10, 2024).

```
GCTAGCGTTTAAACTTAAGCTTGGTACCGAGCTCGGATCCACCATGGAAGGGGATTCTTACCACAATGCAACCACCGTCAAT
GGCACCCACAGTAAATCACCAGCCTTTGGAACGCCACAGGTTGTGGGAAGTCAACACATTGCAGCTGTGACTGCTGTGGTA
AGCCTGATCACCATTGTGGGCAATGTCTTGGTCATGATCTCCTCAAAGTCAACAGCCAGCTCAAGACAGTAAACAACTATTA
CCTGCTCAGCTTAGCCTGTGCAGATCTCATCATTGGAATCTTCTCCATGAACCTCTACACCACCTACATCCTCATGGGACGC
TGGGCTCTCGGGAGTCTGGCTTGTGACCTTTGGCTTGCACTGGACTACGTGGCCAGCAACGCTTCTGTGATGAACCTTCTG
GTGATCAGTTTTGACCGTTACTTTTCCATCACAAGACCCTTGACATATCGGGCCAAGCGTACTCCGAAAAGGGCTGGCATCA
TGATTGGCTTGGCCTGGCTGATCTCCTTATCCTCTGGGCCCCAGCAATCCTCTGCTGGCAGTACTTGGTTGGGAAGCGGA
CAGTCCACTGGATGAGTGCCAGATCCAGTTTCTCTGAGGCCACCATCACTTTTGGCACTGCCATTGCTGCCTTCTACAT
CCCTGTTTCTGTGATGACCATCCTCTACTGTGCAATCTACCGGGAACAGAGAAGCGAACCAAGGACCTGGCTGACCTCCA
GGGTTCTGACTCTGTGACCAAAGCTGAGAAGAGAAAGCCAGCTCATAGGGCTCTGTTGAGATCCTGCTTGGCCTGTCTCG
ACCCACCTGGCCAGCGGGAAAGGAACCAGGCCTCCTGGTCATCCTCCCGCAGGAGCACCTCCACCACTGGGAAGCCAT
CCCAAGCCACTGGCCCAAGCGCAATTGGGCCAAAGCTGAGCAGCTCACCACCTGTAGCAGCTACCCTTCTCAGAGGAT
GAGGACAAGCCCGCCACTGACCCTGTCTCCAAGTGGTCTACAAGAGTCAAGGTAAGGAAAGCCAGGGGAAGAATTCAG
TGCTGAAGAGACTGAGGAACTTTTGTGAAAGCTGAAACTGAAAAAGTACTATGACACCCCAAACCTTCTGTCTCCA
GCAGCTGCTCATAGACCCAAGAGTCAGAAATGTGTGGCCTATAAGTTCCGATTGGTGGTAAAAGCTGACGGGAACCAGGAG
ACCAACAATGGCTGTGACAAGGTGAAAATCATGCCCTGCCCTTCCAGTGGCCAAGGAACCTTCAACGAAAGGCCAAT
CCCAACCCAGCCATCAATGACCAAACGAAAGAGAGTGGTCTAGTCAAAGAGAGGAAAGCAGCCAGACACTGAGTGCC
ATTCTCCTGGCCTTATCATCATGACCCCGTATAACATCATGGTCTGTTTCTACCTTCTGTGACAAGTGTGTCCAGT
CACCTGTGGCACTTGGGCTATTGGTTGTGCTATGTCAATAGCACTGTCAACCCCATCTGCTATGCCCTGTGCAACAGAACC
TTCAGGAAGACCTTAAAGATGCTGCTTCTGCCGATGAAAAAGAAAAAGTGGAAAGAGAAGTTGACTGGCAGGGGAACA
GCAAGTACCCTGACTCGAGTCTAGAGGGCCCGTTTAAAC
```

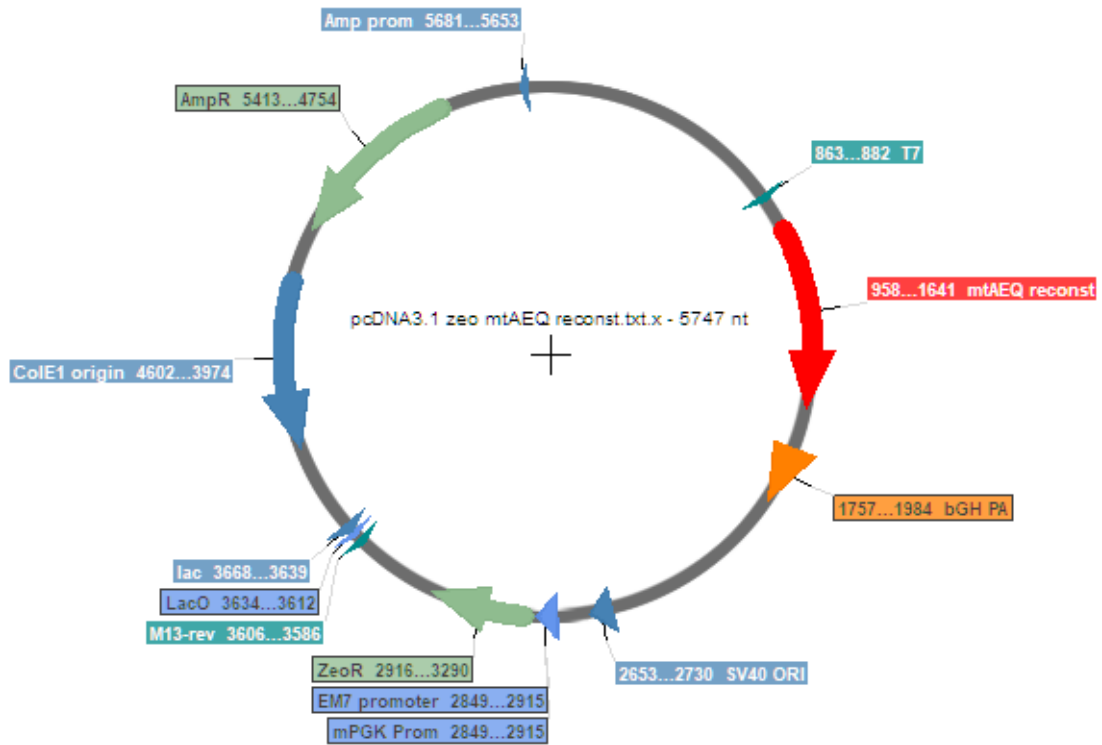
Appendix 2. DNA sequence encoding for the M5R used in the pcDNA3.1/M5R vector for the generation of CHO M5R cells (cdna.org; August 10, 2024).



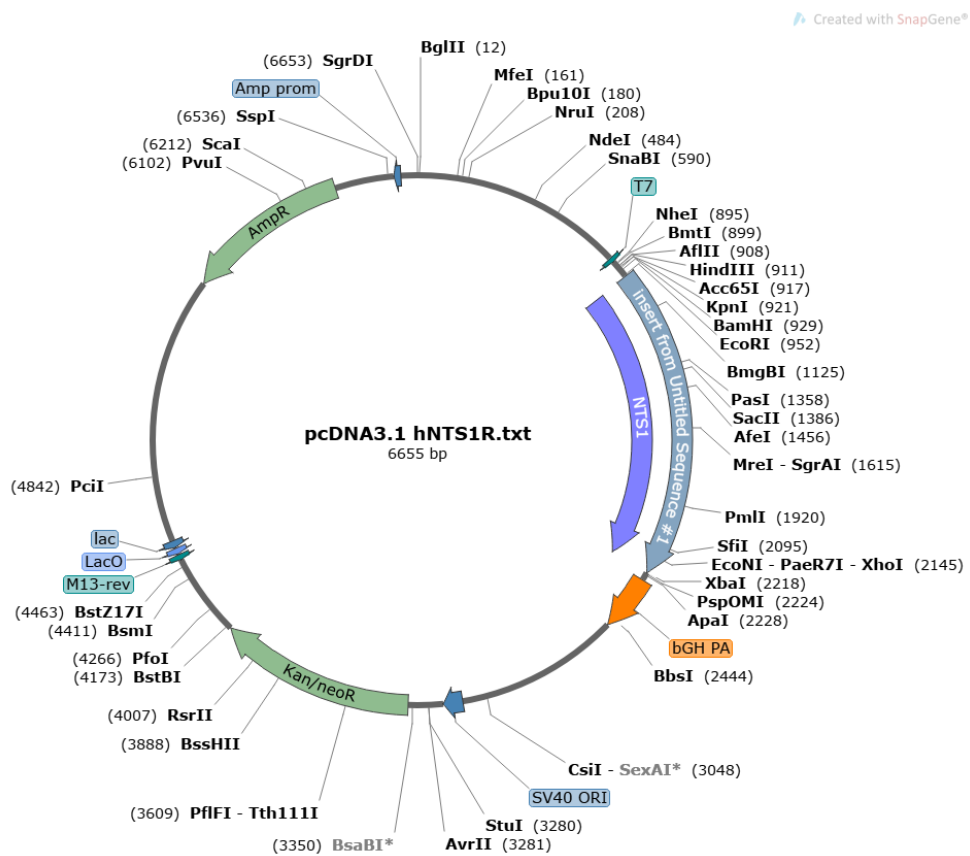
Appendix 3. Vector map of the pcDNA3.1/Y4R plasmid encoding for the neuropeptide Y4 receptor (Y4R) used in CHO NPY cells. The vector map was created with the Snapgene Viewer.



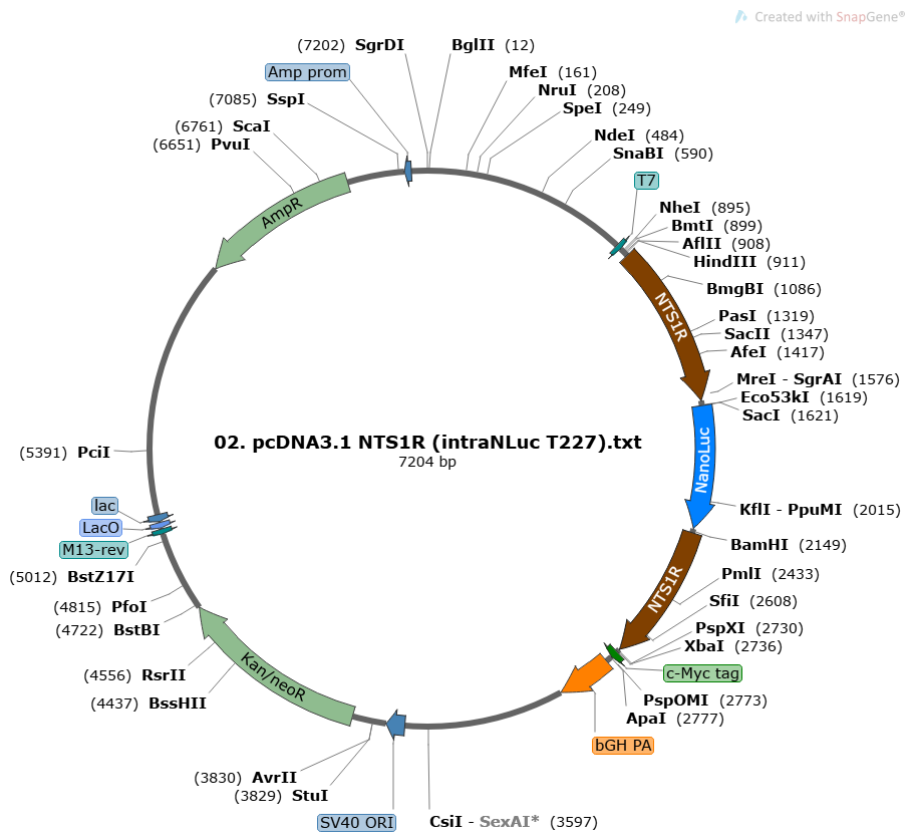
Appendix 4. Vector map of the pcDNA3.1/hygro-G<sub>qi5</sub> plasmid encoding for the chimeric G protein G<sub>qi5</sub> used in CHO NPY cells. The vector map was created with the Snapgene Viewer.



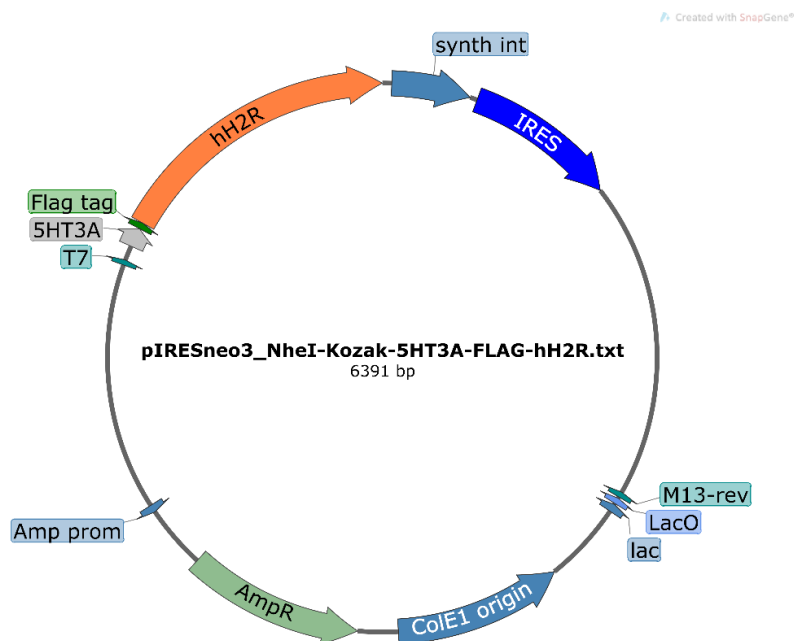
Appendix 5. Vector map of the *pcDNA3.1/zeo-mtAEQ* plasmid encoding for the mitochondrially targeted apoaequorin used in CHO NPY cells. The vector map was created with the Snapgene Viewer.



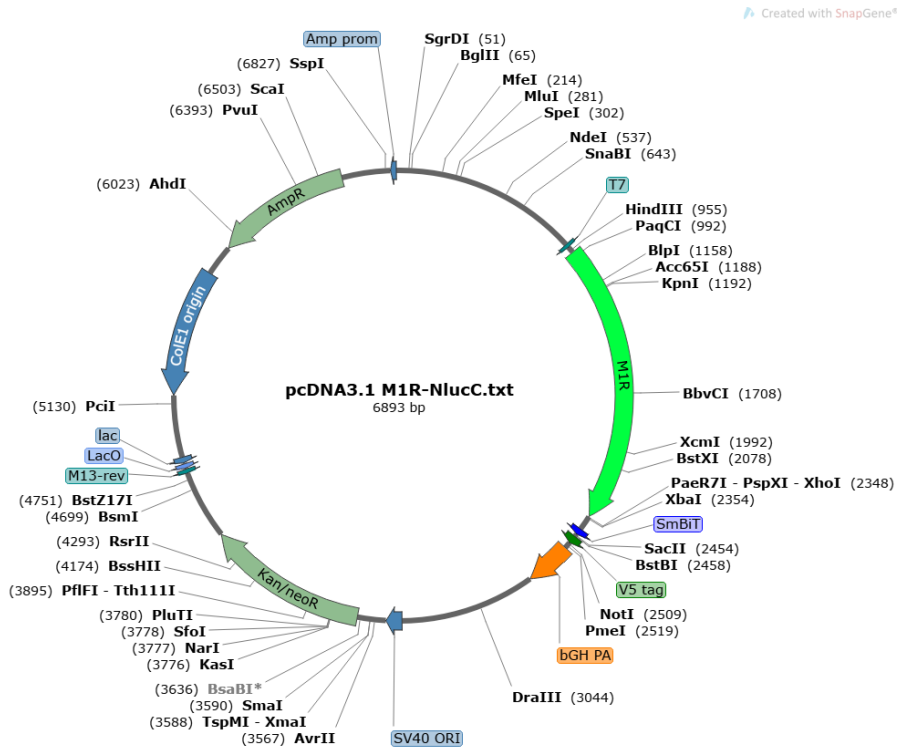
Appendix 6. Vector map of the *pcDNA3.1/NTS1R* plasmid encoding for the neurotensin 1 receptor (NTS1R) used in CHO NTS1R cells. The vector map was created with the Snapgene Viewer.



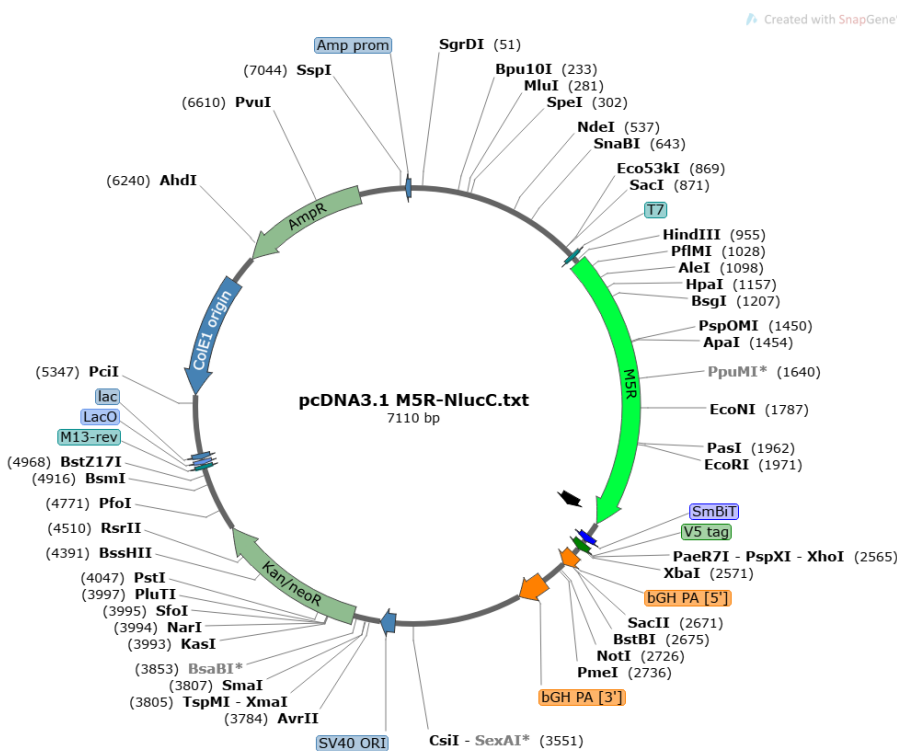
Appendix 7. Vector map of the pcDNA3.1/NTS1R (intraNLucT227) plasmid encoding for the NanoLuc-labeled neurotensin 1 receptor (NTS1R). NanoLuc was inserted at position 227 (threonine). The vector was used to create HEK NTS1R intraNLucT227 cells. The vector map was created with the Snapgene Viewer.



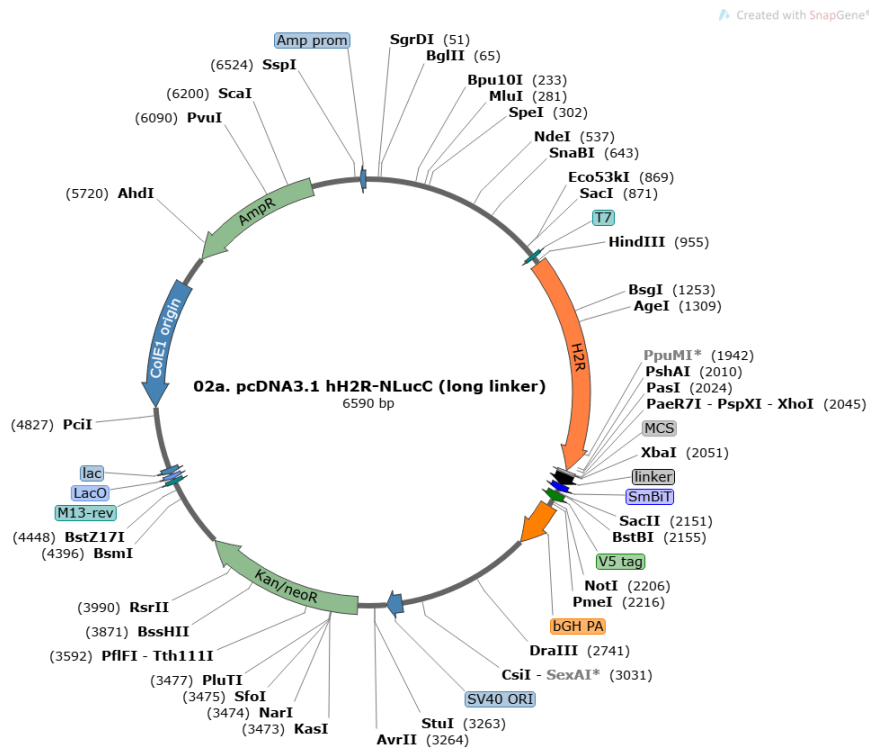
Appendix 8. Vector map of the original pIRESneo3/H2R vector encoding for the histamine 2 receptor (H2R), which was used in HEK H2R cells and was kindly provided by Dr. Ulla Seibel-Ehlert (University of Regensburg). This vector was modified in chapter 3.2.1. The vector map was created with the Snapgene Viewer.



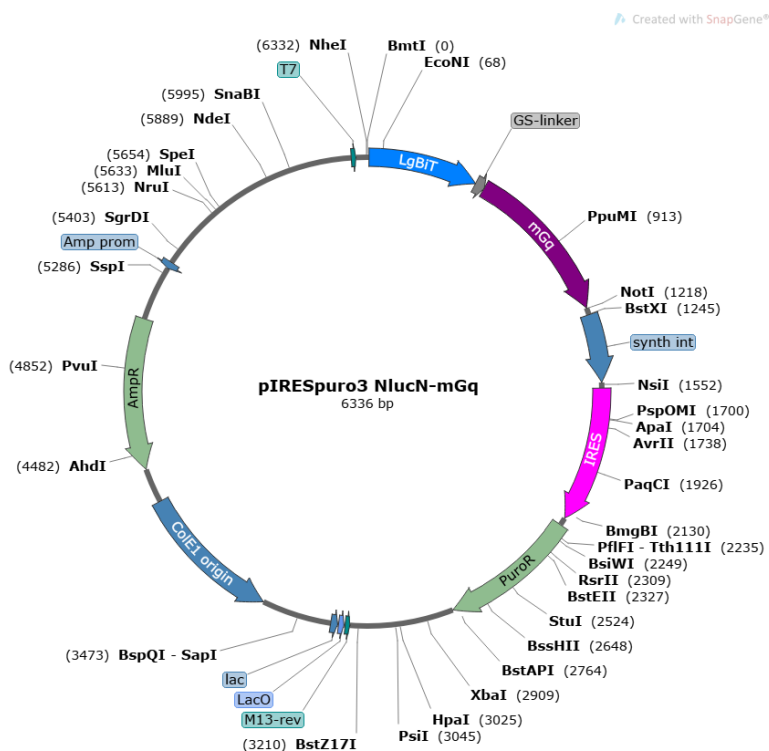
Appendix 9. Vector map of the pcDNA3.1/SmBiT-M1R plasmid encoding for the SmBiT-labeled muscarinic acetylcholine 1 receptor (M1R) used in HEK M1R/mG<sub>q</sub> cells. The vector map was created with the Snapgene Viewer.



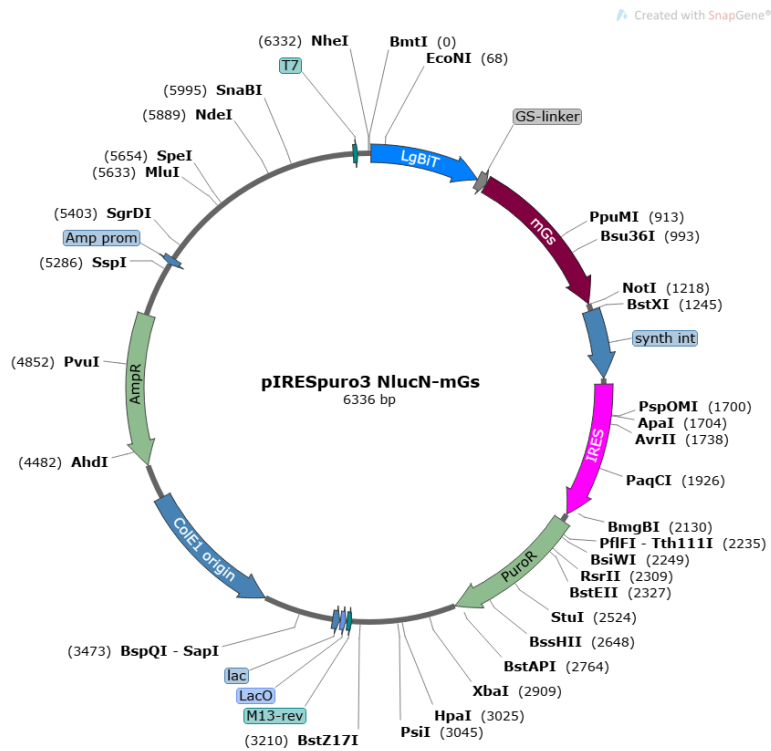
Appendix 10. Vector map of the pcDNA3.1/SmBiT-M5R plasmid encoding for the SmBiT-labeled muscarinic acetylcholine 5 receptor (M5R) used in HEK M5R/mG<sub>q</sub> cells. The vector map was created with the Snapgene Viewer.



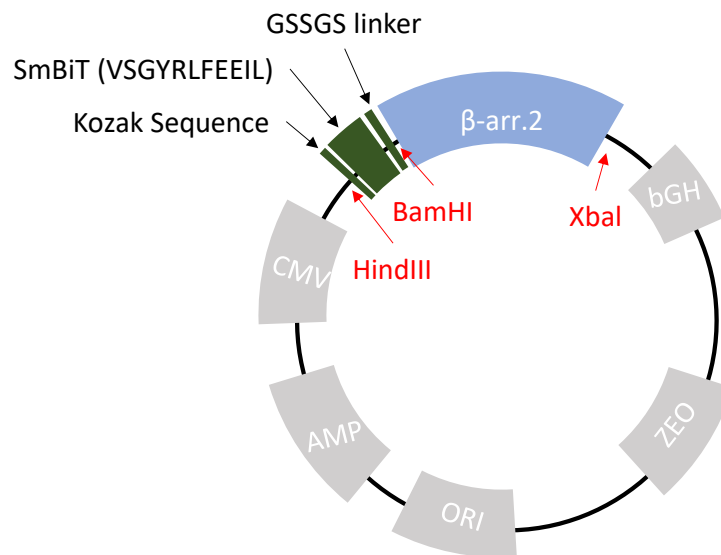
Appendix 11. Vector map of the pcDNA3.1/SmBiT-H2R plasmid encoding for the SmBiT-labeled histamine 2 receptor (H2R) used in HEK H2R/mG<sub>s</sub> cells. The vector map was created with the Snapgene Viewer.



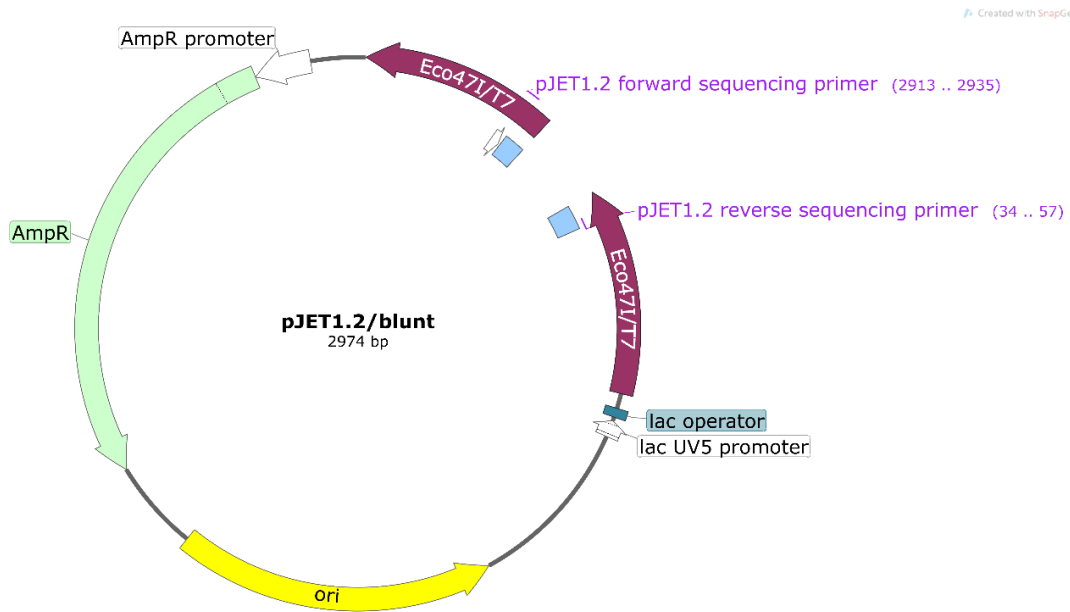
Appendix 12. Vector map of the pIRESpuro3/LgBiT-mG<sub>q</sub> plasmid encoding for the LgBiT-labeled miniG<sub>q</sub> protein used in HEK M1R/mG<sub>q</sub> and HEK M5R/mG<sub>q</sub> cells. The vector map was created with the Snapgene Viewer.



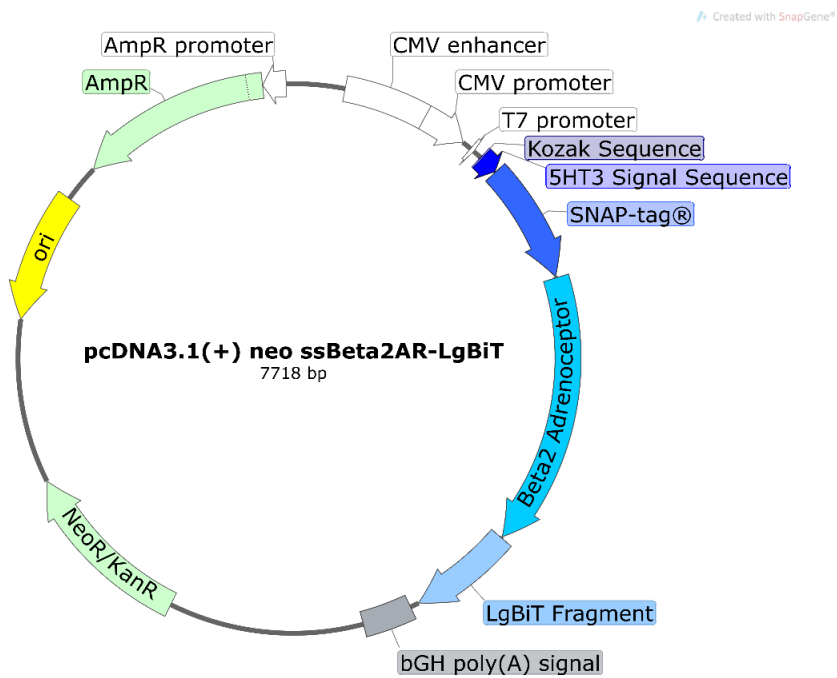
Appendix 13. Vector map of the pIRESpuro3/LgBiT-mG<sub>s</sub> plasmid encoding for the LgBiT-labeled miniG<sub>s</sub> protein used in HEK H2R/mG<sub>s</sub> cells. The vector map was created with the Snapgene Viewer.



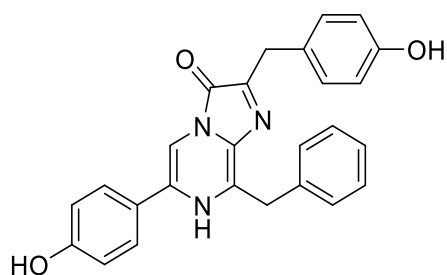
Appendix 14. Vector map of the pcDNA3.1/SmBiT- $\beta$ -arrestin2 plasmid encoding for SmBiT-labeled  $\beta$ -arrestin2 used in HEK293T SmBiT  $\beta$ -Arrestin2 cells. For more details please refer to (Dijon, 2022).



Appendix 15. Vector map of the pJET1.2/blunt vector (see **chapter 3.2.1.2**). The vector map was created with the Snapgene Viewer.

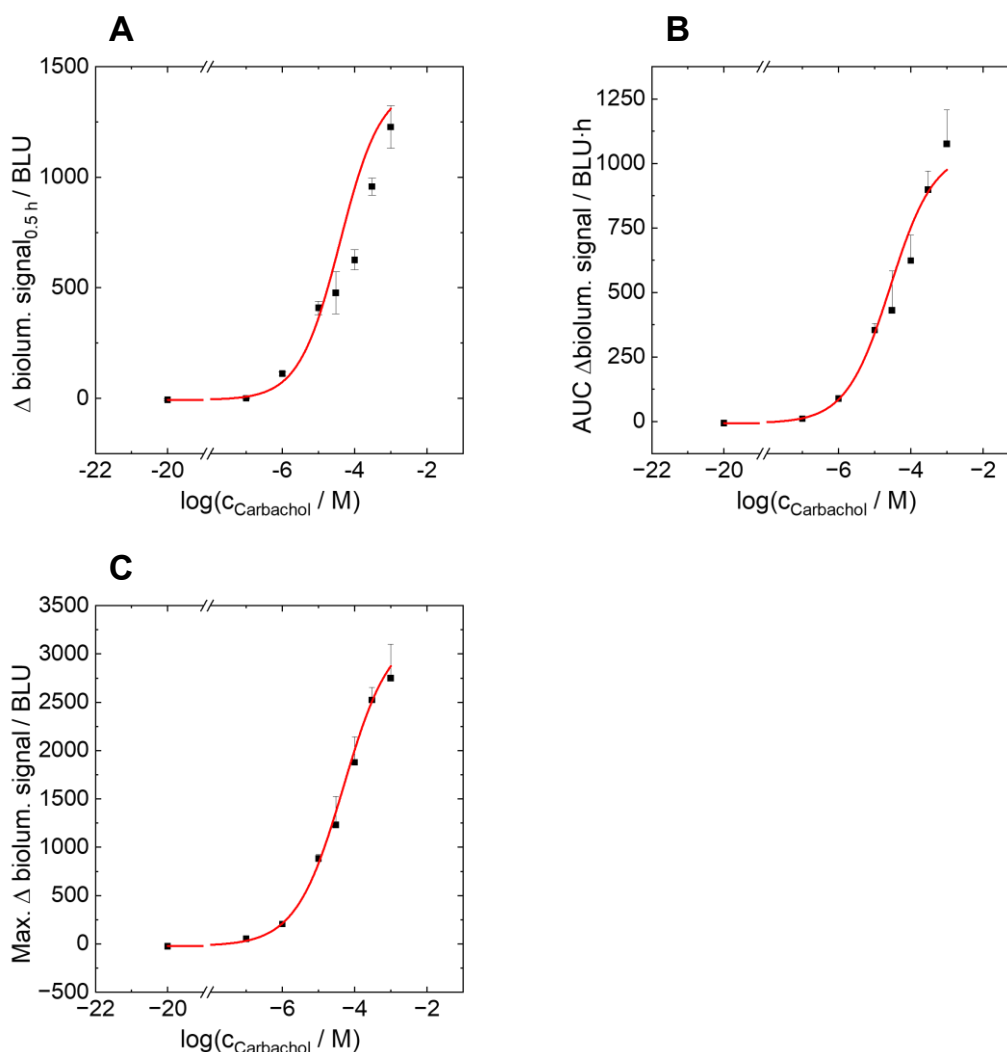


Appendix 16. Vector map of the pcDNA3.2/SNAP- $\beta$ 2AR-LgBiT encoding for a LgBiT-labeled  $\beta$ 2-adrenoceptor ( $\beta$ 2AR, see **chapter 3.2.1.4**) used in HEK  $\beta$ 2AR/ $\beta$ -Arr.2 cells. The vector map was created with the Snapgene Viewer.

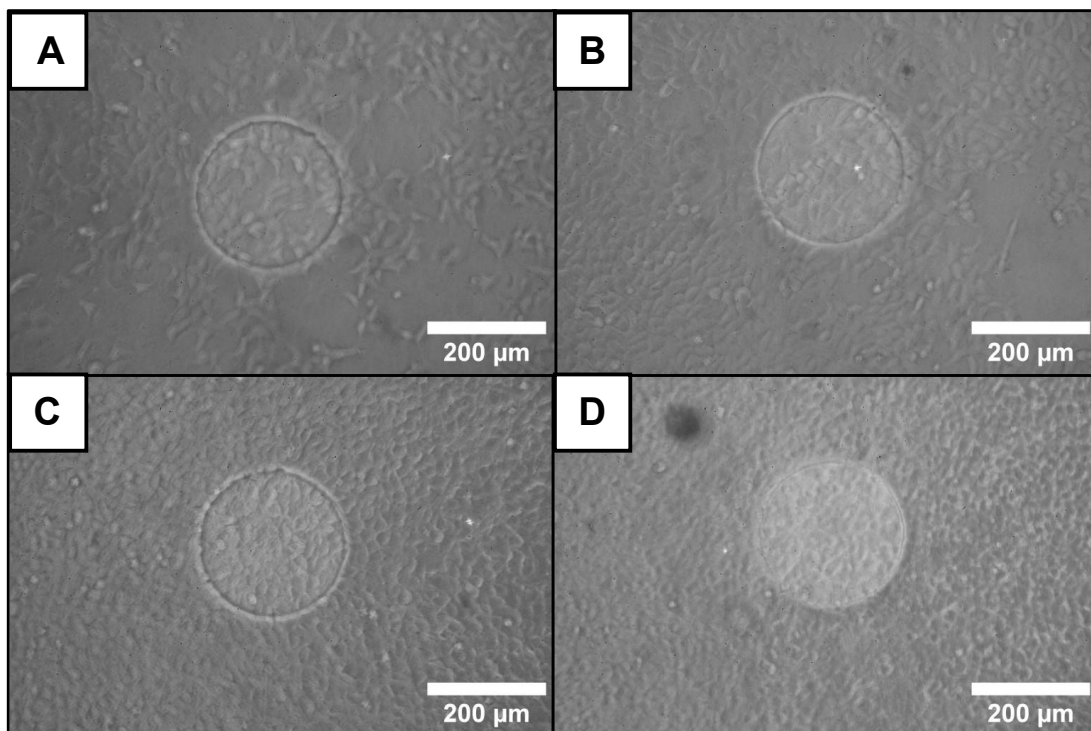


Coelenterazine

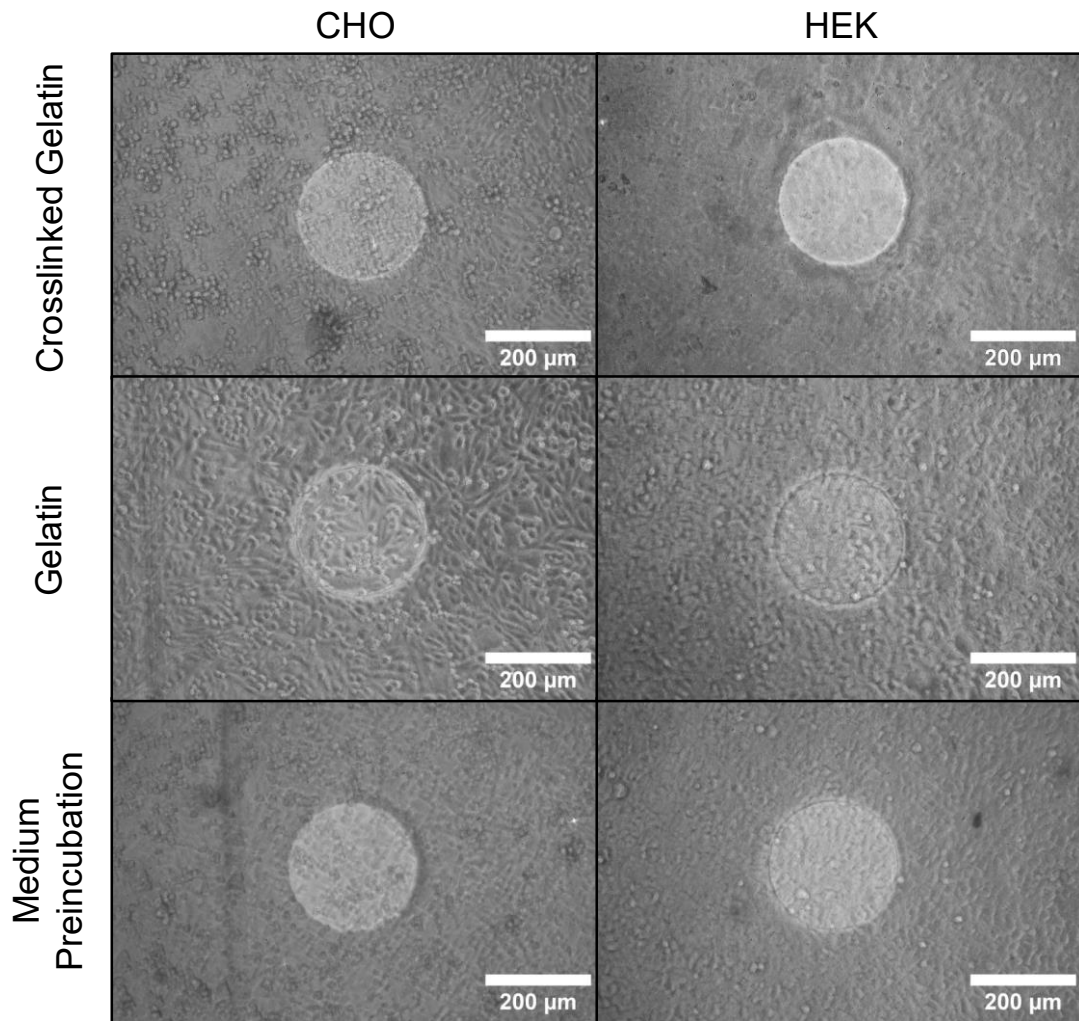
Appendix 17. Structure of coelenterazine. Coelenterazine *h* is derived from this molecule. This structure was created with ChemDraw (Perkin Elmer).



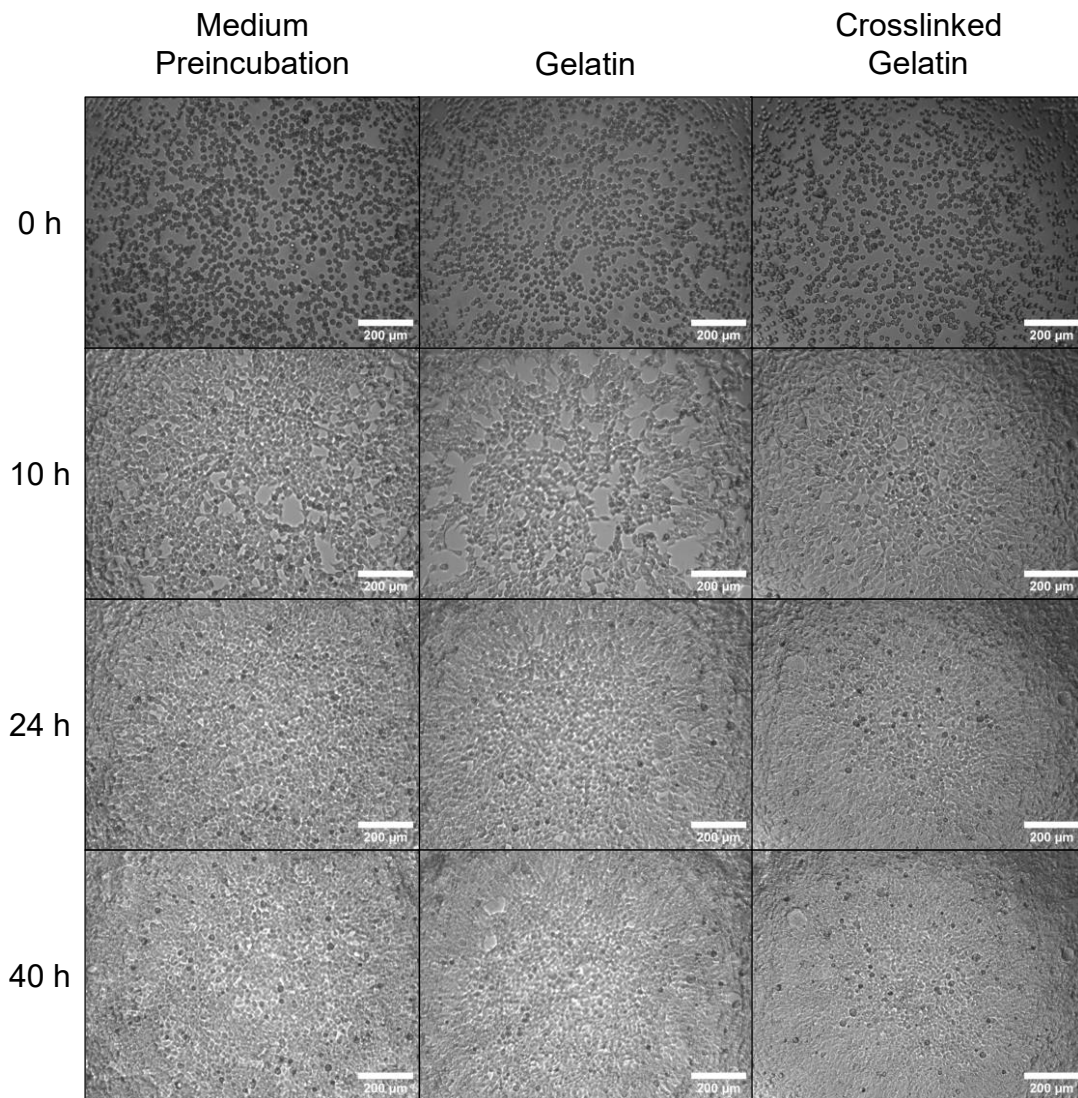
Appendix 18. Comparison of bioluminescence concentration-response analysis of **HEK M1R/mG<sub>q</sub> cells** after preincubation with 1  $\mu$ M **coelenterazine *h*** and stimulation with different concentrations of **carbachol** (cf. **chapter 4.3**, miniG protein recruitment). **A**: Analysis of time point 0.5 h after stimulation. **B**: Area under the curve (AUC) analysis for a time interval of 0-0.75 h. **C**: Analysis of bioluminescence maximum. The fits reveal similar pEC<sub>50</sub> values of  $4.4 \pm 0.3$  (A),  $4.6 \pm 0.1$  (B) and  $4.3 \pm 0.2$  (C).



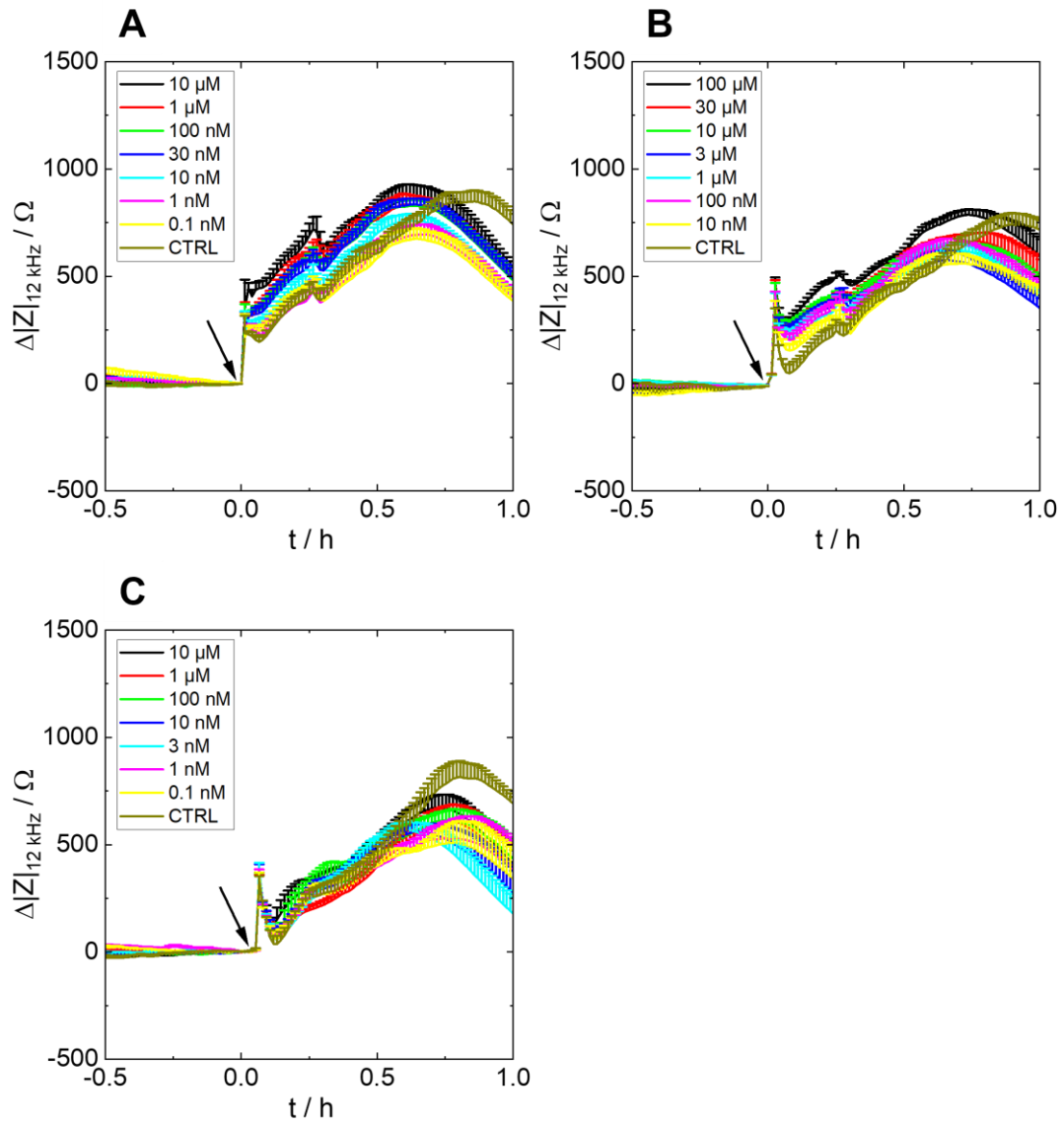
Appendix 19. Phase contrast micrographs of **HEK M1R/mG<sub>q</sub>** cells that were seeded with densities of **A:  $5 \cdot 10^4$  c/cm<sup>2</sup>**, **B:  $10^5$  c/cm<sup>2</sup>**, **C:  $2 \cdot 10^5$  c/cm<sup>2</sup>** and **D:  $3 \cdot 10^5$  c/cm<sup>2</sup>** on 8W1E arrays coated with crosslinked gelatin. The pictures were taken 2 d after cell seeding. Shown is the working electrode in the center of the well.



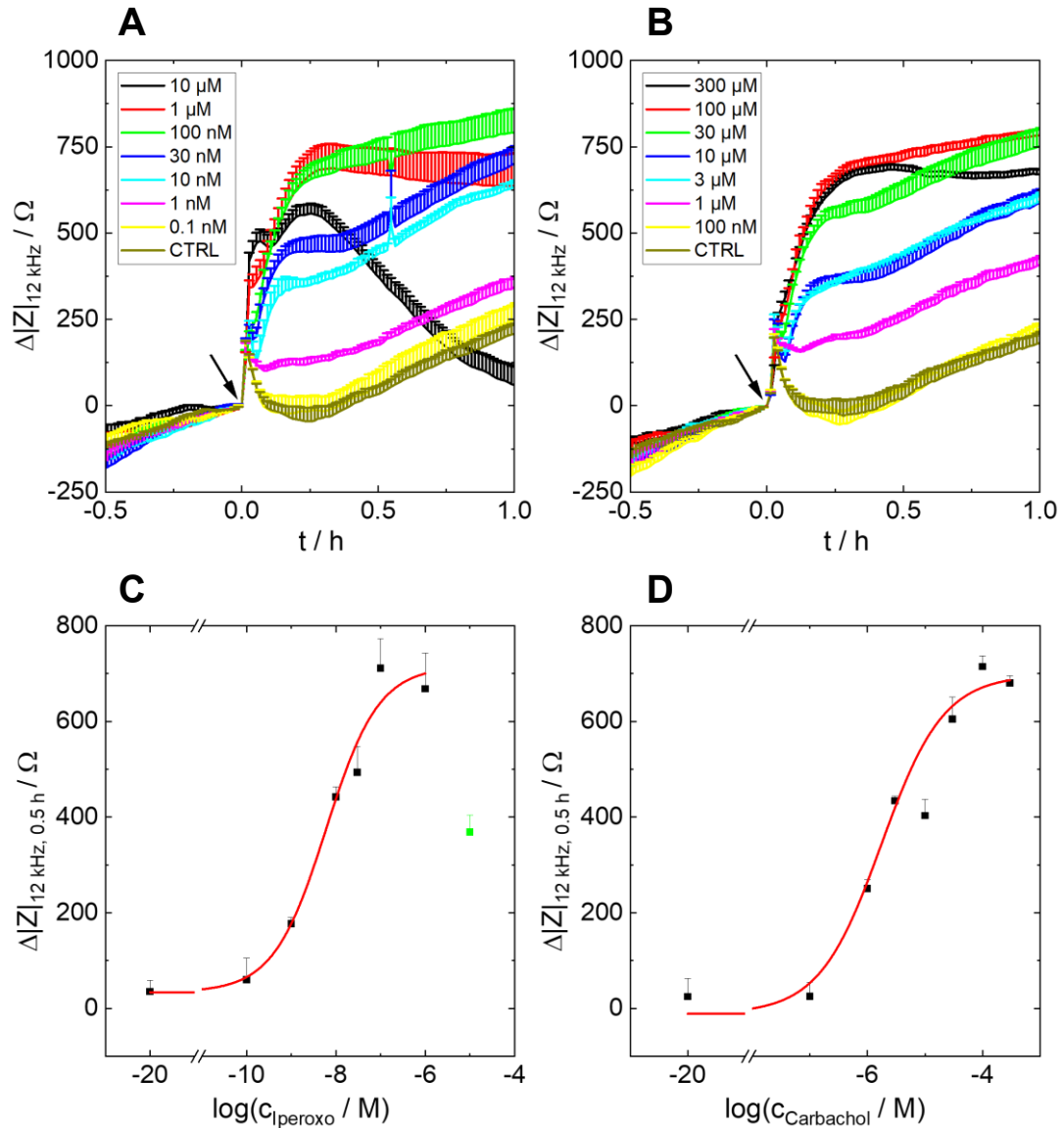
Appendix 20. Phase contrast micrographs of **CHO NTS1R (left) and HEK NTS1R iL (right)** cells that were seeded with densities of  $10^5$  c/cm<sup>2</sup> (CHO) or  $3 \cdot 10^5$  c/cm<sup>2</sup> (HEK) on 8W1E arrays, which were coated with **crosslinked gelatin (top row), gelatin (middle) or preincubated with serum-containing medium (bottom row)**. The pictures were taken 2 d after seeding. Shown is the working electrode in the center of the well.



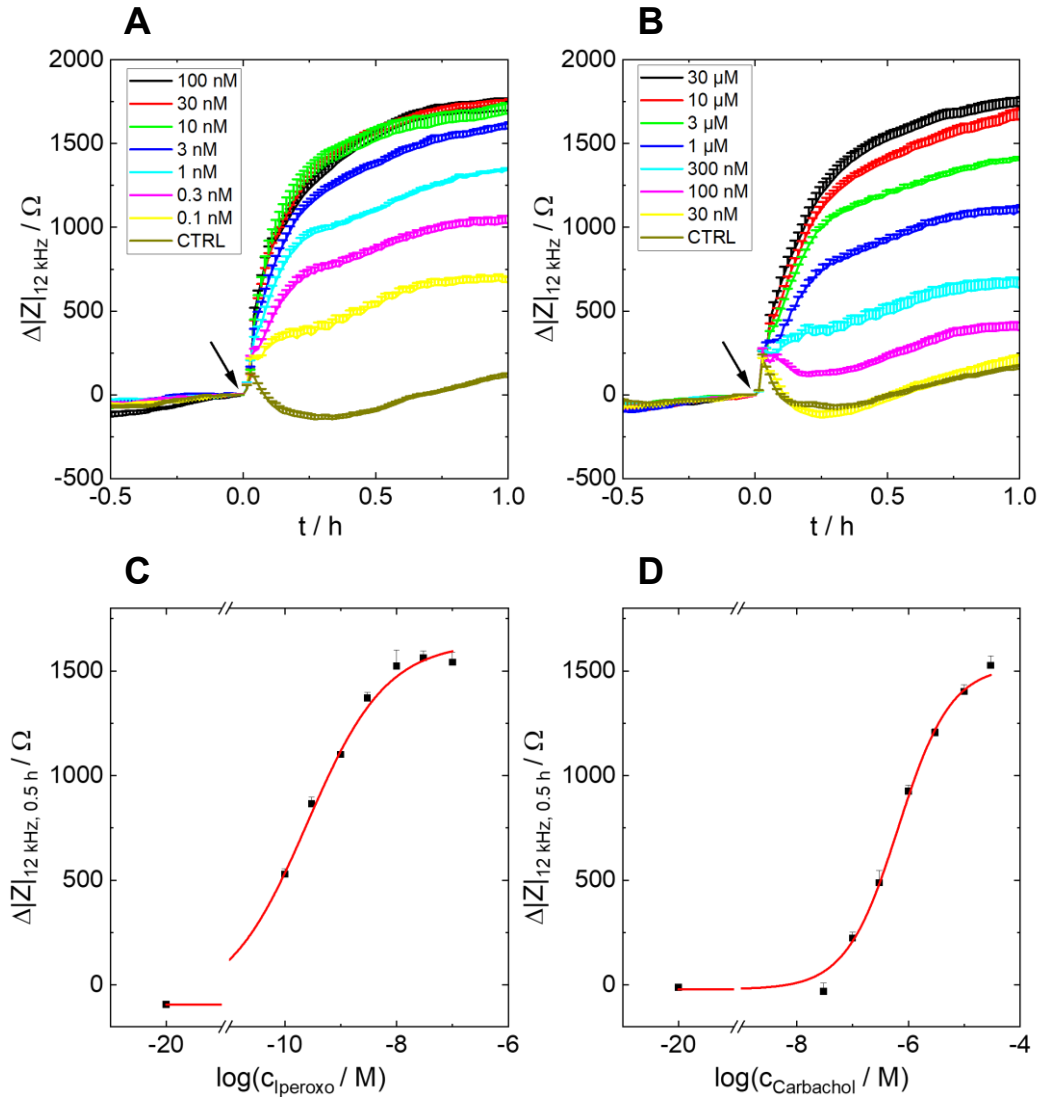
Appendix 21. Microscopic study of **HEK M1R/mG<sub>q</sub>** cells with the zenCELL owl device (innoME). The cells were seeded with a density of  $3 \cdot 10^5$  c/cm<sup>2</sup> on a 24-well plate **preincubated with serum-containing medium (left column) or coated with gelatin (middle column) or crosslinked gelatin (right column)**. Adhesion was monitored by taking pictures 0 h, 10 h, 24 h and 40 h after seeding. Scale bar: 200 μm.



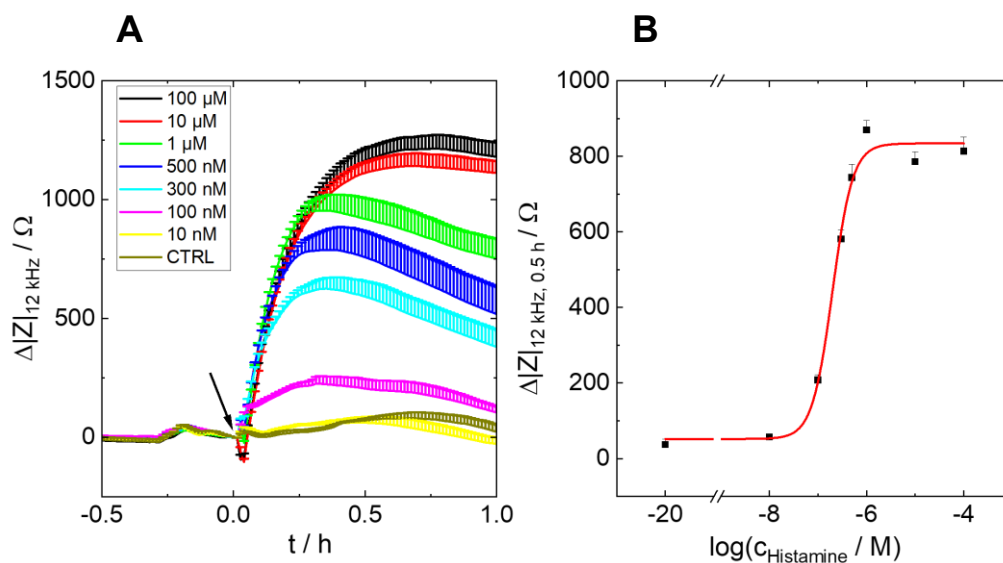
Appendix 22. Impedance change over time of **HEK wt** cells. The cells were cultivated on a 96W1E+ electrode array coated with gelatin. After a baseline measurement, at  $t = 0$  h different **iperoxo (A)**, **carbachol (B)** and **histamine (C)** concentrations were added. A: black 10  $\mu\text{M}$ , red 1  $\mu\text{M}$ , green 100 nM, blue 30 nM, cyan 10 nM, pink 1 nM, yellow 0.1 nM, brown CTRL. B: black 100  $\mu\text{M}$ , red 30  $\mu\text{M}$ , green 10  $\mu\text{M}$ , blue 3  $\mu\text{M}$ , cyan 1  $\mu\text{M}$ , pink 100 nM, yellow 10 nM, brown CTRL. C: black 10  $\mu\text{M}$ , red 1  $\mu\text{M}$ , green 100 nM, blue 10 nM, cyan 3 nM, pink 1 nM, yellow 0.1 nM, brown CTRL. Baseline from A to C:  $(5530 \pm 10) \Omega$ ,  $(5569 \pm 8) \Omega$ ,  $(5227 \pm 9) \Omega$ . Mean + SE,  $N = 5-6$ , single experiment. CTRL = vehicle control. Temperature: 37°C.



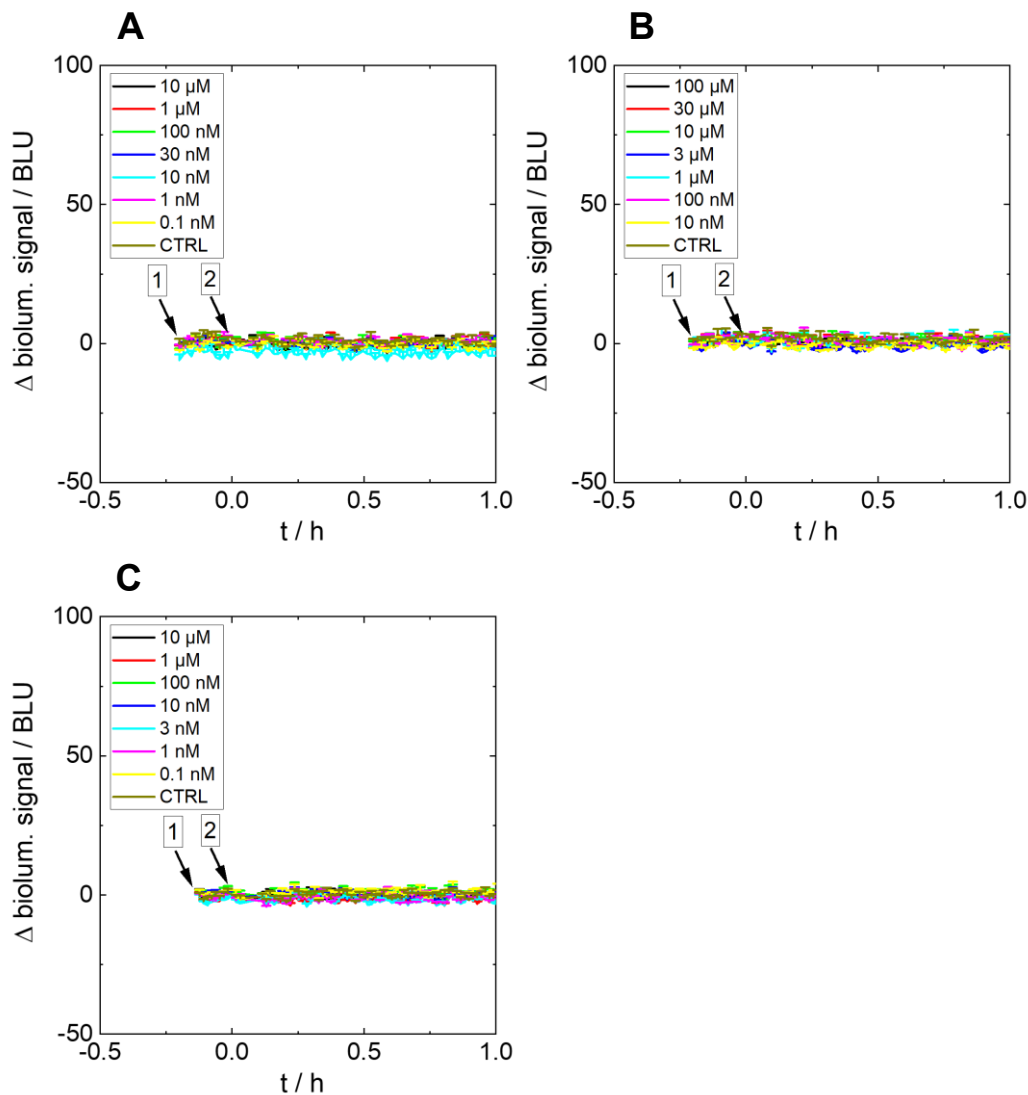
Appendix 23. Impedance change over time of **CHO M1R** cells at a frequency of 12 kHz. The cells were cultivated on a 96W1E+ electrode array that was coated with gelatin. At  $t = 0$  h, the cells were stimulated with different concentrations of **iperoxo (A) or carbachol (B)**. A: black 10  $\mu\text{M}$ , red 1  $\mu\text{M}$ , green 100 nM, blue 30 nM, cyan 10 nM, pink 1 nM, yellow 0.1 nM, brown CTRL. B: black 300  $\mu\text{M}$ , red 100  $\mu\text{M}$ , green 30  $\mu\text{M}$ , blue 10  $\mu\text{M}$ , cyan 3  $\mu\text{M}$ , pink 1  $\mu\text{M}$ , yellow 100 nM, brown CTRL. The concentration-response curves for **iperoxo (C) and carbachol (D)** were obtained by plotting the data at  $t = 0.5$  h (black squares) against the logarithmic ligand concentration. A four-parametric dose-response fit (red solid line, **equation 15**) reveals  $p\text{EC}_{50}$  values of  $8.2 \pm 0.2$  for iperoxo and  $5.8 \pm 0.2$  for carbachol. The  $E_{\text{max}}$  lie at  $(720 \pm 70) \Omega$  for iperoxo and  $(700 \pm 50) \Omega$  for carbachol. The highest iperoxo concentration (green) was excluded from fitting. Baseline A and B:  $(5159 \pm 7) \Omega$  and  $(5066 \pm 9) \Omega$ . Mean + SE,  $N = 6$ , single experiment. CTRL = vehicle control. Temperature: 37°C.



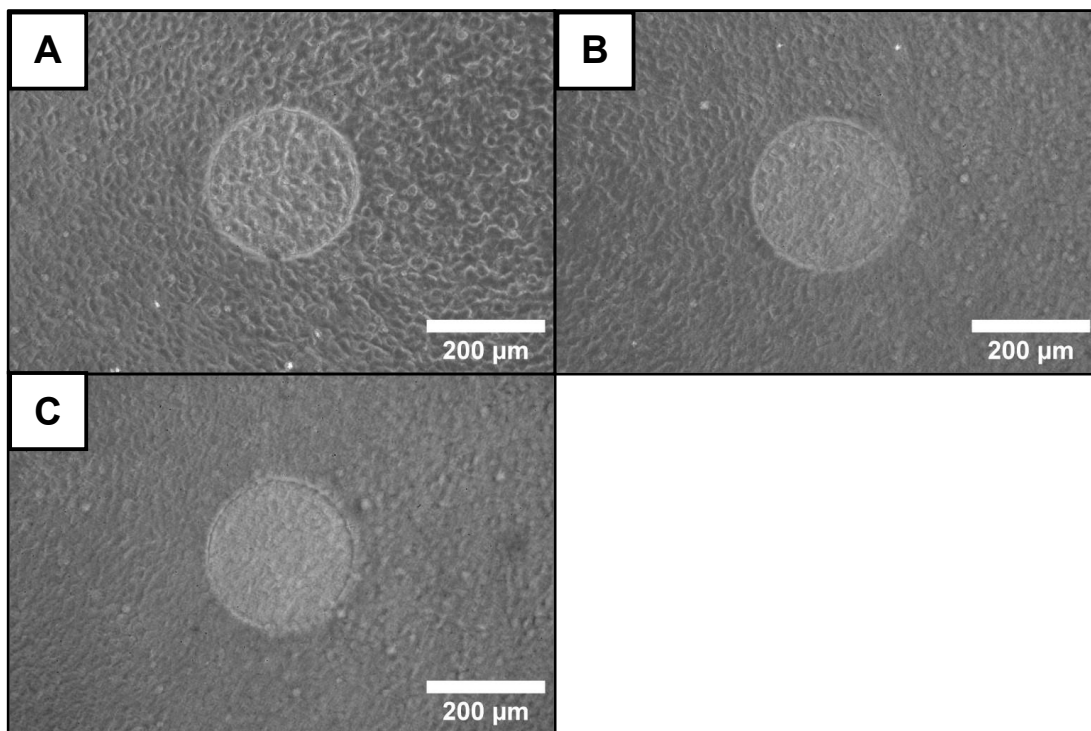
Appendix 24. Impedance change over time of **CHO M5R** cells at a frequency of 12 kHz. The cells were cultivated on a 96W1E+ electrode array that was coated with gelatin. At  $t = 0$  h, the cells were stimulated with different concentrations of **iperoxo (A)** or **carbachol (B)**. A: black 100 nM, red 30 nM, green 10 nM, blue 3 nM, cyan 1 nM, pink 0.3 nM, yellow 0.1 nM, brown CTRL. B: black 30  $\mu$ M, red 10  $\mu$ M, green 3  $\mu$ M, blue 1  $\mu$ M, cyan 300 nM, pink 100 nM, yellow 30 nM, brown CTRL. The concentration-response curves for **iperoxo (C)** and **carbachol (D)** were obtained by plotting the data at  $t = 0.5$  h (black squares) against the logarithmic ligand concentration. A four-parametric dose-response fit (red solid line, **equation 15**) reveals  $pEC_{50}$  values of  $9.60 \pm 0.06$  for iperoxo and  $6.18 \pm 0.07$  for carbachol. The  $E_{max}$  lie at  $(1640 \pm 60) \Omega$  for iperoxo and  $(1530 \pm 60) \Omega$  for carbachol. Baseline A and B:  $(4260 \pm 10) \Omega$  and  $(4360 \pm 10) \Omega$ . Mean + SE,  $N = 6$ , single experiment. CTRL = vehicle control. Temperature: 37°C.



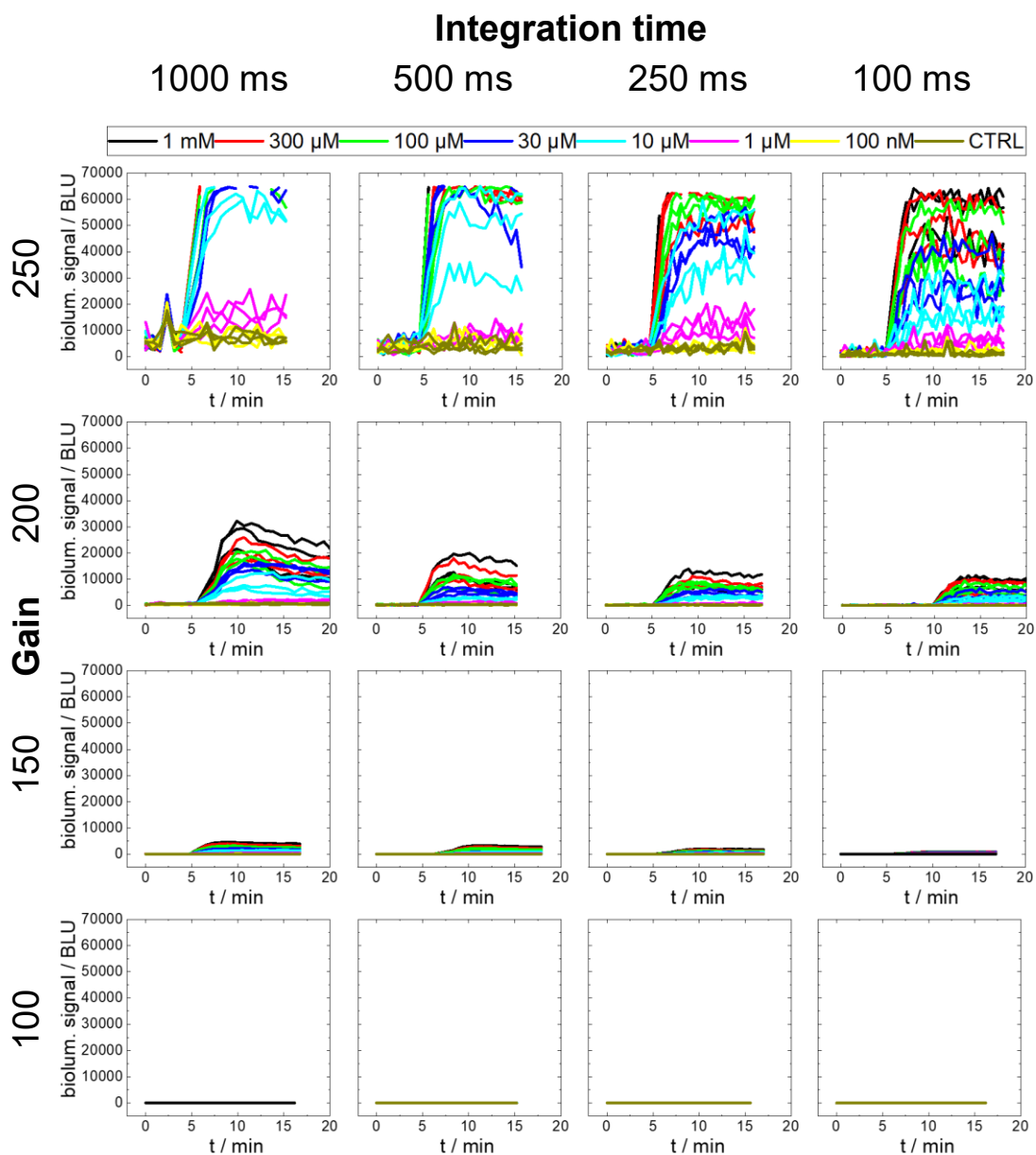
Appendix 25. Impedance change over time of **HEK H2R** cells at a frequency of 12 kHz. The cells were cultivated on a 96W1E+ electrode array that was coated with crosslinked gelatin. At  $t = 0$  h, the cells were stimulated with different concentrations of **histamine** (A). Black 100  $\mu\text{M}$ , red 10  $\mu\text{M}$ , green 1  $\mu\text{M}$ , blue 500 nM, cyan 300 nM, pink 100 nM, yellow 10 nM, brown CTRL. The experimental data after  $t = 0.5$  h is plotted against the logarithmic histamine concentration to generate a concentration-response curve (B). By fitting the experimental data (black squares) with a four-parametric dose-response fit (red solid line, **equation 15**), a  $p\text{EC}_{50}$  of  $6.70 \pm 0.04$  and an  $E_{\text{max}}$  value of  $(830 \pm 30) \Omega$  were determined. Baseline:  $(3185 \pm 5) \Omega$ . Mean + SE,  $N = 4$ , single experiment. CTRL = vehicle control. Temperature:  $37^\circ\text{C}$ .



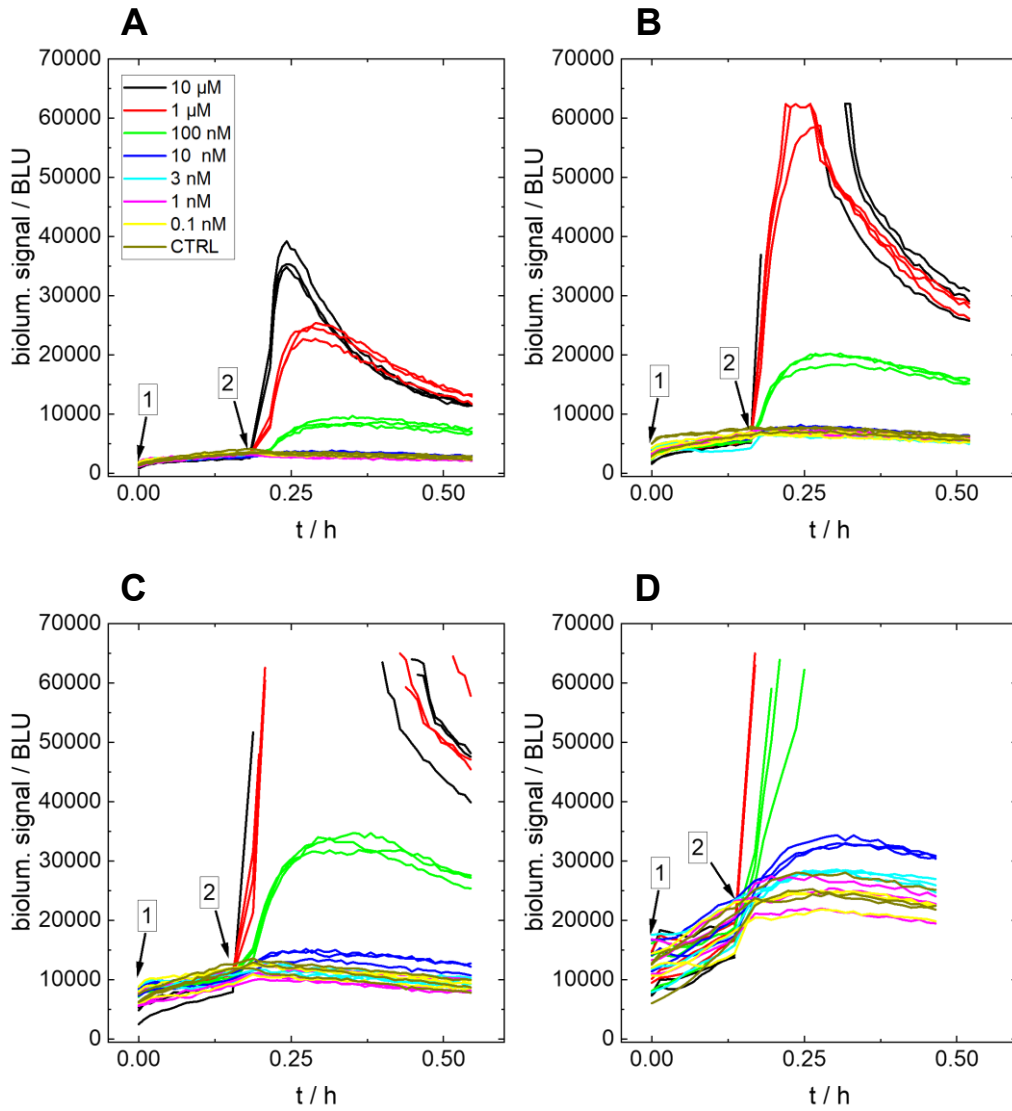
Appendix 26. Luminescence change of **HEK wt** cells seeded on a white 96-well plate. After addition of 1  $\mu\text{M}$  **coelenterazine h** (arrow 1), different concentrations of **iperoxo (A)**, **carbachol (B)** or **histamine (C)** were added (arrow 2). A: black 10  $\mu\text{M}$ , red 1  $\mu\text{M}$ , green 100 nM, blue 30 nM, cyan 10 nM, pink 1 nM, yellow 0.1 nM, brown CTRL. B: black 100  $\mu\text{M}$ , red 30  $\mu\text{M}$ , green 10  $\mu\text{M}$ , blue 3  $\mu\text{M}$ , cyan 1  $\mu\text{M}$ , pink 100 nM, yellow 10 nM, brown CTRL. C: black 10  $\mu\text{M}$ , red 1  $\mu\text{M}$ , green 100 nM, blue 10 nM, cyan 3 nM, pink 1 nM, yellow 0.1 nM, brown CTRL. All curves remain at the baseline level. Analogous experiments were done for CHO M1R, CHO M5R and HEK H2R with the same luminescence outcome. Baseline from A to C: ( $4.4 \pm 0.2$ ) BLU, ( $4.6 \pm 0.3$ ) BLU, ( $4.2 \pm 0.3$ ) BLU. Mean + SE, N = 6, single experiment. CTRL = vehicle control. BLU = bioluminescence units. Temperature: 37°C.



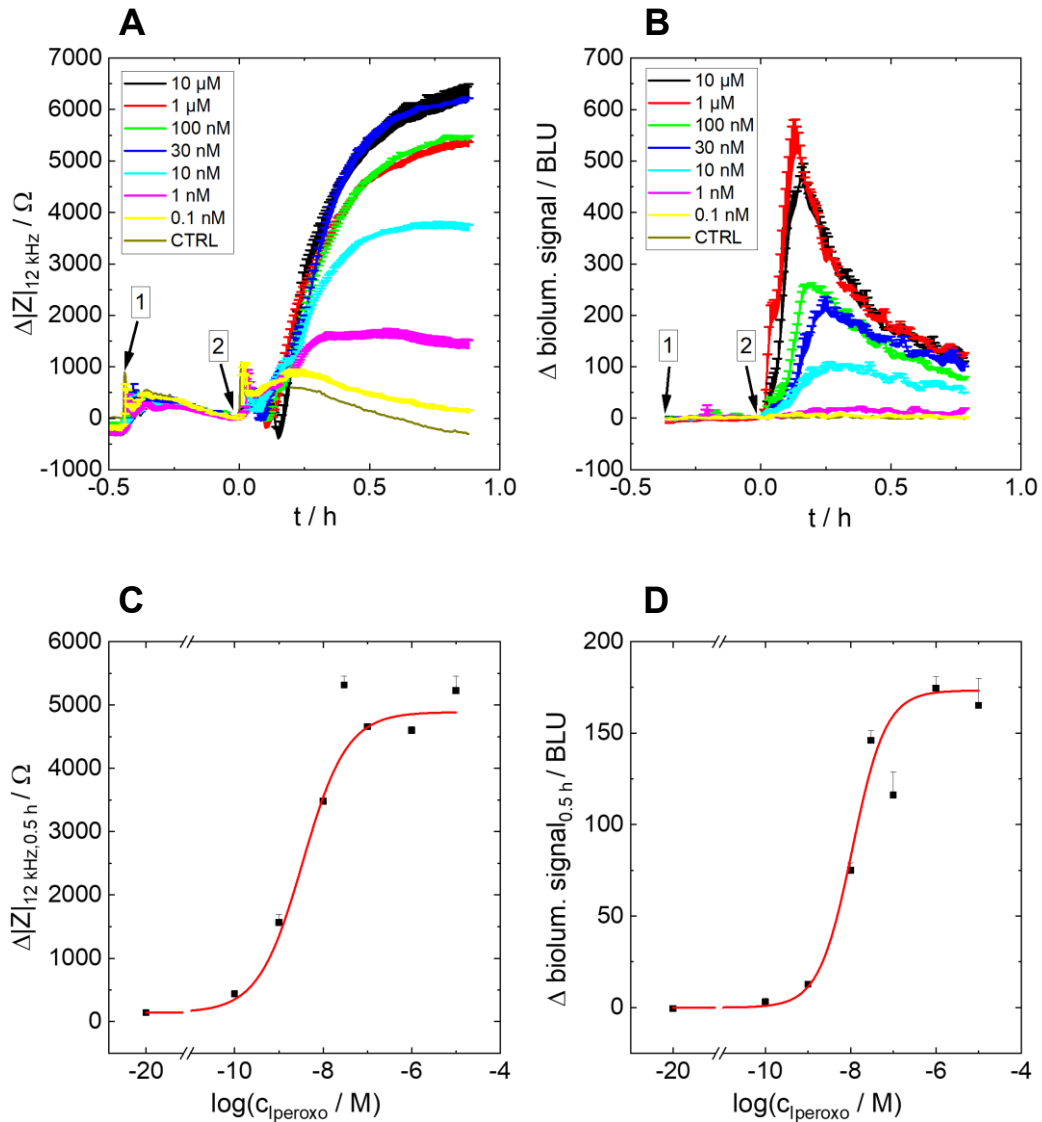
Appendix 27. Phase contrast micrographs of **HEK M1R/mG<sub>q</sub>** cells that were seeded with a density of  $3 \cdot 10^5$  c/cm<sup>2</sup> on 8W1E arrays that were coated with crosslinked gelatin. The pictures were taken **one (A), two (B) or three (C) days after seeding**. Shown is the working electrode in the center of the well.



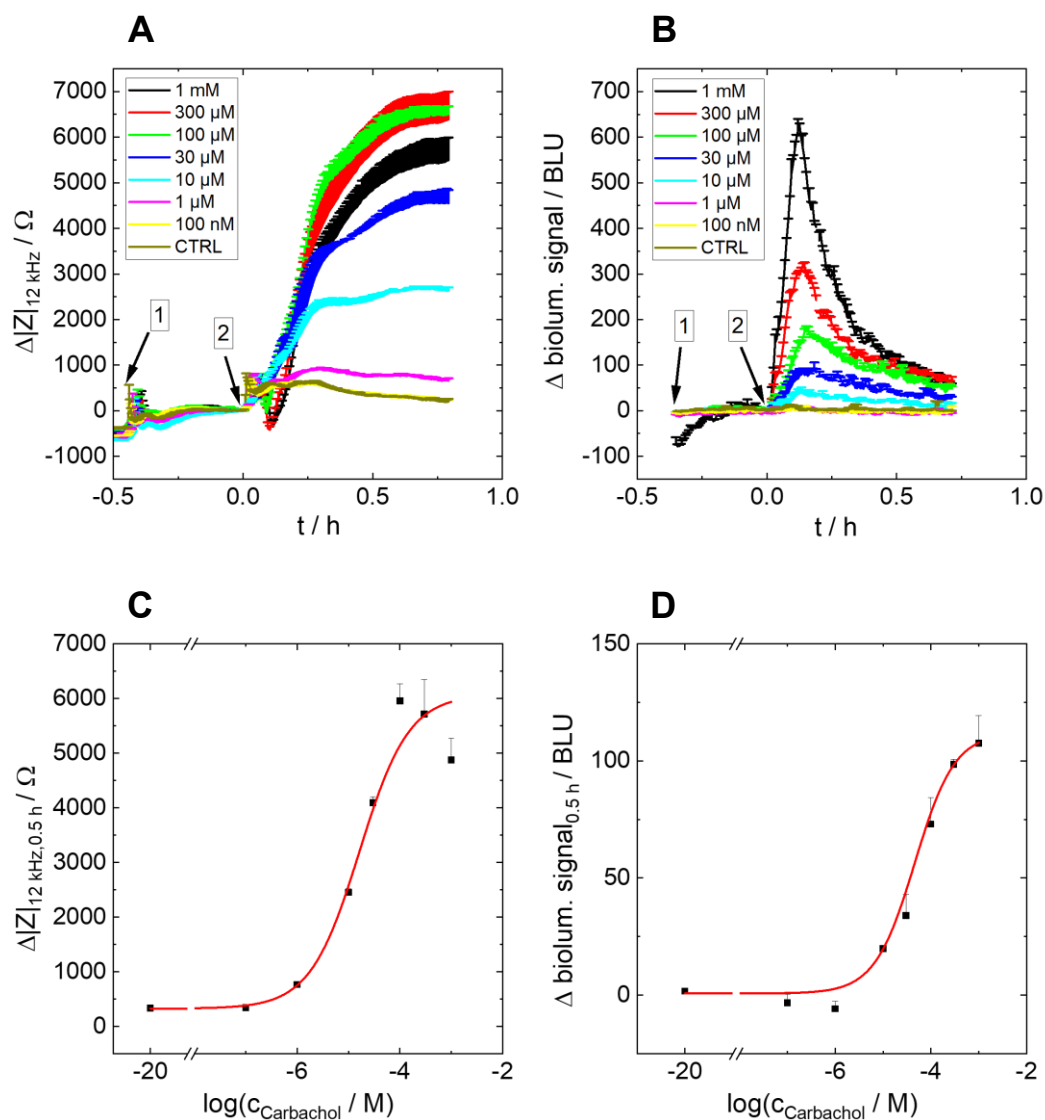
Appendix 28. Luminescence raw data of **HEK M1R/mG<sub>q</sub>** cells over time. The cells were cultivated on a white 96-well plate. At  $t = 0$  h, 1  $\mu$ M coelenterazine h was added. At  $t = 4.7$  min, the cells were stimulated with different concentrations of carbachol. Black 1 mM, red 300  $\mu$ M, green 100  $\mu$ M, blue 30  $\mu$ M, cyan 10  $\mu$ M, pink 1  $\mu$ M, yellow 100 nM, brown CTRL. Different **integration times (100 ms, 250 ms, 500 ms, 1000 ms) and gains (100, 150, 200, 250)** were set. The integration time increases from right to left. The gain increases from the bottom row to the top row. The scale on the y-axis is the same for every graph.  $N = 3$ , single experiment. CTRL = vehicle control. BLU = bioluminescence units. Temperature: 37°C.



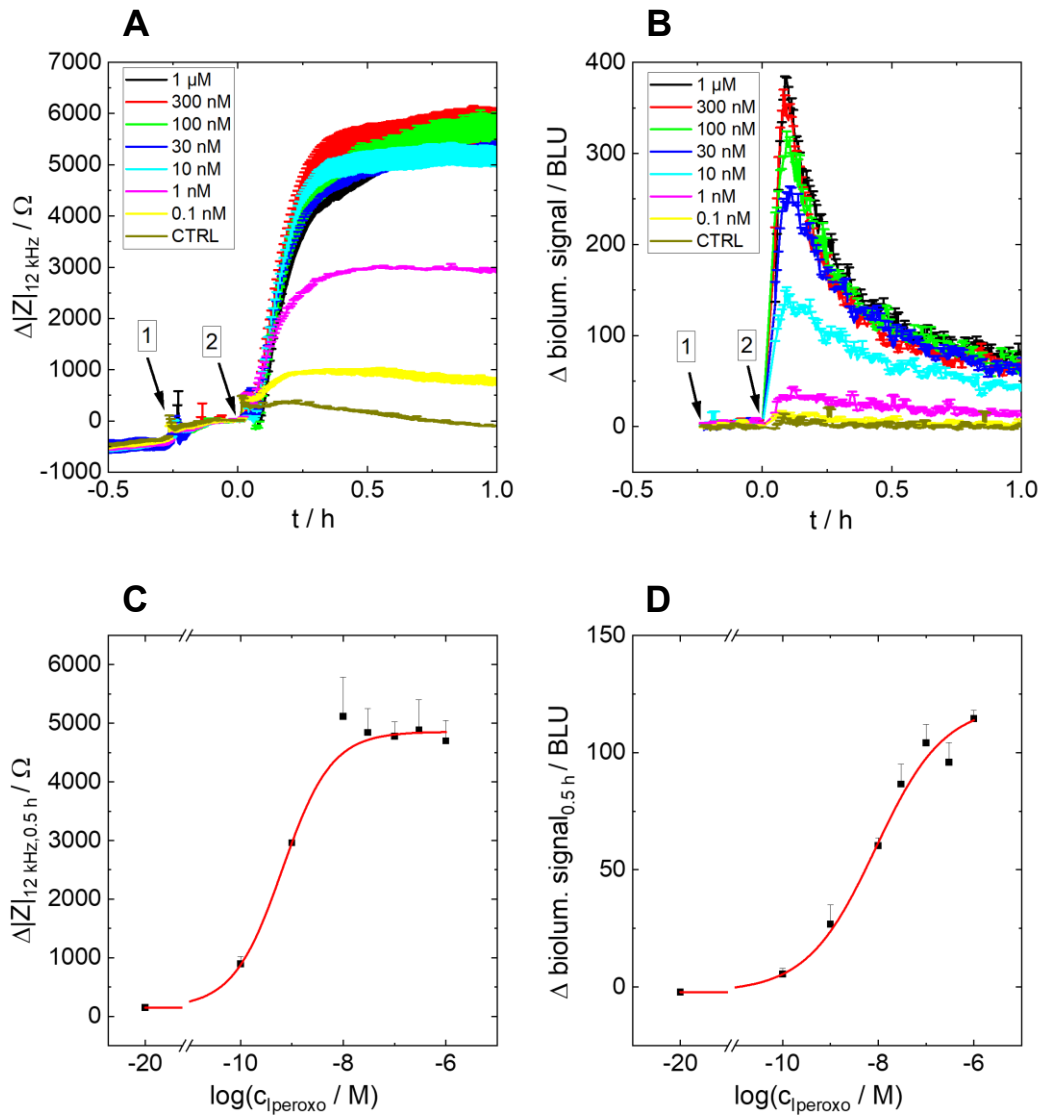
Appendix 29. Luminescence raw data of **HEK H2R/mG<sub>s</sub>** cells over time. The cells were cultivated on a white 96-well plate. At  $t = 0$  h, 1  $\mu$ M coelenterazine h was added (arrow 1). At  $t = 0.15$  h, the cells were stimulated with different concentrations of histamine (arrow 2). Black 10  $\mu$ M, red 1  $\mu$ M, green 100 nM, blue 10 nM, cyan 3 nM, pink 1 nM, yellow 0.1 nM, brown CTRL. **Different integration times were set (A: 100 ms, B: 250 ms, C: 500 ms, D: 1000 ms).** For 10  $\mu$ M and 1  $\mu$ M (B,C) and 10  $\mu$ M, 1  $\mu$ M and 100 nM (D) of histamine, the signal threshold is partially exceeded.  $N = 3$ , single experiment. CTRL = vehicle control. BLU = bioluminescence units. Temperature: 37°C.



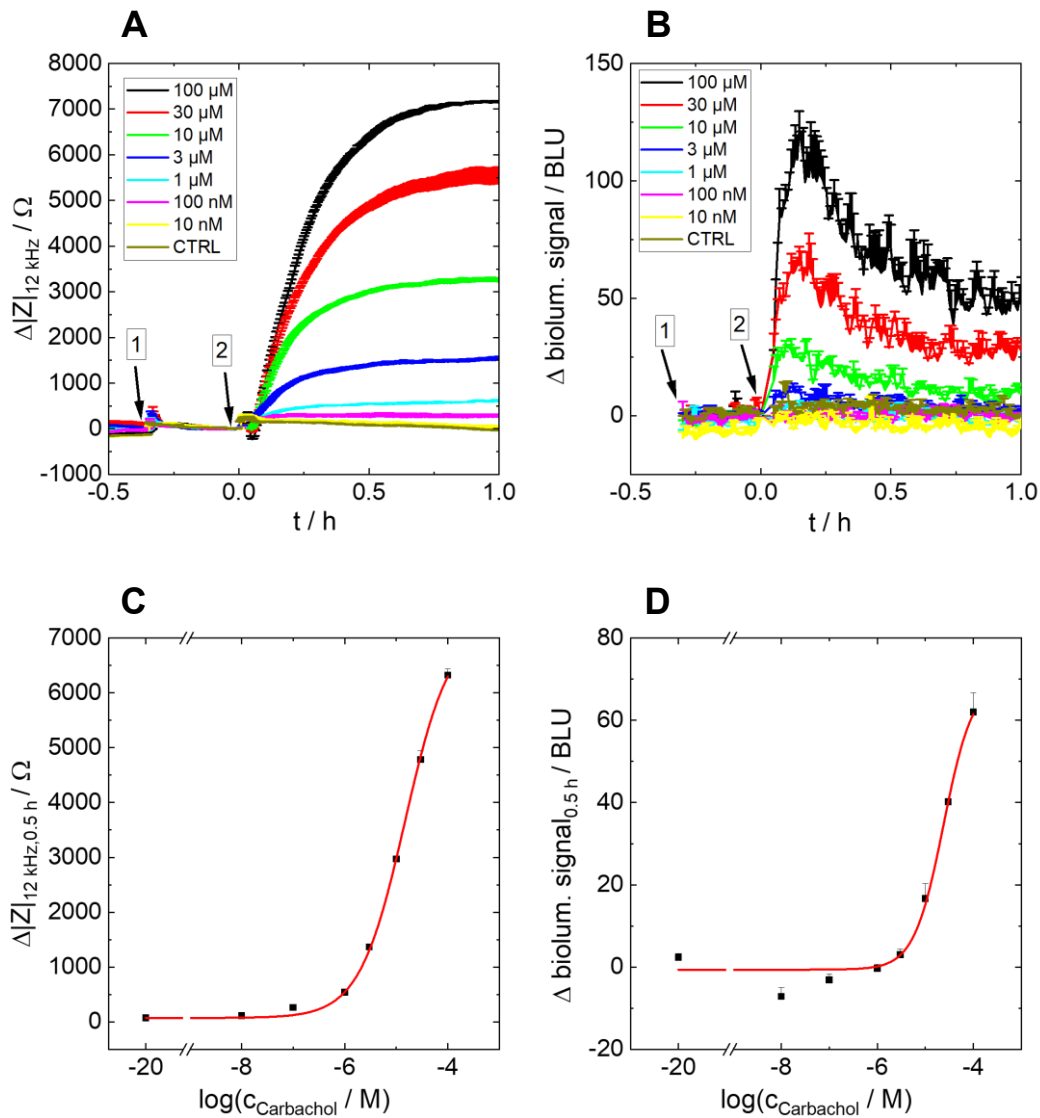
Appendix 30. Change of impedance (A) and luminescence (B) of **HEK M1R/mG<sub>q</sub>** cells after preincubation with 1  $\mu\text{M}$  **coelenterazine h** (arrow 1) and stimulation with **iperoxo** (arrow 2). Black 10  $\mu\text{M}$ , red 1  $\mu\text{M}$ , green 100 nM, blue 30 nM, cyan 10 nM, pink 1 nM, yellow 0.1 nM, brown CTRL. Both measurements were performed in parallel with the **dual** luminescence-impedance setup. From the data at time point  $t = 0.5$  h, concentration-response curves of impedance (C) and luminescence (D) were extracted. The experimental data (black squares) was fitted with a four-parametric dose-response fit (red solid line, **equation 15**). The  $p\text{EC}_{50}$  value determined for impedance is  $8.5 \pm 0.1$ . For luminescence, a value of  $8.0 \pm 0.1$  was found.  $E_{\text{max}}$  lies at  $(4900 \pm 200) \Omega$  and  $(170 \pm 10) \text{BLU}$ , respectively. Baseline A and B:  $(6640 \pm 30) \Omega$ ,  $(7.5 \pm 0.3) \text{BLU}$ . Mean + SE,  $N = 1-2$ , single experiment. CTRL = vehicle control, BLU = bioluminescence units. Temperature:  $37^\circ\text{C}$ .



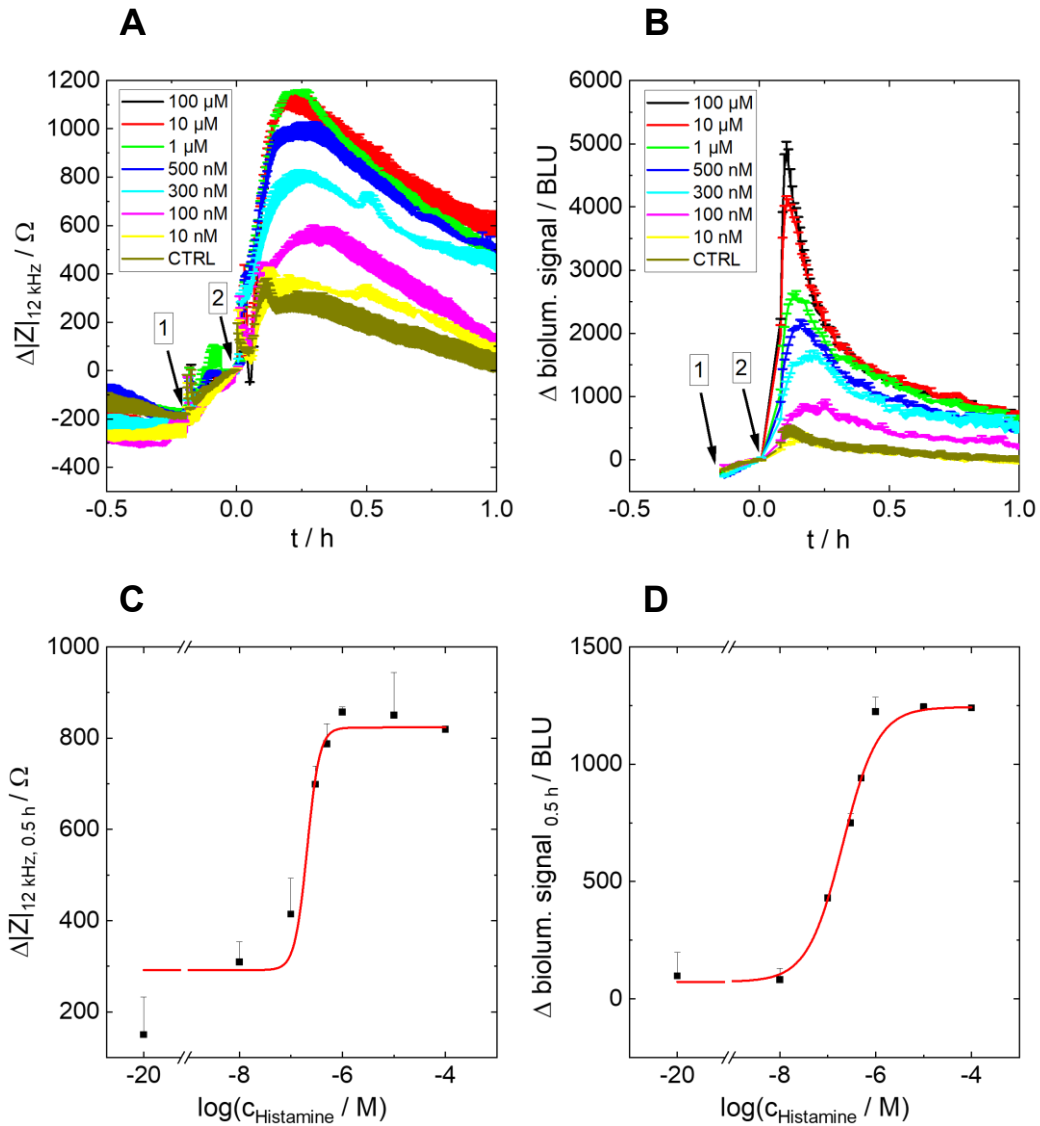
Appendix 31. Change of impedance (A) and luminescence (B) of **HEK M1R/mG<sub>q</sub>** cells after preincubation with 1  $\mu\text{M}$  **coelenterazine h** (arrow 1) and stimulation with **carbachol** (arrow 2). Black 1 mM, red 300  $\mu\text{M}$ , green 100  $\mu\text{M}$ , blue 30  $\mu\text{M}$ , cyan 10  $\mu\text{M}$ , pink 1  $\mu\text{M}$ , yellow 100 nM, brown CTRL. Both measurements were performed in parallel with the **dual** luminescence-impedance setup. From the data at time point  $t = 0.5 \text{ h}$ , concentration-response curves of impedance (C) and luminescence (D) were extracted. The experimental data (black squares) was fitted with a four-parametric dose-response fit (red solid line, **equation 15**). The  $p\text{EC}_{50}$  value determined for impedance is  $4.8 \pm 0.1$ . For luminescence, a value of  $4.3 \pm 0.3$  was found. The  $E_{\text{max}}$  values amount to  $(6100 \pm 700) \Omega$  and  $(110 \pm 20) \text{BLU}$ . Baseline A and B:  $(8270 \pm 30) \Omega$ ,  $(11.8 \pm 0.5) \text{BLU}$ . Mean + SE,  $N = 2$ , single experiment. CTRL = vehicle control. BLU = bioluminescence units. Temperature:  $37^\circ\text{C}$ .



Appendix 32. Change of impedance (A) and luminescence (B) of **HEK M5R/mG<sub>q</sub>** cells after preincubation with 1  $\mu\text{M}$  **coelenterazine h** (arrow 1) and stimulation with **iperoxo** (arrow 2). Black 1  $\mu\text{M}$ , red 300 nM, green 100 nM, blue 30 nM, cyan 10 nM, pink 1 nM, yellow 0.1 nM, brown CTRL. Both measurements were performed in parallel with the **dual** luminescence-impedance setup. From the data at time point  $t = 0.5$  h, concentration-response curves of impedance (C) and luminescence (D) were extracted. The experimental data (black squares) was fitted with a four-parametric dose-response fit (red solid line, **equation 15**). The  $p\text{EC}_{50}$  value determined for impedance is  $9.19 \pm 0.02$ . For luminescence, a  $p\text{EC}_{50}$  value of  $8.06 \pm 0.10$  was found. The  $E_{\text{max}}$  values are  $(4900 \pm 100) \Omega$  and  $(120 \pm 5) \text{BLU}$ . Baseline A and B:  $(7320 \pm 30) \Omega$ ,  $(5.9 \pm 0.2) \text{BLU}$ . Mean + SE,  $N = 2$ , single experiment. CTRL = vehicle control. BLU = bioluminescence units. Temperature:  $37^\circ\text{C}$ .



Appendix 33. Change of impedance (A) and luminescence (B) of HEK M5R/mG<sub>q</sub> cells after preincubation with 1 μM coelenterazine h (arrow 1) and stimulation with carbachol (arrow 2). Black 100 μM, red 30 μM, green 10 μM, blue 3 μM, cyan 1 μM, pink 100 nM, yellow 10 nM, brown CTRL. Both measurements were performed in parallel with the dual luminescence-impedance setup. From the data at time point t = 0.5 h, concentration-response curves of impedance (C) and luminescence (D) were extracted. The experimental data (black squares) was fitted with a four-parametric dose-response fit (red solid line, **equation 15**). The pEC<sub>50</sub> value determined for impedance is  $4.83 \pm 0.05$ . For luminescence, a value of  $4.6 \pm 0.2$  was found. The  $E_{max}$  analysis yielded  $(7200 \pm 300) \Omega$  and  $(70 \pm 20) \text{BLU}$ . Baseline A and B:  $(6420 \pm 30) \Omega$ ,  $(5.7 \pm 0.2) \text{BLU}$ . Mean + SE, N = 2, single experiment. CTRL = vehicle control. BLU = bioluminescence units. Temperature: 37°C.



Appendix 34. Change of impedance (A) and luminescence (B) of HEK H2R/mGs cells after preincubation with 1  $\mu\text{M}$  coelenterazine h (arrow 1) and stimulation with histamine (arrow 2). Black 100  $\mu\text{M}$ , red 10  $\mu\text{M}$ , green 1  $\mu\text{M}$ , blue 500 nM, cyan 300 nM, pink 100 nM, yellow 10 nM, brown CTRL. Both measurements were performed in parallel with the dual luminescence-impedance setup. From the data at time point t = 0.5 h, concentration-response curves of impedance (C) and luminescence (D) were extracted. The experimental data (black squares) was fitted with a four-parametric dose-response fit (red solid line, equation 15). The pEC50 value determined for impedance is  $6.7 \pm 0.2$ . For luminescence, a value of  $6.69 \pm 0.05$  was found. The  $E_{\text{max}}$  values are  $(823 \pm 7) \Omega$  and  $(1243 \pm 9) \text{BLU}$ . Baseline A and B:  $(5240 \pm 30) \Omega$ ,  $(279 \pm 5) \text{BLU}$ . Mean + SE, N = 2, single experiment. CTRL = vehicle control. BLU = bioluminescence units. Temperature: 37°C.

Appendix 35. Overview over  $pEC_{50}$  (point of inflection) and  $E_{max}$  (upper asymptote  $A_2$ ) values detected in **chapters 4.2.1, 4.3, 4.4 and 4.5** for the impedance and luminescence measurements of HEK M1R/mG<sub>q</sub> cells that were stimulated with carbachol. \* = for a reliable fit, the carbachol concentration 100  $\mu$ M was excluded. n.d. = not determined. BLU = bioluminescence units.

Experiment	Impedance		Luminescence		
	$pEC_{50}$	$E_{max} / \Omega$	$pEC_{50}$	$E_{max} / BLU$	
<b>Standard Conditions</b>	$5.55 \pm 0.06$	$5340 \pm 90$	$4.4 \pm 0.3$	$1400 \pm 300$	
<b>Coelenterazine h Aging</b>	<b>Control</b>	n.d.	n.d.	$3.8 \pm 0.2$	$800 \pm 200$
	<b>Three warm-cold-cycles</b>	n.d.	n.d.	$3.9 \pm 0.3$	$600 \pm 100$
	<b>4°C dark</b>	n.d.	n.d.	$4.7 \pm 0.2$	$210 \pm 30$
	<b>r.t. illuminated</b>	n.d.	n.d.	$4.4 \pm 0.2$	$8 \pm 1$
<b>Measurement Buffer</b>	<b>L15</b>	$6.4 \pm 0.1$	$4800 \pm 200$	$4.7 \pm 0.1$	$1300 \pm 100$
	<b>PBS</b>	$6.05 \pm 0.06$	$5400 \pm 100$	$4.5 \pm 0.2$	$2100 \pm 200$
	<b>HBSS</b>	$6.0 \pm 0.2$	$5200 \pm 300$	$4.64 \pm 0.05$	$2740 \pm 90$
<b>Plate Coating (white)</b>	<b>Crosslinked gelatin</b>	n.d.	n.d.	$4.72 \pm 0.08$	$1370 \pm 80$
	<b>Gelatin</b>	n.d.	n.d.	$4.5 \pm 0.1$	$1130 \pm 90$
	<b>Medium</b>	n.d.	n.d.	$4.68 \pm 0.10$	$1000 \pm 80$
<b>Plate Coating (transparent 96W1E+)</b>	<b>Crosslinked gelatin</b>	$5.8 \pm 0.2$	$7600 \pm 400$	$4.5 \pm 0.1$	$160 \pm 10$
	<b>Gelatin</b>	$6.4 \pm 0.3$	$3600 \pm 400$	$4.5 \pm 0.2$	$120 \pm 10$
	<b>Medium</b>	$6.2 \pm 0.1$	$4700 \pm 200$	$4.4 \pm 0.1$	$130 \pm 10$
<b>Plate Coating (black 96W1E+)</b>	<b>Crosslinked gelatin</b>	n.d.	n.d.	$4.73 \pm 0.06^*$	$163 \pm 9^*$
	<b>Gelatin</b>	n.d.	n.d.	$4.5 \pm 0.2$	$130 \pm 10$
	<b>Medium</b>	n.d.	n.d.	$4.40 \pm 0.08$	$129 \pm 6$
<b>Coelenterazine h Concentration</b>	<b>0.25 <math>\mu</math>M</b>	n.d.	n.d.	$4.4 \pm 0.1$	$230 \pm 20$
	<b>0.5 <math>\mu</math>M</b>	n.d.	n.d.	$4.2 \pm 0.4$	$800 \pm 200$
	<b>1 <math>\mu</math>M</b>	n.d.	n.d.	$3 \pm 2$	$2000 \pm 2000$
	<b>2 <math>\mu</math>M</b>	n.d.	n.d.	$4.4 \pm 0.2$	$3400 \pm 300$
<b>Cultivation Time</b>	<b>One day</b>	n.d.	n.d.	$4.44 \pm 0.08$	$1470 \pm 50$
	<b>Two days</b>	n.d.	n.d.	$4.2 \pm 0.4$	$800 \pm 200$
	<b>Three days</b>	n.d.	n.d.	$4.0 \pm 0.3$	$700 \pm 100$
<b>Washing Step</b>	<b>Washed</b>	n.d.	n.d.	$4.2 \pm 0.4$	$500 \pm 200$
	<b>Non-washed</b>	n.d.	n.d.	$4.3 \pm 0.3$	$290 \pm 70$

Appendix 36. Overview over lower asymptote ( $A_1$ ) and Hill slope ( $p$ ) values detected in chapters 4.2.1, 4.3, 4.4 and 4.5 for the impedance and luminescence measurements of HEK M1R/mG<sub>q</sub> cells that were stimulated with carbachol. \* = for a reliable fit, the carbachol concentration 100  $\mu$ M was excluded. n.d. = not determined. BLU = bioluminescence units.

Experiment		Impedance		Luminescence	
		$A_1 / \Omega$	$p$	$A_1 / \text{BLU}$	$p$
Standard Conditions		730 $\pm$ 50	0.84 $\pm$ 0.07	-7 $\pm$ 9	0.8 $\pm$ 0.1
Coelenterazine h Aging	Control	n.d.	n.d.	-41 $\pm$ 4	1.1 $\pm$ 0.2
	Three warm-cold-cycles	n.d.	n.d.	-55 $\pm$ 5	0.7 $\pm$ 0.1
	4°C dark	n.d.	n.d.	-27 $\pm$ 8	0.9 $\pm$ 0.2
	r.t. illuminated	n.d.	n.d.	-1.3 $\pm$ 0.4	2 $\pm$ 3
Measurement Buffer	L15	700 $\pm$ 200	0.8 $\pm$ 0.2	-20 $\pm$ 10	0.67 $\pm$ 0.07
	PBS	190 $\pm$ 40	0.81 $\pm$ 0.06	-20 $\pm$ 10	0.72 $\pm$ 0.07
	HBSS	100 $\pm$ 600	0.7 $\pm$ 0.2	-18 $\pm$ 5	0.82 $\pm$ 0.04
Plate Coating (white)	Crosslinked gelatin	n.d.	n.d.	-16 $\pm$ 6	0.73 $\pm$ 0.05
	Gelatin	n.d.	n.d.	-13 $\pm$ 5	0.75 $\pm$ 0.06
	Medium	n.d.	n.d.	-9 $\pm$ 5	0.82 $\pm$ 0.07
Plate Coating (transparent 96W1E+)	Crosslinked gelatin	800 $\pm$ 100	0.6 $\pm$ 0.1	-2 $\pm$ 1	0.62 $\pm$ 0.08
	Gelatin	200 $\pm$ 200	1.0 $\pm$ 0.5	1.3 $\pm$ 0.8	0.7 $\pm$ 0.1
	Medium	400 $\pm$ 100	0.9 $\pm$ 0.1	-0.5 $\pm$ 0.9	0.65 $\pm$ 0.07
Plate Coating (black 96W1E+)	Crosslinked gelatin	n.d.	n.d.	1.7 $\pm$ 0.5*	0.90 $\pm$ 0.04*
	Gelatin	n.d.	n.d.	0 $\pm$ 2	0.8 $\pm$ 0.2
	Medium	n.d.	n.d.	-2.3 $\pm$ 0.4	0.67 $\pm$ 0.04
Coelenterazine h Concentration	0.25 $\mu$ M	n.d.	n.d.	-4 $\pm$ 3	0.63 $\pm$ 0.09
	0.5 $\mu$ M	n.d.	n.d.	-10 $\pm$ 10	0.5 $\pm$ 0.1
	1 $\mu$ M	n.d.	n.d.	-20 $\pm$ 10	0.4 $\pm$ 0.1
	2 $\mu$ M	n.d.	n.d.	-20 $\pm$ 10	0.69 $\pm$ 0.08
Cultivation Time	One day	n.d.	n.d.	-13 $\pm$ 3	0.70 $\pm$ 0.04
	Two days	n.d.	n.d.	-7 $\pm$ 3	0.7 $\pm$ 0.1
	Three days	n.d.	n.d.	-5 $\pm$ 4	0.64 $\pm$ 0.08
Washing Step	Washed	n.d.	n.d.	-21 $\pm$ 5	0.8 $\pm$ 0.3
	Non-washed	n.d.	n.d.	-19 $\pm$ 6	0.8 $\pm$ 0.2

Appendix 37. Overview over lower asymptote  $A_1$ , upper asymptote  $A_2$  or  $E_{max}$ ,  $pEC50$  value and Hill slope  $p$  for concentration-response fits of **impedance** of HEK M1R/mG<sub>q</sub>, HEK M5R/mG<sub>q</sub> and HEK H2R/mG<sub>s</sub> cells stimulated in **chapters 4.2.1, 4.2.2 and 4.6**.

Chapter	Cellular System	Added Compound(s)	$A_1 / \Omega$	$E_{max} / \Omega$	$pEC50$	$p$
4.2.1	HEK M1R/mG <sub>q</sub>	Iperoxo	690 ± 70	5400 ± 100	8.39 ± 0.06	0.91 ± 0.08
4.2.1	HEK M5R/mG <sub>q</sub>	Iperoxo	500 ± 100	6000 ± 100	9.0 ± 0.2	0.7 ± 0.2
4.2.1	HEK M5R/mG <sub>q</sub>	Carbachol	430 ± 30	6300 ± 100	5.46 ± 0.04	0.91 ± 0.05
4.2.1	HEK H2R/mG <sub>s</sub>	Histamine	340 ± 40	1400 ± 100	6.3 ± 0.2	2 ± 1
4.2.2	HEK M1R/mG <sub>q</sub>	Coelenterazine h + Iperoxo	430 ± 80	5730 ± 80	8.28 ± 0.07	0.71 ± 0.06
4.2.2	HEK M1R/mG <sub>q</sub>	Coelenterazine h + Carbachol	500 ± 300	5300 ± 100	5.5 ± 0.1	0.9 ± 0.1
4.6	HEK M1R/mG <sub>q</sub>	Iperoxo	143 ± 5	4900 ± 200	8.5 ± 0.1	0.9 ± 0.2
4.6	HEK M1R/mG <sub>q</sub>	Carbachol	330 ± 40	6100 ± 700	4.8 ± 0.1	0.90 ± 0.08
4.6	HEK M5R/mG <sub>q</sub>	Iperoxo	150 ± 10	4900 ± 100	9.19 ± 0.02	0.91 ± 0.05
4.6	HEK M5R/mG <sub>q</sub>	Carbachol	74 ± 5	7200 ± 300	4.83 ± 0.05	0.98 ± 0.03
4.6	HEK H2R/mG <sub>s</sub>	Histamine	290 ± 80	823 ± 7	6.7 ± 0.2	4 ± 4

Appendix 38. Overview over lower asymptote  $A_1$ , upper asymptote  $A_2$  or  $E_{max}$ ,  $pEC50$  value and Hill slope  $p$  for concentration-response fits of **luminescence** of HEK M1R/mG<sub>q</sub>, HEK M5R/mG<sub>q</sub> and HEK H2R/mG<sub>s</sub> cells stimulated in **chapters 4.3 and 4.6**.  
\* =  $E_{max}$  value was set to the given value. BLU = bioluminescence units.

Chapter	Cellular System	Added Compound	$A_1 / BLU$	$E_{max} / BLU$	$pEC50$	$p$
4.3	HEK M1R/mG <sub>q</sub>	Iperoxo	-6 ± 2	2300 ± 100	8.14 ± 0.06	1.21 ± 0.07
4.3	HEK M5R/mG <sub>q</sub>	Iperoxo	-7 ± 3	360 ± 20	8.3 ± 0.1	1.0 ± 0.2
4.3	HEK M5R/mG <sub>q</sub>	Carbachol	-14 ± 2	90 ± 10*	4.8 ± 0.3	0.40 ± 0.09
4.3	HEK H2R/mG <sub>s</sub>	Histamine	-1500 ± 100	4100 ± 400	7.4 ± 0.2	1.3 ± 0.3
4.6	HEK M1R/mG <sub>q</sub>	Iperoxo	0 ± 2	170 ± 10	8.0 ± 0.1	1.1 ± 0.2
4.6	HEK M1R/mG <sub>q</sub>	Carbachol	1 ± 2	110 ± 20	4.3 ± 0.3	1.0 ± 0.4
4.6	HEK M5R/mG <sub>q</sub>	Iperoxo	-2 ± 1	120 ± 5	8.06 ± 0.1	0.61 ± 0.07
4.6	HEK M5R/mG <sub>q</sub>	Carbachol	-1 ± 2	70 ± 20	4.6 ± 0.2	1.4 ± 0.5
4.6	HEK H2R/mG <sub>s</sub>	Histamine	70 ± 70	1243 ± 9	6.69 ± 0.05	1.18 ± 0.08

Appendix 39. Overview over lower asymptote  $A_1$ , upper asymptote  $A_2$  or  $E_{max}$ ,  $pEC50$  value and Hill slope  $p$  for concentration-response fits of **impedance** of HEK H2R/mG<sub>s</sub> cells stimulated in **chapter 5.1.2**. CTX = cholera toxin.

Chapter	Cellular System	Added Compound(s)	$A_1 / \Omega$	$E_{max} / \Omega$	$pEC50$	$p$
5.1.2	H2R/mG <sub>s</sub>	Carbachol	86 ± 7	3500 ± 100	6.42 ± 0.03	1.43 ± 0.05
5.1.2	H2R/mG <sub>s</sub>	1 ng/mL CTX + Carbachol	100 ± 20	3200 ± 100	6.50 ± 0.04	1.6 ± 0.1
5.1.2	H2R/mG <sub>s</sub>	10 ng/mL CTX + Carbachol	138 ± 4	3190 ± 30	6.49 ± 0.01	1.65 ± 0.04
5.1.2	H2R/mG <sub>s</sub>	100 ng/mL CTX + Carbachol	120 ± 20	3200 ± 100	6.46 ± 0.03	1.46 ± 0.08

Appendix 40. Overview over lower asymptote  $A_1$ , upper asymptote  $A_2$  or  $R_{max}$ ,  $pEC50$  value and Hill slope  $p$  for concentration-response fits of **calcium-induced fluorescence** of HEK M1R/mG<sub>q</sub>, HEK H2R and HEK wt cells stimulated in **chapter 5.2**. FLU = fluorescence units.

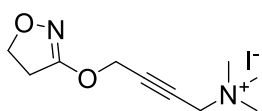
Chapter	Cellular System	Added Compound(s)	$A_1 / FLU$	$R_{max} / \%$	$pEC50$	$p$
5.2	HEK M1R/mG <sub>q</sub>	Acetylcholine	-0.8 ± 0.7	96 ± 4	7.2 ± 0.1	1.1 ± 0.2
5.2	HEK M1R/mG <sub>q</sub>	Carbachol	-0.5 ± 0.6	105 ± 5	6.2 ± 0.1	1.0 ± 0.2
5.2	HEK M1R/mG <sub>q</sub>	Iperoxo	-0.5 ± 0.6	104 ± 4	9.1 ± 0.1	1.2 ± 0.2
5.2	HEK H2R	Histamine	Set to 0	110 ± 10	6.2 ± 0.2	0.5 ± 0.1
5.2	HEK wt	Acetylcholine	-2 ± 4	92 ± 6	6.1 ± 0.1	1.3 ± 0.4
5.2	HEK wt	Carbachol	-5 ± 2	120 ± 10	4.9 ± 0.1	1.0 ± 0.2
5.2	HEK wt	Iperoxo	-1 ± 2	133 ± 6	7.52 ± 0.08	0.9 ± 0.1

Appendix 41. Overview over lower asymptote  $A_1$ , upper asymptote  $A_2$  or  $R_{max}$ ,  $pEC50$  value and Hill slope  $p$  for concentration-response fits of **luminescence** of HEK  $\beta 2AR/\beta$ -Arr.2, HEK H2R/ $\beta$ -Arr.2 and HEK M1R/ $\beta$ -Arr.2 stimulated in **chapter 5.3**. BLU = bioluminescence units.

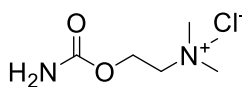
Chapter	Cellular System	Added Compound(s)	$A_1$ / BLU	$R_{max}$ / %	$pEC50$	$p$
5.3	HEK $\beta 2AR/\beta$ -Arr.2	Isoprenaline (comparison with histamine)	$0.0 \pm 0.07$	$108 \pm 5$	$7.66 \pm 0.09$	$1.02 \pm 0.08$
5.3	HEK H2R/ $\beta$ -Arr.2	Histamine (comparison with isoprenaline)	$0.1 \pm 0.5$	$100 \pm 10$	$6.0 \pm 0.1$	$1.2 \pm 0.2$
5.3	HEK H2R/ $\beta$ -Arr.2	Histamine (control for cimetidine experiment)	$0.2 \pm 0.8$	Set to 100	$5.79 \pm 0.03$	$0.77 \pm 0.04$
5.3	HEK H2R/ $\beta$ -Arr.2	1 $\mu$ M Cimetidine + Histamine	$1 \pm 1$	Set to 100	$5.36 \pm 0.06$	$0.81 \pm 0.08$
5.3	HEK H2R/ $\beta$ -Arr.2	3 $\mu$ M Cimetidine + Histamine	$0.4 \pm 0.5$	Set to 100	$4.92 \pm 0.02$	$0.89 \pm 0.04$
5.3	HEK H2R/ $\beta$ -Arr.2	10 $\mu$ M Cimetidine + Histamine	$-0.1 \pm 0.2$	Set to 100	$4.43 \pm 0.02$	$0.87 \pm 0.03$
5.3	HEK H2R/ $\beta$ -Arr.2	100 $\mu$ M Cimetidine + Histamine	$-1.1 \pm 0.7$	Set to 100	$3.35 \pm 0.04$	$0.91 \pm 0.06$
5.3	HEK M1R/ $\beta$ -Arr.2	Carbachol (control for pirenzepine experiment)	$0.0 \pm 0.5$	Set to 100	$5.49 \pm 0.08$	$0.58 \pm 0.06$
5.3	HEK M1R/ $\beta$ -Arr.2	100 pM Pirenzepine + Carbachol	$1 \pm 1$	Set to 100	$5.78 \pm 0.08$	$0.67 \pm 0.06$
5.3	HEK M1R/ $\beta$ -Arr.2	1 nM Pirenzepine + Carbachol	$2 \pm 3$	Set to 100	$5.79 \pm 0.09$	$0.66 \pm 0.09$
5.3	HEK M1R/ $\beta$ -Arr.2	10 nM Pirenzepine + Carbachol	$1 \pm 1$	Set to 100	$5.09 \pm 0.08$	$0.56 \pm 0.05$
5.3	HEK M1R/ $\beta$ -Arr.2	100 nM Pirenzepine + Carbachol	$2 \pm 2$	Set to 100	$3.8 \pm 0.1$	$0.46 \pm 0.07$
5.3	HEK M1R/ $\beta$ -Arr.2	1 $\mu$ M Pirenzepine + Carbachol	$0 \pm 2$	Set to 100	$1.7 \pm 0.7$	$0.3 \pm 0.1$

Appendix 42. Overview over lower asymptote  $A_1$ , upper asymptote  $A_2$  or  $R_{max}$ ,  $pEC50$  value and Hill slope  $p$  for concentration-response fits of impedance of CHO D2L and CHO NPY cells stimulated in **chapter 6.2**.

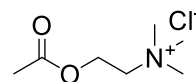
Chapter	Cellular System	Added Compound(s)	$A_1$ / %	$R_{max}$ / %	$pEC50$	$p$
6.2	CHO D2L	Ligand 1 ( <i>closed</i> )	$-9 \pm 2$	$100 \pm 10$	$7.11 \pm 0.05$	$2.7 \pm 0.7$
6.2	CHO NPY	Ligand 2 ( <i>cis</i> )	$9 \pm 5$	$111 \pm 7$	$7.9 \pm 0.1$	$1.1 \pm 0.3$
6.2	CHO NPY	Ligand 2 ( <i>trans</i> )	$9 \pm 3$	$110 \pm 10$	$7.3 \pm 0.1$	$1.2 \pm 0.3$



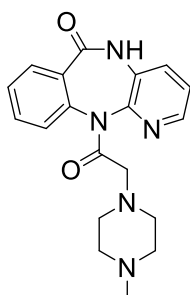
Iperoxo



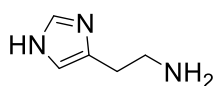
Carbachol



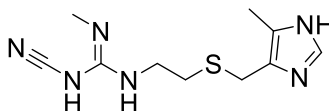
Acetylcholine



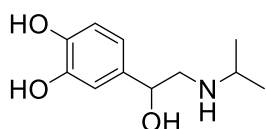
Pirenzepine



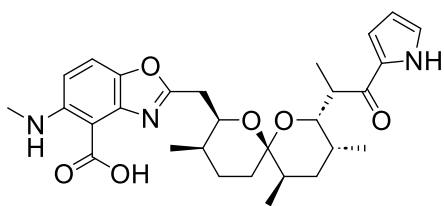
Histamine



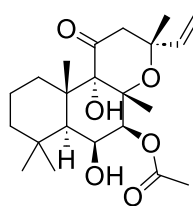
Cimetidine



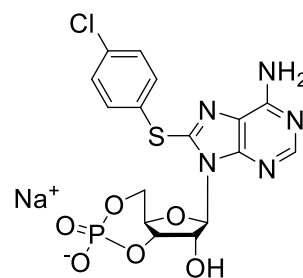
Isoprenaline



Calcimycin



Forskolin



8-CPT-cAMP

Appendix 43. Structures of ligands and molecules used throughout this work. In the red box the muscarinic acetylcholine receptor agonists iperoxo, carbachol and acetylcholine and the selective M1R antagonist pirenzepine are depicted. In the blue box the endogenous histamine receptor agonist histamine and the selective H2R antagonist cimetidine is depicted. In the black box the  $\beta$ 2AR agonist isoprenaline is shown. In the green box the structures of calcimycin, forskolin and 8-CPT-cAMP are shown. The structures were created with ChemDraw (Perkin Elmer).

## 9.2 Abbreviations

Abbreviation	Full Description
-	Minus
%	Percent
% (v/v)	Volume Percent
% (w/v)	Weight Percent
*	Statistical Significance
Z	Impedance Magnitude
€	Euro
+	Plus
<	Smaller/Less Than
>	Larger/More Than
≤	Smaller than
≥	Larger than
°	Degree
°C	Degree Centigrade
μ	Micro, 10 <sup>-6</sup>
<sup>125</sup> I	Iodine-123
<sup>35</sup> S	Sulfur-35
3D	Three-dimensional
<sup>3</sup> H	Tritium
8-CPT-cAMP	8-(4-Chlorophenylthio) Adenosine 3',5'-Cyclic Monophosphate
96W1E+	96-well Electrode Arrays (Applied Biophysics Inc.)
A	Ampere
A <sub>1</sub> , A <sub>2</sub>	Lower/Upper Asymptote (Sigmoidal Fit)
A23187	Calcimycin, Calcium Ionophore
AC	Alternating Current, Adenylate Cyclase
AD	Activating Domain
ADP	Adenosine Diphosphate
AM	Acetoxymethyl Ester
AMP	Adenosine Monophosphate
A <sub>n</sub>	CPE Parameter in F·s <sup>n-1</sup>
AP-1	Activator Protein 1
ATP	Adenosine Triphosphate
AUC	Area Under the Curve
BAEC	Bovine Aortic Endothelial Cells
BamHI	Restriction Enzyme
BAPTA	1,2-Bis( <i>o</i> -aminophenoxy)ethane- <i>N,N,N',N'</i> -tetraacetic acid
BD	Binding Domain
BERKY	BRET Biosensors with ER/K Linker and Yellow Fluorescent Protein
Biolum. (signal)	Bioluminescence
BL	Bioluminescence
BLU	Bioluminescence Units
bp, bps	Base Pair(s)
BRET	Bioluminescence Resonance Energy Transfer
BSA	Bovine Serum Albumin
c	<i>Closed</i> , Concentration
C	Capacitor, Capacitance
c/cm <sup>2</sup>	Cells per Square Centimeter
Ca <sup>2+</sup>	Calcium
CaCl <sub>2</sub>	Calcium Chloride
cAMP	Cyclic Adenosine Monophosphate
CBLuc	Click Beetle Luciferase
C <sub>cl</sub>	Capacitance of Cell Layer
CE	Counter Electrode
CE96	CardioExcyte 96 (Nanion Technologies)
cf.	<i>Confer</i>
CHO (K1)	Chinese Hamster Ovary Cells
cl	Cell Layer
Cl <sup>-</sup>	Chloride
CLSM	Confocal Laser Scanning Microscopy
cm	Centimeter
C <sub>m</sub>	Membrane Capacitance
CMO	Common Main Objective
CNS	Central Nervous System

CO <sub>2</sub>	Carbon Dioxide
cos	Cosine
CPE	Constant Phase Element
CRE	cAMP Response Element
CRISPR/Cas9	Clustered Regularly Interspaced Short Palindromic Repeats/CRISPR-associated protein 9
cryo-EM	Electron Cryo-Microscopy
CTRL	Vehicle Control
CTX	Cholera Toxin
d	Day
D2L	Dopamine Receptor 2 (Long Splicing Variant)
D2R	Dopamine Receptor 2
D2S	Dopamine Receptor 2 (Short Splicing Variant)
DAG	Diacylglycerol
DMEM	Dulbecco's Modified Eagle Medium
DMR	Dynamic Mass Redistribution
DMSO	Dimethyl Sulfoxide
DNA	Desoxyribonucleic Acid
dNTPs	Deoxynucleotide Triphosphates
DpnI	Restriction Enzyme
DR	Dose Ratio
e	Euler Number
e.g.	<i>Exempli Gratia</i>
ebBRET	Enhanced Bystander BRET
EC50	Concentration with Halfmaximal Effect
ECIS	Electric Cell-Substrate Impedance Sensing
ECL	Extracellular Loop
ECM	Extracellular Matrix
EDTA	Ethylenediaminetetraacetic Acid
EGTA	Ethylene glycol-bis(β-aminoethyl ether)- <i>N,N,N,N</i> -tetraacetic acid
EIS	Electrochemical Impedance Spectroscopy
em	Emission
E <sub>max</sub>	Efficacy
ER	Endoplasmic Reticulum
ERK1/2	Extracellular Signal-Regulated Kinases 1 and 2
EtOH	Ethanol
ev	Empty vector
exc	Excitation
F	Fluorescence
f	Frequency
F12, Ham's F12	Ham's F12 Medium
F-bottom	Flat-bottom
FBS	Fetal Bovine Serum
FDA	Food and Drug Administration
FITC	5/6-Fluorescein Isothiocyanate
FLU	Fluorescence Units
FLuc	Firefly Luciferase
FR	FR900359
FRET	Förster Resonance Energy Transfer
FSK	Forskolin
g	Gram, Gravitational Acceleration
G protein	Guanosine Triphosphate Binding Protein
GABA	γ-Aminobutyric Acid
GDP	Guanosine Diphosphate
GEMTA	G Protein Effector Membrane Translocation Assay
GFP	Green Fluorescent Protein
GLuc	<i>Gaussia</i> Luciferase
GPCR	G Protein-Coupled Receptor
GPCR intraNLuc x	Nanoluciferase fused to N-terminus of a GPCR; x Represents the Amino Acid the Nanoluciferase is Connected to
G <sub>q/5</sub>	Chimeric Protein G <sub>q/5</sub>
GRAFS	Glutamate (G), Rhodopsin (R), Adhesion (A), Frizzled/Taste2 (F) and Secretin (S)
GRK	GPCR Kinase
GRM	Metabotropic Glutamate Receptors
GTP	Guanosine Triphosphate
Gα <sub>q/11</sub> , Gα <sub>s</sub> , Gα <sub>i/o</sub> and Gα <sub>12/13</sub>	G protein Families
h	Distance between Cell Layer and Substratum, Hour

H <sub>0</sub>	Null hypothesis
H1R	Histamine 1 Receptor
H2R	Histamine 2 Receptor
H3R	Histamine 3 Receptor
H4R	Histamine 4 Receptor
HBS	HEPES-Buffered Saline
HBSS	Hank's Balanced Salt Solution
HEK (293T)	Human Embryonic Kidney Cells
HEPES	4-(2-Hydroxyethyl)-1-Piperazineethanesulfonic Acid
HiBiT	High Affinity Nanoluciferase Fragment
hPP	Human Pancreatic Polypeptide
Hz	Hertz
hν	Light Quantum
i	$\sqrt{-1}$
I	Current, Ionic Strength
I <sub>0</sub>	Current Amplitude
IBMX	3-Isobutyl-1-Methylxanthine
ICL	Intracellular Loop
iL	intraNLuc
Im	Imaginary Part of Impedance
IP <sub>1</sub>	Inositol Monophosphate
IP <sub>2</sub>	Inositol Diphosphate
IP <sub>3</sub>	Inositol Triphosphate
IP <sub>3</sub> R	Inositol Triphosphate Receptor
ITO	Indium Tin Oxide
k	Kilo, 10 <sup>3</sup>
KAZ	19 kDa fragment of OLuc with catalytic activity
K <sub>B</sub>	Equilibrium Dissociation Constant, Affinity (Functional Assay)
KCl	Potassium Chloride
K <sub>D</sub>	Equilibrium Dissociation Constant, Affinity (Saturation Binding)
kDa	Kilodalton
KH <sub>2</sub> PO <sub>4</sub>	Monopotassium Phosphate
L	Inductor, Inductance, Liter
L15	Leibovitz' 15 Buffer
LED	Light Emitting Diode
LF	Lipofectamine™ 3000
LgBiT	Large Nanoluciferase Fragment
L-glu	L-Glutamine
Li <sup>+</sup>	Lithium
log	Logarithm
m	Milli, 10 <sup>-3</sup> , Meter
M, mol/L	Molar, mol per Liter
M1R	Muscarinic Acetylcholine Receptor 1
M2R	Muscarinic Acetylcholine Receptor 2
M3R	Muscarinic Acetylcholine Receptor 3
M4R	Muscarinic Acetylcholine Receptor 4
M5R	Muscarinic Acetylcholine Receptor 5
MAPK	Mitogen-Activated Protein Kinase
Max.	Maximum, maximal
MDCK	Madin-Darby Canine Kidney
MFT	Multi-Frequency vs. Time
Mg <sup>2+</sup>	Magnesium
MgCl <sub>2</sub>	Magnesium Chloride
MgSO <sub>4</sub>	Magnesium Sulfate
min	Minute
miniG	Minimal G Protein
mG	Minimal G Protein
n	Nano, 10 <sup>-9</sup> , CPE Order (0 < n < 1)
N	Number of Repetitions
n.d.	Not Determined
NA	Numerical Aperture
Na <sub>2</sub> HPO <sub>4</sub>	Disodium Phosphate
NaCl	Sodium Chloride
NaHCO <sub>3</sub>	Sodium Bicarbonate
NanoBiT	Nanoluciferase Binary Technology
NanoLuc	Nanoluciferase
NLuc	Nanoluciferase
NFAT	Nuclear Factor of Activated T-Cells

NLucC-GPCR	GPCR fused to C-terminal Fragment of Nanoluciferase, SmBiT
NLucN-miniG <sub>x</sub>	miniG <sub>x</sub> Protein Fused to N-terminal Fragment of Nanoluciferase, LgBiT
NP	Native Peptide
NPY	Neuropeptide Y
NTS1R	Neurotensin Receptor 1
o	<i>Open</i>
O <sub>2</sub>	Oxygen
OLuc	<i>Oplophorus gracilirostris</i> , Deep-Sea Shrimp Luciferase
OM	Opti-MEM
p	Pico, 10 <sup>-12</sup> , Hill Slope, Probability that Null Hypothesis is Rejected
PBS <sup>-</sup>	Phosphate-Buffered Saline without Calcium and Magnesium Ions
PBS, DPBS	(Dulbecco's) Phosphate-Buffered Saline
PBS <sup>++</sup>	Phosphate-Buffered Saline with Calcium and Magnesium Ions
PCA	Protein Fragment Complementation Assay
pcDNA 3.1	
pIRESneo3	Plasmids, e.g. Plasmid Cloning DNA
pIRESpuro3	
PCR	Polymerase Chain Reaction
PDE	Phosphodiesterase
pEC50	Negative Logarithm of EC50
pH	pH Value
Photoswitch	Photoswitchable Ligand
PI3K	Phosphoinositide 3-Kinase
PIP <sub>2</sub>	Phosphatidylinositol Phosphate
PKA	Protein Kinase A
pK <sub>B</sub>	Negative Logarithm of K <sub>B</sub>
PKC	Protein Kinase C
PLC-β	Phospholipase C-β
PMT	Photomultiplier Tube
POI	Protein of Interest
PP	Pancreatic Polypeptide
PSS	Photostationary State
PTX	Pertussis Toxin
px	Pixel
r <sub>s</sub>	Spearman Correlation Coefficient
R	Resistor, Resistance
r.t.	Room Temperature
R <sup>2</sup>	Coefficient of Determination
R5P	Riboflavin 5'-Phosphate
R <sub>b</sub>	Barrier Function/Resistance
R <sub>bulk</sub>	Bulk Resistance/Medium Resistance
r <sub>c</sub>	Radius of Cells
R <sub>cl</sub>	Resistance of Cell Layer
Re	Real Part of Impedance
RET	Resonance Energy Transfer
RGS	Regulators of GPCR Signaling
RhoGAP	RhoGTPase Activating Proteins
RhoGEF	RhoGTPase Enhancing Factor
RLuc	<i>Renilla</i> Luciferase
R <sub>max</sub>	Relative E <sub>max</sub>
RNA	Ribonucleic Acid
RNase	Ribonuclease
ROCK	Rho Kinase
rpm	Rounds per Minute
RWG	Resonance Waveguide Grating
s	Second
S/N	Signal-to-Noise Ratio
SA	Self-assembled
SD	Standard Deviation
SE, SEM	Standard Error (of the Mean)
SFT	Single-Frequency vs. Time
sin	Sine
SmBiT	Small Nanoluciferase Fragment
SNAP	SNAP-Tag
SPASM	Systematic Protein Affinity Strength Modulation
SPR	Surface Plasmon Resonance
t	Time
T	Temperature
t <sub>1/2</sub>	Time After Which Half-Maximal Response is Observed

T227	Threonine 227
T25 or T75	Culture Flask with an Area of 25 cm <sup>2</sup> or 75 cm <sup>2</sup>
TAS1/2	Taste Receptors of Type 1/2
TBE	Tris-Borate-EDTA Buffer
TE	Tris-EDTA Buffer
TM	Transmembrane (Domain/Helix)
TRUPATH	Transducer Pathway Assay
U	Voltage
U <sub>0</sub>	Voltage Amplitude
U-373 MG	Human Glioblastoma Cells
UV	Ultraviolet
V	Volt
Vis	Visible Light
vs.	Versus
W	Watt
w/	With
w/o	Without
WE	Working Electrode
wt	Wild Type
X	Reactance
XhoI	Restriction Enzyme
Y2H	Yeast Two-hybrid
Y4R	Neuropeptide Y4 Receptor
YFP	Yellow Fluorescent Protein
YM	YM-254890
YY	Peptide YY
Z	Impedance
Z <sub>cl</sub>	Impedance of Cell Layer
Z <sub>el</sub>	Impedance of Electrode
Z <sub>i</sub>	Ionic Charge
Z <sub>m</sub>	Impedance of Membranes
Z <sub>n</sub>	Impedance of Cell-Free Electrode
α	Impedance from Cell Adhesion Sites
αH	α-Helical Domain
αN	N-Terminal Helix
β2AR	Beta-2 Adrenoceptor
β-Arr.2	β-arrestin2
Δ	Difference, Change
ΔT	Temperature Rise
λ	Wavelength
π	Pi
ρ	Specific Medium Resistivity
φ	Phase Shift
Ω	Ohm
ω	Radial Frequency in s <sup>-1</sup>

## 9.3 Materials and Instrumentation

### Materials and Instrumentation

0.5/1/2 mL Tubes

10x objective  
(E, 10x, NA = 0.25)

15/50 mL Tubes

30 mL Tubes

4x objective  
(Plan, 4x, NA = 0.13)

8-CPT-cAMP

96W1E+, 8W1E

Acetylcholine

Agar, Agarose

Ampicillin

Autoclave DX-45

Automated Cell Counter Luna™

Balances

BamHI

BenchTop 1kb Ladder

Benchtop Centrifuge

Black 96-well, black bottom

Black 96-well, transparent bottom

Bovine Serum Albumin

Bunsen Burner

Calcimycin

Camera Nikon D 5000

Carbachol

Carbon Dioxide

CardioExcyte 96 Sensor Plates 0.6 mm

CardioExcyte96, CE96

Centrifuge 5418

Centrifuge 5810 R

Centrifuge Heraeus

Multifuge 1S-R

Centrifuge MiniSpin®

ChemDraw Software

CHO K1 cells

Cimetidine

Circuit Boards

Clamps

CLARIOstar plate reader

Coelenterazine h

Compressed Air

Copper Wires

Cryo Vials

CTX

Deoxyribonucleotide triphosphates, dNTPs

D-Glucose

Disposable Pipettes (2/5/10/25 mL)

DMEM

DMEM/F12

DMSO

Dpnl

E. coli, One Shot® Top10F Chemically Competent Cells

### Company

Sarstedt AG & Co. KG, Nümbrecht, Germany

Eppendorf Inc., Hamburg, Germany

VWR GmbH, Radnor, USA

Nikon Instruments Europe, Amsterdam, Netherlands

Greiner Bio-One GmbH, Frickenhausen, Germany

Sarstedt AG & Co. KG, Nümbrecht, Germany

Thermo Fisher Scientific Inc., Waltham, USA

Nikon Instruments Europe, Amsterdam, Netherlands

Sigma-Aldrich Chemie GmbH, Taufkirchen, Germany

Applied BioPhysics Inc., Troy, USA

Sigma-Aldrich Chemie GmbH, Taufkirchen, Germany

Sigma-Aldrich Chemie GmbH, Taufkirchen, Germany

Sigma-Aldrich Chemie GmbH, Taufkirchen, Germany

Systec, Wetzlar, Germany

Logos Biosystems, Anyang, South Korea

Scaltec Instruments GmbH, Göttingen, Germany

OHAUS Europe GmbH, Nänikon, Switzerland

Thermo Fisher Scientific Inc., Waltham, USA

Promega Corporation, Madison, USA

Carl Roth GmbH & Co. KG, Karlsruhe, Germany

neoLab Migge GmbH, Heidelberg, Germany

Greiner Bio-One GmbH, Frickenhausen, Germany

Corning Inc., Corning, USA

VWR GmbH, Radnor, USA

Carl Roth GmbH & Co. KG, Karlsruhe, Germany

WLD Tec., Arenshausen, Germany

Sigma-Aldrich Chemie GmbH, Taufkirchen, Germany

Nikon GmbH, Düsseldorf, Germany

Sigma-Aldrich Chemie GmbH, Taufkirchen, Germany

Linde AG, Dublin, Ireland

Nanion Technologies GmbH, Munich, Germany

Nanion Technologies GmbH, Munich, Germany

Eppendorf Inc., Hamburg, Germany

Eppendorf Inc., Hamburg, Germany

Thermo Fisher Scientific Inc., Waltham, USA

Eppendorf Inc., Hamburg, Germany

Perkin Elmer Inc., Waltham, USA

cDNA Resource Center, Bloomsberg, USA

Sigma-Aldrich Chemie GmbH, Taufkirchen, Germany

Electronics Workshop (University of Regensburg)

Mechanics Workshop (University of Regensburg)

BMG LABTECH GmbH, Ortenberg, Germany

Promega Corporation, Madison, USA

Linde AG, Dublin, Ireland

Conrad Electronic Regensburg GmbH & Co. KG, Regensburg, Germany

TPP Techno Plastic Products AG, Trasadingen, Switzerland

Sigma-Aldrich Chemie GmbH, Taufkirchen, Germany

New England Biolabs Inc., Ipswich, USA

Sigma-Aldrich Chemie GmbH, Taufkirchen, Germany

Greiner Bio-One GmbH, Frickenhausen, Germany

Sigma-Aldrich Chemie GmbH, Taufkirchen, Germany

Sigma-Aldrich Chemie GmbH, Taufkirchen, Germany

Carl Roth GmbH & Co. KG, Karlsruhe, Germany

Thermo Fisher Scientific Inc., Waltham, USA

Invitrogen, Waltham, USA

ECIS Software		Applied BioPhysics Inc., Troy, USA
ECIS Z, ECIS Z0		Applied BioPhysics Inc., Troy, USA
Ethidium Bromide		Fisher BioReagents, Thermo Fisher Scientific Inc., Waltham, USA
EtOH		Sigma-Aldrich Chemie GmbH, Taufkirchen, Germany
FBS		Sigma-Aldrich Chemie GmbH, Taufkirchen, Germany
FD Green Buffer		Thermo Fisher Scientific Inc., Waltham, USA
Female Plugs		Amazon.com Inc, Seattle/Arlington, USA
Flexstation 3		Invitrogen, Waltham, USA
Fluo-4 Assay Kit		Invitrogen, Waltham, USA
Forskolin		Sigma-Aldrich Chemie GmbH, Taufkirchen, Germany
Freezing Container Mr. Frosty™		Thermo Fisher Scientific Inc., Waltham, USA
FuGENE6		Roche Molecular Biochemicals, Mannheim, Germany
Furimazine		Promega Corporation, Madison, USA
Gas Cartridges		Cavagna Group UK, Derbyshire, UK
Gel Tank/Chamber		Bio-Rad Laboratories Inc., Hercules, USA
Gelatin from Bovine Skin		Sigma-Aldrich Chemie GmbH, Taufkirchen, Germany
GenElute™ Gel Extraction Kit		Sigma-Aldrich Chemie GmbH, Taufkirchen, Germany
GenElute™ PCR Clean-up Kit		Sigma-Aldrich Chemie GmbH, Taufkirchen, Germany
GenElute™ Plasmid Miniprep Kit		Sigma-Aldrich Chemie GmbH, Taufkirchen, Germany
Geneticin		Sigma-Aldrich Chemie GmbH, Taufkirchen, Germany
Glutardialdehyde		Sigma-Aldrich Chemie GmbH, Taufkirchen, Germany
Ham's F12		Sigma-Aldrich Chemie GmbH, Taufkirchen, Germany
Hank's Balanced Salt Solution		Sigma-Aldrich Chemie GmbH, Taufkirchen, Germany
Heat Block Dri-Block® DB-2D		Sigma-Aldrich Chemie GmbH, Taufkirchen, Germany
Hemocytometer		Marienfeld Superior, Lauda-Königshofen, Germany
HEPES		Sigma-Aldrich Chemie GmbH, Taufkirchen, Germany
HERAsafe Biological Safety Cabinet		Thermo Fisher Scientific Inc., Waltham, USA
Histamine		Carl Roth GmbH & Co. KG, Karlsruhe, Germany
hPP		Sigma-Aldrich Chemie GmbH, Taufkirchen, Germany
Humidity and Gas Control		ibidi GmbH, Gräfelfing, Germany
Hygromycin B		Sigma-Aldrich Chemie GmbH, Taufkirchen, Germany
Image Analysis Software <i>ImageJ</i>		InvivoGen Europe, Toulouse, France
Incubator Heraeus Function Line		Wayne Rasband, NIH
Iperoxo		Thermo Fisher Scientific Inc., Waltham, USA
Isoprenaline		Sigma-Aldrich Chemie GmbH, Taufkirchen, Germany
LabView-based Software		Tocris Bioscience, Bristol, UK
LB Broth		Kindly Provided by Prof. Dr. J. Wegener
LB Broth w/ agar (Lennox)		Sigma-Aldrich Chemie GmbH, Taufkirchen, Germany
LEDs		Sigma-Aldrich Chemie GmbH, Taufkirchen, Germany
Leibovitz' 15		Kindly Provided by Prof. Dr. B. König; Electronics Workshop (University of Regensburg)
L-Glutamine		Sigma-Aldrich Chemie GmbH, Taufkirchen, Germany
Ligation Buffer		Thermo Fisher Scientific Inc., Waltham, USA
Lipofectamine™ 3000		Sigma-Aldrich Chemie GmbH, Taufkirchen, Germany
Loading Dye		Thermo Fisher Scientific Inc., Waltham, USA
Multimeter Voltcraft VC220		Invitrogen, Waltham, USA
Multipipette		New England Biolabs Inc., Ipswich, USA
N <sub>2</sub> Tank		Conrad Electronic SE, Hirschau, Germany
NaHCO <sub>3</sub>		Eppendorf Inc., Hamburg, Germany
NanoBiT (LgBiT, SmBiT)		german-cryo GmbH, Jüchen, Germany
Nanodrop™ Spectrophotometer		Merck KGaA, Darmstadt, Germany
Nanoluciferase (NanoLuc®, NLuc)		Promega Corporation, Madison, USA
Opti-MEM		Promega Corporation, Madison, USA
OriginLab Software		Invitrogen, Waltham, USA
P-3000™		OriginLab Corporation, Northampton, USA
Pasteur Pipettes		Invitrogen, Waltham, USA
Penicillin and Streptomycin		VWR GmbH, Radnor, USA
Phase Contrast Microscope Nikon	Nikon	Sigma-Aldrich Chemie GmbH, Taufkirchen, Germany
Diaphot		Nikon Instruments Europe, Amsterdam, Netherlands
Phase Contrast Microscope Zeiss	Zeiss	Carl Zeiss AG, Oberkochen, Germany
Axiovert 25		
PHERAsar FS plate reader		BMG LABTECH GmbH, Ortenberg, Germany
Phosphate-Buffered Saline		Sigma-Aldrich Chemie GmbH, Taufkirchen, Germany
Photoswitchable ligand 1		Synthesized by Dr. Daniel Lachmann
Photoswitchable ligand 2		Synthesized by Dr. Ulrike Wirth

Pipetman	Brand GmbH Co Kg, Wertheim, Germany
Pipettes (Single or 8/12-Well) & Tips	Brand GmbH Co. KG, Wertheim, Germany
	Eppendorf Inc., Hamburg, Germany
	Sarstedt AG & Co. KG, Nümbrecht, Germany
Pirenzepine	Tocris Bioscience, Bristol, UK
pJET1.2/blunt vector	Thermo Fisher Scientific Inc., Waltham, USA
Plasma Cleaner PDC-002	Harrick Plasma, Ithaca, USA
Pluronic F-127	Sigma-Aldrich Chemie GmbH, Taufkirchen, Germany
Poly-D-Lysine	Greiner Bio-One GmbH, Frickenhausen, Germany
Polystyrene Flasks (25 cm <sup>2</sup> , 75 cm <sup>2</sup> )	Greiner Bio-One GmbH, Frickenhausen, Germany
Probenecid	Sarstedt AG & Co. KG, Nümbrecht, Germany
Puromycin	Sigma-Aldrich Chemie GmbH, Taufkirchen, Germany
Q5 High-Fidelity DNA Polymerase	New England Biolabs Inc., Ipswich, USA
Q5 Reaction Buffer	New England Biolabs Inc., Ipswich, USA
QIAfilter Plasmid Maxi Kit	Qiagen GmbH, Hilden, Germany
Quick-Load® Purple 1kb Ladder	New England Biolabs Inc., Ipswich, USA
Quinpirole	Sigma-Aldrich Chemie GmbH, Taufkirchen, Germany
Shrimp Alkaline Phosphatase	Thermo Fisher Scientific Inc., Waltham, USA
Silver Conductive Paint	Busch GmbH & Co. KG, Viernheim, Germany
SoftMax Pro 7.1 Software	Invitrogen, Waltham, USA
Solartron Si-1260	Schlumberger Instruments, Farnborough, UK
Soldering Iron	Chilitec GmbH, Essenrode, Germany
SpectraControl Software	Nanion Technologies GmbH, Munich, Germany
Stereomicroscope Nikon SMZ 1500	Nikon Instruments Europe, Amsterdam, Netherlands
Sterile Filters (Pore Size: 0.2 µm)	TPP Techno Plastic Products AG, Trasadingen, Switzerland
	Thermo Fisher Scientific Inc., Waltham, USA
T4 Ligase	Sigma-Aldrich Chemie GmbH, Taufkirchen, Germany
TBE Buffer	Sigma-Aldrich Chemie GmbH, Taufkirchen, Germany
TE Buffer	Tecan Group AG, Männedorf, Switzerland
Tecan Genios Plate Reader	Thermo Fisher Scientific Inc., Waltham, USA
Transparent 24-well	Corning Inc., Corning, USA
Transparent 6-well	Corning Inc., Corning, USA
Transparent 96-well, F-bottom	Greiner Bio-One GmbH, Frickenhausen, Germany
Transparent 96-well, U-bottom	Corning Inc., Corning, USA
TRIO-Thermoblock	Biometra GmbH, Göttingen, Germany
Trypan Blue	Sigma-Aldrich Chemie GmbH, Taufkirchen, Germany
Trypsin-EDTA	Sigma-Aldrich Chemie GmbH, Taufkirchen, Germany
UV Chamber	Syngene, Cambridge, UK
Vortexer	Heidolph Elektro GmbH & Co. KG, Kelheim, Germany
Water Bath TW12	Julabo GmbH, Seelbach, Germany
White 96-well	Brand GmbH Co Kg, Wertheim, Germany
White 96-well, transparent bottom	Greiner Bio-One GmbH, Frickenhausen, Germany
Xhol	Thermo Fisher Scientific Inc., Waltham, USA
zenCELL owl	InnoME GmbH, Espelkamp, Germany
Zeocin	InvivoGen Europe, Toulouse, France

# Curriculum Vitae

## Personal Information

Name

**Saphia Sarah Azzam**

Date of Birth

**23<sup>rd</sup> of June, 1996**

Place of Birth

**Munich, Germany**

## Career

May 2015 – August 2018

**Nursing Assistant** in a Retirement Home  
(BRK Seniorenheim Ergoldsbach)

April 2018 – September 2019

**Tutor and Laboratory Assistant** for  
Students of Chemistry and Human Medicine

Since December 2023

**Application Engineer** at MueTec GmbH

## Education

September 2006 – June 2014

**A Levels**

Grammar School Mallersdorf-Pfaffenberg,  
Germany

October 2014 – August 2017

**Bachelor of Science, Chemistry**

University of Regensburg, Germany

Thesis: *Impedimetrische in vitro Studien zur  
Bioaktivität von Bisphenol A*

Lab: Prof. Dr. J. Wegener

Institute of Analytical Chemistry, Chemo- and  
Biosensors

October 2017 – September 2019

**Master of Science, Chemistry**

University of Regensburg, Germany

Thesis: *Entwicklung und Anwendung eines  
photochemischen Wundheilungsassays*

Lab: Prof. Dr. J. Wegener

Institute of Analytical Chemistry, Chemo- and  
Biosensors

January 2020 – March 2023

**Doctor of Philosophy, Natural Sciences  
(Dr. rer. nat.)**

Member of the Research Training Group  
*GRK1910*

University of Regensburg, Germany

Thesis: *Dissecting the Wholistic Impedance  
Profile of GPCR Signaling by Combining  
Functional Assays*

Doctorate Supervisor: Prof. Dr. J. Wegener

Institute of Analytical Chemistry, Chemo- and  
Biosensors

## Further Education

March 2019	<b>Spring School Industrial Analytical Chemistry</b> GDCh, Krefeld, Germany
October 2019 – December 2019	<b>Internship Atomic Force Microscopy</b> Wacker, Burghausen, Germany
September 2020	<b>Certificate for Project Manager for Biological Safety</b> University of Regensburg, Germany
January 2022 – February 2022	<b>Business Administration for Engineers</b> Strategische Partnerschaft Sensorik, Regensburg, Germany
February 2022	<b>Imaging Basics</b> Optical Imaging Centre, Erlangen, Germany
December 2022 – January 2023	<b>Research Stay Abroad</b> Supervisors: Associate Professor Dr. N. Holliday, Dr. N. Dijon University of Nottingham, UK

## Skills

**Languages:** German (Native Speaker), English (Level C1)

**Computational Skills:** OriginLab, AutoCAD, ImageJ, Citavi, Microsoft Office

**Technical Skills:** Spin Coating, Photolithography, Wound Healing/Migration Assays, Molecular Biology, Impedance Spectroscopy, Atomic Force Microscopy, Stereomicroscopy, Cell-based Assays, Confocal Laser Scanning Microscopy, Fluorescence Microscopy, Phase Contrast Microscopy, Cell Culture Techniques, Radioligand Binding Assays, Calcium Assays, Transfections, Luminescence Assays

## Publications and Posters

- [1] Poster: Zinkl, M., Sauer/Pütz, L., Azzam, S., Wegener, J.: Monitoring the toxicity of bisphenol A using multiple impedance-based cellular assays **2018**.
- [2] Poster: Azzam, S., Wegener, J.: Dissecting the wholistic impedance profile of GPCR signaling: combining functional assays **2023**.
- [3] Wirth, U., Erl, J., Azzam, S., Höring, C., Skiba, M., Singh, R., Hochmuth, K., Keller, M., Wegener, J., Koenig, B.: Monitoring the Reversibility of GPCR Signaling by Combining Photochromic Ligands with Label-free Impedance Analysis. *Angew. Chem.* **2023**.
- [4] Azzam, S., Tomasova, L., Danner, C., Skiba, M., Klein, M., Guttenberg, Z., Michaelis, S., Wegener, J.: A High-Precision Wound Healing Assay Based on Photosensitized Culture Substrates. *Scientific Reports* **2024**.

## Eidesstattliche Erklärung

Ich erkläre hiermit an Eides statt, dass ich die vorliegende Arbeit ohne unzulässige Hilfe Dritter und ohne Benutzung anderer als der angegebenen Hilfsmittel angefertigt habe; die aus anderen Quellen direkt oder indirekt übernommenen Daten und Konzepte sind unter Angabe des Literaturzitats gekennzeichnet.

Weitere Personen waren an der inhaltlich-materiellen Herstellung der vorliegenden Arbeit nicht beteiligt. Insbesondere habe ich hierfür nicht die entgeltliche Hilfe eines Promotionsberaters oder anderer Personen in Anspruch genommen. Niemand hat von mir weder unmittelbar noch mittelbar geldwerte Leistungen für Arbeiten erhalten, die im Zusammenhang mit dem Inhalt der vorgelegten Dissertation stehen.

Die Arbeit wurde bisher weder im In- noch im Ausland in gleicher oder ähnlicher Form einer anderen Prüfungsbehörde vorgelegt.

---

Ort, Datum

---

Unterschrift